CRANFIELD UNIVERSITY

SCHOOL OF INDUSTRIAL AND MANUFACTURING SCIENCE

PhD THESIS

Academic year 2002-2005

S LANDI

Reactive ion etching techniques for uncooled pyroelectric detectors

Supervisors: P B Kirby and R W Whatmore

March 2005

This thesis is submitted in partial fulfilment of the requirements
for the degree of Doctorate of Philosophy

© Cranfield University 2005. All rights reserved. No part of this publication may be reproduced without the written permission of the copyright owner.

ProQuest Number: 10820941

All rights reserved

INFORMATION TO ALL USERS
The quality of this reproduction is dependent upon the quality of the copy submitted.

In the unlikely event that the author did not send a complete manuscript
and there are missing pages, these will be noted. Also, if material had to be removed,
a note will indicate the deletion.



ProQuest 10820941

Published by ProQuest LLC (2019). Copyright of the Dissertation is held by Cranfield University.

All rights reserved.
This work is protected against unauthorized copying under Title 17, United States Code
Microform Edition © ProQuest LLC.

ProQuest LLC.
789 East Eisenhower Parkway
P.O. Box 1346
Ann Arbor, MI 48106 – 1346

ABSTRACT

This research presents the design and microfabrication of a novel pyroelectric IR array detector. Micromachined concentrators are incorporated in the device to focus incoming radiation. Patterning of the sensing elements is introduced to reduce thermal losses. According to the physical theory of IR detection, these improvements can enhance the response of a pyroelectric detector.

The device is designed to be fabricated using state of the art micro systems technology. The design and fabrication route build partially on a previous primitive version of the device, which has been used as a case study.

An array of 3 – d structured non-imaging collectors is coupled to the sensing array. A survey of concentrators identified the most suitable contours, which were subsequently analysed. An original series of "suspended" collectors were especially developed for incorporation in this device. The calculations demonstrated that, generally, the Compound Parabolic Concentrator outperforms any other system. In all cases, truncated or suspended systems would show lower efficiency than the respective full systems.

The search for a viable microfabrication route focussed on methodologies based on Deep Reactive Ion Etching. Experimental trials, using both 3 – d sacrificial masks and conventional binary masks demonstrated a range of interesting structures, some of which had not been previously showed in literature. Long etching cycles in pure SF_6 could only approximate a tenth of the ideal contour and lacked flexibility, but demonstrated the lowest surface roughness (300 nm to 2 μm), highest reliability and are easy to implement and optimise. Being the processes of choice, these were analysed further and chosen as a quick route for producing working prototypes of the device. A chemical model of the process was built, based on mass balance considerations.

Calculations demonstrated that, by isolating each sensing element of the array on a spiral microbridge, the responsivity of the device could be increased up to 100 times. Conventional Reactive Ion Etching was used for patterning the entire active layer (pyroelectric material and electrodes). Suspended spiral elements were successfully incorporated in the final prototypes.

To produce the final device, two wafers (250 μm thick) were stacked to approximate a collector with 37 % truncation, leading to a maximum theoretical collection efficiency of 2.36. The electrical properties and response from the prototypes were measured and the results compared with the theoretical performance of the device, calculated using rough approximations in 2 – d. Using a home made testing rig, the best responses obtained were between 5 to 25 mV. Unfortunately, the model used is not sophisticated enough to allow straightforward comparison with the experimental results. Recently, better agreement has been demonstrated using a 3 – d model.

ACKNOWLEDGMENTS

I would like to thank all the people at the Nanotechnology Group at Cranfield University for their help. A particular thanks goes to my supervisors for their guidance throughout this research work.

TABLE OF CONTENTS

Chapter 1 INTRODUCTION p. 1

Chapter 2 UNCOOLED PYROELECTRIC DETECTORS: PHYSICS, DESIGN, CASE STUDIES AND STATE OF THE ART 5

2.1 The detection of IR radiation 5

2.2 The pyroelectric effect for uncooled thermal imaging 9

2.3 The physics of pyroelectric detectors 10

2.4 Figures of merit of pyroelectric materials 12

2.5 Choice and optimisation of the pyroelectric material 14

2.6 The technology of pyroelectric thermal imaging: case studies 17

2.7 State of the art in IR Detection: an integrated device with a concentrating collector for each individual array element 21

2.8 Conclusion 23

Chapter 3 LITERATURE SURVEY: THE SEARCH FOR A ROUTE TO DEVICE MICROFABRICATION 25

3.1 The theoretical background of non-imaging concentrators and the design of systems with high collection efficiency 26

3.2 The fabrication of micro-concentrators: a general overview 34

3.3 Deep Reactive Ion Etching Techniques based on Inductively Coupled Plasmas 39

3.4 3 - d structures obtained by using 3 - d masks 43

3.4.1 Deposition and patterning of 3 – d contoured photoresist masks on inorganic substrates 44

3.4.2 Transfer of 3 – d contoured photoresist masks into inorganic substrates by unidirectional dry etching 49

3.4.3 Process modelling and simulation of the 3 – d sculpting process 50

3.4.4 Road map for the experimental trials 56

3.5 3 - d cavities directly etched using binary masks 58

3.6 Design of microbridges for thermal isolation of the inner active areas of the elements of the focal plane array 63

3.7 The search for a microfabrication route to pattern the array of microbridges 67

3.7.1 Basic Concepts 67

3.7.2 RIE of conventional microelectronics materials 69

3.7.3 RIE of lead Zirconate Titanate based materials 70

3.8 Conclusion 71

Chapter 4 EXPERIMENTAL DETAILS p. 73
4.1 Microfabrication Of The IR Sensing Array Device 73
4.1.1 Details of the microfabrication process 73
4.1.2 Poling of the pyroelectric material 77
4.1.3 Methods for characterising the results and metrology techniques 78
4.2 Active Area Isolation 79
4.3 Microfabrication Of Concentrators 82
4.3.1 The DRIE-ICP machine 82
4.3.2 The grey-scale technique 82
4.3.3 The direct DRIE method with decreases anisotropy 86
4.3.4 Production of cavities to be used as concentrators 88
4.3.5 Characterisation of the results and metrology techniques 89
4.4 Conclusion 92

Chapter 5 DESIGN AND ANALYSIS OF NON-IMAGING COLLECTORS FOR INCORPORATION IN THE INFRARED SENSING DEVICE 93
5.1 The enlarged concentrator with a suspended inner active area 94
5.2 The effects of power distribution on power collection 95
5.3 Physics of concentrators and Ray Tracing technique application 99
5.4 Acceptance of direct rays 102
5.5 Acceptance and transmission of the 2 – d CPC-based design types 104
5.6 Acceptance and transmission of the "V" concentrator 108
5.7 Comparison of relative performance for different types of concentrator designs 111
5.8 Conclusion 113

Chapter 6 MICROFABRICATION OF CONCENTRATING NON-IMAGING COLLECTORS 115
6.1 3 – d Contoured Features obtained by Grey Scale Photolithography & Deep Reactive Ion Etching 117
6.1.1 Deposition and patterning of 3 – d contoured sacrificial masks made by photoresist 117
6.1.2 Sacrificial masks made of thermally grown silicon oxide 122
6.1.3 Transfer of 3 – d contoured masks into silicon by unidirectional dry etching 122
6.1.4 Post-etching treatments 127
6.1.5 Comment: suitability of the results for the microfabrication of collectors 133

Chapter 6 (continued)
6.2 Modified DRIE cycles with reduced anisotropy p. 134
6.2.1 *Assessment of the capabilities of the ICP-ASE multiplex ® equipment* 134
6.2.2 *Cavity profiles obtained by unbalancing the etch-passivation equilibrium* 136
6.2.3 *Isotropic etching in pure SF_6* 141
6.2.4 *Cavity profiles obtained by coupling long anisotropic and isotropic cycles* 143
6.2.5 *Other trials* 145
6.2.6 *Comparison of the methods attempted and choice of the most promising technique* 147
6.2.7 *Comparison between the results reported above and the results published in literature* 157
6.2.8 *Suitability of the techniques attempted for the microfabrication of concentrators* 159
6.3 Arrays of through-the-wafer cavities to be used as concentrators, produced by SF_6-based plasma etching in absence of passivation 160
6.3.1 *Shape of large cavities obtained by long isotropic etching cycles* 161
6.3.2 *Surface roughness of large cavities obtained by SF_6 etching* 163
6.3.3 *Variation of cavity dimensions across the area of the wafer* 169
6.3.4. *Approximation to the CPC contour* 171
6.3.5 *Evaluation of the performance of the two-stages collector* 174
6.4 **Conclusion** 177

Chapter 7 ISOLATION OF THE ACTIVE ELEMENTS OF THE ARRAY BY REACTIVE ION ETCHING 181
7.1 System design (spiral bridges) 181
7.2 Early stage trials: feasibility of PZT patterning by reactive ion etching 185
7.3 Patterning of Au/PZT/Pt/TiO_x/SiO_x membranes 189
7.4 Conclusion 192

Chapter 8 THE IR SENSOR PROTOTYPE DEVICE: MICROFABRICATION, SIMULATION AND TESTING 195
8.1 The microfabrication process for building the device 196
8.1.1 *The microfabrication process, up to the patterned array* 197
8.1.2 *The etching of the spiral bridges within the overall microfabrication process* 199
8.1.3 *Problems of dimension control in the microfabrication process* 200
8.1.4 *Full view of the final prototype* 206

Chapter 8 (continued)
8.2 Simulation of device response p. 209
8.2.1 Performance of 2 – d elliptical collectors 210
8.2.2 Simulation of single element performance: Responsivity and Detectivity 216
8.2.3 Theoretical analysis of the detection of IR collimated beams 223
8.3 Experimental testing of the prototype 226
8.3.1 Experimental result: general performance 227
8.3.2 Experimental results: use of collimated beams 229
8.4 Conclusion 230

Chapter 9
A DEEPER LOOK AT THE PROCESS OF SILICON ETCHING BY RADICAL FLUORINE IN INDUCTIVELY COUPLED PLASMA REACTORS 233
9.1 Etching of Si with fluorine-based plasma: additional experimental results 234
9.1.1 Shape of the cavities and the trends of vertical and lateral etch rates with time and aperture dimension 234
9.1.2. Direct evidence of etching related to the orientation of preferential crystalline planes (CODE) 238
9.1.3 Indirect evidence of etching related to the orientation of preferential crystalline planes I: analysis of surface roughness 239
9.1.4 Indirect evidence of etching related to the orientation of preferential crystalline planes II: evolution of the 3 – d shape of the cavities 241
9.2 Comparison between the results presented and the major findings and trends reported in literature 245
9.2.1 Shape of the cavities and the trends of vertical and lateral etch rates with time and aperture dimension 245
9.2.2. Direct evidence of etching related to the orientation of preferential crystalline planes (CODE) 246
9.2.3 Indirect evidence of etching related to the orientation of preferential crystalline planes I: analysis of surface roughness 248
9.2.4 Indirect evidence of etching related to the orientation of preferential crystalline planes II: evolution of the 3 – d shape of the cavities 249

Chapter 9 (continued) **9.3** **Analysis and model for the etching of silicon using fluorine radicals** p. 249
9.3.1 Kinetic balance, etch rates and the evolution of the etching front 250
9.3.2 Phenomena ascribed to CODE: a model that includes CODE? 259
9.3.3 Production of complex cavities obtained coupling long anisotropic and isotropic cycles 265
9.4 **Conclusion** 267

CONCLUSION 271

FUTURE WORK 275

REFERENCES 279

Appendix A 291
Appendix B 293
Appendix C 295
Appendix D 299
Appendix E 301
Appendix F 321
Appendix G 325
Appendix H 331
Appendix I 337

List Of Abbreviations

2 – d:	Two Dimensions
3 – d:	Three Dimensions
ARDE:	Aspect Ratio Dependent Etching
ASE:	Advanced Silicon Etching
CODE:	Crystalline Orientation Dependent Etching
CPC:	Compound Parabolic Concentrator
DRIE:	Deep Reactive Ion Etching
FET:	Field Effect Transistor
FBAR:	Ferroelectric Bulk Acoustic Resonator
IADF:	Ion Angular Distribution Function
IEDF:	Ion Energy Distribution Function
IR:	Infra Red (Radiation)
NEP:	Noise Equivalent Power
NETD:	Noise Equivalent Thermal Difference
PZT:	Lead Zirconate Titanate
RADF:	Radical Angular Distribution Function
RF:	Radio Frequency
RIE:	Reactive Ion Etching
ROIC:	Read Out Integrated Circuit
STS ltd:	Surface technology Systems limited

List of symbols used throughout the text:

α	loss due to adsorption
A	entry cross section of a radiation beam
A'	exit cross section of a radiation beam
A_c	cross sectional area of the radiation flux
A_e	exposure dependent adsorption term
$\mathcal{A}$	thermal admittance
a	half-width (or radius) of the entry of a radiation collector
a'	half-width (or radius) of the exit of a radiation collector
a^{T}	half-width (or radius) of the entry of a truncated radiation collector
AR	aspect ratio of a cavity
B	power flux crossing a given point x along the entry of a concentrator
B_e	exposure independent adsorption term
C	concentration ratio of a radiation beam
C_{A}	capacity of a transistor
C_{E}	capacity of the sensing element of an IR sensor
C_{I}	fractional decay rate of inhibitor per unit intensity
c	velocity of light in vacuum
c'	specific heat
δ	electric loss of a dielectric material
D	detectivity
D^*	standard detectivity
ε	dielectric constant
ε_0	dielectric constant of the vacuum
ED	etch depth of a cavity
EL	undercut or lateral etch of a cavity
$\Delta\phi$	frequency bandwidth
φ	incidence angle of a radiation beam
ϕ_R	local radical flux hitting on a surface
F_D	figure of merit of a pyroelectric material
γ	incidence angle between the surface and the incoming radiation
γ_{s}	radiation lost by scattering
G	thermal conductance
H	photoresist remaining thickness after development
H_I	root-mean-square of the fundamental component of the irradiance
H_m	thermal capacity of the element
h	Planck's constant
I_{lamp}	constant lamp intensity
i_p	current in a circuit

κ	thermal conductivity of the material
k	Boltzmann's constant
k_R	generic kinetic constant
λ	wavelength of the radiation
M	local concentration of inhibitor
P	amplitude of the incoming power flux
$\boldsymbol{P}_s$	polarisation
P_ω	radiant flux
$\boldsymbol{p}$	pyroelectric coefficient
q	power transferred to the element
ρ_A	increment of the spiral of Archimedes
ρ	material density
R	local etch rate
R_G	resistance at the gate of a transistor
R_I	etch rate related to the synergetic effect of the ions
R_R	etch rate related to the action of the primary radicals
R_{Riso}	etch rate related to the action of the secondary radicals
R_{rms}	means square roughness of a surface
$\mathcal{R}_i$	intensity responsivity
$\mathcal{R}_V$	voltage responsivity
σ_e	extinction coefficient
σ	Stefan's constant
S_R	sticking coefficient
s	extent to which a suspended collector has been extended
τ	spectral transmittance
τ_T	thermal time constant
τ_E	electrical time constant
Θ	differential temperature from the element to its surroundings
θ	acceptance angle of a concentrator
T	transmittance
V_n	root-mean-square of the noise voltage at the output of the detector
V_r	total volume of the cavity eroded by etching
V_s	root-mean-square of the fundamental component of signal voltage
χ_R	relative amount of surface sites occupied by fluorine atoms
ω	cut-off angle of a power distribution
W_λ	spectral emittance.

NOTE: The above list does not include the most common symbols, which have been used to denote the generic time, length, radius, area, volume, temperature, voltage etc. throughout the text.

Chapter 1: INTRODUCTION

This project researched a new concept in Infra-Red radiation collection. The novelty of the IR sensing device produced during this PhD work involved the use of micromachined concentrators to collect incoming radiation to active sensing elements and thermal isolation of these elements by using a spiral bridge.

Pyroelectric infra-red detectors have been of interest for many years because of the wide wavelength response, good sensitivity and lack of need for cooling. Historically limited to the defence sector, they have achieved a wide market acceptance in the 1990s. Uncooled thermal imaging arrays have a range of civil applications, which include people, flame and fire sensing, environmental monitors, spectrometry and energy management.

The application to infrared systems of technologies and concepts derived from microelectronics was instrumental to the growth of this sector. Although the boom in microelectronics technology started in the 1970s, IR detectors caught up only a decade later. This technology transfer was beneficial in many ways: IR detectors could now be produced in batch and integrated within the circuitry of the system. Broadly speaking, this led to a large increase in the dimensions of the arrays (i.e. scale integration), an improvement in the design and a general reduction of the production cost. This revolution hit photon detectors first, but spread to thermal detectors after a few years: it was instrumental in shifting the ambit of IR detectors from purely military applications to the wider commercial use.

A new technology is available today: Micro-Systems Technology. This PhD research was aimed to present an example on how MST might lead, if applied to IR sensors, to further improvement in sensitivity and reduction in cost. MST started in the 1980s as a visionary science, aimed at extending microelectronics techniques in order to produce mechanical and physical devices of micrometric scale. Of interest to this research, there is the capability of producing three-dimensional structures, whereas conventional microelectronics technologies are mainly pattern-based. Initially a secondary product of microelectronics, the large success of MST justified the growth of a backing industry so that nowadays a range of new microfabrication techniques is specifically produced and designed for the MST engineer. For example, twenty years ago wet etching was the only technique available to obtain through-the-wafer cavities. Nowadays, Deep Reactive Ion Etching of silicon is just one of a range of techniques available that allow micromachining of high aspect ratio features with nanometre precision. A list would include micro-injection moulding, mechanical micromachining and others. The pyroelectric device object of this research was conceived to be fabricated using MST. Microfabrication routes typical of MST allowed the introduction of two major improvements in the design of the classical hybrid IR detector array.

The device was conceived for being incorporated in the series of hand held universal thermal imagers produced by the company Irisys, UK. The device contains an array of 16 by 16 elements and represents the core of such IR cameras. The image is created by sensing local differences in temperature across the active elements of the array. The small scale integration (16 by 16) would lead to a pretty rough image, as showed in the

left photograph of figure 1.1. After graphic software interpolation, the resolution is increased as showed in the right picture of the same figure.

A sensing element of the pyroelectric device object of this PhD research is showed in figure 1.2. The two innovations can be clearly observed in this sketch. First, an array of concentrators collects the incoming IR radiation incident on the detector front side, with absorption taking place in the element on the other surface of the wafer. The design of the collectors is based on the Compound Parabolic Concentrator (CPC) profile. CPCs are non-imaging collectors that yield a concentration ratio near to the thermodynamic maximum. The background theory of Infra Red radiation detection demonstrates that an increase in the density of the power collected onto the elements can enhance the response of a pyroelectric detector.

In order to machine arrays of collectors in silicon, the range of 3 – d structures that can be produced by bulk micromachining of silicon have been mapped out. The research has entailed a broad review of microfabrication techniques for micromachining of cavities with complex contours in silicon, including grey scale photolithography and deep pattern transfer using Deep Reactive Ion Etching (DRIE).

The other innovation concerns the patterning of the individual elements. Spiral bridges isolate the active elements from the thermal sink maximizing the length of the heat transfer path. This is expected to decrease the thermal losses through the array and enhance the sensitivity of the detector. Detector performance is modelled for different types of bridges and concentrators design.

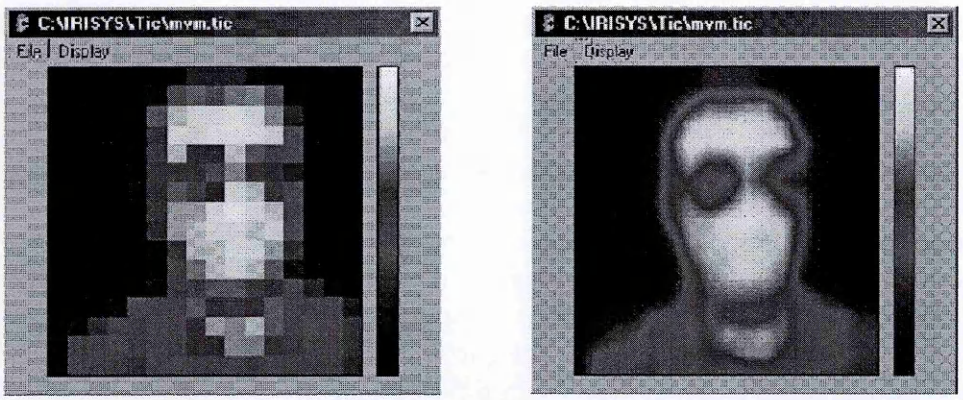


Figure 1.1 **Image from an IR detecting camera of the series produced by Irisys, UK. *Left*: crude image obtained from the array, *Right*: after digital graphic interpolation**

This thesis is organised in the following way. The first part (chapters 2 and 3) reports the general survey of the pertinent literature. Chapter 2 introduces the background of IR systems and the main concepts of the physical theory of IR sensing: the pyroelectric effect, the definitions of responsivity and detectivity and the figures of merit of pyroelectric materials. The chapter offers an historical survey of case studies in IR detecting technology. The survey concludes with the presentation of an early, primitive version of the device object of this research. That primitive design was accomplished before this research started and it is described in order to present the state of the art

upon which the new device is built. Chapter 3 is a structured presentation of the body of literature reviewed in order to find promising routes to set up the microfabrication process. The chapter introduces the theory of non-imaging concentrators and presents a series of effective collector profiles widely used in large optical systems. It then discusses the constraints the design will put on the microfabrication route. Many routes are discarded after being surveyed. Two routes, based on Deep Reactive Ion Etching looked promising at this preliminary level and a more detailed survey follows. The chapter concludes presenting a series of case studies in thermal isolation of the elements in IR devices and a study on the patterning of the active layer and electrodes.

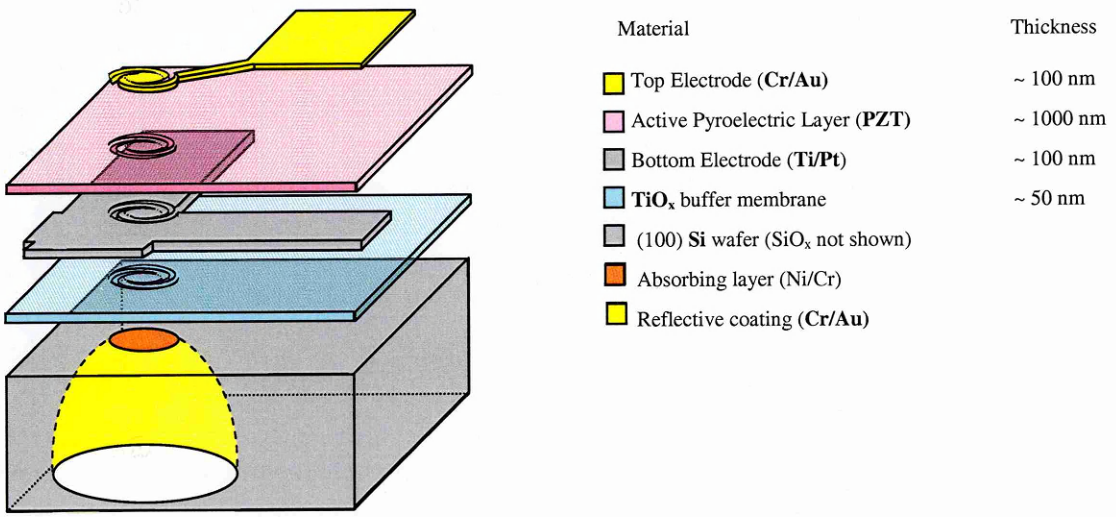


Figure 1.2 Exploded schematic of a sensing element of the pyroelectric device object of this PhD research

The experimental details of the research are reported (without discussion or comment) in chapter 4, which is a bare description of the methods and techniques used. The microfabrication process for building the sensing array is briefly reported, followed by a discussion on the methodologies used for characterising the device. Subsequently, the processing conditions are reported for the main trials conducted during this research.

A certain amount of time was devoted to analyse and clarify the physics of non-imaging collectors. An original series of collectors was conceived and ways of assessing the performance expected from a given profile were developed. These computations are described in chapter 5. The chapter, however, reports mainly the general topics and results whereas the detailed calculations are removed in a specific appendix.

Chapters 6 and 7 describe the empirical results obtained. Chapter 6 discusses the route for producing contoured structures in silicon wafers. The results of chapter 6 are particularly detailed because most techniques attempted were completely new. A large range of structures was produced, some of which, albeit not useful to be used as concentrating collectors, were nevertheless interesting. In fact, the development of a reliable technique for 3 – d micromachining would be beneficial to many MEMS

applications. It is the author's opinion that the novelty of most processes and structures described in chapter 6 would be enough to justify this research. One process in particular was chosen for further investigation. This set of more advanced trials is subsequently reported. The chapter concludes with the presentation of a viable route to produce arrays of contoured cavities in silicon that can be integrated into the IR device as micromachined collectors. Chapter 7 deals with the thermal isolation of the individual elements of the array, obtained by patterning the membranes (where the elements lay after DRIE). After a brief section that describes the design of the microbridge pattern, the rest of the chapter is devoted to the presentation of the empirical results of reactive ion etching of the active layer and electrodes and to the optimisation of the etching recipes.

Chapter 8 describes the last stage of the research, i.e. the production and testing of the full working device. The chapter start by describing the main microfabrication issues. The typical structures obtained are measured and a rough simulation is used to calculate the expected performance of the prototype. Subsequently, the performance is measured experimentally and compared to the calculated one. Due to the primitiveness of the model, the comparison is not straightforward and a measurement expedient (i.e. the use of microcollimators) has to be introduced.

The thesis concludes with the modelling of the dry micromachining of silicon by using fluorine inductively coupled plasmas. The model is based on the balance between mass flow and surface kinetics. A relevant part of the results and trends were interpreted on the basis of this model, which justified also some of the operative choices. Chapter 9 can be considered as an overall discussion on the physics involved in the etching of the collectors. The chapter opens with the presentation of additional results that are needed to corroborate the model. It then compares these results (and the results previously presented in chapter 6) with the major findings and trends reported in literature for similar processes. Finally, a model is presented and the results interpreted.

To summarise, after the literature survey and the presentation of the experimental details, the results presentation consists of three main parts. The microfabrication routes are presented in chapters 6 and 7. Chapter 8 presents the core of the research and the wrapping up, in terms of prototype fabrication and testing. Chapter 9 presents the scientific interpretation of the results obtained in chapter 6. In a way, chapters 6 and 9 could have been presented as a single, very long chapter but the author was convinced that it would be clearer for the reader to follow a rational path to the fabrication of the device and postpone the scientific discussion on the chemistry of the process at the end of the thesis.

CHAPTER 2 UNCOOLED PYROELECTRIC DETECTORS: PHYSICS, DESIGN, CASE STUDIES AND STATE OF THE ART

This section presents a survey of the principles, theory and technology of the thermal detection of Infra Red (IR) radiation. The presentation is limited to the information required to understand and discuss the major issues of this research work. Thermal imaging systems are complex devices made of different parts. The fundamental elements of thermal imaging systems will be examined briefly in section 2.1. Among the different elements, the pyroelectric sensing array represents the core of the thermal imaging camera: section 2.2 will provide a definition of the pyroelectric effect, upon which the sensing action of the detector is based. The basic physics of the system is treated in section 2.3 in order to predict the performance of the system as a function of the design parameters and the materials used. The theory presented in section 2.3 leads to the calculation of figures-of-merit for the pyroelectric materials, which are briefly introduced in section 2.4. The material issues will be discussed in section 2.5. The section will first present a comparison of the performance of various pyroelectric materials and subsequently address the problems of material integration in the device. The objective of section 2.6 is to demonstrate the role of factors such as the densification of incoming radiation and the thermal isolation in the design of IR sensing systems. To this end, an overview of thermal imaging systems technology is presented with selected case studies. A case study of particular relevance is represented by the IR sensing device that had already been designed and partially produced at Cranfield before this research started. The device included individual pyramidal concentrators coupled to each element of the array and the design did not allow reticulation of the elements. In the results part, it will become clear how the device object of this research was built largely on the knowledge and processing already developed for the previous prototype. (This is the reason why it is presented here in the background part.) The case study relative to the primitive version of the device is presented in section 2.7.

2.1 The detection of IR radiation

A schematic of the main elements that can be identified in a thermal imaging system is reported in figure 2.1.

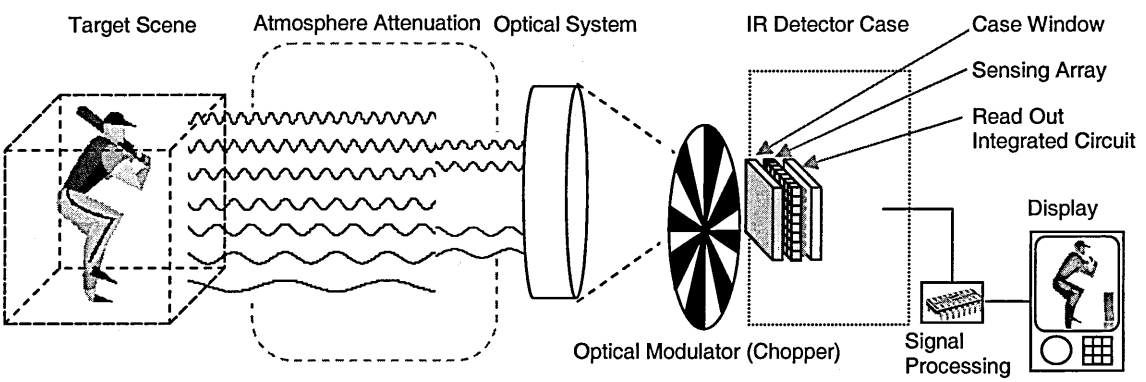


Figure 2.1 Schematic of the elements of the IR thermal imaging system

Infrared electromagnetic radiation is emitted from all bodies as a consequence of the second principle of thermodynamics. When the temperature of a body is above the thermal equilibrium (i.e. the temperature of the background), the additional emission of radiation from it can be collected and detected. The radial emittance, W (flux of energy emitted per unit area of emitter surface) depends generally on the wavelength of the emitted radiation. The black body is an ideal body that absorbs all the incident radiant energy. Consequently, it radiates the maximum emission at all wavelengths. Planck's law describes the behaviour of a black body, introducing the quantisation of the energy of the atomic harmonic oscillators [*Hudson, 1969, Chapter 1*]:

$$W_\lambda = \frac{2\pi hc^2}{\lambda^5\left(e^{\frac{ch}{\lambda kT}} - 1\right)} \qquad [\mathrm{Wcm^{-2}\mu m^{-1}}] \quad (2.1),$$

where W_λ is the spectral emittance. λ is the wavelength of the radiation emitted, h is Planck's constant, c is the velocity of light in vacuum and k is Boltzmann's constant. T represents the absolute temperature of the radiator. Emission curves, obtained from equation 2.1 are reported in figure 2.2. The spectrum of emission from a conventional body contains generally only a few bandwidths (e.g. grey curve of figure 2.2), but the trend remains similar.

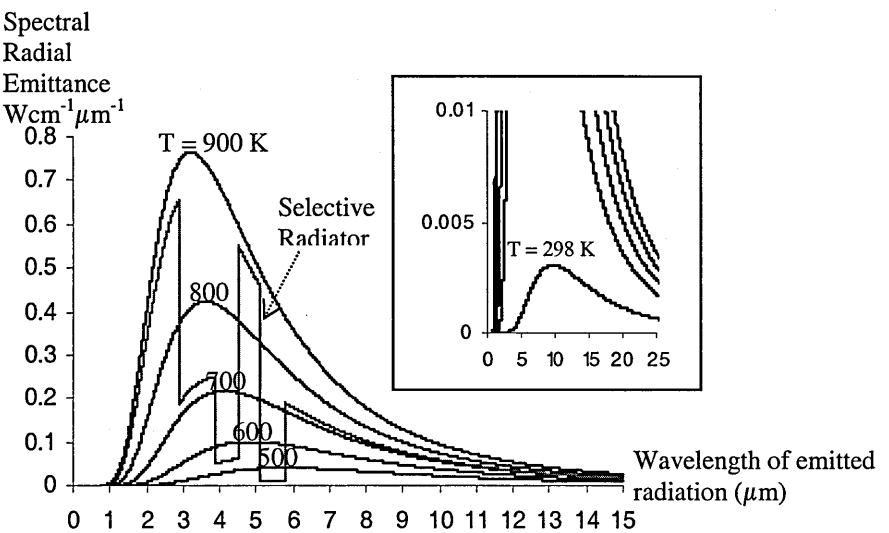


Figure 2.2 Emission from a blackbody at different temperatures according to equation 2.1 and example of emission from a selective radiator (grey curve). Inset: particular of the emission curve at 298 K (same units as for the larger diagram)

The radiation energy is attenuated before reaching the detector because of scattering and absorption by the atmosphere. The attenuation can be described by the equation

$$\tau = e^{-\sigma_e x} \qquad (2.2),$$

where τ is the spectral transmittance and x represents the length of the radiation path. σ_e is the extinction coefficient. σ_e is equal to $(\alpha + \gamma_s)$, where α represents the loss due to adsorption and γ_s is the radiation lost by scattering. If the particles suspended in atmosphere are reasonably smaller than the wavelength of the radiation, the scattering coefficient (γ_s) increases with the reciprocal of the fourth exponent of the wavelength

(Rayleigh scattering). Under these circumstances, IR radiation penetrates farther than light and scattering can be generally disregarded in comparison with absorption.

Absorption by CO_2 and H_2O gases in air occurs across a large band: a typical IR transmittance spectrum is reported in figure 2.3 [*Hudson, 1969, Chapter 4*]. The two wavelength intervals of maximum transmission (atmospheric windows) are in the ranges 3 – 5 and 8 – 14 μm. Generally, since the black-body emission spectrum at 298 K has a maximum at about 9 μm (see inset of figure 2.2), thermal imaging will be targeted to the 8 – 14 μm wavelength atmospheric window [*Whatmore and Watton, 2001*]. On the contrary, high temperature applications (e.g. military target recognition) may exploit windows of shorter wavelengths.

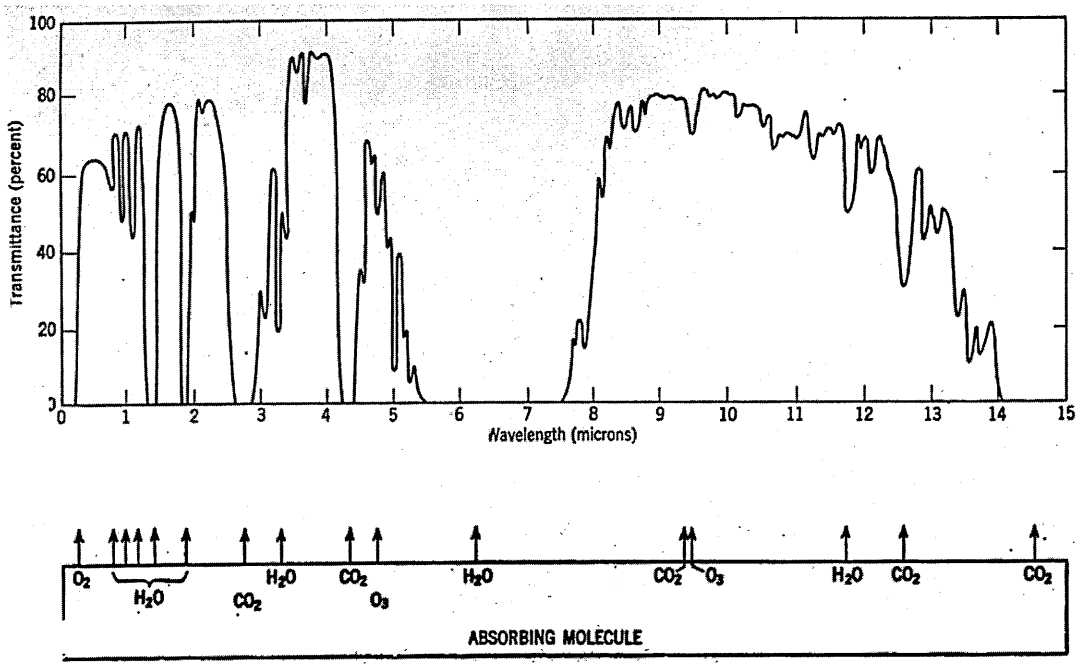


Figure 2.3 **Transmittance spectrum of the atmosphere at 6000 ft above sea level containing 17 millimetres of precipitable water** (reproduced from [*Hudson, 1969*])

The radiation is generally focussed onto the detector focal plane by means of a large scale optical system. In the most basic case the optics consist of a single lens [*Whatmore and Watton, 2001; Goss, 1987*]. A large, macroscopic non-imaging concentrator has been applied in one instance [*Ning, 1991*]. The optical materials must show satisfactory transmittance to IR radiation at the wavelengths of interest. In addition, they must meet the requirements of system manufacturing and use. Reduced variation of refraction index with temperature, hardness, thermal and chemical resistance, and low thermal expansion coefficient are among the main requirements. Germanium lenses demonstrate total transmittance up to ~ 45 % for wavelengths between 2 and 15 μm. This value can rise up to more than 90 % when antireflection coatings are applied [*Hudson, 1969, Chapter 5*].

Optical modulation systems (also called reticules or choppers) have been used since the Second World War to resolve the signal of a moving target from larger objects or

background radiation [*Hudson, 1969, Chapter 6*]. In the case of thermal pyroelectric detectors, which respond to a difference of temperature, a chopper has the function of modulating the signal in order to prevent the elements of the detector from reaching a thermal steady state, beyond which no signal would be produced. Thermal imaging of a static scene requires radiation chopping [*Whatmore, 2001*]. Without chopping, only warm moving objects can be detected.

The detector is the core of the system. Basically, it is a transducer that absorbs the incoming IR radiation to yield an electrical signal. This secondary signal can be directly processed and displayed in some way that can be appreciated by human senses. Detectors can be broadly classified into two types according to the way in which the IR radiation induces the production of a signal: thermal detectors respond to an increase in temperature of the elements whereas in quantum (or photon) detectors the IR photons interact directly with the electrons of the atoms of the active material. The response of thermal detectors increases with the amount of energy absorbed whereas that of photon detectors is proportional to the number of photons absorbed. The pyroelectric effect is a well known thermal phenomenon, exploited for the device developed by this project. (It will be analysed in detail in section 2.2.) However, to build thermal detectors other transduction effects had been exploited far before the pyroelectric effect. Among them are the thermoelectric effect (thermopile) and the variation of electrical conductivity with temperature (bolometer). It is clear that thermal detectors have a slower time of response in comparison with photon detectors, due to the inherent thermal loading. Conversely, their performance is expected to be practically independent of the wavelength of radiation absorbed.

Depending upon the principle of image formation, the detectors can be classified as point detectors and imaging detectors. A point detector contains a single element (or pixel). Dynamic scanning is required to form an image. On the contrary, imaging (or staring) collectors contain an array of elements, each corresponding to a pixel of the final image displayed.

Since the performance of thermal detectors is generally lower, photon detectors have always represented the choice for thermal imaging applications. However, they need to be cooled to very low temperatures (and cooling technology raises enormously the cost). Up to the late 1980s, due also to the general secrecy surrounding IR research (funded by defence in the greater part and classified in the United States until 1992 [*Kruse, 2001*]), thermal detectors were solely employed for robust, low cost applications for single point detection [*Rogalski, 2003; Muralt, 2001*]. A major exception was represented by the pyroelectric vidicon [*Goss, 1987*], a classic thermal imaging system that will be described in section 2.6. Although single point thermal detectors perform necessarily worse than photon detectors, this difference is less important for a focal plane array. Staring arrays can be more easily manufactured for thermal detectors and this gave thermal detectors a point of advantage [*Kruse, 2001*]. In particular, pyroelectric detectors benefited from the early development of processes for integrating the active materials onto the silicon-based micro-circuitry. (The attempts were mostly aimed to the production of ferroelectric non-volatile random access memories [*Muralt, 2001*].) Attempts to produce IR sensor arrays using thermal sensing materials became more widespread in the 1990s. More recently, good results were demonstrated for

thermal imaging in a large range of wavelengths using large arrays of pyroelectric elements [*Rogalski, 2003*].

Staring (focal plane) arrays are generally employed in current IR cameras. The elements are electronically scanned by a Read Out Integrated Circuit (ROIC). For example, in the traditional architecture each individual sensing element is connected to its relative Field Effect Transistor, which amplifies and transmits the signal. Techniques for connecting the ROIC to the sensing array were established two decades ago for photon detectors containing matrices up to 10^6 pixels [*Rogalski, 2003*]. In hybrid technology the ROIC and detector array are built onto different substrates and joined later. Monolithic devices, on the contrary, contain both sensing layer and circuitry on the same chip. Both routes have been exploited for thermal detectors and examples will be reported in section 2.6. The choice of fabrication routes depends on many factors. If the active layer is obtained from a bulk ceramic, then it has to be incorporated in the system using hybrid technology. Conversely, the monolithic route is suitable for fully micromachined IR sensors. The ROIC is generally specific to the final application and may incorporate, besides pixel addressing, the initial step of signal processing (amplification, signal integration or multiplexing) and conversion of the signal from analog to digital [*Kruse, 2001*].

2.2 The pyroelectric effect for uncooled thermal imaging

The pyroelectric effect is normally observed in polar dielectric materials, i.e. materials that have a net electric dipole different from zero. In a polar dielectric element, charges appear at the surfaces. These charges are neutralised by stray charges so that the element maintains its external electroneutrality and it is not possible to measure the dipole directly [*Putley,* 1970]. However, if the dipole $\boldsymbol{P}_s$ is subjected to a change, e.g. due to a variation in temperature ΔT,

$$\Delta \boldsymbol{P}_s = \boldsymbol{p}\,\Delta T \qquad (2.3)$$

(where $\boldsymbol{p}$ [C cm^{-2} K^{-1}] is the pyroelectric coefficient), then the stray charges at the surfaces are slower to react to this change and a partial imbalance is induced. If the element is connected to an external circuit, a current (i_p) can be detected until the equilibrium is reached again (and the current is extinguished). If the direction of $\boldsymbol{p}$ is normal to the focal plane of the element (or array), the vector notation can be omitted [*Whatmore and Watton, 2001*]:

$$i_p = Ap\frac{dT}{dt} \qquad (2.4),$$

where A is the area of the element cross section perpendicular to the direction of $\boldsymbol{p}$.

Since all polar dielectrics may exhibit pyroelectric effect, there is a vast range of materials available under different forms [*Whatmore and Watton, 2001*]. Both inorganic and organic materials have been used. Single crystal organic materials have been widely used in the past, but they are not robust for many applications. Ferroelectric polymers are also exploited. Ceramics (bulk and thin films) are in common use today. The novel pyroelectric device described here employs a thin film ceramic material based on the Lead Zirconate – Lead Titanate solid solution (PZT) [*Whatmore and Watton, 2001*]. More information about these materials and their properties will be given in section 2.4.

2.3 The physics of pyroelectric detectors

This section presents a brief introduction to the physics of pyroelectric detectors in order to build the theoretical basis upon which system architecture is designed and detector performance modelled. The final target of this research is to produce a detector with enhanced characteristics. The ways to improve the performance were briefly presented in the introduction (Chapter 1). These design improvements will become clear throughout this section. In particular, the theory will demonstrate how higher signals are achieved by increasing the power collected and thermally isolating the active elements.

The performance of IR detectors is generally described by the following terms [*Hudson, 1969, Chapter 7*].

- The (Voltage) Responsivity is defined as the output signal produced relative to the incoming power flux per unit of detector surface:
  $\mathcal{R}_V = V_s / H_I A_d = V_s / P$ [VW^{-1}] (2.5).
  Where: V_s is equal to the Root-Mean-Square of the fundamental component of signal voltage [V]. H_I represents the root-mean-square of the fundamental component of the irradiance on the detector from the scene [Wcm^{-2}] and A is the sensitive area of the detector [cm^2].
- The noise equivalent power (NEP) indicates the minimum detectable signal from a detector. The NEP is introduced as
  $NEP = [\, H_I A_d / (V_s / V_n) \,] = V_n / \mathcal{R}_V$ [W] (2.6).
  In other words, the NEP represents the radiant flux necessary to produce an output signal equal to the detector noise. V_n is the RMS value of the noise voltage at the output of the detector.
- The detectivity is a figure of merit, defined as the reciprocal of the NEP. Since the detectivity is a function of the sensing material used, the detector architecture and the conditions of measurement, it is customary to define a standard detectivity (D^*) for a detector area of 1 cm^2 and a bandwidth (Δf) equal to 1 Hz:
  $$D^* = \frac{A^{1/2} \Delta f^{1/2}}{NEP}$$ [W^{-1} cm $Hz^{1/2}$] (2.7),

These terms are applicable to all types of IR detectors, independently on the sensing principle. However the expressions of $\mathcal{R}_V$, *NEP* and *D* depend on detector type and system architecture. The analysis of a full system is beyond the scope of this thesis, which is concerned with the design and fabrication of the sole sensing array. For this reason, no analysis of the *NEP* (equation 2.6) will be attempted. Equation 2.7 will be used to compare the performance of detectors of different design, after assuming the constancy of *NEP*. (The theoretical analysis of device performance will be carried out in section 8.2.2.)

It is easier to demonstrate the enhancement in detector performance due to thermal isolation of the sensing elements using the expression of the responsivity. For this reason, the expression for the responsivity of a pyroelectric detector will be hereby introduced.

The theory of the pyroelectric detector was elaborated from the theory of bolometer-based IR detectors [*Smith et al., 1968, Chapter II*]. The principles of functioning for a single element are illustrated in figure 2.4 [*Whatmore and Watton, 2001*]. A thin slice (or a film) of pyroelectric material is sandwiched between two conductive electrodes. One side of this structure receives the oncoming radiation. The radiation is directly absorbed by the element liberating an energy equal to ηP (where P is the power flux in watts and η is the emissivity of detector surface). The element is thin and small so that it can be considered to reach instantly the inner thermal equilibrium [*Putley, 1970*], whereas it is not in equilibrium with the surroundings (thermal sink at temperature T), which support the element by means of bridges (or similar structure). Radiance and conductance to the thermal sink tend to lower the temperature of the element. (The nature of thermal losses will be further discussed in sections 3.6 and 7.1.) The overall term can be here indicated with G [WK^{-1}] and the energy transferred is equal to $G\Theta$ (Θ represents the differential temperature from the element to its surroundings, i.e. ΔT). Imposing the energy balance between the radiation absorbed, the heat transferred and the increase in temperature one obtains:

$$\eta P = H_m \frac{d\Theta}{dt} + G\Theta \tag{2.8}$$

where H_m is the thermal capacity of the element. It is assumed that the incoming energy flux is modulated with frequency ω, and power $P = P_0 e^{-j\omega t}$. A solution of equation 2.8 is given by [*Whatmore and Watton, 2001*]:

$$\Theta = \frac{\eta P_0}{G\left(1+\tau_T^2\omega^2\right)^{1/2}} e^{j\omega t} \tag{2.9},$$

where $\tau_T = H_m / G$ is called thermal time constant [s]. The analysis of thermal circuits up to equation 2.9 is satisfactory enough for the scope of this discussion. Introducing 2.9 in equation 2.4, one obtains the expression for the current induced by the change in polarisation:

$$i_p = \frac{\eta p A \omega P_0}{G\left(1+\tau_T^2\omega^2\right)^{1/2}} e^{j\omega t} \tag{2.10}.$$

The element, therefore, is equivalent to a generator (figure 2.4) with a difference of phase with respect to the modulation of incoming power equal to atan ($\omega H_m / G$). From equation 2.9 it is immediately apparent how the increase in temperature (Θ) induced by a modulated incoming radiation is directly proportional to the amplitude of incoming power flux (P) and inversely proportional to the thermal conductivity. The current responsivity of the detector can be introduced as:

$$\mathcal{R}_i = \frac{i_p}{P_0} = \frac{\eta p A \omega}{G\left(1+\tau_T^2\omega^2\right)^{1/2}} \tag{2.11}.$$

It is clear from equation 2.11 that $\mathcal{R}_i$ increases with ω at low frequency while, at high frequencies it reduces to $\eta p A / H_m$ (constant).

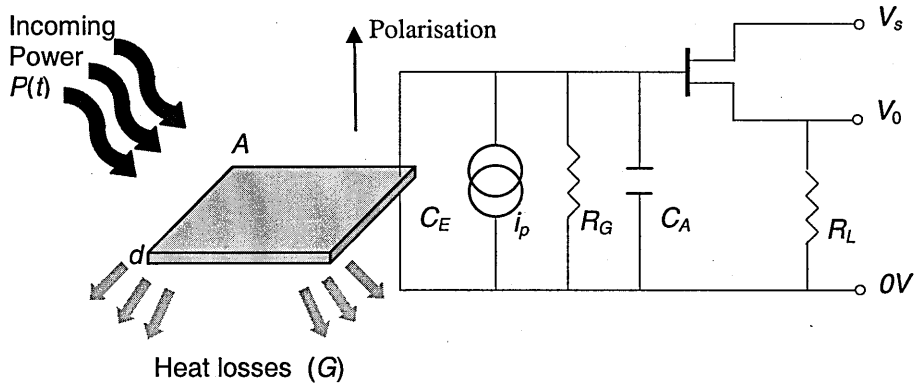


Figure 2.4 Schematic of a pyroelectric detector element at a temperature *T* above its surroundings. Redrawn from [*Whatmore and Watton, 2001*].

To evaluate the figures-of-merit of a detector one needs to introduce the properties of the electronic circuitry. Generally, the signal i_p is amplified by an electronic amplifier. For thermal imaging purposes (where a large 2 – d array of sensing elements is used) each element is connected to its Field Effect Transistor, which amplifies the signal. The combined equivalent circuit can be represented with the capacities of the element (C_E) and of the transistor (C_A) in parallel with a resistance (R_G), which is the gate resistor. The electrical time constant (τ_E) is given by $\tau_E = R_G\,(C_E + C_A)$, [s]. The voltage across R_G is given by:

$$V = i_p\,|Z| = i_p\,R_G\,(1 + \omega^2\tau_E^2)^{-1/2} \qquad (2.12).$$

Introducing relation 2.12 in the definition of responsivity (equation 2.5) one obtains:

$$\mathcal{R}_V = \frac{\eta p A \omega R_G}{G\left(1+\tau_T^2\omega^2\right)^{1/2}\left(1+\tau_E^2\omega^2\right)^{1/2}} \qquad (2.13).$$

The voltage responsivity appears to be proportional to the reciprocal of the thermal conductance. Once again it is demonstrated how a decrease in thermal diffusion from the element to the surroundings (i.e. a decrease in *G*) induces an increase in the detector's performance.

2.4 Figures of merit of pyroelectric materials

Different figures of merit emerge from the above treatment, according to design and the requirements of the final application [*Whatmore and Watton, 2001*]. For example, at high frequency ($\omega >> 1 / \tau_T$ and $\omega >> 1 / \tau_E$) equation 2.13 reduces to:

$$\mathcal{R}_V = \frac{\eta p}{c' d\left(C_E + C_A\right)\omega} \qquad (2.14),$$

where *c'* is the volume specific heat [J K^{-1} cm^{-1}]. For $C_E >> C_A$ it is:

$$\mathcal{R}_V = \frac{\eta}{A\omega}\frac{p}{c'\varepsilon\varepsilon_0} \qquad (2.15).$$

With ε relative dielectric constant of the material and ε_0 permittivity of the vacuum. F_V is a material figure of merit equal to ($p / c'\ \varepsilon\,\varepsilon_0$) [$m^2$ C^{-1}] usually employed for comparing different pyroelectric materials.

The detectivity is inversely proportional to the minimum power that can be sensed. The theoretical limit to the detectivity is given by the overall noise of the instrument. The overall noise voltage (V_n) has a composite spectrum. V_n is a combination of the main internal noise sources affecting a detector such as statistical fluctuations in thermal conductance, Johnson noise, amplifier current noise and amplifier voltage noise. A detailed discussion on intrinsic noise sources is not inherent to the topics of this research: expressions for computing the noise components are reported in [*Whatmore and Watton, 2001; Putley, 1970*]. A figure of merit specific of the dominant noise has to be used since different components are dominant depending on the materials used, the design of the system and the frequency of operation. For example, for high frequency operations (i.e. $\mathcal{R}_V$ expressed by equation 2.14) and in the case that Johnson noise is dominant, the detectivity is given by [*Whatmore and Watton, 2001*]:

$$D^* = \frac{\eta d}{(4kT)^{1/2}} \frac{p}{c'(\varepsilon\varepsilon_0 \tan\delta)} \frac{1}{\omega^{1/2}} \tag{2.16}$$

The figure-of-merit F_D defined as p / [c' ($\varepsilon\,\varepsilon_0$ tan δ)$^{1/2}$] in [Pa$^{-1/2}$], which contains the dielectric loss of the element (tan δ) can be used for comparing different materials.

If the element of figure 2.4 is part of a large array for thermal imaging, thermal conductance will tend to spread the heat across the plate uniformly and the differences in temperature among pixels will tend to disappear. To include the heat diffusion phenomena, the figures of merit must be divided by the thermal conductivity of the material (κ). But if a form of thermal isolation among the elements is provided, there is no need to divide by κ, hence the introduction of element separation techniques (such as reticulation), which will be treated in section 2.6.

In conclusion, it is not possible to give a general figure of merit to assess the performance of any pyroelectric detector or material because the expression depends on the set up of the entire device (including the electronics of the ROIC) and the operating frequency (i.e. the angular frequency of the chopper). In other words, while equations 2.6 to 2.11 can be applied to any pyroelectric detector, as one proceeds to equation 2.13 one looses progressively in generality. However, it is possible to make $\mathcal{R}_V$ independent of the frequency by finding its maximum value for $\omega = (\tau_E \tau_T)^{-1/2}$:

$$(\mathcal{R}_V)_{max} = \frac{\eta p A R_G}{G} \frac{1}{\tau_E + \tau_T} \tag{2.17}$$

Equation 2.17 demonstrates that, independent of the frequency, the maximum $\mathcal{R}_V$ achievable is increased by reducing the thermal losses.

The maximum detectivity (D^*) theoretically attainable from a thermal detector was calculated to be about 1.8 x 10^{10} W^{-1}cm Hz$^{1/2}$ in the case where the only noise is due to thermal radiation from the element to the thermal sink [*Whatmore and Watton, 2001; Putley, 1970; Rogalski, 2003*]. Deviations from this ideal performance are inevitable due to the encapsulation of the active element, the conductance from the electrical contacts and the presence of a support structure. External noise sources are particularly detrimental for detectivity: it is crucial to enclose the detector in an earthed conductive package to screen it from external electromagnetic sources of noise. The external window should be conductive as well: germanium represents an optimal choice as it is conductive and has relatively low absorption at the wavelengths of interest (as stressed

in section 2.1) [*Hudson, 1969*]. Ultimately, most authors agree the experimental detectivity of real pyroelectric IR detectors lies in the range 10^8 to 10^9 W^{-1} cm $Hz^{1/2}$ (depending on modulation frequency).

As stated above, equations 2.4 to 2.17 refer to a single point detector. The figure of merit for focal plane arrays is called Noise Equivalent Temperature Difference (NETD): it represents the minimum change in scene temperature required to yield a signal equal to the root mean square noise voltage (V_n). The treatment of imaging detectors is complex and the expression for NETD is generally peculiar to the single system and ROIC architecture. However, in most cases it is possible to demonstrate the same improvement in performance with thermal isolation of the elements and increase in power density [*Whatmore and Watton, 2001; Rogalski, 2003*]. Micromachined integrated detectors (of the kind reported in figure 2.6) have demonstrated NETD of about 140 mK [*Watton, 1989*]. Detailed treatment of thermal imaging systems is beyond the scope of this introduction. Moreover, although it was initially planned, the arrays produced within the time frame of this research have not been integrated into a fully working IR camera. On the contrary, they have been individually tested. (This problem will be detailed in the experimental part, in section 4.1.3.)

The simplified physical model relative to a single point detector (equations 2.4. to 2.17) is largely used for the design and analysis purposes of this thesis. In particular, in the results part the performance relative to various system designs will be predicted and compared to the experimental results (see section 8.2).

2.5 Choice and optimisation of the pyroelectric material

The previous section demonstrated that the choice of the active (pyroelectric) material is crucial in order to optimise the performance of the detector. The choice of the best material is generally driven by the final application. However, for example in [*Putley, 1970*] the author outlines the pyroelectric material properties that would generally improve the performance of any detector: large pyroelectric coefficient, high resistivity, small dielectric constant, low thermal capacity and, of course, maximum emissivity (i.e. maximum power absorption). Other considerations, such as the cost, the thermal and chemical stability and the safety of handling have also to be taken into account.

Many pyroelectric materials employed in the last 10 years for thermal imaging applications are based on the perovskite system. The crystals have formula ABO_3 (O stands for oxygen). In most pyroelectric materials A is lead. B may be one or a mixture of cations (e.g. in a solid solution) [*Moulson and Herbert, 1990*]. The elementary cell of a perovskite (PZT) is showed in figure 2.5. PZT is a solid solution of $PbTiO_3$ and $ZrTiO_3$. Across most of the compositional range, the cell is tetragonal at room temperature, with the dipole aligned with the (001) direction [*Whatmore and Watton, 2001*]. Above the transition temperature (Curie temperature or T_C) the structure becomes cubic and the net dipole disappears. The temperature of cubic transition depends on the composition of the solid solution and so do many other properties [*Moulson and Herbert, 1990*]. The best pyroelectric properties are exhibited around the 30/70 Zr/Ti ratio for thin films and near 100% $PbTiO_3$ or 100% $PbZrO_3$ for bulk ceramics [*Whatmore and Watton, 2001*]. Often dopants are added to these basic

formulations, in order to enhance or tune the properties. The pyroelectric properties for these materials are compared to the properties of other typical pyroelectric materials in table 2.1 [*Whatmore, 2001*]. PZT-based materials usually show pyroelectric properties high enough to be used at room temperature (well below the Curie temperature). Recently, our group at Cranfield University demonstrated a sol-gel deposited PZT thin film, doped with manganese, showing a figure of merit F_D equal to $3.85 \cdot 10^{-5}$ $Pa^{-1/2}$ [*Zhang et al., 2003*].

Table 2.1 demonstrates the large gap in pyroelectric properties between bulk ceramic and thin film materials. This difference arises because of the major constrains in thin film processing, in particular the low thermal budget required and the effects of interaction with the substrates.

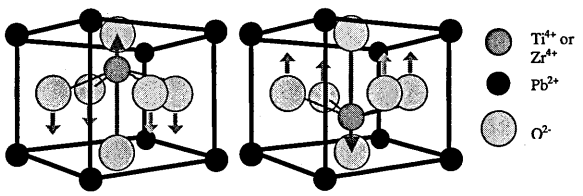


Figure 2.5 The elementary crystalline cell of a perovskite showing the two stable states of polarisation (below the Curie temperature)

Material	p	ε	tan δ	Meas.	c'	T_C	F_V	F_D	Deposition	
	10^{-4} $Cm^{-2}K^{-2}$			frequency Hz	10^6 $Jm^{-3}K^{-1}$	°C	m^2C^{-1}	10^{-5} $Pa^{-1/2}$	Method	T °C
ATGSAs	7	32	<0.01	1000	2.6	51	0.99	>16	Bulk	
$LiTaO_3$	2.3	47	10^{-3}	1000	3.2	665	0.17	11.1	Bulk	
VDFTrFE	0.33	7.4	0.017	1000	2.3	121	0.22	1.36	Bulk	
Mod PZ	4.0	290	0.003	1000	2.5	230	0.06	5.8	Bulk	
		300	0.014	33			0.06	2.6	Bulk	
Mod PT	3.5	220	0.01	1000	2.5	230	0.07	3.2	Bulk	
		220	0.03	33			0.07	1.8	Bulk	
PZT 30/70	3	380	0.008	33	2.7		0.032	2.1	Sol-Gel	510
PZT 25/75	2.2	350	0.008	33	2.7		0.025	1.7	Sol-Gel	510
PZT 20/80	1.8	260	0.011	33	2.7		0.028	1.3	Sol-Gel	510
PZT 25/75	2	300	0.01	1000	2.7		0.026	1.4	Sputt'd	450

ATGS = Triglycine sulphate doped with Alanine and Arsenic Acids (single crystal)
$LiTaO_3$ = Lithium Thallium Oxide (Perovskite, single crystal)
P(VDFTrFE) = Copolymer between vinylidene fluoride and trifluoroetilene – 70/30
Mod PZ = PZT ceramic, solid solution almost 100 % lead zirconate
Mod PT = PZT ceramic, solid solution almost 100 % lead titanate

Table 2.1 Properties of common pyroelectric materials for IR imaging [*Whatmore and Watton, 2001*]. All measurement performed at 25 °C

Many methods for depositing PZT-based materials have been reported. Sol-gel techniques are attractive for their low cost and versatility. Sputtering and Chemical Vapour Deposition are more expensive methods and present the problem that the compositions tend to change in an unreliable way. (Above all it is difficult to supply an

adequate amount of lead during sintering.) More reliable routes, such as Pulsed Laser Deposition, may only be suitable for small areas. The properties of a thin film may be dramatically influenced by the way it has been deposited. A general review is in [*Paz de Araujo, 1996*].

Ceramic thin films are generally polycrystalline and do not show any conspicuous spontaneous polarisation. The net dipole (***P***) is zero because the domain orientation (and their overall dipoles) is randomly distributed (figure 2.6*a*). Polycrystalline materials need therefore to be polarised in a strong field (coercive field) until they are mostly aligned along the direction of the detection (perpendicular to the focal plane of the array) as schematised in figure 2.6*b*. Once the field is removed, a large part of the domains remains aligned with the field, so that a net polarisation P_{rem} can be detected (figure 2.6*c*). Values of coercive fields for the films used in this device were found of the order of 20 – 40 V [*Zhang and Whatmore, 2001*]. The pyroelectric coefficient increases with temperature since the domains have more energy and orientate more easily. The pyroelectric coefficient peaks at the Curie temperature (T_C), while dropping to zero immediately after. If a film is sandwiched between two patterned electrodes (such as for the device object of this research), it is not possible to pole the sample by contact since this would require poling all the elements individually. Alternative processes, such as the corona poling, have to be employed [*Waller and Safari, 1988*]. The corona poling procedure is briefly detailed in the experimental part (section 4.1.2).

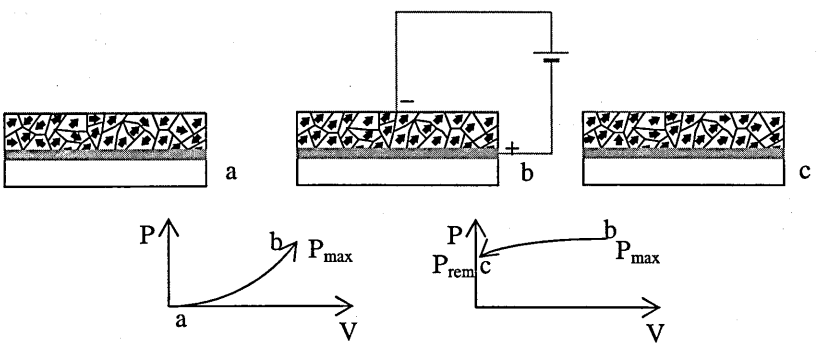


Figure 2.6 **Schematic of a poling process of a ferroelectric thin film. *a*) unpoled & disordered (P ~ 0), *b*) poling at the coercive field ($P = P_{max}$) and *c*) after removing the field ($P = P_{rem} < P_{max}$)**

The best performance is achieved by strongly (111) oriented PZT thin films. This is not directly evident, since the cell is tetragonal with the polar axis along the (001) direction. However, if films are deposited with (001) orientation, then the tensile stress in the film forces the polar axis to be in the substrate plane. This will greatly reduce the net polarisation since the domains subjected to a 90 degrees switching generally return to the original direction once the coercive field is removed [*Whatmore and Watton, 2001*].

Once the active material is chosen, the electrodes have to be optimised. If the pyroelectric material is grown as a thin film on silicon, the bottom electrode material (i.e. the electrode between the substrate and the PZT layer) must demonstrate chemical inertia, maximum stability and minimum diffusion at the temperature of crystallisation of the PZT (> 500 °C), good adhesion to the substrate and adhesion promotion for PZT. A well-chosen electrode should also induce the required texture in the PZT film. It is

known that a strongly (111) oriented Pt layer may favour the growing of PZT thin films in the (111) orientation [*Fox et al., 1995*]. (111)-oriented Pt can be grown by sputtering in absence of oxygen at room temperature. In many cases, the substrate is silicon with a layer of thermally grown oxide (SiO_2) (as in the device produced in this research). Unfortunately, Pt shows very bad adhesion on SiO_2, hence the use of a titanium buffer layer [*Madsen et al., 1998*]. The top electrode entails fewer problems because it is generally deposited at the end of the process.

2.6 The technology of pyroelectric thermal imaging: case studies

The theory of pyroelectric detectors (section 2.3) demonstrated how increasing the density of absorbed power and reducing the thermal conductance from the single active element represent two ways of improving the performance of the detector. In this section some case studies in pyroelectric detector technology will be presented. The survey will not be detailed: examples of systems and devices are presented here only to stress the practical importance of power collection and thermal isolation.

The first, obvious solution to increasing the density of incoming power flux, is to resort to large focussing optical systems. Germanium lenses have been generally applied to pyroelectric thermal imagers after the vidicon [*Whatmore and Watton, 2001*; *Gloss, 1987*]. In one instance [*Ning, 1991*], a single large non-imaging concentrator (dielectric totally internally reflecting concentrator) has been applied to a point element detector, leading to a theoretical increase in detectivity (in case internally generated noise is dominant) equal to $C^{½}$. (C is the concentration ratio of the collector, as explained in section 3.1)

Expressions 2.11, 2.13 and 2.17 show that detector performance increases with the amount of power absorbed and, in particular, with the emissivity of the element (η). The emissivity can be increased by coating the elements with one of the following [*Whatmore and Watton, 2001*].

- Thin metal layers with resistivity equal to 377 Ω/□. This value of resistivity corresponds to the layer thickness that yields the maximum in radiation absorbance [*Lang et al., 1991*; *Bly and Cox, 1994*].
- High IR absorbing "black" coatings.
- So-called "interference" absorbing thin films.

The third type is of particular relevance to micromachined detectors for thermal imaging arrays. Interference absorbers consist of a dielectric layer of thickness equal to a quarter of the wavelength of the targeted IR radiation, sandwiched between a metallic absorber (R = 377 Ω/□) and a reflective layer. The ideal set up depends on the thickness of the pyroelectric layer and various examples exist in literature [*Whatmore and Watton, 2001*]: for suspended elements about ~ 1 μm thin, the pyroelectric material itself can be used as an interference absorber and there is no need for an additional material.

The pyroelectric vidicon (figure 2.7) pioneered the application of thermal detectors to IR imaging and had represented the only example of imaging thermal detector for decades [*Whatmore and Watton, 2001*; *Goss, 1987*]. The vidicon is essentially a vacuum tube where the differences in surface charge are read out by a scanning electron beam. A germanium lens focuses the beam onto the detector (a thin pyroelectric plate).

The plate is suspended in vacuum to minimise the conductive losses and reduce *G*: the thermal loss is dominated by radiative conductance. Reticulation of the plate can be introduced to improve the thermal isolation among the elements [*Whatmore and Watton, 2001*; *Goss, 1987*].

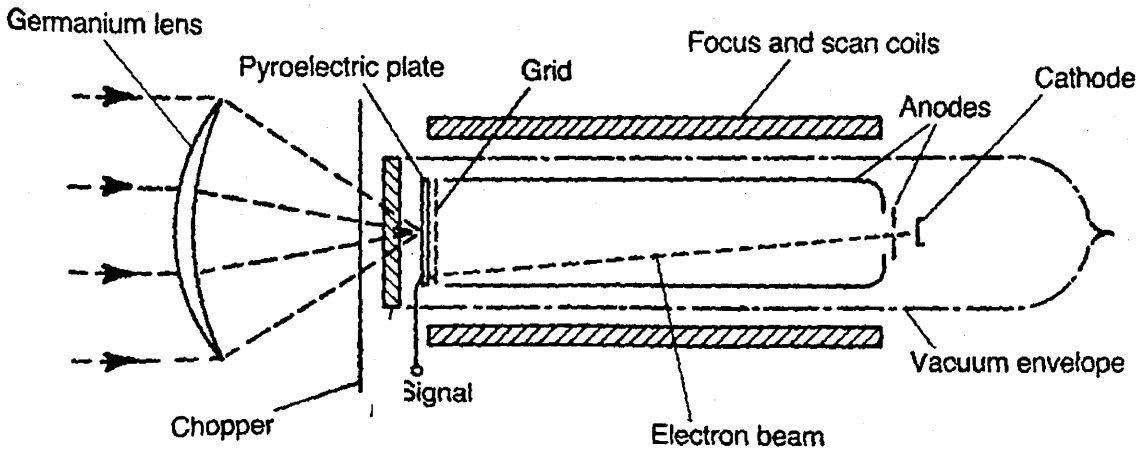


Figure 2.7 Scheme of the Vidicon device showing the focussing Germanium lens
Reproduced from [*Moulson and Herbert, 1990*]

A single element of a typical array structure, produced by "hybrid" technology (see section 2.1) is shown in figure 2.8 [*Moulson and Herbert, 1990; Whatmore and Watton, 2001, Rogalski, 2003*]. The pyroelectric thick plate is obtained from a bulk ceramic (PZT and other titanates have been used) and bonded to the ROIC through an array of solder bumps. This technique called "flip chip" bonding is well schematised in [*Whatmore, 1991*]. The features introduced to reduce the thermal losses are:
1) small diameter of the solder bumps,
2) isolation of the single bump from the element using a polymer plinth,
3) reticulation of the pyroelectric plate and
4) packaging of the array in low conductivity Xenon atmosphere.
The thermal conductance through the bumps sets a severe limit to detector performance. Increasing the distance between the element and the bump was a solution attempted. Values of NEDT for devices reported in literature are in the range 50 – 100 mK [*Whatmore and Watton, 2001, Rogalski, 2003*] with a best value achieved of 38 mK. The thickness of the pyroelectric plate is above 10 μm. The use of thinner films requires monolithic integration with the ROIC. Most pyroelectric materials display a degradation of properties as thickness is reduced, but PZT still maintains acceptable characteristics [*Rogalski, 2003*].

A typical element of an integrated (or monolithic) array is shown in figure 2.9 [*Moulson and Herbert, 1990*]. The process was originally developed for bolometer detectors [*Rogalski, 2003, Kruse, 2001*]. The fabrication method uses techniques peculiar to microelectronics, such as photolithography, surface micromachining and thin film deposition. In imaging detectors, the array of sensing elements has to be connected to a ROIC with a connection for each element to its individual FET (see figure 2.1 and section 2.1). Electrical connection entails the use of metal strip or solder bumps that will inevitably induce thermal losses by conduction. In the monolithic design, the element is

connected to the ROIC by microbridges. Bridges assure a better thermal isolation than that achievable by hybrid detectors [*Ploss et al., 1995*]. Element suspension by surface micromachining creates a vacuum that provides isolation between the active layer and the read-out integrated circuit. If the element itself is used as a $\lambda / 4$ absorbing layer [*Whatmore and Watton, 2001*], then the pyroelectric layer must be ~ 1 μm thick; this places a limit to the minimum thermal conductance achievable. On the contrary, if the vacuum between the element and the substrate is used as a resonant structure (interference absorber), then the element may be made as thin as possible. In this second case, the predicted NETD can be as low as 13 mK depending on material figures of merit [*Whatmore and Watton, 2001*]. However, in a recent survey [*Rogalski, 2003*] the author claims that devices actually produced have shown poor performance with NETD of about 400 mK.

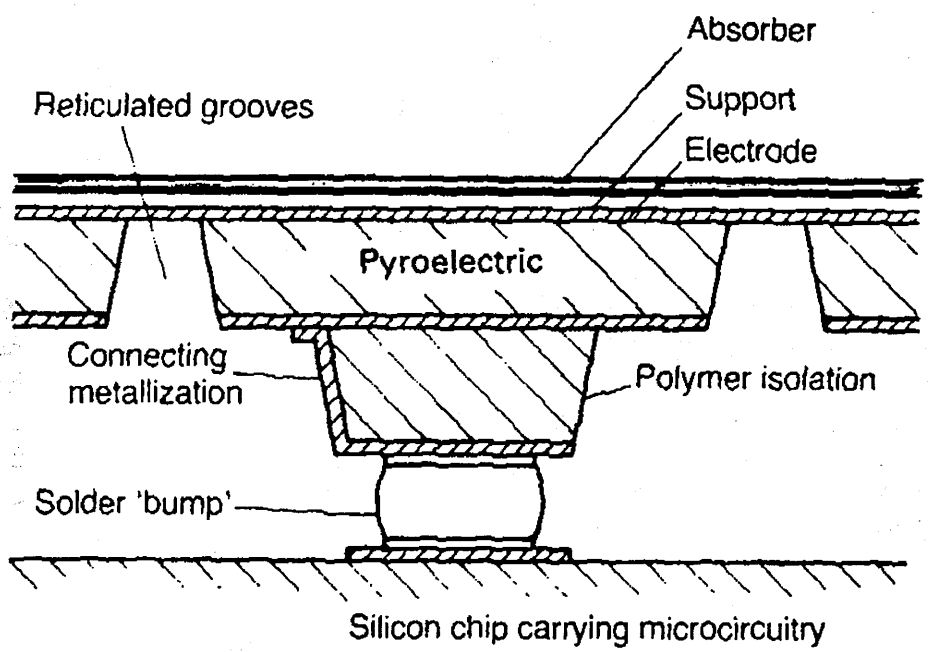


Figure 2.8 Thermally isolated and reticulated detector element of a typical hybrid device. Reproduced from [*Moulson and Herbert, 1990*]

The thermal compromise between ideal annealing temperature of the pyroelectric thin films (generally around 600 °C) and the resistance to the thermal treatment of the ROIC (down to 450 °C for long treatments) may prevent achieving good material properties. This could be one of the reasons for the gap between NETD prediction and the actual result achieved. In a composite design, developed in the UK [*Rogalski, 2003*], the microbridge structures are produced in a backing wafer, which is in turn connected to the ROIC as in the hybrid process (figure 2.10). The interconnections are micromachined through the wafer (probably using Deep Reactive Ion Etching). In this way the pyroelectric thin film can be annealed separately and the advantages of microbridge suspension are maintained. Finally, the bump is physically removed from the element. A NETD of 20 mK was predicted for this design [*Rogalski, 2003*].

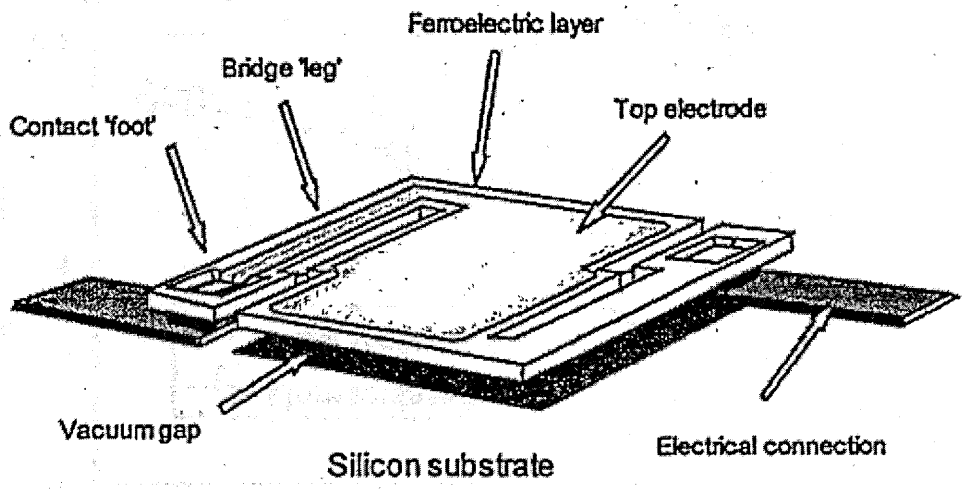


Figure 2.9 **A typical integrated IR detector element**
Reproduced from [*Moulson and Herbert, 1990*]

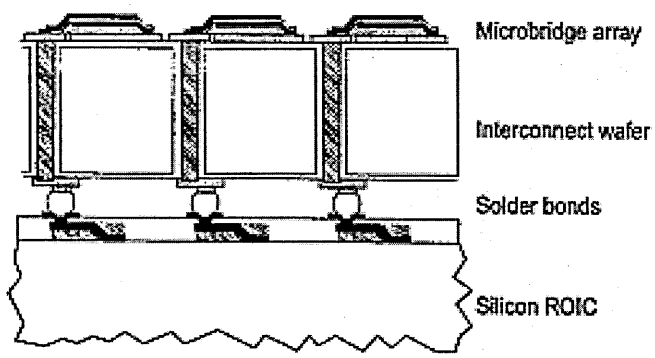


Figure 2.10 **Elements from a composite IR device**
Reproduced from [*Rogalski, 2003*]

The suspension of elements on a thin membrane has also been attempted. In [*Takayama et al., 1983*] thin lead-lithium tantalate films are deposited on a thick MgO substrate. The substrate is then wet bulk-micromachined in phosphoric acid to free the membrane containing the active array. The IR radiation reaches the active layer through the cavity, from the etched side of the MgO wafer. More recently, wet bulk micromachining was used to release suspended membranes in thermal imaging linear arrays based on PZT [*Kohli, 1997*] or ferroelectric polymers [*Neumann et al., 1995*]. These prototypes are generally characterised by the large dimensions of the membranes, so that the entire array is contained within a single etched cavity. In [*Bell et al., 1995*] for example, the membranes were up to 5 mm in width. Another group applied wet etching from the front (i.e. the side of the wafer containing the array) to create an IR sensing element, suspended by four thin bridges above the pyramidal etch pit [*Iborra et al., 2002*]. The technique of suspending the active elements on membranes has a large potential for improving the thermal isolation. The device developed in this research exploits largely such suspension technique, but it entails a single membrane for each individual element of the array. A primitive type of device that includes this design is reported in section 2.7.

One of the aims of this research is to use non-imaging concentrators in order to increase the density of incoming power flux. The advantage of this configuration can be demonstrated also considering that each element will receive (if the collection is ideal) the power incoming onto a larger area (i.e. the entry aperture of the collector, if round: $A = \pi a^2$) but the noise will be associated with a smaller area (the effective area of the element: $A' = \pi a'^2$). An example of the application of this principle was found in a photovoltaic device, [*Gordon et al., 1991*], which uses arrays of spherical immersion microlenses (i.e. image-forming concentrating systems) to enhance sensor performance. Each lens is coupled to a single element of the array, as shown in figure 2.11. Needless to say, this set up is not suitable for thermal detectors, as it does not allow the required thermal isolation of the elements.

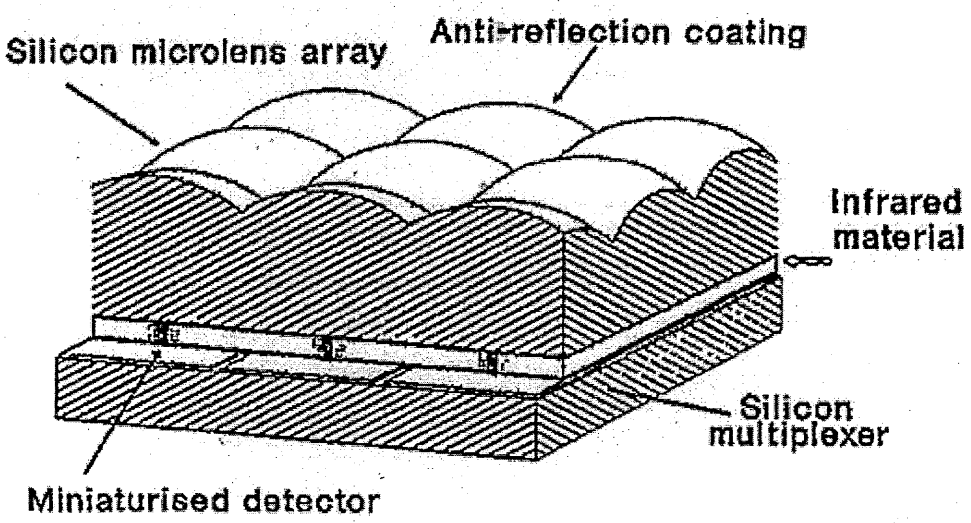


Figure 2.11 Microlens arrays applied to IR photovoltaic sensors
Taken from [*Gordon, 1991*]

2.7 State of the Art in IR Detection: an integrated device with a concentrating collector for each individual array element

The previous section showed various solutions adopted to increase the densification of the collected IR radiation or provide thermal isolation of the elements. If effectively achieved, these two targets can largely improve the performance of a pyroelectric detector. This would suggest that a device that includes both thermal isolation and power collection might represent the state of the art in pyroelectric detection of IR radiation. In fact, no example of such a device was found in literature. However, when this research started, such a device had already been fully designed at Cranfield University. Prototypes were produced as early as 2001, but a full account was only published three years later, when results were made available, demonstrating effective IR detection [*Shaw et al., 2004*].

The development of this original device had already highlighted and solved the main design and processing issues (such as the materials issues presented in section 2.5). The device object of this research builds on the knowledge developed and the design strategies of the original device presented in this section. There was no contribution to

producing this early device: all the work reported in this section had been accomplished before this PhD research started. For this reason the device is presented as a case study in this background chapter.

The IR sensor array was designed for being directly incorporated in a thermal imaging camera of the kind fabricated by IRISYS, UK [*IRISYS, 2004*]. The original camera design prescribes a "hybrid" detector (of the kind depicted in section 2.6, figure 2.8). The array was designed for being "flip-chip" coupled to the ROIC using an array of solder "bumps". Each bump connects an individual element to an individual FET, which collects and amplifies the current signal and transforms it into a voltage difference. An exploded view of a representative single element from the device design is in figure 2.12. It can be observed how the device contains an individual concentrating collector coupled to each element of the array. Each element is suspended on its own thin membrane, thereby enhancing the thermal isolation. However, such a design makes reticulation of the elements almost impossible.

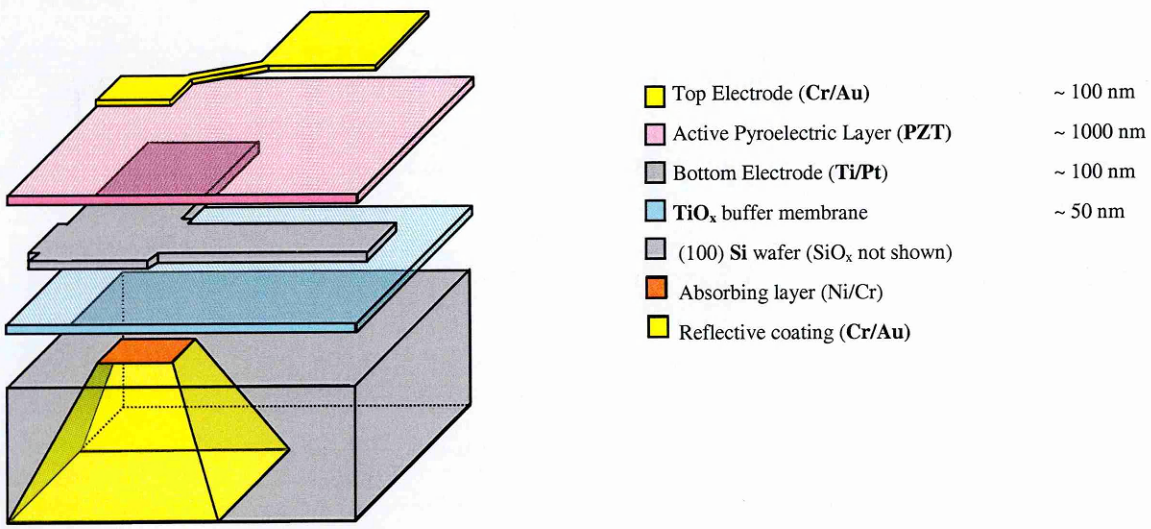


Figure 2.12: Exploded view of the early device design representing a single array element

In the previous section it was showed how the direct contact between the element and the bump limits considerably the performance of hybrid detectors. In this device, the bumps are physically removed from the detector. In fact, each bump is deposited onto the respective large pad that lies beside the membrane element. This greatly improves the thermal isolation of the elements.

The architecture of the infrared imaging camera puts some constraints to the design of the array. Each array has to be a square of 16 by 16 elements. The pitch of the array (500 μm) is determined by the pitch of the ROIC used in the system (see section 2.1). The maximum area of the elements is therefore limited by the pitch. A further limitation of the area is induced by the presence of the concentrators. The concentrators are pyramidal cavities, produced by wet anisotropic etching of silicon [*Shaw, 2004*]. In a silicon wafer 250 μm thick, the fixed etching angle of 54.74 degrees leads to a maximum available side of 125 μm for the entry aperture of the collector.

Each element is a small capacitor, with its respective top electrode electrically isolated. (Each gold electrode has to be individually bonded to the respective bonding pad.) To avoid etching the PZT layer, the elements were delineated by designing the top and bottom electrodes so that they overlapped only on the areas of the effective elements. The electrodes were patterned by lift off using a process that had previously been optimised for the production of FBAR devices: a long running project at Cranfield [*Kirby et al., 2001*]. The active material was a sol-gel deposited PZT-based material with high figures of merit, which had been developed at Cranfield [*Zhang and Whatmore, 2001*]. The Pt/Ti layer was patterned previous to the deposition of the blanket PZT. This entailed deposition of PZT partly on Pt covered areas and partly directly on SiO_2. Since PZT is not compatible with SiO_2, a TiO_2 buffer layer was introduced [*Madsen et al., 1998; Kirby et al., 2001*]. TiO_2 is known to induce low quality perovskite or even the formation of pyrochlore, but at least assures adhesion of the PZT thin film across all wafer area. This step, however, is expected to lead to a general decrease in process reliability and device performance.

2.8 Conclusion

This chapter presented the background theory and technology of IR radiation sensing using uncooled pyroelectric detectors. Thermal detectors are complex systems that allow the transduction of temperature differences of a scene to a detectable signal (which can be a visual image in IR cameras). The core of a 2 – d imaging (staring) detector consists of an array of sensing elements, each corresponding to a pixel in the image. The image emerges from a distribution of surface temperatures across the focal plane.

The sensors object of this research convert infrared to electrical signals using the pyroelectric effect, whereby temperature variations in a polar dielectric material generate changes in the electrical dipole moment. The fundamental model of a pyroelectric element demonstrates that, in order to enhance performance, the radiation power reaching the detector should be maximized and the thermal conductance of the sensor elements to their surroundings minimised. In early commercial designs these issues were addressed by using a germanium lens to focus infra-red radiation and packaging in vacuum for thermal isolation. In the "hybrid" technology, thermal isolation is provided by reticulation of the thinned pyroelectric ceramic plate. Another solution proposed was to machine the elements to thin membranes by wet or dry bulk micromachining. "IR black" or resonant structures have been used to increase the absorption of power.

The device described in this study builds on the above ideas and technology. It also builds on the design and development of an earlier device produced at Cranfield. This device represented the state of the art in IR sensing since it coupled a concentrator cavity micromachined in silicon to collect the incoming IR radiation to each element and it provided suspension of each element of the array onto an individual thin membrane that improved thermal isolation.

The device object of this research elaborates on that original design do develop a novel concept device with the following features:

1) An array of 3 – d structured collectors is coupled to the sensing array. The collectors are designed to yield the maximum collection efficiency.
2) Each element is suspended in a thin membrane. The membranes are patterned so that's the elements lay on inner active areas that are thermally isolated from the background.

The design of these features is optimised after a theoretical analysis. Subsequently, to develop a viable microfabrication route the available techniques have to be researched and compared. The literature surveyed is critically reported and discussed in the next chapter.

CHAPTER 3 LITERATURE SURVEY: THE SEARCH FOR A ROUTE TO DEVICE MICROFABRICATION

The theory of IR detection, presented in the previous chapter, demonstrated how the performance of a pyroelectric IR sensor could be improved by thermally isolating the sensing elements or by focussing the incident radiation. The analysis of a series of case studies showed the relevance of these two issues to IR sensing technology. Both solutions are incorporated in the design of the novel device object of this research. Initially, a device had been conceived at Cranfield that incorporated an array of pyramidal cavities to collect the incoming IR radiation and provided suspension of each element of the array onto an individual thin membrane that improved thermal insulation (see section 2.7 and figure 2.12). The design of this early prototype had been accomplished before this research started.

The device object of this research elaborates on that original design do develop a novel concept. An innovative design has been developed. In particular, the aim of this research is to incorporate an array of 3 – d structured collectors, whereas the concentrators in the primitive version of the device (of figure 2.12) were simple pyramidal etch pits produced by anisotropic wet etching of silicon. Furthermore, the novel device puts forward a design that allows isolation of each individual element on an inner active area by means of micromachined bridges (this was practically impossible in the early design).

This chapter collects the bulk of literature that was surveyed in order to design the device structure and outline feasible microfabrication routes to achieve a working prototype. The chapter will focus mainly on two issues: the microfabrication of arrays of suitable micro-collectors and the patterning of the active layer to yield an array of thermally isolated elements.

Concentrating collectors have been historically used to focus radiation beams in optical systems. In this project, however, a class of concentrators has been considered with a concept completely different from the traditional optical systems (such as macroscopic lenses or parabolic mirrors). Non-imaging collectors are curved mirrors with an entrance and an exit: radiation is concentrated by means of reflection from the sidewalls. These systems, which have such a high aberration as to be completely incapable of producing an image of the source, can nevertheless achieve collection efficiency higher than the conventional imaging systems. The literature on non-imaging concentrating collectors was reviewed in order to assess the most suitable profiles for the purposes of the application. The physics and the design of non-imaging collectors are detailed in section 3.1.

Traditionally, with a few exceptions, the applications in the literature concern large-scale collectors. The manufacturing of IR-collecting micro cavities for incorporation in microsystems presents peculiar problems, different from the requirements of meso-scopic systems. In fact, micro-concentrators would be deep (through-the-wafer) and narrow 3 – d microstructures, with aspect ratio (ratio between depth and maximum width) higher than one. Sidewalls would be highly sloped but necessarily smooth to achieve the maximum reflectivity. The main issues relative to the microfabrication of

concentrator cavities in silicon wafers will be discussed in section 3.2. Not all the suitable profiles are achievable by using conventional microfabrication techniques. Therefore, after a brief review on the spectrum of available microfabrication techniques, section 3.2 will conclude by identifying a few routes that are promising and within the capability of this group.

The most promising routes entail at least a step involving Deep Reactive Ion Etching of silicon. DRIE is a process that allows the etching of high aspect-ratio micromachined cavities in silicon using plasma-based chemical methods. An overview of this technique will be presented in section 3.3. The specific microfabrication routes that could potentially lead to a successful integration of arrays of concentrators in the device are discussed in details in sections 3.4 and 3.5.

In section 2.3 it was demonstrated how the performance of pyroelectric detectors increases when the thermal conductance of the element to the surroundings is reduced (see in particular equations 2.11, 2.13 and 2.17). Although this was demonstrated for a single point detector, similar arguments were developed for focal plane 2 – d arrays. Since one of the objectives of this research is to improve the thermal isolation of the pixels, the nature of G is investigated in more detail in section 3.6. The increase in device performance when microbridges are introduced is demonstrated after theoretical analysis.

The microfabrication route for elements patterning is analysed in section 3.7. First, available microfabrication techniques for providing thermal isolation to the elements are surveyed. After this brief survey, conventional Reactive Ion Etching is presented as the process of choice. RIE is an ideal technique for patterning thin films of inorganic materials. It is very versatile thanks to the synergy between chemical etching by activated radicals and the effect of the ionic flux induced by the RF plasma. The technique is briefly described and the literature on plasma etching of PZT-based materials is reviewed.

3.1 The theoretical background of non-imaging concentrators and the design of systems with high collection efficiency

Independent from its actual design, a concentrating system can be defined as a "black box" (figure 3.1). A beam of section A passes through the system: it is assumed that all rays with angle below a certain angle θ (called "acceptance angle") will enter the system. The concentration ratio (or collection efficiency) can be defined as the power density of the emerging ray (H') divided by the power density of the incoming ray (H). If all the radiation is passed by the optics (ideal case) of the system, the emerging beam will have the same total power (P) as the accepted beam, but its section will be equal to A'. Under these assumptions:

$$C = H'/H = (P/A')/(P/A) = A/A' \qquad (3.1).$$

The quantities A and A' of equation 3.1 refer to the area of beam section. Conversely, the ratio between the entry and exit aperture areas of the system is called the "geometric" concentration ratio. It is crucial to clarify that the geometric concentration ratio may differ from the physical concentration ratio since part of the rays that enter the system can be lost or rejected. The geometrical concentration ratio is a dimensional

parameter of the systems whereas the concentration ratio is related to the actual beam densification (i.e. the physics of the system). As a matter of fact, they do not coincide for most of the systems treated below.

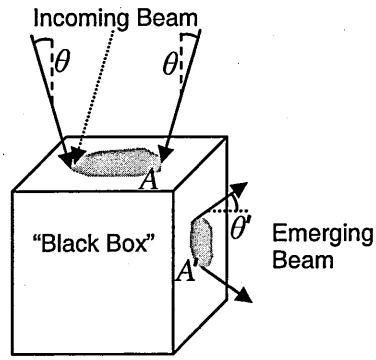


Figure 3.1: A generic concentrator intended as a "black box". *A* and *A'* represent the sections of the collected and emerging beams respectively.

The maximum theoretical concentration ratio that an ideal system can yield was calculated by Winston from phase space conservation (energy conservation) as [*Winston, 1970*]:

$$C_{\max} = (n' \sin\theta') / (n \sin\theta) \tag{3.2}$$

for a 2 – d system and

$$C_{\max} = (n' \sin\theta')^2 / (n \sin\theta)^2 \tag{3.3}$$

for a 3 – d system possessing axial symmetry.

Since the collectors of interest for this research are basically curved mirrors with no dielectric filling, the ratio of the refractive indices of environment (n) and medium (n') is equal to 1. If the emerging beam is totally concentrated, then it is also totally diffused. (Otherwise, it could be concentrated more by adding a subsequent concentrator, thereby violating the first principle of thermodynamics.) The cut-off angle of the emerging beam must be equal to $\pi/2$ (isotropic distribution). Substituting $\pi/2$ in 3.3 yields [*Welford and Winston 1989, Chapter 1*]:

$C_{max} = [\, 1 / \sin(\theta)\,]^2$ (3.4).

For a 2 – d concentrator (using equation 3.2):

$C_{max} = 1 / \sin(\theta)$ (3.5).

It is important to stress that this value is a true physical limit: it cannot be overcome by any (even ideal) system. Equations 3.4 and 3.5 show that the concentration ratio decreases with the acceptance angle: this means that a collector designed to accept radiation over wider angles (i.e. more radiation power) will necessary pay the price of a wider emergent beam (i.e. be less concentrated). In other words, when the acceptance angle tends to $\pi/2$, then C_{max} tends to one. Eventually, a system that accepted all the incoming radiation from an isotropic distribution would not be able to concentrate it at all. To assess whether there could exist concentrators that achieve that maximum ideal ratio, it is necessary to look into the "black box" of figure 3.1. Winston showed that all

practical image forming systems, if used as concentrators, fail to approach the maximum; although it is not theoretically impossible to produce a perfect image-forming concentrator [*Welford and Winston 1989, Chapter 3*].

Winston then analysed the design of non-imaging collectors [*Winston, 1974*]: concave mirrors with very large aberrations. They do not project any coherent image of the source. The cone concentrator is the most basic version of a non-imaging collector. A 3 – d conical cavity is produced by the revolution of a straight line generator around the axis of the concentrator. A possible 2 – d generator ("V" collector) is shown in figure 3.2*a*. If the generator is the arc of a parabola (figure 3.2*b*), then a parabolic concentrator is obtained. The figures 3.2*a* and 3.2*b* can be also intended as meridian cross sections of the respective 3 – d systems. Both types of design yield concentration ratios lower than the theoretical maximum.

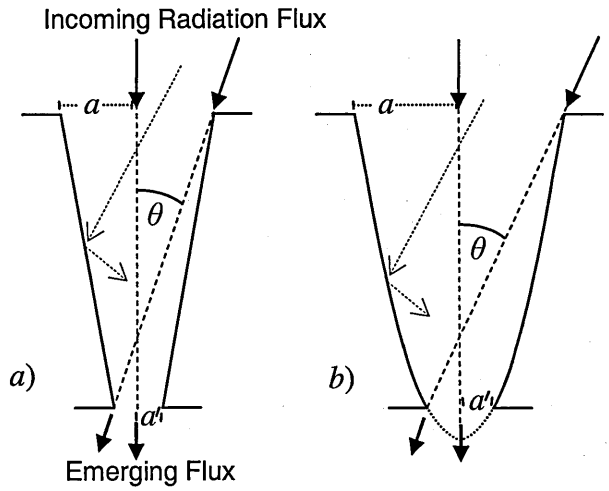


Figure 3.2 Meridian cross sections (or generators) of cone (a) and a parabolic (b) concentrators

More efficient systems can be designed by coupling the Fermat principle to the Edge-Ray principle [*Welford and Winston 1989, Chapter 4, Gordon, 1996*]. The construction of the 2 – d system will be shown first. In figure 3.3 a propagating wave front is shown. The front is at the extreme angle, below which the radiation has to be collected (i.e. the acceptance angle of the beam entering the concentrator). Given a system with a fixed exit aperture width (*FF'*), the dashed line represents the left reflector of a 2 – d concentrator with no particular geometry. The reflector has to be designed so that all the rays within the front at the extreme angle θ (acceptance angle) pass, after reflection, through the rim (in this case the point *F*) of the exit aperture. If this happens, then the Edge-Ray principle assures that all the rays with incidence angle within the acceptance angle (that is all the fronts at angle below θ) will eventually pass within the exit aperture and therefore through the concentrator.

Figure 3.3 suggests also how such a result could be achieved. The segments *IF'* and *BA'* represent the extreme rays, passing through the inner and outer rims of the reflector respectively. *DE* is a generic ray at the acceptance angle. The reflector has to be designed to collect all these rays in *F*. Applying the Fermat principle of the shortest path

the reflected rays will pass through F only if $BA' + A'F = DE + EF = IF' + F'F$. If the reflector is part of a parabola with director line r parallel to the front at θ and focus in F, then for the properties of the parabola $A'F = A'C$; $EF = EG$ and $F'F = F'L$. Substituting these equalities in the above sums yields the expressions $BA' + A'F = BA' + A'C = BC$; $DE + EF = DE + EG = DG$ and $IF' + F'F = IF' + F'L = IL$. Since r is parallel to the front, then $BC = DG = IL$. Therefore, the Fermat principle is satisfied by an arc of parabola of the type reported in figure 3.4 [*Welford and Winston 1989, Chapter 4*]. The angle between the parabola axis and the axis of the concentrator is equal to the acceptance angle θ. Winston called the class of concentrator based on this principle "Compound Parabolic Concentrators" (CPCs). The 2 – d system (with mirror symmetry) is built by placing in F a second reflector, arc of a parabola whose axis intersects the concentrator axis at an angle equal to – (θ).

The 2 – d CPC has four degrees of freedom that determine its profile:
1. θ, the angle within which the rays are collected into the inner aperture;
2. a', the half-width of the exit aperture of the CPC;
3. a, the half-width of the entry aperture of the CPC and
4. L, the overall depth of the CPC.

The following geometrical relationships among these parameters, emerging from the construction detailed in figure 3.4, reduce the four degrees of freedom to two:

$$a = a' / \sin\theta \tag{3.6};$$

$$L = (a + a')\cot\theta_i = a'(1 + \sin\theta_i)\cos\theta_i \frac{1}{\sin^2\theta_i} \tag{3.7}.$$

The parametric equations describing the profile of the concentrator can be obtained from the parabola equation by a translation and rotation of the axes [*Welford and Winston 1989, Chapter 4*]. If one of the four degrees of freedom is saturated, then families of CPCs can be generated. Generally, it is the acceptance angle that determines the CPC construction. The importance of the acceptance angle becomes clear when the actual cut-off angle of the flux power distribution is introduced. In section 5.2, it will be demonstrated how the largest power collection is attained by matching the CPC acceptance angle to the cut-off angle of the incoming power flux distribution. However this is not always possible or practical because other constraints may reduce the available range of design choices. For example, to produce the diagrams of figures 3.5 and 3.6, respectively a and a' have been kept fixed. The units in the plots are symbolic. They can be considered in μm, for the purposes of the application. Large 2 – d CPCs were actually manufactured, in the form of very long trenches bounded by mirror-like sidewalls [*Winston, 1974*; *Welford and Winston, 1989, Chapter 4*].

In equation 3.1, the geometric concentration ratio was introduced as the ratio of the entry and exit areas for a 3 – d concentrator. In an analogous way, C can be defined, in two dimensions, as the ratio of the entry and exit aperture widths. For the 2 – d CPC:

$$C = a / a' = 1 / \sin\theta \tag{3.8}$$

Under the assumption that all rays accepted from $2a$ are transmitted through $2a'$, equation 3.8 demonstrates that the 2 – d CPC is an ideal concentrator since it yields the maximum theoretical concentration ratio. In fact, that the 2 – d CPC is ideal follows directly from its geometrical construction.

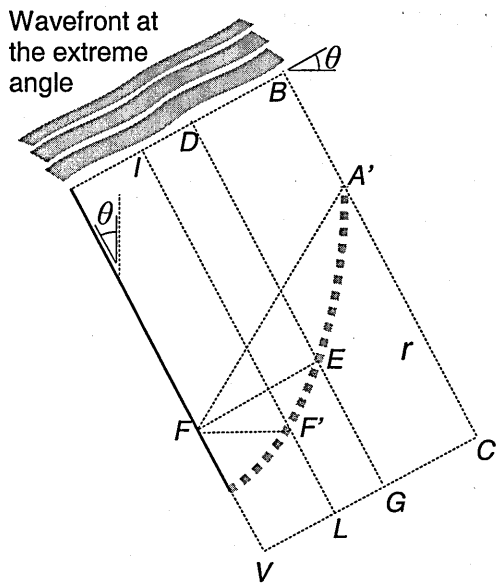


Figure 3.3 Construction of the CPC by means of the Edge-Ray and Fermat principles

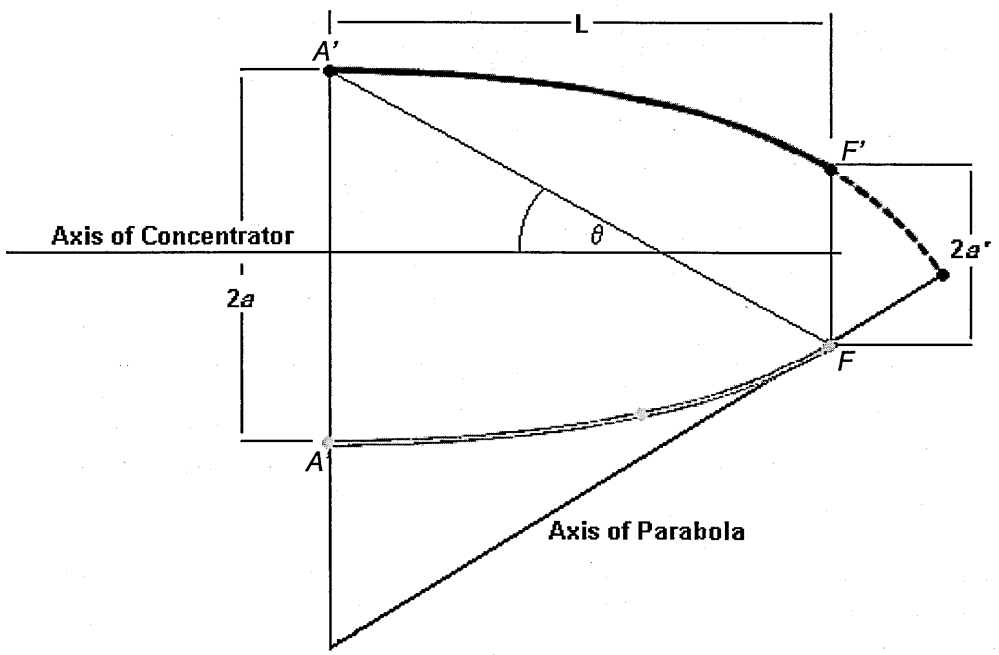


Figure 3.4 2 – d CPC profile and main design parameters

The 3 – d CPCs can be built either by rotating the reflectors of a 2 – d generator about the CPC axis as in figure 3.7*a* (in analogy with the cone and parabolic concentrators of figure 3.2) or by "intersecting" perpendicularly two 2 – d CPC trenches as in figure 3.7*b*. From now on, anytime a generic 3 – d CPC is referred to, the shape of figure 3.7*a* will be always considered unless specified. A 3 – d CPC is not especially built to obey the Edge-Ray principle (as the 2 – d CPC was). Although the meridian cross section is a

2 – d CPC, there are no degrees of freedom left to adjust the design to compensate for the reflections of the skewed rays. It is therefore expected that a proportion of these rays will eventually be rejected. In other words, the total transmittance of an ideal 2 – d CPC is equal to one, while for a 3 – d CPC T is necessarily below 1.

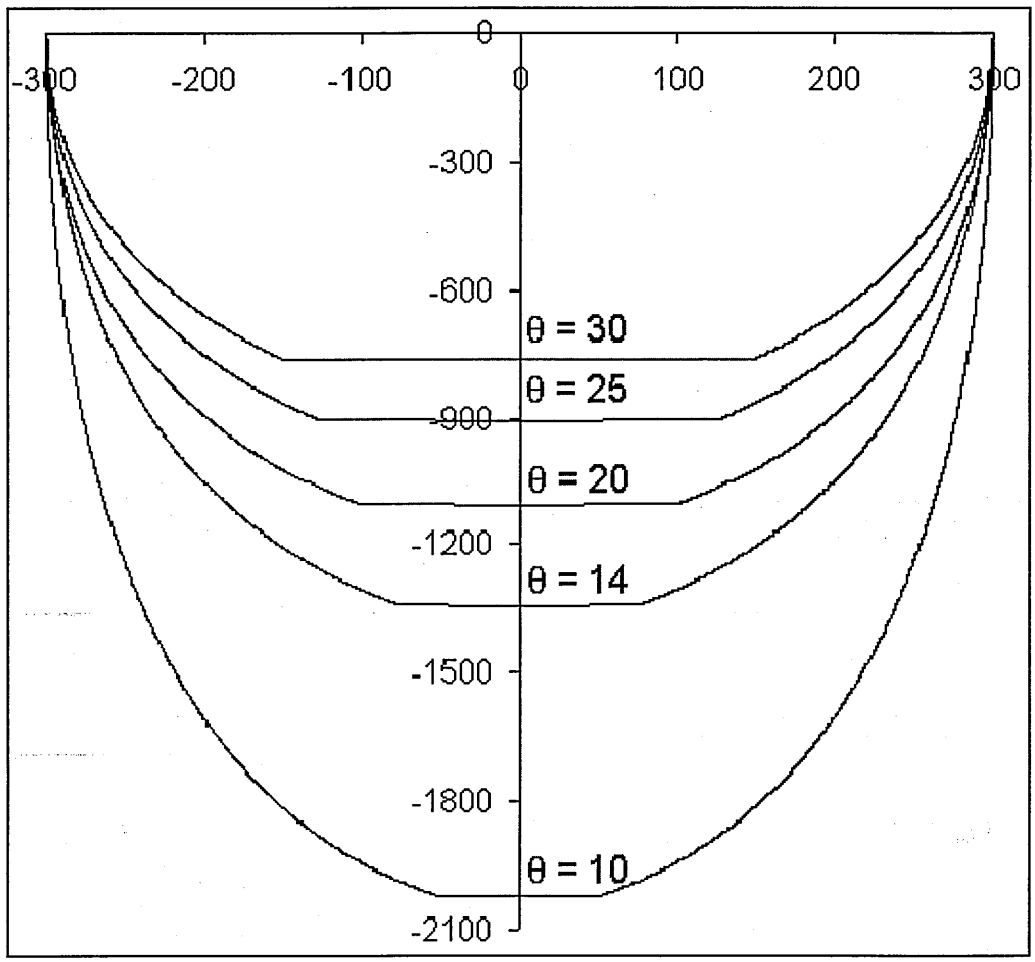


Figure 3.5 **A series of 2-d CPCs with fixed entrance aperture width (600 units) and variable acceptance angle. Arbitrary units (same unit for x and y).**

It is interesting to show also that, for the 3 – d CPC, the ratio of the aperture areas is (geometrically):

$$\pi a^2 / \pi a'^2 = (a / a')^2 = [1 / \sin (\theta)]^2 \qquad (3.9).$$

However, since $T < 1$, the area $\pi a'^2$ does not coincide with the section of an outgoing uniform beam: for the 3 – d CPC, the geometrical concentration ratio does not coincide with the actual beam power densification. Ray tracing analysis (a statistical technique that will be detailed below) showed that a part of the skewed rays is effectively rejected and, therefore, the 3 – d CPC does not represent an ideal concentrator [*Welford and Winston 1989, Chapter 4*]. Subsequently, Winston et al. offered a semi-intuitive explanation of this non-ideality by making use of the geometrical vector flux $\boldsymbol{J}$. Using $\boldsymbol{J}$ they also gave a more rigorous demonstration that the 2 – d CPC is an ideal concentrator [*Winston, 1979*].

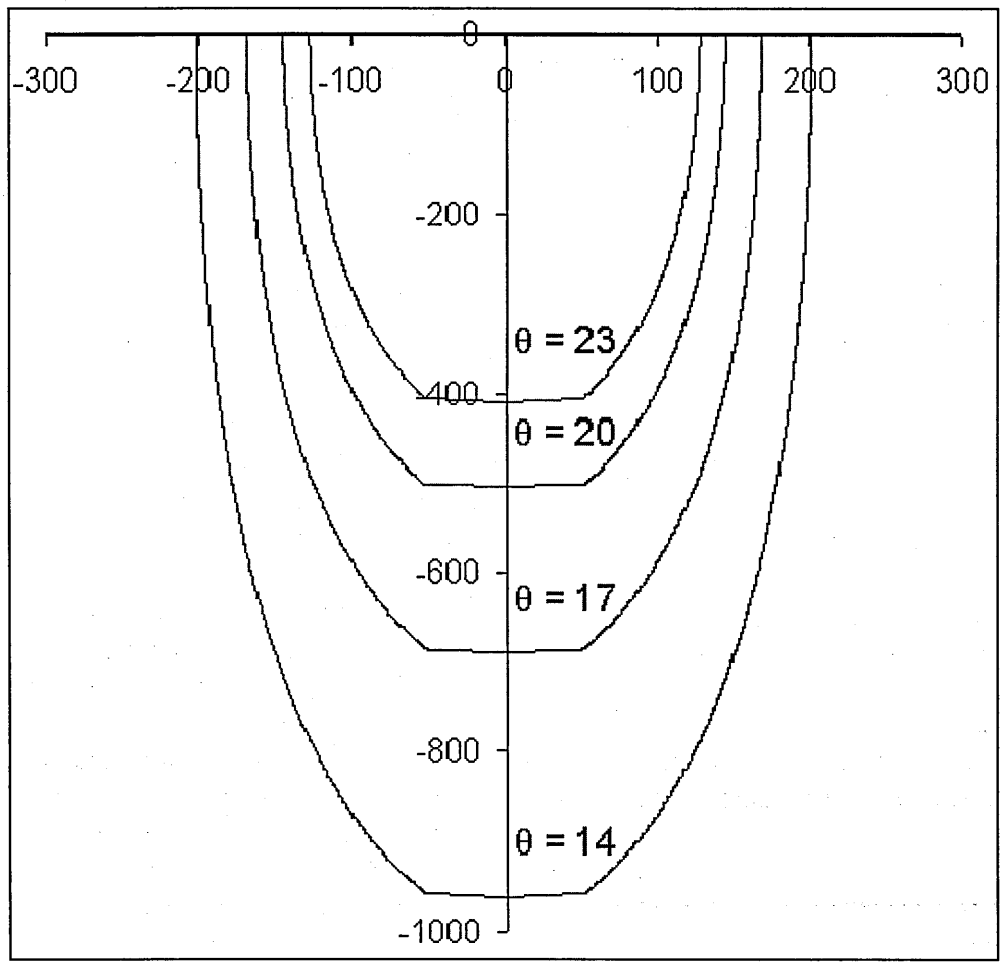


Figure 3.6 **A series of CPCs sections with fixed exit aperture width (150 units) and variable acceptance angle. Arbitrary units (same unit for *x* and *y*).**

Various advanced types of design have been proposed since the classic CPC was first discovered [*Welford and Winston 1989, Chapter* 10; *Norton, 1991*]. New profiles, presenting high concentration ratios were also discovered by making use of the geometrical vector flux approach. The trumpet collector represents an actual 3 – d ideal collector [*Gordon, 1996; Winston, 1979*]. Many designs are specifically developed for peculiar applications (mostly solar energy collection) and are generally not interesting or viable to be applied to the micromachined IR sensing array. These types of design will not be treated here.

In conclusion: non-imaging collectors are promising for incorporation in infrared devices for their high performance, relative simplicity and freedom of design. The 2 – d CPC design, built on the application of Edge-Ray principle yields the maximum concentration ratio. It is convenient, therefore, to model the collectors for the IR sensing device on these concentrators. Although constraints in the design exist, entire families of CPCs can be available to suit the application requirements.

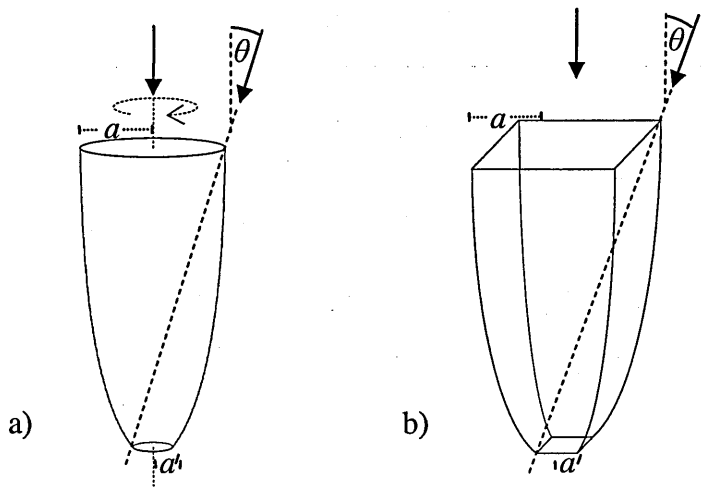


Figure 3.7: 3 –d concentrators originated by rotation of the 2 – d CPC about its axis (a) and by the crossing of two perpendicular trenches with 2 – d CPC cross section.

Before concluding this section, it is important to spend some words on the techniques used for predicting the performance of a concentrator of a given design. Above it was demonstrated how the rough use of geometric concentration ratio is not satisfactory as it could be misleading (see e.g. equation 3.9). Power densification must be assessed using more rigorous physical arguments and keeping into account the total transmittance of the system. However, analytic solutions may be available only for highly symmetric concentrator or 2 – d systems. Profiles that cannot be directly expressed in analytical form require computational methods, e.g. the ray-tracing method. A more rigorous treatment of this method will be given in chapter 5, where it is extensively used as a computational tool. This technique simply consists in tracing the trajectories of numerous rays inside the concentrator using geometric optics. After the analysis of the path of a consistent sample of rays is accomplished, plots of transmittance Vs incidence angle of the rays may be produced. In figure 3.8, transmittance – angle plots obtained by ray – tracing are reported for 2 – d and 3 – d CPCs with $\theta = 10$ degrees [*Welford and Winston, 1989, Chapter 4*]. The performances of a cone and a paraboloid of revolution are also reported. For better comparison, all the systems have equal apertures diameters ratio ($a / a' = 5.76$). The cone concentrator cut-off angle is equal to the CPC acceptance angle. The results of the ray-tracing analysis show that the 2 – d CPC is ideal (perfect cut-off at the acceptance angle), whereas the other systems, although accepting rays at angles above θ, reject part of the radiation at smaller angles thereby failing to achieve the thermodynamic maximum. The diagram of figure 3.8 is taken from the literature but similar diagrams are calculated in the framework of this research for types of design of interest and for a new series of profiles especially developed for the IR sensor device. These diagrams will be reported and discussed in the results part, throughout chapter 5. In the literature, concentrator's performances have also been evaluated using the theory of heat transfer and finite element module analysis [*Norton et al., 1991*]. Ray tracing and the other computational methods are chiefly important to predict the performances of concentrators actually manufactured. The fabrication of collectors and their incorporation in a silicon-based device will be treated in the next sections.

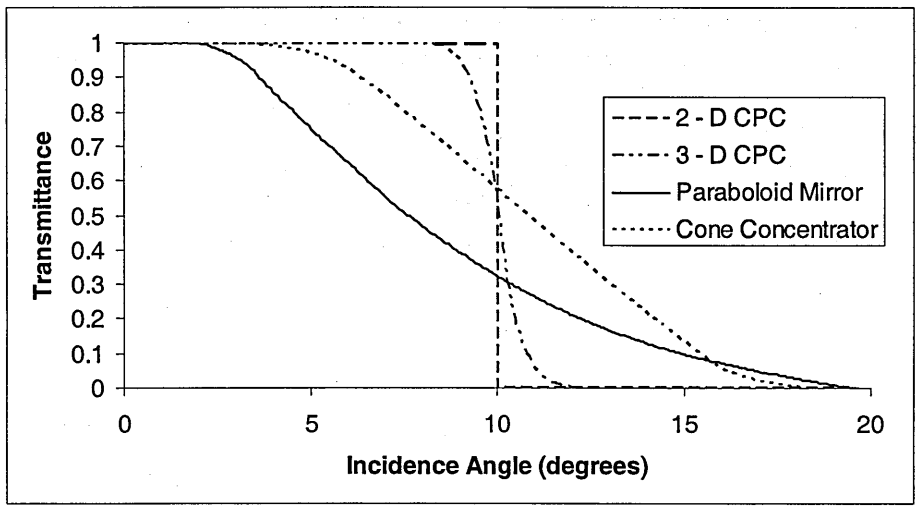


Figure 3.8 Plots of Transmittance Vs Incidence Angle for different concentrator designs. (Obtained by ray-tracing in [*Welford and Winston 1989*]**.)**

3.2 The fabrication of micro-concentrators: general overview and survey

As stated in the introduction, with a few exceptions the applications in the literature concern large-scale collectors [*Welford and Winston 1989, Chapter 11*]. (Solar cells, for example require collectors with dimensions of few inches at least [*Rabl 1979; Welford and Winston, 1989, Chapter 10*].) Non-imaging microscopic concentrators were considered for laser fibre optic surgery [*Gordon et al., 1998*] and incorporated in Light Emitting Diode devices [*Nash et al., 2002*]. However, these examples are concerned with protruding features rather than cavities.

In this section, the issues concerning the fabrication of collectors will be presented. Manufactured collectors are complex systems. The actual contour may differ in many ways from the original design profile. The reflectivity of the sidewalls is likely to be less than ideal, due to inherent roughness (hence scattering of the radiation) or partial absorption of the radiation. Therefore, more sophisticated computational methods are required in order to predict the performance. In particular, at the end last section the ray tracing technique was introduced. Winston called "optical concentration ratio" the datum obtained by ray tracing computation [*Welford and Winston 1989*]. A non-imaging concentrator functions as a mirror, i.e. upon pure reflections and independent of the wavelength of the radiation transmitted. In order to compute the collection properties of such systems by ray tracing, it is sufficient to obtain the local value of the normal to concentrator surface for generating the reflected ray for a given incidence of the incoming ray. It is clear that the tracing of elementary bundles of rays across the system can be accomplished also when the profile cannot be analytically described as long as the local curvature of concentrator contour is known for all the points of interest. Providing the real contour has been well characterised by some morphological assessment technique, ray tracing can be applied to profiles of manufactured concentrators, which may be far from the original equation of the design. The practical concentration ratio, eventually, has also to make allowances for the manufacturing

errors (reflection losses) [*Welford and Winston 1989, Chapter 2, Rabl 1979*]. Due to intrinsic random variability of many of these properties, the concentration ratio of the individual collector as a manufactured product has often to be assessed experimentally.

This section analyses the problems that are expected to arise when attempting to fabricate arrays of micro-structured concentrators in the silicon wafer. These issues are introduced here in order to justify the choice of the most promising techniques. The search for a suitable microfabrication process can be considered as a series of subsequent refining steps. First, routes have to be identified capable of producing arrays of through-the-wafer cavities that can be used as concentrators. Then, the best technique has to be chosen to approximate, among all the routes, the shape of the concentrator sought. The choice of the concentrator type plays a fundamental role at this stage: if the CPC represents somewhat the most demanding contour, rough approximations based on the cone or paraboloid could be more easily produced [*Welford and Winston 1989, Chapter 4*]. After a technique capable of producing rough collectors has been identified, a viable process has to be set up. The last step entails tuning the process parameters to enhance the performance of the concentrators produced (in terms of profile and surface smoothness). Unfortunately, achieving high-collection concentrators represents just a part of the requirements: in fact the compatibility of the process with the other steps of the production process has to be taken into account too. Furthermore, the microfabrication process has to be viable within the capabilities of the laboratory (or group) and it has to entail a reasonable cost. Time is also an important issue. The choice of a suitable microfabrication route is illustrated in picture 3.9 by means of sets.

In this section, the inevitable degradation of performance from the design to the final manufactured device is discussed. The main constraints expected to arise during the actual fabrication experiments recalled will be analysed in detail in the following. The exposition follows the same path that was actually followed by the preliminary investigation (during the first months of this research). This survey led eventually to the selection of a few promising routes.

The main requirements of the cavities that have to be micromachined are the following.

1) SCALE: The cavities produced must cross through the entire wafer thickness because the active elements lie on the side of the wafer opposite to the infrared source (see for example the schematic of the device presented in chapter 1). To achieve such depth with a satisfactory reliability, a bulk microfabrication technique is needed.

2) SHAPE: Non-imaging concentrators have a well-defined parametric contour. Since the radiation is collected by means of reflection, the efficiency is inherently related to the fidelity of the profile to the parametric design. In particular, the CPC is a complex 3 – d structure, with slope of profile varying from zero (at the absorber) to 90 degrees (at the entrance). Among the bulk microfabrication techniques, wet etching in alkaline solutions can only produce pyramidal etch cavities [*Madou, 2003; Chapter 4*] as dictated by the etch rate minimum at the (111) planes. A device with collectors produced by wet anisotropic etching was presented in section 2.7 (figure 2.10). However, such a process is not useful for producing contoured profiles with complex

curvature and it is not of interest for this research. For this reason the production of wet etched collectors will not be reported in the results section.

3) SMOOTHNESS: Surface roughness must be minimised to achieve the minimum scattering and the maximum reflectance. This is a crucial issue that has dominated through all the steps of the research, both at the stage of the preliminary survey and at the time of judging the suitability of a technique on the basis of the experimental results. For this reason it extends well beyond the scope of this literature survey, and it will be discussed in detail in the results part (see for example sections 6.2.6 and 6.3.2).

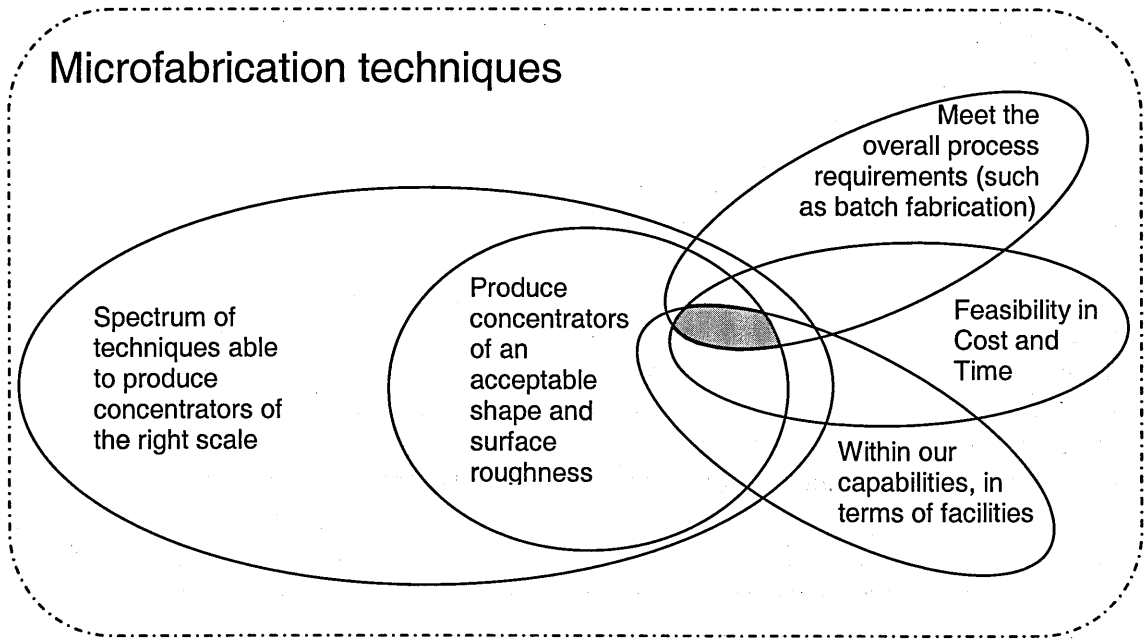


Figure 3.9 The choice of the most promising technique highly constrained by a series of requirements pertaining to needs of a different nature. The grey area identifies, symbolically, the intersection of constraints. This intersection might not exist, as the sets might not intersect.

It is anticipated that approximating exact contours and achieving smooth surfaces will represent the hardest requirements to meet. Although a high impact technique such as powder blasting is capable of very high etch rate, it was excluded due to the relative immaturity of process application to silicon, the low quality of the surfaces and the difficulty in controlling the contours [*Wensink et al, 2000*]. Furthermore, a technique that etches silicon at a fast rate is required, but it has to stop gently once the membrane that contains the active elements is reached. This rules out etching methodologies with inherent low selectivity such as the ones based purely on ion beams [*Madou, 2003; Chapter 2*].

The followings constraints are imposed in order to make the route compatible with the overall device building process.

1) BATCH FABRICATION: The device wafer contains 45 arrays of 16 by 16 elements for a total of 11520 active elements. Each element must be coupled to the respective

concentrator cavity. A fabrication method is needed that could produce all these cavities in batch. This definitely rules out contact microfabrication techniques such as microdrilling and micromilling. In fact, ultraprecision machining by using numeric controlled tooling machines is the only technique that has a proven capability to achieve 3 – d features in single-crystal Silicon [*Weck et al., 1997*]. However, it would be inconceivably time consuming if applied to the production of such a large array of structures. Furthermore, the progressive approximation to the compound parabolic concentrator is likely to require a trial and error approach. This entails the chance of varying the cavities contours many times and excludes the use of techniques that would need a permanent expensive mould (e.g. hot embossing, injection moulding or electro-discharge-machining).

2) WAFER THICKNESS: Single crystal silicon wafers are commonly available in a range of thickness. A thickness of 500 – 600 μm can be considered as the upper limit above which machining through-the-wafer cavities with a non-contact technique becomes difficult.

3) LAYOUT PITCH: The pitch is already constrained to specific values because of the subsequent flip-chip bonding step [*Whatmore, 1991*]. The dimensions of the CPC must adhere to this pitch requirement. The CPC families of figures 3.5 and 3.6 possess suitable entry apertures. The problem of matching the acceptance angle of the CPC with the cut-off angle of the incoming power distribution will be detailed the results part. As the length of the CPCs decreases, their concentration ratio decreases because $C = [\ 1 / \sin(\theta)\ ])$. Looking at figures 3.5 and 3.6 there do not seem to exist CPCs with a suitable wafer thickness that maintain high collection efficiency. In figure 3.5, for example only the CPC with $\theta = 23$ degrees satisfies both requirements of pitch and depth. For this CPC design the maximum theoretical concentration ratio is a mere 2.6. Fortunately one can add a degree of freedom in CPC design and relative choice by introducing the concept of truncation.

Truncation is an alternative solution to the problems of concentrator's fabrication. In particular, truncation leads to a reduction in aspect ratio (i.e. lateral dimensions divided by depth of a cavity). As usual, ray tracing may be used to assess the concentration ratio of truncated 3 – d systems. However, equations were derived to give the length and width of a truncated collector as a function of the truncation angle for 2 – d CPCs [*Welford and Winston 1989, Chapter 5*]. These equations are employed here according to the formulation given by Carvahlo et al. to calculate the ratio between the new entrance width ($2a^T$) and the exit width ($2a'$) [*Carvahlo et al., 1985*]. Similar formulae will be employed in the results part to calculate the expected performances of a series of truncated CPCs (section 5.5). The a^T / a' ratio (i.e. the geometrical concentration ratio) is plotted it as a function of relative length for different CPC profiles in figure 3.10. From the plot it is evident that one third of CPC length can generally be eliminated without appreciable loss in concentration ratio.

In this section, many microfabrication techniques were excluded a priori since they are not expected to meet the various requirements of the application or the constraints of the process. Little available choice is left: non-contact techniques based on high-density plasma etching seem to represent a route worth pursuing. Laser micromachining

although promising, was discarded because it was scarcely affordable and because the technology was not available. Furthermore, laser micromachining is a technique entailing physical erosion, unsuitable for a gentle etch-stop on a thin oxide membrane [*Rizvi et al., 1999*]. Routes with a stronger chemical nature were sought in order to achieve high selectivity. Gas etching (XeF_2 based) is known to yield isotropic etching [*Chu et al., 1997*]. XeF_2 etching has therefore narrow versatility. There was little interest in acquiring the equipment and the route was not investigated further.

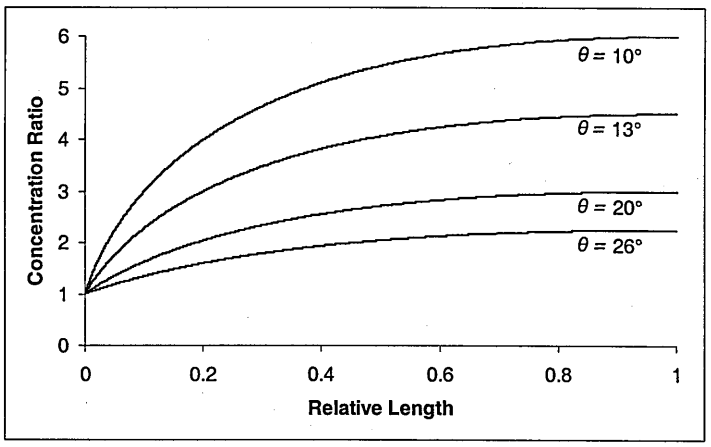


Figure 3.10: Decrease of geometrical concentration ratio for 2 – d CPCs with different acceptance angle (i.e. different geometry) as a function of truncation length

Recent evolution in Reactive Ion Etching equipment and chemistry has allowed the development of processes that couple high silicon etch rate with minimum oxide and photoresist mask erosion and optimal uniformity [*McAuley et al., 2001*]. An overview of these techniques is reported in section 3.3, where it will be shown how most of the constraints and requirements of figure 3.9 may be effectively met. An Inductively Coupled Plasma reactor [*Ashraf et al., 2000*] had been acquired by this group at Cranfield University a few months after this research started. For this reason, at that moment, a technique based on high-density plasma seemed to represent the most suitable route for producing the concentrators array. The applications of the technique to microfabrication of 3 – d microstructured cavities will be treated the following sections of this chapter. In section 3.4 the literature concerning the use of 3 – d structured sacrificial masks will be reviewed. Subsequently, published attempts to produce contoured cavities using conventional binary masks will be analysed in section 3.5.

3.3 Deep Reactive Ion Etching Techniques based on Inductively Coupled Plasmas

Plasma is defined as a homogeneous state of matter, made of particles of different nature, charge and distribution. All these particles are subjected both to macroscopic electromagnetic fields (externally applied) and to microscopic fields generated by the mutual interactions of the same particles. These forces affect the collective behaviour of gaseous plasma. Plasma electrodynamics is a complex field of physics (see e.g. [*van Roosmalen et al., 1991*]): no detailed discussion is required here; neither would there be enough space. In this section, some basic concepts will be introduced as a background for the presentation of the literature on silicon etching.

In capacitively coupled plasma, a collimated, steady beam of ions is induced normally to every surface immersed in plasma, thanks to the formation of capacitive "dark sheaths". The flux of ions may play different roles in the surface reactions depending on the mean energy of the beam. Generally speaking, as the pressure in the process chamber increases, the energy of the ions decreases and their angular distribution function becomes less sharp (because they are subjected to a higher degree of scattering). At the pressures typical of the Reactive Ion Etching processes for bulk micromachining, the energy of the ions is low enough to prevent any direct sputtering of the etching material (e.g. silicon) [*Ashraf et al., 1999*]. On the contrary, the etch rate due to surface chemical reactions with radicals increases with the reactant concentration and hence with the density of the plasma. Unlike the ions, the radicals, which generally do not possess any charge, tend to display an isotropic distribution: chemical etching is inherently not directional. Also the selectivity towards the mask depends on the nature of the etching mechanism: chemical etching may show maximum selectivity towards slowly etching layers (such as the photoresist or oxide). On the contrary, the etching induced by a physical mechanism (due to ions) is less selective.

The highest etch rates for silicon were achieved by using fluorine etchants due to the favoured formation of the by-products [*Flamm et al., 1981*]. In Reactive Ion Etching, anisotropy is achieved thanks to the synergetic action of ions and etching radicals. Working at pressures lower than 50 mTorr is desirable for many reasons. Firstly, it yields an ion flux with sharp angular distribution and high energy, thereby improving anisotropy and profile control for cavities with large depth or aspect ratio. Secondly, low pressure enhances volatilisation of by-products (e.g. SiF_4) and reduces coating deposition and contamination. Unfortunately, the etching of silicon in fluorine is a process that shows predominant chemical nature, so that the etch rate is directly dependent on fluorine flow. (On the other side, the flow is related to the density of fluorine in the bulk of plasma.) It is clear that, as pressure decreases, the fluorine density decreases and so does the etch rate. On the contrary, working at high pressure reduces the energy of the ion flux below the anisotropy threshold and induces loading. (In a loaded process, the etch rate decreases when the surface of unmasked silicon increases.)

In a conventional parallel plate capacitor, it is simply not possible to increase the power indefinitely in order to accelerate the ions: this would result in a strong lack of uniformity across the wafer area and a dramatic decrease in selectivity. To couple fast etch rate with high selectivity, anisotropy and uniformity, high density plasma sources

that work at low pressures were developed at the end of the 1980s [*Ogle, 1990*; *Keller and Foster, 1993*]. These technologies were first developed for decreasing the critical dimensions of vias in microelectronics while increasing the dimensions of the wafers processed [*Comello, 1993*]. Subsequently, they have been successfully applied to the etching of deep features. In ICP sources, the electrons are excited by coupling with the electromagnetic field originated by a coil that runs around the process chamber. Capacitive coupling that would lead to inhomogeneous ion distribution is avoided as the energy is transferred inductively [*Bhardwaj and Ashraf,1995*]. More information about the ICP dry etching equipment acquired by our group is reported the experimental part in section 4.3.1.

The use of high-density plasma in the 20 – 50 mTorr range is not enough to assure unidirectional etching. On the contrary, it was shown how, under these conditions, the contribution of direct physical sputtering of silicon would be minimal (or absent) and etching would be inherently chemical and therefore not directional, leading to (almost) isotropic etching profiles [*Ashraf et al., 2000*]. This was unacceptable for the MST community: they were seeking for a highly anisotropic etching technique that could allow large scale integration of very deep and narrow features. Deep trenches with straight sidewalls were chiefly important for comb actuators and inertial sensors: two leading applications with a major commercial drive (see e.g. [*Rai-Choudhury, 2000*]). In order to achieve deep cavities with straight sidewalls, a mechanism had to be introduced to induce anisotropy.

Two different successful methods were devised. The cryogenic method entails the introduction of passivating species in the mixture [*deBoer et al.*, 2002]. For example, CF_2 was shown to cause deposition of a carbon-based polymer over silicon surfaces. Oxygen radicals may induce the growth of a SiF_xO_y coating [*Elwenspoek and Jansen, 1998, Chapter 12*]. Under ordinary conditions, this coating may be too volatile to cause a serious decrease in etch rate. On the contrary, at cryogenic regimes, volatility drops: the deposited species stick onto the surfaces unless the local action energy supplied by the ion beam facilitates their eliminations. Since the ion flux is highly collimated, the etching tends to become unidirectional. On the other hand, the ICP equipment our group recently purchased runs a process that promotes anisotropy in a different way. This method was created at Bosch GmbH (hence the designation as the "Bosch Process") [*Larmer and Schilp, 1993*] and subsequently developed by STS ltd. for the Advanced Silicon Etching (ASE ©) process. The room temperature process consists of a sequence of passivation and etching steps, as illustrated in figure 3.11. During the passivation step (figure 3.11-*left*), an organic fluorocarbon coating is deposited onto all the surfaces from carbon-fluoride precursors [*Bhardwaj et al., 1997*]:

$$n\mathrm{CF_x^{\cdot}} \rightarrow n(\mathrm{CF_2})_{ads} \rightarrow n(\text{-}\mathrm{CF_2}\text{-})_{ads} \qquad (3.10).$$

Each passivation step is then followed by an etching step (figure 3.11-*right*), during which the coating is locally removed by the synergetic action of the ion flux and the fluorine radicals:

$$n(\text{-}\mathrm{CF_2}\text{-})_{ads} + \mathrm{F^{\cdot}} \xrightarrow{(\mathrm{SF_x^+})} n(\mathrm{CF_2})_{ads} \xrightarrow{(\mathrm{SF_x^+})} n\mathrm{CF_x^+} \qquad (3.11).$$

Once exposed, the silicon is chemically etched by fluorine radicals,

$$\mathrm{Si} + \mathrm{F^{\cdot}} \rightarrow \text{Si-}n\mathrm{F} \rightarrow (\mathrm{SiF_x})_{ads} \rightarrow \mathrm{SiF_x} \qquad (3.12).$$

Reaction 3.12 advances only on those areas deprived of the coating (figure 3.11-*right*). The reaction of coating consumption is activated by the ion beam, which has a sharp angular distribution function. In this way, a balanced alternation of etching and passivation prevents the etching on the silicon sidewalls, yielding high anisotropy even for very deep and narrow structures. The use of unbalanced processes (with passivation or etching times in excess) for producing sloped sidewalls will be treated in section 3.5.

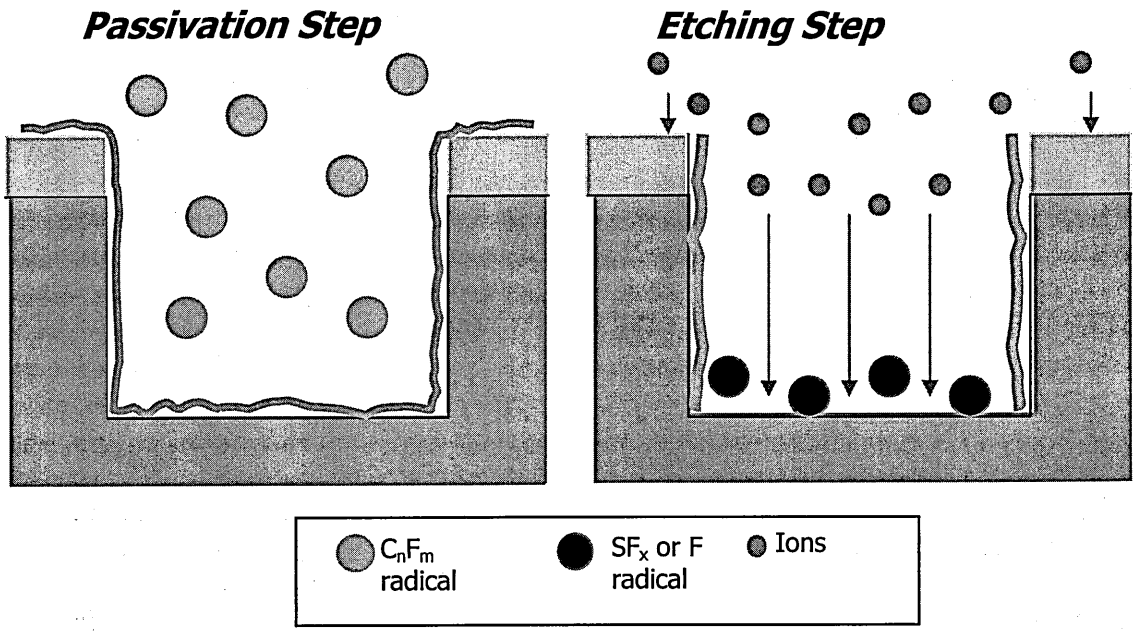


Figure 3.11 The mechanism of Advanced Silicon Etching developed by STS after the Bosch Process

Applications of this technique were presented as early as 1997 [*Bhardwaj et al., 1997*]. The capabilities were: etch rate from 1.5 to 3 μm/min; selectivity to thermally grown oxide from 120 to 200; selectivity to resist around 50 to 100; feature size from 1 to above 500 μm; and finally, etch depth up to 800 μm. Comparing this performance with the constraints reported in section 3.2 it is easy to see how the ASE process meets all the requirements for CPC microfabrication.

The major drawbacks affecting the ASE process are the following [*Elwenspoek and Jansen, 1998; Chapter 12*]:
1) Aspect Ratio Dependent Etching (ARDE). Generally, for a well balanced anisotropic process, the etch rate decreases with the aspect ratio (depth / width) of the cavities. Different causes were adduced for this phenomenon affecting all deep dry etching techniques. A general review and discussion are in [*Bailey and Gottscho, 1995*].
2) Bowing and tapering of profiles. These deviations from anisotropy were ascribed to ion deflection by the sidewalls and are prominent in very narrow trenches [*Elwenspoek and Jansen, 1998; Chapter 14*].
3) Bottling. This defect leads to a large undercut in the mask. It is typical of very deep features and it is due to the large number of ions that deviates from the collimated trajectory and hits the sidewalls [*Elwenspoek and Jansen, 1998; Chapter 14*].

Process optimisation and sidewalls evolution control have been achieved in the past by extensive experimental investigation. Nowadays analytic, phenomenological and experimental models are employed to integrate the experimental analysis. Modelling of plasma etching is a complex field that has originated hundreds of papers and at least three successful commercial software packages. Some recent reviews of the state of the art in the simulation of plasma processing may be found in [*Meeks and Ho, 2000; Sukharev, 2002*]. An older but very articulated review on the simulation of all plasma processes in general is in [*Kline and Kushner, 1989*]. As for every complex system, there are different levels of modelling. An overview of these levels is sketched in figure 3.12, with an indication of the sphere of competence of each model. The level of complexity and the aspect of the process addressed vary from model-to-model. Similarly, the purpose (i.e. the application) of the models may vary: general models or models based on fluid dynamics are generally used for reactor design or optimisation whereas feature scale level simulation is required to predict and control the evolution of cavities profile.

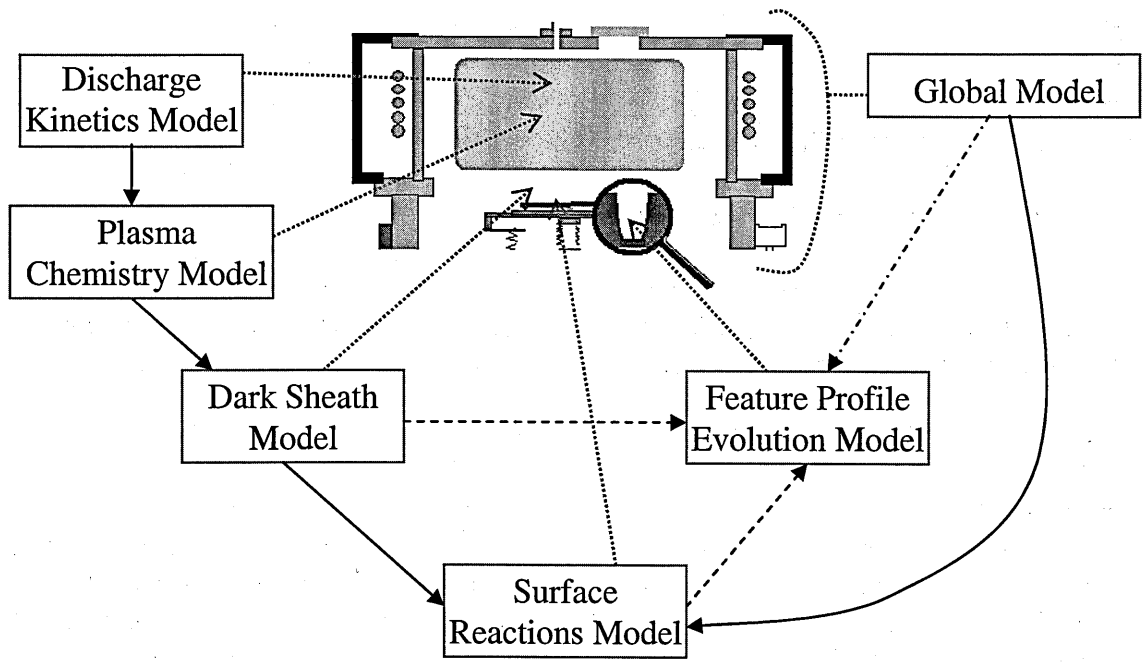


Figure 3. 12 Hierarchy of plasma etching models with indication of the different phenomenology they address within a reactor. The connecting arrows indicate that the output of a model can be used as an input for the model indicated.

Simulation can be accomplished at the scale of the entire reactor, the local sheath or the feature micro-reactor. A model may address the physics or the chemistry of the process (or both). Global models address the fundamental physics and chemistry of plasma bulk. Global models and other reactor scale models may yield the distribution of ion and neutral fluxes to be used as a boundary condition for sheath or topography (feature scale) simulators. An advantage of global models is that operating parameters (such as pressure, gas mixture etc) can be input directly. As a model increases in complexity and addresses more specific parts of a reactor, the approach becomes somewhat removed

from the fundamental physics and the input becomes removed from the direct process settings. For example, a model that addresses the electrodynamics of the dark sheath may need the distribution of the particles of interest in the bulk of plasma as an input. Similarly, the simulation of surface chemistry kinetics requires the local flow of all the interacting species. These inputs have to be generated either using a model of higher hierarchy or experimentally assessed by using specific diagnostic techniques (such as mass spectroscopy).

Feature-scale level is of particular interest for this research since it is aimed at controlling profile evolution. The simulation of etching at the feature level requires knowledge of the local etch rate as a function of the energy and angular distribution of ions and reactants at the entrance of the cavity (sample surface) and within the cavity itself. An adequate model of the kinetics of surface reactions is also necessary. Since the etch rate is a complex function of time and spatial coordinates, it is not practical to calculate the integrated analytical expression for the evolving surface. On the contrary, most simulation tools compute the surface step by step, using surface advancement algorithms. There is a large gap in the integration between the levels of plasma simulation due to the enormous variation in the scale of space and time across the different aspects of plasma phenomenology. Simplifications apply often to feature scale level modelling: if the required input cannot be predicted or measured, a completely phenomenological model can be used. In this case, all the fitting parameters of the surface advancement algorithm are experimentally assessed.

In section 9.3 a simple qualitative model is presented to address the feature-scale reaction of fluorine with silicon. The model is built on various feature-scale models presented in the literature.

3.4 3 - d structures obtained by using 3 - d masks

In section 3.2, suitable techniques were chosen for micromachining arrays of concentrators in silicon wafers. Aiming to identify methods that possess the capabilities of producing 3 - d structured cavities of the required scale and shape many available microfabrication techniques were reviewed. The technique pursued, it was stressed, needs also to be versatile, fast, repeatable and suitable for batch fabrication and optimisation by trial and error procedure. All the above constraints, related to the device fabrication process and the requirements of the application, pushed the choice towards the use of microfabrication methods based on high-density plasma etching. The route surveyed in this section entails the use of intermediate masks, which contain the 3 - d features. These sacrificial masks are generally made of photoresist. Their contoured features can be transferred into the silicon substrate by anisotropic dry etching as the mask is consumed. The method, schematised in figure 3.13, consists of two main steps: deposition and patterning of a sacrificial mask and subsequent unidirectional (or fully anisotropic) transfer.

This section is divided into four subsections. Section 3.4.1 briefly reviews the techniques available to obtain 3 - d photoresist features on silicon wafers to be used as a sacrificial layer. Many procedures for structuring 3 - d masks on various substrates can be found in literature. Although most techniques meet the requirements presented in

section 3.2, fewer among them are time or cost effective and within the capabilities of the available facilities. Subsequently, the transfer of 3 - d features into the substrate is considered in section 3.4.2. It is clearly showed in figure 3.13 how the final depth of the cavities etched in silicon is far higher than any achievable mask thickness. The concentrators are cavities hundreds of microns deep whereas most commercial photoresists are optimised for the production of layers thinner than a few tenths of microns [*Madou, 2003, Chapter 1*]. (A notable exception is represented by the SU8 photoresist [*Bogdanov and Peredkov, 2000*], which is unsuitable for the process, for reasons that will become clear in the following.)

It can be seen in figure 3.13 how the 3 - d features in the mask end up being vertically stretched in the substrate. The extent of the deformation depends on the ratio between the etch rate of the substrate and the rate of consumption of the mask (selectivity). Unlike 3 - d masks production, no previous experience of transfer of 3 - d structures at high selectivity was found in the literature: 3 - d features such as blazed gratings and microlenses have been successfully transferred into inorganic substrates from 3 - d organic masks in the framework of binary optics, but at very shallow etch depths (i.e. selectivity below or equal to 1). The conclusion of the survey will be that, given the scarcity of experience collected from the literature, 3 - d mask transfer at the very deep scale (hundreds of microns) lies at the forefront of research in the MEMS community. Control over process outcome is chiefly important for obtaining the required shape. This entails the capability of predicting the outcome of each single process step as a function of the input variables. The physics of the process and the potential for process modelling and simulation represents the subject of section 3.4.3. After the essential literature has been reviewed, a road map for the experimental trials is drafted in section 3.4.4.

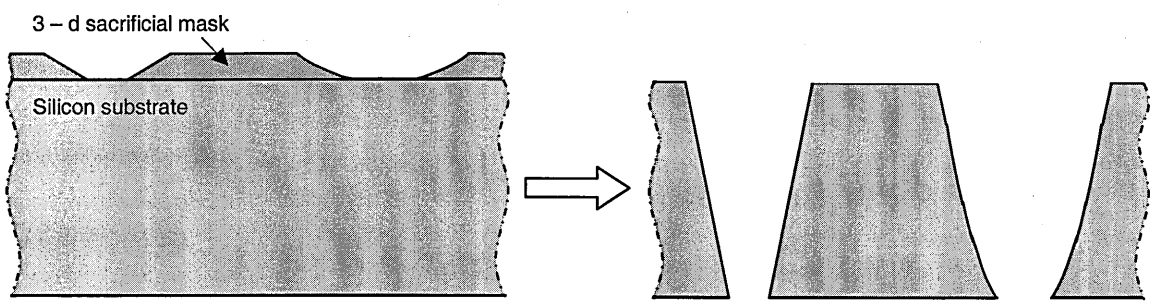


Figure 3.13 **Schematic of 3 - d bulk micromachining by transferring 3 - d structures from a sacrificial mask into an inorganic substrate using deep unidirectional etching. The thickness of the mask is exaggerated respect to the final depth after etching**

3.4.1 *Deposition and patterning of 3 – d contoured photoresist masks on inorganic substrates*

Before reviewing the techniques for 3 – d mask patterning, it is opportune to assess the ideal geometry for a mask that, once transferred into the substrate by dry etching, would originate arrays of cavities suitable to be used as concentrators. The CPC (or an approximated contour with similar geometry) is the shape eventually sought. Families of suitable CPCs were reported in figures 3.5 and 3.6. It can be observed how the entry

aperture diameter would be in the range 400 to 600 μm and the exit aperture diameter would vary between 100 and 150 μm. The silicon wafer is expected to be 400 – 600 μm thick. To achieve a similar geometry by purely unidirectional etching, with reasonable selectivity values (50 to 70) the mask thickness has to range between 5 and 12 μm (if it is completely consumed) [*Ashraf et al., 2000; Bhardwaj et al.*, 1997]. A suitable mask would contain 3 – d contoured holes with aspect ratio less than 0.05. The rim of these cavities will be 100 – 200 μm wide: thus the aspect ratio of the contoured part will be less than 0.12. It is impossible to render such feature graphically while maintaining the same scale between width and depth, therefore no sketch is presented. The actual mask cross section is similar to the mask reported in figure 3.13, maintaining the same horizontal scale but dividing the thickness by 8. An approximate idea of the required mask shape is important in order to identify the methodologies that are likely to yield suitable results.

As previously introduced, the research in the production of contoured features in photoresist on inorganic substrates is a well-established field, which started more than a decade ago for binary optics applications [*Veldkamp and McHugh, 1992*]. Aiming to the production of diffractive lenses and blazed gratings, the literature is generally focused on features tens of microns wide and less than a micron deep [*Veldkamp and McHugh, 1992*]. The aspect ratio was generally less than 0.1. The more recent advent on the market of photoresist materials that can be deposited in layers up to many micrometers thick and the emerging of new applications allowed an increase in the aspect ratio up to 4 ~ 5 [*Wagner et al., 1995; Rotich et al., 1998; Gimkiewicz et al., 1999*].

It seems reasonable to divide the techniques for obtaining 3 – d photoresist features on the basis of the means by which the complex contours are imposed onto the photoresist layer. The more widespread and consolidated set of techniques entails modifications to the traditional photolithographic patterning process. Methods of more sparse evidence in the literature involve photoresist deformation. The deformations can be thermally induced (flowing) [*Daly et al., 1990; Popovic et al., 1988*] or mechanically imposed (moulding) [*Gale, 1997*]. Less conventional techniques, such as microsterolithography [*Bertsch, 2001*] and direct writing (using laser or electron beams [*Horiuchi and Yaguchi, 2001*; *Steingrüber and Ferstl, 2000*]) were not considered, since these methods require specific apparatus (not affordable within this research project). Furthermore, these techniques are more suitable for prototyping than manufacturing very large arrays.

Implementations of the conventional photolithographic process for 3 – d contouring are finalised to induce planar variations in the dose of energy provided during exposure, i.e. a varying degree of advancement of the photonic induced reaction. For positive diazotype photoresist (the type used in this research), this variation results in local differences in the thickness of photoresist residual after development. The physics of this process will be introduced section 3.4.3. The procedure for obtaining local variations in exposure dose may concern the modality of exposure (introducing supplementary steps into conventional binary photolithography) or being limited to the use of a special kind of mask (grey scale masks).

The multiple photolithographic process (the first technique developed historically) consists of consecutive repeated exposures with binary masks (figure 3.14) [*Veldkamp*

et al., 1992]. This results in a stepped profile that approximates the continuous curve: the higher the number of steps (and the number of masks) the better the approximation. However, the large number of masks required entails a very large cost, particularly if these are produced in the traditional way (by e-beam patterning). Low-cost methods have been used for the fabrication of diffractive optical elements [*O'Shea et al., 1993*]. Desk-top publishing techniques enable fast and low cost rapid generation of binary masks on acetate or photographic film and, by subsequent photoreduction, onto photographic glass plates. These cheap masks can only achieve a poor resolution. (Critical dimension is above 40 μm for reproduction onto acetate and 5 μm on high precision photographic glass plate [*O'Shea et al., 1993*].) This low cost technique increases the flexibility of the process, opening the route for trial and error implementation. An alternative method employs a dynamic exposure, where the sample is actually moved between exposures. In no way the latter method could be viable for producing features with cylindrical symmetry: it was discarded at an early stage.

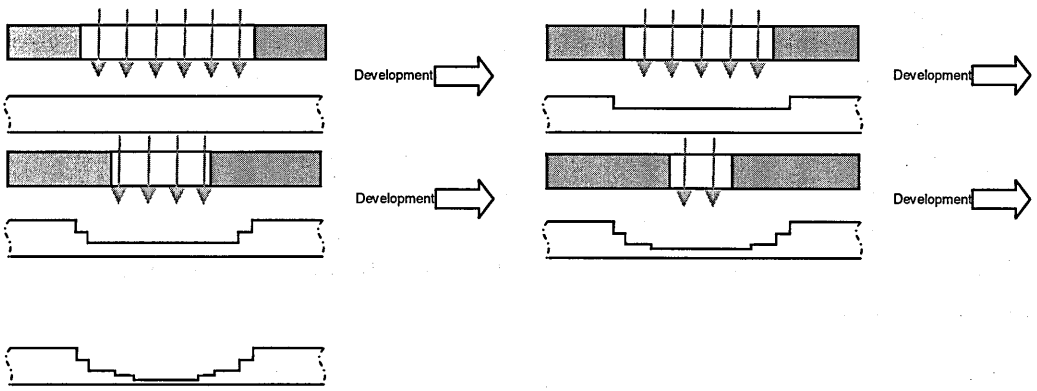


Figure 3.14 Schematic of the multiple photolithographic process

A major drawback of the multiple photolithography process is the need for various masks and relative alignment steps. On the contrary, grey scale lithography (figure 3.15) achieves planar variations of local exposure dose in a single step by using special types of masks that possess variable transmittance. The intensity I_0 reaching the mask is modulated by the transmittance T, so that the intensity at the photoresist top surface (I) is equal to $I_0\, T\,(x, y)$. The 3 – d profile of the final photoresist layer is encoded in a 2 – d array on the grey masks (see section 3.4.3). There are currently two ways of varying mask transmittance.

1) High Energy Beam Sensitive (HEBS) masks represent true grey masks [*Wu, 1989*]. The HEBS glass becomes opaque upon exposure to an e-beam. The opacity is due to the reduction reaction of Ag^+ ions in silver-alkali-halide crystal specks dispersed in the glass matrix. The optical density of the crystal decrease upon exposure as the reaction proceeds. Local transmittance decreases with increasing e-beam exposure dose. The dimension of these complex crystals is generally less than 10 nm (i.e. well below the resolving power of conventional photolithography). Therefore, the grey tone is almost perfect and no graininess can be observed in the resulting photoresist contour [*Däschner et al., 1996*]. More information on the characteristics and use of HEBS masks is reported in the experimental part (section 4.3.2) and in appendix A. Due to the enormous cost of producing a single HEBS mask, the process must be completely set up

and optimised before the HEBS mask is designed and produced. (In other words the calibration curve of photoresist remaining thickness vs. local mask transmittance has to be fully assessed.)

2) Half tone masks reduce the intensity by diffracting the light on a grid with holes so small they cannot be resolved by the optical system (smaller than 500 nm for contact photolithography). The transmittance is increased by increasing the size (Pulse Width Modulation) or the pitch (Pulse Density Modulation) of the holes, or both (figure 3.16 [*Opplinger et al., 1994*; *Wagner et al., 1995*]). Traditional chrome masks (produced by e-beam lithography) have an elevated cost that hardly allows trial and error procedure [*Opplinger et al., 1994*]. The process parameters must be optimised and the optimal transmittance assessed before the mask is designed [*Yao et al., 2000*; *Wagner et al., 1995*]. However, simulation tools are not satisfactory enough: experimental assessment and trial and error optimisation is often required [*Yao et al., 2000*; *Purdy, 1994*; *Wagner et al., 1995*]. Projection photolithography in a stepper is usually employed for best results. A low cost alternative is a three-stage process, which entails the reproduction of a coarse digital grating onto polymeric support and a subsequent photo-optical reduction on high precision photographic glass plates [*Sulesky and O'Shea, 1995*]. This technique is fast and cheap and can be used for process set up. The agility of the procedure allows experimental trial and error optimisation of the process, through fabrication of numerous masks. Once the parameters are optimised and the suitable transmittance modulation curve is found, the results can be exploited for designing an expensive chrome mask.

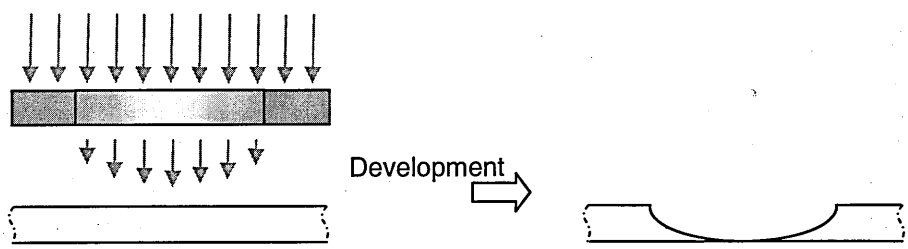


Figure 3.15 Schematic of grey scale photolithographic process

It was affirmed that the main limitation of multiple photolithography is that a continuous profile cannot be obtained directly. Similarly, grey scale masks must necessarily contain a finite number of steps: up to 500 for HEBS masks [*Canyon Materials, 2004*] and 10,000 for half tone masks [*Purdy, 1994*]. (But often only a few hundred grey levels are practically used [*Wagner et al., 1995; Nicolas et al., 1998*].) The high development contrast, typical of most photoresist materials, magnifies the discontinuity among the grey levels: ripples, kinks and steps can be easily observed in the 3 – d contours finally produced. This effect is worsened when half-tone masks are used because the reticule is coarser [*Waits et al., 2003*]. It has to be said that the presence of steps becomes crucial for high aspect ratio features. Conversely, this represents a lesser problem for the CPC-mask geometry presented at the beginning of this section: a maximum aspect ratio of 0.12 was contemplated for the sacrificial mask. For such an aspect ratio, for a 10 μm thick photoresist layer, even using a mere 50 grey levels, the average height of each step would be 0.2 μm, whereas the average width will be 10 to 15 μm (still a ratio of less than 0.02). It is true that the CPC presents a slope

varying continuously from 0 to 90 degrees, but the presence of steps may represent a problem for the most external rim of the CPC, which would be probably eliminated anyway in the design stage after truncation. Finally, blurring the projected pattern during exposure may improve contour smoothness. Blurring may be achieved by defocusing in a stepper [*Yao et al., 2000*] or by increasing the gap between wafer and mask in proximity printing. Post exposure treatments (thermal or chemical) may also be effective in eliminating ripples or steps [*Yao et al., 2000; Stern et al., 1997; Gimkiewicz et al., 1999*].

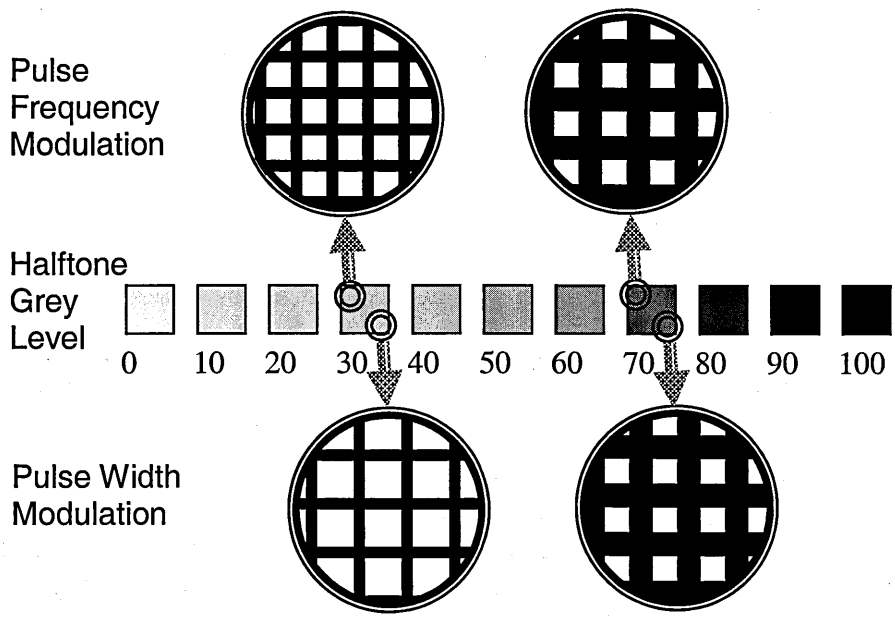


Figure 3.16 Principles of coding a grey tone in a half-tone grey mask. Redrawn from [*Opplinger et al, 1994*]

Economical half-tone masks, obtained by photographic reduction of grey reticules onto high precision glass plates are particularly coarse, the pixel dimension being larger than 5 μm [*Sulesky and O'Shea, 1995*]. The pixels are coarse enough to be resolved by photolithography. A projection printing system, which could de-magnify the pattern at least 10 times to reduce the pixel dimension below the resolution limit. If such a system is not available, the pattern shadow onto the photoresist must be blurred so that the overlapping of diffracted shadows, cast from the edges of the pixels, produces the grey shade effect. In this way, also very rough half tone masks can yield contoured features [*Rotich et al., 1998*]. (Blurring, however, reduces process accuracy greatly.)

The defocused exposure suggests a very economical way of producing sloped zones on a photoresist layer with proximity exposure. If the photoresist is exposed to a binary chrome mask with a gap introduced with the modalities of figure 3.17, then the edges of the imaged features will be blurred and sloped. Although totally unsuitable for producing accurate slopes, the method is nevertheless useful for testing the general transfer of sloped contours into silicon (i.e. the second step of the process).

Another economical method for imposing sloped sidewalls to photoresist binary patterns is suggested by the post exposure treatment used for smoothing the steps. In

particular, phothoresist re-flowing by thermal annealing has been exploited to produce hemispherical shapes from circular 2 – d features [*Daly et al., 1990, Popovic et al., 1988*]. Replication techniques (moulding, embossing and casting) impose a shape on the sacrificial mask without the need of a photolithographic step. These methods are largely established: a review is in [*Gale, 1997*]. Replication techniques need specific equipment and a 3 – d structured master mould, which leaves little room for trial and error. The master needs to be micromachined with the correct 3 – d contoured surface.

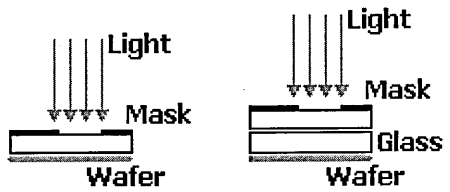


Figure 3.17 Modality of blurring mask pattern in shadow exposure

To summarise this brief survey, many methods exist to deposit and pattern sacrificial photoresist mask containing 3 – d structures. Generally the most accurate methods are costly and time consuming. More economical techniques exist. These methods produce low quality contours with a large number of defects and more evident steps, but they can be used for process set up, calibration and optimisation of exposure dose and transmission curve. Furthermore, major defects may be reduced by a blurred exposure or by post development treatment (e.g. thermal reflowing). Very cheap photoresist patterns with sloped sidewalls may be produced by blurring a conventional binary mask during exposure or re-flowing a digital photoresist pattern after development. The latter methods afford little or no control over sidewall contours.

3.4.2 Transfer of 3 – d contoured photoresist masks into inorganic substrates by unidirectional dry etching

The first stage of the 3 – d microfabrication process is well established, although not yet mature within the MEMS community. The same cannot be affirmed of the second stage: no reports were found concerning the transfer of 3 – d photoresist patterns at high selectivity to produce structures hundreds of microns deep. Traditionally, as anticipated in the introduction of this section, the selectivity of the transfer is below unity [*Stern, 1997; Opplinger et al., 1994; Andersson et al., 1990 Gimkiewicz et al., 1999*]. This means that the depth of the structure etched in the substrate is equal to or smaller than that of the original mask. Däschner et al. increased the selectivity up to 6, leading to a depth of 24 μm [*Däschner et al., 1996*]. Very recently, ramps produced in thick photoresist have been transferred into silicon by RIE with a selectivity up to 5.3 [*Waits et al., 2003*]. In [*Waits et al., 2003*] it is made apparent that roughness increases and defects intensify when the selectivity of the transfer increases. Many authors claim that the highest quality of transfer is achieved by working at unitary selectivity. It seems that the best practice would be to deposit a sacrificial mask with thickness equal to the depth of the cavity to be etched, so that there is no vertical stretching of the geometrical features and curvature. Unfortunately for cavities hundreds of microns deep (as required for the concentrators) no photoresist of comparable thickness can be used. Negative SU8 can be deposited up to hundreds of microns but patterned with straight sidewalls

[*Bogdanov and Peredkov, 2000*]. Only recently grey scaling was demonstrated using SU8 [*Kudryashov et al., 2003*]. However, this was limited to a thickness of a few microns.

3.4.3 Process modelling and simulation of the 3 – d sculpting process

The physics of the grey scale technique will be briefly discussed here. The steps of the process are indicatively exemplified in figure 3.18 for a grey scale photolithographic process. The variables to be controlled are reported beside each step, with their symbolic variation in the x direction (perpendicular to the line of exposure). The modulation of transmission will be treated in two dimensions. z is the axis of projection and x represents a radial direction.

The first step is the modulation of mask transmittance. HEBS masks allow direct control of optical density. Conversely, when half-tone masks are used, transmittance is encoded in pixels pitch or width distribution (as showed in figure 3.17). The encoding expression (T as a function of pixels size or pitch) can be obtained from first principles by using the theory of coherent light [*Yao et al., 2000*] or experimentally by trial and error producing a sequence of many half-tone low-cost masks [*Suleski and O'Shea, 1995*].

Once a suitable profile of mask transmittance is assessed as T (*% grey tone*), the photolithographic step has to be controlled. The literature presents plenty of models for photolithography simulation with various degrees of sophistication: from largely phenomenological models that approximate roughly the physics of the process to highly sophisticated software suites that address the phenomenology at the wavelength scale. The choice of a model depends on the final application of the process. The more advanced models are generally used for simulating Very Large Scale Integration processes where the critical dimensions of the patterns are comparable with the wavelength of the radiation used for exposure. The cost and time involved in the most advanced simulation tools are not justified at this preliminary level of research. On the contrary, rough phenomenological models can be directly employed to set up and optimise the process successfully if accompanied to experimental optimisation by trial and error. In this case a large number of trials is required. The results obtained at this stage are used to recursively optimise the transmission modulation of the mask produced at the first stage.

In the following, the basics physics of the photolithography process will be introduced with two aims: first, to provide the notions upon which the treatment of the experimental results of section 6.1 will be based and second, to introduce the main concepts of the photolithographic and etching processes. The elaboration will refer to the coordinate system showed in picture 3.19. This treatment follows the classic model developed by Dill et al. in the 1970s [*Dill et al., 1975*]. The phenomenology is divided into two successive steps: *exposure* (a photochemical reaction changing the nature of the film) and *development* (a surface dissolution process which removes the photoresist at a rate dependent on the ratio of inhibitor altered in the previous step).

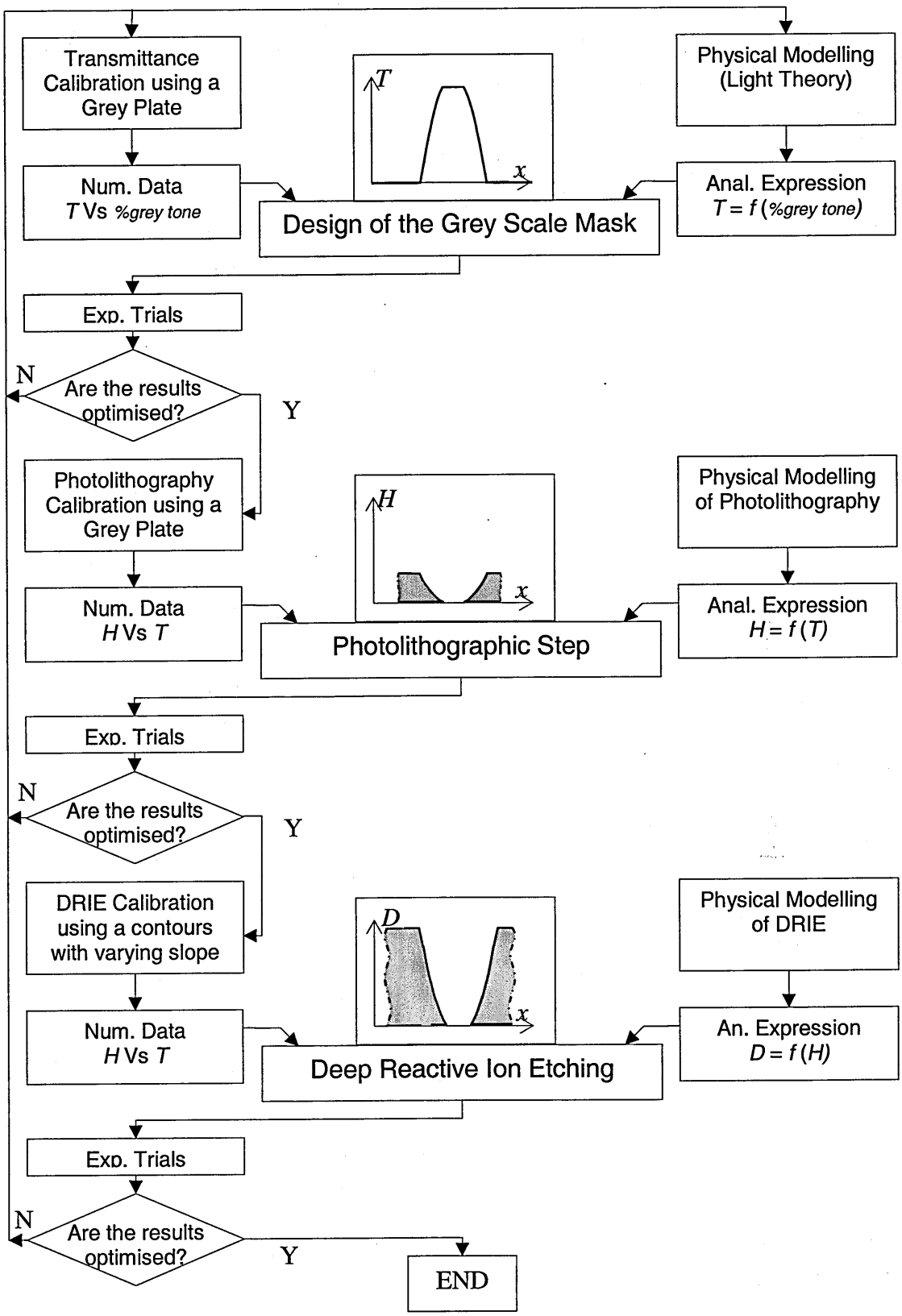


Figure 3.18 **Process flow chart of a generic process for 3 – d photoresist mask production using methods for varying the exposure dose across the film during conventional photolithography.**

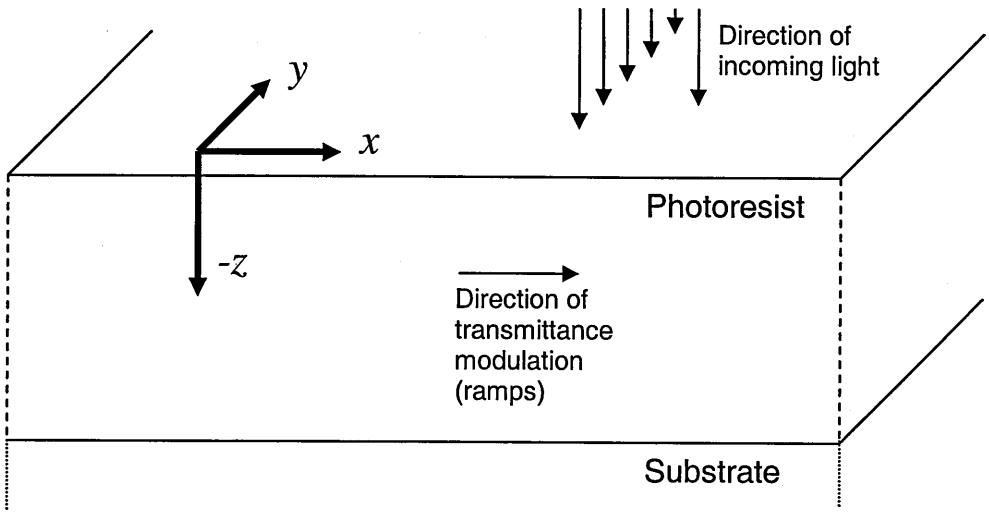


Figure 3.19 The coordinate system for the physical modelling of photoresist exposure and development

As with every commercial property formulation, photoresist materials are very complex suspensions with a composition often only partially disclosed. Positive-type photoresist can be considered, for the purposes of understanding grey scale photolithography, to contain three main components [*Madou, 2003 Chapter 1*]: a structural base-resin (which is usually a novolac-type such as the polymer formula shown in figure 3.20), a photoactive compound (a typical formulation is in figure 3.21) and a mixture of casting solvents. The photoactive compound works as a solubility inhibitor: the particles of novolac-polymer, impregnated by the unexposed inhibitor show very small solubility towards the developer (usually a mildly basic solution in water). As the photoresist layer is struck by light (figure 3.21*b*), the inhibitor undergoes decomposition to highly soluble products (figure 3.21*d*). The absorption starts from the top surface of the photoresist and proceeds towards the interface as the inhibitor is depleted. The exposed parts of the photoresist film are hundreds of times more soluble than the unexposed parts and the etch rate is directly proportional to the amount of inhibitor destroyed and therefore to the dose received during exposure. Since the absorption of photons is localised in the site of the reaction, the kinetics of exposure and development can be treated separately. Therefore, the local concentration of inhibitor (M (x, z, t)) after exposure is a sole function of the overall energy absorbed in that point. As underlined in section 3.4.1, the patterning of negative type photoresist follows a different phenomenology, which cannot be described by this model. Negative resist is therefore not immediately suitable for grey scaling.

Dill's model of exposure is mechanistic in that describes the physics of the process, under certain assumptions, with the use of three parameters (A_e, B_a and C_1), experimentally determined and typical of the photoresist material used.

The following assumptions are made:

- constant lamp intensity I_{lamp}. The transmittance (T) is modulated in x,
  $I(x,0,t) = I_0(x) = I_{lamp}T(x)$ (3.13).
- initial inhibitor uniformity;
- resin uniformity and integrity during exposure.

These assumptions allow normalisation of the model using $M(x, z, t)$ as the fractional inhibitor concentration and setting the adsorption coefficient of radiation equal to $A_eM(x, z, t) + B_a$, where A_e is the exposure dependent adsorption term [μm^{-1}] (representing the absorption by the inhibitor) and B_a the exposure independent adsorption term (the absorption by the base resin). The variation in the intensity within the dry film along the z direction is given by the extinction law of Lambert & Beer:

$$\frac{\partial I(x,z,t)}{\partial z} = -I(x,z,t)[A_eM(x,z,t) + B_a] \quad (3.14).$$

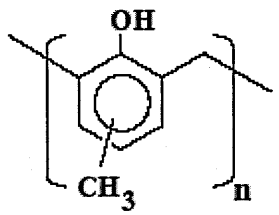


Figure 3.20 The structural formula of the typical base-resin of a positive-type photoresist

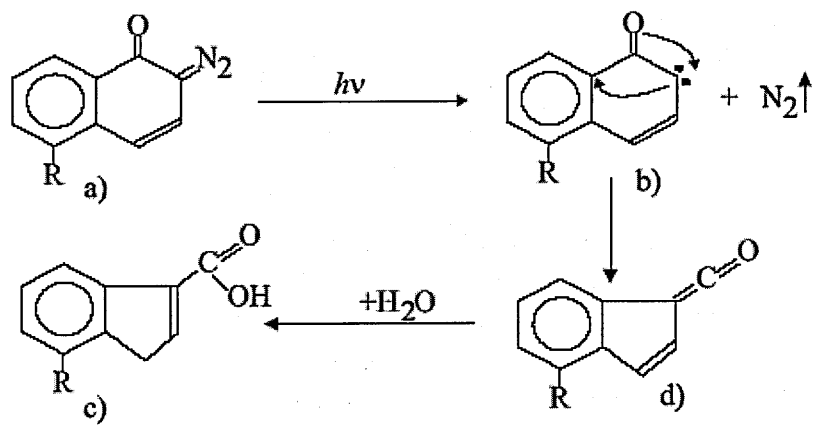


Figure 3.21 The structure of the typical diazo-component (photoactive compound) in positive-type photoresist materials and its reaction to yield highly soluble products.

On the other side, the rate of M consumption by photo-induced reaction is given by:

$$\frac{\partial M(x,z,t)}{\partial t} = -I(x,z,t)M(x,z,t)C_I \quad (3.15).$$

Where C_I represents the fractional decay rate of inhibitor per unit intensity (or photochemical quantum efficiency) in [$\mu m^2 J^{-1}$]. Equations 3.14 and 3.15 determine completely the exposure mechanism, with initial conditions $M(x, z, 0) = 1$ and

$I(x,z,0) = I_0(x)e^{-[A_e+B_a]z} = I_{lamp}T(x)e^{-[A_e+B_a]z}$. The boundary conditions are $M(x,0,t) = e^{-I_{lamp}T(x)C_I\ t}$ and $I(x,0,t) = I_{lamp}T(x)$.

Conventionally, numerical methods have been used to solve equations 3.14 and 3.15 for given A_e, B_a, C_I and boundary conditions [*Neureuther and Dill, 1974*]. An analytic solution was given in [*Babu and Barouch, 1986*] but in an implicit form not directly suitable. The parameters A_e, B_a and C_I must be provided by the photoresist supplier or have to be evaluated experimentally from photoresist transmittance using a special set up [*Dill et al., 1975*]. The initial A_e, B_a and C_I have often to be optimised experimentally by fitting them to a series of development rate curves obtained at different dose. The output of the exposure model is the distribution of relative inhibitor concentration ($M(x, z)$) along the z and x directions (y as well for a three dimensional modelling) for a given exposure time equal to t_{exp}.

The photoresist etch rate after exposure (R) depends on:
1) photoresist properties and chemistry;
2) developer nature, dilution and chemistry;
3) process settings and parameters (soft bake pre exposure or after exposure time and temperature, solution temperature, modality of developing, stirring, ageing of developer);
4) dose received during exposure, that is amount of inhibitor transformed.

Surface reaction is often assumed to represent the limiting step in the kinetic of development. Once the process is set up, the development rate can satisfactorily be expressed as $R(M)$. The form of this function is related to the kinetic of the dissolution process. Dill initially introduced an expression for $R(M)$ obtained by regression, with no physical meaning [*Dill et al., 1975*]. Many groups have tried to improve the expression for $R(M)$ by introducing the kinetics mechanism of the development. The group who developed the software simulator SAMPLE ® postulated a difference between bulk development rate and surface development rate, introducing a dependence on depth of development [*Kim et al., 1984*]. Mack postulated a steady-state regime between the diffusion of reactant to the developing surface and the surface reaction [*Mack, 1987*]. Main feature of these models is that the distribution of M has to be input in the expression of R, and thus A_e, B_a and C_I must be known. The values of the parameters figuring in the expression of development rate are usually obtained in the following way [*Fahey, 1996*; *Thornton and Mack, 1996*]:

- a series of development rate (R) measurements are taken under different exposure and development time conditions,
- the values are adjusted so to yield the variation of R as a function of depth into photoresist z (i.e. thickness residual),
- a distribution of M Vs depth into photoresist z is generated using numerical solutions of Dill's model (or with a photolithography simulation software),
- the expression of M Vs z is inserted in the experimental data of R Vs z to produce a set of experimental data of R Vs M,
- the sample of data thus elaborated are fitted with the expression for $R(M)$, obtained applying one of the above development models [*Dill et al., 1975*; *Kim et al., 1984*; *Mack, 1987*]. Least square analysis is used to optimise the parameters.

Some parameters of the first model by Dill did not possess any direct physical meaning. Subsequent models tried to express the regression parameters in some physical way so that part of them could be experimentally obtained under certain conditions [*Kim et al., 1984*; *Mack, 1987*]. (Parameters might represent, e.g. the development rate of the unexposed photoresist or the development rate of fully exposed photoresist.) Usually, the first step of this computation requires special equipment such as a Development Rate Monitor or painstaking experimental work (the so-called poor-man-DRM [*Arthur et al., 1998*]). Using an HEBS mask with hundreds of grey tones, hundreds of exposure dose data can be obtained from a single sample. Development rate curves could be easily obtained in this way.

All these early models fail in some way to address the problem of the standing waves. Standing waves are due to interference between the primary wave-front and the waves reflected from the substrate. Furthermore, those simple models were optimised for thin resist: for photoresist layers thicker than 2 microns the prediction becomes less accurate [*Arthur et al., 2001*]. Far more sophisticated photolithography models are used in current simulation packages such as PROLITH ® or SAMPLE ® [*Arthur et al., 1998*]. (SAMPLE can be used on-line at http://cuervo.eecs.berkeley.edu/Volcano/.) These models use the aerial image concept and wave propagation physics to predict the local properties of exposed photoresist and the M distribution in 3 - d. Subsequently, complex development kinetic models produce an expression for the local R. As the solution is numeric, the etching surface is advanced at each time interval using appropriate algorithms such as string methods, cell techniques or the more recent level set method. However, these advanced simulation tools are generally useful for very small features in VLSI and their use is redundant in this research. On the contrary, the simple models detailed above can be largely applied to understand the evolution of coarse features (in the order of tens of microns) without appreciable loss in approximation.

The outcome of the photolithographic step modelling is an expression of the photoresist residual thickness H as a function of mask transmittance and process set up. Once the process is optimised and settings as exposure dose and development time are fixed, H is a sole function of T. At this point, it is clear that the process can be set up for a given system and given settings in a totally experimental way by using the HEBS calibration plate (or other calibration device) to find $H(T)$ without the need to resort to physical modelling. This method requires a large number of trials, it has no predictive capabilities and lacks applicability to a different system (e.g. a different photoresist thickness or exposure dose). However, being totally depleted of physical meaning, it can be used when the material parameters used in the physical models (e.g. A_e, B_a, C_1) are unknown.

Once a satisfactory expression for $H(T)$ is known, only the relation between the etch depth after DRIE (D) and H is left to be assessed before the modelling of the 3 – d structuring process is complete. The function $D(H)$ may be obtained either experimentally or by using process simulation. In the first case a series of ramps undergo etching under different process conditions and the data are interpolated with expressions that do not possess any physical meaning. In the second case a physical model has to be used. At the end of section 3.3 the models available for the simulation of DRIE processes were briefly surveyed. It emerged that a vast number of models and

simulation tools exist, ranging from purely mechanistic to highly sophisticated. As the CPCs are relatively coarse features, there is no need for advanced models. For example, one can make the following assumptions:

1) stable etch rate and selectivity that change only slightly with process time, etch depth and features aspect ratio,
2) maximum uniformity of etch performance across wafer area,
3) ideally unidirectional process (Anisotropy = 1).

Disregarding other process deviations and random phenomena, the predicted profile is then just produced by multiplying local mask thickness (H) per process selectivity (S) and subtracting the total etch depth (ED):

$$D = H \times S - ED \qquad (3.16).$$

For a given mask contour, the slope developed after etching is therefore just driven by selectivity, as exemplified in figure 3.22. With one exception, in literature the previous examples of 3 - d masks transfer were limited to selectivity values around 1. In this case the maximum linearity is assured and mask random defects are passed on the final contour without amplification: for $S \leq 1$ the linear model of equation 3.16 is certainly suitable for predicting the shape of the etched profiles. If the experimental data show the unsuitability of a linear expression, then a more complex dependence may be introduced, e.g. a dependence on etch depth or on local slope of the etch front.

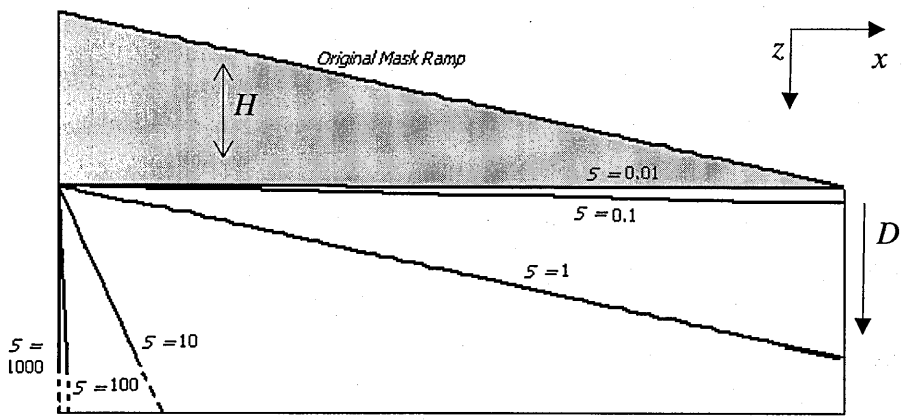


Figure 3.22: Modality of the linear transfer: for a given mask contour $H(x)$, as the selectivity (S) increases, the slope of the final feature increases. The linearity of the slope is maintained.

3.4.4 Road map for the experimental trials

The survey realised in this section allows drafting a roadmap for the experimental trials. This roadmap is sketched in figure 3.23 and will be followed in the results section (section 6.1).

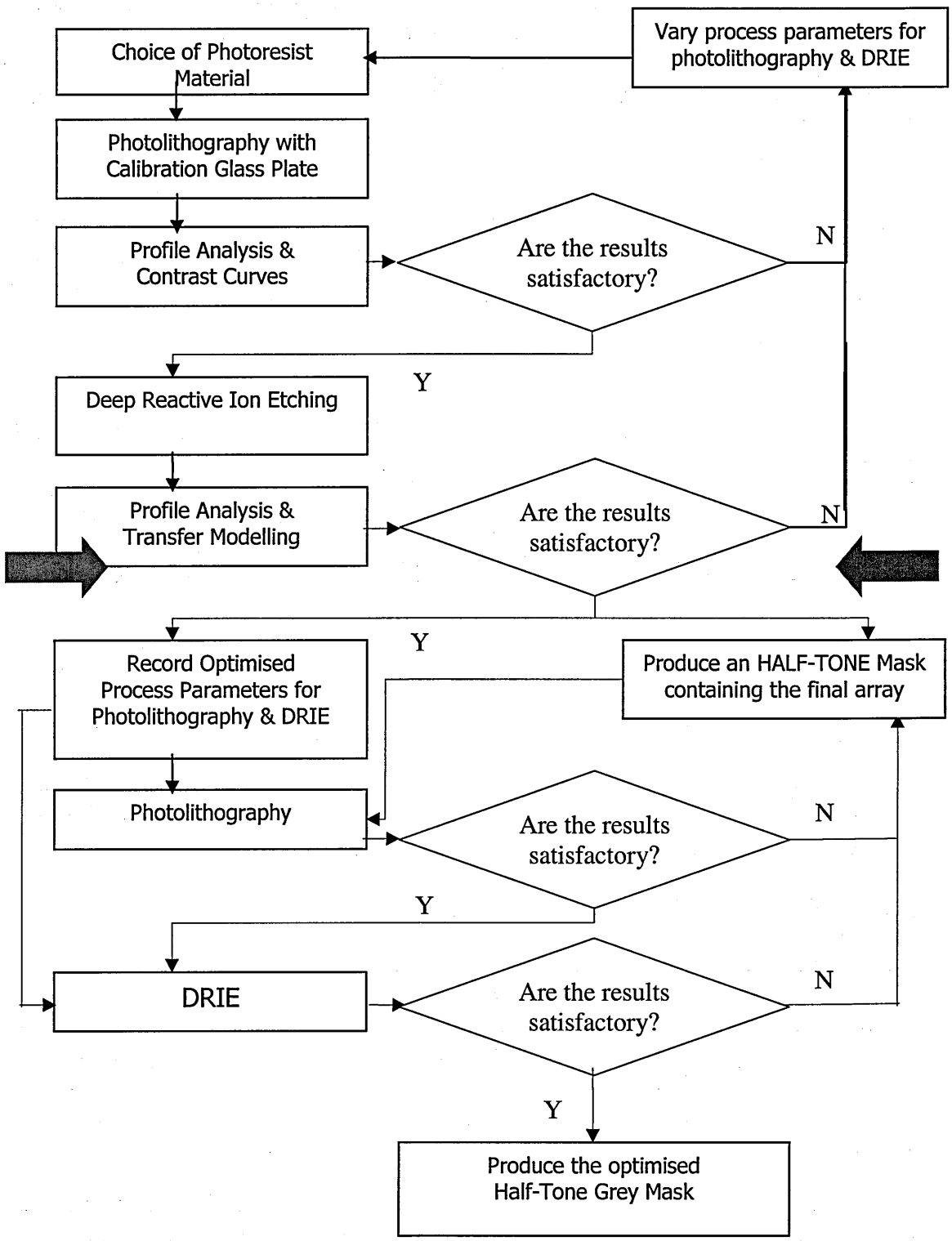


Figure 3.23 Roadmap for the production of 3 – d microstructures using anisotropic DRIE, 3 – d contoured photoresist intermediate sacrificial layers and grey masks.

The main uncertainty of successful performance seems related to the second step, i.e. the transfer of 3 – d structures at high selectivity. It is crucial to assess that the transfer is feasible and viable before embarking on setting up a grey scale process for 3 – d sacrificial mask production. To this end, a large number of samples is needed containing contoured sidewalls with different slope. These can be obtained by blurred exposure or by thermal treatment of original digital photoresist patterns (as specified above). However, a calibration HEBS glass plate was made available from Rutherford Appleton Laboratory. Although it contains features such as microlenses and blazed gratings (far from suitable for producing a concentrator cavity), the mask yields nevertheless 3 – d photoresist features in a wide range of slope, curvature and aspect ratio. The outcome of transfer at high depth/high selectivity by DRIE can be extensively tested by using the features produced by this calibration plate. Once the feasibility of the process in demonstrated, the calibration glass plate can be used to find the experimental relationship that relates the thickness of residual photoresist after development $H(x, y)$ to the original HEBS mask transmittance $T(x, y)$ for given photolithography settings and for a given photoresist. If the DRIE transfer shows satisfactory reproducibility and repeatability, then the depth after DRIE $D(x, y)$ may be experimentally related to the $H(x, y)$. This method is useful for a rough set up of the process. At a second stage, a series of half-tone masks produced in the economical way may be used to optimise the process. Finally, a single chrome mask can be produced. This mask should yield the sought 3 – d sacrificial mask, which originates, under the right DRIE conditions, the cavity that best approximates a CPC.

Unfortunately, as will become clear in section 6.1, it was not viable to go further than the first step because the process was impossible to optimise for many practical reasons. The route was abandoned after the trials of deep etching with 3 – d features produced with the HEBS mask (indicated by a couple of grey arrows in figure 3.23).

3.5 3 - d cavities directly etched using binary masks

In section 3.3 the main features of the deep reactive ion etching process were introduced. In particular, it was stated how the ions have a limited role since, at the range of energy involved, ion flux would not be able to break the bonds among silicon atoms. Indeed, studies on high density plasma etching in SF_6 showed that the nature of the etching reaction is mainly chemical [*deBoer et al., 2002; Ashraf et al., 1999*]. The etching profile tends to evolve isotropically in absence of a mechanism that could induce anisotropy. A true isotropic profile (i.e. equal etch rate in all the directions) occurs only when surface reactions represent the rate limiting step of process kinetics. When reactions are fast and diffusion represents the rate limiting step, radical etching may produce (because of flux shadowing) profiles somewhat far from the full isotropic. Due to partial shadowing of the radical flux, the lateral etch rate of a feature can be smaller than the vertical etch rate. A range of typical profiles produced during deep reactive ion etching in fluorine rich mixtures is reported, as an example, in figure 3.24 [*Singh et al., 1992*]. A detailed analysis of process kinetics and consequent etch front development is beyond the scope of this section. This section explores the versatility of the deep reactive ion etching process, which can potentially yield a range of profiles from the fully anisotropic to the fully isotropic.

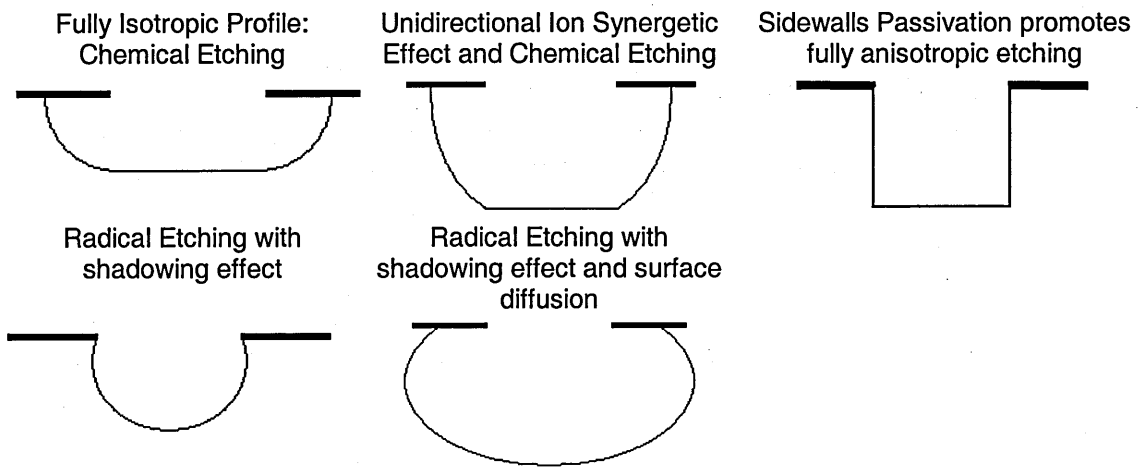


Figure 3.24 Typical profiles achieved in Deep Reactive Ion Etching depending on the main mechanism active during the process (after [*Singh, 1992*]).

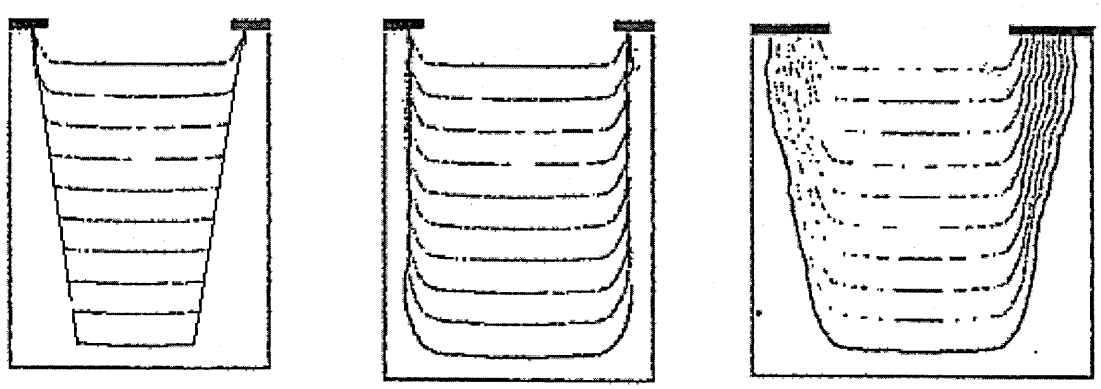
For clarity of terminology, a process (or a profile) will be denominated "isotropic" if it occurs in absence of any anisotropy promoting mechanism (e.g. passivation) independently on whether the profile is truly isotropic or not. It is important to remark that the most common etching effects that induce deviations from unitary anisotropy, such as bowing, bottling and tapering of sidewalls are not interesting for producing concentrators of the kind reported in section 3.1: these effects usually occur at very small scale (few microns) or very high aspect ratio (more than 10) [*Elwenspoek and Jansen, 1998, Chapter 14*]. On the contrary, this survey is concerned with larger deviations from anisotropy, purposely tailored to produce large 3 – d cavities with a tight control of the sidewalls contour.

The wide versatility of DRIE makes it very interesting for the production of cavities or microstructures with complex contours. In fact, this capability seems not to be fully explored in literature. Most of the applications concern fully anisotropic profiles. Sidewalls with slope near to 90 degrees (85 ~ 89 degrees) are aimed at for an easy release of cast materials when the silicon sample is used as a mould (e.g. in the DEEMO technique [*Elders et al., 1995*]). On the other hand, isotropic dry chemical etching is generally used for the release of hanging structures (e.g. polysilicon sacrificial etching). To this end, gas etchers have been recently developed that use XeF_2 decomposition to give fluorine radicals in absence of plasma [*Chu et al.,1997*]. No examples of direct use of structures obtained by dry isotropic etching were found in literature. On the contrary, applications of structures obtained by wet isotropic etching are widespread [*Zhao et al., 1999*; *Hannoe et al., 1997*]. It can be expected that wet processes will be substituted by dry isotropic etching in the near future, if XeF_2 etching becomes more affordable. Fewer examples were found of 3 – d structures achieved by modified DRIE processes (neither fully isotropic nor fully anisotropic). These examples will be reported below.

In a complex plasma environment, the shape of the etched structures is a non-linear function of all process parameters. Reliable multi scale modelling (both theoretical and experimental) is required in order to control the results, and extensive characterisation is essential for building the necessary knowledge of the process. Elwenspoek's group at

Twente University conducted a deep and extensive research on cryogenic deep etching [*deBoer et al., 1999*; *Elwenspoek and Jansen, 1998, Chapter 14*]. Unfortunately, there is no such detailed analysis for the Advanced Silicon Etching process and it may be difficult to predict the trend of sidewalls evolution when the equilibrium is removed from the kinetic balance. However, from similarity with Elwenspoek's group work, from the basic STS documentation and from the general process phenomenology reported in section 3.3, it can be roughly expected what follows:
1) Parameters variation will lead to an increase in lateral etch rate (i.e. a decrease in anisotropy) if the deposition rate of passivating coating decreases as a result of the variation. (Indeed, a feature scale model of the Bosch process confirms this trend [*Zhou et al., 2003*].)
2) On the contrary, when the imbalance leads to an increase in passivation, the thicker coating leads to inwardly sloped sidewalls.
The mechanism is schematised in figure 3.25. Analogue results were reported by deBoer et al. [*deBoer et al., 1999*]. In their work, the balance between passivation and etching is acted upon by changing the substrate temperature and the amount of oxygen in the mixture. (In other words, the amount of oxygen that leads to coating deposition takes the place of the deposition-etching step time ratio in the Bosch process: for $O_2 \sim 0$ an almost isotropic profile is obtained. A large undercut is produced for $O_2 \sim 5\%$ and straight sidewalls are obtained at $O_2 \sim 12\%$.)

For such a process, a way of achieving sidewalls with complex slope would be to change the etching parameters until the sought profile is reached. Unfortunately, the commercial DRIE reactors are optimised for unitary anisotropy (i.e. cavities with straight sidewalls): as one moves from the optimal conditions, the results tend to become largely variable and generally unreliable. Furthermore, a series of parasitic effects such as bottling, bowing and "micrograss" appears, which dramatically change the shape and reduce the quality of features surface [*Elwenspoek and Jansen, 1998, Chapter 14*]. This may be one of the reasons why there are no reports of 3 – d large features obtained by artificially deviating from anisotropic equilibrium in DRIE.



Excessive passivation **Balanced Process: Anisotropy equal to 1** **Deficient passivation**

Figure 3.25 **A schematic view of the modification of features profile as a result of the unbalance in the passivation / etching equilibrium in Deep Reactive Ion Etching** (Part of this sketch is taken from [*Zhou et al., 2003*])

Although it is questionable whether the ASE process can produce a continuous range of profiles from the fully anisotropic to the fully isotropic, it has demonstrated good results in the extremes of the range. In particular, in section 3.3 it was showed how ASE is optimised for the production of features with straight sidewalls even for very deep etching. Conversely, isotropic etching may occur in the absence of any passivation-inducing mechanism. Sequences of anisotropic and isotropic cycles provide a reliable way of etching complex shapes, especially for large MEMS. The possibility of introducing intermediate depositions of masking materials between the cycles increases the versatility of the process. A few examples were found of structures produced by this microfabrication route. Historically, isotropic etching was coupled to deep dry etching for releasing movable parts, after a passivation step to protect the vertical sidewalls [*Elewenspoek and Jansen, 1998, Chapter 16*]. More recently, a similar process was used for microchannels fabrication [*deBoer et al., 2000*]. Different types of sequence were devised for the production of microneedles [*Griss et al., 2001*]. Some typical profiles achievable are reported, as an example, in figure 3.26. Although the technique has been used for some years, it was not possible to find an extensive review. The technique seems to be reliable also for large structures and very deep etching. The main constrains are related to the limited range of profiles achievable. The presence of an isotropic step makes it difficult to design and produce asymmetrical features but this does not represent a problem for an application like the concentrators, which possess cylindrical symmetry.

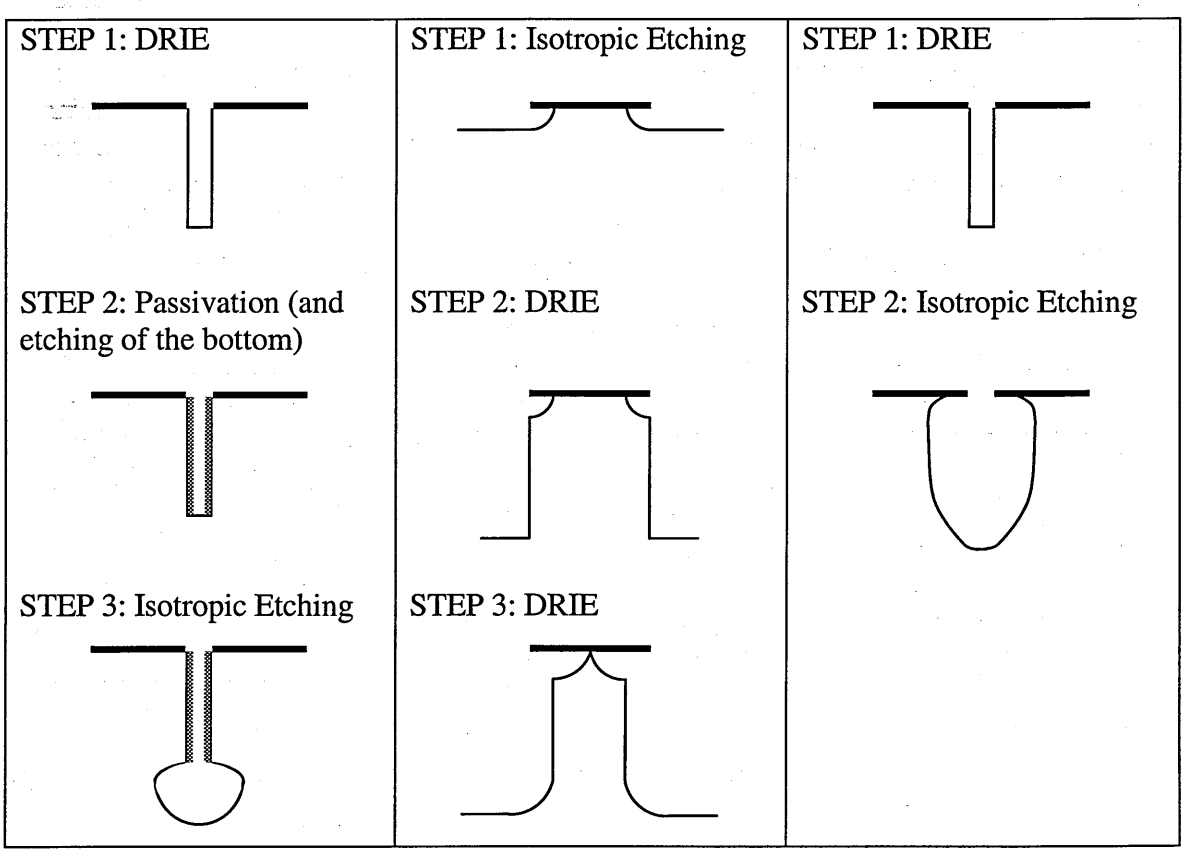


Figure 3.26 **Typical profiles achievable with sequences of isotropic and anisotropic etching and passivating steps**

A kind of approach was reported in literature that stands halfway between the methods described in this section and the grey scaling transfer techniques reviewed in section 3.4. The technique entails starting from a conventional binary pattern and making the photoresist mask recede during etching. The contour is inherently broken into steps. Anisotropic etching cycles are coupled to etching steps in oxygen to gradually consume the mask as showed in figure 3.27. This technique was successfully used for fabricating protruding micromachined optical concentrators for IR negative luminescent devices [*Nash et al., 2002*]. Since photoresist etching is inherently isotropic, the vertical consumption rate of the etch rate is necessarily equal to the lateral consumption, and process selectivity drops considerably. Therefore the amount the mask is allowed to recede is dictated by the thickness of the photoresist. Conventional photoresist materials cannot withstand this process for deep etching and this method is not directly suitable for through the wafer etching.

Finally, in [*Chou and Najafi, 2002*], an elegant way was reported to produce mesoscopic 3 – d structured contours by exploiting the reactive ion etching lag (also called Aspect Ratio Dependent Etching). A sketch of the methodology is in figure 3.28. A series of mask apertures with varying width is etched by anisotropic DRIE. The nature of the process is such that the etch rate decreases with aspect ratio, with a trend that depends on process chemistry, machine settings and reactor configuration. Parallel trenches or concentring rings of varying depth are produced. The thin walls that separate them are removed afterwards by isotropic etching. The final result is a 3 – d cavity with a contour defined by the initial number and geometry of mask apertures. An experimental calibration curve allows the control over the contour produced.

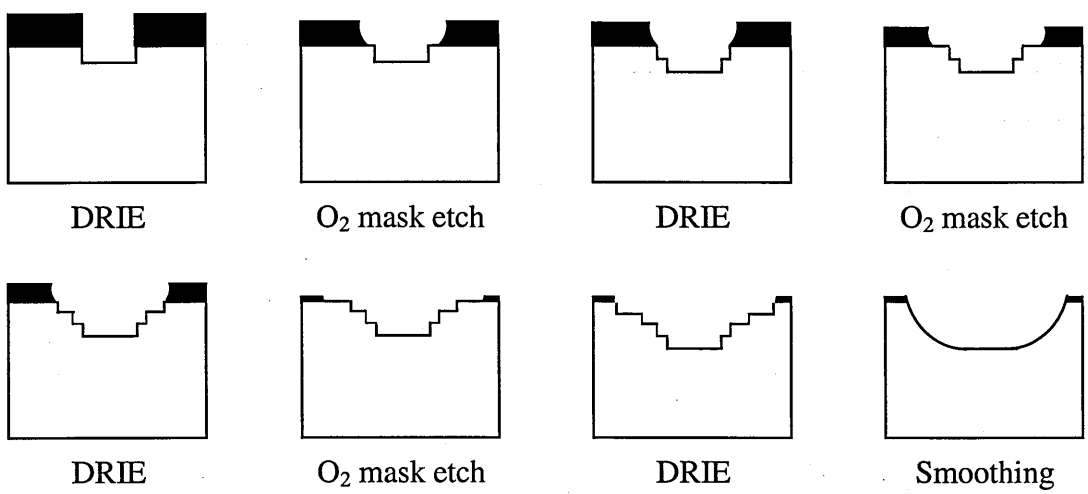
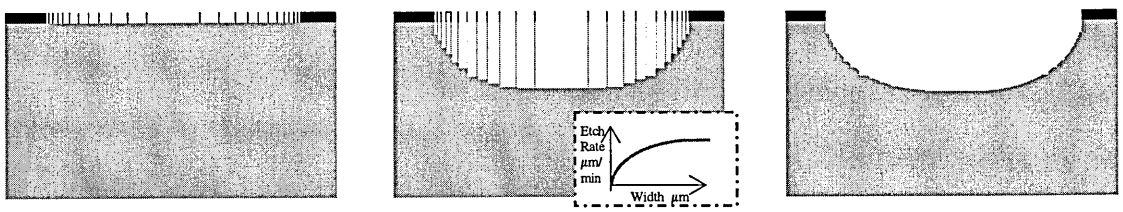


Figure 3.27 Schematic of DRIE with a receding mask: intermediate oxygen etching steps consume the mask inducing stepped sidewalls

However, the authors reported the microfabrication of a very shallow contour [*Chou and Najafi, 2002*]. The curved contour achieved is 400 μm wide and 11 μm deep, with an aspect ratio of ~ 0.03. On the contrary, a typical CPC (for example the series reported in figures 2.5 and 2.6) has a sidewalls profile that goes through the wafer, which can be around 600 μm with a width of less than 200 μm. This corresponds to an

aspect ratio higher than 3. Thus, the CPC geometry is quite far from the feature reported in [*Chou and Najafi, 2002*] and additional problems are expected to arise. Furthermore, figure 3.28 suggests that residual steps are likely to roughen the contour also after isotropic etching. This problem is expected to worsen when the slope of the curve to be approximated increases because a smaller number of steps and a higher difference between the steps are required. In conclusion, the method is not directly applicable to deep and highly sloped features such as the concentrators.



STEP 1: Mask Patterning STEP 2: DRIE STEP 2: Isotropic Etching

Figure 3.28 Schematic of the process for producing 3 – d structured cavities by exploiting the RIE lag (Aspect Ratio Dependent Etching effect)

3.6 Design of microbridges for thermal isolation of the elements of the focal plane array

One of the aims of this research is to identify a route to pattern the active layer of a pyroelectric sensor. This would enhance the performance of the detector by decreasing the thermal lateral spread from the elements. This section sets the theoretical background for the design of microbridges to support the active area elements. First, the nature of G is investigated. Subsequently the theoretical increase in performance obtained from a suspended single element is reported, thereby demonstrating the advantages of introducing microbridges.

Losses of thermal energy from a sensing element to its surroundings may occur by conduction or radiation. The total thermal loss G_{tot} is obtained by the linear combination of all the losses. Losses of different nature may be considered to lie in parallel within the thermal circuit (with an analogy to the electrical circuit), so that:

$$G_{tot} = 1 / R_{tot} = 1 / R_{radiation} + 1 / R_{conduction} = G_{radiation} + G_{conduction} \quad [WK^{-1}] \quad (3.17).$$

$G_{radiation}$ represents the loss of heat from the element by radiation. The maximum power irradiated from a small element of area A that has a small difference in temperature with its surroundings (Θ) is equal to the power emitted by the classical black body, i.e. $4A\sigma T^3\Theta$, where σ is Stefan's constant.

The energy loss due to conduction from the element to the surroundings is equal to $G_{conduction}\Theta$. $G_{conduction}$ is given by two contributions: conduction along the material or membrane to the thermal sink and conduction to the air surrounding the element. A complete thermal modelling of heat conduction entails solving the heat flow equation in three dimensions [*Holman, 1997*]. For the purposes of this discussion, it is possible to use the one-dimensional equation:

$$\frac{\partial \Theta}{\partial t} = \frac{\kappa}{\rho c} \frac{\partial^2 \Theta}{\partial x^2} \qquad (3.18)$$

where x represents the direction along the connection (of length l) between the element and the thermal sink (figure 3.29), κ is the thermal conductivity of the material in [W °C m^{-1}], ρ is the density of the material in [kg m^{-3}] and c the specific heat in [J °C Kg^{-1}]. The boundary conditions are $\Theta = \Theta_0$ for $x = 0$ and $\Theta = 0$ for $x = l$. The temperature distribution, obtained from equation 3.18 can be used for calculating the heat flow in [J sec^{-1}] along the connection, using Fourier's equation [*Holman, 1997*]:

$$q = -\kappa A_c \frac{\partial \Theta}{\partial x} \qquad (3.19)$$

Where A_c represents the cross sectional area of the flux. With reference to figure 3.29, A_c is equal to $w\,d$. The value of $G_{conduction}$, which is obtained from the integration of equation 3.19, depends largely on the geometry of the connection. At steady state, the first member of equation 3.18 is equal to zero and the solution is simply given by $\Theta = \Theta_0 [\, 1 - (x / l) \,]$, which, after substitution in equation 3.19, yields upon integration a total energy transfer rate of:

$$q = \frac{\kappa w d}{l} \Theta \qquad (3.20)$$

and therefore $G_{conduction} = \kappa w d / l$.

In the case of the temperature of the element varying along a sinusoidal (as for equation 2.9) the heat exchange is given by the thermal admittance ($\mathcal{A}$), multiplied by the difference in temperature. The thermal admittance has a real and an imaginary part in analogy with the electrical admittance [*Smith et al., 1968, Chapter II*]:

$$\mathcal{A} = G + j\omega C \qquad (3.21),$$

where ω is the angular frequency of the chopper and C the thermal capacitance of the element. Equation 3.21 leads to the treatment of section 2.3. However, the real part G can be assumed to be equal to $\kappa w d / l$ in most cases.

It is now possible to compare the radiation contribution to thermal loss with the contribution due to conduction, for a system of the kind depicted in figure 3.29. A square element of 100 μm side, at a temperature 1 °K higher than the background is assumed. (The background is at room temperature.) The maximum value of $G_{radiation}$ (given by the black body radiation) is equal to $4A\sigma T^3\Theta = 6.2 \cdot 10^{-8}$ W K^{-1}. The element is connected to the surroundings with a bridge 10 μm wide (w), 2 μm thick (d) and 100 μm long (l). The diffusivity of the material constituting the bridge is equal to 50 WKm^{-1} (a reasonable value, if compared with the actual diffusivities of the materials used for the device: see table 7.1 of section 7.1). After these assumptions, equation 3.20 yields $G_{conduction} = 1.0 \cdot 10^{-5}$ W K^{-1}. This value is more than two orders of magnitude higher than the contribution due to radiation. Since the element emits less energy than the black body, the thermal loss due to radiation can be disregarded.

The focus of this research was on the reduction of conduction, which represents the largest contribute to thermal losses. The simple term G will be used to indicate the loss by conduction. For an ideally isolated element, conduction is set to zero. However, thermal losses by radiation would occur even in such a system. The thermal exchange

between the ideally isolated element and the thermal sink leads to a background thermal noise that sets a theoretical upper limit to the performance of thermal detectors. The theoretical limit to the detectivity of thermal detectors (1.8×10^{10} W^{-1} cm $Hz^{1/2}$ [*Putley, 1970; Whatmore and Watton, 2001; Kruse, 2001;Rogalski, 2003*]) reported in section 2.3 is calculated in conditions of dominant thermal noise, assuming ideal absence of conduction from the single element to the background (i.e. $G_{conduction} = 0$).

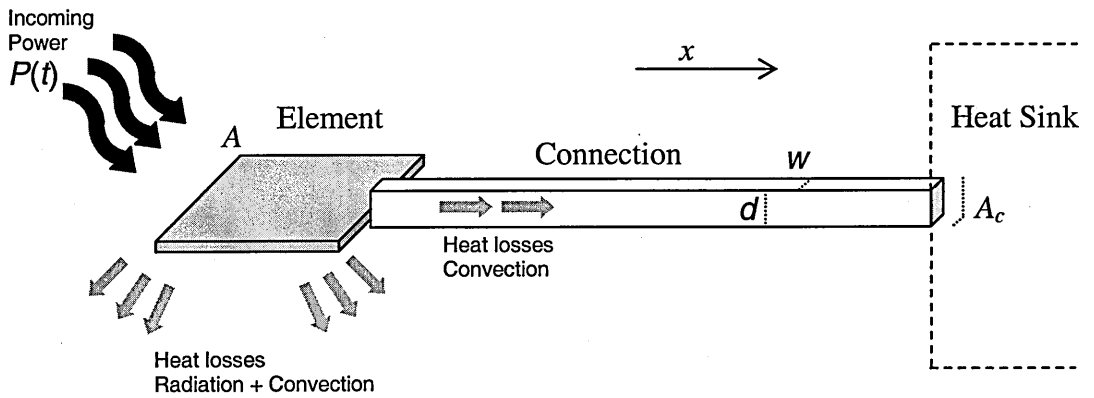


Figure 3.29 Schematic of the connection between the element and the thermal sink, with indication of the nature of the thermal losses

For the device objective of this research, enhancement of thermal isolation due to the introduction of microbridges can be simply demonstrated using Fourier's equation, solved for the steady state. A full membrane element is compared with a micromachined membrane in figure 3.30. The power is assumed to be collected in a central (active) area of radius r_i, at a temperature higher than the thermal sink (Θ represents the temperature difference). The heat spreads towards the heat sink so that at the rim of the membrane (of radius r_o) the difference in temperature Θ is zero. In figure 3.30*b* two microbridges of angular extent ϕ are micromachined into the membrane. The Fourier's equation for the full membrane is [*Holman 1997*]:

$$q = -\kappa A_c \frac{d\Theta}{dr} = -\kappa\, 2\pi\, r\, d \frac{d\Theta}{dr} \tag{3.22}$$

The thermal conductance is given by solving equation 3.22 (using the boundary conditions specified above). Considering that the power transferred (q) is equal to $G_{memb}\Theta$:

$$G_{memb} = \frac{2\pi\, \kappa\, d}{\ln(r_o / r_i)} \tag{3.23}.$$

Fourier's equation, applied to the micromachined membrane yields (for a single bridge):

$$q = -\kappa A_c \frac{d\Theta}{dr} = -\kappa\, \phi\, r\, d \frac{d\Theta}{dr} \tag{3.24}.$$

The thermal conductance for the entire system (two bridges) is given by:

$$G_{bridge} = \frac{2\phi\, \kappa\, d}{\ln(r_o / r_i)} \tag{3.25}.$$

So the gain in thermal resistance by micromachining the membrane (in the case of figure 3.30) is given by:

$$\frac{G_{memb}}{G_{bridge}} = \frac{\pi}{\phi} \qquad (3.26).$$

The gain in thermal resistance is ≥ 1 for $\phi \leq \pi$. (The case for $\phi = \pi$ represents a full membrane.) A numerical example can provide a better picture of the kind of gain involved. If $r_i = 50$ μm and $r_o = 100$ μm and $\phi = 9$ degrees, each bridge will have a minimum width of 16 μm and a maximum width of 31 μm (fully within the critical dimensions achievable with conventional dry etching techniques). The gain will be equal to 20. In other words: the micromachined element will have a thermal conductivity 20 times lower (at the steady state).

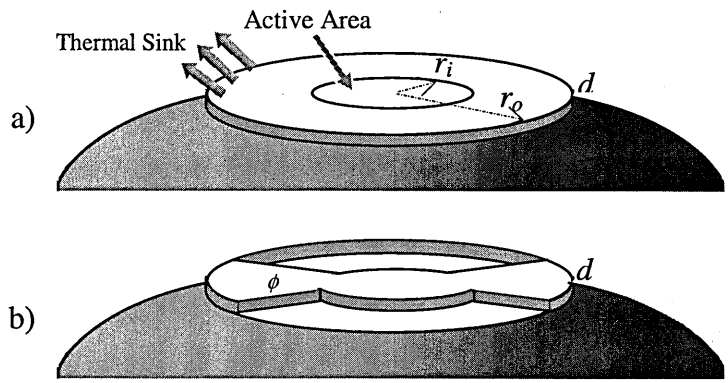


Figure 3.30 Geometry of a full membrane element (figure *a*) and of an element suspended by microbridges (figure *b*)

If the conductance through a solid bridge at the steady state is rewritten (from equation 3.20) as

$$G = \kappa \frac{A_c}{l} = \kappa\, d\left(\frac{w}{l}\right) \qquad (3.27),$$

it becomes evident that the thermal conductance from the element to the surroundings decreases with the length of the bridges (l) and increases with the width of the bridges (w). In the results part, the geometric factor between brackets (w / l) will be largely employed as a figure of merit for calculating the expected performance of various types of microbridge design (see section 7.1).

The thermal conductance of a system with more than one bridge is given by the composition of the conductance in parallel (analogous to the electrical circuit): $G_{tot} = \sum G_i$ [*Holman, 1997*]. Similarly, for a bridge composed of many layers (silicon oxide, buffer layers, bottom electrode, PZT and top electrode) the overall conductance is given by the sum of the conductance for each layer. It means that an individual layer with very high conductance would dominate the conductance of the entire bridge.

Finally, for a complete modelling of device performance, the contribution to losses, due to conduction from the surface of the membrane to the atmosphere has to be kept into account. The conductance through air (or other types of atmosphere) from the element is in parallel with the other losses and can be linearly combined with G_{tot}. The role of this contribution will be discussed in the results part (see section 8.2.2).

3.7 The search for a microfabrication route to pattern the array of microbridges

Structures that incorporate microbridges were described in the case studies of figures 2.7 and 2.8. Generally, suspended structures and microbridges were produced with techniques analogue to those developed for the micromachining of cantilevers or resonant membranes [*Madou, 2003, Chapter 3*]. Bridges were first introduced in the design of the thermal bolometer detector developed at Honeywell, USA [*Kruse, 2001*]. The isolation of the pixel element was attained by surface micromachining of a sacrificial silicon oxide layer. A similar design was later applied to integrated pyroelectric detectors [*Whatmore, 2001*]. Few examples exist of microbridges produced by bulk micromachining. In [*Iborra et al., 2002*] a thermal bolometer was suspended in the centre of a cross shaped structure, over a pyramidal cavity produced by wet etching from the face containing the active bolometer element. The microbridges were defined by undercutting the arms of the cross. In [*Méchin et al., 1996*], superconductor-based bolometers were suspended on a patterned meander bridge, undercut by large scale dry isotropic etching in SF_6.

The design of the device object of this research entails that each element is contained in an individual membrane, which represents the exit pupil of the respective concentrator cavity. These membranes result after the bulk micromachining of the concentrators from the front side of the wafer. For such a design, the most direct way of isolating the element from its surroundings appears to be the micromachining of bridges by etching holes through the membranes. This process is straightforward and does not require any sacrificial layer. The membranes can be etched by using e.g. a focussed ion beam [*Xie et al., 2004*]. In this case each single element has to be individually machined. This process, although ideal for prototyping, is unsuitable for machining the entire array. A surface patterning technique (wet or dry etching) represents a low-cost alternative.

It is well known that dry etching techniques offer many advantages over wet etching (see e.g. [*Madou, 2003, Chapter 4*]). Dry patterning demonstrates better etching performance (in terms of anisotropy and pattern fidelity) and higher reliability (due to the possibility of quenching the reaction instantly). There is a vast range of techniques and equipment that extends from purely physical to purely chemical etching. Within the spectrum of etching techniques, Reactive Ion Etching (RIE) shows interesting characteristics. A complete treatment of plasma physics and plasma-based techniques is beyond the scope of this thesis. In this section the main concepts that differentiate RIE from other plasma-based etching technologies will be introduced. The details of RIE processes will be briefly discussed in section 3.7.1. Most procedures for etching semiconductor materials using RIE were established more than 20 years ago. These well-established processes are reviewed in section 3.7.2. The main literature concerning the etching of PZT-based materials will be reviewed in section 3.7.3.

3.7.1 Basic Concepts

This research involves the use of low pressure plasmas (1 to 100 mTorr) ignited by electromagnetic fields. For the purposes of this discussion, a plasma can be defined as a gas containing charged particles, which exhibit collective behaviour due to the effects of

the electromagnetic field [*van Roosmalen et al., 1991*]. The formation of plasma is a self-sustaining chain-reaction, which produces radicals (stable and metastable), molecules, ions (negative and positive), charged molecules and electrons. Due to their small mass, large acceleration and high relative mobility, the electrons are responsible for sustaining the chain reaction thanks to the collision with larger particles. Of particular interest for RIE are ions and metastable species.

The etching techniques used in this research are based on plasmas induced by RF power in AC currents. Plasma electrodynamics predicts the formation of "dark sheaths" (or dark spaces) along every material surface immersed in the discharge. The characteristics of this dark region are essentially different from those of bulk plasma. In particular it can be roughly said that the sheath is almost free of electrons for most of the RF cycle time as they are accelerated towards a floating surface faster than ions. Due to the higher frequency of electron collisions, every surface immersed in the plasma acquires a negative potential, which reaches a steady state. At this point, the dark sheath acts as a capacitor, inducing a steady collimated flow of positive ions accelerated towards every surface.

The generic term "dry etching" includes various techniques, according to the predominant mechanism. The kinetic energy of the oncoming particles and the nature of the substrate dictate the mechanism that is more likely to take place at the bombarded surface. Particles reaching the substrate with energies below 3 eV are either reflected or physically adsorbed. (In the latter case chemical reactions may subsequently occur.) In the 3 to 10 eV range, surface migration and surface activation are triggered. The surface thus activated, may lead to chemical reactions. At energies higher than 10 eV, substrate heating and surface damage occur. Physical ejection of material (sputtering) may take place in this region. In general only ionic species may acquire a large energy since they are accelerated by the electrodynamics of the discharge. The energy and angular distributions of the ion beam become broader as the extent of the scattering increase. Therefore, the etch rate due to physical etching decreases with pressure (i.e. with the scattering of the ions). Physical etching, due to ions, is generally not selective and highly directional (leading to anisotropic etching). The etch rate can be very low at low energies whereas high energy would damage the substrates and increase mask consumption rate (thus decreasing process selectivity). Radicals are neutral: they reach the surfaces immersed in plasma by diffusion. Therefore, they collide with energies far below 10 eV. Chemical etching due to neutrals may be highly selective. (It may be stopped on a given layer and masks may be protected longer.) Generally, it yields etch rates higher than physical etching. However, radical etching is inherently isotropic: the undercut of the mask (lateral etching) is generally equal to the etch depth. Variations in pressure do not affect chemical etch rates as much as physical etch rates.
In the conventional technology, plasma is induced capacitatively by a parallel plate (anode – cathode) configuration. An RF generator produces an alternate current (generally 13.56 MHz) exciting the charged particles in the gas. The behaviour of the glow discharge is electrically analogous to a diode. The ions acquire energy and are accelerated towards each surface floating in plasma (since surfaces immersed in a plasma acquire a negative steady-state voltage). As stressed above, acceleration energies typical of RIE processes are not sufficient to produce any direct sputtering of the etching materials. On the contrary, metastable radicals may be used to etch chemically

the materials. In a classic experiment, Coburn et al. [*Coburn and Kay, 1979*] demonstrated that the synergy between ions and chemical reactants may result in an etch rate higher than that occurring in the presence of either of the two species. This large etch rate improvement may be due to any of these mechanisms: weakening of the atomic bonds by ion diffusion in the uppermost material layers, local provision of energy by ion collision during the chemical reaction or sputtering of reaction by-products by the ion flux [*van Roosmalen et al., 1991*]. The etch rate is enhanced where the ion flux hits the substrate: RIE couples the advantage of chemical etching (versatile, selective and fast) with the anisotropy typical of ion etching. It has to be clarified that anisotropy has a simple geometrical definition in this context (i.e. one minus the ratio lateral etch rate / vertical etch rate) [*van Roosmalen et al., 1991*]. It is different from the crystalline-plane-related anisotropy found, for example, in silicon wet etching in potassium hydroxide/propan-2-ol solutions [*Madou, 2003, Chapter 4*].

3.7.2 RIE of conventional microelectronics materials

The selective etching of thermally grown oxide on silicon was one of the first processes to be characterised, because, of the crucial application to the etching of the vias in microelectronic circuits. Historically, the vast majority of dry etching processes for silicon oxide are based on fluorocarbon discharges. Silicon is etched by fluorine radicals according to the following exothermic reaction [*van Roosmalen et al., 1991*]:

$$Si_s + 4\,F_g \rightarrow SiF_{4\,g} \qquad (3.28).$$

The kinetic mechanism of this reaction had been the subject of many speculations. Thermally grown oxide, on the other hand, is not etched by fluorine radicals. CF_2 radicals may etch SiO_2 according to:

$$SiO_{2\,s} + 2\,CF_{2\,g} \rightarrow SiF_{4\,g} + 2\,CO_g \qquad (3.29).$$

CF_4, a typical gas used for RIE, decomposes in plasma as:

$$CF_4 \rightarrow CF_2 + 2\,F \qquad (3.30).$$

In plasma etching, the species CF_2 tends to be adsorbed on the silicon surface causing the subsequent passivation of the etching front. Eventually, the etch would stop. In RIE, instead, the ion flux wipes out the absorbed species (F but also CF_2) avoiding the build up of CF_2. Thus a CF_4 plasma would etch indiscriminately Si and oxide where the surface is hit by the flux. If free H is added to the etching mixture then the fluorine is captured through the reaction:

$$F + H \rightarrow FH \qquad (3.31),$$

which is largely favoured. The etch rate of silicon would decrease. On the contrary, the CF_2 radicals would still etch the thermally grown oxide. The F/C ratio of an etching mixture was introduced as a parameter to be optimised for etching selectively different materials. CHF_3 (tri-fluoro-methane) yields the correct F/C ratio (~ 2) [*Coburn, 1982*] for etching SiO_2 selectively.

Generally speaking, when refractory or highly stable metals, such as Pt and Au are etched in reactive environments, the process has a strong physical (sputtering-related) character [*van Glabbeek et al., 1993*; *Shibano et al., 1999*]. This is due to the difficulty of finding a viable chemical path to stable by-products. However, some authors claim that experimental evidence exists of a chemically activated component in presence of chorine or chlorine-fluorine mixtures. Kwon et al. found consistent presence of chlorine atoms bound to Pt after etching [*Kwon et al., 1998*]. The increase in etch rate with the

addition of fluorine to Ar/Cl plasmas seems to suggest a partial chemical nature in the etching reaction [*Wuu et al., 2001*]. Finally, Milkove et al. found evidence of chemically assisted sputtering in the patterns of formation and dissolution of a fence during etching of micrometric features [*Milkove et al., 1997*]. In this research it was decided to etch the entire Au/PZT/Pt heterostructure using CHF_3-based etching. Metals such Pt and Au are expected to show a very low etching rate; however, the etching of Pt and Au does not represent an obstacle, given the thinness of these layers. Furthermore, the large decrease in etch rate from PZT to Pt can be exploited as an etch stop mechanism.

3.7.3 RIE of lead Zirconate Titanate based materials

Roughly, an etching process can be divided into the following main steps: production of active species, adsorption of the active species and diffusion to the surface, diffusion of these into the uppermost layers of the lattice, formation of reaction products, desorption of the by-products and out-diffusion of these into the gas bulk. In RIE, it was said above, ion-surface interactions may play a role during some of these stages, enhancing the reaction rate. The gas chosen for etching must originate radicals that could react with at least some of the species the material to be etched is composed of. The volatility of the by-products is even more important. If the products have a relatively high vapour pressure and stability, they are easily desorbed and eliminated. On the contrary, if they stick onto the surface they build up, filling the surface sites: elimination of low volatility by-products represents the rate-limiting step for many RIE processes.

There are numerous reports on PZT-type materials etching in literature. However, the outcome of the process is not as straightforward as for silicon oxide and there is scarcely agreement on the mechanism of the process. The group who pioneered the dry etching of lead-based ferroelectric materials, highlighted the need for a synergetic chemical-physical effect to obtain and adequate etch rate [*Title et al., 1986*]. Later, van Glabbeek et al., studying the dependence of PZT etch rate on the CF_4/Ar gas flow ratio, concluded that chemical etching by fluorine plays a minimal part although, for pure Ar etching the etch rate would fall considerably with pressure [*van Glabbeek et al., 1993*]. Subsequently, some researchers agreed [*Vijay et al., 1993; Suchaneck et al., 1999*] and others disagreed [*Saito et al., 1992*] with the picture of a mainly physical process. A recent literature survey concluded that, ions contribute to between 50 and 80 % of the etching process, although their density is smaller than that of neutrals [*Suchaneck et al., 1999*].

Various gases and mixtures have been experimented with for etching PZT thin films. A theoretical determination of reactivity of different radicals towards PZT [*Macé et al., 1999*] showed that (at pressures of 1.0×10^{-3} mbar) the PbO-Zr_2O-TiO_2 ternary system is not generally etched homogenously. All atomic halogens etch PbO primarily, but only fluorine attacks Ti and Zr oxide bonds successfully. Others claimed, on the contrary, that fluorine attacks the Ti-O and Zr-O bonds only and the Pb residual is later eliminated by sputtering [*Suchaneck et al., 1999*]. Some authors chose CHF_3 because the coexistence of F and H is known to be suitable for the etching of oxide materials [*Lin et al., 2000; Suchaneck et al., 1999*]. Since it was decided to use CHF_3 for the etching of silicon oxide, it seemed reasonable to try to set up a process for PZT etching using the same gas.

Many researchers identify the desorption of by-products as the rate-limiting step. Adsorbed lead fluoride [*Vijay et al., 1993, Lin et al., 2000*] and zirconium fluoride [*Poor et al., 1991*] were still found adsorbed onto the surfaces after etching. Other authors stress the low volatility of Pb, Ti and Zr fluorides as opposed to SiF_4, even at temperatures up to 300 °C [*Saito et al., 1992;Vijay et al., 1993; Mace' et al., 1999; Poor et al., 1991*]. This suggests that the high relevance of the ion effect in PZT etching is due to the role of ions in desorbing the fluorides produced by the chemical reaction.

Due to the preferential nature of the etching, the relative stability of the material and the low volatility of the by-products, the etch rates obtained are not expected to be high. In fact in conventional RIE, rates were found around 5 – 10 nm/min while higher rates were achieved with the use of more advanced dry etching techniques [*Lee et al., 2000*] or using gases containing both chlorine and fluorine [*Jung et al., 2001*]. The etch rate may depend strongly also on the structure and density of the PZT [*Vijay et al., 1993*]. For thin films, it generally depends on the deposition technique and consequent film stress and adhesion [*van Glabbeek et al., 1993; Poor et al.,1991*].

3.8 Conclusion

This section presented a survey of topics from the literature with the following aims:

1) to clarify the issues involved in the design of the concentrators and microbridges and
2) to identify viable microfabrication routes to produce arrays of contoured concentrating cavities and to pattern arrays of microbridges onto the active layer.

Three kinds of non-imaging concentrators were considered. Different types of concentrator design and ways of expressing the relative figures of merit were discussed. Theoretic designs with highly symmetrical contours can be treated analytically, whereas statistical ray tracing technique is needed for more complex types or for profiles that cannot be expressed in analytical form (e.g. profiles of actually manufactured devices). The concentrator that offers the maximum collection efficiency is the compound parabolic concentrator. The geometrical construction of the CPC was introduced and families of CPCs suitable for integration in the device were generated (based on the technical literature). The 2 – d CPC demonstrates the maximum concentration thermodynamically achievable. The manufacturing of concentrators presents peculiar problems, due to the design. These cavities are very narrow with high aspect ratio. Sidewalls are necessarily tapered, but require maximum smoothness since the system works on reflection. Not all the suitable profiles are achievable by using conventional microfabrication techniques. If 3 – d CPC cannot be achieved with satisfactory approximation, cone or parabolic collectors might represent an adequate alternative. Truncation is also an option that does not decrease the collection efficiency in a dramatic way.

After a survey, many microfabrication techniques were excluded a priori because they were not expected to meet the requirements of the application. Incorporation of concentrators microfabrication in the overall device fabrication process imposed other constrains on selecting the suitable techniques. It was decided that non-contact

techniques, based on high-density plasma etching would be explored. A DRIE-ICP etcher had been made available at Cranfield after this research started. The etching principle of this machine is based on the Bosch process, which consists of a sequence of passivation and etching steps. The capabilities of the system, as reported in literature, meet the main requirements of CPC microfabrication.

A technique that entails the intermediate use of 3 – d photoresist masks, which are subsequently transferred into silicon was surveyed and discussed. Various methods for imposing 3 – d contoured patterns onto photoresist layers were reviewed. Based on this review, an experimental road map was established. First, a series of sloped microstructures has to be produced using a HEBS calibration glass plate. The shape of these structures is very far from a suitable concentrator profile, but they would be useful for testing the feasibility of the process. In particular, the transferring of these masks at very high selectivity (i.e. to produce very deep cavities) presents the less secure outcome since it has never been reported in literature. Once the feasibility is established and the process set up, a subsequent optimisation by trial-and-error is envisaged, using low-quality, low-cost half tone masks. The final half-tone mask would be produced by conventional e-beam after a successful optimisation of the whole photolithographic process.

The fabrication of 3 – d cavities using both partially anisotropic plasma etching and slightly modified DRIE demonstrated to be a less explored route as fewer examples were found in the literature. Examples were found in literature of tapered (or 3 – d) cavities and protruding features produced by coupling fully anisotropic and fully isotropic cycles. Since these contours were similar to those of the CPCs, it was decided that this route was very promising. Other routes that entail exploiting the ARDE phenomenon or creating a receding mask in-situ during etching were far less promising.

The advantage of isolating thermally the elements of a pyroelectric array was demonstrated theoretically. The problem of element isolation was applied to the structure of the device object of this research. After consideration of a few case studies, a suitable fabrication method was chosen: parallel plate reactive ion etching in capacitively induced plasmas (i.e. traditional RIE). A suitable etching recipe had to be considered for the etching of the electrodes and the active material. The etching of materials typical of microelectronics (such as SiO_2 or Pt) is a long established technique and a detailed literature review was not required. On the contrary, etching of PZT-based materials has been developed only in the last decade. The literature on PZT etching was fully reviewed. After that, a suitable etching environment was chosen.

Chapter 4 EXPERIMENTAL DETAILS

The bare experimental details of the research are reported in this chapter without comment or presentation of results.

The fabrication process of the device is detailed in section 4.1. This section reports the procedures up to the sandwiched structure, i.e. the deposition and patterning of the active pyroelectric layer. Subsequently, section 4.1 discusses the practicalities of poling the PZT film. Finally, the section concludes with the description of the techniques used for assessing the outcome of the fabrication in terms of quality of the materials and structures and performance of the detectors.

Section 4.2 deals with the isolation of the elements by means of surface patterning. The various recipes used for etching the PZT layer and the full PZT-electrode stack are reported. The section concludes outlining the practical differences between the etching of full wafer (i.e. not micromachined) and the etching of thin membranes.

Finally the development of a microfabrication route for incorporating the array of concentrators is discussed in section 4.3. First, the section provides the technical details of the equipment for DRIE owned at Cranfield. In section 3.4, a route to fabricating contoured features in silicon by making use of grey masks was outlined and section 4.3 details the attempts carried out to produce such features. After this route was abandoned, most trials were aimed at machining the concentrators directly using a conventional binary mask. The literature (surveyed in section 3.5) suggested some promising routes to obtained contoured cavities by unbalancing the anisotropy-producing equilibrium or coupling fully isotropic and fully anisotropic cycles. The experimental procedure for these trials is specified. Section 4.3 concludes outlining the ways by which the contours of the 3 – d structures and cavities produced were measured.

4.1 Microfabrication Of The IR Sensing Array Device

In this section, the microfabrication process of the detector array is reported in detail. The experimental details relative to the conventional process for device microfabrication are reported in section 4.1.1. Section 4.1.2 deals with the practicalities of poling the active layer. Finally, section 4.1.3 lists and describes the methods used for characterising the IR device in general. In other words, this section does not report the experimental details relative to the micromachining of the elements membranes or the microfabrication of the array of concentrator collectors. (These will be discussed respectively in sections 4.2 and 4.3.)

4.1.1 Details of the microfabrication process

The main steps of the microfabrication process are illustrated in figure 4.1*a* to *g*. The process starts with <100> double-sided polished silicon wafers, 10 cm in diameter, with 400 nm thermally grown silicon oxide on both sides. Wafers in a range of thicknesses were used, but the final process would use 250 μm thick samples because this represents an optimal value for the micromachining of the concentrators. (This issue is explained

in section 4.3.4). The wafers are cleaned with acetone and isopropyl alcohol (IPA), followed by a 5 minutes plasma ashing in a Polaron barrel etcher using Ar/O_2 (80/20 %) mixture. After plasma cleaning the wafers are immediately loaded in a Nordiko sputtering equipment for deposition of a titanium layer (figure 4.1*a*). (No reference to a specific model is made since the equipment is old and was refurbished many times.) The reasons for introducing this buffer layer were introduced in the background part (see section 2.5 and also [*Madsen et al., 1998*]). Titanium is sputter RF deposited at 300 Watts from a pure Ti target (rectangular, 10-by-20 cm), in argon, up to a thickness of circa 50 nm. After deposition, the layer is oxidised by annealing in air on a hot plate at 520 °C. After a treatment of circa 7 minutes the oxidation of metallic titanium is checked visually. (The film becomes transparent when totally oxidised to TiO_2).

Subsequently, the Pt electrode is patterned by lift off (figure 4.1*b*). A double layer of photoresist is spun onto the $TiO_x/SiO_x/Si$ wafers, using an EMS spinner (Mod. 4000). A layer of Microchem LOR2A [*MicroChem, 2004*] is deposited at 3000 rpm for 30 seconds and then baked onto hot plate (EMS 1000) at 115 °C for 5 minutes. A second layer of Shipley S1818 [*Shipley, 2004*] is spun at 4000 rpm for 60 seconds and then baked on a hot plate at 115 °C for 90 seconds. The double layer is contact exposed in a mask aligner (Karl Suss MJB21) to a dose of about 130 mJ cm^{-2}. The patterns are developed in undiluted Shipley MF319 (a Tetra-Methyl-Ammonium-Hydroxide-based developer). The LOR2A is pre-exposed, so that it tends to dissolve also on the unexposed areas, causing an undercut of the pattern. The undercut is controlled by controlling the development time. After 45 seconds of development, the pattern is visually checked under the optical microscope: if the development is complete, the sample is overdeveloped for an additional 10 seconds, until the LOR2A has receded slightly under the S1818 to yield an undercut of about 1 – 2 μm. The overall operation is schematised in figure 4.2.

After a satisfactory undercut is produced, the samples are barrel etched for 3 minutes in an Ar/O_2 (80/20 %) mixture then immediately loaded in the sputtering equipment. A thin adhesion layer of titanium (~ 5 nm) is deposited by RF sputtering at 300 Watts in argon. Subsequently, platinum is deposited, up to a thickness of ~ 100 nm by DC sputtering, at 700 mV, in pure argon. Finally, the float off is accomplished in acetone ultrasonic bath until all the features are cleared. If the undercut is optimised during development, then the continuity of the metallic film will break along the sidewalls of the pattern and the elimination is unproblematic. LOR2A residual is eliminated by a subsequent 2 minutes dipping into the same developer.

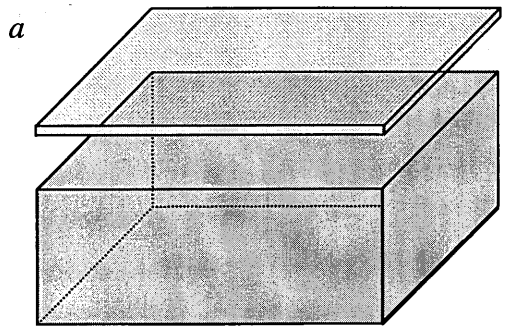
Before depositing PZT, the samples undergo a cleaning step with the same modality (acetone, IPA and plasma etching). A blanket layer of Lead Zirconate Titanate (PZT) is then deposited onto the samples. The layer is sol-gel spin deposited. The sol is produced by mixing two solutions of organometallic complexes in casting solvents [*Huang et al., 1999*]. One solution contains zirconium isopropyl-oxide plus titanium n-propyl-oxide. The second solution contains lead acetate. The Zr/Ti composition ratio was 30/70. Pb was in excess. The resulting solution was diluted to 0.4 M in Pb. Alternatively a small amount of manganese complex was added for producing a series of Mn-doped PZT films [*Zhang et al., 2001*]. The sol was spun at 3000 rpm for 30 seconds using a Headway spinner. In this way the samples were coated in a thin layer of gel. The

organic components were partially eliminated by burnout on a hot plate (make: Cerimec) at 200 °C for 60 seconds. The samples were then crystallised on a second hot plate (custom built). Since reaching the optimal temperature can be problematic, the annealing time is varied to compensate for temperatures lower than optimal. For example, 5 minutes are required for crystallising the first layer and 3 minutes for the subsequent layers at a temperature of 530 °C. Conversely, annealing at a temperature of 510 °C requires up to 10 minutes for the first layer and 5 minutes for the successive layers. The approximate thickness of each layer is 70 nm. Fourteen sequential depositions are required to achieve a thickness of 1 micron.

Each array (or device) contains a single via for connecting the circuit with the read out array. The via is a squared hole of 150-by-150 μm i.e. a reasonably coarse feature, which can be easily produced by wet etching the PZT layer. The successive step is therefore the patterning of PZT by wet etching (not indicated in figure 4.1). After deposition and patterning of a layer of S1818 (with modality similar to that reported above for the double layer), the samples are first soaked for 30 seconds in a solution containing HF (0.5%vol) and HCl (4.5%vol) in H_2O and, subsequently, in a solution of concentrated HNO_3 50% vol in water for 10 seconds, according to a process outlined by [*Mancha, 1992*; *Miller and Bernstein, 2000*]. After removing the photoresist, the gold electrode is patterned by lift off (figure 4.1*d*). The usual bi-layer mask is deposited and patterned. Chrome is RF sputtered at 300 Watts as an adhesion-promoting layer circa 5 nm thick. Gold is then RF sputtered at 100 W up to 100 nm. The photoresist is floated off in acetone ultrasonic bath. Residual LOR2A is stripped using the usual developer.

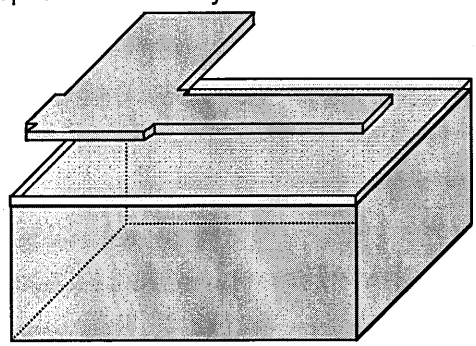
The following steps (incorporation of concentrating cavities and patterning of membranes) are symbolically illustrated in figures 4.1 (*e, f*). However, they will not be detailed here since the set up of these two microfabrication steps is the main object of this research. The experimental issues relative to these two steps will be discussed in detail in sections 4.2 and 4.3.

The alignment of the concentrators with the respective elements represents an essential step. In the final prototype, the production of the concentrators entails the use of a binary bi-layer mask (thermal silicon oxide plus photoresist). The concentrators are etched from the front side of the wafer (i.e. the side opposite to the one containing the active heterostructure). The patterning of this side (and consequent double-side alignment) may be introduced at any stage during the above process. The mask aligner Karl Suss MJB21 has the capability of aligning two patterns at the opposite sides of a wafer. However, if the patterning of the back side is followed by operations that would strip the photoresist from the wafer (e.g. patterning by lift-off of the top electrode), then it is necessary to transfer the front pattern from the photoresist into the thermal oxide by RIE and patterning a new layer of photoresist (aligned with the thermal oxide) just before machining the concentrators.



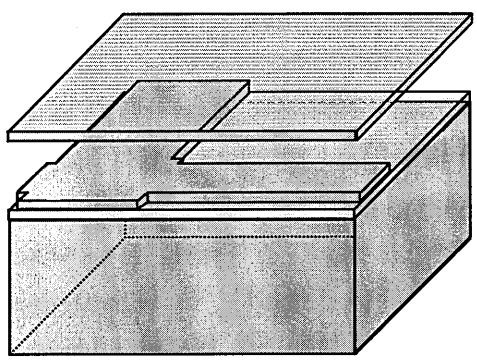
a

Deposition of a Ti layer and oxidation to TiO_x



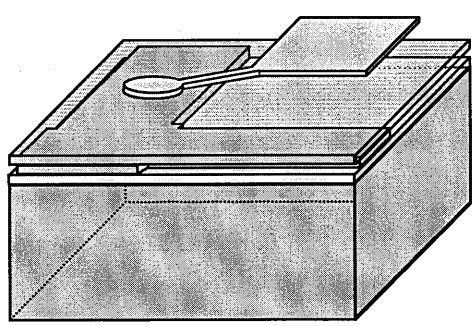
b

Patterning of a Pt layer by sputtering & lift off



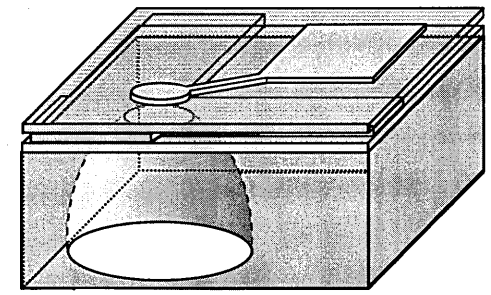
c

Deposition of a PZT layer by sol–gel spin coat



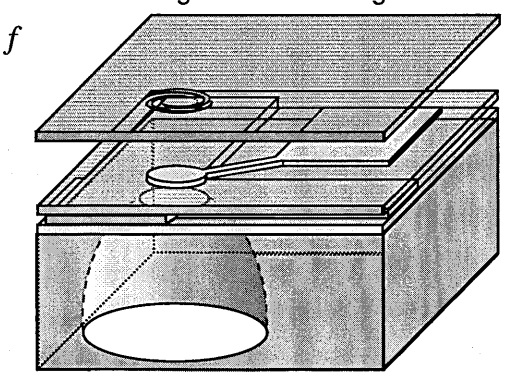
d

Patterning of an Au layer by sputtering & lift off



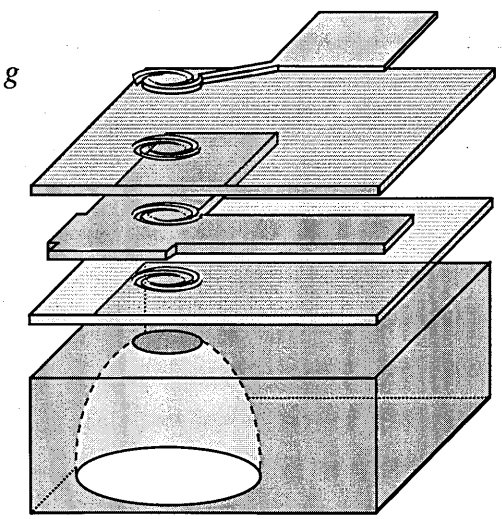
e

Micromachining of concentrating collectors



f

Patterning of the membranes (microbridges)



g

Deposition of absorbing layer on the element and reflective coating on the sidewalls (exploded view)

(The etch may proceed through the entire membrane or stop on the SiO_2)

Figure 4.1 Main steps of the microfabrication route to the IR sensor

Finally, an absorbing layer is deposited onto the cavities by evaporation using a partly modified Edwards equipment. The absorbing layer is nickel / chrome with a resistivity of 377 Ω/□. A subsequent deposition step is required to assure that the sidewalls of the concentrator have the maximum reflectivity. A gold reflective layer is deposited by evaporation over a chrome adhesion layer. A metallic shadow mask is employed to protect the exit pupil of the concentrator. The exploded view of the final device is reported in figure 4.1*g*.

At the end of the microfabrication process, the individual arrays need to be separated. The dies were diced using a numerically controlled sawing machine. Although sawing trials were performed only at the very end of this research, an array of sawing marks had been opportunely incorporated within the device design since the beginning of the project. The issues inherent to the dicing of the wafer are not reported here. (They are briefly discussed in the results part: see section 8.1.2.)

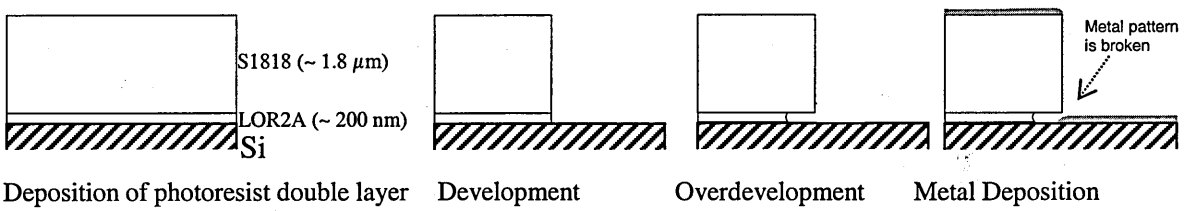


Figure 4.2 Optimisation of the lift off process by using a double-layered mask

4.1.2 Poling of the pyroelectric material

In this section, the procedures for poling the PZT layer will be briefly reported. In section 2.5, it was detailed how poling of the active layer (PZT) is required to attain a suitable pyroelectric coefficient. A poling step has to be introduced at some stage in the microfabrication process of the device. Traditionally, film and bulk PZT samples are sandwiched between two electrodes and then poled by simple contact with two circuit electrodes (in a way similar to that schematised in figure 2.6). However, if the top electrode is patterned with large arrays of mutually isolated structures (e.g. capacitors), then it is not possible to provide individual contact to each capacitor. In a research environment, where the elements can be individually tested, they can also be individually poled by contact poling. This technique has been used for most devices: individual elements were poled using a home-built probe station. An Isotech *ips*1603D generator was used, which can provide DC voltage up to 40 volts (far higher than the coercive field required by this kind of film [*Zhang et al., 2001*]). However, when device microfabrication process has to be scaled up for industrial production, a way of poling all the array elements at once has to be provided.

Corona poling is a way of poling the entire sample at once without the need to deposit an upper electrode [*Waller and Safari, 1988*]. In this way, the PZT layer can be poled previous to the deposition and patterning of the top electrode. Following this method, the negative electrode is made up by a number of pins positioned very near to the surface of the film to be poled. The number may vary from a single pin to a large array of tens of pins. When direct current is provided to the circuit, the immediate

surroundings to the pins become very rich in electrons. Sometimes plasma is ignited. This concentration of charges acts as an electrode to close the circuit with the film. Corona poling is a method that presents some complexities. Although it was invented quite a long time ago, the technique is far from established. This method is not detailed here; neither it is discussed in the rest of this thesis since it was used only for two device wafers. More information on the application of this method to the first version of the device produced here can be found in [*Shaw et al., 2004*].

4.1.3 Methods for characterising the results and metrology techniques

Throughout the entire microfabrication process, the device wafer is visually inspected by optical microscopy using the various tools available in the clean room environment. Profilometry (Dektak 3st) is used for checking the thickness of the films deposited, in particular for photoresist, bottom electrode, top electrode and PZT, after the wet etching of the vias.

The usual material characterisation techniques are employed for assessing the structure and the quality of the films deposited. In particular, the degree of preferential orientation of the PZT and Pt layers are measured by x-ray diffraction spectrometry. In fact, the orientation of the PZT affects the pyroelectric properties (as specified in section 2.5). Since this process step was already optimised before this research started and a very small amount of work was devoted to the structural and material characterisation of the device, these issues are treated only marginally here. Therefore the x-ray diffraction techniques used will not be further discussed. Scanning electron microscopy was used to assess the structural integrity of the films.

The electrical properties of the individual elements of the arrays were tested in a home-built probe station using a GenRad 1689 RLC DigiBridge impedance analyser. The probe allows individual testing of each element of the arrays. The pyroelectric responses of individual elements were tested in a home-built apparatus, sketched in figure 4.3. All the elements of the system are mounted on a graduated optical bench in order to control the distance and the alignment. The IR radiation is produced by a hot plate (mounted vertically). The radiation may be partially collimated using a macroscopic shutter. A rotating disc (chopper) is employed to modulate the radiation. The sensing array is mounted on a board that allows the connection of a single element to the overall circuitry. Therefore the apparatus is able to test just a single element at a time. The circuit connected to the single element includes a single FET to amplify the signal. Both the board and the element are encased in a metallic box to minimise the external noise. The amplified signal is fed to an oscilloscope. The final result is a waveform signal as in figure 4.4. The amplitude of the wave is used as the measurement result. This equipment yields qualitatively valid results and it is useful to compare different arrays. However, it was not possible to implement it to obtain quantitative results within the time frame of this research. For more details on the major problems affecting this apparatus and the possible implementations see the future work part.

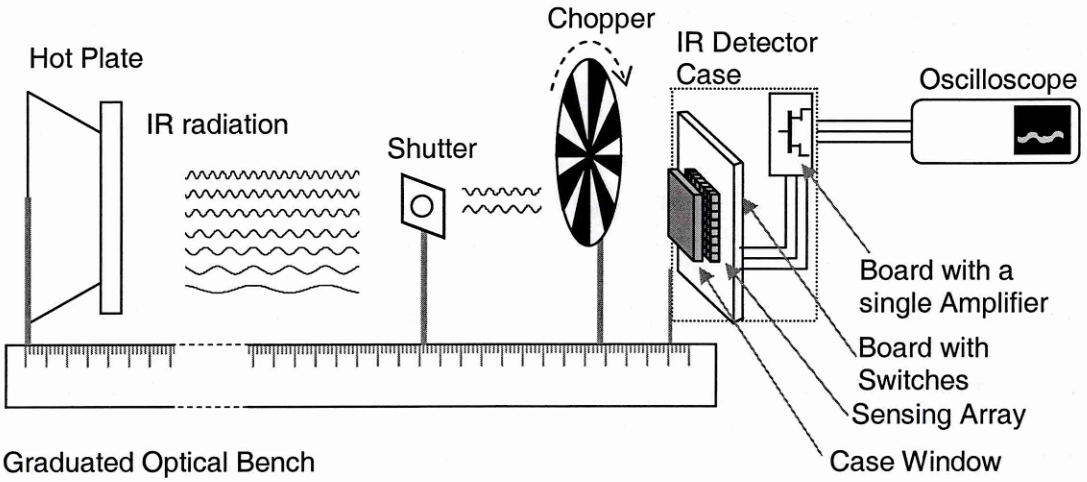


Figure 4.3 **Apparatus for testing of the pyroelectric response of single elements of a focal plane array**

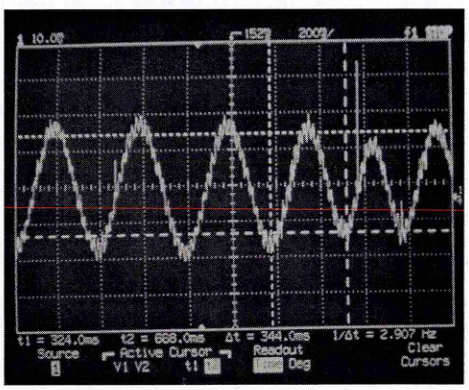


Figure 4.4 **Example of the signal attainable from the oscilloscope. The signal is an example of an actual signal obtained from a working device. The sine wave is produced by the rotation of the chopper.**

4.2 Active Area Isolation

After the detector array has been completed on the "back" face of the wafer, arrays of cavities are machined from the opposite face (i.e. the "front" side). As a consequence of through-the-wafer etching, each element of the focus plane array is expected to lie on a thin membrane that corresponds (roughly) to the exit pupil of the respective concentrator (see figure 4.1*e*). After concentrators are machined, the device undergoes patterning by using conventional Reactive Ion Etching. Etching the membranes means etching through a "stack" of different layers (see figure 4.1*f*). Etching through the electrodes, and PZT was of extreme importance as these layers dominate the thermal conductance. Possibly the etching could be allowed to proceed into titanium oxide and thermally grown silicon oxide, if this does not cause secondary problems (e.g. weakening of the elements structure or shorting between the electrodes). The main issues concerning the patterning of the membranes are discussed, within the framework of the overall device microfabrication process, in the results part (section 8.1.2). The etching of thermally grown silicon oxide is a well-established technique. (It was reviewed in section 3.7.2.) Likewise, RIE of stable metals as Pt and Au is generally a

physical process that does not require extensive development to be set up. On the contrary, although vast research has been published on dry etching of PZT and PZT-like materials, a clear picture of the process mechanism has never been established. (The literature was discussed in section 3.7.3). The set up of the etching process for the Au/PZT/Pt stack represents the bulk of the research. First, the trials were made on full wafers and not on membranes. Then, once the process was set up, the step was tried on actual device wafers (both before and after the micromachining of concentrators).

All wafers used were <100> cut single crystal silicon. Samples were etched in a range of configurations. An overview is given in table 4.1. Due to the huge number of samples etched, references for each single sample are not reported here. On the contrary, each different set up describes an entire set of samples (or trials). The equipment used for the etching was a conventional parallel plate system (Series 80 - Plasma Technology - Vacuum General Inc. San Diego, CA). Ionisation is induced by means of an AC current flowing between two electrodes at a frequency of 13.56 MHz. The reduced pressure is maintained by a system that couples a rotary pump to a Roots blower. The pressure (in a range of 10 to 200 mTorr) was monitored with a capacitance manometer under periodic calibration. Gas flows were controlled by feed back loop, using hot filament flow meters. The samples were attached onto the cathode (using vacuum grease) and back-cooled with water flow to assure a satisfactory dissipation of the heat induced by ion flux. The gases used in the etching mixtures were Argon, Oxygen and Trifluoromethane (CHF_3). The samples were masked by photolithography, using Microposit S1818 [*Shipley, 2004*] or Clariant AZ4562 [*Clariant, 2004*] photoresist materials, under various deposition and patterning conditions. S1818 was employed for the early explorative trials. The maximum mask thickness was 3.5 μm for S1818 and 13 μm for AZ4562.

The optimal recipes for etching thermally grown silicon oxide and Pt were set up after a minimal number of trials (not described here). Two standard recipes were set up for SiO_x etching. In both cases the forward power to the electrodes was 150 W (and the reverse power is nominally equal to zero). Chamber pressure was set to 100 mTorr reducing the pumping throughput by means of a throttle valve. A mixture of Ar and CHF_3 of composition 20 / 5 (SCCM) yields high selectivity towards Si and high uniformity, but it causes the deposition of a fluoro-carbon coating on Si (see section 1.3.4.2). Conversely, a mixture Ar / CHF_3 / O_2 (15 / 5 / 5 SCCM) yields clean etched surfaces, albeit showing lower selectivity towards Si and low uniformity. In both cases, etch rates were found around 40 nm / min. A thin layer of Pt (~ 100 nm) is easily etched in pure Ar using a power of 150 – 200 W at a pressure of 30 to 60 mTorr, with an etch rate ranging from 5 to 10 nm / min. (Etch rates decrease with pressure whereas the selectivity towards the mask increases with pressure). Once the PZT etching process was characterised, a standard recipe was chosen (for the set up of the PZT process, see section 3.1.2). The standard recipe entails an RF power of 100 Watts. The mixture is Ar / CHF_3 in proportions 20 / 5 (SCCM). The pressure is about 35 to 40 mTorr (throttle fully open).

Sample Configuration	Etching Gases	Etching Recipe	Masking Materials	Trials Purpose
Silicon Oxide on Silicon	Ar / CHF_3 or Ar / CHF_3 / O_2	Conventional Recipes	Shipley S1818	Set up a standard process
Pt on SiO_x/Si	Ar	Conventional Recipes	Shipley S1818	Set up a standard process
PZT on Pt/SiO_x	Ar / CHF_3	Various conditions	Shipley S1818 and AZ4562	Feasibility study
Full Stack	Ar / CHF_3 / O_2	Optimised Cycle	AZ4562	Feasibility Study
Full membrane	Ar / CHF_3	Optimised Cycle	AZ4562	Set up a standard process

Table 4.1 Experimental conditions for the etching of different samples / materials using conventional RIE

Etching of the entire stack or membrane requires a very long time; therefore an AZ4562 layer about 10 μm thick was used as a mask. AZ4562 was spin coated at 1500 RPM for 40 seconds, baked onto hot plate at 90 °C for 150 seconds and then exposed for 45 seconds (equivalent to a dose of ~ 600 $mJcm^{-2}$), using a mask aligner (Karl Suss MA56). Photoresist was developed in AZ400K (a NaOH based developer) 20 % volume in water for 3 to 4 minutes (until the features are clear). Since the membranes would not withstand the vacuum induced by the spin coater, before spinning, the wafer was mounted on a second backing wafer using a thick layer of photoresist (AZ4562).

The samples with stack or membranes were subjected to etching cycle using the above recipe for PZT. The top electrode (Au) was etched with the PZT recipe because low power avoids the initial carbonisation of photoresist. The etching cycle is carried on until Pt is reached and all (or most) features are clear. This usually requires 7 to 9 hours: the sample is inspected at different stages of the process. After the PZT layer is fully etched, either the process stops or the sample undergoes etching using the recipe for Pt etching for 20 minutes (or more if needed). After checking that the elimination of Pt is complete, the TiO_x/SiO_x layer can be eliminated (if required) using the conventional recipes reported above. Generally, over 70 % of mask thickness survives etching. The interface between photoresist and sample is not damaged and photoresist can be easily removed by soaking in acetone, which removes the backing wafer as well. Maximum care should be taken to avoid breaking the structures. A cycle of 24 to 48 hours soaking in acetone is sufficient to clear the sample and allow gentle separation of the sample and the backing wafer.

In the early trials (etching attempted on full wafers), the etch rate was assessed, through the etch depth, by profilometry (Dektak 3st). Conversely, it was not possible to obtain a sensible result from profilometric measurement on the membranes: the membranes, in fact, would bend under the load of the tip. For this reason, the results of the etching of membranes could only be assessed visually, i.e. qualitatively. The quality of the etched surfaces and sidewalls was checked by visual inspection (optical microscopy) and scanning electron microscopy.

4.3 Microfabrication Of Concentrators

A general overview of the methodologies for the micromachining of the concentrators is reported in this section. First, preliminary trials to assess the capabilities of the process were performed: section 4.3.1 of this chapter describes the equipment for DRIE at Cranfield. Subsequently, a grey-scale technique was attempted and the experimental details are in section 4.3.2. A wider series of trials followed, aimed at machining the concentrators directly using a conventional binary mask: the experimental procedure for these trials is specified in section 4.3.3.

4.3.1 The DRIE-ICP machine

A sketch of the equipment used for all the deep etching trials is reported in figure 4.4. The main chamber is cylindrical, with a diameter of about 50 cm. The inner (processing) chamber is made by alumina. A coil runs around the upper part of the chamber, where the plasma is ignited and maintained by inductive coupling. Alternated current passes along the coil, during operation, with a RF frequency of 13.56 Mhz. The equipment includes a low-pressure clustered module for the loading of the wafers. (The carousel is not depicted in figure 4.4). The wafer is automatically loaded and mechanically clamped onto the holder. The sample holder is cooled by a flux of highly pressurised helium. Should the wafer break during the process, helium would leak into the chamber, affecting the outcome of the etching. The ion flux is specifically driven to the sample by a supplementary source power connected to the platen. The RF bias applied to the sample can therefore be controlled independently on the power of the plasma. The gas flows are controlled by hot filament mass flowmeters. Reduced pressure is maintained by a pumping system that includes a turbomolecular pump, backed by a rotary pump. The whole system is remotely controlled by a processor unit.

4.3.2 The grey-scale technique

The preliminary trials devoted to 3 – d pattern microfabrication by Grey Scale Photolithography and subsequent Deep Reactive Ion Etching have been partly performed at the Central Microstructure Facility of the Rutherford Appleton Laboratories (UK). The experimental work entailed production and characterisation of intermediate 3 - d masks and transfer of these shaped patterns into silicon wafers. 3 - d photoresist masks were patterned by Grey-Scale Photolithography on bare silicon and silicon oxide coated wafers. A High Energy Beam Sensitive calibration plate, owned by RAL was used [*Canyon Materials, 2004*]. The performance of two different photoresist materials was evaluated. For some samples, photoresist patterns were transferred into a silicon oxide layer by Reactive Ion Etching step in CHF_3/Ar plasma. The SiO_x contoured 3 - d masks were used as an intermediate layer between photoresist and silicon. All the samples were subsequently processed in the ICP-ASE machine at Cranfield University, in order to transfer anisotropically the 3 – d mask patterns into the silicon substrate. As stressed in section 3.4.4, this branch of the research had to stop at the preliminary level because serious problems emerged, which would make the technique not viable for the production of concentrating collectors. (The problems affecting this technique are discussed in section 6.1.4.)

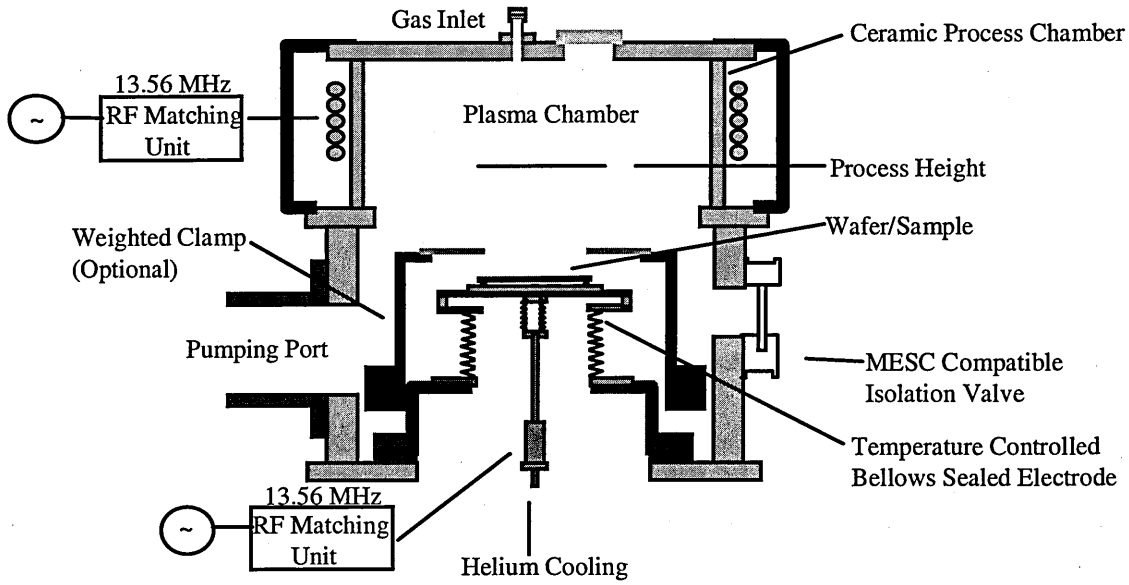


Figure 4.4 Sketch of the multiplex ASE® STS machine with ICP [*Bhardwaj et al, 1997*]

Clariant AZ4562 [*Clariant, 2004*] and JSR IX575 [*JSR, 2004*], positive diazotype photoresist materials were used (exemplary formulas were reported in figures 3.20 and 3.21). The photoresist was spun onto bare Si and silicon-oxide-coated Si wafers (10 cm in diameter, <100> orientation cut) under different process conditions, reported in table 4.2 (*a* and *b*). 1,1,1,3,3,3-Hexa-Methyl-DisilAzane (HMDS) was spun onto some samples to improve the adhesion of the photoresist [*Bauer et al., 1996*]. In order to enhance the contrast, soft bake time was minimised to reduce the thermal bleaching of the photoactive compound (soft bake at 90 °C for 90 seconds). The uniformity of the photoresist coating across the wafer was assessed by ellipsometry. The spin coating equipment employed (Gyrset RC8) maintains a saturated vapour pressure environment to reduce the elimination of the solvent during spinning. In this way the viscosity of the photoresist increases slowly and the film is more uniform. After pre-baking on a hot plate, the thickness of the photoresist layer was measured along four concentric rings on eight equidistant points per ring. The analysis of variance on the data (not reported here) demonstrated that most of the samples coated with AZ4562 showed evidence of thickness variation with the distance from the centre. On the contrary, for JSR IX575, only the set of points on the outermost ring demonstrated evidence of difference. JSR IX575, therefore, can be spun with higher uniformity. This could be expected since a far thinner layer is deposited using JSR IX575.

The samples were patterned by contact photolithography on a Karl Suss MA6 mask aligner using a High Energy Beam Sensitive calibration plate [*Canyon Materials, 2004*]. The nominal intensity of the lamp was constant at 10.0 mJ/cm^2. (The dose was not assessed quantitatively using an external probe). The optical density of the HEBS mask varies locally to create 3 – d features in a range of different shapes and slopes on the wafer surface. The details of the patterns on the HEBS calibration plate can be found in appendix A. The developing solution (Shipley MF319) was diluted in water by a factor of two in volume to lower the contrast during development.

Sample reference	JSR 5X60	JSR 6.5X40	JSR 7.5X45	JSR 10X20	JSR 15X75	JSR-oxi 4X45	JSR-oxi 25X70	JSR-oxi 7.5 X 45
Substrate configuration	Si	Si	Si	Si	Si	Si/SiO_2	Si/SiO_2	Si/SiO_2
HMDS spun	yes	yes	yes	yes	no	yes	yes	yes
Speed (RPM)	3000	3000	3000	3000	1000	4000	1000	3000
Spinning *t* (s)	20	20	20	20	20	20	20	20
Thickness before exposure (Å)	9000	9000	9000	9000	27000	6000	27000	9000
Exposure *t* (s)	5	6.5	7.5	10	15	4	25	7.5
Development *t* (s)	60	40	45	20	75	45	70	45

Table 4.2a Photolithography parameter settings for JSR IX575 photoresist

Sample reference	AZ 20 X 90	AZ 30 X 90	AZ 30 X 150	AZ 25 X 240	AZ 45 X 120	AZ 65 X 120	AZ- oxi 45 X 120
Substrate configuration	Si	Si	Si	Si	Si	Si	Si/SiO_2
HMDS spun	yes	yes	yes	yes	yes	yes	yes
Speed (RPM)	3000	3000	3000	2000	2000	2000	2000
Spinning *t* (s)	40	40	40	40	40	40	40
Thickness before exposure (Å)	80 K	80 K	100 K	> 100 K	> 100 K	> 100 K	> 100 K
Exposure *t* (s)	20	30	30	25	45	65	45
Development *t* (s)	90	90	150	240	120	120	120

Table 4.2b Photolithography parameter settings for AZ4562 photoresist

After exposure and development, the samples were subjected to a long baking onto hot plate at 115 degrees for 10 minutes. It was carefully checked that the treatment did not affect dramatically the original contour. To attain samples with smoother 3 – d contours, thermal annealing cycles were attempted on some samples.

An alternative route entailed the preliminary transferring of the photoresist 3 – d features into a silicon oxide layer, which was subsequently employed as the 3 – d sacrificial mask. The transfer was obtained by parallel plate RIE. The selectivity of the process (Etch Rate SiO_x / Etch Rate photoresist) was reduced to ~ 0.10 by increasing the amount of oxygen in the etching mixture. The samples were clamped to the (water cooled) electrode using polyimide tape. RF power was set to 150 watts and the chamber overall pressure was around 65 mTorr. Other process conditions are shown in table 4.3.

Sample reference name	JSR 4 X 45 oxi	JSR 25 X 70 oxi	JSR 7.5 X 45 oxi
Substrate configuration	JSR/SiO_x/Si	JSR/SiO_x/Si	JSR/SiO_x/Si
RIE time with mask (min)	17.5	10	10
After mask removal (min)	0	5	2
Ar flow (SCCM)	15	15	15
CHF_3 flow (SCCM)	5	5	5
O_2 flow (SCCM)		5	2

Table 4.3 Reactive Ion Etching parameter settings for transfer of JSR sacrificial masks into the oxide layer thermally grown on silicon

Part of the samples underwent Deep Reactive Ion Etching in Inductively Coupled Plasma equipment. The recipes were devised following the standard ASE process in order to achieve maximum unidirectional etching, i.e. anisotropy near to one. The recipes were modelled on the original recipes contained in the database of the software that controls the ASE equipment. Coil Power was set to 600 Watts (reflected power is considered to be zero). The etching gas mixture was composed by SF_6 (130 SCCM flow) and O_2 (13 SCCM flow). Pure C_4F_8 (85 SCCM flow) was used as passivation gas. The process conditions for the samples realised using JSR photoresist directly as a sacrificial mask during etching are shown in table 4.4a. The samples with 3 – d masks made by AZ4562 photoresist were etched under the conditions reported in table 4.4b. Finally, the process conditions relative to the samples with hard silicon oxide 3 – d sacrificial masks are shown in table 4.5.

Sample reference name	JSR 5 X 60	JSR 7.5 X 45	JSR 10 X 20
Substrate configuration	JSR mask on Si	JSR mask on Si	JSR mask on Si
Process Time (min)	30	20 (10 + 10)	10
Etching Step Time (s)	7	7	7
Passivation Step Time (s)	5	5	5
Platen Power (W)	12	12	12

Table 4.4a Parameter settings for DRIE of sample using JSR photoresist as a sacrificial mask

Sample reference name	AZ 20 X 90	AZ 30 X 90	AZ 30 x 150	AZ 25 X 120	AZ 45 X 120
Substrate configuration	AZ on Si	AZ on Si	AZ on Si	AZ on Si	AZ on Si
Process Time (min)	60	60	50	180	180
Etching Step Time (s)	7	12	12	12	12
Passivation Step Time (s)	5	8	8	8	8
Platen Power (W)	12	15	15	15	15

Table 4.4b Parameter settings for DRIE of sample using AZ4562 photoresist as a sacrificial mask

Sample reference name	JSR 4 X 45 oxi	JSR 25 X 70 oxi	JSR 7.5 X 45 oxi
Substrate configuration	JSR/SiO_x/Si	JSR/SiO_x/Si	JSR/SiO_x/Si
Process Time (min)	10	10	11 (3+1+3+1+3) (*)
Etching Step Time (s)	7	7	7
Passivation Step Time (s)	5	5	5
Platen Power (W)	12	12	12

(*) the cycle has been particularly devised to alternate 3 minutes of common anisotropic cycle (process conditions expressed in table) and 1 minute of isotropic etching (only SF_6 with 500 Watt coil power and 10 Watt platen power without passivation step).

Table 4.5 Parameter settings for DRIE of sample using AZ4562 photoresist as a sacrificial mask

It can be noticed from the above tables how two kinds of recipe were used. The first (denominated "shallow") requires a platen (bias) power of 12 Watts and each cycle includes 7 minutes of etching followed by 5 minutes of passivation. The second (denominated "deep") entails a platen power of 15 Watts and 12 seconds of etching followed by 8 seconds of passivation for each cycle.

4.3.3 The direct DRIE method with decreases anisotropy

Following the literature survey of section 3.5, a series of trials were realised for investigating the direct microfabrication of cavities with complex contour using a conventional binary mask.

A photomask was specially designed. The pattern contains arrays of circular holes, with diameters of 30, 58, 86, 114, 142, 200, 300 and 400 μm and squared holes with sides ranging from 100 to 500 μm. A second mask containing squares and circles in a range from 5 to 20 μm (in side or diameter) was also used.

In all the trials <100> cut bare Silicon wafers were used (except in a single case). Clariant AZ4562 [*Clariant, 2004*] was used as a mask. The conditions of deposition and patterning are reported in table 4.6.

Parameter	Settings	Unit
Spinning Speed	4000	RPM
Spinning Time	40	Seconds
Pre Bake T	90	Degrees C
Post Bake t	90	Seconds
Exposure Dose	~ 270	mJ/cm^2 @ ~ 13.4 mW/cm^2
Development t	~ 120	Seconds
Post Bake T	90	Degrees Celsius
Post Bake t	600	Seconds
Final Thickness	~ 6.5	μm

Table 4.6 Parameters for mask deposition (AZ4562 photoresist) for the early direct etching trials

The standard process, denominated "deep", was set up by the company (STS) and recorded in the database of the equipment software. As recalled above (section 4.3.2), it is the same process used for the unidirectional transferring of photoresist ramps in AZ4562. The settings were optimised to yield the maximum anisotropy (straight sidewalls) also for very deep cavities. The main parameters characterising the "deep" process are reported in table 4.7.

First, the effect of unbalancing the etch/passivation equilibrium was explored, which leads to deviation from unidirectional etching. The passivation step time was first increased, and subsequently reduced to various extents. Oxygen was also added to the mixture. The conditions for all the samples produced are reported in table 4.8.

Isotropic etching cycles were performed in absence of any passivation mechanism. For characterising the isotropic process, numerous samples were produced varying the bias power applied to the sample and the process time. The etching mixture was generally composed of pure SF_6. Pressure was generally kept at 30 mTorr. Coil power was kept at 500 Watts. The main emphasis was on the characterisation of the results as a function of the bias power applied to the sample and the etching time. The overall processing conditions for the samples etched in absence of passivation steps are reported in table 4.9.

Standard Settings	Etching Step	Passivation Step	Unit
Coil Power	600	600	Watts
Platen Power	12	12	Watts
Gas Composition	$SF_6 + O_2$	C_4F_8	
Flows	130 + 13	85	SCCM
Pressure	23 to 25	25 to 37	mTorr
Step Length	12	8	sec

Table 4.7 Main settings of the "Deep" DRIE process for unidirectional etching

Sample	Pass step length	Etch step length	Process length	Other notes
	sec	sec	min	
Pass1	10	10	~ 120	
Pass2	12	10	~ 120	
O2	8	12	~ 120	10 % O_2 in etch mixture
Etch1	4	12	~ 60	
Etch2	2	12	~ 90	
Etch3	2	20	~ 90	

Table 4.8 Processing conditions for the samples etched by unbalancing the standard "Deep" process towards

Finally, samples were produced coupling long anisotropic cycles to full isotropic cycles. The settings of the anisotropic step were the same as the "deep" cycle. During the isotropic step the parameters were the same as those reported above (the bias power was set to 10 Watts). A first sample was etched anisotropically for 90 minutes, followed by an isotropic cycle 30 minutes long at 25 W bias. A second sample was etched

anisotropically for 60 minutes and then isotropically for 55 minutes with a bias power of 25 watts. Finally, a third sample was etched for 60 minutes in anisotropic fashion followed by 90 minutes at 10 W bias in pure SF_6.

Sample	Platen Power (Watts)	Time (minutes)	Other notes
ISO 0 - 60	0	60	(*)
ISO 2 - 60	2	60	
ISO 5 - 60	5	60	
ISO 10 - 30	10	30	
ISO 10 - 60	10	60	(*)
ISO 10 - 120	10	120	
ISO 10 - 180	10	180	
ISO 15 - 60	15	60	
ISO 25 - 15	25	15	
ISO 25 - 30	25	30	
ISO 25 - 60	25	60	
ISO 40 - 30	40	30	
ISO 10 mT	10	60	Pressure kept at 10 mTorr
ISO 0 110	0	60	Wafer < 110 > cut
ISO 10% O2	10	60	Etch mixture: O_2/SF_6 (13/135) SCCM (*)
ISO 20% O2	10	60	Etch mixture: O_2/SF_6 (26/135) SCCM

(*) Two samples were produced using two different masks so that the range of mask apertures varied from 5 μm up to 500 μm.

Table 4.9 Overall processing conditions for the samples etched in absence of passivation steps ("isotropic" etching)

4.3.4 Production of cavities to be used as concentrators

After the results were analysed it was decided to investigate further the etching in absence of passivation ("isotropic" etching). For this reason, a series of samples etched for a very long time was produced. A self-aligned double layer mask was used: the patterns were transferred into the thermally grown oxide (originally present on the wafers) by Reactive Ion Etching. The conditions for the dry etching were similar to those reported in sections 4.2 and 4.3.1: the power was set to 150 watts, the pressure to 100 mTorr and a $CHF_3/Ar/O_2$ mixture was fed to the chamber in a ratio of 5/15/5 SCCM. The etch rate of SiO_2 was around 40 nm per minute. Although the layer nominal thickness was 400 nm, the samples were etched for 15 to 20 minutes to allow for a uniform etching through the SiO_2 layer across the whole area of the wafer. The process consumed less than two microns of photoresist and the integrity of the bi-layer was preserved. The samples were then etched in the ICP-ASE Multiplex Machine by STS in absence of any carbonaceous gas so that deposition is ruled out on the surface being etched. The pressure was set to 30 mTorr and the power (to the coil) to 500 Watts for all the samples.

During the "isotropic" process, the selectivity of SiO_2 and AZ4562 over Si is above 100 and 50 respectively. However large variations may occur depending on the presence of O_2 in the etching mixture, on wafer thickness and on the presence of a backing support wafer. The first problem encountered when a backing wafer is introduced is a severe drop in selectivity. Since in earlier attempts photoresist masks ~6.5 μm thick were used, the masks were completely swept away in less than 90 minutes. Therefore the first series of attempts to produce arrays of through-the-wafer cavities concluded in a

complete failure. A second series of samples was realised devising the following improvements:

- wafer thickness was reduced to 250 μm,
- backing wafer thickness was also reduced to 250 μm,
- silicon-oxide-coated wafers were used, creating in this way a double mask during etching. (The pattern is partially transferred into the SiO_2 by RIE: see conditions of table 4.3.)
- photoresist thickness was raised up to ~13 μm (~11.5 μm after RIE of Si). The conditions for the deposition and patterning of thick AZ4562 masks are reported in table 4.10.

Samples could then withstand longer etching times (up to 4 hours) and through-the-wafer cavities could be obtained from mask apertures with diameter as low as 86 μm. The arrays of holes larger than 114 μm in diameter and all the arrays containing squares were shadowed during photolithography so that only the smaller holes remained on the mask. The SiO_2 mask was protected by AZ4562 until the end of the etching preventing mask breakdown. The conditions under which these samples were produced are shown in table 4.11.

Parameter	Settings	Unit
Spinning Speed	1500	RPM
Spinning Time	60	Seconds
Soft Bake T	90	°C
Soft Bake t	120	Seconds
Exposure Dose	~ 600	mJ/cm^2 @ ~ 13.4 mW/cm^2
Development t	~ 120	Seconds
Hard Bake T	90	°C
Hard Bake t	600	Seconds
Final Thickness	~ 13	μm

Table 4.10 Parameters for mask deposition (AZ4562 photoresist) for the advanced trials (thick layers)

Sample Name	Dev 3	Dev 4	Dev 5	Dev 6	Dev 0	Dev O_2
Etching mixture	SF_6	SF_6	SF_6	SF_6	SF_6	SF_6/O_2
Composition (SCCM)	150	150	150	150	150	130/13
Bias Power (W)	5	10	10	10	0	10
Etch Time (min)	90	120	180	210	270	180

Table 4.11 Processing conditions for the samples of the series "Device"

4.3.5 Characterisation of the results and metrology techniques

Many problems with the characterisation of the results are due to the complex topography of the cavities (or features) produced. In fact, these may present a slope varying locally across a wide range, largely asymmetric 3 – d contours or narrow concavities hard to inspect. These issues affect particularly the cavities with complex shape produced by direct etching, which will be treated in the second part of this section. Conversely, the features produced by unidirectional etching of grey scale

sacrificial masks (section 4.3.2) are easier to characterise: first, because they protrude (i.e. they are positive features); and second because they possess a generally higher symmetry than the cavities of section 4.3.3. The blazed gratings (or ramps), in particular, may be characterised by the simple cross section, since the slope is expected to be constant for all the sections perpendicular to the length of the ramp.

Ramp slope was assessed by profilometry using a Dektak 3st along a direction perpendicular to ramp length. However, the tip of the profilometer has a radius of curvature of ~ 2 μm and such coarseness produces a detectability limit when ramp profiles are measured. The results were validated for the photoresist ramps by comparison with the profiles produced by Atomic Force Microscopy (Digital Instruments Nanoscope 3000). The comparison between the profiles obtained by profilometry and the results of the AFM demonstrated that the accuracy of the mechanical method is satisfactory for the purposes of this research. The details and results of the validation procedure are reported in appendix B.

Additional problems arise when attempting to assess the slope of the ramps transferred into silicon at high depth. Very large discrepancies may occur if the bottom of the feature is very rough. For example the presence of "micrograss" can mask the real etch depth. "Micrograss" may be hundreds of microns high and therefore selectivity and etch rate values smaller than usual may be derived. Furthermore, above a certain slope, the accuracy of the mechanical instrument drops. If the profiles are compared with the slope calculated from scanning electron micrographs of cross sections, the results shows generally good agreement, providing the ramp gradient is below 50 degrees and there is a small amount of defects (like "micrograss"). Finally, the upper limit of the instrument is 120 μm; therefore the etch depth and slope of features higher than that can only by assessed by SEM (perspective views or cross sections).

A series of additional issues arise when attempting to analyse the cavities obtained by direct etching. Firstly, the shapes possess generally a complex 3 – d symmetry, so that SEM analysis of the cross section does not provide enough details to reconstruct the true contour. Secondly, quantitative analysis of surface roughness is awkward because of the complex topography. Profile metrology systems (and related software) are generally designed for characterising mainly plane and easily accessible surfaces. Measuring a rounded surface, with slope largely varying between 0 and 90 degrees is almost impossible for common profilometry. For these reasons, besides the usual qualitative inspection of the samples and cavities produced by scanning electron microscopy and optical microscopy, an entire series of characterisation methods were set up to acquire quantitative information about the cavities produced.

The first problem is the identification of the actual shape. Simple wafer cleaving is a way of producing cross sections neither reliable nor representative of the real contours produced. If one breaks the wafer mechanically or by scribing, then inclined cutting sides can mask the real contour, revealing different shapes when SEM pictures are taken. Use of a cutting rotary blade is ineffective since the thinner parts of the features are destroyed during the process, as exemplified in figure 4.5. The fastest and lowest cost solution was to cast a polymer in order to replicate a negative image of the cavities. Using a silicone-based elastomer, three-dimensional protruding replicas of the features

are produced [*Allen, 1981*]. Not only convex microstructures allow a perspective view, which is partly obstructed when cavities or trenches are observed, but it yields also a reliable way of assessing the major cross section of a cavity. The cross sections can be digitised and expressed by numerical matrixes. An exemplification of the procedure is reported in appendix C. In the results part, a large use is made of cross sections obtained in this way (see for example figures 6.22, 6.24, 6.26, 6.28 to 6.30, and 6.48). If one assumes that the cavities possess central symmetry, the major cross section may describe completely the shape of a cavity. Unfortunately, this is not true of most of the cavities produced. Sources of errors that may affect the results obtained using this method are discussed in the same appendix C.

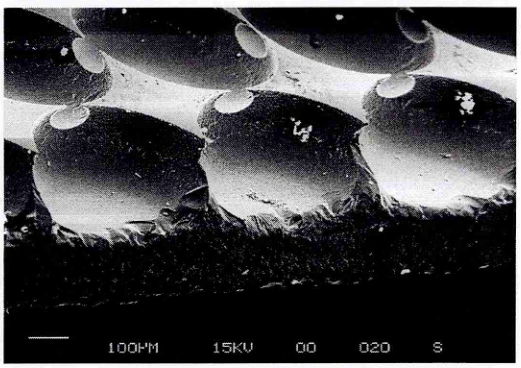


Figure 4.5 SEM photograph showing the heavy damage to the cross section due to action of the cutting wheel blade

The determination of surface roughness presents additional problems. Firstly, it is difficult to discriminate between roughness and actual deformations of the sidewalls. Some results showed extremely irregular cavities, with roughness ranging from a few microns to an extent of the same order of magnitude as cavity dimensions. However, for highly reproducible methods, such as the etching in pure SF_6 it was possible, in principle, to separate the contour of the sidewalls from the proper roughness. Secondly, even when it was possible to distinguish the roughness from the shape, it was not possible to assess the roughness directly. For this reason, an indirect method was applied. The method is detailed in appendix D. This method presents problems that limit its validity in drafting quantitative or absolute conclusions. In particular, although the scale of the first set of data is taken in microns, the deformation due to the filtering operations is not taken into account. A far more sophisticated algorithm would be required to transform the data in a way that the original scale (microns) is respected. Commercial software used for profilometry (such as Talysurf ©) use this method to deconvolute the roughness from the waviness. However, these techniques are generally used for the analysis of mechanically polished surfaces, where the radiuses of curvatures of waviness are 4 or 5 order of magnitude higher than the root mean square roughness. Conversely, for these cavities the roughness, in the best case, is at least one or two order of magnitude lower than the dimensions of the cavity. Nevertheless, the results may be used for comparing the relative quality of different surfaces. In any case, a validation is required by comparison with optical or SEM images.

Finally, the statistical analysis of cavity dimensions was attained by use of commercial image acquisition software (distributed with the Leica series optical microscopes). This software allows the simultaneous processing of many features (in this case the optical image of an array of membranes), to yield the dimensions of the marked features in the image. The area of individual features is calculated by computing directly the amount of pixels occupied by each feature. The "length" (i.e. the maximum Feret diameter) and the "breadth" (i.e. the minimum Feret diameter) are determined by an approximation algorithm, which yields discrete values.

4.4 Conclusion

This section reported the experimental details of the research. The process, up to the fabrication of the active layer, had already been already optimised before this research started. Therefore a small number of trials have been carried out. However, a large number of devices were produced using the process outlined in section 4.1.1. An apparatus for testing the pyroelectric response of the sensors was developed in the course of the research and was in use by the second half of 2003.

A series of trials was devoted to optimising the process for etching, the PZT layer, first, and, subsequently the full electrode–active layer stack. Attempts and definitive recipes were reported. Patterning an array of thin suspended membranes presented peculiar practical problems: the practicalities of the procedures were discussed.

The experiments to obtain 3 – d structures and cavities were presented in their experimental details (no reference to the results). The process details for producing 3 – d protruding features using grey scale masks were presented. The parameters of the etching recipes were collected in tables. Details of the masking materials used and of the practicalities involved were given.

Chapter 5 DESIGN AND ANALYSIS OF NON-IMAGING COLLECTORS FOR INCORPORATION IN THE INFRARED SENSING DEVICE

This section reports the results of the elaboration of a series of concentrator design types that might be suitable for incorporation in the final device. The work reported in this chapter is theoretical. The computations draw on the literature survey reported in section 3.1. The work was developed in parallel with the search for a microfabrication route. Compound Parabolic Concentrators and V concentrator design were analysed in terms of collection efficiency. A second class of concentrators was derived from the design of the original CPC. (This novel design was termed *suspended* or *enlarged* collector.) This class, introduced in section 5.1, is conceived to show better compatibility with the thermal isolation (i.e. the suspension) of the sensing elements.

The theoretical performance of a concentrator design can be evaluated analytically, from its contour. However, the increase in overall power collected depends on the distribution of the flux power that reaches the concentrator. The effect of flux distribution on collection efficiency is exemplified for a series of 2 – d CPC collectors in section 5.2.

Since concentration ratio is a function of the shape (of the sole shape at the design stage), it is reasonable to use the shape as a direct figure of merit. During the preliminary survey stage, many microfabrication techniques were judged unsuitable for the application because they were not expected to produce results near to the required geometry. The estimations made in section 3.2, based on the literature survey, were very rough. Once results approximately near to the required shape (i.e. the CPC) are produced, more sophisticated techniques are necessary for predicting and comparing the performances of the collectors. In fact, it would be inconceivably time consuming to test experimentally the performance of the infrared detectors by producing and testing devices that incorporate every attempted concentrator shape. (For a deeper discussion on the way of testing the collectors efficiency experimentally see sections 8.3 and the future work section.) The ray tracing technique, which was introduced briefly in section 3.1, is discussed in details in section 5.3 in its physical principles. Ray tracing represents a fast method for predicting the collection efficiency as a function of the concentrator contour. Ray tracing will be applied here anytime it is not practical or possible to obtain results using an analytical route. Conversely, it is always possible to compute analytically the acceptance of direct rays (i.e. the rays that pass through without hitting the reflectors). The collection of the direct rays is discussed in section 5.4.

The mathematical elaboration of sections 5.1 to 5.4 represents a personal contribution: the material presented was not found in literature but it was developed during the research. These equations set the background for the calculation of the theoretical collection efficiency of various systems. The results will be employed to compute the performance of the IR sensor in chapter 8 (section 8.2.2). The analysis of the transmittance of the design types based on the 2 – d CPC and the V collectors are reported in section 5.5 and 5.6 respectively. Full collectors were analysed, as well as truncated collectors and suspended collectors. All the details of the calculations have been removed to appendix E for a better readability of the section. After the properties

of the various types of design have been determined individually, the effects of the incoming power distribution are eventually introduced in section 5.7. There, the efficiency of the collectors is compared and the differences in performance discussed.

5.1 The enlarged concentrator with a suspended inner active area

Two alternative types of collector were analysed for each design considered, namely the *full* (or *original*) and the *suspended* (or *enlarged*) systems. The full system has a full absorber membrane, i.e. all the rays crossing the exit aperture of the collectors are assumed to hit the active sensing element. On the contrary, in the enlarged series the central active area is ideally suspended to allow thermal isolation from the sidewalls. The radiation that crosses the exit aperture outside the central active area is assumed to be lost. The suspended series is introduced because of its compatibility with the spiral-based isolated structures. The design procedure for expanding the original concentrator is showed in figure 5.1 for the 2 – d CPC case: one of the reflectors is translated horizontally to an extent *s*. The edge-ray principle still applies to this enlarged construction: rays incident at the acceptance angle (θ) are focused on the extreme of the suspended active segment (*F'* or *F*). Of course the enlarged 2 – d CPC is no longer ideal because part of the rays will fall outside the active area and get lost. Its transmittance is necessarily lower than 100 %. The 3 – d enlarged concentrator may be thought of as originating from the revolution about the central axis of this wider cross section. The outer ring corresponds to the inactive area of the element (where the spiral bridges lay).

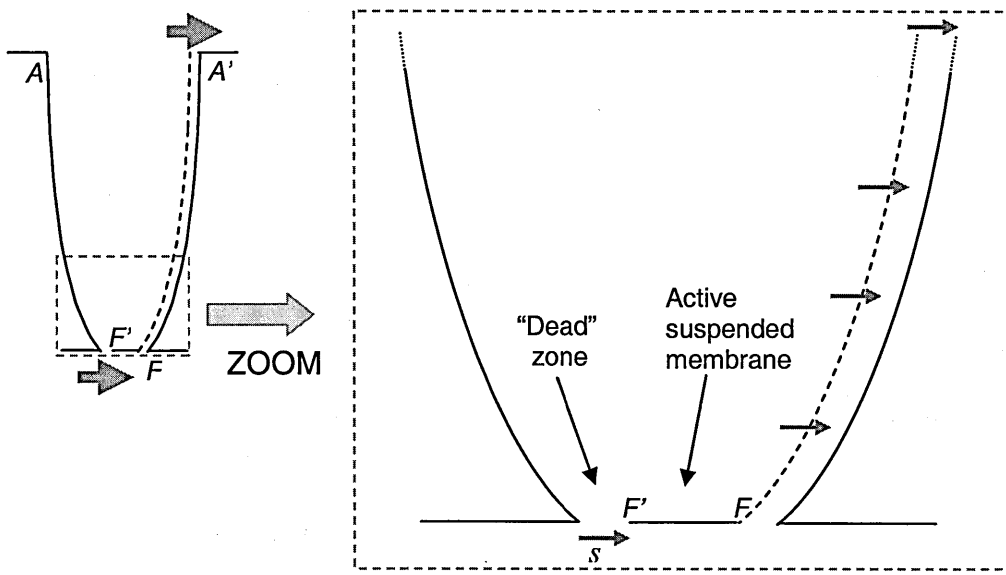


Figure 5.1 Procedure for building a larger CPC maintaining the edge-ray principle (relatively to the inner active area).

A respective enlarged version was analysed for each contour type considered. A gallery of sketches of the profiles evaluated (including the enlarged versions) is in appendix E-1.

5. 2 The effects of power distribution on power collection

In section 3.1 the basics of non-imaging concentrators (in particular Compound Parabolic Concentrators) were introduced following the treatment made by Winston [*Welford and Winston, 1989*]. In that treatment, it was implicit that a concentrator is always designed so that its acceptance angle matches the cut-off angle of the distribution of power flux that reaches the concentrator (if such an angle exists). However, if this matching may be achieved when manufacturing large collectors with conventional techniques, it is certainly not the case for micromachined collectors. In fact, many constraints exist and limit the range of shapes that it is possible to produce. (The main constraints were reviewed in section 3.2.) It might happen that a collector receives a power flux with a variable distribution, or with a distribution that is not exactly matched to the acceptance angle of the collector. For this reason, the effect of the power flux distribution on the performance of a given collector represents an important variable to be considered. Calculations are reported in the following, for the 2 – d CPC design, which yields the most simple and intuitive results. The computation was developed only in two dimensions because working in three dimensions would have entailed devoting large time and resources to the theoretical calculations or acquiring a specific commercial package, such as OptiCAD (www.opticad.com), which was not available (or affordable). The effects of the distribution of the power flux will be calculated for all the systems of interest in section 5.7, once their transmittance has been assessed in sections 5.5 and 5.6.

With reference to figure 5.2 (in two dimensions), the power flux crossing a given point x along the entry of the individual concentrator from a given incidence angle φ is given by $\boldsymbol{B}$ [watts m^{-1} rad^{-1}]. In [*Hudson, 1969*] this measure is called radiance. If the flux is uniform, $\boldsymbol{B}$ is constant in x (for $-a \leq x \leq a$). If the flux is also isotropic, then $\boldsymbol{B}$ is constant in φ. Only the effect of a flux uniform in x will be considered. For the notation of figure 5.2, φ is taken as positive if the incidence angle is taken clockwise from the y axis (and $\varphi < 0$ otherwise). The same notation applies to the cut-off angle of the distribution ω and to the acceptance angle of the concentrator θ. Furthermore, since all the systems analysed here are symmetric along the central axis, only the case for $\varphi > 0$ will be taken into account, unless where especially stated. It is clear that all the considerations that will be expressed in this chapter and relative appendix remain equally valid for the symmetric case, i.e. if all the angles are substituted with their opposite.

The total flux acting on a given infinitesimal segment dx is called irradiance H_I [watts m^{-1}] in [*Hudson, 1969*]. It is given by:

$$H_I = \int_{-\omega}^{\omega} B\cos\varphi \, d\varphi = 2\int_{0}^{\omega} B\cos\varphi \, d\varphi \qquad (5.1)$$

where ω is the cut off angle of the flux distribution (beyond which there is no incoming radiation, i.e. $\boldsymbol{B} = 0$). The integral is reduced since the flux distribution is assumed to be symmetrical along the concentrator axis.

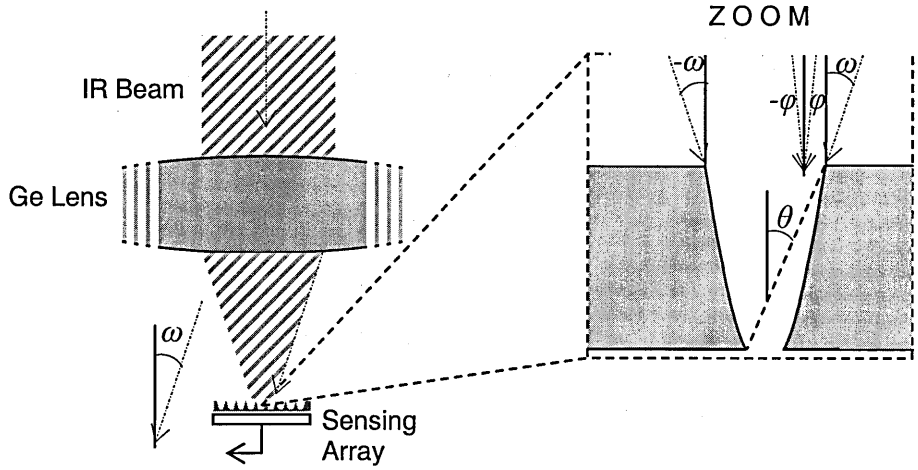


Figure 5.2 Schematic of a set-up made by macroscopic lens and focal plane array of CPC concentrator(s). The geometric optics of the IR beam is indicated. The particular case for which $\theta < \omega$ is illustrated.

If ***B*** is uniform and isotropic then the flux can enter from all directions so that $\omega = \pi/2$ and $H_I(\pi/2) = 2\,B$. The radiant flux (P_ω) [watts] corresponds to the total power incident on a segment of width $2a$ (where $2a$ is the entry aperture of the individual concentrator).

$$P_\omega = \int_{-a}^{a} H_I \; dx = 4 \int_0^a \int_0^\omega B \cos\varphi \; dx \; d\varphi \tag{5.2}.$$

Since B is assumed not depend on x, equation 5.2 simplifies to:

$$P_\omega = 4a \int_0^\omega B \cos\varphi \; d\varphi \tag{5.3}.$$

In analogy with H_I, an isotropic distribution in B yields $P_{\pi/2} = 4\,a\,B$.

Equation 5.3 represents the total power contained into a flux triangle (a cone in 3 – d) of limiting angle ω. However, the total flux that emerges through the concentrator is given by:

$$P = 4a \int_0^\theta B\,T \cos\varphi \; d\varphi \tag{5.4},$$

where T is the transmittance of a beam at incidence φ and θ is the acceptance angle of the concentrator. Of course, the concentrator cannot accept any radiation for $\varphi > \theta$ but a non-ideal concentrator will reject part of the radiation also for $\varphi \leq \theta$.

There are many ways of expressing the performance of a concentrator. In section 3.1 a measure called concentration ratio was introduced. Equation 3.1, applied to the 2 – d case yields

$$C = (P/2\,a') / (P_\theta/2\,a) = \frac{a}{a'} \left(\int_0^\theta B\,T \cos\varphi \; d\varphi \Big/ \int_0^\theta B \cos\varphi \; d\varphi \right) \tag{5.5},$$

where $2\,a'$ represents the exit aperture of the concentrator and P_θ is the total power that enters the concentrator, with analogy to equation 5.3. Another interesting measure of collector efficiency is the ratio between the power that passes through the collector (P) and the power that, under the same power flux, would enter a single isolated element

(with no collector attached) of extent equal to the exit aperture 2 a'. The latter is equal to:

$$P_{a'} = 4a' \int_0^{\omega} B \cos \varphi \, d\varphi \qquad (5.6).$$

In the following, it will be demonstrated how, for the 2 –d CPC the ratio $P / P_{a'}$ depends on the distribution of the power flux that reaches the collector whereas the expression for the concentration ratio is a characteristic of the sole concentrator design.

For the CPC design it was demonstrated in section 3.1 that $T = 1$ for $\varphi \leq \theta$ ($T = 0$ otherwise). Therefore equation 5.4 simplifies to

$$P_{2-d\ CPC} = 4a \int_0^{\theta} B \cos\varphi \, d\varphi \qquad (5.7)$$

and

$$P_{2-d\ CPC} / P_{a'} = \frac{a}{a'} \left(\int_0^{\theta} B \cos\varphi \, d\varphi \Big/ \int_0^{\omega} B \cos\varphi \, d\varphi \right) \qquad (5.8).$$

If the flux is isotropic then $P_{2-d\,CPC} / P_{a'} = a / a' \sin\theta$ and, applying the geometric property of the CPC (equation 3.5), $P_{2-d\,CPC} / P_{a'} = 1$. This demonstrates that a fully diffused flux cannot be further concentrated, as it was claimed in section 3.1. In a non-ideal system T would necessarily be lower than one, so that $P / P_{a'} < 1$. (The non-ideality can be due to the design or to actual deviations from ideality induced by material and surface constrains.) In conclusion, the introduction of a concentrator in a totally diffused flux is always disadvantageous since it leads to the inevitable reduction of the energy collected. For the 2 – d CPC, equation 5.5 reduces to the expression a / a', independently on the expression of B. (Compare with equation 3.1, i.e. $C = A / A'$.)

The advantage of introducing a collector emerges in an anisotropic flux ($B = f(\varphi)$). This can be demonstrated for a very simple square-wave flux distribution, i.e.

$$B = \begin{cases} B \text{ (constant)} & \text{for } \varphi \leq \omega \\ 0 & \text{for } \varphi > \omega \end{cases} \qquad (5.9).$$

For $\omega \leq \theta$, equation 5.8 yields:

$$\frac{P_{2-d\ CPC}}{P_{a'}} = \frac{a}{a'} = \frac{1}{\sin\theta} \qquad (5.10).$$

Equation 5.10 shows that the increase in power collected obtained by introducing a 2 – d CPC is exactly equal to the concentration ratio of the CPC as long as the limit angle of the flux angular distribution is less or equal to the acceptance angle of the CPC. The particular case for which $\omega = 0$ is implicitly contained in the above situation, because for unidirectional distribution $P_{2-d\,CPC} = 2\,a\,B$ and $P_{\pi/2} = 2\,a'\,B$. On the contrary, for $\omega > \theta$:

$$\frac{P_{2-d\ CPC}}{P_{a'}} = \frac{a}{a'} \frac{\sin\theta}{\sin\omega} \qquad (5.11).$$

Introducing the geometrical relation for the 2 – d CPC (equation 3.5) equation 5.11 becomes:

$$\frac{P_{2-d\ CPC}}{P_{a'}} = \frac{1}{\sin\omega} \qquad (5.12).$$

In conclusion, the gain is maximum for $\omega \leq \theta$; it then decreases as the flux becomes less collimated, eventually tending to 1 as $\omega \rightarrow \pi/2$, i.e.

$$\frac{P_{2-d\ CPC}}{P_{a'}} = \begin{cases} \dfrac{1}{\sin\theta} & \text{for } \omega \leq \theta \\ \dfrac{1}{\sin\omega} & \text{for } \omega > \theta \end{cases} \qquad (5.13).$$

A plot of $P_{2-d\,CPC} / P_{a'}$ as a function of distribution cut-off angle is reported in figure 5.3, for the simple distribution of equation 5.9. More complex distributions such as Gaussian or Cosine produce results qualitatively similar (The effects of such distributions are reported, as an example in appendix E-2).

The distribution of equation 5.9 may be thought as produced by an ideal germanium lens. These lenses are used to focus the IR radiation on the plane of the array in conventional infrared sensors (e.g. in the Vidicon, a scheme of which was reported in figure 2.7). Lens aberrations are here disregarded because the scope of this section is just to highlight the qualitative behaviour of the concentrators under different flux conditions. A lens with *f*-number equal to 1 produces a distribution with a cut-off angle of 30 degrees. The maximum theoretical concentration ratio that can be obtained from such distribution is equal to $1 / \sin(\pi / 6) = 2$. This is not satisfactory, considering that an actual concentrator would even probably fail to reach a collection efficiency of 2. Such a small improvement would not justify the expenditure required for prototyping and producing a new device. If a lens with *f*-number equal to 2 is introduced, then $\omega = 14.48$ degrees and the maximum concentration ratio is equal to 4. In fact, figure 5.3 shows that every CPC with acceptance angle (θ) below 14.48 degrees would drive onto the exit aperture 4 times the power that would enter the same aperture in absence of any collector. For $\theta \leq \omega$ the total power collected is simply given by $P = 4\ a\ B \sin\theta$, i.e. $P = 4\ a'\ B$. Therefore the power collected by a CPC with acceptance angle below the cut-off angle of the distribution is always equal to the overall power that would enter the exit aperture isolated if this were immersed in an isotropic flux of equal magnitude B. This confirms what stated above and in section 3.1 about the upper limit of concentration and the ideality of the CPC design. Eventually, all the CPCs with $\theta > \omega$ collect a total power equal to $4\ a\ B \sin\omega$.

In the example of figure 5.3, if $B = 1$ μWatts μm^{-1} rad^{-1} and $\omega = 14.48$ degrees, then the power collected by any CPC with $\theta \leq \omega$ and $a' = 75$ μm is equal to 300 μWatts. On the contrary a CPC with θ equal to 20 degrees is able to collect only 219 μWatts (the extent of the entry aperture is larger but the concentration ratio lower). Similarly a CPC with $\theta = 30$ degrees (concentration efficiency equal to 2) can only collect ~ 150 μWatts. To conclude, from the diagram of figure 5.3 and from what stated above, it is always better to use a CPC with acceptance angle lower or equal to the cut off angle of the

distribution. However, the maximum theoretical concentration achievable (in two dimensions) is always equal to 1 / sin ω.

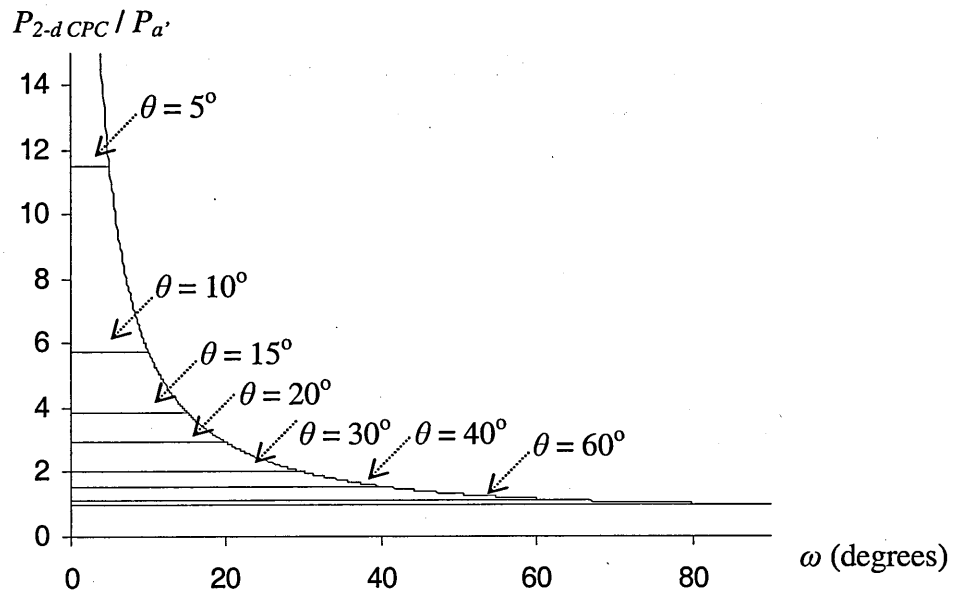


Figure 5.3 **Ratio between the power collected by the 2 – d CPCs and the power that would be collected by the exit aperture in absence of the CPC as a function of the cut-off angle of the incoming power flux distribution. The acceptance angle of the CPCs is indicated beside each curve.**

5.3 Physics of concentrators and Ray Tracing technique application

It is recalled that throughout this chapter, only the 2 – d case for which $\varphi \geq 0$ will be considered. Also, it will be assumed that the flux is uniform along the x direction and its distribution can be described by a simple relation such as equation 5.9. It is important to stress that the computation is carried on ideal systems: the mirror surfaces are assumed to have 100 % reflectance. All the radiation is either rejected or passed through. No energy is lost within the concentrator by scattering of absorption from the sidewalls.

The assumptions made above allow the division of the beam into bundles, which are either fully accepted or fully rejected. This procedure, exemplified (for the enlarged CPC) in figure 5.4, opens the possibility for a partial analytical treatment of the optical phenomena. First, the calculation will discriminate between the portions of the beam that hit the reflectors and the portions that pass through directly. This can be always done analytically: the analysis of the contribution obtained from the direct rays (i.e. rays that enter without reflection) is reported in section 5.4. The assumption of perfect reflectivity entails that in these (simple) systems a finite number of rays (extreme rays) trace the boundary between the parts of the incoming beam which show different optical behaviour. In the example of figure 5.4 (ray tracing from the left sidewall of a 2 – d CPC) there are just two of these extreme rays. In 3 – d concentrators of the type

introduced in section 3.1 (i.e. with cylindrical symmetry) the loci of the extreme rays form continuous surfaces [*Welford, and Winston 1989, Chapter 4*].

The direction of the extreme rays depends on the incidence angle of the beam (φ). In 2 – d they are described by the equation $y = \tan [(\pi / 2) - \varphi]\, x + k_{\text{lim}}$. These rays identify segments of acceptance along the entry aperture (AA'). These segments are clearly marked in figure 5.4. Each of these segments has a width $w = \Sigma\, a_i$, where a_i represents the length of the i^{th} segment of acceptance along AA'. The irradiance coming to the concentrator from a given incidence angle φ is given by:

$$H_{\varphi} = \int_{-a}^{a} B\cos\varphi \, dx = 2aB\cos\varphi \qquad (5.14).$$

The quantity $2a \cos \varphi$ represents (geometrically) the width of the incoming beam, which enters the concentrator at an angle φ. The part of the beam that passes through the concentrator (i.e. effectively collected) is equal to $\Sigma\, a_i \cos \varphi$, that is $w \cos \varphi$, and the total power carried by this beam is equal to $B\, w \cos \varphi$. The transmittance at a given incidence angle is then simply given by:

$T(\varphi) = B\, w \cos \varphi \,/\, 2\, a\, B \cos \varphi = w\,(\varphi) \,/\, 2a \qquad (5.15).$

This expression can be demonstrated in two other ways as detailed in appendix E-3.

If the values of $k_{\text{lim}}(\varphi)$ are known, then analytical expressions for all the acceptance segments can be found, eventually leading to an explicit analytical expression for T as a function of the incidence angle (φ). Although theoretically possible for all the highly symmetric systems presented here, this route was found not viable in practice. In fact, the search for $k_{\text{lim}}(\varphi)$ for most systems led very soon to expressions of such complexity that the roots could not be found by symbolic resolution (see, e.g. appendix E-5).

Anytime the equations were too complex to be solved, the ray tracing technique was employed, after solving separately the parts of the problem for which the analytical solution was practical (e.g. the bundle of rays that pass through the concentrator without hitting the sidewalls). Ray tracing is a statistical method based on the iteration of simple rules of geometrical optics. A number of rays are virtually shot through the system. The trajectory of each individual ray is assessed. The number of rays crossing a surface represents the total power flux (each ray represents a "bundle" of radiations, associated with a prescribed amount of power). In 2 – d, the number of rays per length unit corresponds to the energy density. In the ideal cases evaluated here (where neither refraction nor adsorption phenomena are kept into account), the simple rules of geometrical optics are sufficient to accomplish the ray tracing calculation. The ray tracing algorithm is reported in appendix E-4. In appendix E-3 it is demonstrated how equation 5.15 could be derived also from arguments based on ray tracing.

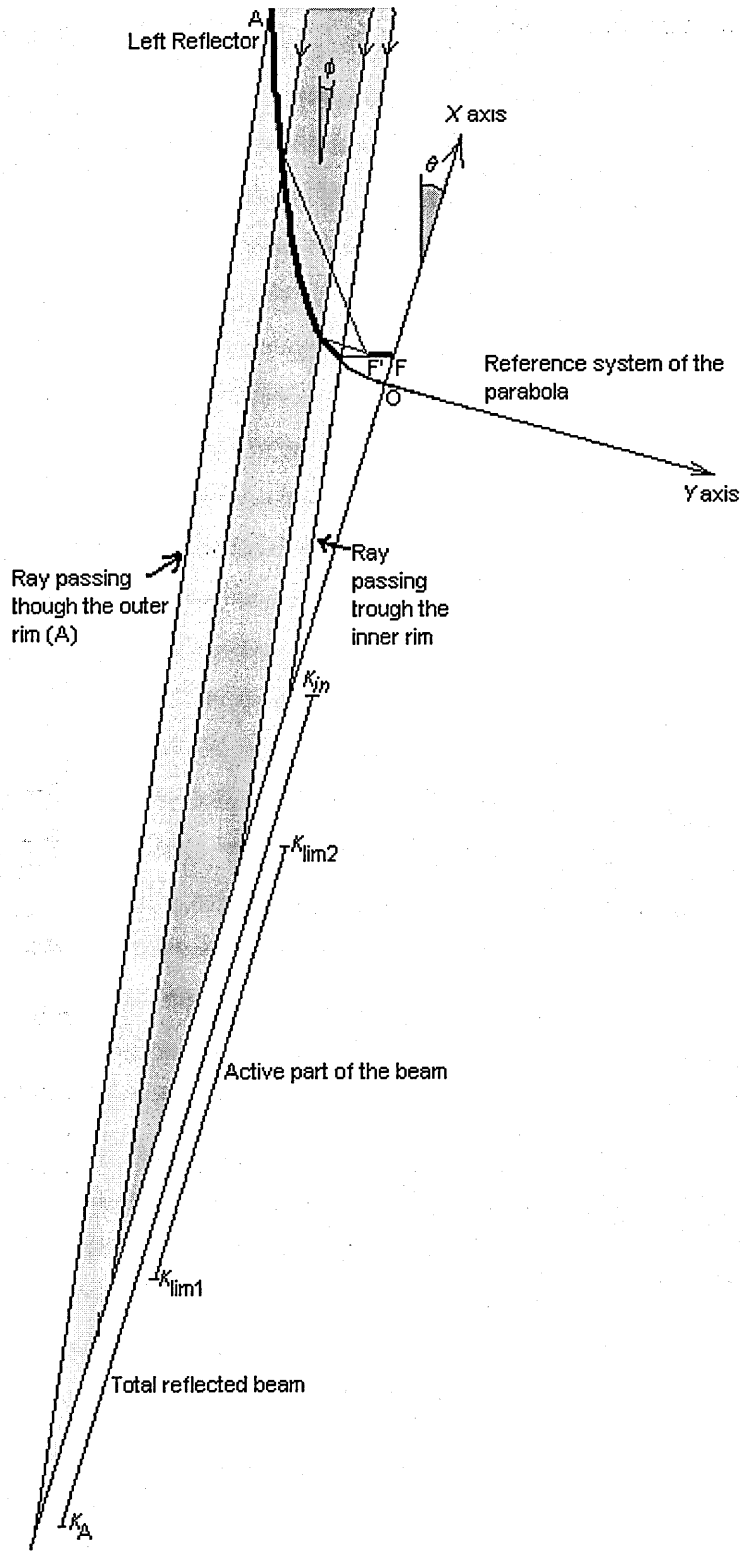


Figure 5.4 **An example of reflection from a 2 – d enlarged CPC that shows the parts of the beam that are rejected (light grey) and the parts that pass through the active area (dark grey)**

5.4 Acceptance of direct rays

The contribution to collection from the radiation that enters directly (without hitting the reflectors) was calculated separately. Not only can this contribution be easily evaluated analytically: it can also be described by a single expression, independently on the concentrator profile (unless the profiles contains cusps that scatter the radiation). The geometry of a generic 2 – d non-imaging concentrator with mirror symmetry and full membrane absorber is sketched in figure 5.5*a*. The segment of extent a_{direct} lies on the exit aperture (*AA*' direction) and describes the beam part that hits the absorber directly without being reflected. It can be easily demonstrated from simple geometric considerations that a_{direct} is equal to:

$$a_{direct} = \begin{cases} 2\,a' & \text{if } 0 < \varphi \leq \arctan[\,(a-a')/L\,], \\ (a+a'-L\tan\varphi) & \text{if } \arctan[\,(a-a')/L\,] < \varphi \leq \arctan[\,(a+a')/L\,], \\ 0 & \text{if } \varphi > \arctan[\,(a+a')/L\,]. \end{cases} \quad (5.16).$$

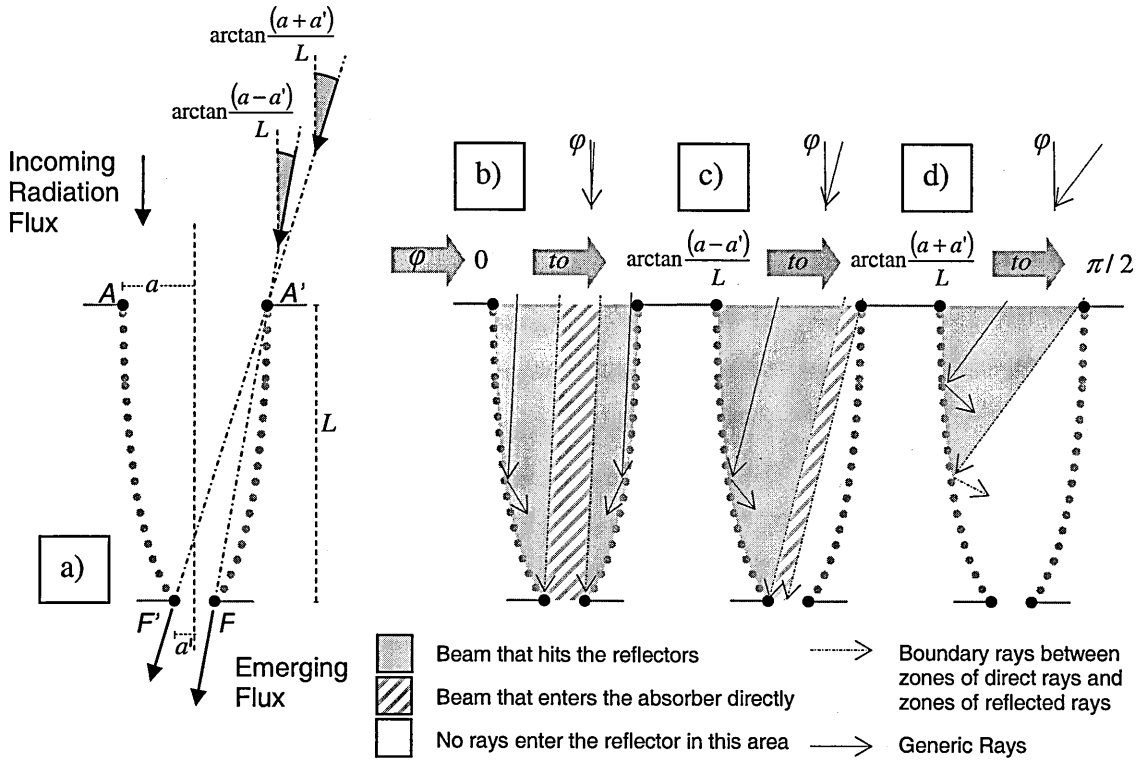


Figure 5.5 **(a) Direct acceptance (without reflection) of rays in a generic generic 2 – d concentrator with mirror symmetry. For discussion on the role of the two angles indicated see text. The three intervals of full acceptance (figure 5.5b), partial acceptance (5.5c) and no acceptance (5.5d) are reported with indication of the range of incidence angle.**

The three cases of equation 5.16 are symbolically illustrated in figure 5.5. In the first case (figure 5.5b) there is no shadowing of the direct rays. In the second case (figure 5.5c) there is partial shadowing whereas in the third case (figure 5.5d) the shadowing is

complete and all the incoming rays hit one of the reflectors. In the CPC, the expression arctan[$(a + a') / L$] corresponds to the acceptance angle (θ). A 2 – d CPC would not accept any radiation above that incidence angle, even after reflection. The same expression is valid for both the cone and the parabolic concentrator by geometrical construction, although rays with higher incidence angle may still be transmitted after reflection.

The extreme angles for the suspended structure are reported in figure 5.6. The different cases are as follows.

$$a_{direct} = \begin{cases} 2a' - s & \text{if } 0 < \varphi \leq \arctan[(a - a' + s)/L], \\ (a + a' - L\tan\varphi) & \text{if } \arctan[(a - a' + s)/L] < \varphi \leq \arctan[(a + a')/L], \\ 0 & \text{if } \varphi > \arctan[(a + a')/L]. \end{cases} \quad (5.17).$$

Equations 5.16 and 5.17 demonstrate that:

1) The extent of radiation that enters directly is independent on the reflectors profile (for the simple systems reported here and as long as the contours do not contain convexities or cusps that would induce scattering).
2) The collection of direct rays depends only on the shadow the entry aperture casts on the exit aperture: therefore, only on the geometrical parameters of the collector (a, a', and L).

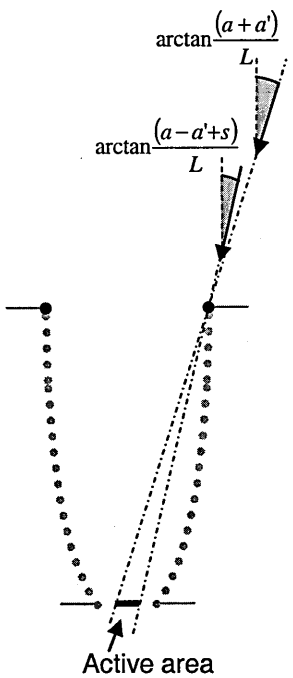


Figure 5.6 **Geometry of a generic enlarged concentrator with suspended central structure. For discussion on the role of the two angles indicated see text.**

Plots of a_{direct} vs. φ for a full generic concentrator are reported in figure 5.7. a and a' are fixed at respectively 300 and 75 μm and L varies from 200 to 1600 μm. The overall power transmitted through the concentrator without reflection is equal to $a_{direct}\, B \cos \varphi$. To compute the overall transmittance, one has to add to the segment a_{direct} all the contributions from the bundles accepted after one or more reflections. This will be accomplished individually for each specific design type in sections 5.5 and 5.6.

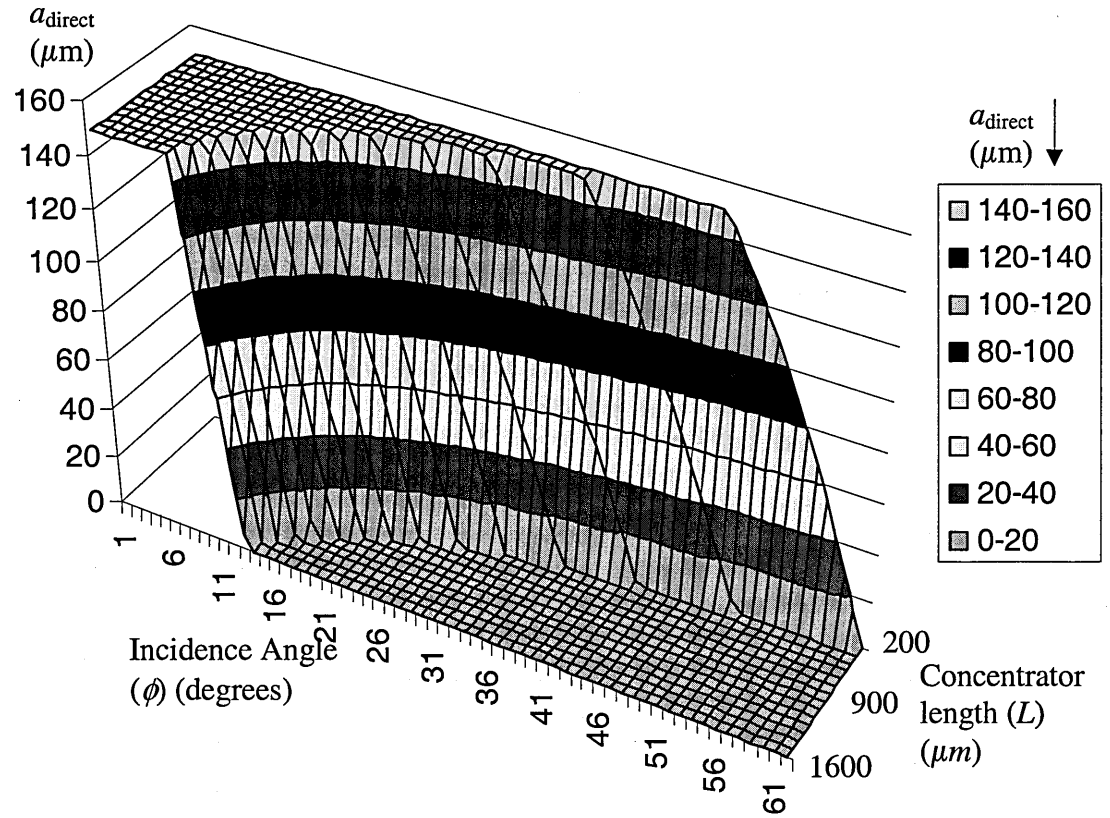


Figure 5.7 **The width (along AA') of the directly accepted beam (a_{direct}) as a function of the incidence angle and depth of the concentrator. This plot refers to a generic symmetric 2 – d concentrator, with no reference to the particular reflectors profiles. Geometric concentration ratio (a / a') is constant. Length (L) varies from 200 to 1600 micrometers.**

5.5 Acceptance and transmission of the 2 – d CPC-based design types

This section will discuss the performance of different types of design derived from the 2 – d Compound Parabolic Concentrator. The first step is to choose a suitable CPC design. In section 5.2 it was shown how a possible value for the cut-off angle of the power flux distribution was ~ 14.48 degrees. However, the geometry has to be chosen to meet the constraints of the overall process, which were extensively discussed in section 3.2. As a compromise between these two issues, a CPC design with angle near to 14.48 degrees was chosen. Its geometric parameters are shown in table 5.1. (This CPC corresponds to the second curve from the bottom of the family of CPCs originally built in figure 3.5.)

Parameter	Value
θ (Acceptance Angle) [deg]	14.47751
a' (Exit half width) [μm]	75
a (Entrance half width) [μm]	300
Concentration ratio (2 – d)	4
Geometric concentration ratio (3 – d)	16
Full Length [μm]	1452

Table 5.1 The geometric parameters upon which the 2 – d CPC design and the systems derived from it are constructed.

Due to the geometrical properties of the 2 – d CPC, which is an ideal concentrator, a beam of width equal to 2 a cos φ is always accepted for $\varphi \leq \theta$ whereas no rays are accepted for $\varphi > \theta$. Similarly, the suspended CPC accepts no radiation at incidence above θ (or below - θ), neither directly nor upon reflection. If these rays may pass through the entry aperture, they will certainly fall into a dead zone (i.e. beyond F or F') due to the geometrical construction of the system. Conversely, all rays are accepted for $\varphi = \theta$: the reflections fall all onto the edge of the active segment (F') for the geometrical properties of the CPC reflectors. For $\varphi < \theta$ the incoming rays can be accepted or rejected depending on the position at which they cross the entry aperture AA' (as exemplified in section 5.3 and figure 5.4).

Once the acceptance of direct rays is assessed (this was accomplished in section 5.4), the calculation of $T(\varphi)$ requires the determination of the extreme rays that divide the parts of the beam that are reflected on the active area (i.e. the bundles coloured in dark grey in figure 5.4) from the parts of the beam that are reflected onto the "dead" zones (i.e. the bundles coloured in light grey in figure 5.4). This is a simple problem of analytic geometry and various attempts were made to solve it analytically. Although a viable route was found (the details are in appendix E-5), it was not possible to solve the final equation analytically. Assessment of the transmittance by ray tracing represented an alternative way. Graphic displays reporting ray tracing examples are reported in appendix E-5.

The ray tracing calculations followed the algorithm reported in appendix E-4 and the details of the calculations are reported in appendix E-5. The geometrical parameters used for the computation are reported in table 5.1. The results are plotted in figure 5.8 (plot of transmittance as a function of the incidence angle). Since the system is assumed to be symmetrical along the axis of the collector, the results are displayed only for $\varphi > 0$. The contributions for the reflectors are evaluated separately (see appendix E-5). Eventually, the contribution from the direct rays is added (evaluated with the modality reported in section 5.4). In analogy with equation 5.15, the overall transmittance is equal to $w / (2\,a + s)$. Note that the overall transmittance of the enlarged 2 – d CPC is always below 100 % because the presence of dead zones in the collecting membrane leads to the inevitable loss of part of the rays for any incidence angle, even for $\varphi = \theta$.

Since a value of 600 μm represents an ideal upper limit to wafer thickness, it is clear that CPCs cannot be easily produced with the depth specified in table 5.1 unless a layer of different material is bonded to the primary silicon-based structure. In literature, truncation has been proposed as a viable route to design shorter concentrators. (Truncation was discussed in section 3.2.) Figure 5.9*a* schematises the generic operation of truncation on the CPC built with the parameters of table 5.1. The performance of a truncated 2 – d CPC can be assessed from purely geometric considerations as follows. It is clear from figure 5.9 that, as the degree of truncation increases, the width of the beam that enters the concentrator at a given incidence angle φ, that is $2a^T \cos \varphi$, decreases (plot of figure 5.9*b*). On the contrary, as the CPC becomes shorter, the angular extent of acceptance increases. In particular, both quantities $\arctan[(a^T - a') / L^T]$ and $\arctan[(a^T + a') / L^T]$ increase, as showed in the diagram of figure 5.9*b*. The new half-width, a^T, can be easily calculated using the CPC geometrical properties. (The method proposed by Carvahlo et al. was employed [*Carvahlo et al., 1985*].) The transmission behaviour of direct rays, being independent on the actual profile, is expressed by equations 5.16 and 5.17 (substituting a with a^T). Rays are totally collected for $\varphi \leq \theta$ because the reflectors still possess the CPC contour. For the same reason, only direct rays are collected for $\varphi > \theta$. In conclusion the width of accepted beam (along AA') for the may be written as:

$$w = \begin{cases} 2\,a^T & \text{if } 0 < \varphi < \theta \\ (a^T + a' - L^T \tan\,\varphi) & \text{if } \theta < \varphi < \arctan[(a^T + a') / L] \\ 0 & \text{if } \arctan[(a^T + a') / L] < \varphi \end{cases} \qquad (5.18).$$

w is reported in the diagram of figure 5.10 as a function of incidence angle and length for a series of concentrators built by truncating the 2 – d CPC of table 5.1.

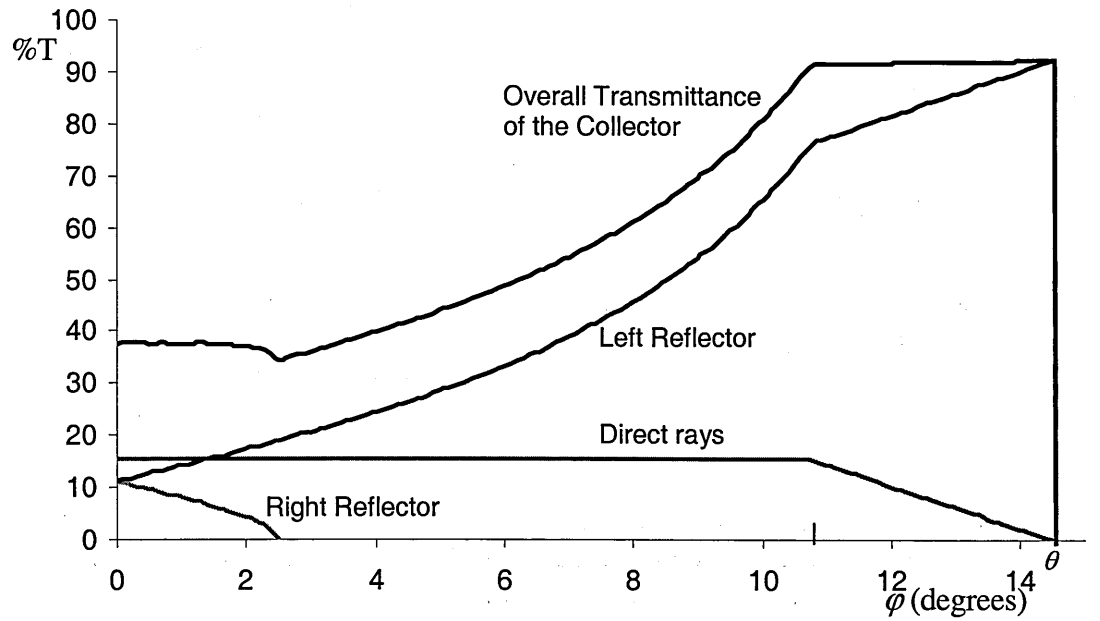


Figure 5.8 **The transmittance as a function of incidence angle for different parts of a 2 – d enlarged CPC and for the whole systems (geometrical parameters in table 5.1, s = 50 μm)**

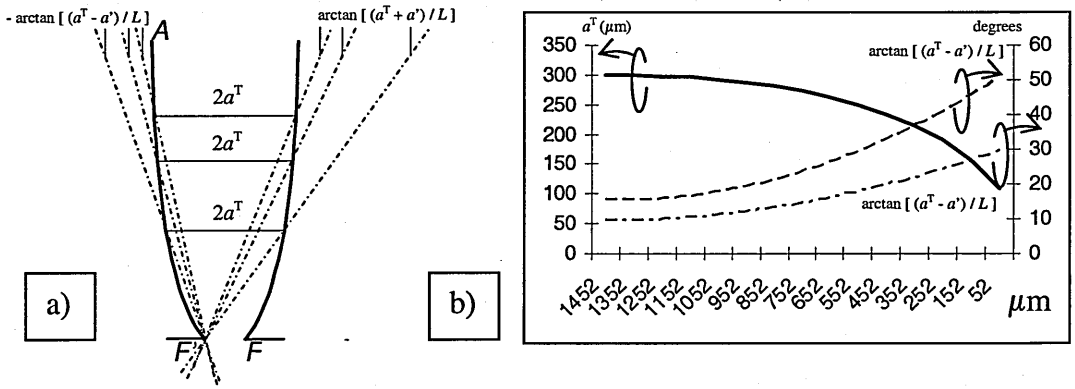


Figure 5.9 Procedure of 2 – d CPC truncation, with plot indicating the variation of geometrical parameters with truncated length.

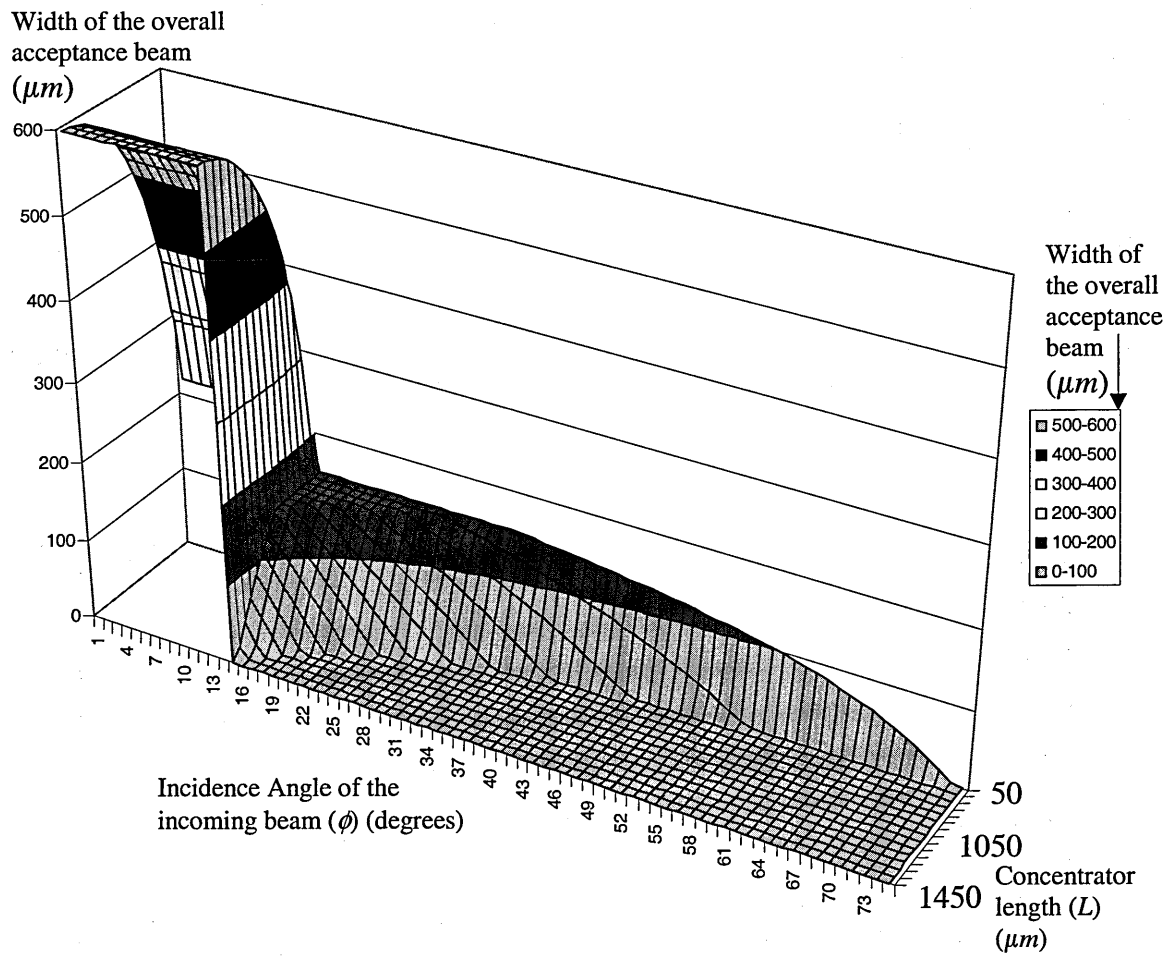


Figure 5.10 Width of the total accepted beam as a function of incidence angle and relative length of the truncated CPC. The original 2 – d CPC parameters are reported in table 5.1.

After assessing the general characteristics of the truncated CPC with full membrane, the truncated length was set to 580 μm, which leads to a value of a^T of 254 μm. The

enlargement shift (s) is equal to 50 μm as above. The expression of the transmittance for the truncated full CPC is simply given by $w / 2\, a^T$ (where w is given by equation 5.18). On the contrary, ray tracing has to be applied again to evaluate the contribution from the reflected rays in the enlarged truncated CPC (see appendix E-5). The transmittance is given by: $T = w / (2\, a^T + s)$. The results are reported in figure 5.11. Also in this case the overall transmittance of the enlarged truncated 2-d CPC is always below 100 %.

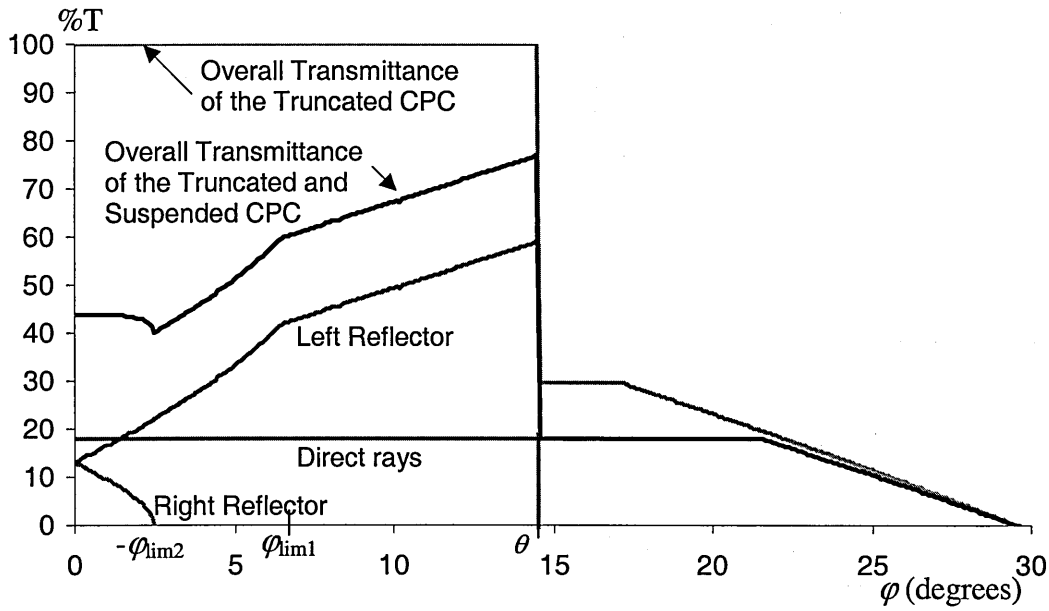


Figure 5.11 The transmittance as a function of incidence angle for different parts of a 2 – d enlarged truncated CPC compared to the CPC with a full membrane (geometrical parameters in table 5.1, s = 50 μm, L^T = 580 μm, a^T = 254 μm)

5.6 Acceptance and transmission of the and "V" concentrator

The 2 – d generator of the cone concentrator, also called V concentrator, was presented in figure 3.2*a*. Analytical treatment is complex because rays that enter after multiple reflections have to be taken into account. Williamson [*Williamson, 1952*] introduced a 2 – d geometrical construction that simplifies the calculations greatly. The construction considers, instead of the reflected rays, the virtual extension of the respective primitive rays into virtual V collectors, which are originated by mirror symmetry from the original V collector. The calculation is detailed in appendix E-6, where Williamson's construction is applied. (Witte introduced a similar construction for the 3 – d cone collector [*Witte,1965*].) This graphical device consents the calculation of the extreme rays that define beams of total rejection or total acceptance. A suitable V concentrator was designed with the same entry aperture, exit aperture and length of the 2 – d CPC used of table 5.1. A second collector was designed with the geometry of the truncated CPC (i.e. entry aperture ~ 254 μm and length ~ 580 μm). The transmission curves for these two structures are reported in figure 5.12.

A V collector has two important angles: all rays are accepted for incidence angle below α whereas no ray is accepted at incidence above β. As the length of the V is decreased

(thereby decreasing the slope of the sidewalls), the limit angle of total acceptance (α) is pushed towards smaller angles and the total rejection limit (β) is shifted towards larger angles, so that the interval of partial acceptance increases. The calculations show that V concentrator accepts rays at higher angles than its 2 – d CPC homologous. Conversely, part of the rays at $\varphi < \theta$ is rejected by the V (and the cone concentrator). The results of figure 5.12 are very similar to the results reported by Winston and reproduced in figure 3.8 [*Welford and Winston, 1989, Chapter 4*]. There, a 3 – d cone concentrator was compared with a 2 – d and 3 – d CPC of equal entry aperture, exit aperture and length. The computation based on Williamson construction [*Williamson, 1952*] works in two dimensions and does not take into account the skew rays. Witte's 3 – d application to the cone concentrators has a reference sphere, instead of a reference circle. However, Williamson's construction still applies to the rays that lay in the meridian section of a cone collector.

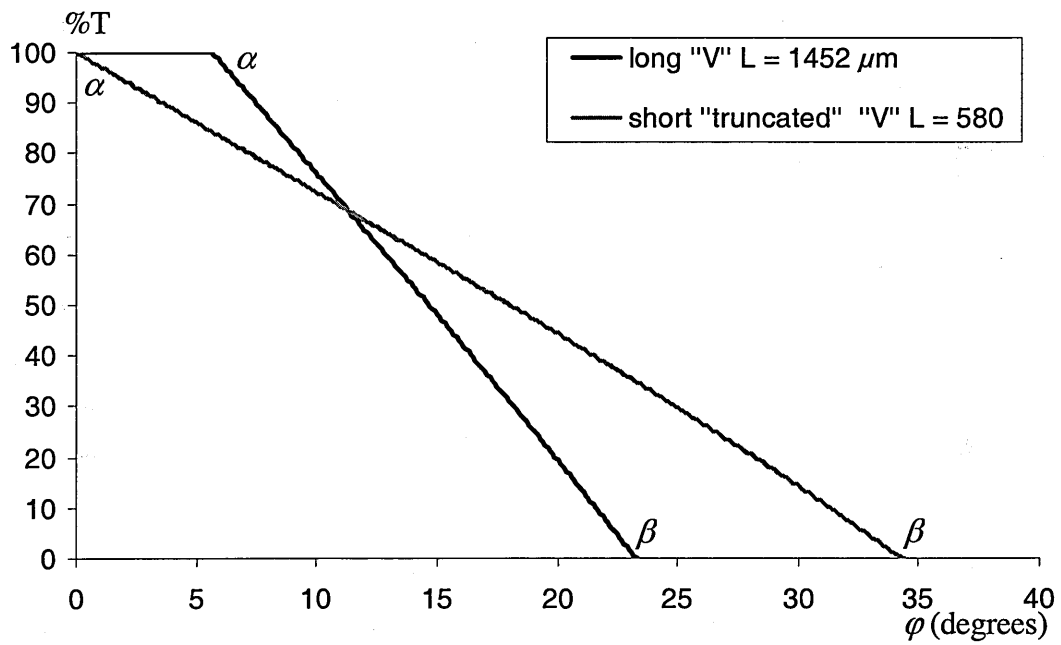


Figure 5.12 Transmittance plot for two V concentrators with geometry modelled respectively on the 2 – d CPC of table 5.1 and on the truncated CPC with length ~ 580 μm.

The two collectors, analysed in figure 5.12, were subsequently enlarged, according to the modality of figure 5.1, with the usual shift of 50 μm. This leads to an exit aperture of 200 μm (in width), with a central active area (representing an ideal suspended structure) of 100 μm. Williamson's construction can be easily modified for evaluating the acceptance curves of enlarged V concentrators. A series of virtual concentrators is built. Each "concentrator" corresponds to a virtual image of the active area. Only rays whose primitive falls within an image of the active area will be collected. The calculation is slightly different than for the full V concentrator. (The calculation is detailed in appendix E-6.) The transmission plots for these enlarged V concentrators are reported in figure 5.13*a* and 5.13*b*. The total transmission is represented by a broken line because the overall thickness of the accepted beam (along *AA'*) is computed as a sum: $w = \Sigma\, a_i$.

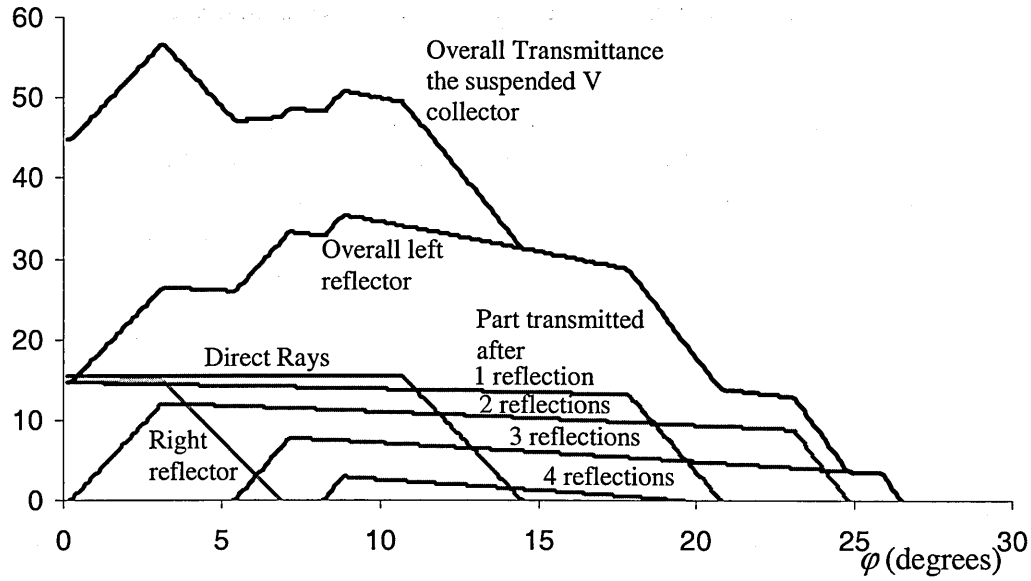


Figure 5.13*a* **Transmittance plots for the enlarged V concentrators with geometry modelled on the 2 – d CPC of table 5.1 and a translation (*s*) of 50 μm**

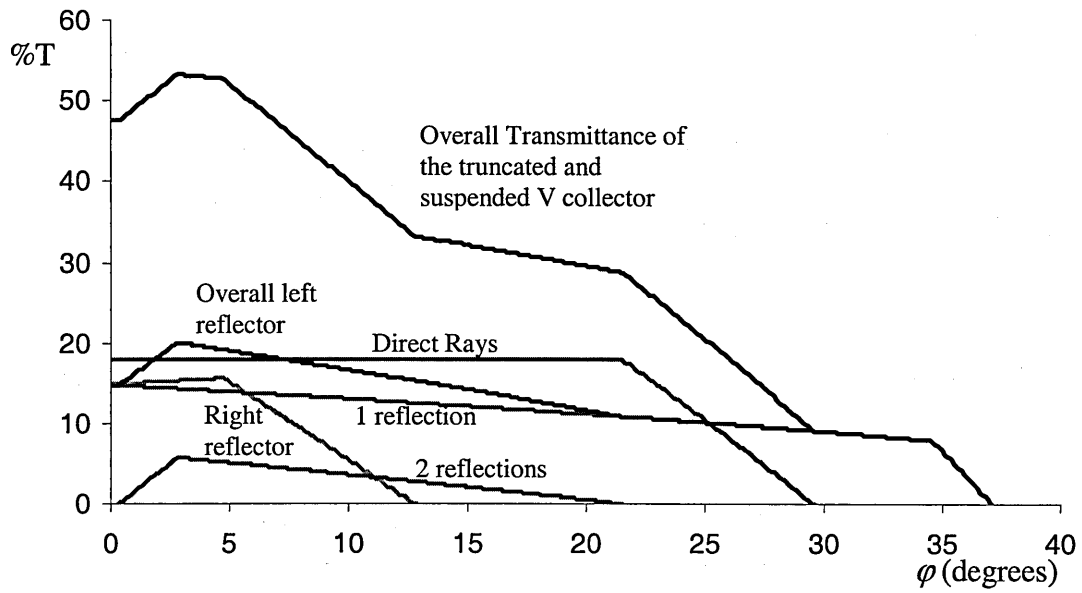


Figure 5.13*b* **Transmittance plots for the enlarged V concentrators with geometry modelled on the truncated 2 – d CPC (length ~ 580 μm) and a translation (*s*) of 50 μm**

The broken line representing the overall transmission for the enlarged V concentrator seems to follow a trend analogous to the full systems of figure 5.12: almost monotone, and decreasing with φ. Similarly, the transmittance for the concentrator with the shorter length (figure 5.13*b*) starts to decrease almost immediately whereas the longest structure demonstrates an initial zone of relative stability centred around 50 % in transmittance. Note also that the truncated V allows fewer reflections (only 2) than the longer V (4 reflections).

5.7 Comparison of the relative performance for different types of concentrator designs

To retain useful information from the above treatment, it is important to achieve a direct comparison of the performance for different concentrator designs. In particular, it is crucial to understand whether an acceptable power density can be achieved using a design that can be realistically manufactured. In this section, the performances calculated in this chapter will be compared using the above results.

Two useful measures of collector efficiency were introduced in section 5.2: namely the concentration ratio and the effective power collected. The concentration ratio was expressed by equation 5.5. In a simple power flux distribution such as the one reported in equation 5.9, the expression for the concentration becomes:

$$C = \frac{a}{a'}\left(\int_0^{\theta} T\cos\varphi\, d\varphi \Big/ \sin\theta\right) \tag{5.19}.$$

Similarly the ratio $P / P_{a'}$ (i.e. the amount of power that reaches the exit aperture from the concentrator divided by the power that would enter a segment of the same extent but isolated) simplifies to

$$P / P_{a'} = \frac{a}{a'}\left(\int_0^{\theta} T\cos\varphi\, d\varphi \Big/ \sin\omega\right) \tag{5.20}.$$

Equations 5.19 and 5.20 can be directly applied to the enlarged concentrators by substituting a with $(2\,a + s) / 2$ and a' with $(2\,a - s) / 2$ (i.e. the effective entry and exit half apertures). In figures 5.14 and 5.15, the ratio $P / P_{a'}$ is plotted for the systems analysed in this chapter as a function of the cut off angle of the incoming power distribution. Finally, the total transmittance can be evaluated as:

$$T_{tot} = \frac{P}{P_{\theta}} = \frac{\int_0^{\theta} T(\varphi)\cos\varphi\, d\varphi}{\sin\theta} \tag{5.21}.$$

And therefore $C = T_{tot}\ a / a'$.

The diagrams of figures 5.14 and 5.15 show the following main features:

1) The 2 – d CPC outperforms all the other systems, which are built using similar dimensions (i.e. the one reported in table 5.1);
2) Shorter systems (either V- or CPC-based) always collect less power (this is due to the reduction in the extent of the entry) although the acceptance angle effectively increases;
3) Enlargement always reduces the efficiency of the collector due to the presence of dead zones;
4) The differences in performance are particularly marked for $\omega << \theta$. Conversely, when the cut off angle increases beyond the acceptance angle of the original CPC (i.e. ~ 14 degrees), then the differences tend to smooth out. Eventually, for isotropic distribution (i.e. $\omega \rightarrow \pi / 2$) the systems tend to the unitary concentration (because of the thermodynamic limit recalled in section 3.1).

The efficiency of different concentrators is compared at the cut off angle of interest. The typical distribution that can be obtained from the germanium lens interposed between

the IR beam and the focal plane array was discussed in section 5.2. In the same section, it was argued that a cut off angle of 14.48 degrees represents a reasonable value. Table 5.2 reports the collection efficiency, the effective power collected and the total transmittance (calculated according to equations 5.19, 5.20 and 5.21) for the systems of interest. The response is analysed for the distribution of equation 5.9 and a cut off angle of 14.48 degrees. The results of table 5.2 will be used for the theoretical analysis of device performance in section 8.2.

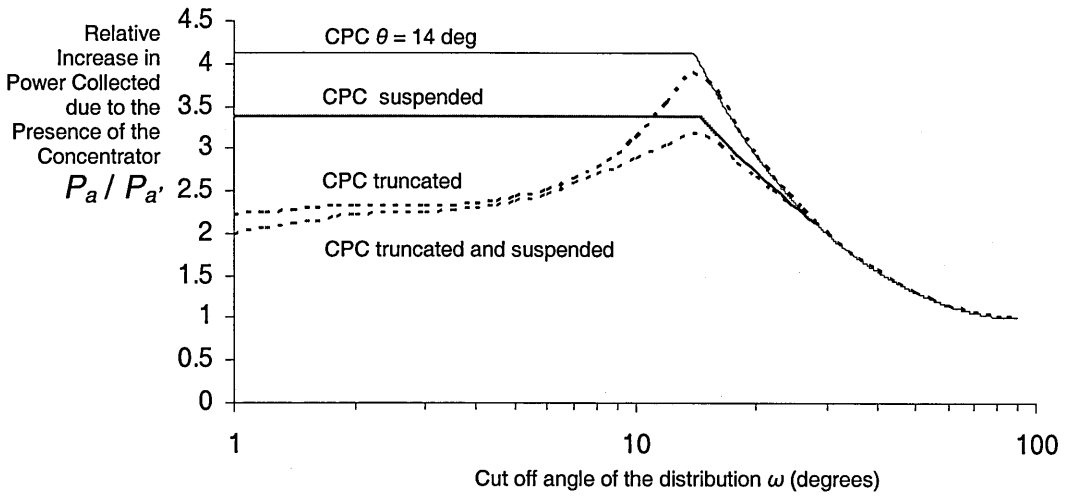


Figure 5.14: Effective concentration power for CPC-based concentrators profiles as a function of the cut-off angle of the radiant power distribution. The incoming flux is assumed to be constant for incidence angle below the cut off angle and zero above

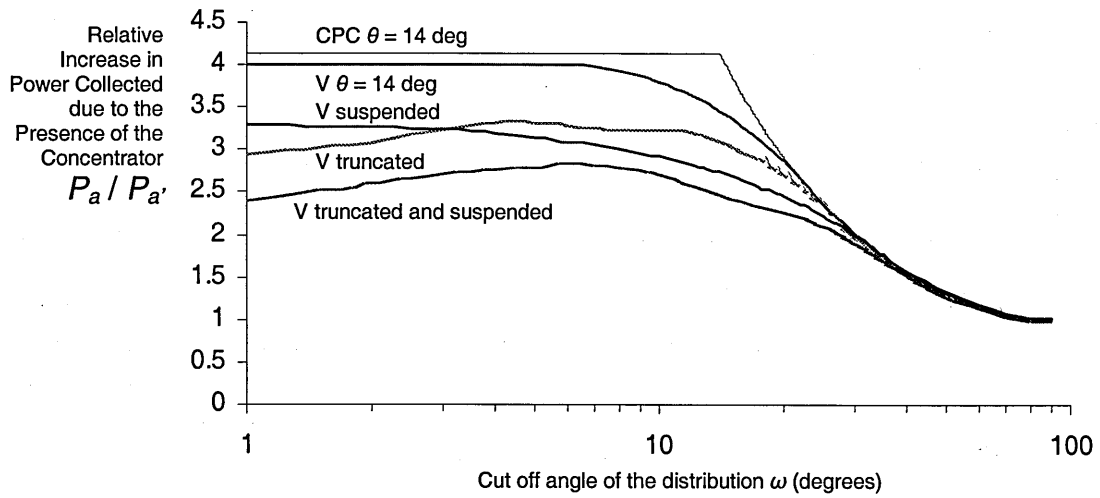


Figure 5.15: Effective concentration power for V concentrators profiles as a function of the cut-off angle of the radiant power distribution. The incoming flux is assumed to be constant for incidence angle below the cut off angle and zero above

Type of collector	T_{tot}	C	$P / P_{a'}$ ($\omega = 14.48$) (*)
2 – d CPC (table 5.1)	1	4	4
2 – d CPC enlarged (shift 50 microns)	0.55	3.57	3.97
2 – d CPC truncated (L^T 580 microns)	0.60	2.02	3.39
2 – d CPC truncated and enlarged (shift 50 microns)	0.33	1.83	3.22
Long V collector (same geometry of the CPC of table 5.1)	0.63	2.51	3.41
Enlarged version of the Long V collector (shift 50 microns)	0.34	2.21	3.08
Short V collector (same geometry of the 2 – d truncated CPC)	0.53	1.78	2.71
Enlarged version of the Short V collector (shift 50 microns)	0.29	1.86	2.47

(*) When $\omega = 14.48$ (i.e. $\omega = \theta$) $C = P / P_{a'}$ (It is demonstrated by equation 5.22, which becomes equal to equation 5.21 after the substitution of ω with θ. So, e.g. the concentration ratio for a 2 – d truncated CPC is reasonably near to 4 for $\omega = \theta$ whereas it is almost half if the cut off angle of the distribution is equal to the effective angle of acceptance of the system, i.e. 29.5 degrees).

Table 5.2 The results for the computation of expected performance for types of concentrators design of interest

5.8 Conclusion

This chapter reported the results of the theoretical analysis of various shapes of concentrators, considered suitable for incorporation in the IR sensor array. A new concentrators design, named the enlarged or suspended collector was introduced. This enlargement can be operated on concentrators with any profile. The geometrical shifting of a reflector is accomplished in 2 – d, and the 3 – d enlarged concentrator may be created after the revolution about the central axis of the suspended cross section. This design allows thermal isolation by suspending the inner active area. It is therefore compatible with the presence of a micromachined element suspended on a microbridge. Since part of the radiation is lost due to the geometrical properties (i.e. it falls onto a "dead" outer ring), the enlarged 2 – d CPC is no longer ideal (i.e. $T < 1$).

The effect of the power flux distribution on the performance of a given collector was assessed. This factor needs consideration when comparing the performance of different types of design. The calculations demonstrated that the introduction of a concentrator in a totally diffused flux is always disadvantageous. However, in an anisotropic flux, such as that produced by a Ge lens in an IR sensor, when an ideal 2 – d CPC is introduced, the increase in power collected is exactly equal to the concentration ratio of the CPC. If the Ge lens has an f-number of 2, then an ideal CPC with an acceptance angle of 14.48 degrees would drive onto the exit aperture 4 times the power that would enter the same aperture in absence of any collector. The maximum collection is always obtained using a CPC with acceptance angle lower or equal to the cut off angle of the distribution.

For the ideal collector profiles assumed in this chapter (i.e. 100% reflectivity from the sidewalls), the IR beam can be divided into bundles, which are either fully accepted or fully rejected; thereby allowing finding an analytical curve that describes the dependence of collection efficiency on the incidence angle. This was not viable in practice (although always possible for such ideal systems). The contribution of the direct rays (rays that are collected without hitting the sidewalls) could always be

evaluated analytically: an expression was found that could be applied to the entire range of profiles analysed independently on the contour. The performances of the V collectors and the enlarged V collectors were calculated analytically using geometrical shortcuts. Conversely, for the 2 – d enlarged CPCs, the solving equations became too complex to be implemented and a computational ray tracing method had to be used.

The results obtained using the above elaborations were gathered in order to compare the different kinds of concentrator design. The overall performance must then be compared with the relative possibility of producing an effective collector by micromachining. Collectors were compared in terms of concentration ratio and relative power collected, i.e. the amount of power that reaches the exit aperture from the concentrator divided by the power that would enter a segment of the same extent but in absence of a concentrator. The concentration ratio was calculated for a cut off angle of 14.48 degrees. The relative power collected was calculated over a range of cut off angle. The results and relative plots showed that the 2 – d CPC outperforms all the other systems (as expected). In all cases, truncated systems collect less power than the respective full systems. Similarly, the suspended design always corresponds to lower efficiency. The differences are maximum for very small cut off angles but tend to smooth as the cut off angle of the distribution increases above 14.48 degrees, until they all tend to 1 for an isotropic distribution (cut off angle equal to 90 degrees).

Chapter 6: MICROFABRICATION OF CONCENTRATING NON-IMAGING COLLECTORS

In the previous chapter, a series of profiles suitable for incorporation in the IR sensor were introduced. This chapter presents the search for a route to fabricate arrays of cavities with profiles similar to those analysed above. The attempts at producing an array of concentrating collectors in silicon wafers are discussed. It has to be remarked that all the trials reported in this chapter did not involve the full-fabricated device but were carried out on bare silicon wafers. In fact, the aim of these early attempts was only to identify the best route and assess the feasibility of the chosen process. Since full wafers were mostly used, it was not possible to attempt these early structures on complete devices for obvious problems of time and cost. The latter problem is further discussed in the future work section.

This chapter consists of three sections. The first section reports the microfabrication of 3 – d structures produced by unidirectional transfer of 3 – d structured sacrificial masks (following the roadmap built after the literature survey of section 3.4; see figure 3.23). The technique entails the production of intermediate 3 – d masks by using a High Energy Beam Sensitive (HEBS) mask. (The mask is described in appendix A.) The 3 – d features are transferred into the substrate (silicon) by unidirectional etching. Main scope of this research was to assess the feasibility of the entire process, with particular attention to the second step (transferring of contours into silicon). The latter process presents unpredictable results, because of its relative novelty. The literature survey of section 3.4.2 revealed crucial differences between the conventional techniques (generally shallow, with selectivity near to one) and the transferring attempted in this research, which involves the fabrication of very deep structures (up to 100 μm and more). Due to the exploratory character of this early part of the research, no articulate discussion of the results will be presented. The physics of the process is sometimes introduced in this section in order to display the results more clearly. Had this piece of research produced satisfactory results, a more rigorous process modelling would have been required. However, this would have happened only at a more advanced stage, i.e. when the grey scale mask would have had to be produced. Although the technique did not provide a successful way to the microfabrication of concentrators, it led to the production of very interesting structures never previously demonstrated in literature.

The experimental details of the trials were reported in the experimental part (in section 4.3.2). The production of 3 – d sacrificial masks in photoresist is reported in section 6.1.1. Since this process has been widely characterized in literature (see e.g. [*Däschner et al., 1996; Opplinger et al., 1994; Purdy et al., 1994*]), the results will be analyzed rather concisely. The physics of photolithography will be briefly employed to gather the results in a more compact form. The transfer of photoresist 3 – d masks into an intermediate layer of thermally grown oxide, to be used as a sacrificial mask is reported in section 6.1.2. Blazed gratings and other features deeply etched into silicon by unidirectional DRIE are characterised in section 6.1.3. The contoured surface of the microstructures often presents irregularities and nonlinearities related to phenomena occurring during process: a series of smoothing post-etching treatments is briefly presented in section 6.1.4. Finally, the suitability of the results achieved for the purposes of the application is discussed in section 6.1.5.

Cavities in a wide range of profiles were produced by unbalancing the DRIE process or coupling isotropic and anisotropic cycles (following the methods outlined in the literature survey of section 3.5). The different typologies of results are reported, commented and compared in the second section of this chapter. Deep dry etching techniques, based on high-density plasma have the capability for etching cavities hundreds of microns deep with a good control over the profile. ICP-DRIE etching seemed the proper equipment for setting up a process for the microfabrication of arrays of concentrators. It seemed reasonable to assess the capabilities of the technology before the equipment was bought. For this reason a series of trials were performed at Rutherford Appleton Laboratory, where a similar piece of equipment is in use (see *www.cmf.rl.ac.uk/facil/layerproc.html*). (The technical details of the machine were reported in the experimental part, in section 4.3.1.) The results of this preliminary feasibility study are reported in section 6.2.1. The literature survey suggested the possibility of inducing contoured sidewalls by unbalancing the equilibrium that would lead to straight sidewalls. The results for etching processes in defect or excess of passivation are reported in section 6.2.2. A subsequent set of trials involved the coupling of fully isotropic and fully anisotropic etching steps. In literature, this method demonstrated to be promising: in fact, some authors have exploited it for producing microsystems with complex shape [*deBoer et al., 2000; Griss et al., 2001*]. Before embarking in trials along this route, a characterisation of the profiles typically obtained by isotropic etching using the STS-ASE machine had to be accomplished. (It has to be reminded that the term "isotropic" etching is used in this dissertation for etching without any passivation promoting mechanism or species, i.e. in pure SF_6.) It is known that the profile of cavities etched in pure SF_6 depends largely on the kinetics of the mechanism at the feature scale. Isotropic etching in pure SF_6 is analysed in section 6.2.3. Once the nature of the isotropic profile is clarified (by an experimental point of view), isotropic cycles are employed to modify the sidewalls of anisotropically etched cavities. The range of cavities achievable by these combinations of long anisotropic and isotropic cycles is discussed in section 6.2.4. Finally, the results obtained from other less common methods are reported in section 6.2.5. The final part of this section (section 6.2.6) is devoted to the comparison among all the methods in order to choose the most promising techniques. The methods will be compared and evaluated on the basis of the constraints associated with the requirements of the application.

Once the most promising routes have been chosen, a series of more advanced experimental trials is accomplished in order to establish the feasibility of the routes proposed for the microfabrication of a device prototype. These trials are reported in the third section of this chapter (i.e. section 6.3) and are consequence of the choices discussed in the previous section (i.e. section 6.2): it is difficult to justify the content of section 6.3 without anticipating the content of section 6.2. It can be anticipated that section 6.3 reports the attempts to etch arrays of through-the-wafer cavities using long "isotropic" cycles, i.e. cycles in absence of passivation of the kind reported in section 6.2.3. Although the profiles produced using this method failed to approximate the greater part of the CPC contour, two good reasons justified the prominence initially accorded to this technique. Firstly, random defects, which may affect the other techniques to a large extent, exert a minimal effect in absence of passivation. Secondly, thanks to its inherent reliability and the predictability of the contours achievable, this method was judged the most functional for producing a series of preliminary "device"

wafers. In other words, it was crucial to assess the practical problems that could arise when the cavities were effectively integrated into a device wafers before more complex etching processes could be attempted. Etching in total absence of passivation was a quick and reliable method to obtain suitable through-the-wafer cavities without the need of further optimisation (or process modelling). In this way, prototype devices would be put through the final steps of sawing and microbridges patterning and the performance of the sensing elements could be experimentally tested. In effects, in attempting to etch through the wafer, some processing difficulties were encountered. After a series of failed attempts, a viable procedure for long-time through-the-wafer etching was set up by increasing mask thickness and using thinner wafers. The samples produced contained arrays of side-to-side etched features, which could hypothetically be used as concentrators. The etch stops on a thermally grown oxide layer. As a consequence, arrays of membranes are formed on the side of the wafer opposite to the etching direction.

The problems arising as a consequence of the longer etching time are discussed in section 6.3.1. The determination of surface roughness is tackled in section 6.3.2. With the final application in mind, a statistical analysis was accomplished of the variation in the dimensions of the membranes across the area of the wafer. The results are in section 6.3.3. Finally, following the statistical analysis, a cavity with average dimensions is compared to the CPC profile in section 6.3.4. The theoretical collection efficiency expected from such "experimentally" obtained profile is calculated in section 6.3.5 by using the ray-tracing technique. (Ray tracing was discussed in section 5.3).

6.1 3 – d Contoured Features obtained by Grey Scale Photolithography & Deep Reactive Ion Etching

As anticipated in the introduction, this section reports the search for a route to produce contoured features in silicon by anisotropic (i.e. unidirectional) etching of 3 – d sacrificial masks. First, 3 – d masks are produced by using different masking materials and by making use of a HEBS mask (section 6.1.1). Subsequently, masks are transferred into silicon wafers directly or after being transferred into an intermediate silicon oxide layer (section 6.1.2). The deep etching of 3 – d features in silicon is reported in section 6.1.3. Post-etching treatments were attempted to smooth the contours of the etched features (section 6.1.4). This section concludes by discussing the suitability of the route attempted for producing arrays of concentrating cavities (section 6.1.5).

6.1.1 Deposition and patterning of 3 – d contoured sacrificial masks made by photoresist

As specified in section 4.3.2 and appendix A, Zone II of the (HEBS) calibration glass plate contains a series of three-dimensional blazed gratings designed to yield ramps with different slope. The widths of the ramps vary from 2 to 500 μm while the number of grey levels that constitute each ramp is equal to 10, 20 or 100 depending on ramp width. Ramps ranging from 50 to 500 μm have a width comparable with the scale of the concentrators. They also contain 100 grey tones and are expected to produce the smoothest contours. The ramps will be named after their designed width, such as 50,100, 200, 300, 400 and 500 respectively. (In most cases the width of the actual ramp

is narrower than the nominal width.) The ramps produced in JSR IX575 photoresist yield a maximum height of circa 900 nm while AZ4562 ramps show a range of heights up to 7500 nm. Local photoresist thickness and therefore ramp slopes depend on many parameters. The most important are: exposure dose, photoresist overall thickness, development time and soft bake temperature and time. Due to the large number of parameters, it is possible to create sloped plane surfaces with a range of gradients. A large variety of features with different shapes were produced. Due to the vast range of features on the mask and the number of samples produced in a range of thickness, it would be impossible and somewhat useless to enumerate here all the results obtained. In the following, some exemplary ramps will be shown in order to represent the typical results achieved. The results are displayed in a compact way in appendix F, by making use of the concept of contrast curve. Zones IV and V of the mask contain arrays of microlenses, which present curved contours. Although the resulting masks features were analysed, the results are not dissimilar from the results obtained from the ramps. In order to save space the results concerning the features contained in Zone IV and Zone V are not reported here. Some examples of the sacrificial masks produced may be found in picture A-3 of appendix A.

AZ4562 photoresist yields ramps with fairly regular slope. A typical series of ramp profiles is represented in figure 6.1. The features are distributed across the wafer surface, but the profiles were gathered, for each sample, on the same diagram for compactness of presentation. The ramps were produced using the set number 1 of zone II of the HEBS mask (see appendix A), therefore the transmittance varies linearly with the x coordinate (and so does the dose received). It is interesting to notice that for most ramps, a large part of the ramp is linear and therefore fits a regression of the following type:

$$H = a_n x + b_n \qquad (6.1),$$

where H is the photoresist thickness remaining after development, i.e. the height of the ramp. Since the transmittance (T) for set number one is equal to $0.0068\, n\, x + 0.0759$ (where $n = 1, 2, 3, 4$ or 5 for the respective ramp 100, 200, 300, 400 and 500) the fitting equation of H as a function of T may be written concisely for all the curves as:

$$H = \frac{a_n}{0.0068\ n} T + \left(b_n - \frac{0.0759}{0.0068\ n} \right) \qquad (6.2).$$

Similar expression may be drafted for the profiles of the ramps produced using the other three sets. In most cases, only the bottom part of the ramp is well approximated by a linear fitting: the top part is better described by a logarithmic regression (as clearly shown in figure 6.1). Conversely, the shape of the extreme top is induced by surface tension during post exposure bake.

Linear ramps are achieved using AZ4562 both on bare silicon and silicon oxide coated samples. On the contrary, the ramps produced patterning JSR IX 575 on silicon present generally three coarse steps in the lower part of the ramp. The contour is linear only towards the top of the ramp. A typical example is in figure 6.2 (obtained with the same modality of figure 6.1). It is not clear whether the large deviations from linearity are due to intrinsic variation in the contrast curve of JSR IX575 or to the effect of the stationary waves (the effect of stationary waves was discussed in the literature survey, in section 3.4.3). This issue was not investigated further since it was beyond the scope of this early

feasibility study. However, the presence of the same steps in the contrast curve obtained measuring the strips of zone I of the HEBS plate (figure 6.3) seems to demonstrate that the steps are caused by some general phenomenon intrinsic to the exposure, rather than local effects. Furthermore, when the ramps were patterned on oxide coated samples, under the same processing conditions, fairly linear profiles were obtained, as showed in figure 6.4. (No large step was detected). Therefore, the cause of these nonlinearities was ascribed to the interference effects of the silicon substrate.

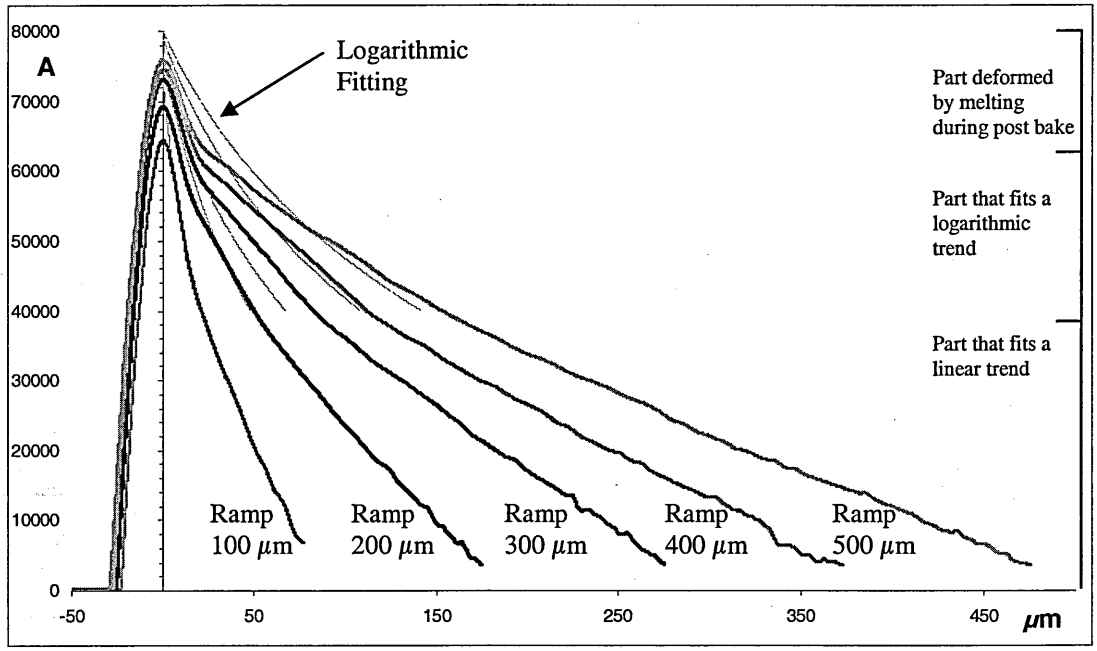


Figure 6.1 **Series of ramps 100 to 500 (nominal width) obtained using the set number one of zone II of an HEBS calibration plate. Photoresist is AZ4562 on bare silicon, spun at 2000 RPM, exposed for 45 s and developed for 120 s. Transmittance varies linearly with x as: $T = 0.0068\, n\, x + 0.0759$. The features were scattered across the wafer surface but the profiles are gathered, for each sample, on the same diagram for compactness of presentation.**

The above examples have demonstrated how the ramps may present kinks and steps that can be very coarse. To smooth the ramps, cycles of thermal annealing have been attempted. Part of the samples underwent thermal re-flowing cycles on a hot plate in order to assess the results of smoothing the initial ramp profile. A treatment of 5 minutes at 200 degrees produced ramp contours of the kind shown in figure 6.5, for JSR IX 575. Although thermal treatment can actually produce smoother ramps, it is ineffective against the major steps. Furthermore, thermal treatment tends to yield a surface-tension induced contour. The original contour results heavily altered. A similar phenomenon was previously reported in the literature [*Daly et al., 1990*].

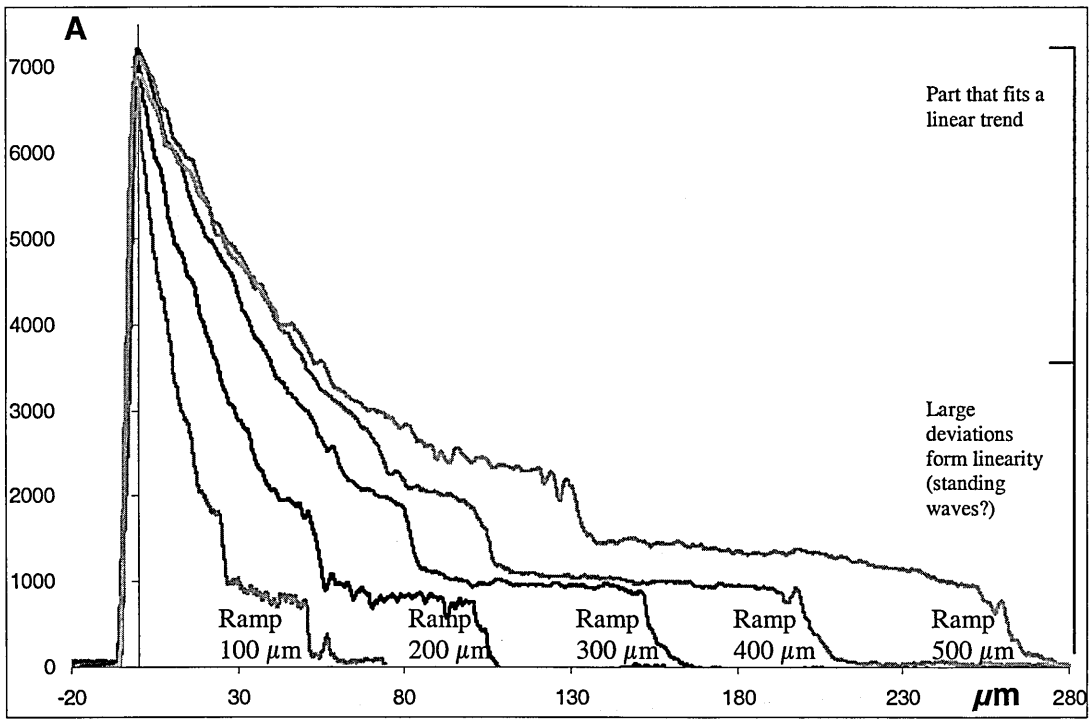


Figure 6.2 **Series of ramps 100 to 500 obtained using the set number one of zone II of an HEBS calibration plate. Photoresist is JSR IX575 on bare silicon, spun at 3000 RPM, exposed for 10 s and developed for 20 s. Other information is in figure 6.1.**

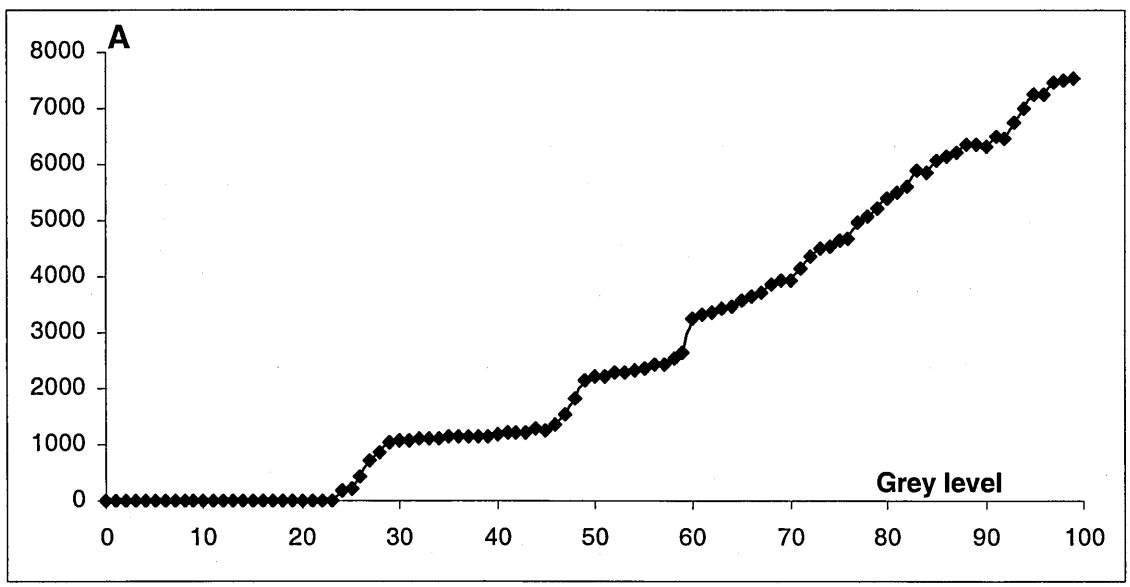


Figure 6.3 **Photoresist remaining thickness Vs grey level measured on strips obtained using zone I of HEBS calibration glass plate. Photoresist is JSR IX575 on bare silicon, spun at 3000 RPM, exposed for 10 s and developed for 20 s.**

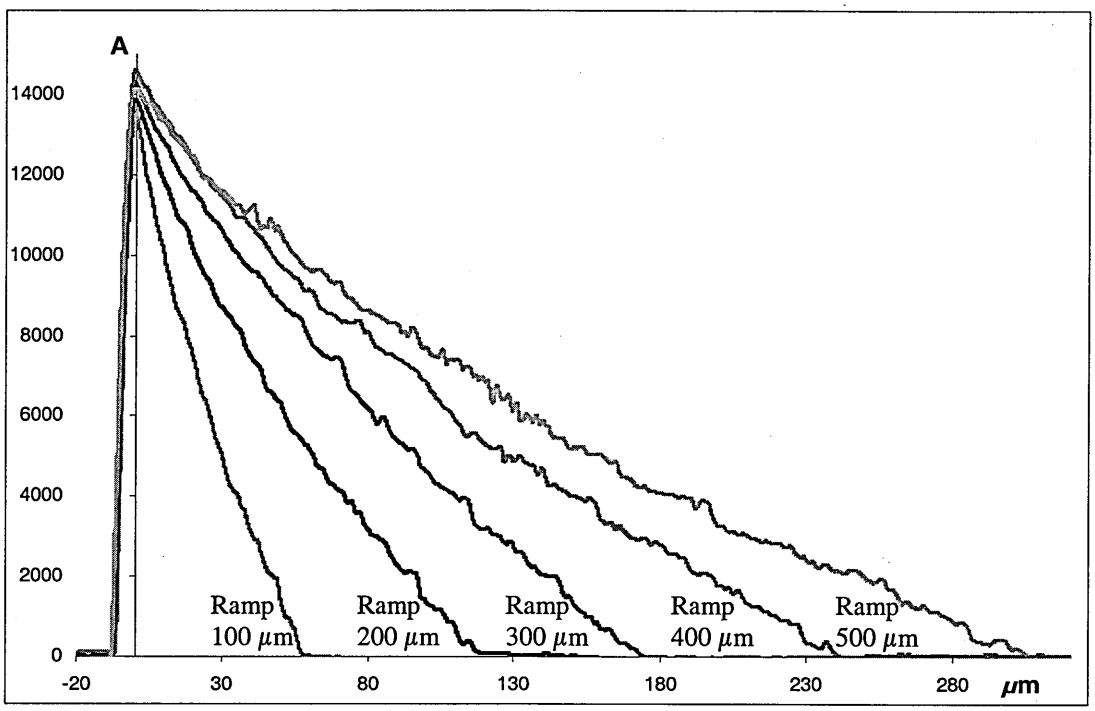


Figure 6.4 **Series of ramps 100 to 500 obtained using the set number one of zone II of an HEBS calibration plate. Photoresist is JSR IX575 on thermally grown oxide, spun at 1000 RPM, exposed for 25 s and developed for 70 s. Other information is in figure 6.1.**

The presence of steps and the fact that exposure dose and development time are not optimised limit the degree of grey scale attainable: it can be clearly observed from the above diagrams that the actual (usable) ramps width is often lower than the nominal width of the ramps in the HEBS calibration plate. Diagram 6.6 reports the percentage of usable ramp width plotted against the nominal width of the ramps for some of the samples produced. The data show that only in one instance (AZ 4562 spun at 2000 RPM, exposed for 45 s and developed for 120 s) it was possible to use the whole ramp nominal width. In all the other instances less than a third of the nominal width is actually usable. In other words, in most samples only one third of the grey level was effectively usable. (This corresponds to about 30 grey steps.) This demonstrates that the process needs a long optimisation procedure before it can be incorporated in a device building process.

The ramps of figures 6.1 to 6.4 represent effective contrast curves. These can be compared with the kind of curves used in literature for photolithography process modelling [*Fahey, 1996; Arthur et al., 1998; Thornton and Mack, 1996*]. In fact, equation 6.2 shows that the photoresist remaining thickness (H) can be directly expressed as a function of the local transmittance. Equation 3.13 (section 3.4.3) showed that, for a grey mask, $T(x)$ can be expressed as the ratio between the local intensity transmitted to the film (I_0) and the general lamp intensity (I_{lamp}). Introducing equation 3.13 in equation 6.2, the ramps profiles taken by profilometry may be transformed in data reporting photoresist remaining thickness Vs dose, i.e. experimental contrast curves. The measurement of contrast curves under different process conditions (in

particular development time) represents the first step for modelling the photolithographic behaviour of a photoresist material. Representation of data using the exposure dose allows a large compactness of display since the profiles become independent on the width of the single ramp. Under the assumptions of Dill's model, the development rate depends only of the exposure dose ($I_{lamp}Tt$) and so local areas that have received the same dose should develop at the same speed although being exposed for different times; the contrast curves are therefore expected to overlap partially where points of different samples received equal dose (at equal development time). Plots of H vs. Dose (contrast curves) obtained transforming the ramps profiles are reported in appendix F, where the issues of process modelling are briefly presented.

6.1.2 Sacrificial masks made of thermally grown silicon oxide

Sacrificial masks were produced in thermally grown silicon oxide by transferring the 3 – d shaped photoresist mask by Reactive Ion Etching. Conventional recipes exist for optimised etching of silicon oxide. The recipes and process settings used are reported in the experimental part (see table 4.3 of section 4.3.2). The selectivity (the ratio between SiO_x etch rate and photoresist etch rate) is around 0.10. The amount of oxygen content in the etching mixture allows controlling the selectivity of the process. Transfer of 3 – d shaped photoresist masks at such low selectivity represents a straightforward process. (In the literature survey it was stressed how such a process has been widely characterized in the past, see e.g. [*Opplinger et al., 1994*; *Daschner et al., 1996*].) In general, mask contours are faithfully reproduced into the inorganic substrate. As an example, the ramps obtained after RIE using the ramps of figure 6.4 as sacrificial masks are reported figure 6.7. A linear projection of the original mask profile represents a good approximation of the actual profiles: a simple linear expression can be used to model this step of the process. (The linear expression derived in equation 3.16 was used, i.e. $D = H \times S - ED$.)

6.1.3 Transfer of 3 – d contoured masks into silicon by unidirectional dry etching

The samples containing 3 – d structures sacrificial masks underwent DRIE. Conventional recipes were used (optimised for achieving unidirectional etching). The parameters settings for the etching processes were reported in tables 4.4a, 4.4b and 4.5 of the experimental part. The etching processes applied can be roughly divided into two types, which are denominated "deep" and "shallow". Typical parameters of the two typologies are reported in table 6.1. Averaged Etch Rate and Selectivity values (obtained from different samples and features with the modality reported in section 4.3.5) are presented in table 6.2. The etch rate was lower than usual etch rates reported for ASE®, which should range from 3000 to 4000 nm per minute [*Bhardwaj et al., 2000*]. This is not unexpected, due to the prominent positive nature of the patterns that may induce a very strong loading effect. The selectivity towards AZ4562 and silicon oxide was within the range usually observed [*Bhardwaj et al., 2000*]. From the results of table 6.2, it can be concluded that only AZ4562 is suitable for through-wafer etching. JSR IX575 cannot be deposited up to the required thickness. Also dry thermally coated silicon oxide cannot be grown up to a sufficient thickness. Wet silicon oxide might be used instead.

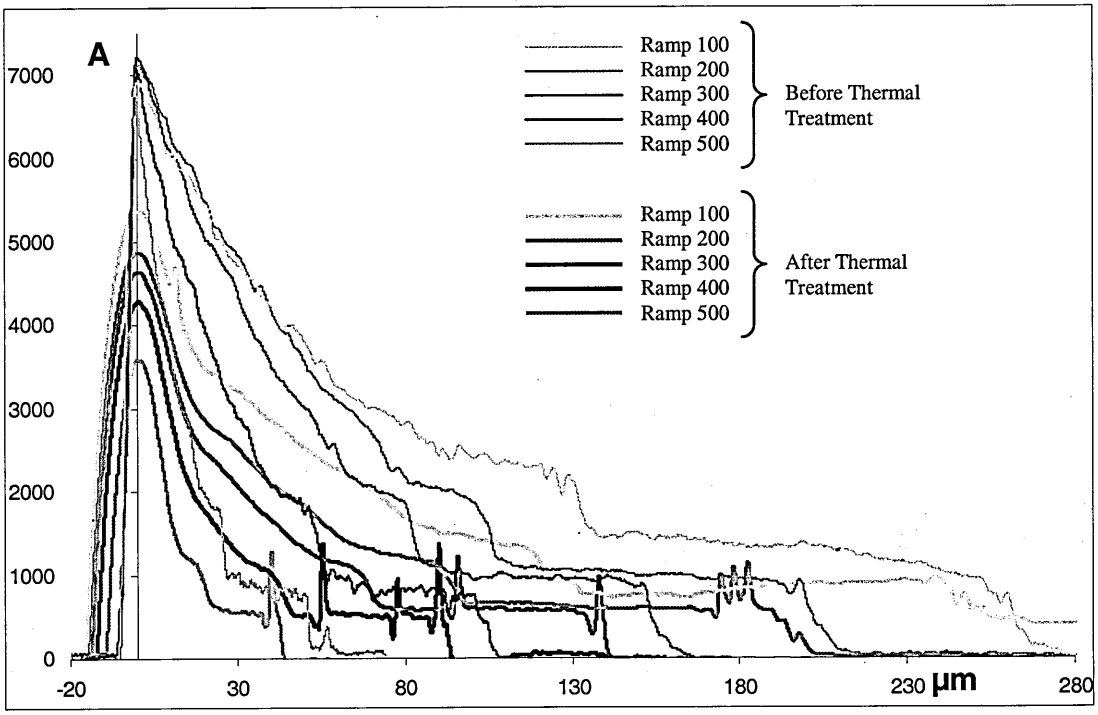


Figure 6.5 **Series of ramps 100 to 500 obtained using the set number one of zone II of an HEBS calibration plate: comparison before and after the thermal treatment. Photoresist is JSR IX575 on bare silicon, spun at 3000 RPM, exposed for 10 s and developed for 20 s. Photoresist baked onto hot plate at 200 degrees for 5 minutes. Other information in figure 6.1. The thin line represents the ramps profile before thermal treatment and the thick line represents the same ramps after treatment.**

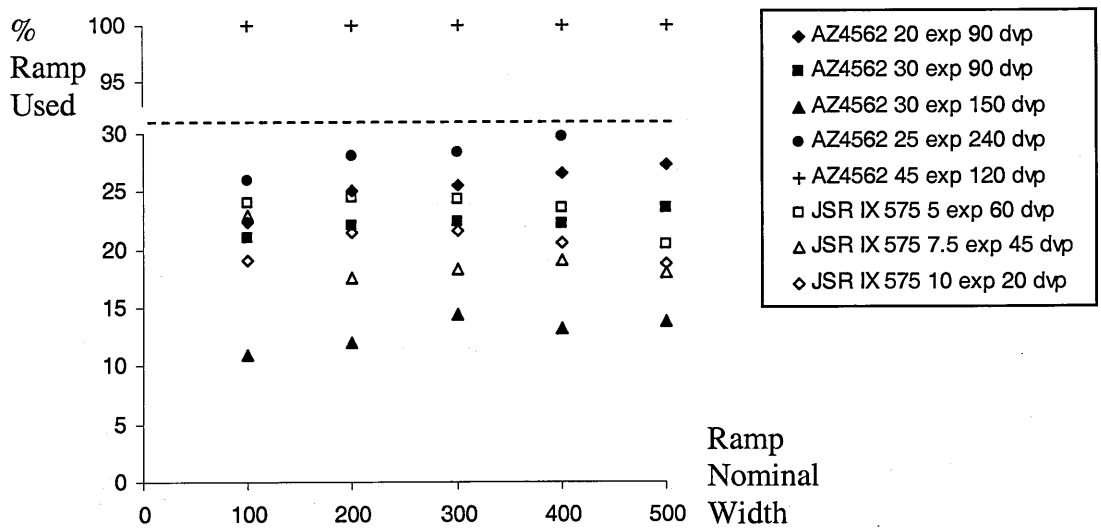


Figure 6.6 **Percentage of grey tones actually used vs. width of the original ramps on the set I of HEBS plate.**

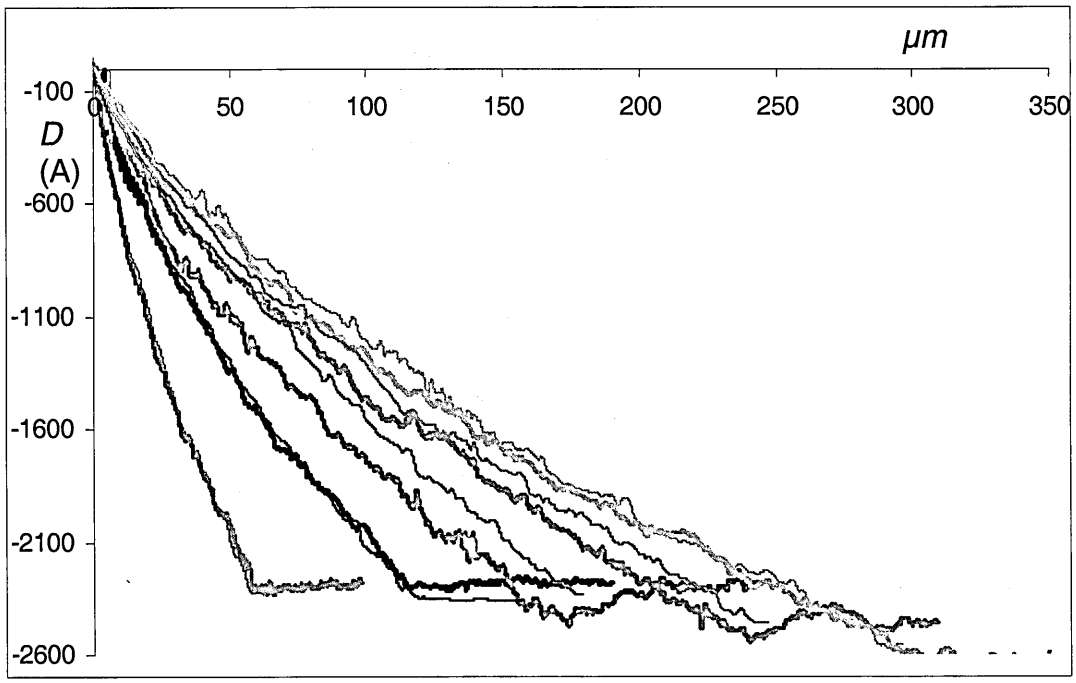


Figure 6.7 **Ramps in thermally grown oxide, obtained by RIE. Original mask ramps are in figure 6.4 (see caption for mask deposition and patterning conditions). The thick line represents the actual profile; the thin line represents the projection of the original mask profile.**

Parameter	Shallow	Deep	Unit
Platen Power	12	15	Watts
Etching step time	5	7	seconds
Passivation step time	8	12	seconds
Pressure etching step	13 to 15	23 to 25	SCCM
Pressure passivation step	15 to 16	25 to 37	SCCM

Table 6.1: **Machine settings peculiar of the "shallow" and "deep" processes**

Mask material	Process Label	Etch rate (nm/min)	Selectivity
AZ 4562	Deep	1442	86
AZ 4562	Shallow	1074	45
JSR IX575	Shallow	1980	66
Dry Silicon Oxide	Shallow	2100	131

Table 6.2: **General Etch Performance: averaged values for the samples etched under different conditions and process time**

In section 6.1.1 it was showed how a vast range of ramps of different slope were produced on each sample, which is individually subjected to a different etching cycle, yielding a particular etch depth and selectivity. In addition, three different mask materials were used (a thick photoresist – AZ4562 – a thin photoresist – JSR IX575 – and thermally grown oxide). It is clear that the amount of features produced is very

large. Trying to display all the results presents a series of problems. In particular, there is no space here for detailing the results for all the features on each sample. Therefore, although this may affect the objectivity of results presentation, a synthesis had to be reached in presenting the results. Ramps slope after etching seems to be the main variable affecting the microstructure, therefore the effects of the increasing steepness of the gradient on the morphology of contours will be discussed first. On a second instance, the effects related to the nature of the mask will be addressed. Finally, evidence of a difference induced by the different process conditions ("deep" or "shallow") will be investigated.

Generally speaking, deeply etched samples contain features with high slope and shallowly etched samples contain features with gentle slope. However, this is not always true since the range of slopes of the ramps in the 3 – d mask is very large: for example a ramp 5 μm wide on a sample etched up to a depth of 10 μm would exhibit the same slope of a ramp 50 μm wide on a sample etched up to a depth of 100 μm (namely ~ 63 degrees). Interestingly, if the results are arranged in order of increasing ramp steepness (after etching), then four typologies of results can be observed independent of the type of process. These are presented in figure 6.8 to 6.11. Very shallow contours present apparently smooth surfaces (figure 6.8) but, as slope increases, microscopic steps arise (figure 6.9). At even higher slope, these steps increase in height and occupy most of the contoured surface (figure 6.10). Silicon filaments emerge too, induced by micromasking effects during etching ("micrograss"). This phenomenon was widely observed in the literature (see e.g. [*Elwenspoek and Jansen, 1998, Chapter 12*]). Beyond a certain slope, large defects and micrograss completely cover the contours, which cannot be observed at all (figure 6.11). Besides pictures of the ramps, microphotographs representing the curved features (microlenses etc.) have been introduced to show that the findings follow the same trends as for the ramps. The diagram of figure 6.12 reports the typology of each ramp as a function of ramp slope. The classification of a result within a certain category is attained visually by inspection at the SEM. The gradient is derived from the ratio between the height and the base of each individual ramp. The value thus obtained shows generally good agreement with the slope revealed by contact profilometry, providing the ramp gradient is below 50 degrees and there is a small number of defects (such as micrograss). This measurement technique was discussed in the experimental part (section 4.3.5). For the masks realised using JSR IX575 on bare silicon (e.g. figures 6.2 and 6.4) the slope was calculated using only the linear part of the ramps. The coarse steps that affect the bottom part of the mask ramps have been disregarded.

The diagram of figure 6.12 reveals that the quality of the contours produced generally worsens with slope and the degradation of smoothness proceeds differently according to the type of 3 – d sacrificial mask used. The best performance is achieved when the contours are produced using thermally grown oxide and JSR IX575 after thermal smoothing treatment (sample JSR 10X20). Using these materials as masks, steps arise when the slope is steeper than 45 degrees. On the contrary, when AZ4562 is used, the performance is generally poor. Even at lower slopes, ramps and features produced using AZ4562 present a large amount of micrograss that conceals the contour.

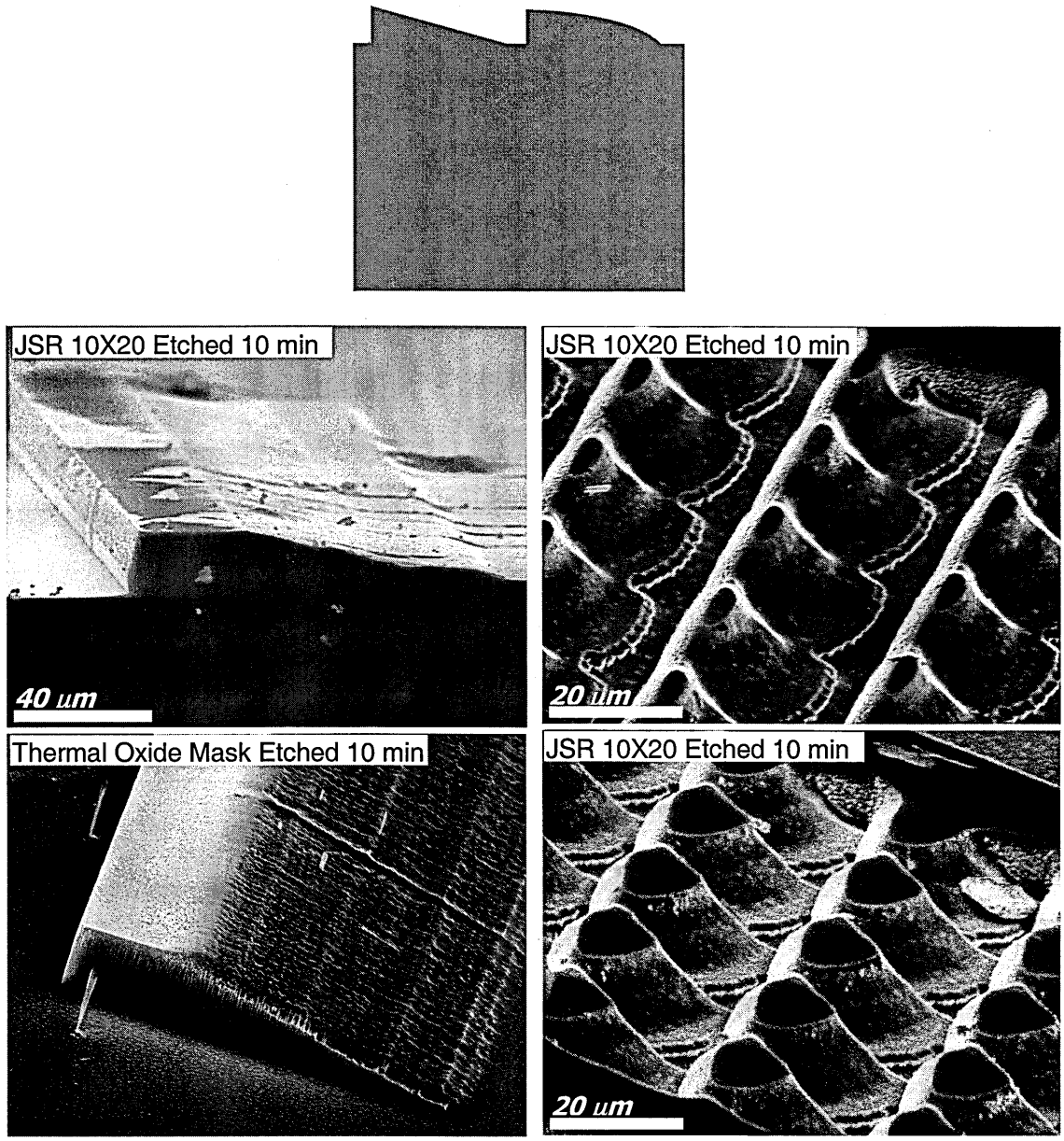


Figure 6.8 **First typology of results: smooth ramps and features. A large part of the contour is smooth and free from defects**

The effect of the masking material is exemplified in figure 6.13, where ramps of approximate slope of 30 degrees obtained using different masking materials are compared. The sequence of materials from the best to the worst performer appears to be: thermally treated JSR IX575, thermally grown oxide, JSR IX575 and, finally, AZ4562. Thermal treatment on AZ4562 does not seem to improve the quality of contours produced. Roughening of contours and emergence of steps and micrograss are phenomena related to the initial roughness of the mask and the mechanism of mask consumption during etching. A speculation on these issues would be very interesting to elucidate the phenomenology of DRIE: unfortunately this is beyond the scope of this early stage research.

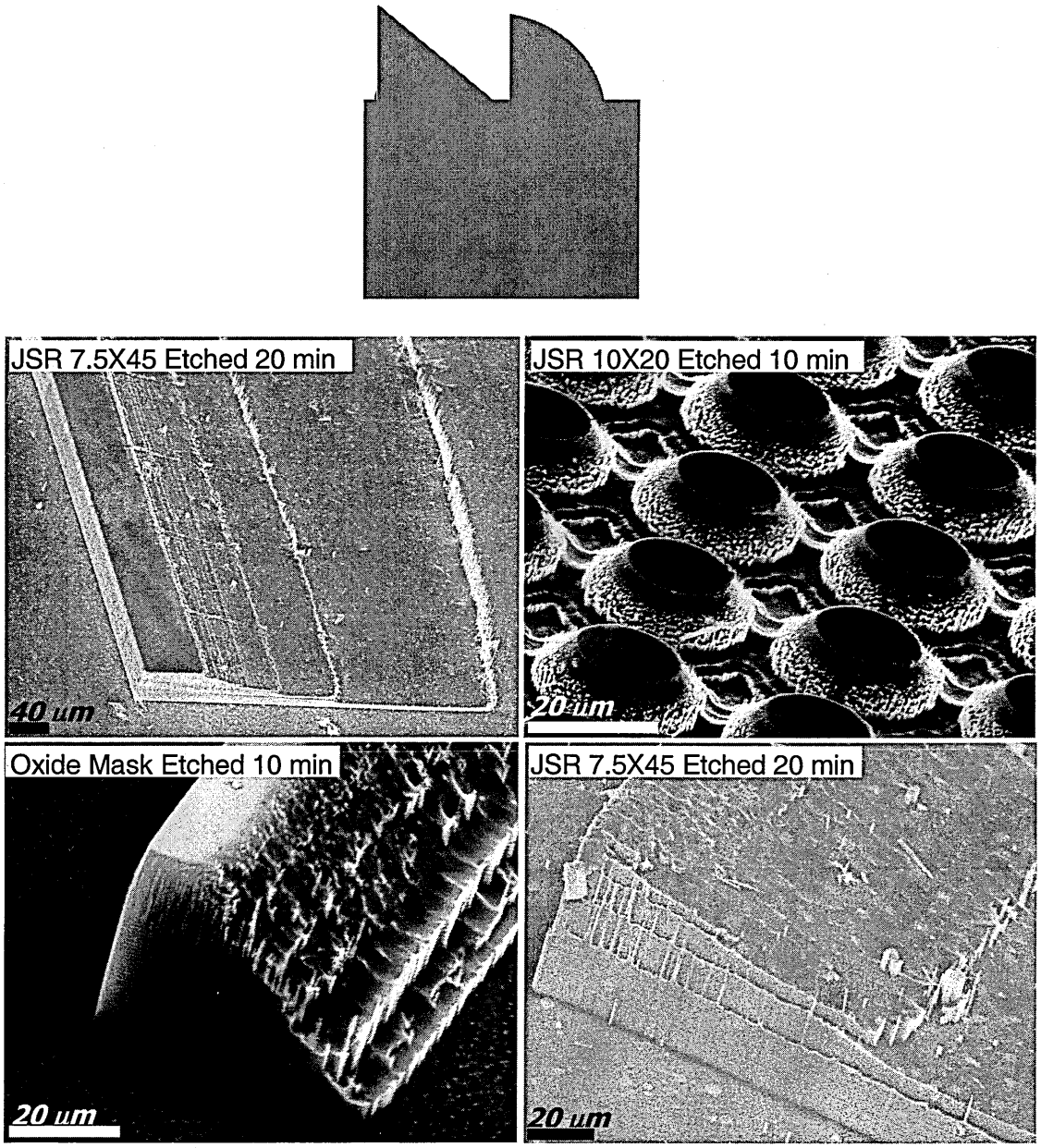


Figure 6.9 **Second typology of results: non-linear ramps and features. Jagged steps affect the contour that is only partly smooth.**

6.1.4 Post-etching treatments

The results showed that it is not possible to produce smooth features when slope exceeds 60 degrees. The contours present huge steps and, when AZ4562 is used, relevant amounts of micrograss are formed. On the contrary, concentrators require smooth contours. A subsequent step to eliminate micrograss and steps has to be introduced. Smoothening of contour surfaces was attempted using different techniques.

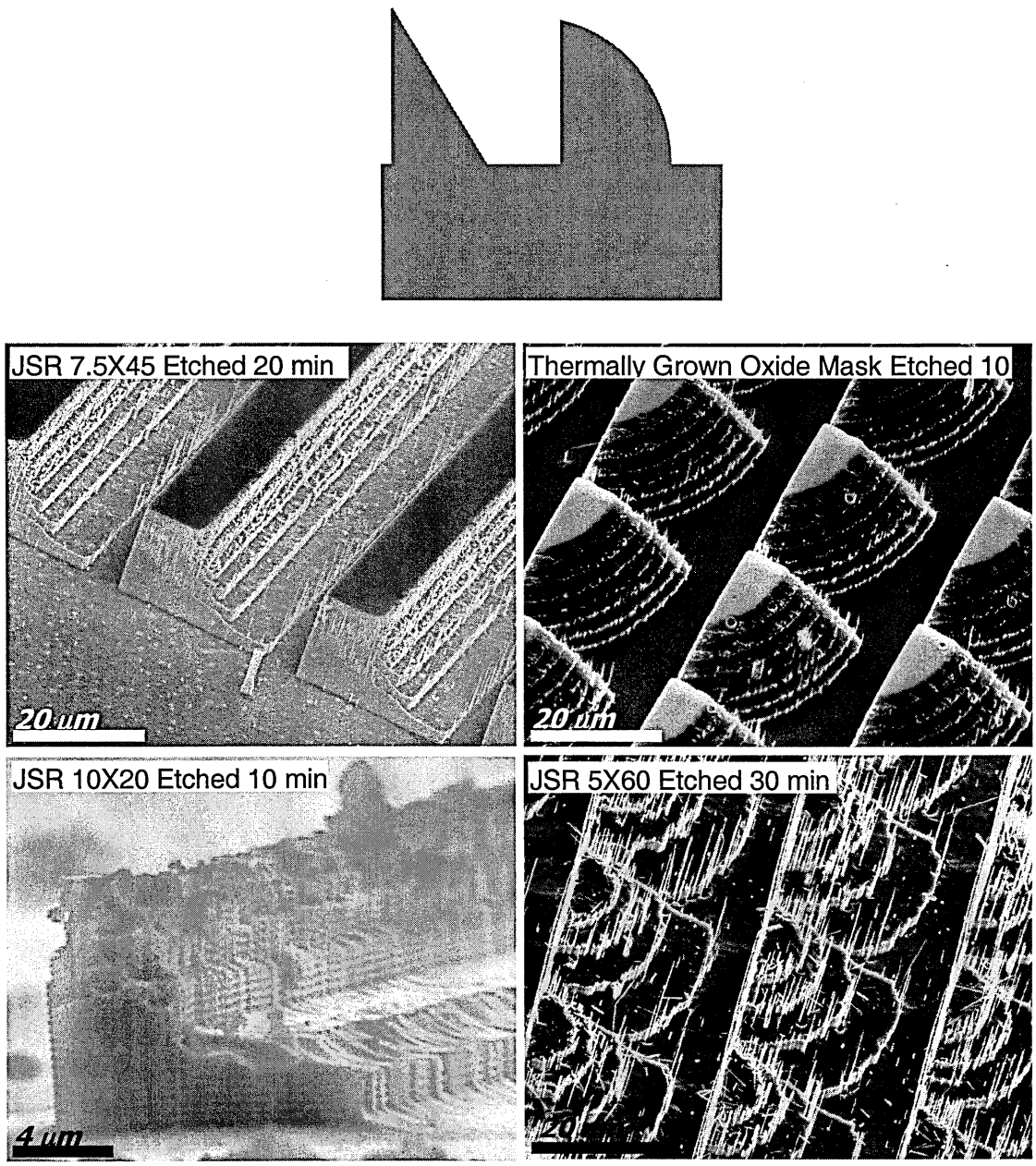


Figure 6.10 **Third typology of results: stepped ramps and features. The contour is definitely broken into a series of steps and continuity is definitely lost. Filaments start to emerge for the edges of the steps.**

An ultrasonic bath in water at room temperature was first used to remove the grass filaments from the ramps. The treatment is unable to smooth the contour, thus as the grass is removed the steps underneath become visible. After a 6 hours treatment the ramps microstructure appears as showed in picture 6.14. It is evident how the massive amount of silicon microfilaments that originally crowded the sloped surface arise generally from the edge of the steps. Furthermore, the steps tend to be coarser at the bottom of the ramp and smaller at the top. The treatment, although successful in removing most of the "micrograss", yields an unsatisfactory performance since it cannot eliminate the steps.

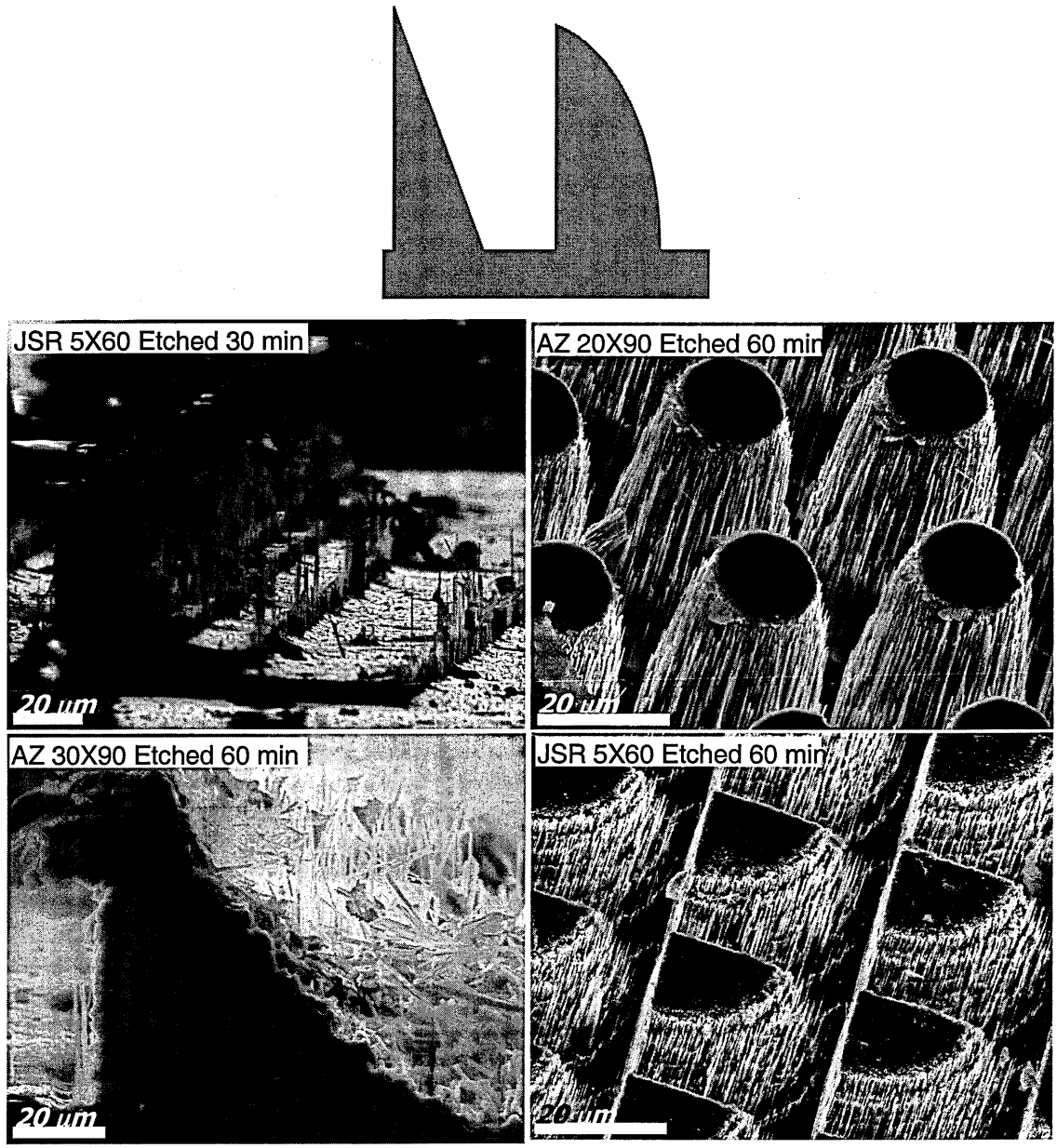


Figure 6.11 Fourth typology of results: completely hidden slope. Large defects and silicon filaments (micrograss) cover completely the contours

Anisotropic wet etching of silicon using KOH based solutions can produce very smooth surfaces (see e.g. [*Madou, 2003, Chapter 4*]). The <111> planes are far the slowest to be etched. Therefore in a <100> silicon wafer, features aligned to the <110> direction tend to be eventually bounded by inclines with slope 35.26 degrees. The delimiting surfaces are ideally smooth. The wet etching process may be able to smooth the steps and eliminate micrograss.

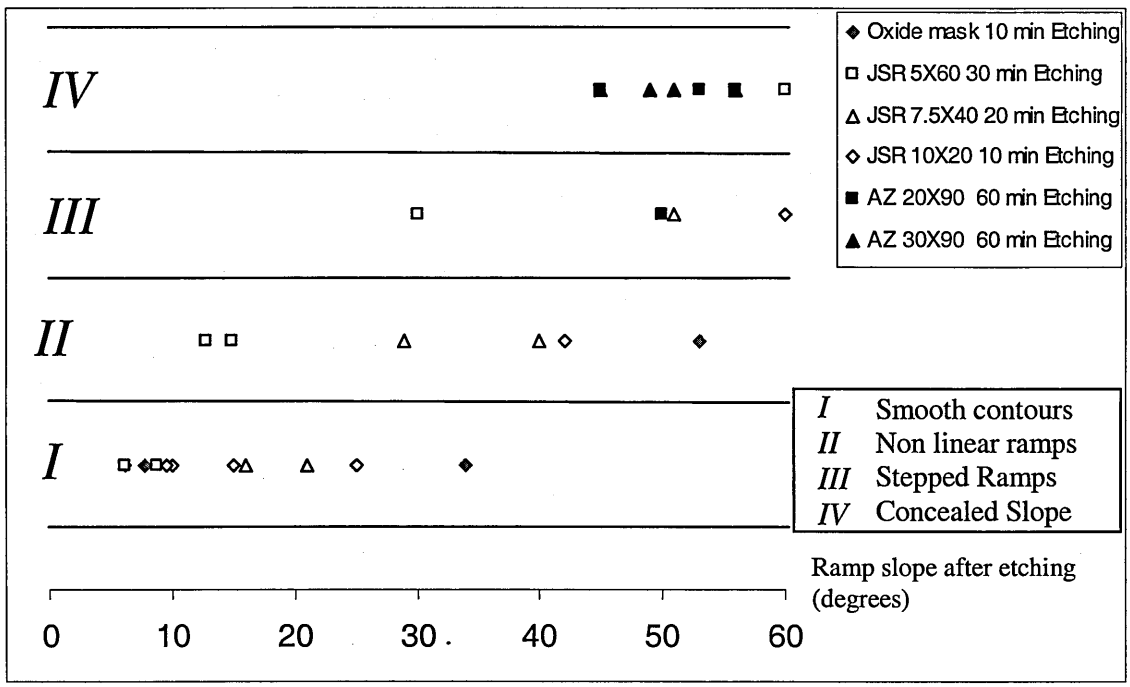


Figure 6.12 Diagram representing the typology of results for different samples as a function of ramps slope after etching

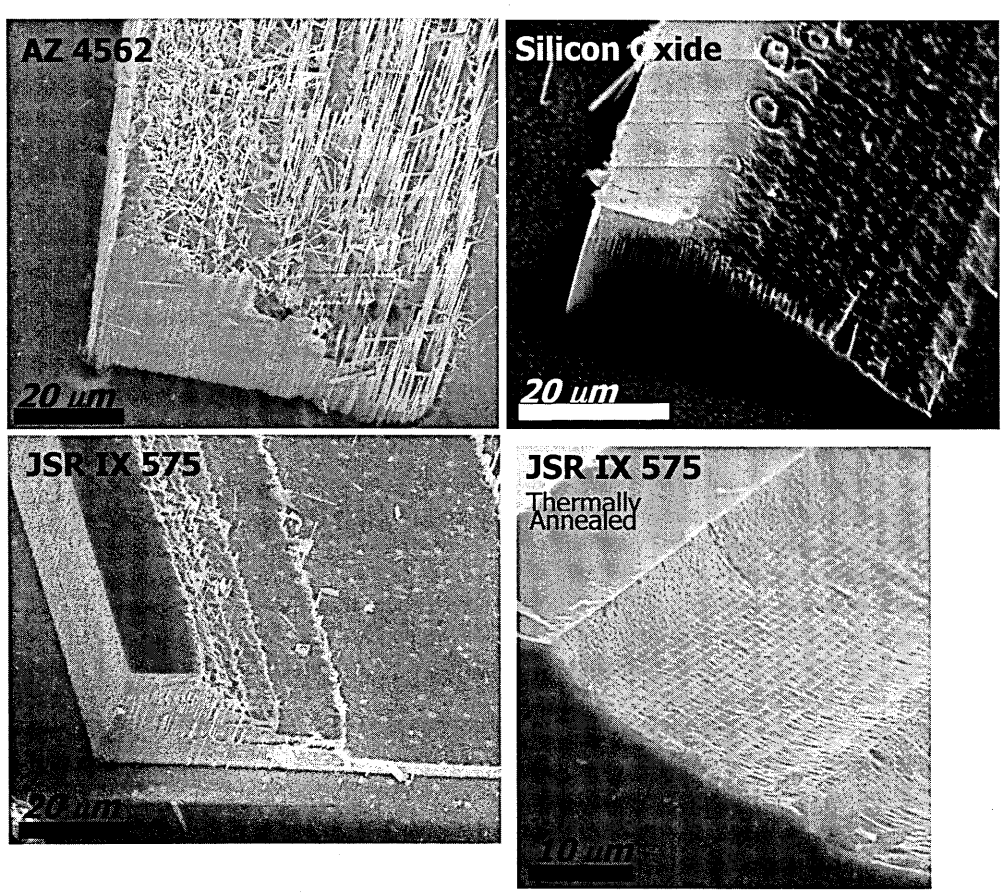


Figure 6.13 Ramps of similar slope obtained in Silicon using different sacrificial masking materials

Samples were etched for various times in a KOH solution 36 % volume in water under constant agitation at a temperature of 70 degrees Celsius. Typical results are shown in figure 6.15. A short process (5 minutes), as in figure 6.15a, may be effective in removing micrograss but it is unable to eliminate ramp steps. Ramps contour is still generally very rough. In fact a closer zoom on ramps side shows the spresence of many steps. As for figure 6.14, the steps are bigger and less concentrated at the bottom and become smaller and denser near the top of the ramp. The steps seem to be bounded by horizontal plateaus (probably <100> planes) and inclined sidewalls (probably <111> planes). The strong kinetic drive towards <111> planes emergence strongly modifies features contour. At longer etching times, therefore, the contour becomes even rougher because the planes are fast etched until appearance of <111> planes. After 10 minutes of etching ramps with initial slope near to 35.26 degrees have already been etched to the point where the ramp is mainly made of <111> planes. The ramp is very smooth as it can be observed in picture b of figure 6.15. Figure 6.15c demonstrates how relatively large steps may be produced during this process. Anisotropic etching is evidently unsuitable for smoothing out the above defects.

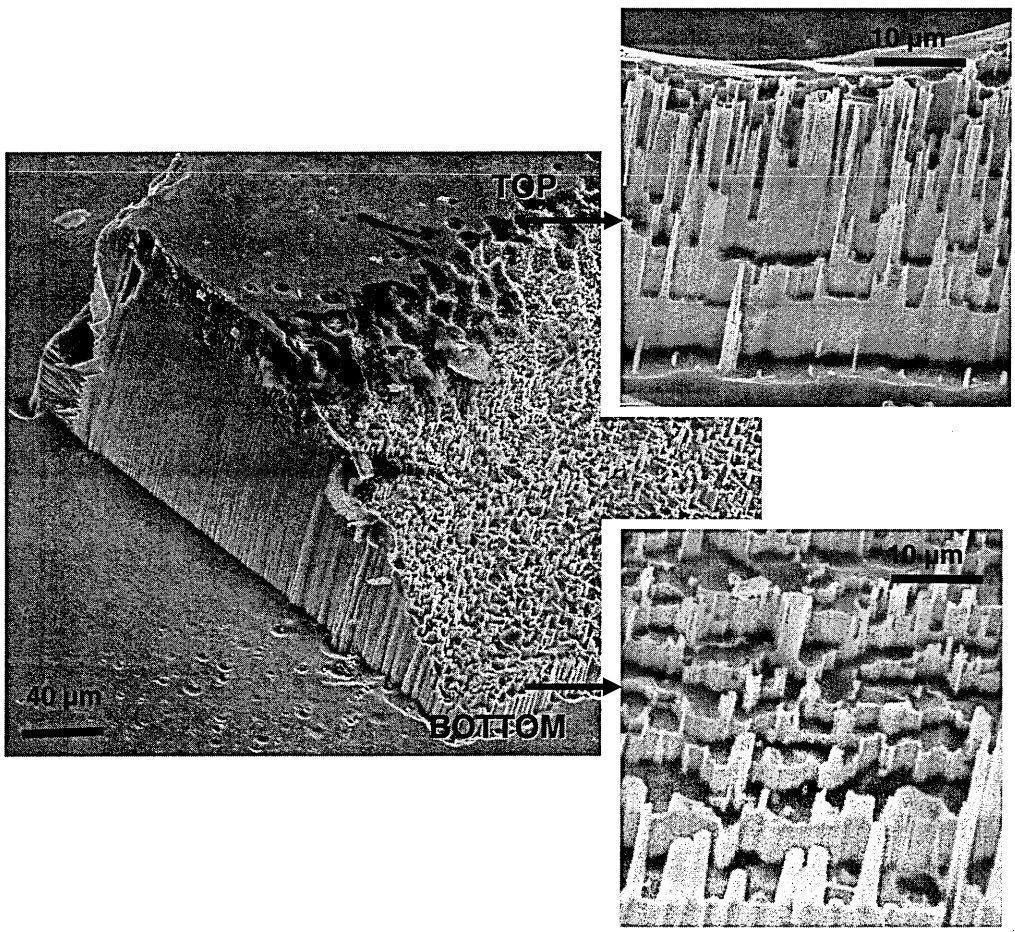


Figure 6.14: Deep ramp, originally obtained using a AZ4562 mask, with slope around 50 degrees after 6 hours of ultrasonic treatment. Insets: magnification (front view) of the top and bottom of the ramp.

Surface smoothing by isotropic etching is expected to yield a better performance. Plasma etching can remove the filaments and round the steps. Thanks to the isotropic character, it does not produce flat prominent surfaces. If applied for long times, however, it will tend to modify the original slope. The isotropic cleaning was realised in the STS ASE equipment using pure SF_6. No passivation phase was introduced. The coil power was set to 500 W and the platen power to 10 W. The etch rate of such a process is expected to lie in the range 2 to 2.5 μm/minute. The isotropic cleaning step was applied to deeply etched (up to 300 μm) samples (using AZ 4562 masks) in order to try to smooth very steep features, which were originally heavily grassy. A typical result is in figure 6.16. The major problem was the scarce effectiveness of a very short cleaning step: 1 or 2 minutes are not enough to get rid of all the grass. After 10 minutes, grass is completely eliminated and steps reduced but ramps slope starts to be slightly deformed by the isotropic cycle. Furthermore, a series of characteristic spherical "bites" start a progressive destruction of the feature. For smaller features, the modification of the original slope was more evident.

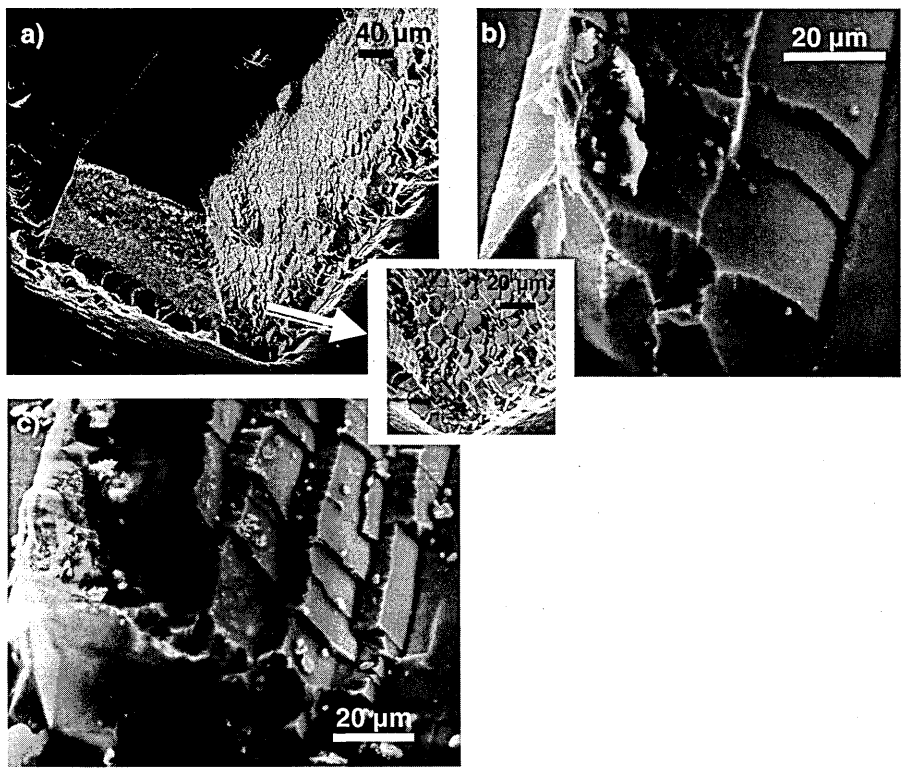


Figure 6.15: a) Deep ramp with slope around 50 degrees, originally obtained using a AZ4562 mask after 5 minutes of wet etching treatment in hot KOH in water. Inset: magnification of the left-bottom corner. As treatment time increases the contour becomes very smooth if it is only made by <111> planes (b) or very rough if delimited by steps (c).

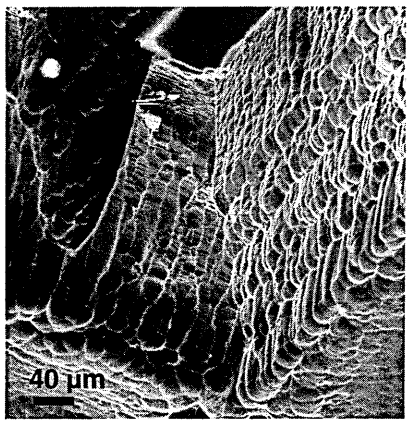


Figure 6.16: Deep ramp with slope around > 70 degrees , originally obtained using a AZ4562 mask, after 10 minutes of isotropic plasma etching treatment.

6.1.5 Comment: suitability of the results for the microfabrication of collectors

The above exploratory work had been accomplished to assess the feasibility of a fast, low-cost and reliable technique for the microfabrication of arrays of real free-form 3 – d microstructures on silicon wafers. Generally, an ideally continuous contour could not be achieved during transfer. The majority of contours produced were actually stepped: a broken sequence of mainly horizontal plateau and vertical sidewalls. Just a few masking materials produced contours that could be defined approximately smooth and only for small slope angles. Every kink, defect or step in the mask ramp or the masking material roughness itself tends to originate vertical edges or plateaus during etching. Micrograss was generally present on the contour. It originated preferentially at the edges of the steps. The phenomenon can be massive depending on the mask material used. It increases greatly with the slope of the feature etched. On planes steeper than 60 degrees the phenomenon may amount to such a great extent that the original 3 – d contour cannot be recognised anymore.

In the following, the major constraints relative to the microfabrication of concentrators are compared with the results reported above in order to assess the suitability of the technique attempted. (The major constraints affecting the microfabrication process were surveyed in the literature part, in section 3.2.)

1) SCALE: Concentrators must cross through the entire wafer thickness and the 3 – d mask must withstand a very long etching cycle. Table 6.2 demonstrated that only AZ4562 can allow through-wafer etching. A very thick oxide layer could be used (~ 5 μm for a 600 μm thick wafer) but a technique capable to produce such thick oxide was not available at Cranfield.

2) SHAPE: Concentrators have a well defined parametric contour. In particular the CPC is a complex 3 – d structure, with slope of profile varying locally from zero (at the absorber) to 90 degrees (at the entrance). As the slope increases - it was shown - contours smoothness is lost. The bottom part of the concentrator could maybe be

produced with an acceptable surface quality, but beyond that the sidewalls would be crowded with micrograss and definitively stepped.

3) SMOOTHNESS: Surface roughness must be minimised to achieve the minimum scattering and the maximum reflectance. The contours reported above are very far from smooth. Although post etching treatments could eliminate the most evident defects, a smooth finish could not be reached.

To conclude, the results achieved by using a "true" grey mask were unsatisfactory. Furthermore, the HEBS mask is expected to produce the smoothest 3 – d contours. An even worse outcome is expected from a digitalised grey mask, which often produces coarse steps and kinks [*Waits et al., 2003*]. After these preliminary trials the methodology was judged not viable and therefore abandoned. There would be still large room for upgrading this process. Some ideas are advanced in the future work part.

6.2 Modified DRIE cycles with reduced anisotropy

The aim of the trials reported in this section was to produce contoured cavities in silicon using a simple conventional binary mask in photoresist or silicon oxide. First, the suitability of the technique chosen (DRIE) is analysed in section 6.2.1. Subsequently, exemplary results are showed and commented for the various methods used: etching in defect or excess of passivation (section 6.2.2), isotropic etching in pure SF_6, (section 6.2.3), combinations of long anisotropic and isotropic cycles (section 6.2.4) and other more elaborated methods (section 6.2.5). Finally, in section 6.2.6, the results from the different methods are compared and evaluated on the basis of requirements and constrains such as scale, shape, surface smoothness, etc. After a comparison with the literature (section 6.2.6), the section concludes with the choice of a method and the presentation of a roadmap for the subsequent trials.

A mask was designed for the trials reported in this section that contained arrays of circles and squares of different size. The layout of the mask was specified in the experimental part (section 4.3.3). <100> bare silicon wafers were used in all the trials. Photoresist Clariant AZ4562 [*Clariant, 2004*] was used as a mask. The conditions of deposition and patterning and the experimental settings for DRIE were reported in the experimental part (section 4.3.3).

6.2.1 *Assessment of the capabilities of the ICP-ASE multiplex ® equipment*

A series of preliminary trials for assessing the suitability of the STS-ASE process for through-the-wafer etching of cavities were performed at Rutherford Appleton Laboratory (Didcot, UK). Typical results are illustrated in the perspective views and cross sections of figure 6.17 *a* to *d*. Figures 6.17*a* and *b* show square apertures with a side of 450 μm deeply etched, using a recipe denominated "deep" (the recipe was described in the experimental part, in table 4.7). The anisotropy of the process is very near to one even for very deep etching (figure 6.17*c*). The close up of figure 6.17*b* from a cross-shaped pattern reveals a defect peculiar of deep anisotropic processes, namely the presence of long silicon filaments. This phenomenon is generally identified as "micrograss" in literature [*Bhardwaj et al., 1997*]. This defect can be clearly observed in

the close up pictures of figure 6.18. Micrograss is generally caused by micromasking during etching, due to the re-deposition of impurities [*Elwenspoek and Jansen, 1998, Chapter 12*]. Micrograss can be easily avoided in the central parts of a cavity by achieving a slight undercutting during etching. However, eliminating micrograss from the sidewalls represents a serious problem.

The horizontal strips, which can be observed on the sidewalls of the features in figure 6.18, are called "scallops". They represent a feature typical of the Bosch process. Scalloping is caused by the sequence of etching-passivation steps (this mechanism was described in the background part, in section 3.3). Finally, the cross section of picture 6.17*d* shows a feature etched in pure SF_6 demonstrating the possibility of producing isotropic profiles. Notice the roughness patterns clearly visible on the front sidewall (this issue will be deeply discussed in the following).

The results of figures 6.17*a* to *d* demonstrate that through wafer micromachining of very deep and large features is well within the capabilities of the STS-ASE equipment. Furthermore, large amounts of silicon can be removed fast: etching almost through wafer (as in figure 6.17*c*) was achieved in slightly less than 4 hours.

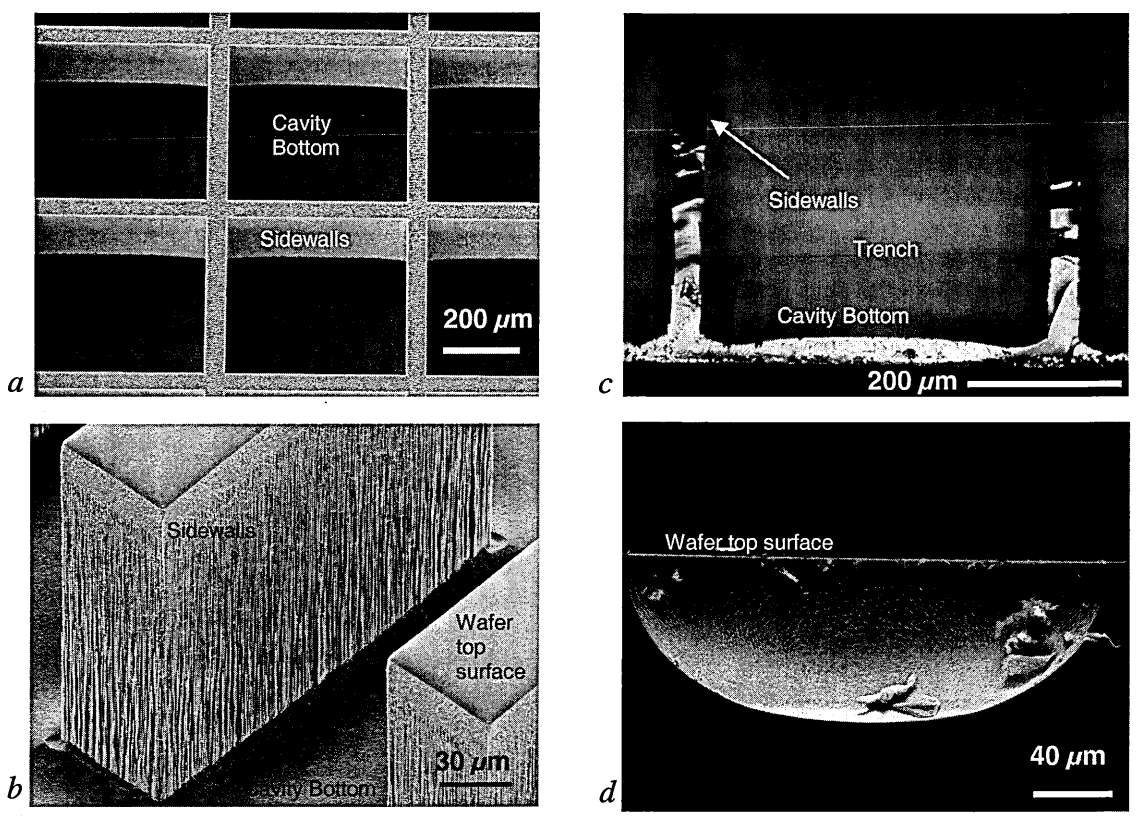


Figure 6.17 Microphotographs presenting perspective views and cross sections of features from samples deeply reactive ion etched under different parameter settings

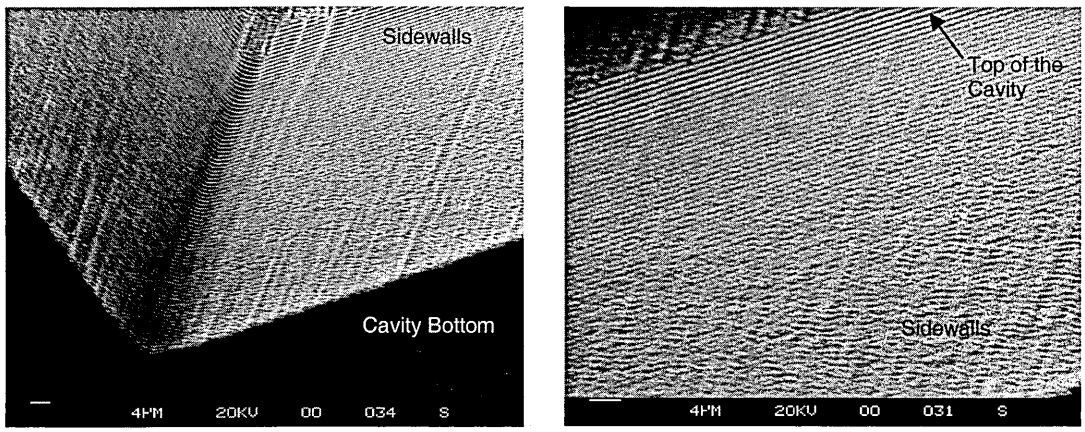


Figure 6.18 Two close up pictures from the sample of figure 6.17*b* showing two typical features of sidewalls obtained by anisotropic DRIE: scallops (horizontal strips on the sidewalls of the features) and micrograss (columnar filaments at the bottom of the of the sidewalls).

6.2.2 Cavity profiles obtained by unbalancing the etch-passivation equilibrium

Opportune deviations from standard unidirectional STS recipes may lead to sidewalls bowed inward ("undercut") or outward ("overcut" or "tapering"). Both overcut and undercut decrease the degree of anisotropy of the features produced and could offer a way of approaching the shape of a CPC or another approximated concentrator. Different samples were realised under process conditions slightly varied (generally one or two factors at a time) from the original "standard" settings (the conditions were reported in section 4.3.3, table 4.8).

The trials were addressed towards increasing the amount of passivation by increasing the time of the passivation cycles or increasing the amount of oxygen in the etching mixture. (A SiO_xF_y coating is known to be deposited during the etching cycle [*Elwenspoek and Jansen, 1998, Chapter 14*].) Although a conic cavity was expected, these modifications did not yield a satisfactory performance. Typical results obtained are reported in figure 6.19. The cross section relative to a sample obtained with two seconds in excess in the passivation cycle length (10 seconds instead of 8) is in figure 6.19*a*. Figure 6.19*b* shows the sidewall between two cavities for a sample etched in excess of oxygen.

In both cases the sidewalls seem slightly bowed: in fact, observation of rubber replicas obtained from the features demonstrated that the cavities have straight sidewalls. The curved sidewalls of the features of figure 6.19 must be due to an artefact occurring during wafer cleaving.

The features are filled with a massive amount of filaments. When passivation step length is increased, the profiles tend to be positively tapered and the slight undercut usually produced in the standard process does not occur. All contaminant particles deposited on the silicon surface act as a mask thereby originating filaments, which, instead of being undercut and etched away survive and populate the cavities. This approach resulted in a dead end: every increase in passivation time could only lead to an

increase in micromasking, yielding features filled with filaments, without any appreciable bowing of the sidewalls. It would be possible to eliminate micrograss using one of the smoothing methods attempted in section 6.1.4. However those methods were unable to achieve a good finishing of the sidewalls. Similarly, no satisfactory result could be obtained in this instance.

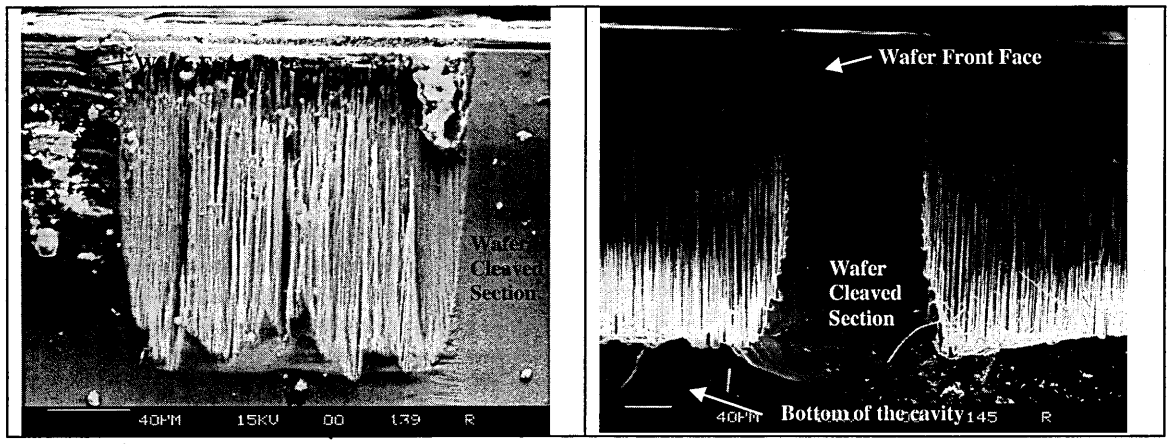


Figure 6.19 Cross sections of features from a sample obtained in excess of passivation

In a second series of trials, the length of the passivation step was decreased, first to 4 seconds (without an observable tapering of sidewalls) and then to 2 seconds. The length of the etching step was fixed at 12 seconds. The latter sample was etched for about 90 minutes, corresponding to 386 cycles, i.e. 4632 seconds (circa 77 minutes) total of etching vs. 772 seconds (circa 13 minutes) of passivation. A thinner deposition layer is expected to induce bowing of sidewalls since the nature of SF_6 etching is originally isotropic. Effectively, when the passivation step length was reduced to 2 seconds, curved contours were produced. Perspective pictures of cross sections are reported in figure 6.20. This time, the tapered sidewalls are not an artefact, as they are confirmed by the SEM analysis of the cast replicas. These replicas, shown in picture 6.21, allow appreciation of the actual 3 – d shape of the cavity.

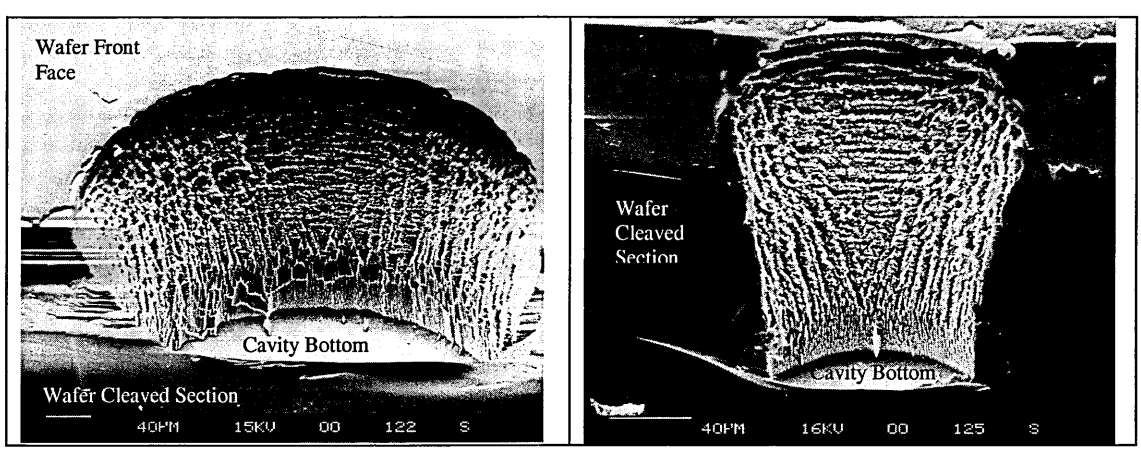


Figure 6.20 Perspective views of cavities cross sections from a sample etched with the passivation cycle reduced to 2 seconds

This process was investigated further: a series of cross sections were transformed in profile data from cast replicas with the method reported in section 4.3.5 and appendix C. After this procedure, it was possible to analyse the evolution of contours as a function of mask aperture. A series of profiles of cavities obtained from circular mask apertures is reported in the diagram of figure 6.22. Notice the similarity of these profiles with the profile reported in figure 3.25*c*, from a software model of the Bosch process [*Zhou et al., 2003*].

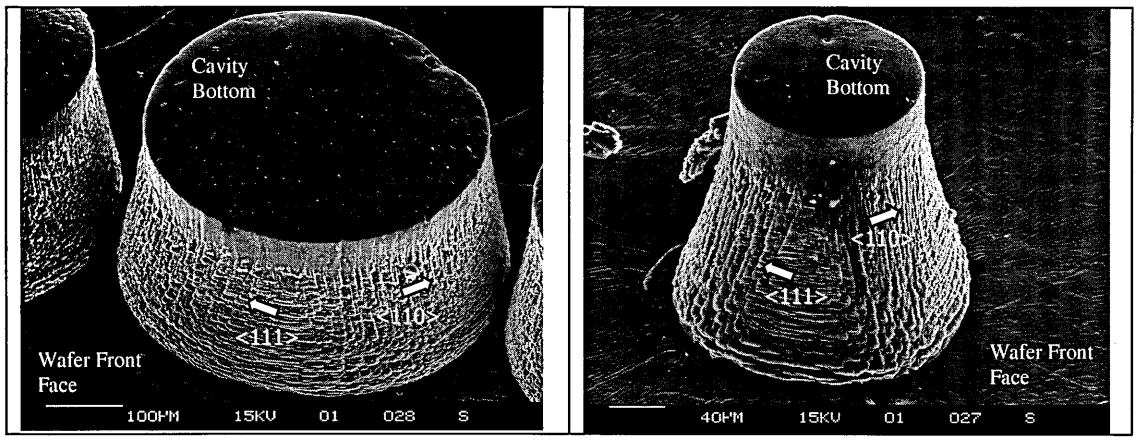


Figure 6.21 **Perspective views of silicone rubber replicas from a sample etched with the passivation cycle reduced to 2 seconds**

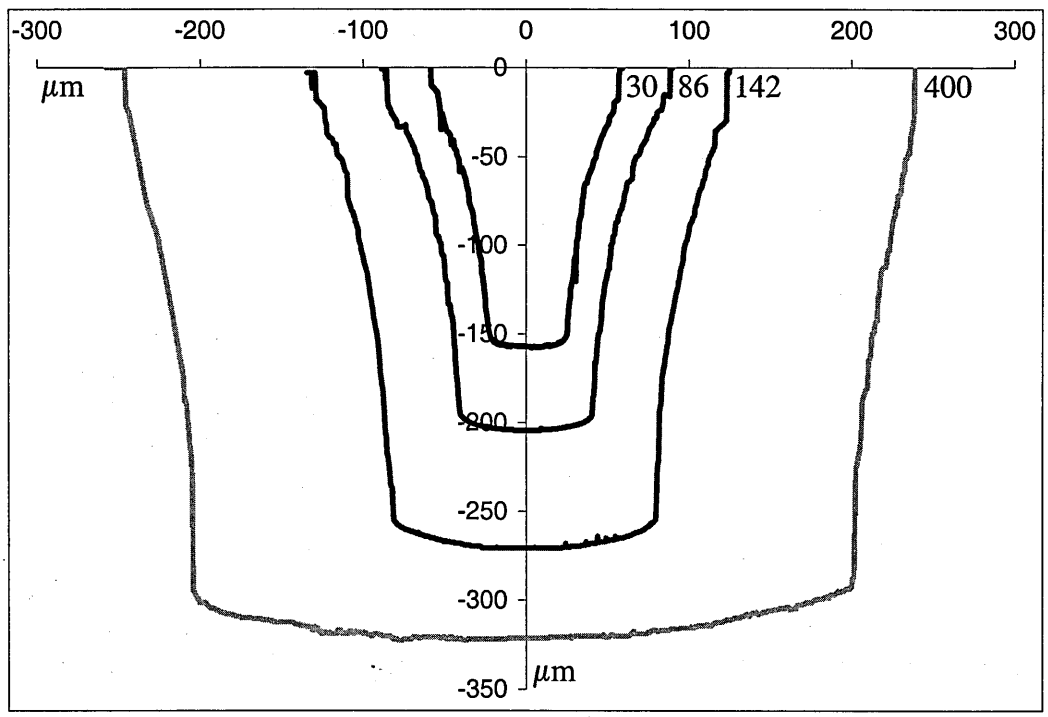


Figure 6.22 **Major cross sections of cavities evolved from different mask circular apertures for a sample etched with the passivation cycle reduced to 2 seconds. The original diameter of the mask aperture is indicated near each curve (in microns).**

A further imbalance towards etching was achieved after increasing the etching step time to 20 seconds while leaving the passivation step at 2 seconds. A cycle of 60 minutes and 8 seconds corresponds to 164 cycles (overall 3280 seconds of etching and 328 seconds of passivation). Shapes similar to the previous case were produced (figure 6.23). The profiles are reported in figure 6.24. The evolution of such profiles can be qualitatively predicted by a simple model of the process based on the balance between the passivation and etching surface reaction and the mass flow within the cavities. (Such a model will be briefly discussed in section 9.3.3.)

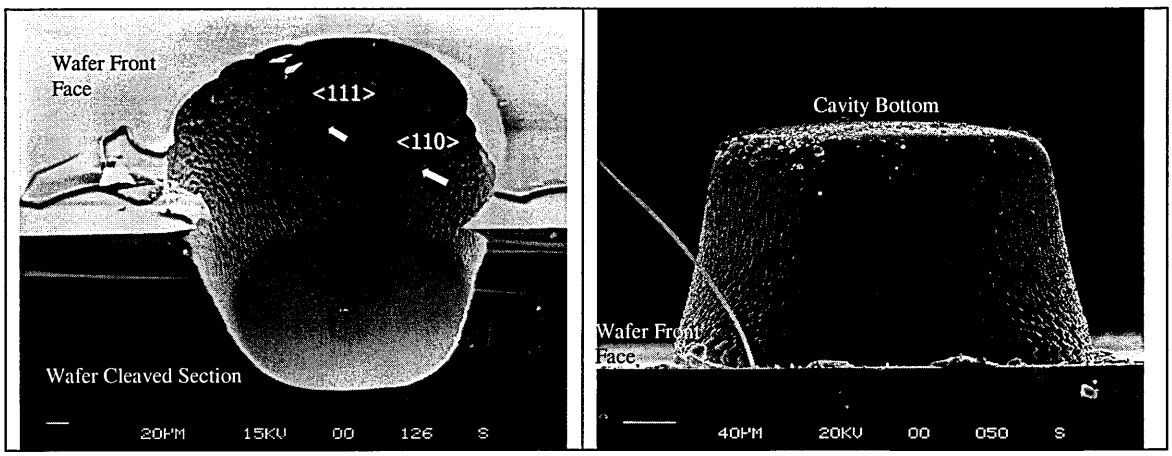


Figure 6.23 Perspective view of cross section (*a*) and front view of a silicone rubber replica (*b*) from a sample etched with the passivation cycle reduced to 2 seconds and the etching cycles increased to 20 seconds.

Characteristics of these cavities that influence the suitability of the process for making concentrators arrays will be discussed in section 6.2.6, where all the methods reported in this chapter will be compared with particular reference to the surface roughness and the shape of the cavities. (These represent two major constrains for the production of suitable concentrators.)

Fundamental physical differences between these processes and the balanced anisotropic process exist. That a different phenomenology is dominant can be demonstrated by the large variation of etch rate with the size of the entry aperture. Although concave sidewalls are developed in all the features analysed, both slope and curvature vary as a function of feature size (i.e. original mask aperture). A large scaling effect in etch rate was observed, which is not normally observed in unidirectional DRIE (see e.g. [*Elwenspoek and Jensen., 1998, Chapter 12; Bailey and Gottscho, 1995*]). Compared to the common ARDE effect for DRIE, the etch rate decreases faster when feature width decreases (diagram of figure 6.25). A deeper discussion of this phenomenon is nor inherent to this chapter. However, attempts to clarify the kinetic of the process at the feature scale level qualitatively will be reported in section 9.3.1.

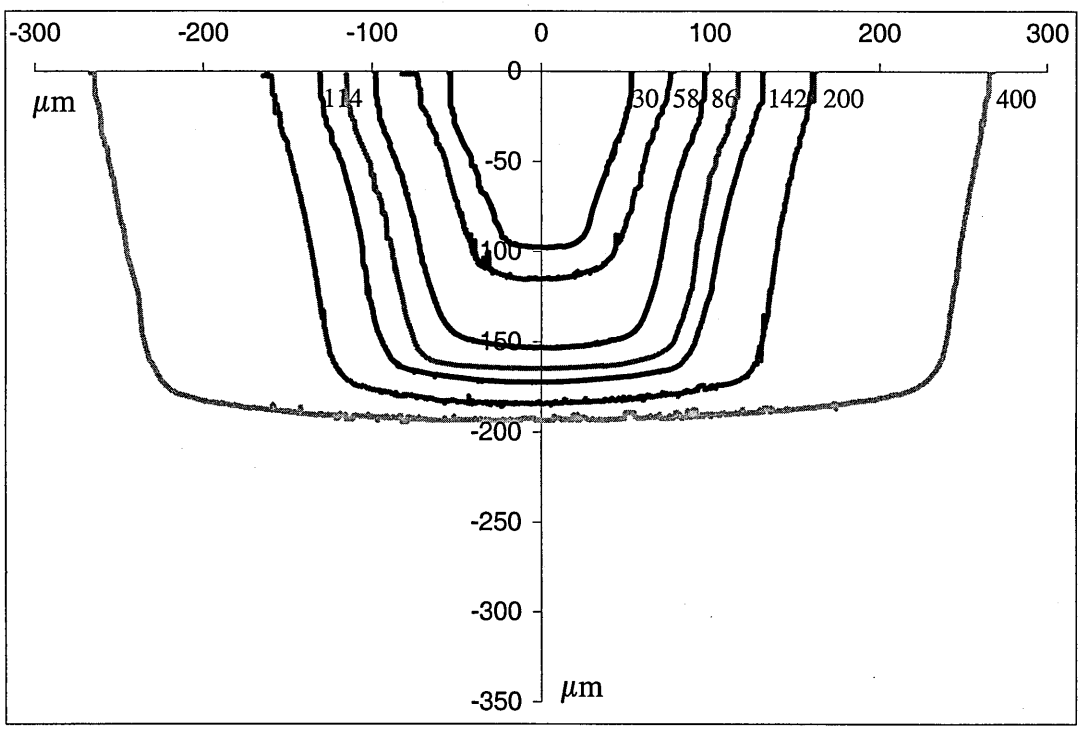


Figure 6.24 **Major cross sections of cavities evolved from different mask circular apertures for a sample etched with the passivation cycle reduced to 2 seconds and etching cycle extended to 20 seconds. The original diameter of the mask aperture is indicated near each curve (in microns).**

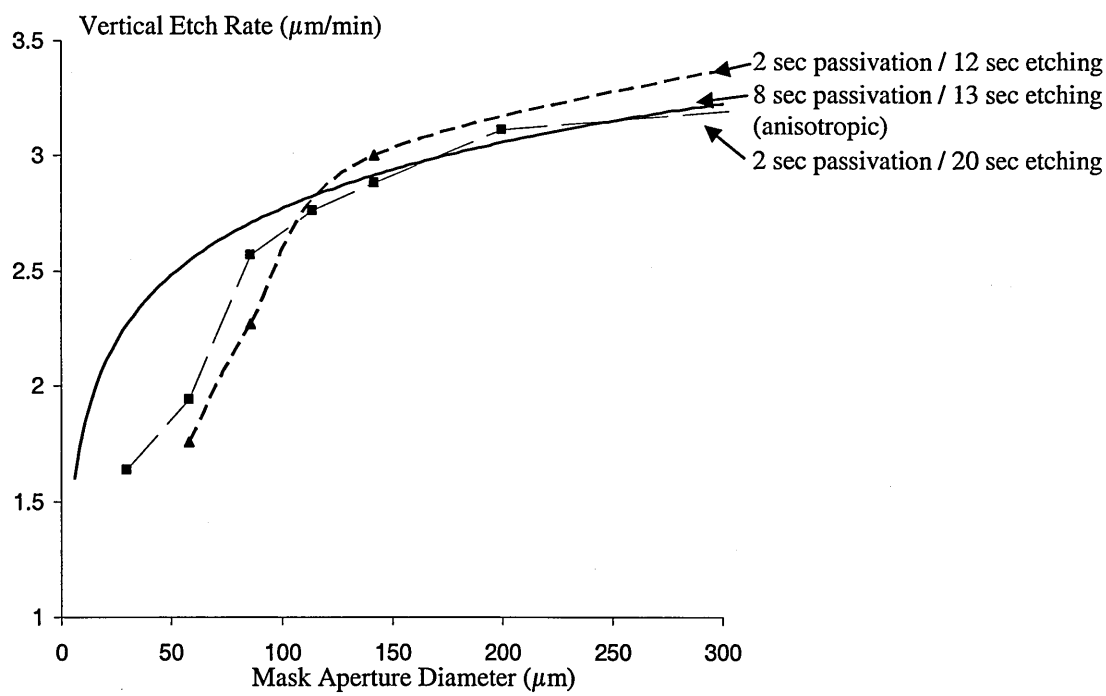


Figure 6.25 **Etch rate for two samples etched with shorter passivation step compared to a sample etched using the standard deep recipe.**

6.2.3 *Isotropic etching in pure SF_6*

If inductively coupled plasma is applied without any passivation-promoting factor, hemi-spheroids with large undercut are produced. Due to the spontaneous nature of the reaction of fluorine with silicon, the etch proceeds also in zones not directly hit by the ion flux or indeed by the radical flux. In the literature survey, it was argued how the shape of the cavities produced is the result of the complex kinetics at the feature scale level. In this section typical results are showed. To characterise the isotropic process, a vast number of samples were produced, by varying the bias power applied to the sample and the process time. The etching mixture was generally composed by pure SF_6. O_2 was added in a few instances. Pressure was kept constant (except in one case) at 30 mTorr. The experimental conditions are reported in the experimental part, in table 4.9.

The contours produced were all roughly similar in shape: in fact, for all the features produced, the etch factor – the ratio between the etch depth (*ED*) and the undercut or lateral etch (*EL*) – ranged from 1.7 to 2.4 regardless of any process parameters or feature size. Therefore, given for example $ED = 2\,EL$, the aspect ratio (*AR*) of a cavity etched from a circular hole of diameter d would be given by:

$$AR = \frac{ED}{2EL + d} = \frac{ED}{ED + d} \qquad (6.3),$$

which shows that the aspect ratio of the cavities decreases with mask aperture original size. The cross section of the etched features can roughly be approximated to a hemi ellipse, which is described by the equation 6.4, in a system with the x-axis aligned along the silicon wafer plane and the y-axis representing the axis of vertical symmetry of the etched profile:

$$y = -ED\sqrt{1 - \frac{x^2}{EL + d/2}} \qquad (6.4).$$

The degree of approximation decreases in accuracy as the features increase in size as demonstrated in the left-hand diagram of figure 6.26, which reports typical contours. In the diagrams of figure 6.26 a series of cavities obtained from mask apertures of different size from a single sample (left hand side) are compared with a series of cavities obtained form a mask aperture of 114 μm in diameter for different etch times from different samples (right hand side). It is apparent how, for similar etch depth, samples obtained from a smaller aperture for a longer etch time present higher aspect ratio.

Etch factor data obtained from optical measurements are reported in figure 6.27. The main feature of the STS-ICP Multiplex®, relatively to the purpose of this research, is represented by the possibility of applying a bias to the platen holding the sample. In this way the ion flux energy can be varied independently on coil power. (The characteristics of the equipment were presented in general in section 4.3.1). An increase from 0 to 40 Watts in the bias power applied to the platen during etching did not show any appreciable increase in aspect ratio. That the ion effect is too weak to contribute to the etching directly is confirmed in the literature produced by STS [*Ashraf et al., 1999*]. On the contrary, the ion flux affects surface evolution in more subtle ways. The effect of ion flux on the shape of the features and on surface quality will be discussed in sections 6.2.6. Only the sample etched at reduced pressure showed a decisively lower etch factor

average. Discarding the data from the samples etched at low pressure or with addition of oxygen, the average etch factor is equal to 2.06 with a standard deviation (σ) of 0.16.

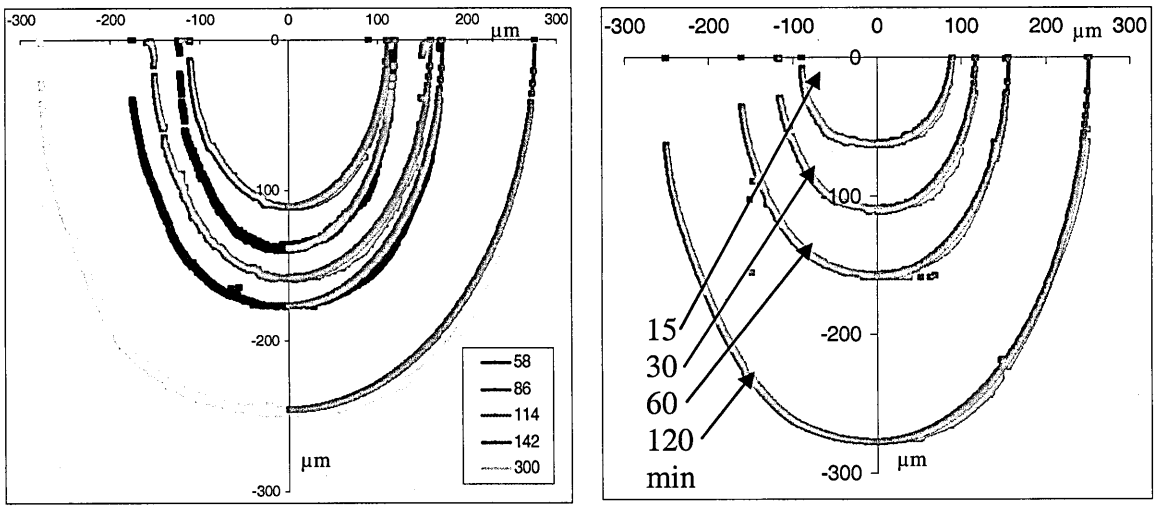


Figure 6.26 **The evolution of cavities etched in SF_6 without passivation promoting mechanism. Left: profiles from cavities etched for 1 hour using a bias power of 10 Watts. The diameter of the original mask apertures is in legend. Right: evolution of cavities etched from a circular mask aperture, 114 µm in diameter, for different etching times.**

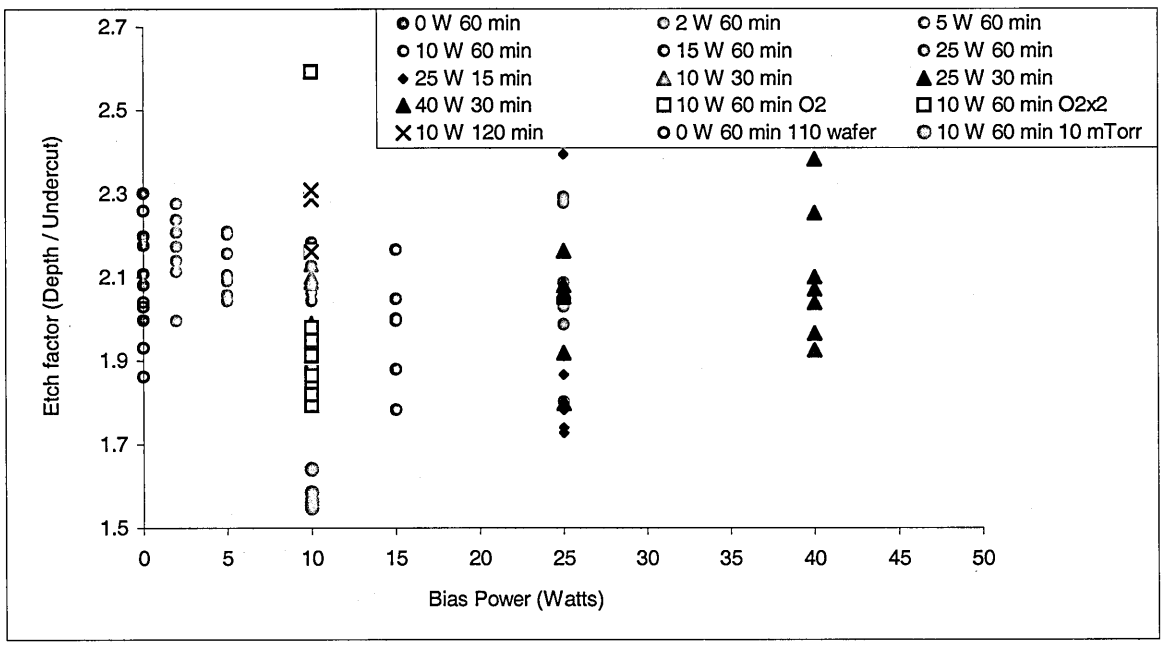


Figure 6.27 **Experimental values of etch factor relative to various mask apertures for different samples etched without passivation mechanism under different process conditions (see table 2.9 for processing conditions)**

The evolution of the roughly hemi-ellipsoidal contours and the aspect ratio higher than for a purely isotropic etching (where $AR = 1$ is to be expected) can be easily explained on the basis of shadowing effects and surface diffusion of fluorine radicals without the need to resort to the action of the ion flux. In fact, etching simulation software can produce similar profiles even in absence of ion bombardment (see e.g. [*Singh et al., 1992*]). Figure 6.26 shows how both etch depth and lateral undercut increase, within each sample, with mask original aperture size and decrease with time. Similar trends were reported for etching by using the fluorine-rich vapour liberated from XeF_2 crystals, i.e. a purely chemical etching [*Chu et al., 1997*]. An extended analysis of the profiles produced and the experimental trends relative to vertical and lateral etch rates is beyond the scope of this section. (A detailed discussion is in chapter 9, where it will be demonstrated how a model based on the mass balance is sufficient to explain the above trends.)

In conclusion, etching time and initial mask aperture appear to be the only two factors controlling the shape of the feature. Other important findings in relation to the application, such as surface roughness and process reliability and reproducibility, will be discussed in section 6.2.6.

6.2.4 Cavity profiles obtained by coupling long anisotropic and isotropic cycles

After preliminary trials at Rutherford Appleton laboratory (not reported here), the coupling of long anisotropic steps to long isotropic cycles was experimented with. Cylindrical cavities with straight sidewalls were produced by conventional anisotropic etching and their profiles subsequently modified by applying cycles in pure SF_6. The conditions of the anisotropic step were standard. The parameters for both cycles were fixed for all the samples: only the respective length of the steps varied. The processing conditions are reported in the experimental part (section 4.3.3, table 4.10). Various series of profiles (obtained from SEM analysis of the replicas, as detailed in section 4.3.5) are shown in figures 6.28 to 6.30.

The contour changes with original mask aperture size. For narrow features, undercut was generally limited to the top of the features. At the bottom, the features tended to maintain the original straight sidewalls. On the contrary when the original aperture was large, the sidewalls were affected more deeply. In the largest cavities the isotropic etching reaches the end of the cavities so that a round bottom is developed. Since both anisotropic and isotropic etch rates depend on aspect ratio and scaling factor respectively, the features become generally deeper and larger as aperture increases. The final etching figure described is not a simple linear combination of the two etching cycles in that it represents an expansion of the original cylindrical cavity. The magnitude and the direction of this expansion depend mainly on the aspect ratio of the original anisotropic feature itself. Notice the striking resemblance of some of the profiles of figures 6.28 and 6.29 with the profiles reported in figures 6.22 and 6.24. Indeed, the phenomenology responsible for the profiles of figure 6.22 and 6.24 presents some analogies with the mechanism involved in the production of the profiles of figures 6.28 and 6.29.

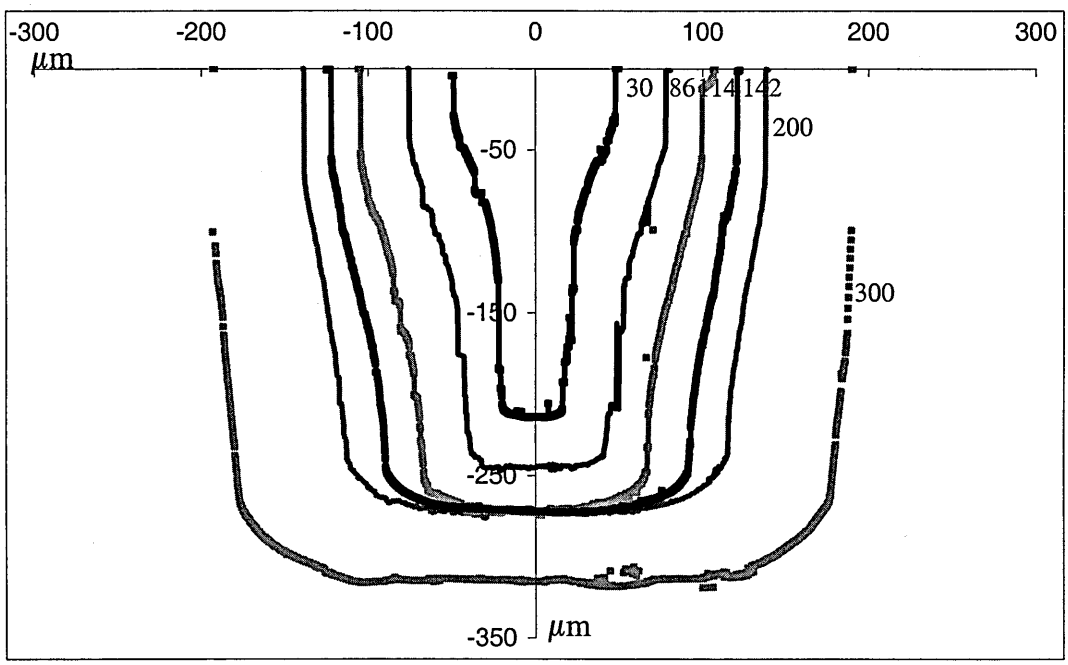


Figure 6.28 **Cross sections of cavities obtained from a sample etched for 90 minutes in deep anisotropic etching followed by 30 minutes in isotropic etching. The aperture diameter is indicated near each curve.**

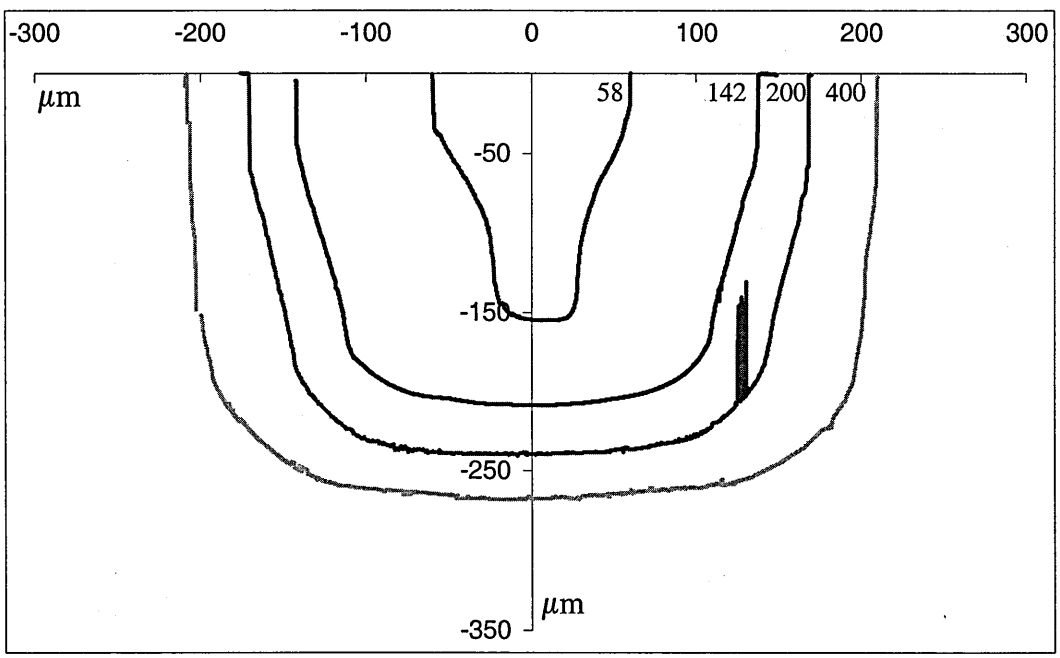


Figure 6.29 **Cross sections of cavities obtained from a sample etched for 60 minutes in deep anisotropic etching followed by 55 minutes in isotropic etching. The aperture diameter is indicated near each curve.**

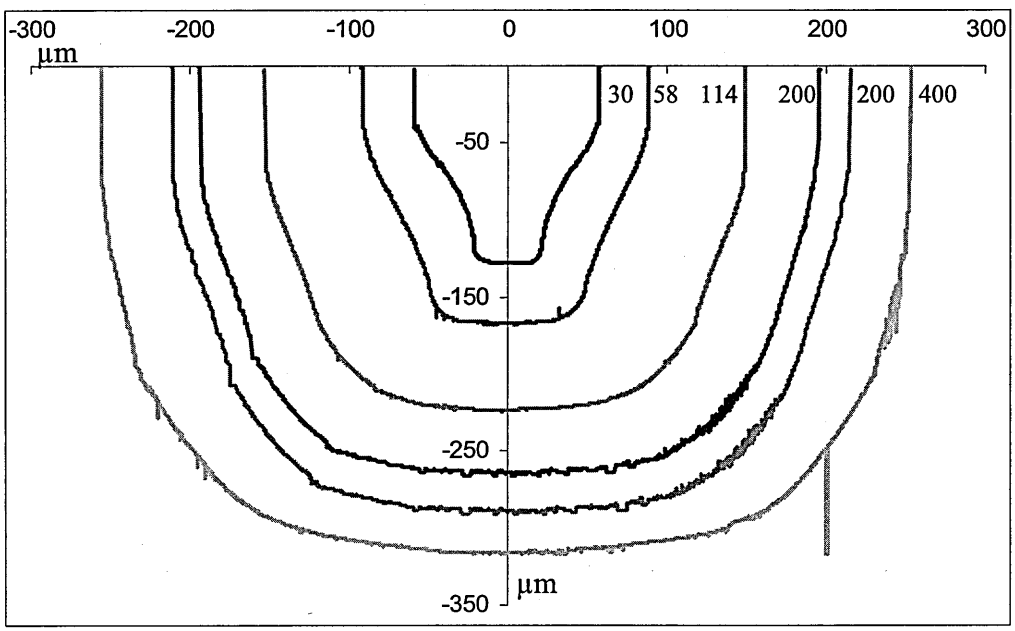


Figure 6.30 Cross sections of cavities obtained from a sample etched for 60 minutes in deep anisotropic etching followed by 90 minutes in isotropic etching. All the scales are in microns.

The above observations are confirmed from the inspection of the cross sections and silicone rubber replicas by Scanning Electron Microscopy (figures 6.31 to 6.33). In particular figures 6.31-*right* and 6.32-*left* show the slight rounding of feature bottom and the deformation on the sidewalls, which tend to the conical shape. Figures 6.32-*right* and 6.33-*right* show how larger apertures (or longer etching times) allow a greater rounding of the bottom of the cavities: the rim of the flat bottom of the original anisotropic (cylindrical) cavity can be clearly observed as a residual feature on the sidewalls. The rubber replicas show that there is a considerable undercut near the entrance of the cavity that is not detected by the method used for assessing the profiles. (appendix C discusses this discrepancy in more details.)

The patterns of surface roughness reveal clearly the evolution of the features. The roughness of the sidewalls and the mechanisms of its formation will be considered in section 6.2.6.

6.2.5 Other trials

A series of samples were etched with a mixture of SF_6 and C_4F_8 continuously fed to the chamber. The overall shape of contours produced was not largely dissimilar from the results obtained in defect of passivation (section 6.2.2). As an example, cross sections from a cavity obtained by etching with a mixture containing SF_6 (100 SCCM) and C_4F_8 (30 SCCM) are reported in figure 6.34. Notice the similarity between these profiles and the samples of figures 6.20 and 6.23.

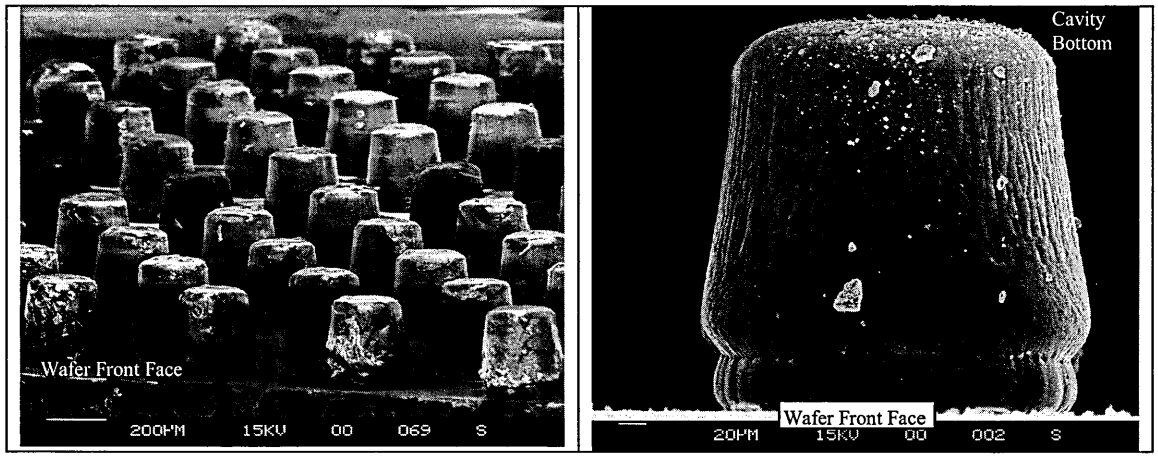


Figure 6.31 Perspective (left) and front view (right) of silicone rubber replicas from the sample etched for 90 minutes in deep anisotropic etching followed by 30 minutes in isotropic etching

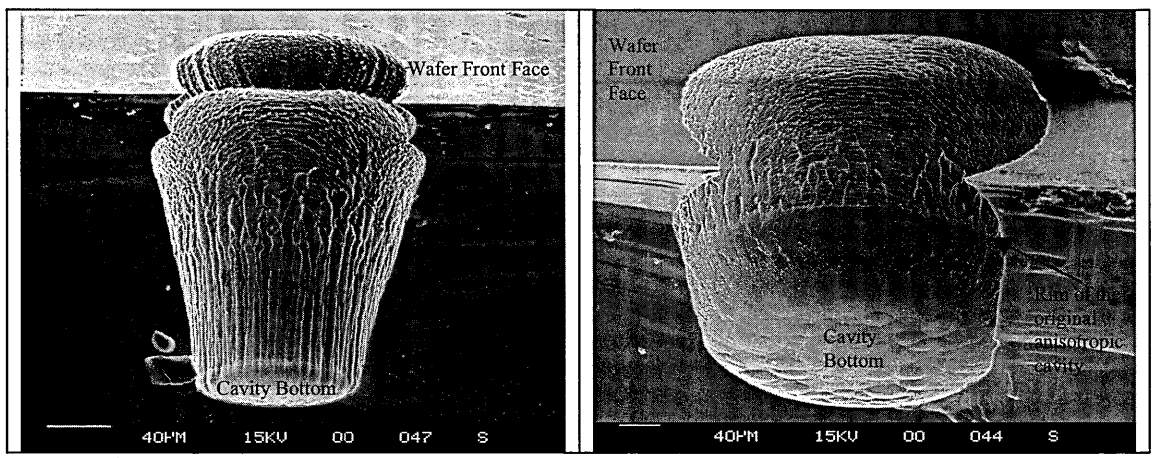


Figure 6.32 Cross section (left) and feature bottom enlarged (right) from sample etched for 90 minutes in deep anisotropic etching followed by 30 minutes in isotropic etching

A completely different set of trials was carried out using the in-situ grey techniques by making the mask recede slightly between sequential anisotropic cycles. Anisotropic etching cycles were coupled to oxygen steps to gradually consume the mask. This economic approach to grey scaling was revealed as being unsuitable for through-wafer etching since the O_2 cycles consume the photoresist, reducing the selectivity greatly. In figure 6.35 a sample obtained with this method is shown. A thick photoresist layer (AZ4562) was only able to withstand a few cycles before disappearing. The total etch depth achieved was ~ 50 μm (one fifth of the minimum depth required). Furthermore, micrograss would often affect the sidewalls.

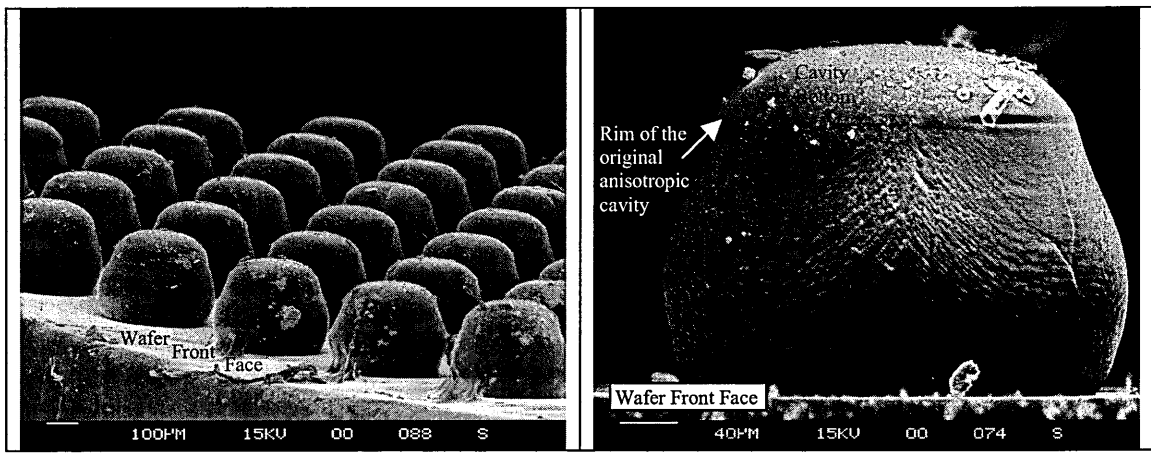


Figure 6.33 Perspective (left) and front view (right) of silicone rubber replicas from sample etched for 60 minutes in deep anisotropic etching followed by 90 minutes in isotropic etching

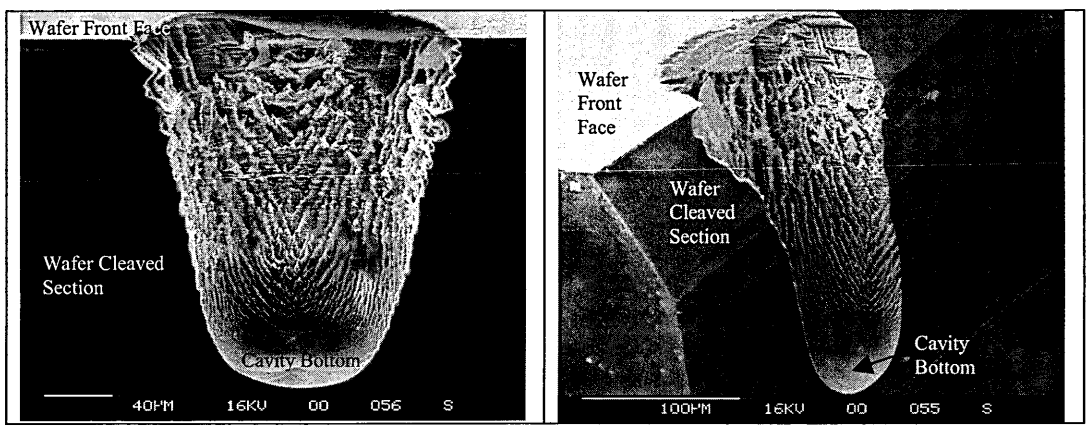


Figure 6.34 Front view (left) and perspective view (right) of cavities cross sections from a sample etched in a continuous cycles with a mixture containing both SF_6 and C_4F_8 (etching time = 180 minutes)

6.2.6 Comparison of the methods attempted and choice of the most promising technique

Once the range of profiles achievable by using modified deep etching processes is mapped, the most promising routes have to be chosen. The choice emerged after the comparison of the different methods. To this end, the considerations upon the microfabrication of concentrators expressed the background part (in section 3.2) are recalled here. In the following, the main requirements of the systems are listed and the above results will be compared with the constraints imposed by the application.

There are two effective ways to assess the suitability of the profiles produced by the different methods for the application as radiation collectors. The first method is fully experimental and would entail a direct testing of the cavities produced. These early cavities were produced on simple silicon wafers, but they could have been integrated

into a working IR device to test the detectivity. In this case, the arrays with the best collectors would show the maximum signal for a given IR source. Unfortunately, the long process for producing a single device wafer does not allow the testing of all kinds of collector shapes achievable. Furthermore, at that stage of the research, when the choice of the route to be investigated further had to be accomplished, there was no equipment available for testing directly a given array without integrating it into a working IR camera. Finally, at this stage, through-the-wafer cavities were not produced, because these would involve the use of SiO_2 coated wafers and a second (or even a third) wafer as a backing wafer. These additions would have represented a fair increase in the cost and time involved, at a stage when it was only required to map out the range of profiles achievable.

On the other side, it could have been possible to assess the expected performance in terms of transmittance, simulating the optical behaviour of the cavities by ray tracing technique as reported in chapter 5. However, the cavities produced are complex 3 – d structures: besides the obvious difficulty in obtaining a numerical matrix representing such complex shapes, we did not have any algorithm available that could be applied to their contours. The simple worksheets compiled for the calculations of chapter 5 were all but useless since they require introducing the profile in analytical form. Furthermore, it is very difficult to address the effect of surface roughness onto the reflection of the rays. In many cavities the roughness is comparable or far above the threshold of scattering, as it will be show below.

For the above reasons, at that stage of the research, the choice of the routes worth pursuing was necessarily based upon qualitative considerations. In this section, the requirements of scale, overall shape and surface smoothness highlighted in section 3.2 will be considered. The results of these trials are judged upon comparison with those requirements in order to identify the most promising route for the microfabrication of the array of concentrators.

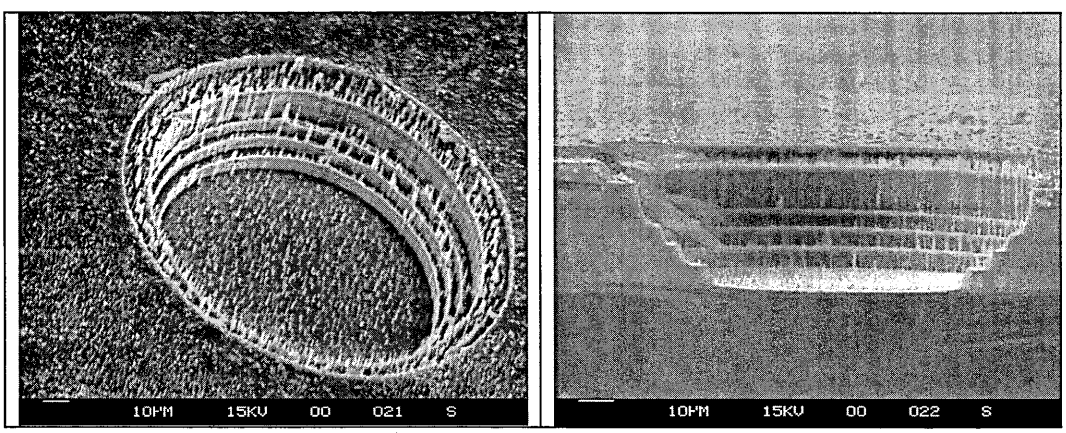


Figure 6.35 Perspective view (left) and front view (right) of cavities from a sample etched using a grey mask produced in-situ.

SCALE

The scale of features achievable represents the first criterion of comparison between methods. The concentrators are necessarily through-the-wafers cavities. These etching trials were not carried out through the entire wafer thickness. It is nevertheless possible to observe that all the methods attempted possess the capability of etching through silicon wafers a few hundreds of microns thick.

A comparison of the aspect ratios of the profiles experimentally achieved and the range of CPC suitable for the integration in the IR array is made difficult by the vast range of features produced and CPC design available. However, a rough qualitative comparison may be a source of precious information. In figures 6.36 to 6.38 part of the profiles produced experimentally are compared with the series of CPCs of figures 3.5 and 3.6. Theoretical considerations reported in section 5.2 demonstrated that a CPC with acceptance angle of about 14 degrees was the optimal choice. In the next pictures, the extremes of the series, i.e. the CPC with the lower and higher acceptance angles are compared to the typical profiles obtained using the above methods. The profiles have been vertically displaced in order to overlap with the experimental profiles. The CPC with 14 degrees of acceptance angle can be though (in both cases) as a profile intermediate between the two profiles indicated.

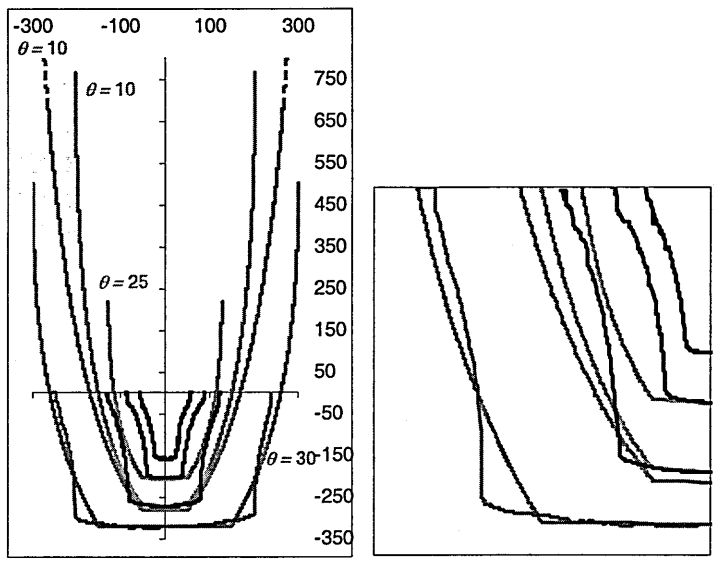


Figure 6.36 Comparison between the profiles of two series of suitable CPCs and the contours of cavities experimentally obtained for the samples of figure 6.22 (etched using shorter passivation steps). All the scales are in microns. Zoom on the right hand side.

Figure 6.36 shows that the etching using shorter passivation steps (reported in section 6.2.2) can produce profiles suitable for approximating up to half a CPC. The diagrams of figure 6.37 (*a* to *c*) demonstrate the extreme versatility of the method that couples long isotropic cycles to anisotropic cycles (reported in section 6.2.4). Since a vast range of aspect ratios is achievable, a good part of the CPC profile can be approximated. Finally, it is interesting to show how much of a CPC profile can be approximated using

a long isotropic cycle in pure SF_6. Figure 6.38 demonstrates that the simple "isotropic" etching, due to very limited range of profiles achievable, is able to approximate a very small part of the CPC profiles.

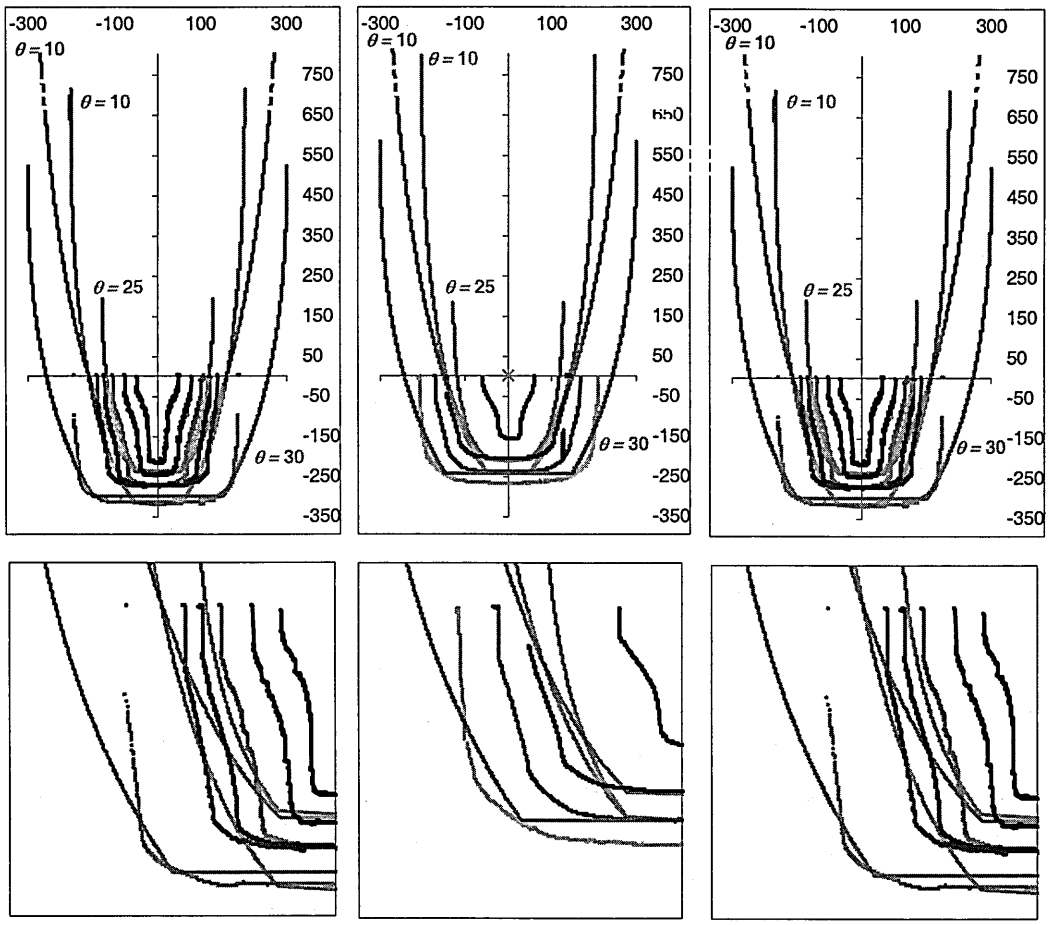


Figure 6.37 Comparison between the profiles of two series of suitable CPCs and the contours of cavities experimentally obtained for the samples of figure 6.28 (a), 6.29 (b) and 6.30 (c). All the scales are in microns. Zoom at the bottom of each diagram.

SHAPE

Besides the correct scale, the cavities have to maintain a local curvature suitable to approximate the CPC (or to concentrate the radiation). The zooms of the respective diagrams of figures 6.36 to 6.38 demonstrate clearly the discrepancy between the local curvature of the typical profiles produced and the curvature required by the CPC design. For example, in figure 6.22 it can be clearly observed how the main problem affecting the profiles obtained in defect of passivation is represented by the convexities of the contour (negative second derivative). These, in fact, would lead to a large scattering of the radiation and should be avoided. For higher etching time, this concavity has a lower extent so that the cavity resembles a cone concentrator (figure 6.23). However, it does not seem possible to produce concave contours by using this method.

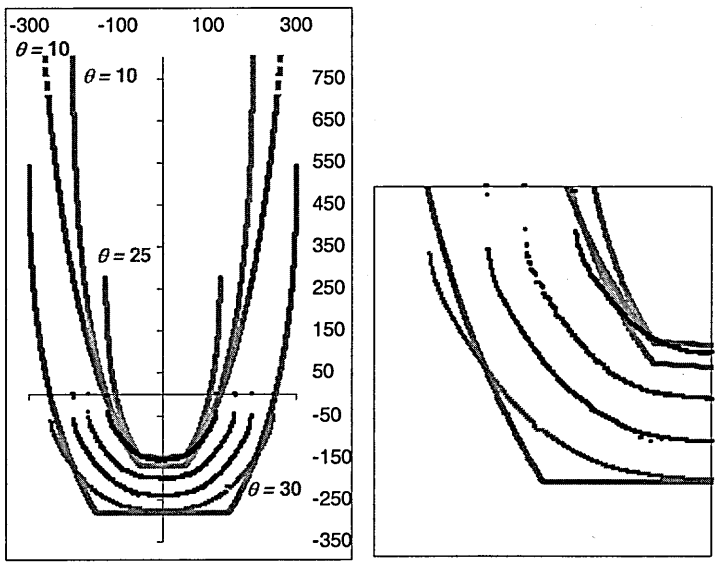


Figure 6.38 Comparison between the profiles of two series of suitable CPCs and the contours of cavities experimentally obtained by etching a sample for 2 hours, by using an "isotropic" cycle (pure SF6 and bias power equal to 10 watts). All the scales are in microns.

The results for the more versatile process, which couples anisotropic etching to a long isotropic cycle (figures 6.28 to 6.30), show that deep through-the-wafer cavities can be achieved either after etching for a short time a very deep cylindrical (anisotropic) hole or by starting from a more shallow anisotropic hole and etch isotropically for a long time. The etching figures obtained in the two cases would be quite different: in the first case, one would obtain profiles of the kind observed in figure 6.28 or similar to the more narrow profiles of figures 6.29 and 6.30. These profiles contain convexities (second derivative less than zero) that are expected to diverge the rays and should be avoided. On the contrary, when long isotropic cycles follow short anisotropic cycles, the profiles possess the right concavity to work as a concentrator. Such profiles correspond to the largest contours of figure 6.29 and 6.30. These profiles present, nevertheless a different problem, in that the isotropic cycles tend to widen the bottom of the feature excessively so that only the widest CPC can be approximated.

It is worth comparing the ideal CPC profiles with a sample etched isotropically for a long time. The profiles obtained from a sample etched for two hours in pure SF_6 (bias power equal to 10 watts) demonstrate not only that the isotropic etching figures show the correct concavity along the whole profile, but also a better approximation to the (small) part of the CPC profiles they overlap.

Besides profile shape (i.e. cross section), which is largely dictated by the local evolution of the etching front, large distortions from the original cylindrical symmetry occur often. In fact, cavities evolve in a fairly complex way: depth, diameter and cross sections do not represent sufficient information to describe the overall 3 - d shape. Two kinds of trend were identified: systematic distortions and random distortions.

Systematic distortions are best observed during etching in pure SF_6. The 2 – d front section does not retain the original circular symmetry: in fact, it is driven towards a deformation with loss of cylindrical symmetry: circular apertures in <100> oriented wafers tend to become squares as the etching proceeds. Conversely, when <110> wafers undergo etching, circular apertures deform towards a fairly hexagonal shape. Comparison between these two markedly different trends is made in figure 6.39. In general, the extent of deformation depends on process parameters. Generally speaking, the deformation is more evident at low bias power and it generally increases with process time. Furthermore, the loss of the original circular shape is generally inversely proportional to original aperture size. The presence of oxygen in the original etching mixture seems to cause a decrease in the extent and an inversion in trend: larger features showed higher deformation. The deformation is limited to the top of the cavity, as shown by the replicas of figure 6.40. In the parts of the cavity subjected to the ion flux (such as the central part of the bottom of the cavities) the deformation is largely less evident.

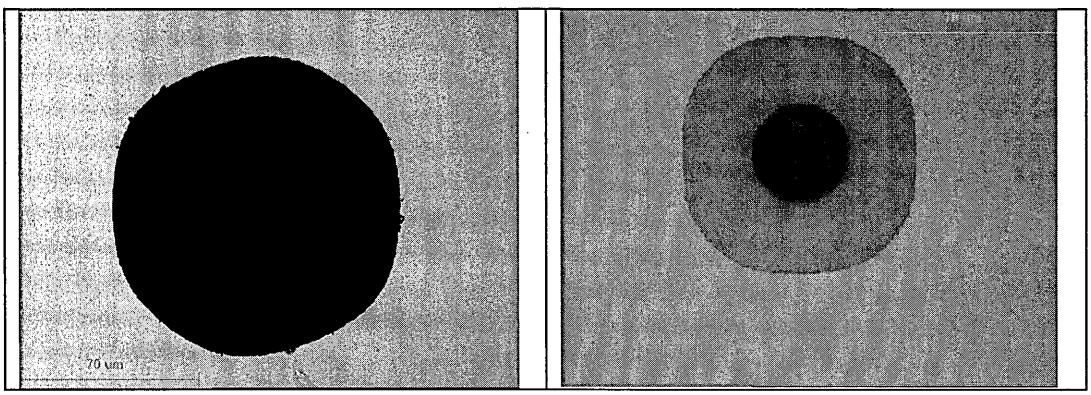


Figure 6.39 Front view of cavities from samples etched with zero bias on in pure SF_6. Cavities developed from a 30 μm original mask aperture. The cavity pictures on the left is from a <110> Si wafer etched for 90 minutes while the cavity on the right-hand side is from a <100> Si wafer etched for 1 hour.

Macroscopic distortions of the symmetry may originate from local differences in etch rate or passivation rate. This problem leads to random variations from the cylindrical symmetry that are difficult to control. The cavities obtained by coupling "isotropic" etching to anisotropic etching (presented in section 6.2.4) are particularly affected by this problem. The passivation coating deposited on the sidewalls during anisotropic etching might develop irregular thickness and be consumed faster in some areas where the etching advances further. Top view of the cavities obtained with this method shows that, beside the systematic deformation, analogous to that already observed for "isotropic" etching, large irregularities of the rim arise (figure 6.41). Large irregularities affect not only the entry aperture, but also the sidewalls of these features. Figures 6.32 and 6.33 show coarse vertical ripples. This phenomenon will be discussed below. Similar variations are found in the samples etched continuously in a SF_6 / C_4F_8 mixture (figure 6.42). Analysis of the cross sections of figure 6.33 demonstrates that the variations in this case may be due to the formation of more regular macroscopic steps bounded by flat planes. This phenomenon will be treated below.

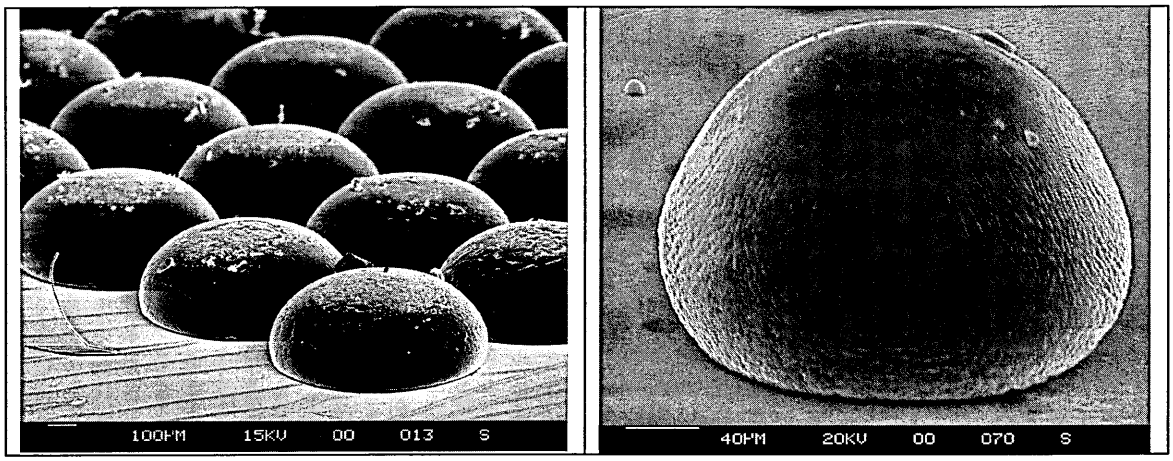


Figure 6.40 **Actual shape of cavities obtained by "isotropic" etching revealed by replicas. a) sample etched for 1 hour in pure SF_6 with 15 watts bias power, b) sample etched for 2 hours in pure SF_6 with 10 watts bias power**

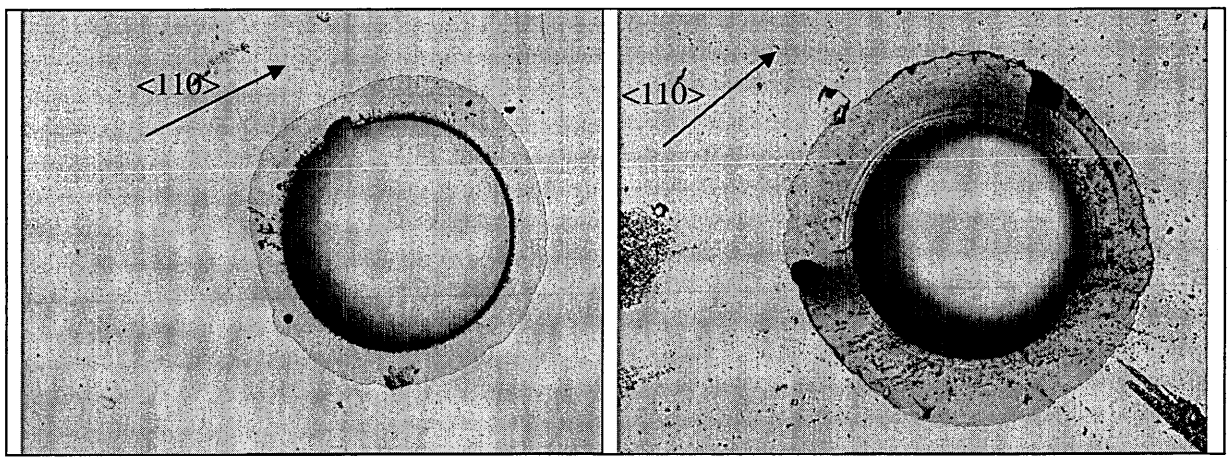


Figure 6.41 **Front view of cavities from samples etched with a sequence of long anisotropic and "isotropic" cycles. Cavities developed from a 142 μm original mask aperture diameter. Left-hand picture, a cavity from a sample etched anisotropically for 90 minutes and then for 30 minutes in "isotropic" etching. Right-hand picture, a cavity from a sample etched anisotropically for 60 minues and then for 55 minutes in "isotropic" etching**

SURFACE QUALITY

The quality of the surfaces represents the issue that most dramatically affects the reflectivity of the sidewalls and, consequently, the collection efficiency of the cavity. Surface roughness must be minimised to achieve the minimum scattering and the maximum reflectance. A quantitative treatment of the reflection phenomena occurring at the sidewalls was largely beyond the scope of this research. However, qualitative considerations can be useful to discuss the results.

The Rayleigh criterion establishes qualitatively that a surface can be considered smooth if:

$$R_{rms} < \frac{\lambda}{8 \sin \gamma} \qquad (6.5),$$

where R_{rms} represents the mean square roughness of the surface, λ is the wavelength of the incoming radiation and γ the incidence angle between the surface and the incoming radiation [*Kerker et al., 1969, Chapter I*]. If $\lambda / R_{rms} > 8$, then one can say that most radiation incoming over any incidence angle is reflected with negligible scattering. For example, in the IR atmospheric window between 8 and 15 μm of wavelength a surface can be considered smooth at every incidence angle if the R_{rms} is respectively less than one (for λ = 8 μm) and 1.875 μm (for λ = 15 μm). The IR absorption spectrum of air was presented in the background part (section 2.1, figure 2.3).

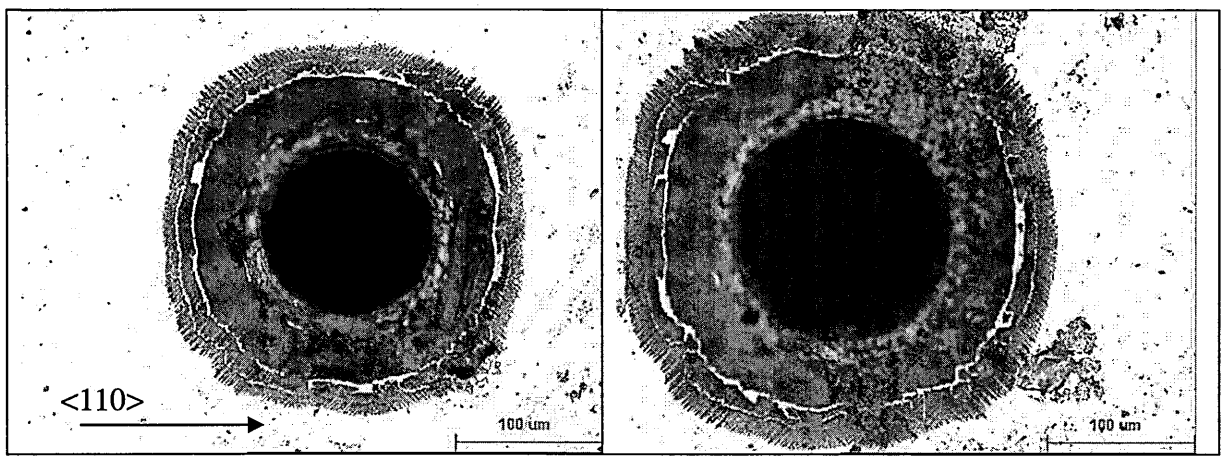


Figure 6.42 Front view of cavities from a sample etched continuously in a mixture containing both SF_6 and C_4F_8

It is clear that most features presented above show a roughness apparently far higher than 2 μm. For example the surfaces of figure 6.20 and 6.21 (sample obtained in defect of passivation) show a series of triangular or trapezoidal steps. These are coarser towards the top of the cavities with dimensions up to 10 μm. Their extent reduces moving towards the bottom of the feature, until any trace of steps disappears. This coarse roughness comes in apparently ordered patterns related to the orientation of preferential crystalline planes with low Miller index. A justification of this phenomenon is beyond the purposes of this section and will be attempted in section 9.3. Besides this "regular" or periodic roughness, there is a roughness of random nature, which becomes apparent as the surfaces are observed at higher magnification. The photographs of figure 6.43 show both the coarse triangular features and the finer pattern of roughness intrinsic to the features themselves. Similar patterns affect the surface of the sample of figure 6.23. The effect of the regular roughness (related to preferential etching) is even more dramatic in the samples produced by etching in a SF_6 / C_4F_8 mixture (section 6.2.5) as testified by picture 6.34. In those cavities the periodic steps and ripples grow to such extent to modify the overall shape of the cavity.

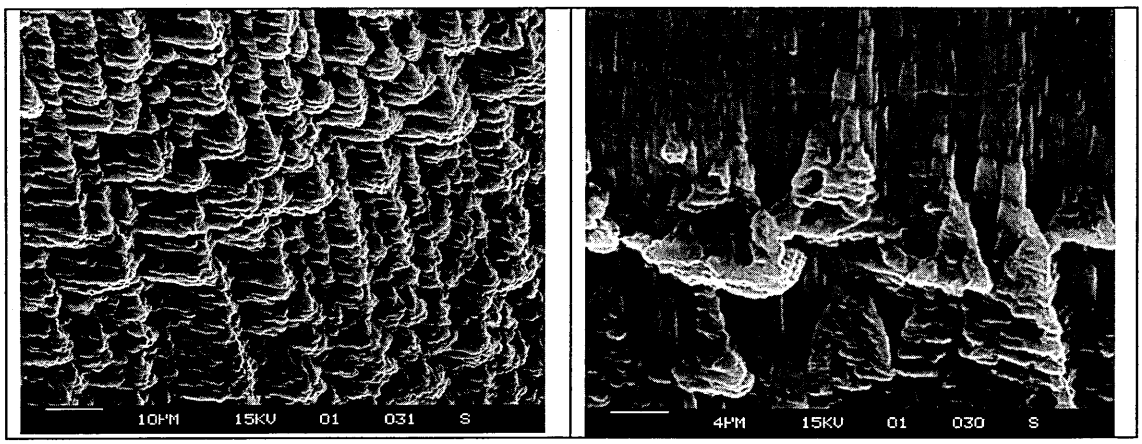


Figure 6.43 Evidence of fine patterns of roughness on the sidewalls of features etched in defect of passivation step time (these close up microphotographs were taken from cast replicas)

At low magnification, cavities obtained in absence of passivation (isotropic etching) seem indeed very smooth (see for example figure 6.40). In fact, at a closer look (figure 6.44), regular patterns of roughness can be observed in these samples too. The surface texture can be qualitatively appreciated in the SEM pictures of the top and bottom part of cavities obtained under different process conditions in figure 6.45. The roughness of the sidewalls is due to patterns of parallel ripples. As the bias power increases, the width and thickness of these ripples decrease and they become denser so that it can be affirmed that the roughness decreases when bias power is increased. A similar "smoothing" effect is obtained when oxygen is added to the mixture. The effect of bias power is particularly striking in the bottom of the cavities, i.e. the area more directly exposed to the ion flux. At zero bias the bottom of the cavities is rough but becomes smooth as soon as a bias is applied. These patterns seem to change along the different directions of the crystalline lattice. This is particularly evident when observing the replicas of the cavities, since many faces can be observed at the same time. A replica from a feature produced by 60 minutes etching with no bias is reported in figure 6.44. (No bias was applied to make the periodic patterns more evident.) A series of zooms along particular crystalline directions detail the varying nature of the patterns.

The problem of surface roughness will be analysed quantitatively in section 6.3.2. A detailed discussion on the mechanism causing this preferential pattern of roughness is beyond the purposes of this section, but it is important to stress how the cavities obtained in absence of passivation mechanism show generally lower roughness. Furthermore these cavities show the most regular kind of roughness and random roughness is minimized. The regular pattern of roughness can be attributed to the preferential etching of silicon along low-index crystalline planes. (This view will be discussed in section 9.3.2.)

Finally, the cavities obtained by sequences of long anisotropic and isotropic cycles show a further kind of roughness. In the samples of figure 6.46 the main effects that roughen the sidewalls can be clearly observed. First, there is evidence of a series of irregular vertical ripples (as in the pictures of figures 6.31 to 6.33). The roughly vertical orientation of the ripples seems to suggest that these originate from the roughness

affecting the straight sidewalls after anisotropic etching. A comparison with the typical aspect of anisotropic sidewalls after DRIE (in particular pictures 6.17 *b* and 6.18 *a*) suggests that the ripples are the residual of the micrograss. In this is true, these patterns of roughness may be difficult to eliminate: very long isotropic cycles would be required. The crater-like irregularities observed in the proximity of the bottom (particularly in figure 6.46-*left*) may be related to subsequent re-deposition of large particles of coating during the isotropic step. When a long "isotropic" cycle is applied, the presence of the typical regular patterns of roughness (similar to those observed for the samples etched in absence of passivation) becomes evident. These patterns can be clearly observed in the cast replica of figure 6.33-*right*.

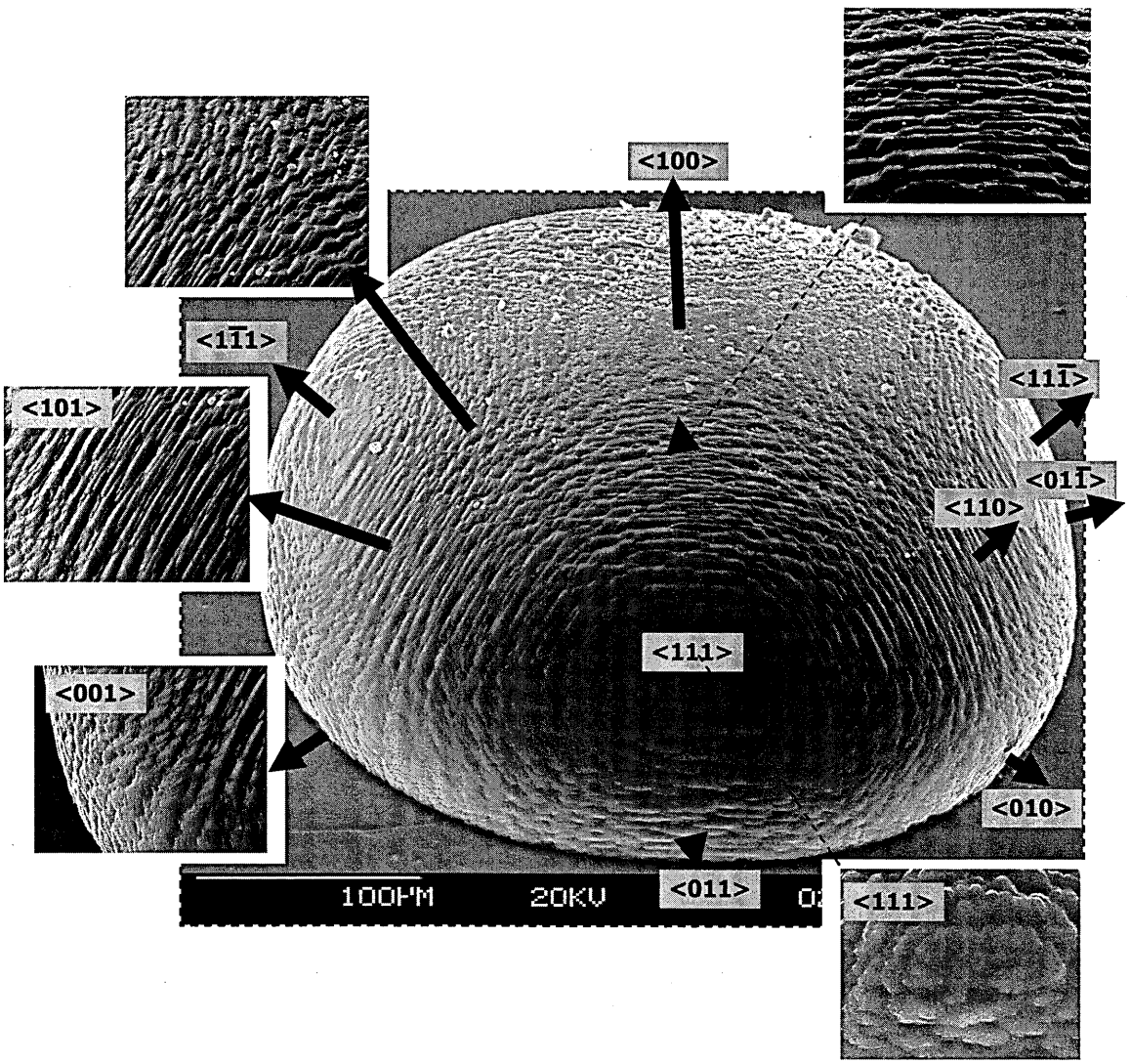


Figure 6.44: Silicone rubber replica of a cavity produced by etching with no bias showing evidence of different patterns in correspondence of different directions in Silicon crystal lattice

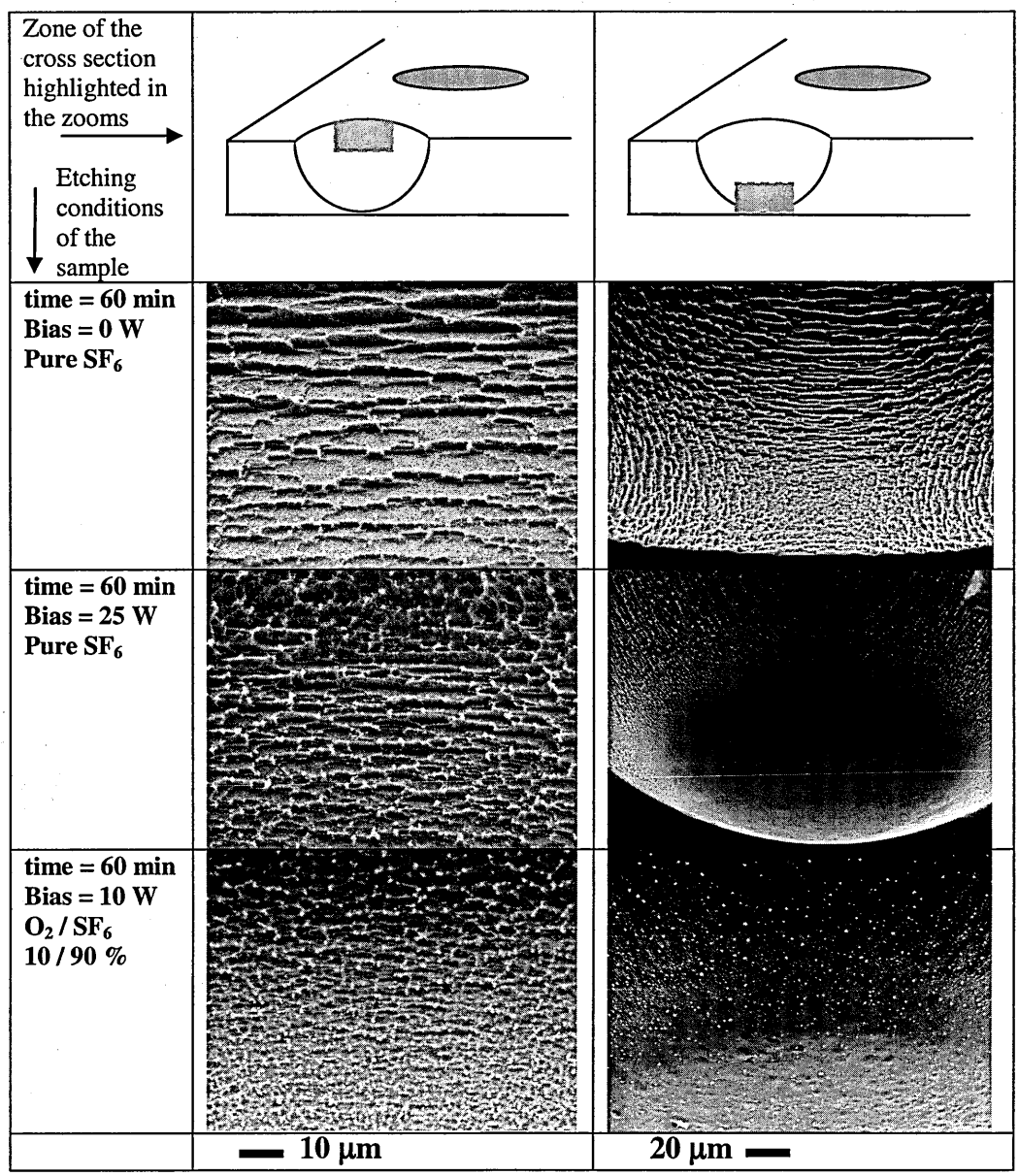


Figure 6.45 **Front views of wafer cross section showing the sidewalls and bottom of the cavities. From samples obtained under different process conditions**

6.2.7 *Comparison between the results reported above and the results published in literature*

Before deciding which microfabrication routes are more worth investigating further it has been useful to compare the range of results achieved by this research with the results published in literature. Methods similar to those reported above were attempted in the past. Although the literature on the field is pretty scarce, a survey was reported in section 3.5.

First, it has to be said that most authors limit their papers to the demonstration that certain results can be achieved. They do not provide detailed analyses of issues such as surface roughness. This may be due to the difficulty of assessing the characteristics of narrow cavities with complex contours. (These practical difficulties were discussed in the experimental part, in section 4.3.5 and in appendixes C and D.)

The authors reporting etching in pure XeF_2 (gas etching: no ion beam involved) report trends in the evolution of the contour of the cavities similar to the findings of section 6.2.3 for pure SF_6 etching [*Chu et al., 1997*; *Sugano and Tabata, 2002*]. It is possible to judge the quality of the surfaces of their cavities after careful examination of the SEM pictures they report although they do not discuss it directly in their paper [*Chu et al., 1997*]. Interestingly, in most cases, the surfaces seem to demonstrate patterns similar to the patterns found for isotropic etching (pictures 6.43 and 6.44). This would confirm that the ion beam has a slight effect on the etching kinetics, which is dominated by the rate of arrival of radicals to the surface.

The authors which couple long isotropic to long anisotropic cycles show devices (such as microneedles and microchannels) with sidewalls far smoother than the results reported here [*deBoer et al., 2000*; *Griss et al., 2001*]. This may suggest that results of the kind reported in section 6.2.4 still offer room for optimisation. In particular, defects such as the roughness demonstrated in the cavities of picture 6.45 might be largely avoided if the initial micrograss is reduced from the anisotropically etched features. A further set of trials (not reported here) showed that the addition of a silicon oxide mask improves surface smoothness. A single paper discussed surface smoothness in some detail [*Richter et al., 2001*]. The phenomena the authors report are strikingly similar to the results reported here. In particular, they reported all three types of roughness that were discussed in section 6.4.6.

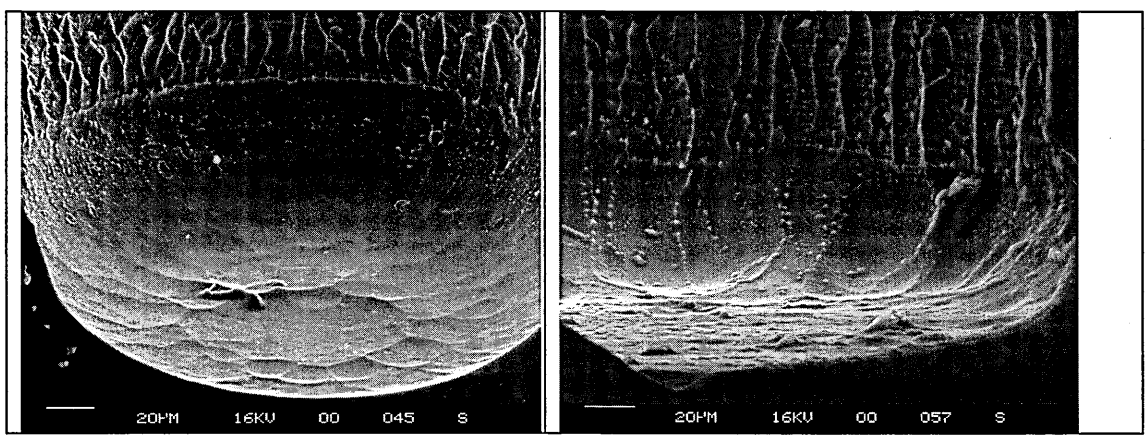


Figure 6.46 **Cross sections of cavities from samples etched with a sequence of long anisotropic and "isotropic" cycles. The cavity pictured on the left is from a sample etched anisotropically for 60 minutes and then for 55 minutes in "isotropic" etching. The cavity pictured on the right is from a sample etched anisotropically for 90 minutes and then for 30 minutes in "isotropic" etching**

6.2.8 *Suitability of the techniques attempted for the microfabrication of concentrators*

It is quite hard to draft definitive conclusions from these preliminary trials. If one observes table 6.1, recalling the comparison accomplished throughout last section, it is possible to say that no methodology attempted was completely successful or satisfactory.

Preliminarily, it can be said that the methodologies that exploit unbalancing the anisotropic equilibrium or that use a SF_6/C_4F_8 mixture have to be excluded: they tend to produce concave sidewalls and very rough surfaces. Furthermore, the periodic roughness related to preferential etching of crystalline planes is expected to worsen with process time and therefore long etching cycles in defect of passivation are expected to lead to such large roughness and steps to modify the shape of the cavity itself (phenomena similar to those observed for the sample of figure 6.34).

Samples produced by sequential anisotropic and "isotropic" steps show many defects. In particular local variation in etch rate due to variation in the thickness of the original coating and micrograss affecting the sidewalls lead to large roughness and distortion of the contour. These defects are more apparent for short "isotropic" cycles, whereas they tend to be reduced by long cycles (although it is difficult to remove the residuals of micrograss from the sidewalls). A first solution could be a short anisotropic cycle followed by a long "isotropic" cycle. However, a cycle of this kind would tend to produce large round cavities not very dissimilar to those produced by "isotropic" etching in absence of passivation mechanism. Surface roughness itself seems very similar in both cases. Since the latter seems to be the most controllable process, it was decided that the etching in absence of passivation deserved further investigation.

Another point for choosing this process is that it is the only one that presents (at least apparently) the sole periodical type of roughness (and not the random). This means that, even if the final roughness will be higher than allowed from the wavelength of the radiation collected, the radiation will be scattered in a regular pattern that can be at least qualitatively predicted and will not be chaotically dispersed.

A schedule for the trials was drafted as follows:
1) the process of etching in absence of passivation would have to be deeply characterised for long etching cycles and through-the-wafer etching.
2) Either this process could be used in itself for the microfabrication concentrators and subsequent integration in device or
3) the knowledge gained from this process could be exploited to set up a process that couples anisotropic to "isotropic" etching.
4) If the surfaces do not reach the required quality, smoothing steps might be tried. Smoothing can be achieved using a truly isotropic finishing (e.g. wet etching [*Madou et al., 2003, Chapter 4*]) or a polymer of some kind can be deposited on the sidewalls [*Bagolini et al., 2002*].
Large, through-the-wafer collectors, obtained by SF_6 are object of the following section, the last section of this chapter.

Figures of merit for assessing the suitability of the cavities produced	DRIE in defect of passivation	"Isotropic" etching (no passivation)	Sequence of anisotropic and "isotropic" cycles	Continuous etching SF_6 / C_4F_8
Overall Scale	May approximate half of the CPC	Worst result: approximates 10 % of the CPC	May approximate half of the CPC or more	
Profile / Local curvature	Some parts are convex: expected to diverge radiation	Concave: expected to converge radiation	Concave in some cases convex in others	Profile broken and highly irregular
Systematic distortion of cylindrical symmetry	A certain extent of systematic deformation can be detected	Generally limited to the entrance of the cavity	High, but generally limited to the entrance of the cavity	A certain extent of systematic deformation can be detected
Random distortion of cylindrical simmetry	High and affecting mainly the top of the cavity	Generally absent	High and affecting all parts of the cavity	High and affecting mainly the top of the cavity
Surface roughness: periodic	Up to 10 μm *rms*	May be up to 10 μm *rms* but smoother sidewalls may be obtained	Present when long "isotropic" cycles are applied	Steps of various dimensions up to tens of microns
Surface roughness: random	Up to 10 μm *rms*	May be present, but it must be very low	Largely present on the sidewalls and difficult to eliminate	Present but very low

Table 6.1 Summary of the results achieved by the early trials for finding routes to machine cavities with complex contours directly from binary masks

6.3 Arrays of through-the-wafer cavities to be used as concentrators, produced by SF_6-based plasma etching in absence of passivation

Long "isotropic" cycles (i.e. cycles in absence of passivation) were reported in section 6.2.3. This method offered the best performance in terms of reliability and surface smoothness, although failing to approximate a large part of the CPC. In section 6.2.6, it was showed how the distortion from the cylindrical symmetry and the roughness of the sidewalls have a regular and predictable behaviour. Long isotropic through-the-wafer etching cycles were deemed the most viable and quick way in order to obtain a series of preliminary "device" wafers that could be processed to further trials (e.g. characterisation in terms of device responsivity). This section deals with the attempts to produce through-the-wafer cavities. Section 6.3.1 describes the problems arising after isotropic etching cycles of such duration. Section 6.3.2 reports the analysis of surface roughness. Section 6.3.3 discusses the statistical analysis of the variation in the dimensions of the membranes across the area of the wafer. A way to obtain a graphical approximation of the ideal collector profile using only cavities etched isotropically is suggested in section 6.3.4. Section 6.3.5 analyses the collection efficiency to be expected from such a system by using the ray-tracing analysis.

6.3.1 *Shape of large cavities obtained by long isotropic etching cycles*

According to the results reported in section 6.2.3, the typical contours obtained in absence of any passivation could be assimilated to a hemi-elliptical section. In particular, the etch factor was in the range between 1.7 and 2.4 regardless of any process parameters. An increase from 0 to 40 Watts in the bias power applied to the platen during etching did not show any appreciable increase in aspect ratio. It was therefore assumed that the ion effect is too weak to contribute to the overall shape of the feature. On the contrary, the energy of the ionic flux affected surface roughness to a certain extent.

The overall 3 – d shape encountered a more complex evolution. The original circular aperture, in fact, tended to become a square as the etching proceeded, and the cylindrical symmetry would degenerate in four-fold rotary symmetry. It was also found that the extent of this phenomenon depended on the process parameters. The deformation seemed mostly evident near the uppermost area of the cavities as the bottom maintained the original symmetry more faithfully. Therefore the overall 3 – d shape was compared to the shape of a dome with squared base.

Conversely, for long etching times, the bias power influenced the shape of the cavities. This is demonstrated dramatically in figure 6.47, which reports the cross sections of two cavities from two samples etched respectively using a platen power of 10 W (sample devO2) and no bias (sample dev0, at zero bias power).

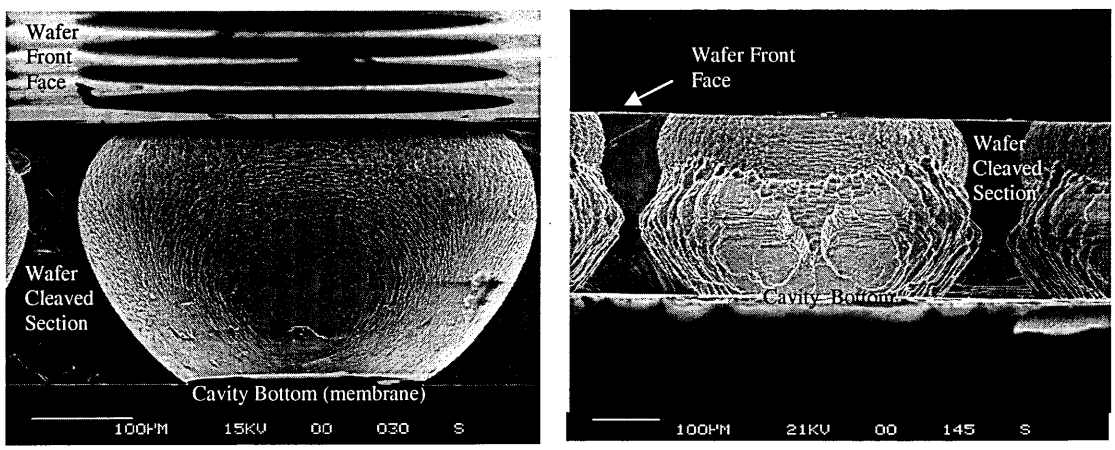


Figure 6.47 SEM microphotographs of cross sections of cavities from the samples "Device O_2" (left) and "Device 0" (right)

The cavities etched with a biased platen still retained a cross section fairly similar to a hemi-ellipse. Typical profiles are reported in figure 6.48. (The curves were obtained from rubber replicas with the modality of appendix C). Conversely, when platen power was set to 0, other kinetic effects prevailed, leading to a large deformation of the contours. The contour of the cavity in the right-hand picture of figure 6.47 is very different from the contours reported in figures 6.44 and 6.45*a*, although those cavities were obtained in absence of bias power too. The aspect of the deformation (larges steps bounded by quasi-flat planes) seems to suggest that the etching along preferential crystalline planes represents the prevailing effect causing the deformation. However, a

detailed explanation of the mechanism is beyond the purposes of this section. An attempt to a complete treatment of this phenomenon (crystalline orientation dependent etching) is in chapter 9.

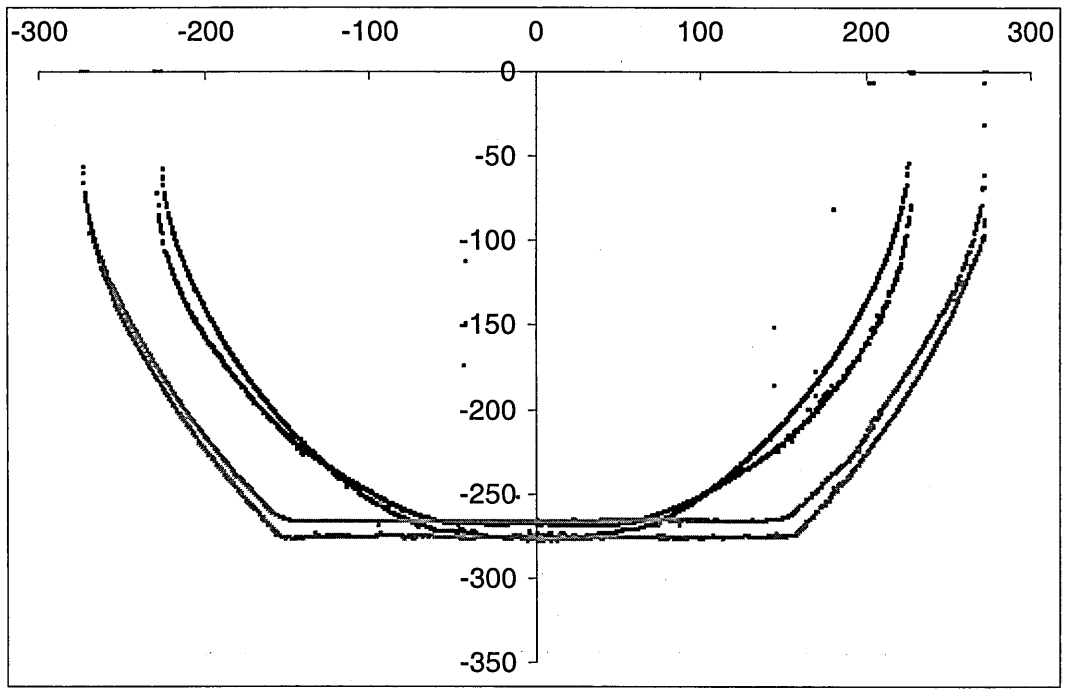


Figure 6.48 Contours of the cavities obtained from sample "Device 6" assessed with the usual method of the PDMS replicas. All the dimensions are in micrometers. Notice that the method fails to detect the upper part of the contour and that it reveals a wafer thickness 10% superior to its actual value (see section 2.3.5 & appendix C for a discussion of the errors produced by the method of replicas observation).

The degeneration from the cylindrical symmetry is not different from that already reported in section 6.2.6. It is easy to evaluate the 3 – d deformation for through-the-wafer cavities such as these, which present a double front section, i.e. entry and exit pupils. Four such "front sections" are compared in figure 6.49 (obtained by optical microscopy). Both the apertures of original diameter of 114 and 86 μm show a certain tendency to develop four-fold symmetry. The bottom membranes (which can be thought of as sections of the cavities parallel to the faces of the wafer) show this tendency to a lesser extent, thus confirming the findings of section 6.2. The membranes can be considered as "slices" of virtual full cavities taken at different depths. It is interesting to notice that the bottom membranes relative to the cavities with 86 μm aperture are more near to a circle, whereas those relative to the 114 μm membranes have developed more fully squared corners. The actual 3 – d shape of these cavities is best described as a truncated dome with a squared base. The cavities originated by the 114 μm aperture have a larger degree of truncation than those originated by the 86 μm aperture. Similarly it was found that etching from a series of square holes of different dimensions produced a series of circular membranes on the opposite side of the wafer. In particular, the membranes originating from the larger squares still retained the squared shape partially

whilst the ones originating from smaller square holes are almost perfectly round. Therefore, below a certain dimension (or beyond a certain etching time) circular and squared holes produced virtually indistinguishable cavities.

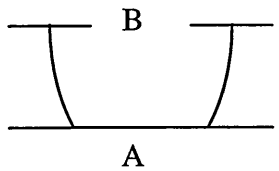
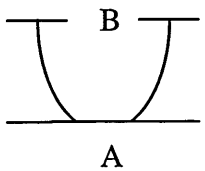
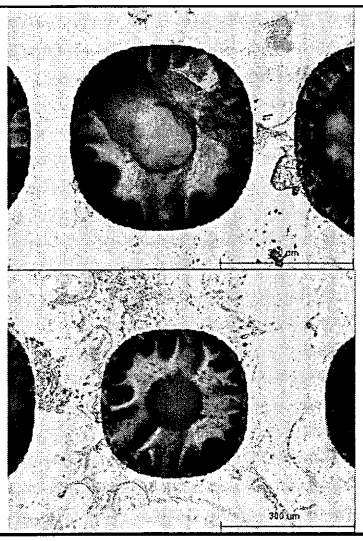
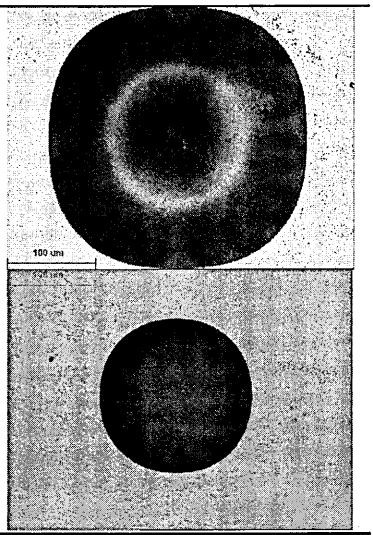
Sample "Device 6" Etched for 210 min Bias = 10W	FRONT MEMBRANE B	BACK MEMBRANE A
Original Aperture 114 μm  Original Aperture 86 μm  		

Figure 6.49 Typical shape of the membranes resulting after through-the-wafer etching in pure SF_6 for the sample "Device 6"

6.3.2 Surface roughness of large cavities obtained by SF_6 etching

The smoothness of the surfaces represents the fundamental requirement for a concentrator. In section 6.2.6, it was demonstrated that, according to equation 6.5, a roughness below 2 μm assures that most IR radiation will be collected within the second atmospheric window. As the roughness increases part of the radiation will be scattered and lost. Scanning Electron Microscopy of the cross sections (as in figure 6.47-*left*) reveals that sidewalls roughness is at least qualitatively similar to that reported for the cavities obtained in absence of any passivation (i.e. the results presented in section 6.2.3). In particular, the bottom of the cavity (where the etching front was constantly exposed to the highly-collimated ion beam) is fairly smooth. On the contrary, roughening patterns appear on the sidewalls in the areas shadowed from the direct ion flux. These ordered fishbone ripples reach the maximum in the annular ring just underneath the mask, i.e. the areas shadowed from both ion and radical direct fluxes.

Quantitative analysis of smoothness is made awkward by the complex topography as stressed in the experimental part. However, an indirect method, based on the elaboration of the optical analysis of the membranes (such as those reported in figure 6.49) may throw some light on the degree of roughness affecting the sidewalls. Two SEM pictures of cavity cross sections are shown in figure 6.50. The pictures show clearly that, near the bottom of the feature, the roughness has the aspect of a series of ridges developed periodically along the <110> directions. The roughness can therefore be calculated from

the boundary of the membrane, which represents an ideal intersection between the ridges and the etch stop layer (i.e. the SiO_2). Essentially, the method consists in analysing the boundaries of the membranes and transforming them into worksheet data files so that the profiles can be directly compared after filtering the shape of the membrane boundary. (The method is detailed the experimental part in section 4.3.5 and in Appendix D.)

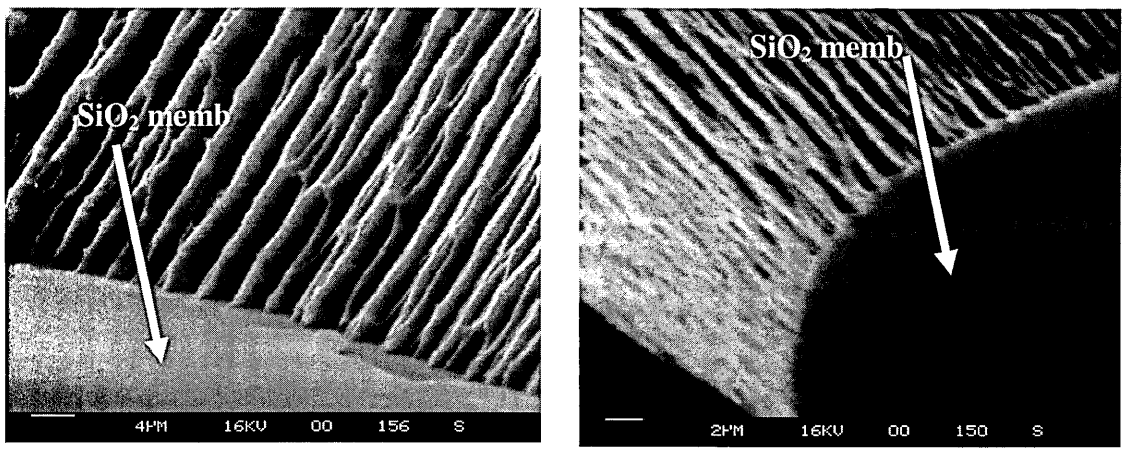


Figure 6.50 Scanning Electron Microphotographs of the bottom of cavities from samples "Device 6" (left) and "Device O_2" (right)

The method gives a fairly approximate idea of the roughness because the grooves are not perpendicular to the membrane and deformations may arise during data computing. Nevertheless, it can be applied to both top and bottom membranes to yield the total range of roughness across the sidewalls of the cavity. The main disadvantage of this method is the large time required for each elaboration. For this reason, it was not possible to produce a set of measurements large enough to accomplish a suitable statistical analysis of the overall process outcome. Although, for these samples the roughness of the bottom membrane (in SiO_2) may be optically assessed, this is not the case in an actual device wafer where the boundary of a multi-layered membrane is scarcely detectable. (This problem will be discussed in section 8.1.4.)

The results of the above method, applied to the samples "device 6" and "device O2" are reported in the diagrams of figures 6.51 to 6.53. Figure 6.51 reports the "boundary roughness" of the bottom membranes originating from an 86 μm cavity. Similar results obtained from cavities with initial mask aperture of 114 μm are reported in figure 6.52. Finally, the boundary roughness of residual top membranes (determined by the undercut due to lateral etch) belonging to initial cavities of 86 and 114 μm are compared, for the sample "Device 6" in the diagrams of figure 6.53. All the curves have been displaced vertically (and variously coloured) for clearness of display. Some qualitative comments follow.

1) for each profile most of the peaks have a very similar height and similar slope suggesting that they might have similar dimensions and shape on the original cavity itself. (In particular, in figure 6.50 the ridges have similar dimensions and orientation).

2) A part from these variations, the peaks are otherwise "smooth", that is the roughness does not have a random appearance. In fact, it can be seen in the pictures of figure 6.50 how the ridges have smooth sides (i.e. they are bounded by reasonably flat planes). Emergence of such a fishbone pattern can be easily explained postulating a preferential etching. (This however is beyond the purposes of this chapter and more details will be presented in chapter 9, in particular in section 9.3.2.)

For these reasons, although the calculation of a root mean square value would be meaningless, it is possible, at least to assess the order of magnitude of the roughness affecting the sidewalls.

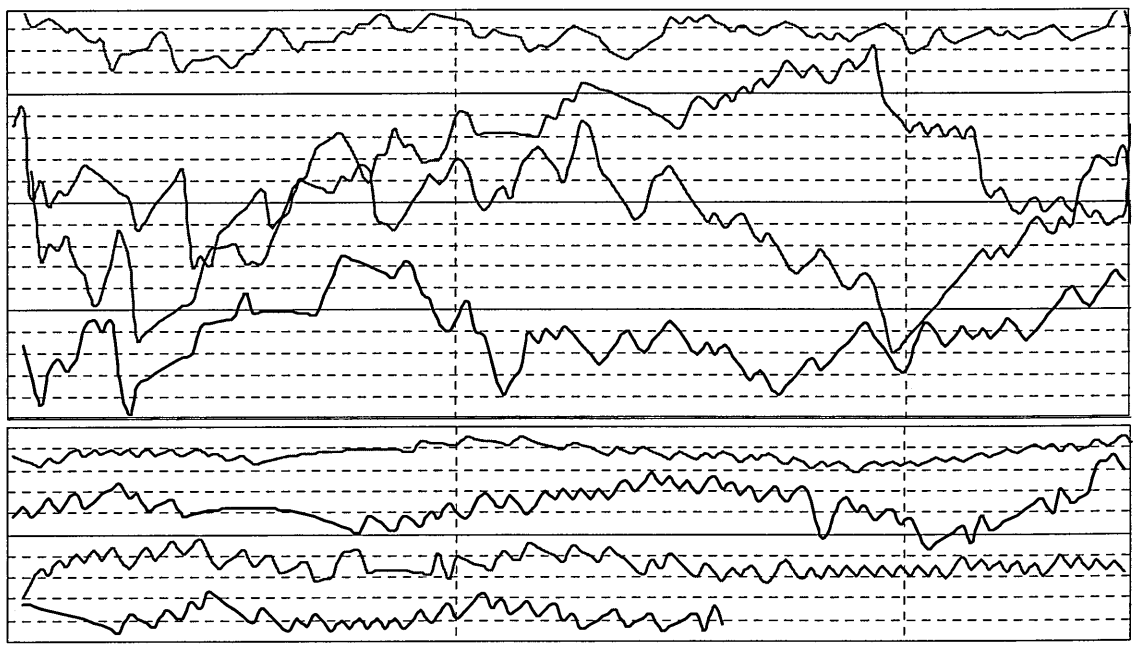


Figure 6.51 Boundary of the membranes filtered from the "waviness" of overall membrane shape in order to highlight the "noise" affecting the boundary, which might be a concrete representation of the roughness of the cavity. Bottom membranes of cavities obtained form a circular hole of 86 μm in diameter, TOP: from the sample "Device 6", BOTTOM: from the sample device O2. Each vertical division corresponds to 2 micrometers and each horizontal division corresponds to 20 micrometers (note the cautions reported in appendix D).

The patterns of roughness seem to be similar in all the diagrams. All the curves present peaks that come in three different sizes. Furthermore, there does not seem to be continuity in the variations of peak dimensions. In the 86 μm cavities, in the sample Device O2 (diagram 6.51*a*) there seem to be a vast majority of peaks with height around 200 nm and a slight number of peaks of about 400 nm. Finally in two instances, peaks with height of approximately 800 nm appear. The sample Device 6 seems to produce more ambiguous results, probably because the levelling was less effective. Although it is possible to identify a few peaks ~ 200 nm in height, one can notice larger peaks very wide and with variable height from 400 nm up to 2 μm.

It is easier to assess the "roughness" from the diagrams of figure 6.52. For the 114 μm cavities, a small number of peaks around 0.2 μm in height appear. However, there is a prevalence of peaks in the range 1.2 – 1.5 μm. Finally, a few peaks with height around 2 – 2.5 μm appear. A similar display occurs in the two curves from the top of figure 6.52*top*, relative to the etching in absence of oxygen (Device 6). However, here some 2 μm peaks appear. Conversely, the first and second curves from the bottom show a majority of peaks around 2 μm in length or slightly above.

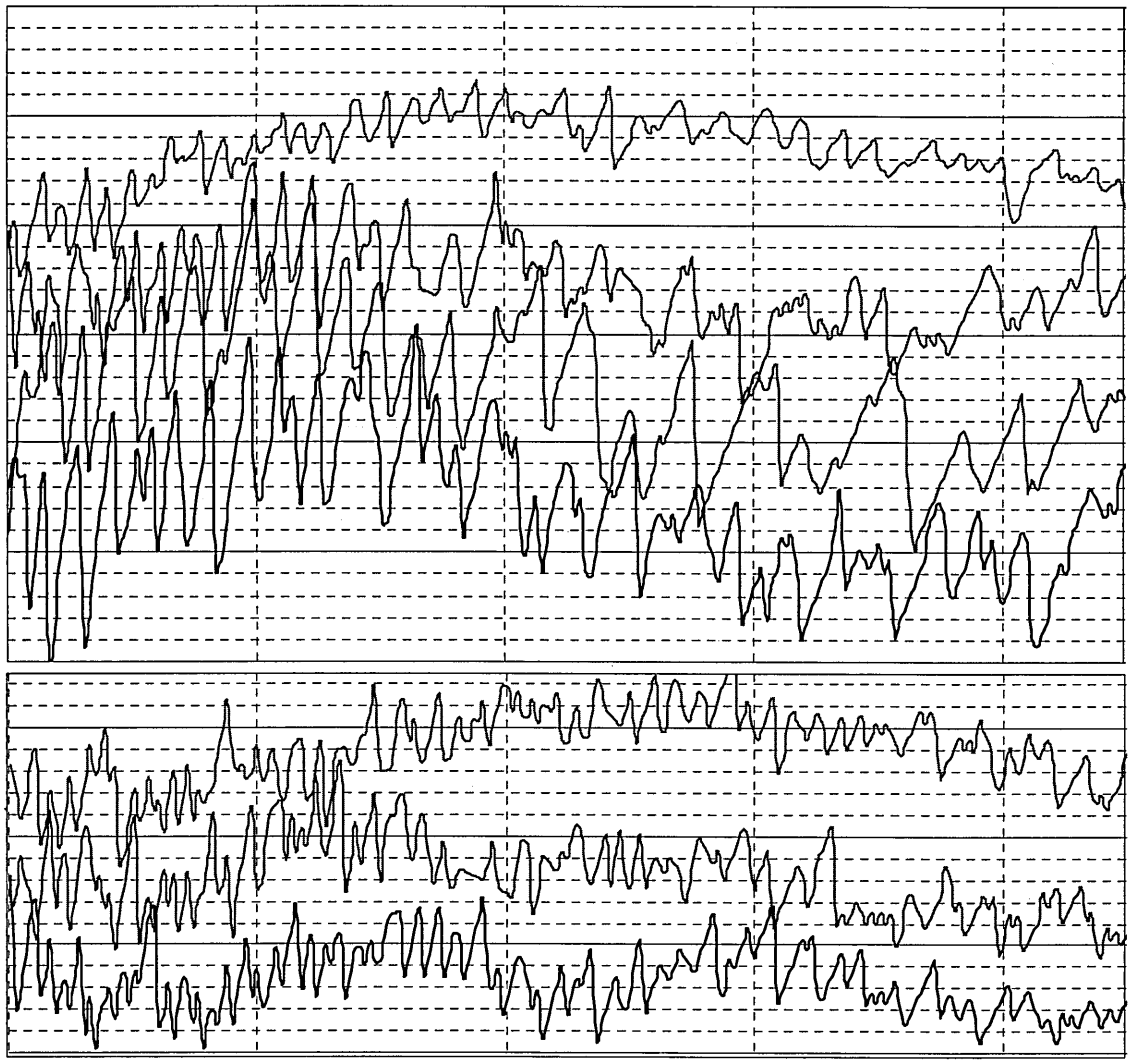


Figure 6.52 Boundary of the membranes filtered from the curvature of the membrane in order to highlight the "roughness" affecting the boundary. Bottom membranes of cavities obtained form a circular hole of 114 μm in diameter, TOP: from the sample "Device 6", BOTTOM: from the sample device O2. Each vertical division corresponds to 2 micrometers and each horizontal division corresponds to 20 micrometers (with the cautions reported in appendix D).

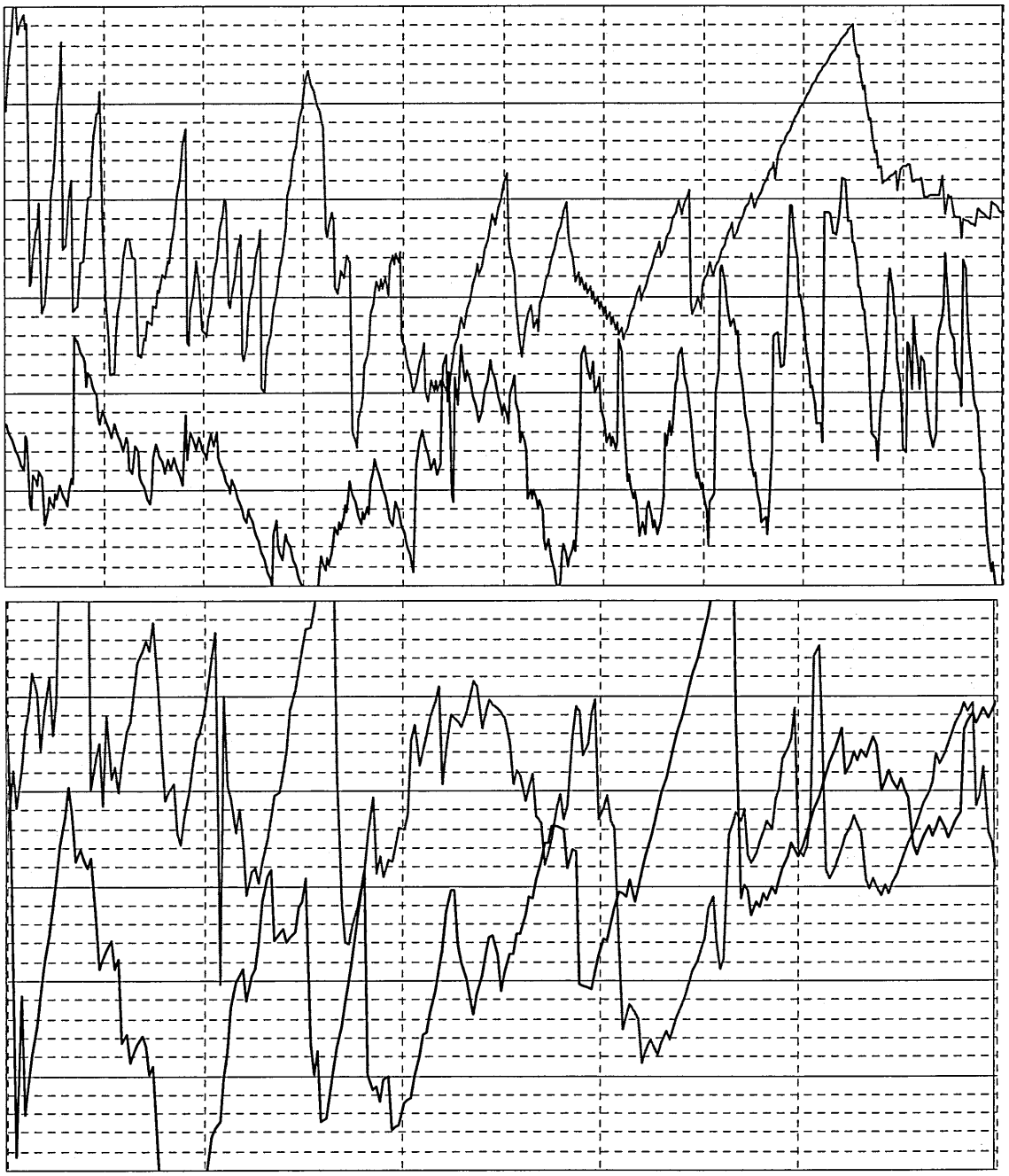


Figure 6.53 **Boundary of the membranes filtered from the curvature of the membrane in order to highlight the "roughness" affecting the boundary. Top membranes of cavities obtained from the sample "Device 6", TOP: from an initial cavity of 114 μm in diameter, BOTTOM: from an initial cavity of 86 μm in diameter. Each vertical division corresponds to 2 micrometers and each horizontal division corresponds to 20 micrometers (with the cautions reported in appendix D).**

The discontinuity breaks down in the results obtained from the top membranes presented in figure 6.53. Here peaks of just 0.2 μm in height lie beside peaks of 0.4 and 0.8 μm, and larger peaks up to two or three peaks of height above 5 μm.

The SEM analysis helps in making sense of the above data. First, the values observed seem to be in concordance with the average dimensions of the ripples qualitatively observed in SEM pictures (such as the ones reported in figure 6.50). Secondly, the "roughness" around the bottom membrane may be considered to represent the minimum value in the cavity contour whereas the boundary roughness of the top membrane should be the highest. Thirdly, the surface patterns depend on the crystalline direction examined and roughness is maximum on the <110> directions and minimum along the <111> directions (figure 6.44). Notice, finally, how most of the peaks of similar height show also similar width, thereby confirming the "non-chaotic" nature of roughness patterns.

It can be safely affirmed that the boundaries of the sample etched in presence of oxygen shows a markedly lower "roughness". Notice that the samples etched in presence of oxygen showed a lower degree of deformation (it was shown in section 6.2.6). The mechanism of preferential etching may explain both findings at once. (This will be discussed in chapter 9, in section 9.3.2).

It is important to judge how such a roughness may affect the performance of the concentrators. Both the small periodic ripples with dimensions below 0.2 μm and their bigger homologous ones with thickness up to 1.2 μm are below the threshold calculated by using the theory of Raleigh. (The threshold was calculated to be 1 to 1.5 μm in section 6.2.6). They are expected not to scatter the IR radiation at the wavelength of interest.

However, for a roughness around 2 μm, the theory of Raleigh (equation 6.5) predicts that, for a wavelength of 8 μm, all the radiation with an incidence angle above 30 degrees may be scattered. For a roughness of 4 μm, at the same wavelength, only the radiation incident at an angle below ~ 15 degrees is not scattered. Due to the geometrical construction of the concentrators, most of the rays hit the collectors at incidence angles beyond 30 degrees. Therefore, a qualitative analysis such as this seems to suggest that, at most wavelengths, most of the radiation would be scattered. However, it can be contested, that a large part of the sidewalls is expected to show a roughness below 2 μm and that the nature of the roughness patterns are not chaotic. The scattering behaviour is similar to the scattering obtained from a regular optical reticule, more than from a randomly rough surface of fractal nature. Therefore the "bundles" of rays may be coherently scattered and finally might be collected. Therefore, the radiation, although scattered, may be assumed to not be completely lost but might eventually cross the exit aperture of the cavity thanks to the nature of the rough patterns. Although the loss due to scattering might eventually be calculated, this would require a highly sophisticated computer model, which is beyond the time frame of this research. In the following, the sidewalls will be considered smooth at the wavelength of operation.

6.3.3 *Variation of cavity dimensions across the area of the wafer*

So far, no information has been provided on the reproducibility and reliability of the process. In particular, no statistical analysis was performed. Whenever typical contours were presented, these were limited to some exemplary profiles chosen randomly across the sample (such as those reported in figures 6.22, 6.24, 6.26, 6.28 to 6.30, and 6.48). This small number of measured cavities can hardly be assumed as a statistically valid representation of the entire population. However, when the process is characterised for a prospective use, such as a microfabrication step in the production of the device prototype, statistical analysis of device dimensions is required; in particular for the following reasons.

1) The variance of dimensions across the wafer must be kept as low as possible to produce the highest number of suitable devices,
2) Similarly the variance within the individual arrays has to be controlled in order to maximise the reliability of the device and maintain homogeneous performance across the array,
3) A value of average of cavities dimensions consistent with the sample is important for the modelling of concentrator (and device) performance, which will be accomplished in section 6.3.5.
4) A consistent average and a narrow distribution allow the determination of an optimal etch time. Conversely, if the dimensions vary largely across the wafer, then it is not possible to establish an optimal etch time.

Average dimensions were collected across the whole wafer area. Since these samples were obtained by using only the smaller holes in the mask, the arrays of original opening of 86 and 114 μm in diameter were used. These cavities proceed through the wafer and produce two SiO_2 membranes: one at the front of the wafer determined by mask undercut (e.g. figure 6.49*b*) and one at the back (e.g. figure 6.49*a*). Sampling is fairly simplified by the presence of these two membranes: optical images can be fast processed by conventional image processing software to yield the dimensions of all the cavities within an array. Three arrays were characterised for the 114 μm cavity and four for the 86 μm cavity. The area is simply computed from the overall number of pixels occupied by each cavity. Conversely, the largest and smallest "cord" (or Feret diameters) are computed using an algorithm, and therefore approximated within certain intervals. For this reason, the linear dimensions are given only on certain discrete intervals of approximately four μm. The complete histograms relative to these samples are reported in appendix G. Given the characteristic shape developed by the cavities, which are mid-way between a circle and a square, the shortest Feret corresponds to the "side" of the square, whereas the longest Feret corresponds to the "diagonal" of the square. The values chosen for further computation/simulation or as a reference for the considerations on the contours (see next section) is the smallest (i.e. the "side" of the square) for two reasons. Firstly, it is the length which ideally corresponds to the diameter of the circle. The second reason will become clear in the next section and it is related to the overall symmetry of the concentrator. It was argued how the actual shape of the 3 – d collector should be thought of as somewhere in between the cylindrical symmetry and the four-fold symmetry (i.e. shapes *a* and *b* of figure 3.7). However, a four-fold symmetric concentrator (such as that depicted in figure 3.7-*b*) is always generated by the perpendicular crossing of two 2-d CPCs with entry length equal to the

side of the square representing the entry aperture, not its diagonal. Therefore, such a concentrator would be related to the 2 – d CPC with width equal to the side of the square.

In each array a few cavities were found with dimensions completely outside a normal range. These were mainly cavities that had not been etched (e.g. because the SiO_2 was still on the mask aperture during deep etching) or cavities largely overetched (due to a complete breakdown of the mask during the etching process). After these few values were discarded, the results of the statistical analysis are reported in table 6.2.

Sample			Device 6	Device O2	
Cavity with original opening of 86 μm	Cavity TOP	μ	340	371	μm
		σ	20	6	
	Cavity BOTTOM	μ	120	100	μm
		σ	30	14	
Cavity with original opening of 114 μm	Cavity TOP	μ	430	460	μm
		σ	30	6	
	Cavity BOTTOM	μ	300	279	μm
		σ	30	5	

Table 6.2 Results of the statistical analysis for the samples "device 6" and "device O2": dimensions of the membranes

The following observations can be made:

1) The bottom membranes show a larger standard deviation (respectively to overall dimension) than the top membranes (this is due to the fact that small deviations in vertical etch rate cause large deviations in the dimensions of the membranes, whereas top membranes are affected only by the lateral etch rate). It is very simple to show this pictorially in 2 – d. For example, if we start with a cavity with average dimensions (340 – 120 μm) and increase the vertical etch rate of 10% by leaving the top membrane extent constant at 340 μm, we obtain a bottom membrane of 215 μm in extent, i.e. an increase of almost 80%.
2) The standard deviations for the sample etched in presence of oxygen are lower than those for the sample etched in pure SF_6. However, there is no evidence that this was inherently due some hidden cause rather than chance.
3) The standard deviation is so high that presenting an average value is sometimes meaningless: the histograms (appendix G) show the large variation in the area of the backside membrane, which leads sometimes to a factor of three between the smaller and the larger value.

Although it was shown many times, and in particular in figure 6.48, how the contours may be quite far from a pure hemi-elliptical profile, nevertheless this is the curve that approximates them most accurately (amongst the simple analytical curves). For this reason it was assumed that the cavities possess an elliptical cross section. The averaged values reported in table 6.2 were used in order to build cavities representative of the sample. The minor semi-axis of these ellipses can be considered a "virtual" etch depth,

which was not reached because of the etch stop layer. The ratio between the actual undercut and this virtual etch depth can be calculated to characterise the etching figure and compare these cavities with the trends already mentioned for the shorter etching time in section 6.2.3 (see in particular figure 6.27). The etch factors are reported in table 6.3. It can be observed how these values are well within the range calculated in section 6.2.3.

Sample	Device 6	Device O2
Cavity with original opening of 86 μm	2.10	1.83
Cavity with original opening of 114 μm	2.21	1.82

Table 6.3 Results of the statistical analysis for the samples "device 6" and "device O2": "virtual" etch factors

The variance between arrays may be induced by inherent variation in radical and ionic flux distribution, leading to local variations in etch rate. The consequent lack of uniformity at the wafer scale level leads to bull's eye effects. Variation between arrays might be slightly improved by rotating the wafer one or more times during the etching. In this case a decrease of the variance between arrays is expected while the variance within arrays should remain more or less the same. The variance within individual arrays is more likely to be due to random factors, e.g. the breakdown of mask rims, leading to an increase in apertures dimensions and subsequent increase in etch rate. This second problem proved more difficult to tackle since it involves a full optimisation of mask deposition and patterning.

6.3.4. Approximation to the CPC contour

Etching in absence of passivation offers a superior performance in comparison with all other methods attempted, especially in terms of reliability and surfaces finishing. Unfortunately, the degree of approximation to the compound parabolic concentrator ideal profiles is very low (due to the limited range of profiles achievable). In fact, it was shown how typical profiles produced by a 2 hours isotropic etching could only overlap a very small part of a suitable CPC (see diagram of figure 6.38). It is clear that such cavities can hardly be used as concentrators directly. A second stage must be added. In this section, the contours presented above will be compared with suitable CPC profiles (of the kind reported in figures 3.5 and 3.6). This section will introduce a viable route to producing a concentrator that approximates the geometry of a truncated CPC by using isotropically etched cavities.

The etch factor for the cavities etched in absence of passivation is almost fixed (varying less than 20% around 2). In a similar way, the slope of the contour varies only slightly, even when O_2 is added to the etching mixture or the pressure is reduced. For a given wafer thickness, once the original mask aperture and the etching time are fixed, so is the shape of the cavities produced. Since the etch rate increases with the dimensions of

mask aperture, it is clear that, for cavities with the same depth (or "virtual" depth), the cavity that was etched for more time starting from a smaller mask aperture is the cavity that shows the higher aspect ratio (that is: it has achieved the same depth but the undercut is lower and so is the aperture diameter; this was demonstrated pictorially in the right-hand diagram of figure 6.26). It is reasonable to seek the maximum achievable increase in aspect ratio to overlap a larger part of the CPC profile. (Picture 6.38 showed that the aspect ratio of a suitable CPC is a lot higher than the aspect ratio of the cavities produced after 2 hours of etching). However, there are constraints in the minimum mask aperture that can be practically used. Firstly, the etch time cannot be indefinitely high because the selectivity of the mask is not infinite. Secondly, the wafer thickness that can be used is not unlimited: the selectivity of the mask reduces the viable etching time to 180 – 240 minutes (depending on the use of oxygen in the mixture, because oxygen consumes the masking material faster). A wafer thickness around 250 μm allows the production of through-the-wafer cavities with backside membranes of a proper dimension. Etching through thicker wafers would be increasingly difficult while thinner wafers would be awkward to manipulate and prone to breaking during processing.

Once the optimal thickness is assessed, the two degrees of freedom (mask aperture and etch time) have to be decided. The ideal way of proceeding would be to choose the ideal CPC profiles (e.g. the profiles corresponding to an acceptance angle of ~14 degrees in the series of figures 3.5 and 3.6) and use simulation software to find the starting conditions to produce such a profile. This route was impracticable: this group did not possess a commercial simulations tool (such as SPEEDIE © or SAMPLE ©) neither there were grounds for acquiring one. Secondly, it would not have been possible to produce a home made tool in a reasonable time since there was no such expertise within this group. Besides, there would not be enough results to validate a fundamental model or build a simply phenomenological one.

Although a simple experimental model was attempted on the basis of least square analysis of the dependence of the vertical and lateral etch rates experimentally obtained (from all the samples etched in pure SF_6, i.e. all the samples reported in table 4.9) on etch time and mask aperture, the forecast did not match the results experimentally obtained in this section. Therefore the experimental model was judged unreliable.

Given the unreliability of the simple regression model, other routes had to be tried. A graphical comparison of the profiles obtained and suitable CPC profiles can help in clarifying the main issues of the problem. The profiles obtained are compared to the CPC profiles in figure 6.54. It must be kept in mind that the profiles reproduced here do not represent actual experimental profiles, such as those reported in figure 6.48. The profiles of figure 6.54 are in fact obtained by interpolating the average dimensions of table 6.3 (i.e. the extent of the entry and exit apertures) with half-ellipses. This may reproduce the average but the actual shape is slightly different, i.e. it is wider and the undercut closes the structures near the top of the cavity. Notice finally that the "cross sections" relative to the original apertures of 114 μm were displaced vertically in order to simulate a second wafer stacked on top of the first.

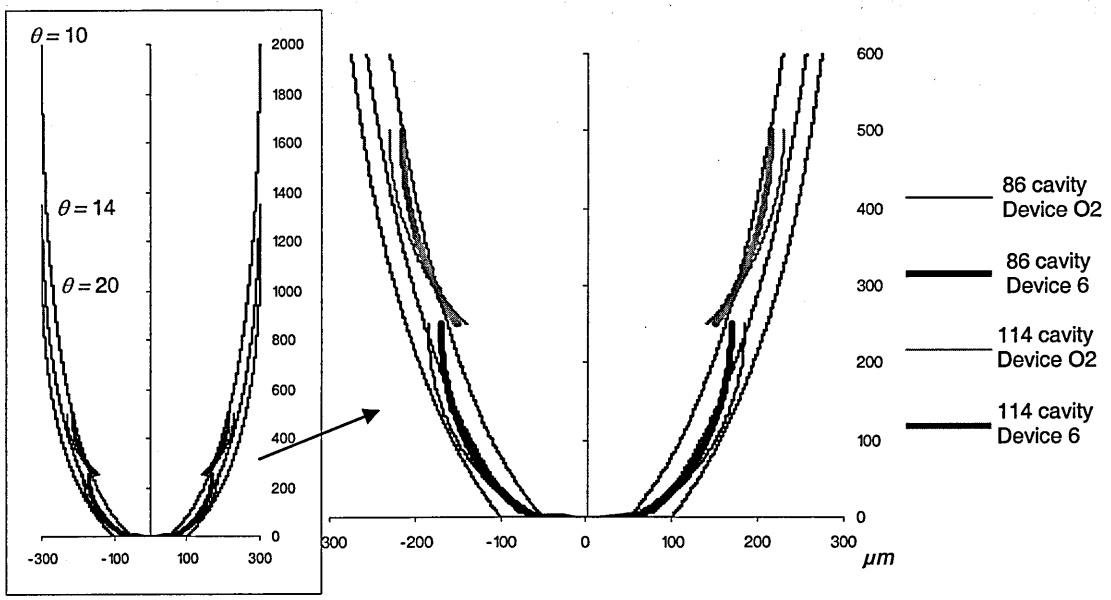


Figure 6.54 Comparison between the profiles of a series of suitable CPCs and the contours of cavities experimentally obtained by etching for long times in absence of passivation mechanism

Graphically the following conclusions can be drafted:

1) The process entailing the use of Oxygen must be ruled out: it makes the aspect ratio decrease to such an extent that the profiles are no longer suitable for approximating the CPC contour. (But the O2 process is ruled out also because of the high consumption of the mask, i.e. the low selectivity, which considerably limits the process time.)
2) The dimensions chosen for the collectors are 120 – 340 for the bottom collector and 330 – 410 for the top collector. These dimensions can be considered to approximate the CPC with 14 degrees of cut off angle (i.e. the "best" CPC following the discussion of section 5.2).
3) The stacking of two wafers as showed in figure 6.54, would approximate a truncated CPC. The truncated CPC would have 37 % of the required height leading to a mere 12 % decrease in concentration ratio (for an ideal 2 – d CPC); in other words, an ideal 2-d CPC originated from a CPC with approx. 14 degrees of acceptance angle and truncated down to 500 μm would produce an effective collection efficiency equal to 3.34.
4) The top collector has to be slightly enlarged. Starting from a mask containing an array of circular holes 120 μm in diameter, one has to etch the top wafer after the bottom collectors have already been machined (in the active-layer-containing wafer). In this way cavities on the top wafer can be tailored to match the correct top dimension of the bottom wafer cavity average.

6.3.5 *Evaluation of the performance of the two-stages collector*

In the previous section, a route was presented for building an array of collectors using dry etching in pure SF_6. Unfortunately, the typical profile achieved in absence of passivation gases could only approximate the extreme bottom of a CPC. However, it is possible to couple (and align) the cavities from two separately etched samples. In this way, it is possible to build arrays of cavities with the contours approximating almost one third of a CPC. This approximation was built graphically in picture 6.54.

The cavities were approximated as hemi-ellipses, although deviations were detected in the actual contour (as clearly shown in figure 6.48). As, previously stressed, there was not enough time to produce software able to apply the ray-tracing algorithm to contours numerically expressed. It was not possible, therefore, to assess the theoretical concentration ratio from experimental boundaries such as those of figure 6.48. However, the validity of results of this kind would have been limited because they would have represented only a few measurements and not a statistically valid sample. On the contrary, the dimensions of the contours reported in figure 6.54 represent the results of a wider statistical analysis. These may be reasonably considered to represent the average of the dimensions of the cavities across the sample.

The performance of the elliptical collectors was simulated by means of ray tracing, i.e. using methods similar to those used in section 5. The details of the calculations can be found in appendix H. The values used for the simulation of the ellipse were the following:
- Bottom ellipse: 126 – 336 and
- Top ellipse: 326 – 414 (the units are arbitrary).

The transmittance plots for the elliptical collectors are reported in figures 6.55 to 6.58. Both the single stage and double stage collectors show a transmittance up to almost 80 % for small incidence angles (< 10 degrees). The transmittance decreases more rapidly for the system with two stages due to the shadow that the boundary of the upper ellipse casts on the bottom ellipse. However, the maximum acceptance angle is similar in both cases. In both cases, the elimination of the outer rim of the active areas (in order to provide thermal isolation) has a dramatic effect on transmittance. The transmittance falls to less than half of the original value. The acceptance angle, on the contrary decreases just slightly more than 10 %.

In figure 6.59 the ratio $P / P_{a'}$ is plotted as a function of the cut-off angle. This diagram can be compared with the diagrams of figures 5.14 and 5.15 (of section 5.7). The increase in power collected for the truncated 2 – d CPC starts in the range 2 – 2.5 as for the elliptical collectors, but then it increases up to almost 4, whereas, for the elliptical collector, it remains almost constant up to a cut-off angle of 10 – 20 degrees. In this respect, the trends are more similar to those of the truncated "V" collectors (figure 5.15).

Table 6.4 reports the collection efficiency, the effective power collected and the total transmittance for the elliptical collectors for a cut-off angle of 14.48 degrees. It can be observed how the two-stage system is effectively able to collect 18 % more power to the

active area than the single stage elliptical collector (although focussed at a slightly lower extent). For the suspended system (inner active area) this value rises to 20%.

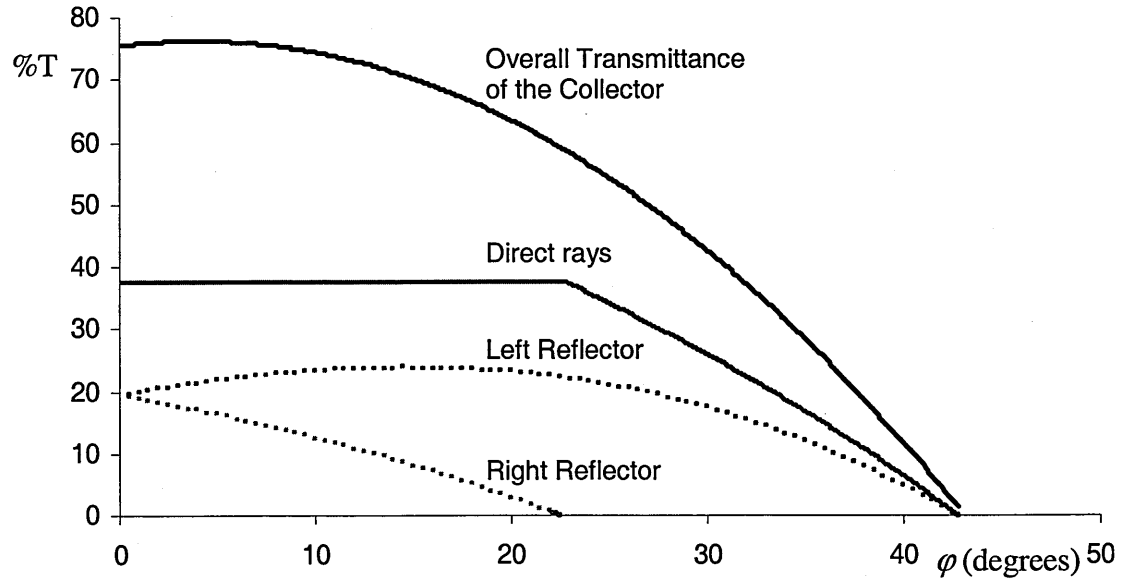


Figure 6.55 Transmittance plot for an elliptical 2 – d concentrator with entry aperture of 336 μm in extent and exit aperture of 126 μm

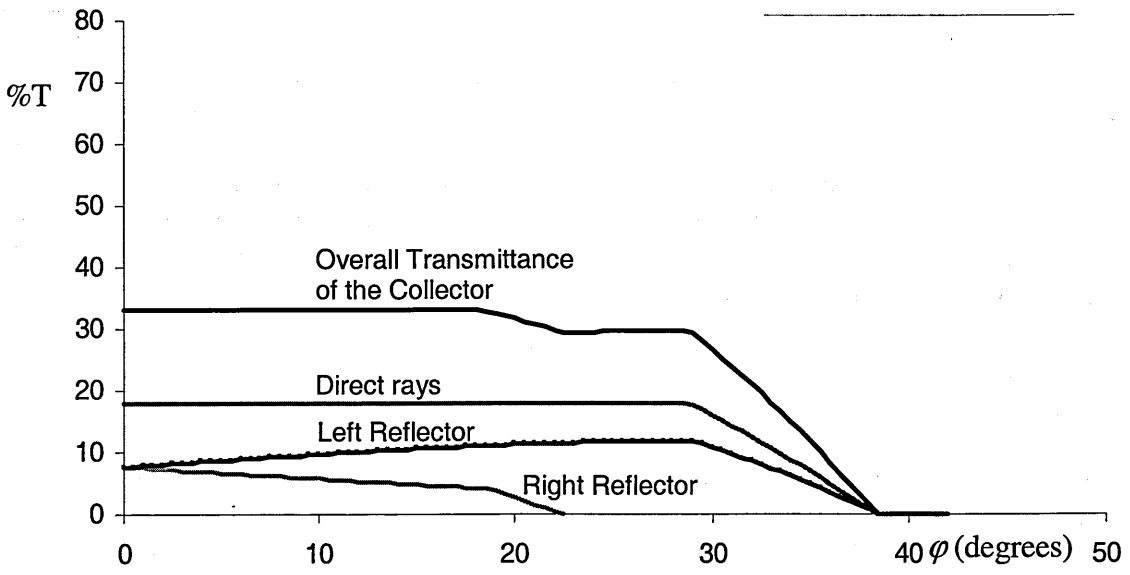


Figure 6.56 Transmittance plot for an elliptical 2 – d concentrator with entry aperture of 336 μm in extent and exit aperture of 126 μm after elimination of the outer structure in order to create an active area of 60 μm in extent

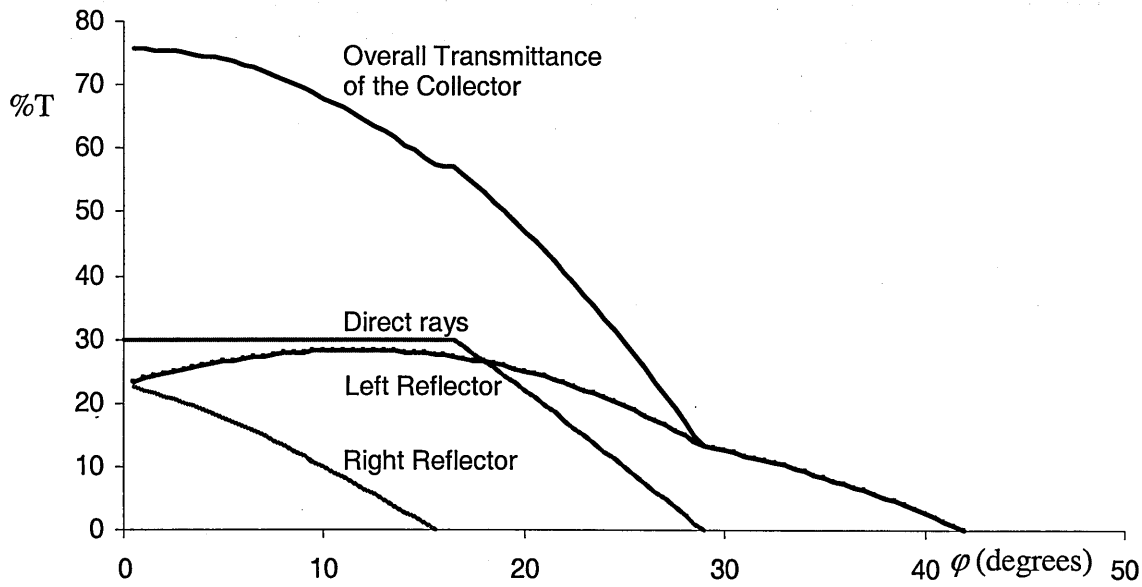


Figure 6.57 **Transmittance plot for a 2 – d concentrator built by coupling two elliptical concentrators. The top cavity has an entry of 414 μm in extent and an exit of 326 μm. The bottom concentrator has an entry aperture of 336 μm in extent and exit aperture of 126 μm.**

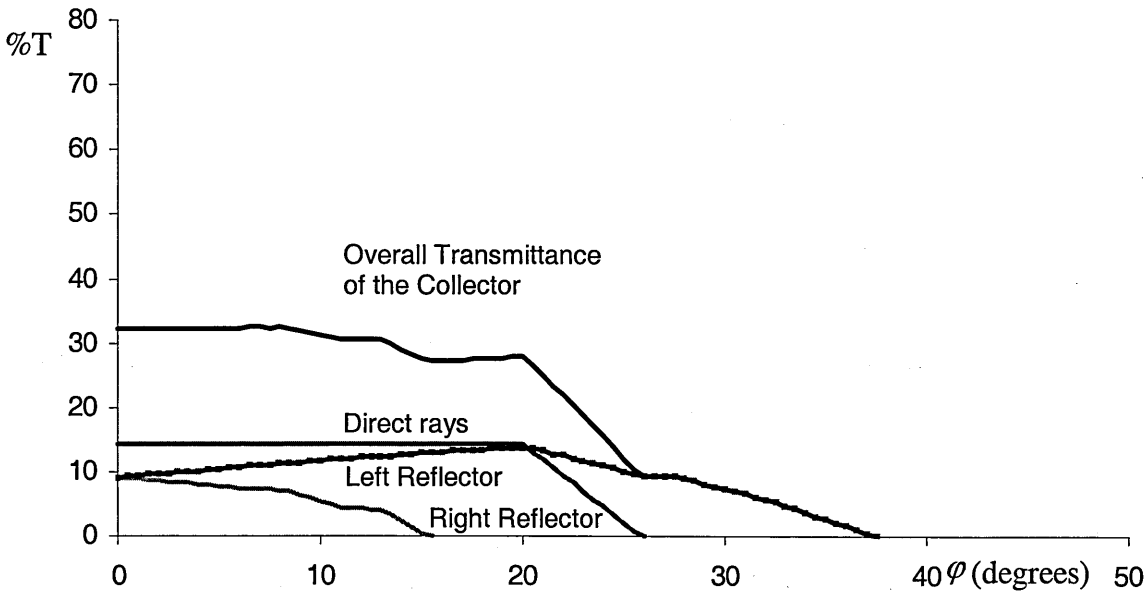


Figure 6.58 **Transmittance plot for the elliptical 2 – d concentrator of figure 6.57 after elimination of the outer structure in order to create an active area of 60 μm in extent**

In this section a route was proposed for achieving arrays of concentrators approximating the profile of truncated CPCs with an acceptance angle of ca 14.48 degrees. Such collectors are expected to collect up to 2.36 times the power that would be collected by

isolated elements of the same dimensions but without collectors. Although problems of surface roughness and loss of cylindrical symmetry exist, the technique elaborated in this section represents a viable way to produce prototype devices. In this way a system for testing the signal can be set up and optimized.

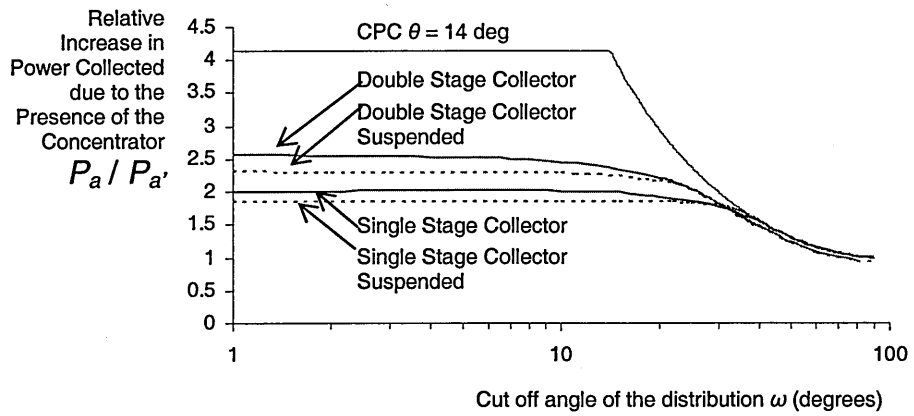


Figure 6.59: Effective concentration power for elliptical concentrators profiles as a function of the cut-off angle of the radiant power distribution. The incoming flux is assumed to be constant for incidence angle below the cut off angle and zero above.

Type of collector	T_{tot}	C	$P / P_{a'}(\omega = 14.48)$
Single ellipse	0.55	1.47	1.99
Single ellipse suspended	0.29	1.59	1.86
Two-stages ellipse	0.42	1.42	2,36
Two-stages ellipse suspended	0.22	1.54	2,24

Table 6.4 The results for the computation of expected performance for four types of 2 – d elliptical collectors

6.3 Conclusion

This chapter presented a series of experimental results, converging towards finding a viable route to fabricate arrays of concentrating collectors in silicon wafers. The results were discussed in order to identify the best route. After a particular process was chosen, it was examined in more detail to assess its feasibility.

The first section of this chapter discussed ways of producing 3 – d structures by unidirectional transfer of 3 – d structured sacrificial masks into silicon substrates. The masks were produced in photoresist by grey scale photolithography. The results presented here did not differ substantially from the results generally presented in literature (a rich literature exists on the production of 3 – d structures in photoresist). The exception is JSR IX575, which shows large deviations from linearity, probably

originated by phenomena intrinsic to the photolithography process. Thermal treatment may be applied to achieve smoother ramps, albeit it is unable to eliminate the coarser steps. Unless exposure and development time are optimised, only part of the overall ramps width can be effectively used. SiO_2 masks (obtained by RIE transferring) reproduce the contours of the sacrificial mask into the inorganic substrate faithfully (i.e. linear projection of the original mask profile).

The subsequent step (micromachining of relatively deep structures by unidirectional DRIE) was hardly characterised in literature. The research was therefore mainly exploratory in aim. The results were characterised as a function of ramps slope and original masking material. Broadly speaking, the quality of the contours produced generally worsened with slope and the degradation of smoothness proceeded differently according to the type of 3 – d sacrificial mask used. It was not possible to produce smooth features when slope exceeded 60 degrees. The contours presented huge steps and relevant amounts of micrograss. Post-processing smoothing steps were unable to achieve a satisfactory level of smoothness. A final comparison between the constraints imposed by the application (concentrators) and the above results demonstrated the unsuitability of the route. Since there was no time for attempting optimisation, this methodology was abandoned after these preliminary trials.

The second part of the chapter presented the outcome of variously unbalanced processes. Most routes were not ideal for various reasons. Albeit it might approximate up to half of an ideal CPC profile, DRIE in defect of passivation or coupling long isotropic and anisotropic etching cycles produced partly convex contours with systematic deformation and high roughness (up to 10 μm rms). Other methods produced broken profiles, highly irregular and with steps of tens of microns. "Isotropic" etching (in absence of passivation) could only approximate a tenth of an ideal CPC contour. However, the profile was concave throughout. The roughness was generally limited to the entrance of the cavity, and the bottom was quite smooth. Cavities produced in pure SF_6 were minimally affected by deformation (only the deformation due to crystal orientation dependent etching) and the shape was largely predictable. Furthermore, this process was the only one that presented evidence of the sole periodical type of roughness. This means that, even if the final roughness will be higher than allowed from the wavelength of the radiation collected, the radiation will be scattered in a regular fashion that can be at least qualitatively predicted and will not be chaotically scattered. This route was chosen as a quick and reliable way of producing devices that could provide a measurable response.

A further series of trials was carried out in order to assess the feasibility of isotropic etching to produce arrays of cavities that could be incorporated in working devices. The length of the etching cycles induced substantial differences with the previous results. In particular, longer etching time meant a larger extent of deformation and a higher roughness. The roughness was minimal in the bottom of the cavities and reached the maximum just underneath the annular ring of the mask. The analysis of the roughness (using an indirect method) showed that the smallest cavities had a roughness in the range 200 – 400 nm whereas the larger ones were affected by a roughness up to 2 – 4 μm. Although these results seemed to demonstrate that most radiation would be dispersed at the wavelength of interest, it has to be stressed that a large part of the

sidewalls is expected to show a roughness below 2 μm and that the nature of the roughness patterns are not chaotic. One would rather expect the "bundles" of rays to be coherently scattered across the "regular" fishbone pattern and possibly collected in the end. The effect of surface roughness on effective collection could not be investigated further without more sophisticated computational tools.

Processing consideration obliged to use wafer 250 μm thick. Two stacked wafers (etched separately) would approximate a truncated CPC with 37 % of the required height. The diameters were 120 – 340 μm for the bottom collector and 330 – 410 μm for the top collector (approximating the CPC with 14 degrees of cut off angle). Such a CPC would produce effective collection efficiency equal to 3.34 (2 – d case). A representative profile of this two-stage cavity was obtained by averaging the actual dimensions of the cavities obtained across an entire wafer. If surface roughness and deviations from the ideal elliptical profile are disregarded, such a collector would provide up to 2.36 times the power that would be collected by an isolated element (in absence of a collector). Actual devices would be produced following this route. (Working prototypes produced in this way will be presented in chapter 8).

Chapter 7 ISOLATION OF THE ACTIVE ELEMENTS OF THE ARRAY BY REACTIVE ION ETCHING

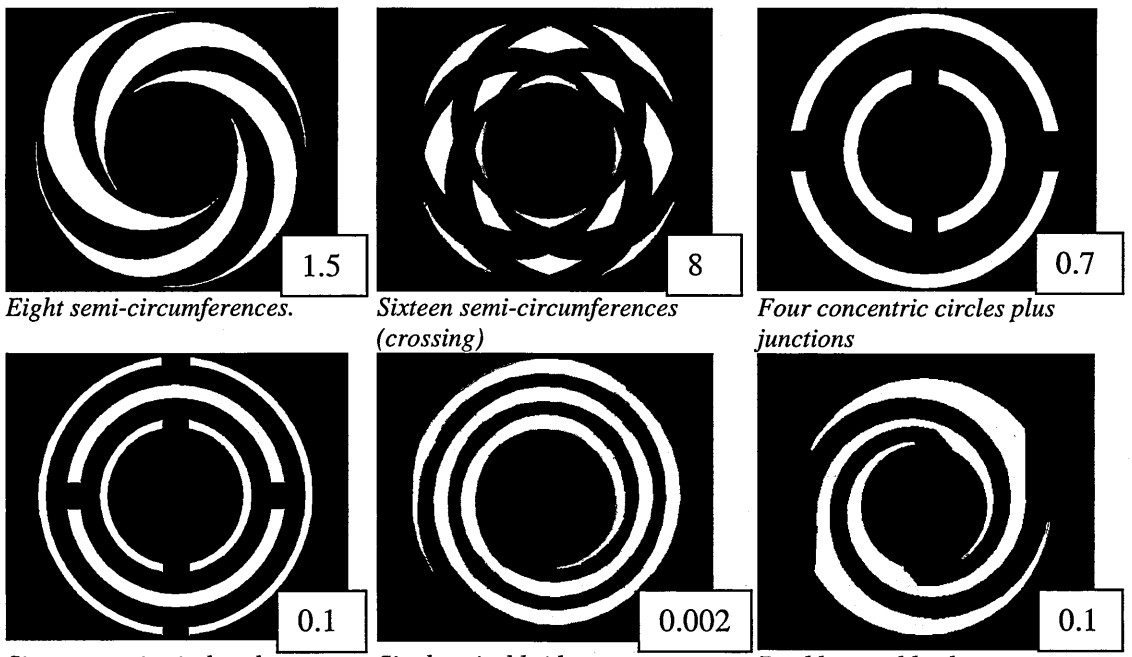
This chapter describes the research carried out in order to pattern the active layer of the pyroelectric detector. It will be recalled how in the introduction (chapter 1) it was stated that one of the aims of this research is to provide thermal isolation for the elements of the pyroelectric detector array. The literature review demonstrated that elements isolation is expected to lead to a large improvement in the performance of the detector. The theory was detailed in section 3.6, where it was demonstrated that conduction dominates the heat losses. It is opportune, therefore, to introduce separation gaps between the active element and the array background. Some case studies of suspension of active elements in thermal sensors were presented in the same section. In the design of the device object of this research, each sensing element of the array lies on an individual membrane (as a consequence of through-the-wafer DRIE). Etching the microbridge pattern onto these membranes directly is the most reasonable way of achieving thermal isolation. The microbridges could carry the required electrode connections to the bonding pad. Conventional Reactive Ion Etching (RIE) was the technique of choice for pattering the PZT/electrodes stack.

This chapter is divided into three sections. Section 7.1 will present the various types of bridge shapes that were compared at the design stage. A particular configuration was chosen among the set proposed: spiral bridges. Structures incorporating spiral bridges are analysed in detail and thermal conductance is calculated. Subsequently, sections 7.2 and 7.3 present the results of the microfabrication process. Although RIE is a well established technique, the etching of PZT-based films still presents some difficulties: setting up a procedure for etching through a stack thicker than one micron required some investigations. Early trials for PZT and electrodes etching are reported in section 7.2. After the correct recipes were identified, the methodology was attempted on the actual element membranes. Only at this level the actual patterning of spiral structures was attempted. Eventually, arrays of elements were etched to produce working devices, and the results are reported in section 7.3.

7.1 System design (spiral bridges)

A bridge configuration separates the active area from the thermal sink thereby providing a drastic reduction of thermal losses. Equation 3.27 (section 3.6) showed that in a single bridge system the conductance is roughly proportional to the ratio between the width and the length of the bridge (w / l). The minimisation of this ratio may be further enhanced with a more elaborated design than a simple straight bridge (a structure incorporating straight bridges was reported in figure 2.9). In the early stage of the design analysis, a range of bridge shapes was proposed and discussed. The design strategy was to divide a circular membrane in various ways. At the preliminary level, the evaluation did not keep into account the properties of the actual materials. A geometrical figure-of-merit proportional to G_T (i.e. w / l) was roughly calculated and the different types of design compared. Since the heat transfer paths are either in series or in parallel (and k and d are assumed to be constant), the overall geometrical figure of merit is computed by a combination of the geometrical factors (i.e. w_i / l_i) relative to every i^{th} segment of the configuration. In this way, very different configurations can be quickly

compared. Of course, a low value of w / l is sought. Typical structures investigated are roughly sketched in figure 7.1 (the figure of merit, proportional to w / l is reported in the bottom-right corner). The overall diameter of the element (outer ring) is 200 μm, compatible with issues that arise during the design of the entire device. The inner diameter is 100 μm. The circular shape of the design is dictated by the cylindrical symmetry of the 3 - d CPC concentrator.



Eight semi-circumferences. *Sixteen semi-circumferences (crossing)* *Four concentric circles plus junctions*

Six concentric circles plus junctions *Single spiral bridge* *Double spiral bridge*

Figure 7.1 Exemplary patterns for isolating the central area of a membrane from the surroundings. The respective geometric figure of merit (see text) is indicated at the corner of each figure (the same factor for the full membrane is circa 9).

The choice of a design is driven not only by thermal considerations. The mechanical properties of the suspended structure must be kept into account: the elements withstand occasional stress, during the microfabrication process and continuous stress, due to the inherent deformation that affects the membranes [*Madou, 2000, Chapter 5*]. A quantitative prediction of the mechanical behaviour of the suspended structures would require knowledge of the material properties, membranes intrinsic stress and, possibly, the use of numerical methods (e.g. finite element module analysis). A complete simulation of the mechanical properties and deformation for various design types (as the ones reported in figure 7.1) is beyond the scope of this early stage research. However some qualitative considerations may be taken into account. Suspended structures would surely be weaker than a full membrane and subjected to a higher extent of strain. An increase in the number of bridges would improve the general mechanical properties of the structure. Breakage of bridges, with loss of active elements, is expected to follow a statistical distribution: longer and thinner bridges are likely to induce a larger number of failures. Finally, the presence of sharp corners has to be avoided as these induce stress concentrations that might provoke cracks.

Consideration of these mechanical issues and geometrical figures of merit (figure 7.1) led to focus on the design types based on spirals. Indeed, the following factors were taken into account:

- Shapes based on spirals are well known to yield good mechanical resistance to loads (as in nature this shape is generally developed for shells);
- A spiral develops a spring-like effect that counteracts the deformation induced by mechanical stress;
- Spiral bridges would allow an increase in length in respect to straight bridges;
- A spiral-based design can be easily implemented to eliminate sharp corners (see e.g. step VI of figure 7.2)

Once the spiral structure was chosen, a second set of patterns was produced. Based on a single or double spiral bridge, the design was produced in the following way:

- the membrane radius was set to 60 μm: this dimension was chosen so that the outer rim should match the exit pupil of the concentrator cavity micro-machined from the other side of the wafer;
- the inner circle radius was set to 30 μm;
- an Archimedes' spiral was centred in the origin of the circular membrane with a certain (constant) increment;
- a second spiral was generated, rotated at 180 degrees clockwise respect to the first spiral: this produces a single bridge;
- to produce two bridges other two spirals were generated rotated at 90 degrees respectively to the previous two spirals.

An example of the construction procedure is reported in figure 7.2.

Thermal conductance was assessed for the spiral-based design using the simplified heat flow equation for the steady state (i.e. $G = \kappa d\, w / l$). First, the thermal conductance for the full membrane was assessed. The full membrane is a multilayered structure, composed as in table 7.1. The diameter is equal to 120 μm. The membrane is considered perfectly circular and flat: the strain is disregarded. Calculated values for each single layer are reported in the last column (according to equation 3.23, i.e. G equal to $2\pi\kappa d / \ln(r_o / r_i)$). The overall conductance for a full membrane is simply given by the sum: $G_{tot} = 3.9 \cdot 10^{-4}$ W K^{-1}. The overall conductance is largely dominated by the conductance of the gold layer. Platinum comes second. The contribution of PZT has the same order of magnitude of Pt, due to the thickness of the PZT layer. The buffer layers can be generally disregarded. The combined contribution of the SiO_x and TiO_x layers is less than half of the contribution of the single PZT layer.

The equations of the spirals of Archimedes of increment ρ_A, which generate the design, are given by (in polar coordinates):

$$r = \rho_A\left(\phi + n\frac{\pi}{2}\right) \tag{7.1},$$

where n takes the values of 0 or 2 for the single bridge and 0, 1 2 and 3 for the double bridge (see steps I to V of figure 7.2). The width of the bridge is constant and equal to (ρ_A / 2) for the single bridge and (ρ_A / 4) for the double bridge. The length of the spiral arc is given by

$$l_{arc} = \frac{\rho_A}{2\pi}\int_{\phi_i}^{\phi_o}\sqrt{1+\phi^2}\,d\phi \qquad (7.2).$$

The extremes of the integration represent the angular coordinates of the intersection between the spiral and the inner circle (ϕ_i) or the outer circle (ϕ_o). The integral 7.2 may be solved numerically or analytically. Although in a rigorous computation one should consider the shortest path available, the thermal path can be roughly assumed equal to the overall length of the spiral arc. The bridges are very narrow for their length so that this approximation is not expected to affect the results dramatically; it should just induce a slight underestimation of G. The calculated values of G are plotted in the diagram of figure 7.3 as a function of bridge width for different configurations. As bridge width decreases, the length increases for geometrical construction. It is clear that the thermal conductance decreases with the length (and thus the inverse of the width) of the bridges. Unfortunately the width of the bridges cannot be decreased below 10 μm because of the mechanical considerations reported above and because of the critical dimensions induced by the microfabrication method chosen. The width of the bridges for the final designs produced ranged between 11.25 μm and 18.75 μm.

Layer material	**Thickness (nm)**	κ (W K m^{-1})	G (W K^{-1}) (full membrane)
Silicon Oxide	400	0.8 [a]	$3.48 \cdot 10^{-6}$
Titanium Oxide	50	8.4 [b]	$3.81 \cdot 10^{-4}$
Ti	5	21.9 [c]	$9.93 \cdot 10^{-7}$
Pt	100	71.6 [c]	$6.49 \cdot 10^{-5}$
PZT	1,000	3.2 [d]	$2.90 \cdot 10^{-5}$
Cr	5	91.7 [c]	$4.16 \cdot 10^{-6}$
Au	100	317 [c]	$2.87 \cdot 10^{-4}$

a – [*Wu, 1980*], *b* – [*Incropera and deWitt, 2002, Appendix A, Table A2*],
c – [*Incropera and deWitt, 2002, Appendix A, Table A2*], *d* - [*Kang et al., 1998*]

Table 7.1 Composition of the element membrane for the calculation of thermal conductance

The prototypal structures are represented in figure 7.4. After the design is completed, a viable microfabrication process has to be established. After evaluating various configurations, it was decided to simply etch the bridges through the full hetero-structure. Both complete etching (free standing structures: thick curves of figure 7.3) and a partial etching that stops on the TiO_2 / SiO_2 layer (thin curves of figure 7.3) were considered. Although a fully isolated structure would yield a conspicuous gain in thermal isolation (as shown in figure 7.3), complete etching may cause secondary problems such as excessive weakening of the structures or shorting between the sandwiched electrodes with loss of the element capacitance. Furthermore, the gain attainable from a complete etching is very high for very narrow bridges, but it tends to decrease as the bridges become wider and shorter. More complex configurations (e.g. a double bridge structure with each bridge carrying only a single electrode layer) were discarded because they would increase the complexity of the process without a substantial gain in thermal isolation.

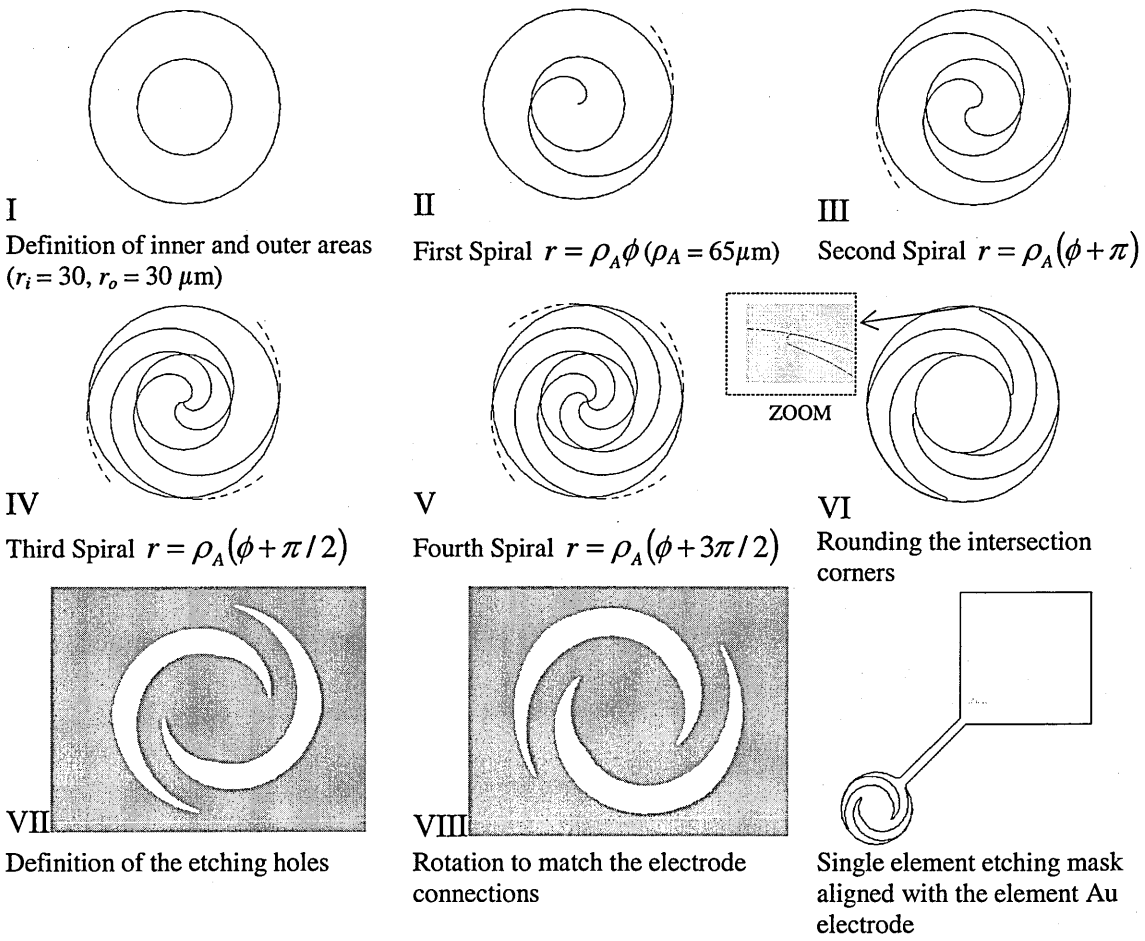


Figure 7.2 Analytical construction of the spiral bridges and sketch of an exemplary element, aligned with the Au electrode pattern. Steps IV and V are missing in a single bridge structure design.

7.2 Early stage trials: feasibility of PZT patterning by reactive ion etching

Patterning the spiral microbridges on element membranes entails etching through a "stack" made of different layers. The typical composition of the stack is reported in table 7.1. It is crucially important to etch through the PZT and gold layers, which represent the higher contribution to the thermal losses. The etching of the buffer layers in the stack does not represent a rate limiting factor: chrome and titanium layers are very thin and most likely to disappear during the various annealing phases (because of diffusion or interface reactions). Techniques for etching silicon oxide and Pt etching have been fully established in the past. Standard recipes for etching thermally grown silicon oxide and Pt were set up after a minimum number of trials, which are not described here. The conventional recipes are detailed in the experimental part (section 4.2, table 4.1). In this section, the results of a first series of attempts to etch PZT and Au/PZT/Pt stacks will be reported and discussed in detail. Experimental set up and methodologies are reported in the experimental part (section 4.2). No transfer of spiral structures was attempted in the first phase. The process was characterised using full wafers and generic patterns. This section will conclude with the set up of a viable recipe for etching the PZT layer and, more generally, the entire stack.

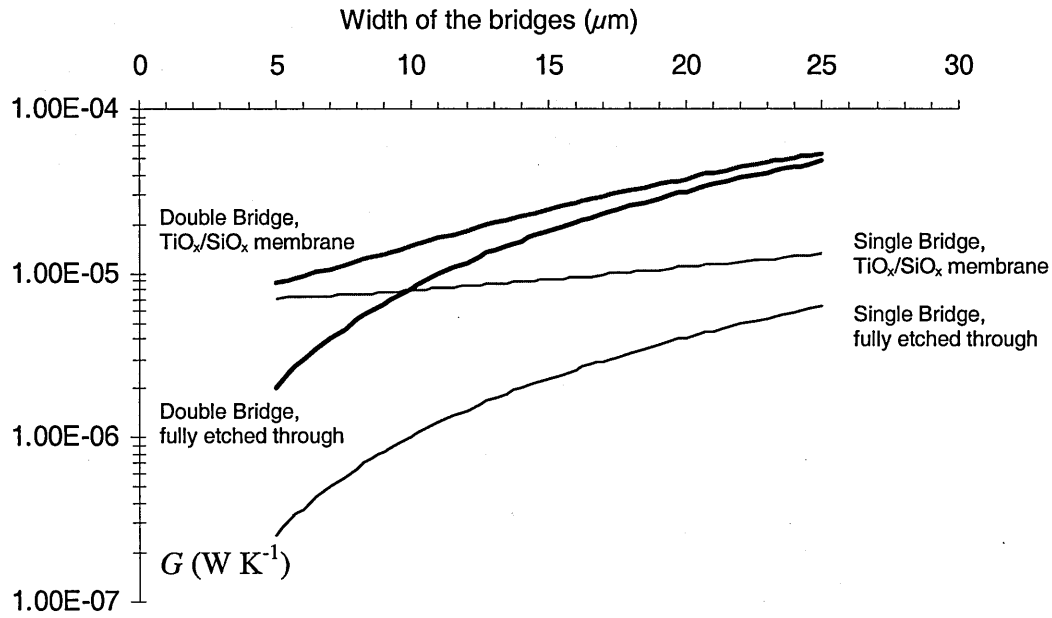
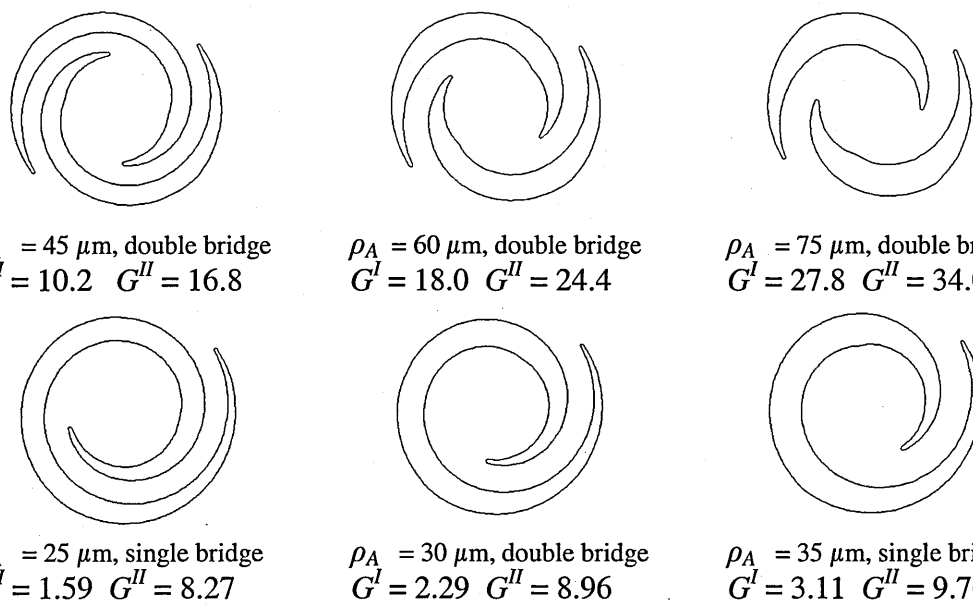


Figure 7.3 **Thermal conductance at the steady state for a central circular structure connected to the thermal sink by one or two spiral microbridges. The computation was made with the values of table 3.1 for two cases: complete etching through the membrane and etching only through PZT and electrode leaving a SiO_2/TiO_2 membrane.**



ρ_A = 45 μm, double bridge
G^I = 10.2 G^{II} = 16.8

ρ_A = 60 μm, double bridge
G^I = 18.0 G^{II} = 24.4

ρ_A = 75 μm, double bridge
G^I = 27.8 G^{II} = 34.0

ρ_A = 25 μm, single bridge
G^I = 1.59 G^{II} = 8.27

ρ_A = 30 μm, double bridge
G^I = 2.29 G^{II} = 8.96

ρ_A = 35 μm, single bridge
G^I = 3.11 G^{II} = 9.76

(*) G^I represents the losses for the fully etched system (spiral suspended). G^{II} is the thermal conductance from the systems where the etch stops at the TiO_x layer. All the values are expressed as $\cdot 10^{-7}$ W K^{-1}

Figure 7.4 **The spiral structures produced for micromachining the arrays**

The etch rate of PZT on Pt/Ti/TiO_x/SiO_x/Si substrates is plotted in figure 7.5 (as a function of RF power) and figure 7.6 (as a function of chamber pressure). The etch rate

was found to increase with RF power and with the inverse of chamber pressure. Both findings were previously reported in literature [*Suchaneck et al., 1999; Title et al., 1986*]. Similarly, slight variations were found in PZT etch rate with the amount of CHF_3 in the mixture. A variation in CHF_3 concentration from 20 to 60 % only caused a maximum of 20 % variation in etch rate. Other researchers reported a similar behaviour [*Van Glabbeek et al., 1993*]. An opaque coating was deposited on all surfaces for CHF_3 rich mixtures at high pressure (>100 mTorr). These findings confirm the model, often advocated in literature, which assumes a strong physical nature of the etching process due to the extremely low volatility of the fluorides of Ti, Zr and Pb [*Saito et al., 1992; Vijay et al., 1993; Macé et al., 1999; Poor et al., 1991*].

The largest values of etch rate obtained are in agreement with those reported in literature [*van Glabbeeck et al., 1995; Vijay et al., 1993; Saito et al., 1992*]. Achieving higher rates would require an increase in power and a decrease in pressure, as suggested by the trends of figures 7.5 and 7.6. (Higher power and lower pressure mean a highly energetic and well-collimated ion flux.) Unfortunately, under these conditions, selectivity problems arise. The thickness of a Shipley S1818 layer (< 2 μm) is unable to withstand a long etching process whereas a thicker photoresist mask (~ 4 μm) gets heavily heated and burns. The carbonisation of the photoresist mask has been previously observed [*Lin et al., 2000*] and it leads to the impossibility of removing the mask after etching.

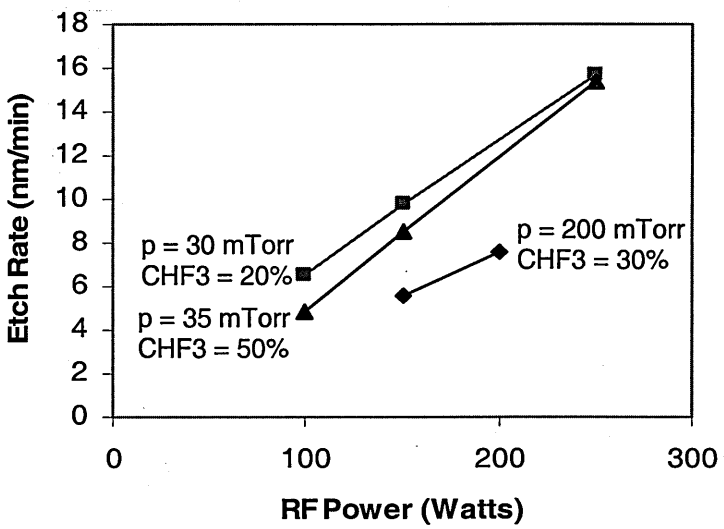


Figure 7.5 Diagram reporting the etch rate for PZT in CHF_3 / Ar mixtures as a function of power. Samples dimensions: approximately 1 centimetre by 2 centimetres.

A decrease in etching power assures a very high selectivity. However, etching at low power requires a long etching time since a dramatic drop in etch rate with time was observed for full wafers (figure 7.7). For a power of 100 watts, it takes ~ 7 hours to eliminate the PZT completely and up to 9 hours for the etching of the electrode/PZT stack. Fortunately, a 10 μm thick AZ4562 layer demonstrated ample capability of withstanding very long etching cycles. (Such a thick mask could resist up to 10 hours at a power equal to 100 Watts with a pressure of circa 40 mTorr.) Furthermore, at such

low power damage and carbonization did not reach the photoresist-PZT interface, thus the photoresist was easier to eliminate afterwards. In figure 7.8, the optical images from two samples etched with the same settings are compared after photoresist removal: using a 3.5 μm thick mask (S1818) produced a badly damaged surface, which was avoided by using a 6.5 μm thick mask (AZ4562).

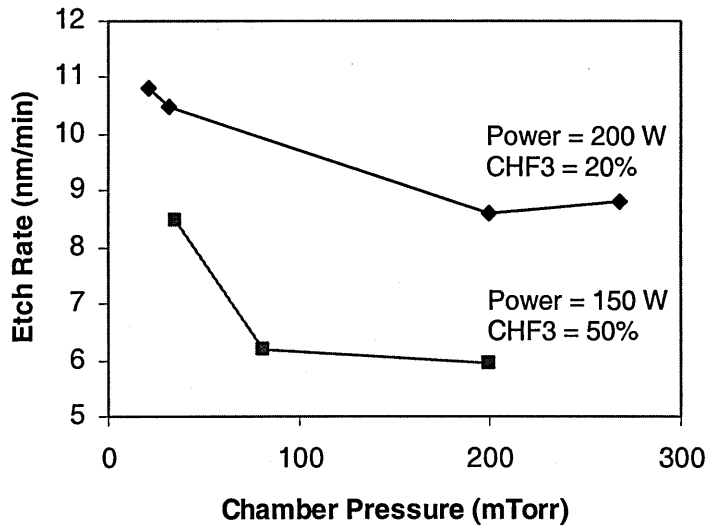


Figure 7.6 **Diagram reporting the etch rate for PZT in CHF_3 / Ar mixtures as a function of chamber pressure. Samples dimensions approximately 1 cm per 2 cm.**

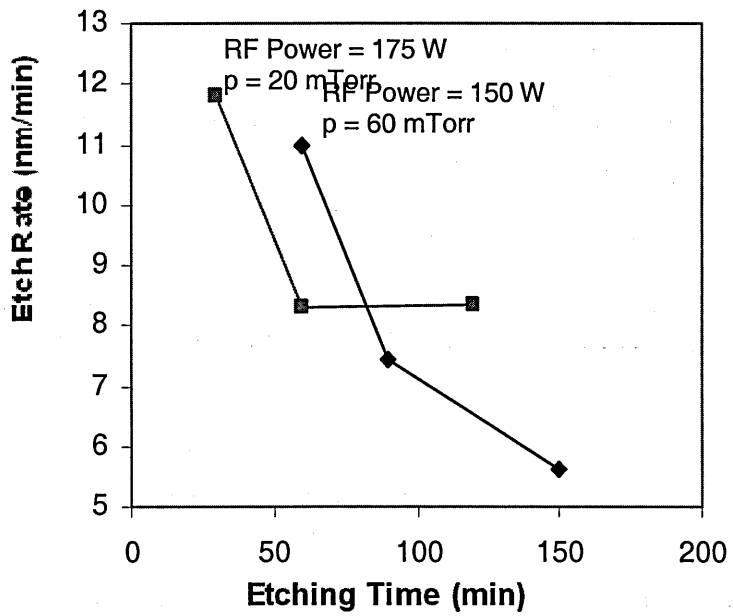


Figure 7.7 **Diagram reporting the etch rate for PZT in CHF_3 / Ar (20/80%) mixtures as a function of etching time. Samples dimensions: entire wafers (10 cm in diameter).**

The problem of mask damage emerges when etching the gold on top of the PZT layer. If the conventional recipe for metal etching (namely etching in pure Ar with very low pressure and high RF power) is applied from the start, then the surface layer of AZ4562 gets immediately carbonised. At this point, cracks occur, which lead to subsequent damage in the film, with production of pinholes in the gold electrode. The solution is to use the PZT etching recipe from the start, which entails using lower ion energy. This avoids the carbonisation of the photoresist mask, albeit increasing the etch time required for patterning through the gold. On the contrary, if the metal recipe is applied to the Pt layer (after the 4 to 6 hours required for etching through the gold and the PZT), then the photoresist does not get carbonised anymore. Probably the long etching process re-flows the photoresist partially and makes it more dense and less prone to partial carbonisation and exfoliation, even under a strong ion flux.

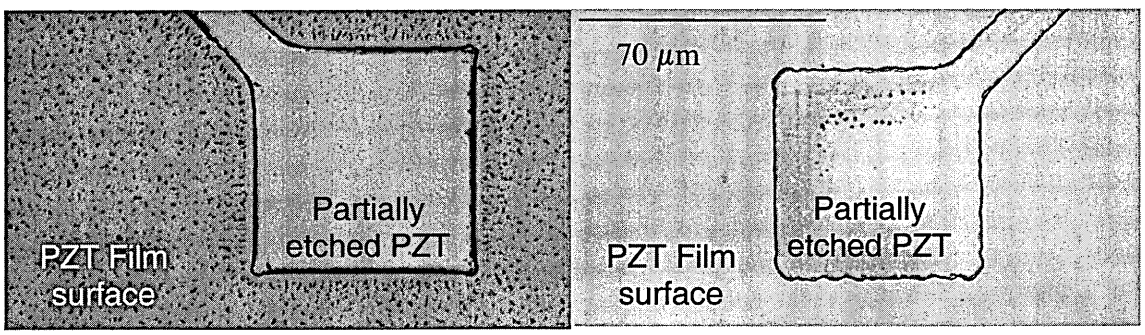


Figure 7.8 PZT patterned surface after etching for 60 min at 150 Watts. The etching mixture was CHF_3/Ar (20/80). Left: using a 3.5 μm thick mask, Right: using a 5.5 μm thick photoresist

In conclusion, using thick AZ 4562 and a low power process, the stack can be fully etched (albeit after a process of 7 to 9 hours) and the photoresist residual easily removed. The standard recipe for etching through a membrane was reported in details in the experimental part in section 4.2 (table 4.1).

7.3 Patterning of Au/PZT/Pt/TiO_x/SiO_x membranes

Patterning the spiral structures on a device wafer originates additional processing issues. In this section, the focus is upon the crucial problems of the uniformity and the fidelity of pattern transfer.

Uniformity represents a major concern for conventional RIE because of the radial variation in the properties of the plasma, which is capacitively induced. Generally, the etch rate depends on the distance from the centre of the wafer. The experimental trials demonstrated a low uniformity even at the early stage and for small samples. Figure 7.9 shows an example: the diagram presents the etch depth relative to a full wafer etched for 6 hours in 20% CHF_3 at a pressure of ~ 40 mTorr with 150 W power. The etch is almost complete at the periphery whereas the PZT residual can be as thick as 300 nm in the centre of the wafer ("Bull's eye" effect). The problem of uniformity may be overcome by etching a single array at a time after sawing the wafer. Unfortunately, the uniformity may be quite poor also across a single array: it is clearly visible in the inset of figure 7.9. For this reason it is not possible to produce a recipe for stack-etching with a fixed,

ideal etching time. On the contrary, the etching process has to be checked visually to assess a suitable ending point. This significant lack of uniformity can be controlled using an etch stop mechanism. In our case the etch stop is provided by the Pt layer, which has a very low etch rate when subjected to the PZT etching recipe.

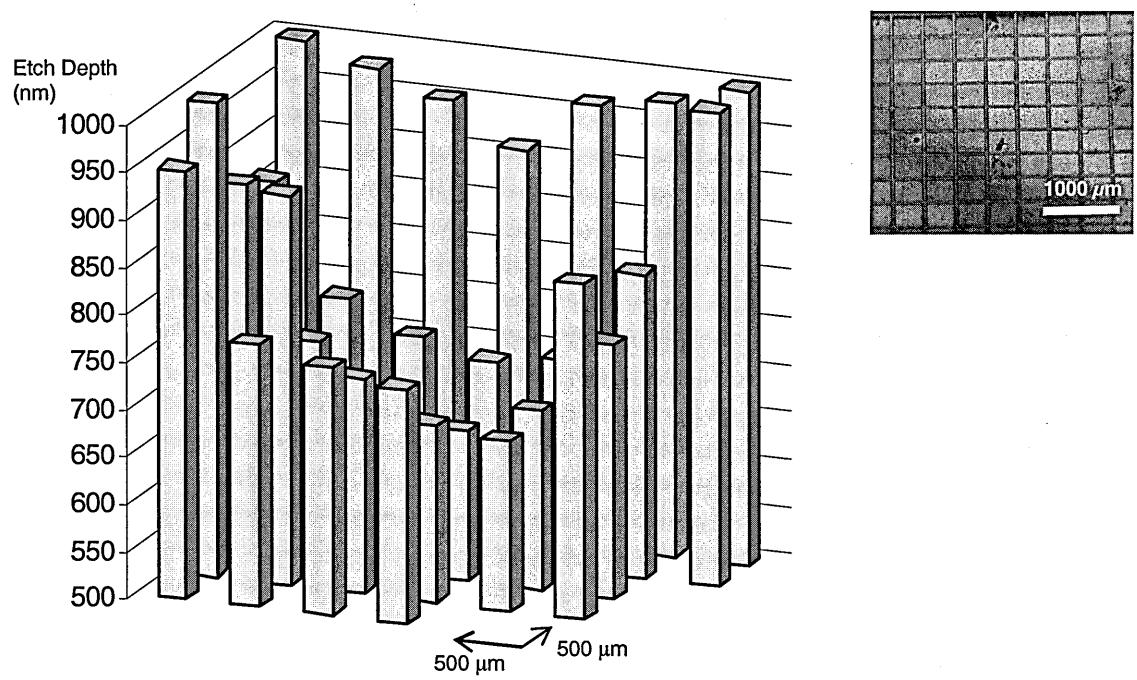


Figure 7.9 **Variations in etch depth across the surface of a 10 cm diameter wafer. Each column represents the average etch depth relative to a different array on the wafer. Inset: the variation of remaining PZT thickness across a single array can be easily observed by noting the change in colour of the partially etched film. See text for etching conditions.**

At this point, it is possible either to etch the stack completely (through titanium and silicon oxide layers) or to leave a full oxide membrane. Unfortunately, since Pt etching is not uniform across the wafer, it is difficult to stop on the oxide layer. The selectivity of SiO_x and TiO_x over Pt must be near to 1 as expected from a purely physical etching. Typically, the oxide layer is partially or totally etched in part of the arrays, while still present in other parts. The outcome is scarcely controllable. Figure 7.10 shows the characteristic outcome of the etching process. The sample was etched for 10 hours using the recipe for PZT etching. The view is from the cavities etched by bulk micromaching, so that the side opposite to the etching is showed. Proceeding from left to right, it can be observed how the etch becomes progressively deeper until fully etched and, finally, overetched structures appear.

Pattern fidelity represents another important issue to be taken into account. It is well known that a certain degree of shape deformation occurs during positive photolithography [*Madou, 2003, Chapter 1*]. In particular, positive features (bridges) become narrower and negative areas (holes) tend to extend, because the limitations due to development induce tapered sidewalls. Tapering may affect thick photoresist such as

AZ4562 to a larger extent: it is clearly evident in the optical pictures of figure 7.11. The features of figure 7.11 are patterned using thick AZ4562 on a PZT layer after optimisation of the photolithographic process. If compared with figure 7.4, they show clearly how the bridges tend to become narrower than the original design while the holes widen. This problem becomes more evident for the long bridges. There are obvious ways of compensating for this loss by modifying the original design.

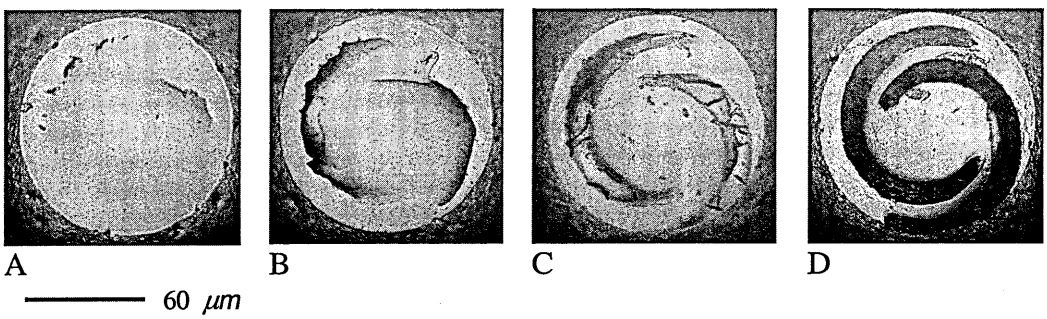


Figure 7.10 Differences in the etch depth through the membranes for elements of the same sample etched for 10 hours using the standard recipe for PZT. The membranes are observed from the side that was bulk micromachined (side opposite to the etching).

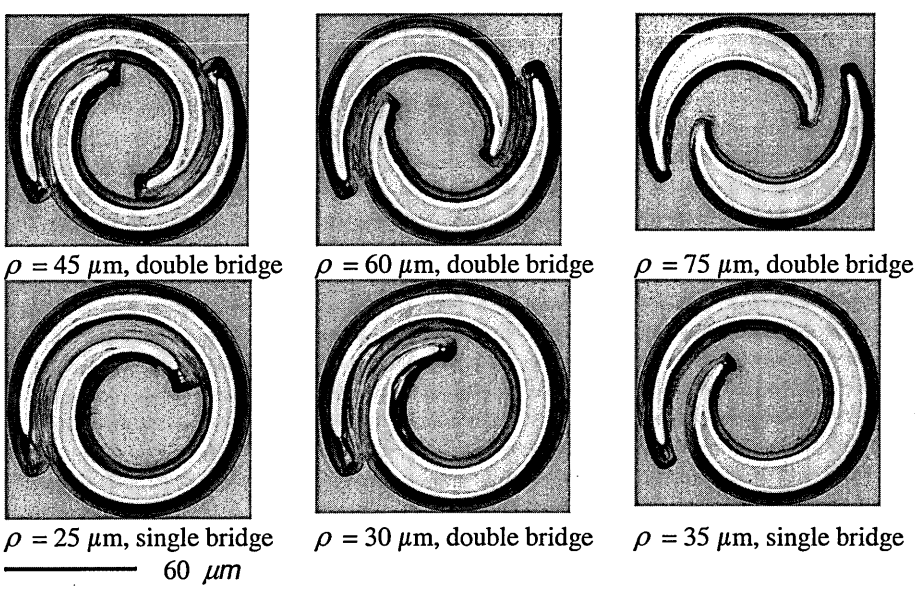


Figure 7.11 Spiral-based microbridges patterned by photolithography using AZ4562 on a PZT layer. The photoresist layer is ~ 10 μm thick.

In spite of the large tapering, the photoresist withstands the etching process and the structures (in particular the ones with wider bridges) can be successfully patterned down to the Pt layer. Once the photoresist is removed, the width of the original design is preserved. Examples are shown in figures 7.12 and 7.13*a*. The SEM picture of figure 7.13*a* demonstrates a neat etching down to the Pt level. However, a close up of a partially etched structure (figure 7.13*b*) reveals that the tapering of the photoresist has been transferred into the PZT layer, which shows contoured sidewalls. Figure 7.13 also

shows that the etching of PZT proceeds preferentially onto the defects of the deposited film. In this case the film was originally cracked and the cracks etch preferentially. This preferential etching was previously observed in [*Title et al., 1986*] along the grain boundaries for a chemically vapour deposited film. When etching through the membranes is attempted (or when the bridges are too narrow to withstand the etching) the gold may be eventually removed from the bridges, leading to the loss of structure functionality. An example is in figure 7.13*c*. There the membrane was partially etched through and it can be clearly observed how the bridges are evidently tapered and thinner than the active area they hold. The close up of figure 7.13*d* demonstrates how the bad outcome of photolithography induced largely irregular sidewalls.

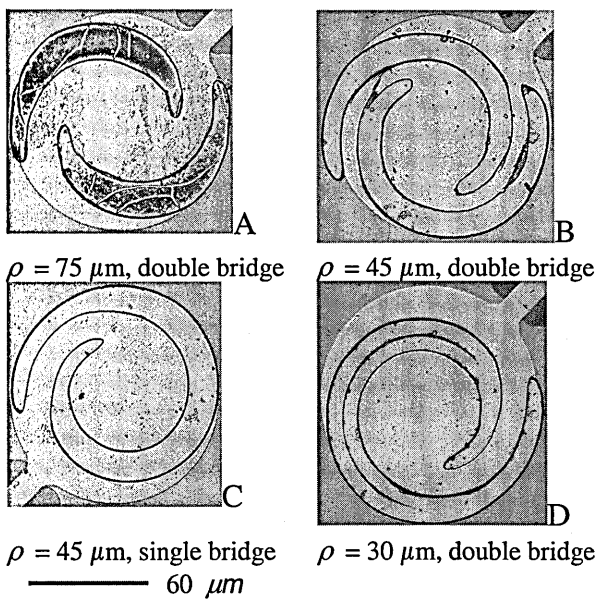


Figure 7.12 Spiral-based microbridges patterned by etching down to the Pt layer using the PZT standard recipe for 9 hours. (the photoresist mask was removed in acetone)

7.4 Conclusion

A viable process was proposed and set up for the thermal isolation of the elements of an infrared sensor focal plane array. The suspension is obtained through patterning of spiral-based microbridges onto membranes (containing the active elements) previously obtained by DRIE bulk micromachining.

Bridges with a shape based on Archimedes' spiral construction allow the maximisation the length while maintaining a width achievable by conventional photolithography of thick photoresist. Theoretical analysis of the thermal loss was accomplished, relative to the design based on a single or double spiral bridge. The analysis showed that the patterning leads to a decrease in thermal losses between 100 and 2000 times (depending on the thickness and number of spiral arms and the etch depth).

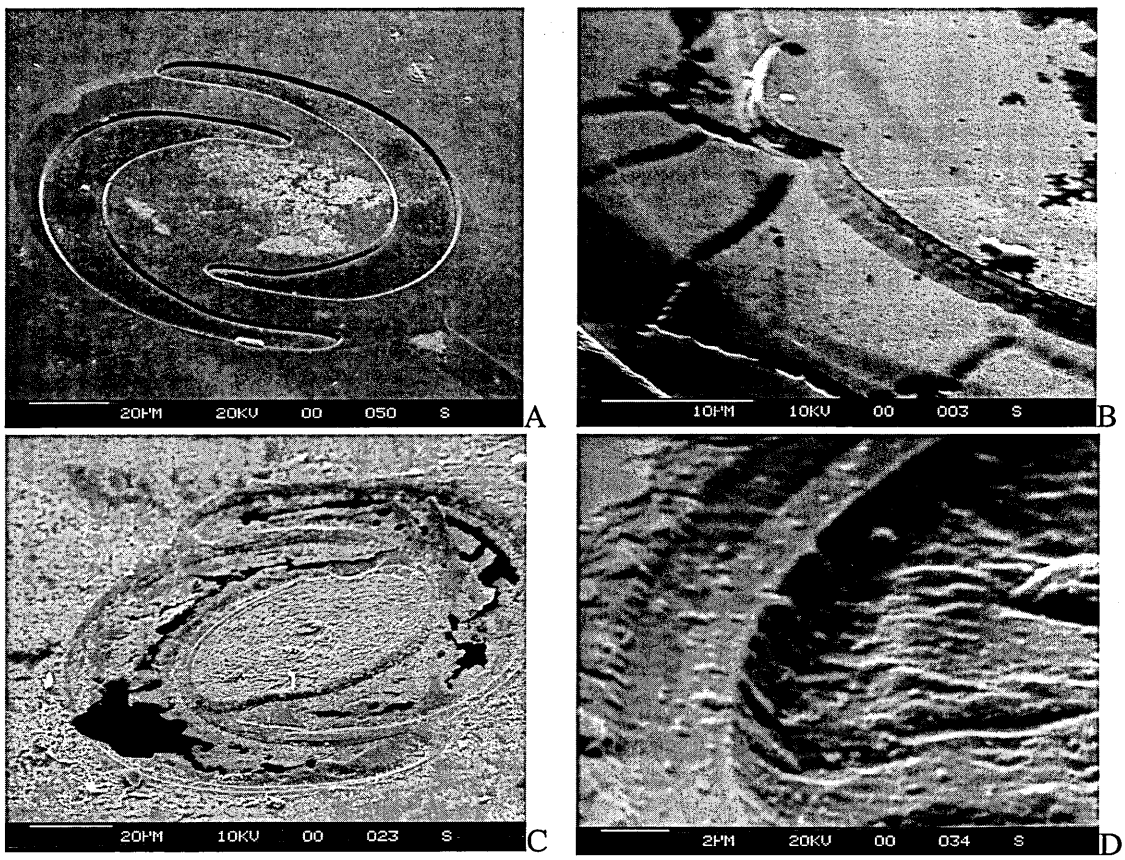


Figure 7.13 Series of SEM pictures of structures with spiral-based microbridges etched for different time using the standard recipe for PZT etching

The suspended structure was produced by etching the whole Au/PZT/Pt heterostructure in conventional RIE (parallel plate reactor). Patterning of thin metal films or silicon oxide could easily be achieved by RIE, but the etching of PZT required careful setting up of process parameters. In particular, the use of a thick photoresist was required, which allowed longer etching times and thereby a more gentle process (after the RF power was lowered).

Attempts to etch full wafers were hampered by poor uniformity, which could be partly overcome by etching individual arrays or by using the platinum electrode as an etch stop layer. The masks produced using a thicker photoresist (AZ4652) demonstrated patterns less sharp and bounded by sidewalls more irregular. As a consequence, the bridges were narrower than the designed width. For this reason, only structures with short and large bridges were successfully etched (and the etch stopped on Pt). There are two ways of overcoming this problem: first, the photolithographic process can be further investigated and optimised; secondly, mask design could be easily changed to compensate the loss of pattern fidelity during photolithography.

Chapter 8 THE IR SENSOR PROTOTYPE DEVICE: MICROFABRICATION, SIMULATION AND TESTING

The previous chapters presented the results relative to the two different streams of this research (namely to incorporate an array of micromachined collectors and to provide thermal isolation for the individual elements of an IR sensing array). So far, these two aspects have been kept separated. This chapter, on the contrary, represents the synthesis of the above trials. The last part of this research was devoted to producing working prototypes and measuring their response to IR radiation.

This chapter consists of three parts three parts. The first section presents the route that leads to the microfabrication of the prototype. The main processing aspects are considered and discussed. First, the main steps of the process are presented. This recalls partly the fabrication of the primitive version of the device, which was presented in the background theory as a case study (in section 2.7). It then adds the novel steps introduced by this research. The order of the steps represents a particular problem. The section discusses whether the micromachining of the collectors should be postponed to the patterning of the active layer or vice versa (both routes were attempted). After a statistical analysis of cavities dimension, the section concludes with an overview of the structure of the prototypes obtained.

The second section of this chapter calculates the performance of the IR device by making use of the results of the computation of thermal losses and the ray tracing analysis of power collection. First, the collection efficiency of the cavities obtained by long isotropic etching is calculated. The calculation uses the average dimensions from the statistical analysis of the previous section. The calculation is pretty rough: it works in 2 – d and for elliptical collectors that only approximate the actual profile (and shape) of the cavities obtained experimentally. 100% reflective sidewalls are assumed. Subsequently, the calculations of heat losses are combined with the results of the ray-tracing procedure in order to produce estimates for $\mathcal{R}_I$, $\mathcal{R}_V$ and $\mathcal{D}$ (thus demonstrating the improvement in performance for the upgraded array). Finally, the theoretical effect on the IR response due to the introduction of micro-collimators is calculated. (Micro-collimators were used to help demonstrating the effectiveness of power collection from the concentrators.)

Working prototypes were obtained and tested. The results are reported in the last section of this chapter. First, the general performance in terms of response to IR radiation is reported. This shows some interesting effects, which are attributed to the presence of the collectors. However, these results did not demonstrate the improvement in performance directly, and micro-collimators were subsequently introduced. Unfortunately, the time for the testing procedures was short and the devices produced could not be fully characterised. The experimental results are compared with the theoretical results obtained in the previous section.

8.1 The microfabrication process for building the device

This section describes the definitive process for the fabrication of a working prototype. After the preliminary trials (presented in the previous chapter), it was established that two routes would be researched further: first, the etching in absence of passivation (or "isotropic" etching) and subsequently the coupling of long anisotropic and "isotropic" cycles. The former route was chosen mainly because of the superior reliability and predictability of the results, the latter because of the higher versatility in designing the profile and potential better approximation to the CPC profile. Both routes present serious drawbacks. In particular, the "isotropic" etching can only approximate the very bottom of a CPC (as shown in figures 6.38 and 6.54) whereas the anisotropic-isotropic process needs significant optimisation.

From the investigation of the isotropic process (section 6.3) an effective solution to the former problem emerged: a second wafer could be stacked on top of the device wafer so that for every collector a second larger "isotropically" etched cavity could be coupled to the first. In this way, structures that could approximate a truncated CPC were achieved. The sequence of long anisotropic and isotropic processes was deemed worth pursuing as long as both a reliable model to predict the results and a method for smoothing the contour could be developed. A series of trials were accomplished to smooth the contours on many of the cavities presented in section 6.2. These trials are not described here. Briefly, these attempts entailed using both dense and diluted photoresist materials to be deposited inside the cavities or etching cycles with different recipes both in the DRIE and the RIE equipment. Unfortunately, all these trials were largely unsuccessful: some needed optimisation and others lacked a satisfactory reproducibility. Since these trials were running out of the time schedule, it was decided to devote most of the resources to building a device using the first method (long isotropic cycles). In addition, prototypes of the device were needed that would effectively deliver a signal in order to set up and characterise the apparatus for testing the pyroelectric sensing arrays. (The equipment was described in the experimental part, in section 4.1.3 and shown in figure 4.3.)

At the end, there was not enough time to set up a process using the second route and device wafers were only produced using the first route, i.e. etching in pure SF_6 and stacking of two wafers. The new microfabrication steps are added to the process flow chart in figure 8.1, which follows ideally from figure 4.1. The microfabrication steps of figure 8.1 represent the production of arrays of isotropic through-the-wafer cavities by etching in pure SF_6. The cavities are then coated with a nickel/chrome reflective coating. After the dies are separated, the top and bottom arrays are stacked together to produce a full device.

Only the main steps are presented in figure 8.1. In particular, the elimination of the SiO_2 mask after DRIE from both wafers is not addressed. SiO_2 can be eliminated by RIE (e.g. using the recipes reported in table 4.3 of the experimental part) or by ultrasonic bath. These methods are optimal for the top wafer but are unsuitable for the device (bottom) wafer as they may lead to a loss of the PZT membranes. It was found that the best method to eliminate SiO_2 from the front side of the device wafer is to peel the mask using simple adhesive tape.

This section presents the main problems arising from the processing point of view, in particular regarding the order of operation of the steps added to the original process set up. The "conventional" process is briefly recalled in section 8.1.1. The main problems (i.e. quality of the electrode and quality of the microstructure of the PZT, bad outcome of the lift-off) are discussed. The practical question of the order of the sequence for the operations *etching of the concentrators – patterning of the spiral microbridges* is addressed in section 8.1.2, relatively to the outcome of the sawing process. In effects, the rate of survival of membranes is strongly related to the sequence of operation. The variation of cavity dimensions across the wafer is discussed in section 8.1.3. (The values emerged from the statistic analysis will be used for the simulation of prototype performance in section 8.2.) Finally, the resulting structures are presented in section 8.1.4 showing the main problems affecting the final device.

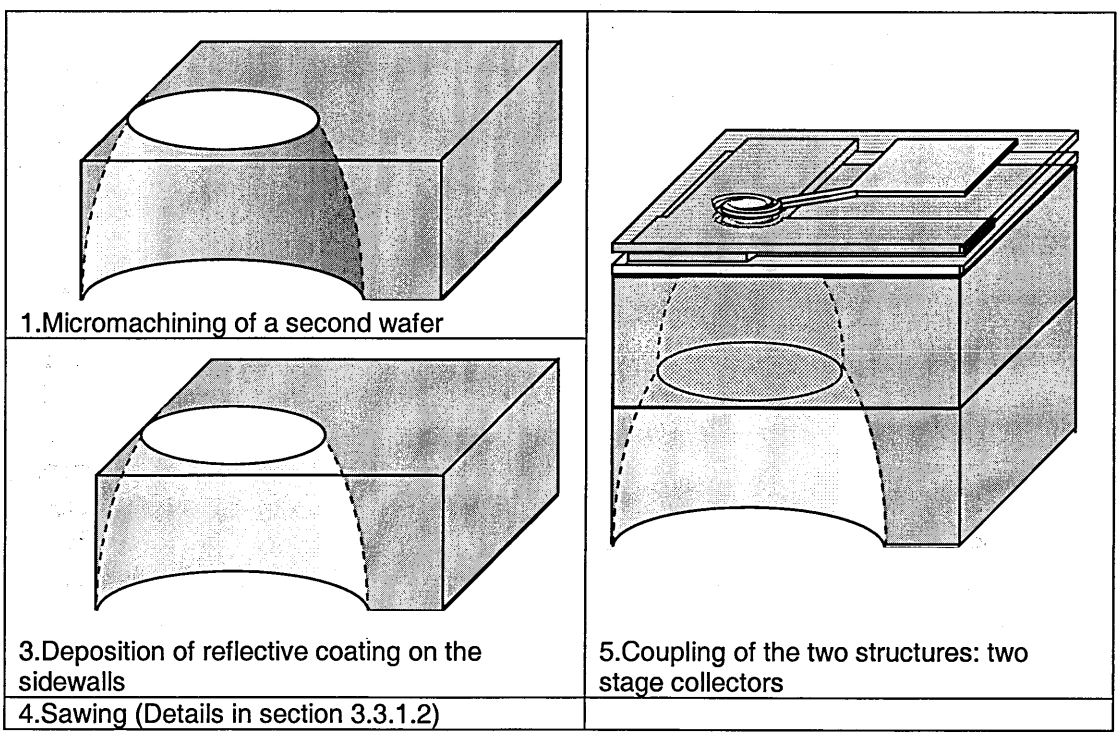


Figure 8.1 New steps introduced in the final microfabrication process of the IR pyroelectric device prototype

8.1.1 The microfabrication process, up to the patterned array

The process, up to the sandwiched structures, does not present unfamiliar problems since it entails fairly conventional techniques. Above all, it is chiefly important to keep the microstructure of the PZT and Pt layers under control during the first phase of device fabrication. The sol-gel process for PZT thin film deposition has been part of the know-how of the group for a long time (see e.g. [*Zhang et al., 2001*]). However, the process drifts may lead to low quality PZT. In particular the temperatures of drying and firing may induce unwanted preferential orientations on the PZT film. Conversely, optimised orientation of the Pt layer (narrow rocking curve) induces highly oriented PZT films. Subsequently, the orientation and the texture of the active layer affect the pyroelectric properties, hence the performance of the sensor. A detailed discussion of

these issues is completely beyond the scope of this thesis. (A more detailed discussion can be found, e.g. in [*Hanson et al., 1996*].)

As an example of the kind of control that is operated on the process at this stage, exemplary x-ray diffraction spectra typical of good and bad PZT are compared in figure 8.2. The blue curve corresponds to a film that has been crystallised below the optimal temperature. (A wide peak appears, corresponding to pyrochlore formation [*Huang et al., 1999*].) This structure is often related to a heavily defected film, such as that shown in the inset, after partial etching of the PZT. Blisters, pinholes and microcracks are clearly visible. (Notice that the etching is preferential along the cracks as stressed in section 7.2.) Lower capacitance and smaller pyroelectric coefficients are to be expected from these low-quality films. On the contrary, in a well-crystallised film, the pyrochlore peak vanishes (grey curve of figure 8.2).

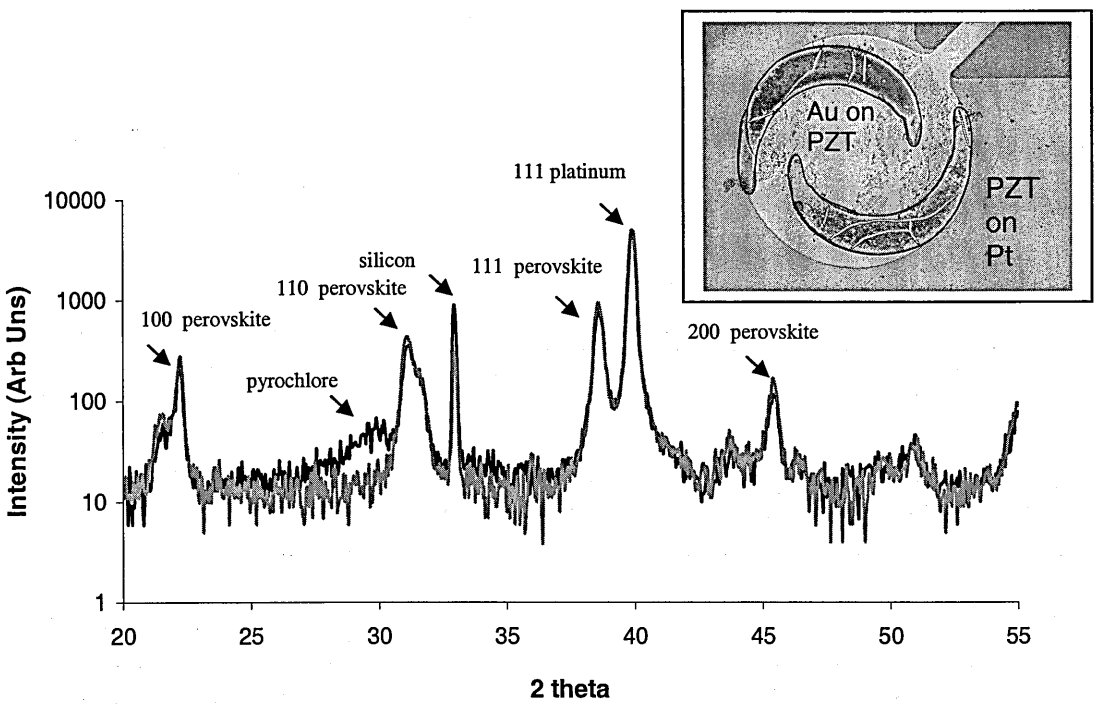


Figure 8.2 **Example of X-ray diffraction spectrum for controlling the quality of the pyroelectric layer in the pyroelectric device. Inset: optical microphotograph of a single element showing clearly the cracks and pinholes related to a low-quality PZT layer**

Typical examples of bad outcomes of the lift-off process are reported in figure 8.3. Firstly, an incomplete elimination of the metal leaves a very rough surface. This may prevent the deposition of a good PZT layer on that zone (picture 8.3 *left*). Secondly, an excessive elimination of the top electrode may lead to a lack of connection from the sensing element to the bonding pad (picture 8.3 *right*). On the contrary, an incomplete elimination of the Au layer may leave two or more elements in contact. These defects lead to the loss of the elements involved. However, the number of the elements lost in this way was never higher than a few units per entire wafer. This loss can therefore be disregarded in comparison with the far higher loss due to the sawing process, which is the object of next section.

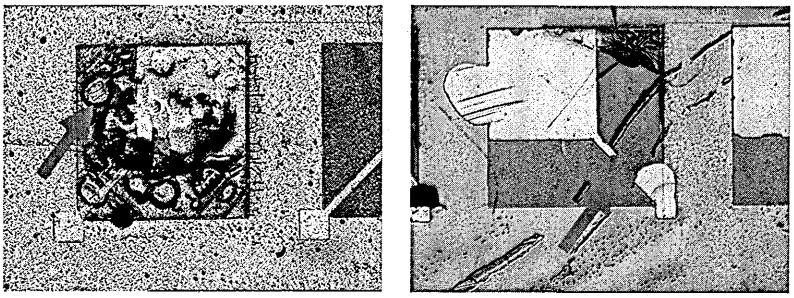


Figure 8.3 Examples of faulty elements after a lift off that showed low performance. Left: incomplete elimination of Pt, leading to bad PZT crystallisation; right: poor Au elimination resulting in disconnection between element and bonding pad.

8.1.2 The etching of the spiral bridges within the overall microfabrication process

The sequence of operations determines the survival rates of the membranes. First, it is crucial to decide whether the suspended system must be etched into the PZT layer before DRIE or micromachined on the membranes after DRIE. The use of a backing wafer is required when etching through-the-wafer cavities. This backing wafer needs to be temporarily attached to the device wafer using vacuum grease or photoresist. The former offers the best performance. Photoresist is difficult to eliminate afterwards. If DRIE is performed after membrane micromachining, then most suspended structures are likely to disintegrate during the separation procedure. Indeed, they could not stand the stress the separation of the backing wafer from the device wafer entails. Therefore, it is necessary to postpone the pattering of microbridges: suspended features are etched directly on the membranes resulting after through-the-wafer DRIE. (An alternative solution is proposed in figure 8.4 *D* and in the future work section.)

Subsequently, one has to choose whether the membranes have to be etched before or after the wafer is sawed. (Sawing is required to allow separation of the individual arrays.) In this case a multiple choice is available, as reported schematically in figure 8.4. Each route presents its own advantages and problems. A survey is presented in table 8.1.

That the breakdown of membranes is intrinsically triggered by the sawing process is demonstrated not only by the improved outcome in presence of a protective photoresist layer, but also by the particular configuration of blown membranes, which tend to cluster toward the outer boundaries of the arrays (see picture 8.5). Although it has not been tried, route *D* seems very promising, in particular for the possibility of performing DRIE on individual arrays, which can undergo subsequently different cycles. In this way up to 45 working arrays for each device wafer are potentially achievable, each with a different concentrator profile. The great potentiality offered by this route will be detailed in full in the future work section. Finally, patterning the spirals on each individual array after sawing represents a highly impractical choice. A single array does not contain enough alignment marks to allow individual alignment.

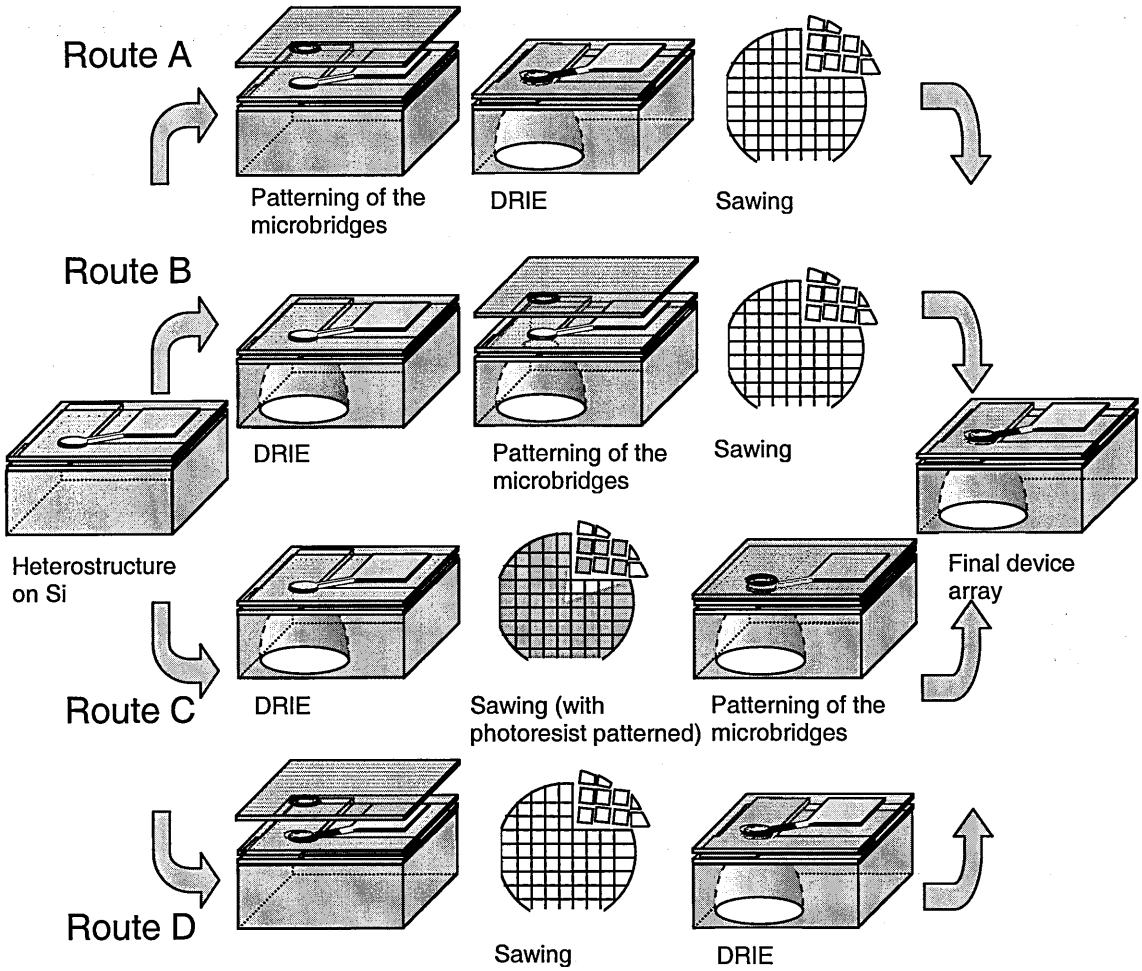


Figure 8.4 Flow sheet comparing the possible sequences of microfabrication procedures leading to arrays of sensing element s with concentrators and spiral micro-bridges

Finally, part of the elements may be lost due to the long etching process. In fact, due to problems inherent to the photolithographic process (e.g. presence of striations), which may become prominent for thick photoresist, local variations in photoresist thickness may be induced. Areas with thinner photoresist are etched deeper than the rest of the wafer. All the arrays contained in these areas will be lost. An example of a large area completely etched on a wafer (induced by an original striation in the photoresist) is showed in figure 8.6. In general, up to 5 – 6 arrays each wafer may be lost in this way.

8.1.3 Problems of dimension control in the microfabrication process

The results obtained in the early trials showed that the dimension (and relative shape) of the concentrators might vary largely across the wafer or even the single array. (The statistical analysis is reported in detail in appendix G). The pictures of figure 8.7*a* to *d* display the problems caused by this variation, in a pictorial way. From *a* to *c*, as the cavity becomes smaller there is no longer space for the microbridges. In *c* the membrane is effectively attached to the rim of the cavity. It is therefore chiefly

important to control the variance in the dimension in order to enhance the performance of the device and improve reproducibility.

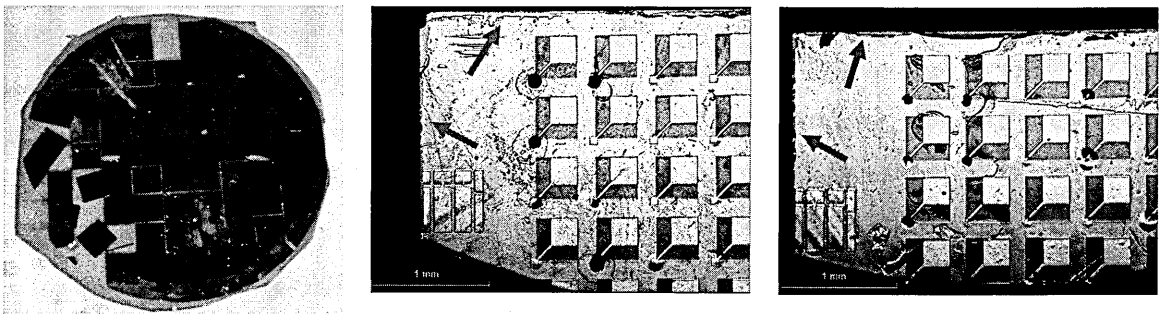


Figure 8.5 Clusters of blown membranes near the edges of sawed arrays (a sawed wafer is pictured at the extreme left; sawed sides are indicated by the grey arrows).

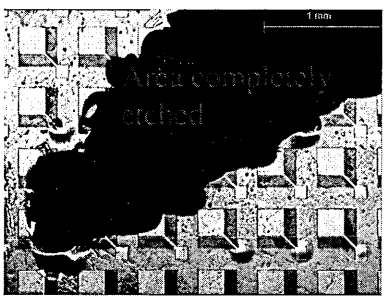
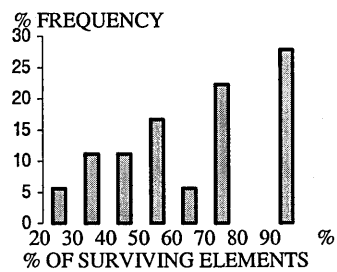
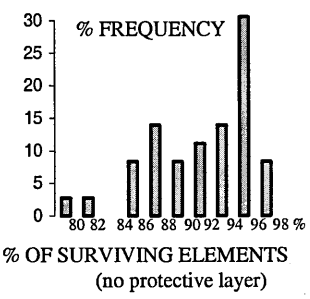


Figure 8.6 Loss of great part of an array due to overetching.

The problem of the etch stop is also strictly dependent on the variance associated with the dimension of the collectors. Due to the inherent variance of the dimensions within a wafer, it is not useful to establish a fixed etch time. On the contrary, the etch has to be stopped when an acceptable average dimension is reached. In this case, one has to check frequently the dimensions of the cavities at the end of the etching cycle (i.e. after 3 and a half hours) so that the process can be controlled within a range of a few microns. However, to compute the average, one has first to build a sensible statistical analysis of the dimensions distribution by sampling many cavities across wafer surface. This process becomes long and scarcely practicable. The reproducibility of the process decreases dramatically. If this method had to be used for production, a more economic way of control the etching outcome should be found. The lack of uniformity in etch rate across wafer area may lead not only to variation in the dimensions and shapes of the collector cavities, but even to the loss of part of the wafer. A dramatic example is showed in figure 8.8. The lack of uniformity, leading to overetching of three quarters of the wafer can be easily observed while the other quarter still retains the full SiO_2 mask.

(*)	Advantages	Drawbacks	Experimental Outcome (survival rate)
A	1 – Wafer easy to handle during photolithography 2 - smaller misalignment	1 - The spirals would break during backing wafer bonding, DRIE or the subsequent separation	Not tried, but almost zero survival rate expected
B	1 - Photolithography and RIE occur in sequence (i.e. less damage to the PR pattern) 2 – an entire wafer undergoes RIE at the same time: time saving and lower cost	1 - Wafer difficult to handle: needs another backing wafer for photolithography 2 - Large misalignment due to difficulty in wafer handling 3 - Fragility of membranes during sawing: a protective coating is needed	65.4 % using a protective coating, zero expected without protective coating 
C	1 - The membranes are far more robust if not etched, furthermore the photoresist layer can protect the membranes 2 – Both arrays with full and etched membrane can be produced from the same device wafer	1 - Wafer difficult to handle: needs another backing wafer for photolithography 2 - Large misalignment due to difficulty in wafer handling 3 – The PR pattern can be damaged during sawing due to the water jet and this, added to the misalignment can worsen the pattern fidelity transfer 4 – The arrays have to be handled individually during RIE	- 92.3 % without protective coating - 99.8 % with the photoresist mask 
D (**)	1 – Eliminates the above problems of misalignment 2 – The arrays can undergo different DRIE cycles allowing a very large number of experimental trials with final working device for each wafer 3 – Similarly, both arrays with full and etched membrane can be produced from the same device wafer	1 – A thicker Au layer has to be produced. If the layer is not enough, a photoresist mask can be re-aligned to the gold pattern, but in this case, the misalignment problems would remain 2 - The arrays have to be handled individually during both DRIE and RIE	Not tried, but expected 100% because the full wafer is etched before micromachining

(*) Route: with reference to figure 8.4
(**) see section *"Future Work"*

Table 8.1 Details & comment on the possible routes of device microfabrication (choice of the order of operations: *wafer sawing – microbridges fabrication*)

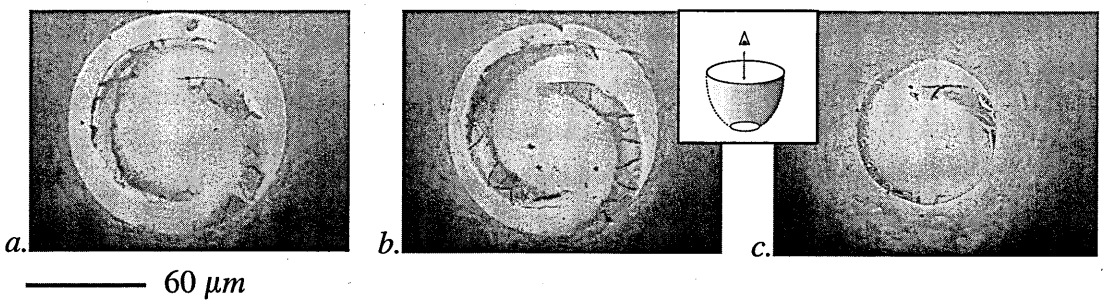


Figure 8.7 **Series of optical microphotographs revealing the effect of the variation in the cavity dimensions across a single array.**

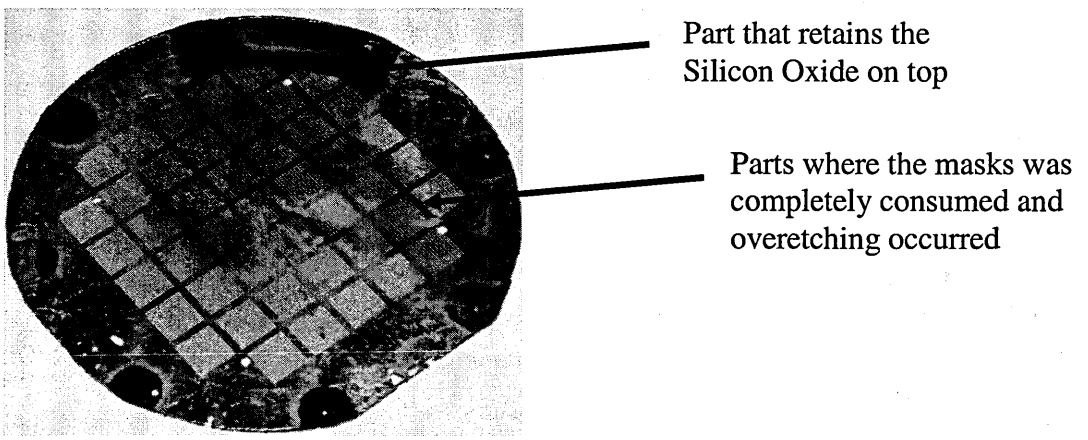


Figure 8.8 **Macroscopic effects of the lack of uniformity in etch rate / selectivity during etching at the wafer scale level**

Sample			PZTDEV 4	PZTDEV 5	PZTDEV 6	TOPWAFER
Etch time			280	210	240	150
Cavity with original opening of 85 microns	Cavity TOP	μ	347	275	282	
		σ	13	8	8	
	Cavity BOTTOM	μ	106	126	118	
		σ	16	18	16	
Cavity with original opening of 120 microns	Cavity TOP	μ				240
		σ				11
	Cavity BOTTOM	μ				411
		σ				8

Table 8.2 **Results of the statistical analysis of cavity dimension for some samples representing device prototypes**

The relative histograms are reported in appendix G. The statistical data are reported in table 8.2. Notice that, also in this case the top membranes are affected by a smaller standard deviation than the bottom membranes. (The same was found for earlier trials, as reported in section 6.3.4 and appendix G.) Note also the large difference in the aspect ratio between the sample PZTDEV4 and the samples PZTDEV5 and PZTDEV6. For the former sample the bottom membrane is 10% smaller in average than the other samples

whilst the top membrane is about 25 % larger. Figures 8.9 *a* to *c* offer a pictorial interpretation of the role of variance in effecting the performance of the device: they compare an exemplary type of microbridge design with the possible dimensions of the bottom membranes in the samples analysed in table 8.2. Finally, the effect of dimension variation on the overlapping between the top and bottom wafer is illustrated in figure 8.10.

Notice that, in figure 8.7*c*, the diameter almost coincides with the $\mu - 3\sigma$ case of figure 8.9*b* or *c*. In these schemes we can see what happens when the dimensions of the exit apertures of the collector are smaller than the average: the length of the thermal path gets progressively shorter so that the losses increase linearly. Conversely, when the concentrator entry aperture becomes larger, the rays falling onto the PZT area without gold electrode are lost. These larger concentrators may be thought of as the enlarged concentrators (of section 5.1, figure 5.1), after further enlargement.

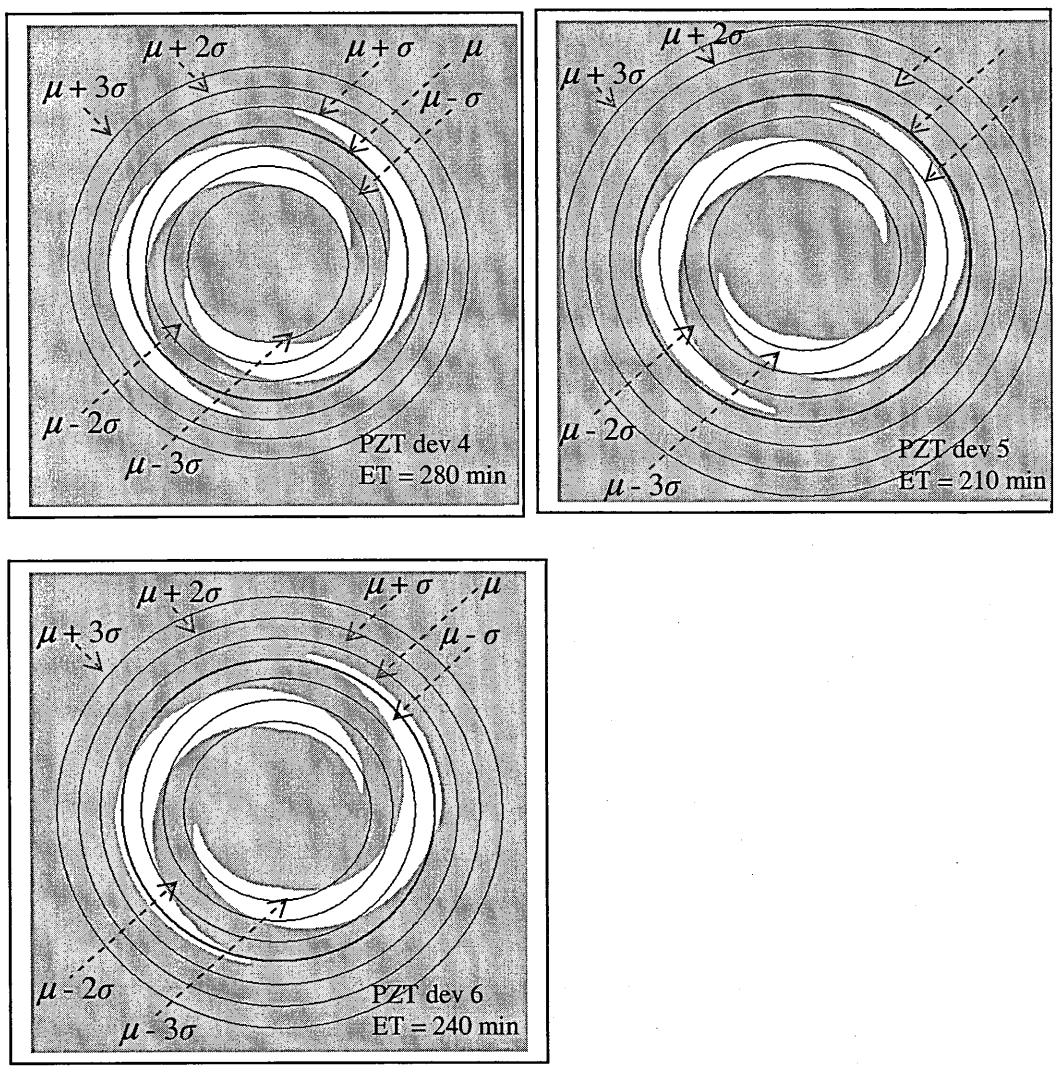


Figure 8.9 Comparison between the geometry of a microbridge set up and the possible dimensions of bottom membranes for the samples of table 8.2

In both cases, anytime the dimensions of the cavities deviate from the average, a concentrator profile different from the modelled one is produced. Such a collector would show a concentration ratio different from that calculated for the ideal profile (which was calculated using averaged dimensions). The actual distribution of dimensions should be taken into account when attempting to model the performance of the IR sensor. However, there are two practical reasons why this was not accomplished. Firstly, as reported in section 6.3.4, it was not feasible to develop a statistical analysis of the true shape of the profiles because they are complex curves that cannot be directly described using simple functions. Furthermore, the method of the replicas (used to assess the true profile of a cavity, i.e. its major cross section and detailed in section 4.3.5) could not possibly be applied to more than 5 – 10 cavities per wafer because of the laborious method involved. Secondly, since there was not enough time to develop an automatic procedure for computing the performance by ray tracing but, on the contrary, the performance was assessed individually for all the profiles (using a ray tracing procedure), it was not conceivable to analyze hundreds of cavities in order to assess a statistical analysis of performance (as a function of the variation in cavity dimensions). For these reasons, the actual distribution was not taken into account and only the averages were used for the modelling of the device.

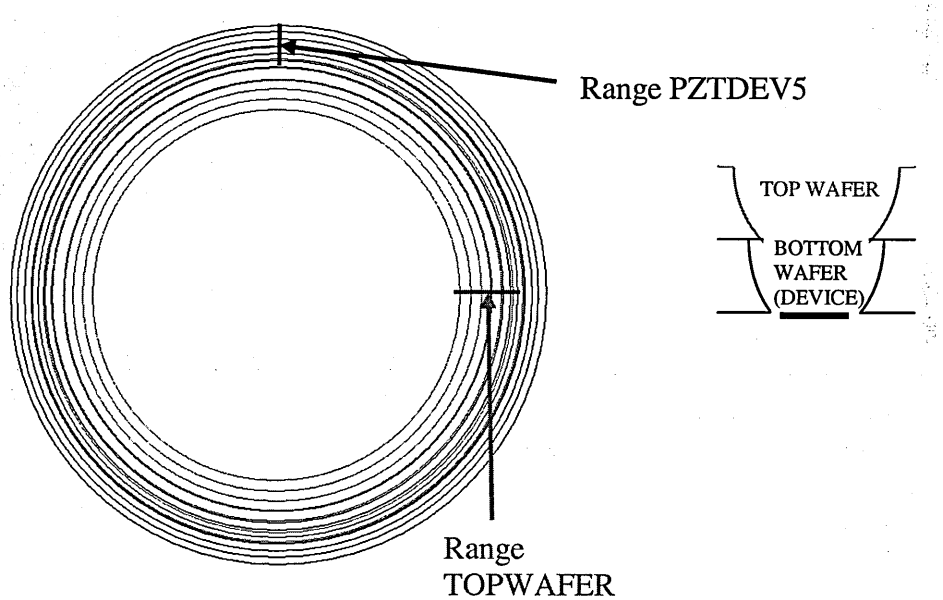


Figure 8.10 Comparison between the dimensions of the entry aperture (top membrane) of the cavities of the sample PZTDEV5 and the dimensions of the exit aperture (bottom membrane) of the sample TOPWAFER

However, there is an important fact that needs to be stressed: if the values of table 8.2 are compared with the values obtained in the early trials (table 6.2 of section 6.3.3), it can be observed that the dimensions distributions gather around markedly different averages. In particular, for the cavity of original aperture of 86 microns in diameter, the ratio between the top and bottom membrane was 2.83. Two samples analysed (PZTDEV5 and PZTDEV6) showed a markedly higher aspect ratio: the ratio between top and bottom membranes being respectively equal to 2.18 and 2.39. The final

prototype produced developed a concentrators shape ~ 18% narrower than predicted, and this will be taken into account in the modelling of device performance. For this reason, the actual dimensions obtained in samples PZTDEVICE5, PZTDEVICE6 and, finally, DEVICETOP (i.e. the top wafer) will be used for simulating the expected performance of the concentrators.

8.1.4 Full view of the final prototype

An individual element from a final prototype array is shown in figure 8.11. The picture is taken from the sample PZTDEVICE6. The array was cleaved so that both a cross section of the collector and the whole PZT-based standing membrane can be observed. An isolated element with a single bridge structure is clearly visible. Notice that the structure was not micromachined through the whole heterostructure: the RIE patterning stopped at the TiO_x/SiO_x membrane. Some of the findings reported in earlier sections can be observed here. Notice the slight tapering of the sidewalls of the microbridge, as observed in section 7.3. (Compare with figure 7.13.) Similarly, the etching was preferential along the microcracks originally present on the PZT layer, which demonstrates that probably the PZT layer did not have an optimal structure and quality.

The patterns of roughness characteristic of the etching in absence of passivation are clearly observed in the main picture. Notice the similarity between these patterns and those exhibited in the replicas of figure 6.44. Qualitatively, the sidewalls here seem rougher than those obtained for earlier samples (see for example figure 6.50-*left*). This can be observed in particular by comparing the two pictures in the insets (reporting the roughness of the steps onto the sidewalls and the top of the feature, near to the membrane and at the edges of the zone not hit by ion or radical flux) and the pictures of figure 6.45.

A quantitative analysis of surface roughness is reported in figures 8.12. This analysis allows the comparison between the roughness of these cavities and the roughness of the cavities previously produced (figure 6.51 – 6.53). The same patterns of roughness seem to be common to all the diagrams. All curves present peaks with similar slope. The top membrane of the sample PZTDEVICE6 (curves of top diagram of figure 8.12) shows the largest roughness. (This demonstrates that the sidewalls are roughest in the areas just underneath the mask. i.e. the areas not reached by ionic or radical flux.) Steps of more than 3 - 4 μm in height abound in this sample. A slight number of smaller peaks appear. It is still possible to observe a few steps of height below 500 nm. They appear somewhere superimposed onto the larger peaks. This roughness is generally higher than those observed for the samples of section 6.3 (figures 6.51 – 6.53). This could be due to the highest etching time. (The qualitative model presented in chapter 9 will attempt an explanation for the increase of surface roughness with etch time.) The bottom membranes of the wafer DEVICETOP show generally lower "roughness": the majority of peaks gather in the range 100 – 500 nm or 2 – 5 μm.

If these results represent a sensible measurement, then the roughness within a cavity is developed in a large range from hundreds of nanometres up to a few microns. Roughness reaches the minimum at the bottom of the cavity. Here, a vast number of small ripples of height around 300 nm can be found. These features are not supposed to

scatter the IR radiation at the wavelength of interest since the roughness is below the scattering threshold. (A threshold of 1 to 1.5 μm was calculated in section 6.2.6 applying the theory of Raleigh.) Approaching the top of the cavity, an increasing number of larger cusps appear, which are big enough to cause scattering. The roughness is expected to increase steadily, until it reaches the maximum just underneath the mask. Here the ripples are well within the range to cause scattering. However, as underlined in section 6.3.2, these ripples have all similar shape and smooth sidewalls, therefore they are expected to scatter the light in an "ordered" way, just like an optical reticule. Qualitatively, one can expect losses lower than those observed after scattering from a "randomly" rough surface.

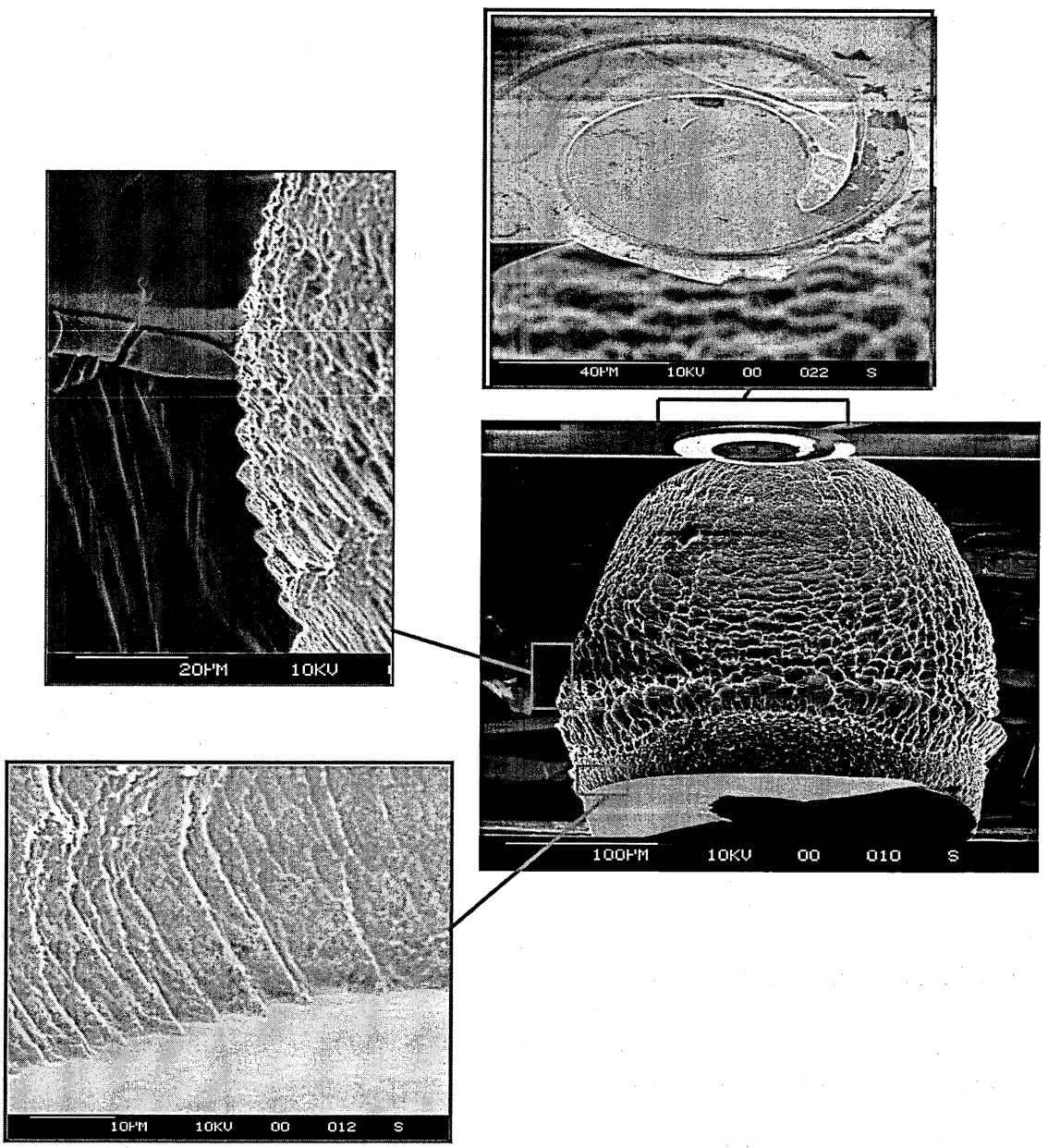


Figure 8.11 SEM View of an element of a final prototype array (sample: PZTDEV6). Insets: close-up pictures demonstrating particular features of the microstructure (see text for details and comment)

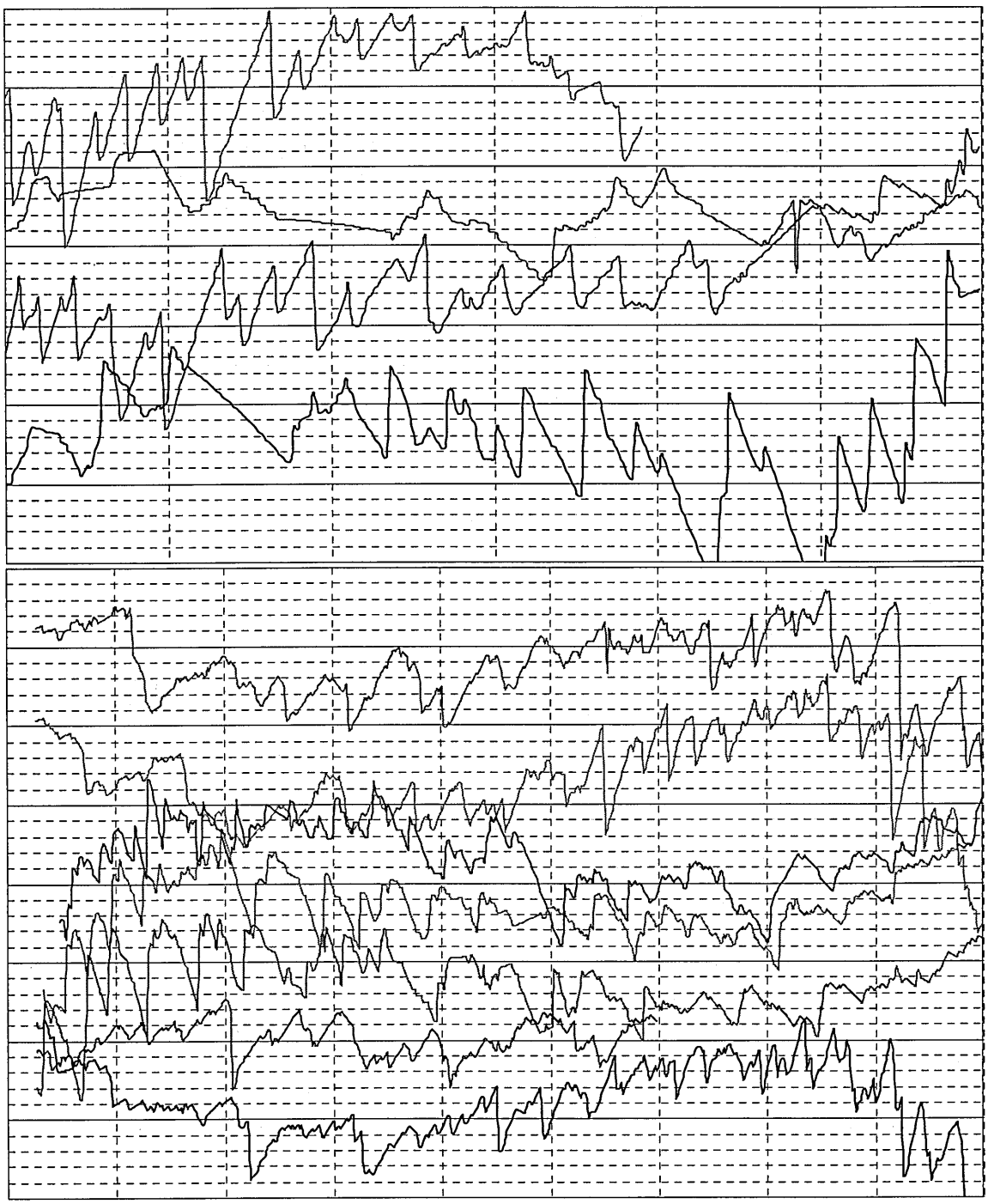


Figure 8.12 **Boundary of the membranes filtered from the "waviness" of overall membrane shape in order to highlight the "noise" affecting the boundary, which might be a concrete representation of the roughness of the cavity. TOP) top cavity of the bottom (device) wafer, for the sample PZTDEVICE6, BOTTOM) bottom cavity for the sample to be used as a top-wafer (PZTDEVICETOP). Each vertical division corresponds to one micron, each horizontal division corresponds to 20 microns.**

8.1 Simulation of device response

The present section introduces the simulation of the performance of the device. Due to the lack of time (a large part of the research was devoted to the empirical trials) and the unavailability of sophisticated computational tools, the simulation was carried out in two dimensions and only for simple cases. The simulation uses values calculated through the whole thesis. It will be normal, therefore to find references to those parts in this section. However, in order to provide a swift reading of this part, the values used will be repeated where possible.

The modelling of system performance has been an important part of this research. The rough analysis of thermal losses from individual elements justified the choice of the spiral design for the suspended structure (PZT-based microbridge) in section 7.1. The subsequent detailed modelling allowed the optimisation, in terms of shape design and etching parameters, of the spiral microbridges.

On the other side, the calculation of the collection efficiency for given concentrating cavities contours was limited to ideal 2 – d cases, where the sidewalls have 100 % reflectance and the contour can be analytically defined by a simple function. (The calculations were carried out in chapter 5, based on the literature survey of section 3.1.) Under these assumptions, the treatment allowed the assessment of the optical performance of 2 – d CPCs and "V" collectors, as a function of the radiation flux distribution. Improving the theoretical model beyond this level of approximation would have involved a large upgrade in the calculations, entailing larger resources of cost and time. This could not be done without interfering with the time schedule for the production of an actual working prototype. (The opportunity of improving and refining the theoretical treatment are discussed in the future work section.)

Due to the highly ideal cases assessed, the estimates of chapter 5 could hardly be useful at a later time when the merits of experimentally obtained complex contours or the role of surface roughness had to be assessed (e.g. sections 6.2.6 and 6.3.2). Nevertheless, the calculations developed in chapter 5 were useful in many ways. Firstly, they clarified the basic physics of the process (e.g. they allowed establishing the upper limits of power collection and the general effect of CPC enlargement). Secondly, they provided the fundamental idea of testing the devices by using collimated beams. The testing set up was described in the experimental part, in section 4.1.3. The technique will be detailed in sections 8.2.3 and 8.3.2. Finally, those calculations represent the basis upon which more refined calculations could be accomplished.

In fact, a potential advanced model would be able to assess the performance of experimental profiles, which can be described only numerically (such as the numerical cross sections reported in figures 6.22, 6.24, 6.26, 6.28 to 6.30, and 6.48). Such a model could be built to process 3 – d contours and address the problems of scattering and absorption of radiation from non-ideal Si (or Au coated-Si) surfaces. A refined analysis of this kind would require programs more elaborate than the simple procedures employed in this research or the use of commercial software packages (such as OptiCAD ® [*www.opticad.com*]). However, such a model would exploit the same principles and algorithms already presented and developed in chapter 5 and relative

appendix. An outline of how such a model could be useful in optimising the prototype fabrication is presented in the future work section.

Given the various arguments reported above, it was important to advance the calculations for modelling device performance up to the level of computing the responsivity and detectivity of individual elements of IR sensors. (Responsivity and detectivity were defined in the background part, in section 2.3.) The performance of hypothetical 2 – d elliptical collectors, built using the average dimensions calculated in section 8.1.3 is computed in section 8.2.1. Section 8.2.2 deals with the core of the simulation of device performance. Combining the calculations of heat losses (section 7.1) with the results of the ray-tracing procedure (chapter 5 and section 8.3.1) estimates for $\mathcal{R}_I$, $\mathcal{R}_V$ and $\mathcal{D}$ can be achieved (thus demonstrating the improvement in performance for the upgraded array). Finally, the role of flux distribution will be discussed in terms of beam collimation in section 8.2.3.

8.2.1 Performance of 2 – d elliptical collectors

This section reports the results of the calculation of collection efficiency from elliptical collectors. In section 6.2.3 (figure 6.26) it was shown how a good approximation of the contours obtained by isotropic etching is demonstrated by a hemi-ellipse with one axis coinciding with the diameter of the aperture and the other semi-axis equal to the maximum depth of the cavity. The collectors analysed here are modelled on the dimensions obtained from statistical data analysis of the experimental results (table 8.2, excluding sample PZTDEVICE4). This represents a higher degree of approximation to the real profile than using an ideal CPC or a V collector. A certain discrepancy still exists in that the actual shape of collecting cavities obtained by etching in pure SF_6 may deviate considerably from the simple elliptical contour (as demonstrated in figure 3.26). Furthermore, the actual 3 – d shape cannot be thought of as originated by a rotation of the major cross section around its axis (i.e. it has no cylindrical symmetry). On the contrary, the actual 3 – d shape is best represented by a dome with an almost squared base. The cavity shows a four-fold axis of symmetry. This was clearly showed in section 6.3.6 and demonstrated in various pictures of original cavities and rubber replicas. Finally, the problems of surface roughness and radiation absorption are not addressed: these ideal elliptical collectors are assumed to have 100% reflectance.

Since the contours are assumed to be ideal (i.e. the surface roughness and emissivity are not taken into account), the simple ray-tracing analysis may be applied. The transmittance is calculated according to the theory elaborated in section 5.3. The acceptance of direct rays (i.e. the beam that passes through the entry aperture directly without hitting any reflector) is assessed analytically. The acceptance from the sidewalls is assessed by ray tracing. All the details of the calculation are reported in appendix H.

The results and comments are reported in the following. However, it is important to stress that there is a crucial difference between the previous types of profiles analysed in chapter 5 and the collectors assessed here. In the latter, the top ellipse shadows the contours of the bottom ellipse partially (not only the entry aperture). In other words, the collector profile contains a concavity, i.e. a centre of scattering that prevents part of the reflected rays from reaching the exit aperture. The presence of a shadowing effect (i.e. a

centre of scattering in the sidewalls) changes completely the nature of the collector and originates profound differences in comparison with all the collectors analysed previously. (See the detailed calculations in appendix H.)

The transmittance plots for the elliptical collectors are reported in figures 8.13 to 8.16. It is interesting to compare these results with those obtained from the previous elliptical cavities analysed (figures 6.55 to 6.58 of section 6.3.5). First, notice that the increase in aspect ratio leads to an increase in transmittance. The single-stage elliptical collector of figure 8.14, in fact, (with a top aperture of 278 microns) demonstrates a transmittance up to 97% (30% more than the elliptical collector of figure 6.55, with an entry aperture of 336 microns). Conversely, the decrease in acceptance angle is slighter (a mere 5 degrees). In section 6.3.5, it was shown that both the single stage and double stage collectors demonstrated a similar trend in transmittance, with almost the same maximum transmittance and acceptance angle. It is not the case now, because of the shadowing effect. Notice that, this time, the two-stages elliptical concentrator (figure 8.15) demonstrated a dramatic decrease in transmittance at angles below 20 degrees. In comparison with figure 6.57, the upper lobe of the curve is missing: a significant decrease in slope occurs and the transmittance then raises only to 60% of the maximum achieved by the single stage collector.

Both in the single-stage and the two-stages cases, the elimination of the outer rim of the active areas (in order to produce the suspended structure) has a dramatic effect on transmittance (similarly to what occurred for the elliptical collectors of section 6.3.5, see figures 6.56 and 6.58). The transmittance falls to less than half than the original value at most incidence angles. Conversely, the decrease in the acceptance angle is slight (a few degrees). A similar decrease in transmittance (at low incidence angles) with suspension was common to all types of profiles analysed, even the theoretical ones (see e.g. figures 5.8 5.11, 5.13*a* and 5.13*b* of chapter 5). However, it has to be remarked that the extent of the inner active segment (in 2 – d) corresponds to one half of the original extent of the exit aperture, whereas the reduction of the available collection extent was limited to one third in the profiles derived from the 2 – d CPC and V collectors.

In figure 8.17 the ratio $P / P_{a'}$ is plotted for the systems analysed as a function of the cut-off angle of the incoming flux distribution. This diagram can be compared with the diagrams of figure 6.59. Also in this case, the transmittance decreases only slightly below incidence angles of 20 degrees. For example, for both curves relative to the full systems, the transmittance in the range 0 – 20 degrees decreases by a mere 10%. The major feature that can be observed in figure 8.17 is that in the curve representing the effective power for the full collector (top ellipse + bottom ellipse) lies always below the line of the effective power for the single bottom ellipse. This means that for the collector without microbridges (i.e. with a full active area) the coupling of an upper ellipse actually reduces the total power transmitted, although increasing the width of the entry aperture by 47%. In particular, for a cut-off angle of 14.48 degrees, the effective power is reduced by 10%. In other words, a longer collector with a larger entry aperture entails an actual loss of collection efficiency. This is believed to be due to the effect of shadowing (i.e. the introduction of a centre of scattering), which prevails over the increase in efficiency provided by the larger entry aperture. Notice also that, probably

for the same reason, the effective power for the two-stages collector lies far below the CPC ideal line even for almost isotropic flux distributions. It is the only instance, for all the profile analysed, in which the curve does not reach the effective power of the CPC beyond a threshold incidence angle. This demonstrates that the presence of a convexity, i.e. a centre of scattering, changes the nature of the collector in a fundamental way. No such deviation was found for the collectors of figure 6.59 (where no shadowing occurred). (This deviation, however, remains in the suspended version of the two-stages ellipse because, although no shadowing occurs for the direct rays, part of the reflected rays are still scattered by the bottom rim of the upper ellipse.)

The theoretical results are summarised in table 8.3. Comparing the performance of these collectors with the performance of the other elliptical collectors (presented in section 6.3, table 6.4), the major feature observed is the increase in effective power collected with suspension for the two-stage system. This was never found previously and it must be caused by the reduction of the extent of scattering (see discussion above). Other usual trends are confirmed, such as the halving of the transmittance with suspension and the converse increase in energy densification.

To conclude, one can affirm that the philosophy of building the concentrator that most approximated the curve of the CPC was, in this case, misleading. (Saving all the differences between the ideal systems analysed here and the actual cavities and devices experimentally produced.) Indeed, by prolonging the length of the CPC we obtain either a very small gain or even a loss in the total power transmitted. However, one has to consider that the profiles finally obtained in the device samples were unexpectedly quite different from the profiles previously obtained in section 6.3. An alternative approach to the approximation to the CPC contour is suggested in the future work section.

Type of collector	T_{tot}	C	$P / P_{a'}(\omega = 14.48)$ (**)
Single ellipse	0.70	1.61	2.15
Single ellipse suspended	0.39	1.78	2.06
Two-stages ellipse	0.40	1.37	1.94
Two-stages ellipse suspended	0.25	1.71	2.18

(**) Notice that the total power collected is compared to the total power that would be collected by a 2 – d element of extent equal to the exit aperture of the collector (but in the absence of the collector itself). The calculations for the suspended collectors entails dividing by the power that would be collected by the active entry (in this case, an extent of 60 μm and not 120

Table 8.3 The results for the computation of expected performance for four types of 2 – d elliptical collectors

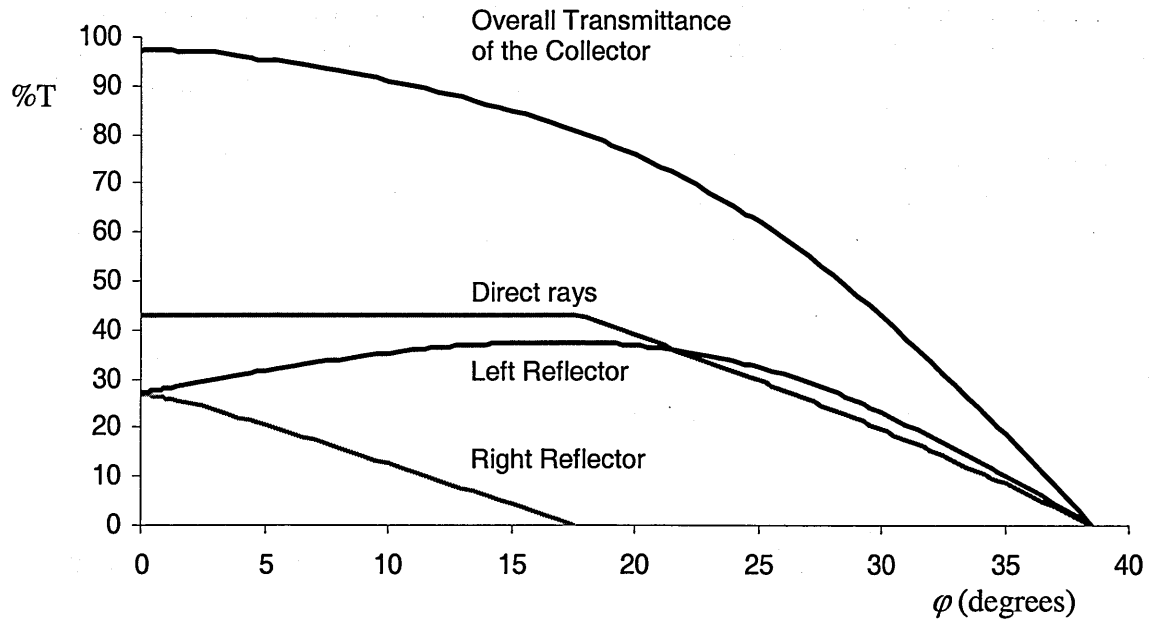


Figure 8.13 Transmittance plot for an elliptical 2 – d concentrator with entry aperture of 278 microns in extent and exit aperture of 120 microns

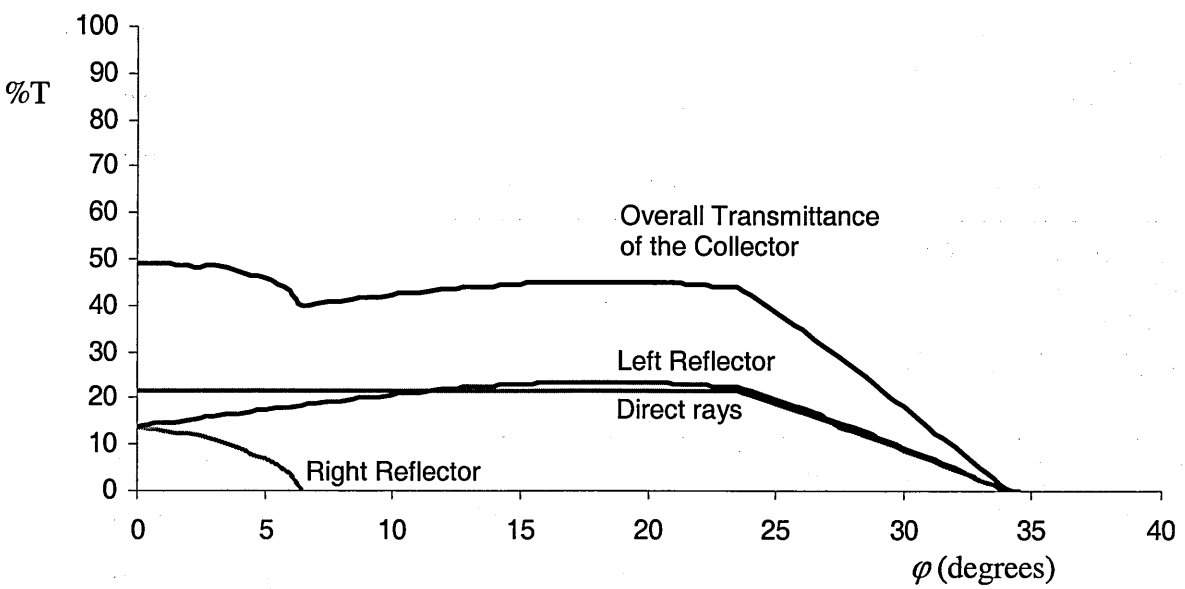


Figure 8.14 Transmittance plot for an elliptical 2 – d concentrator with entry aperture of 278 microns in extent and exit aperture of 120 microns after elimination of the outer structure in order to create an inner active area of 60 microns in extent

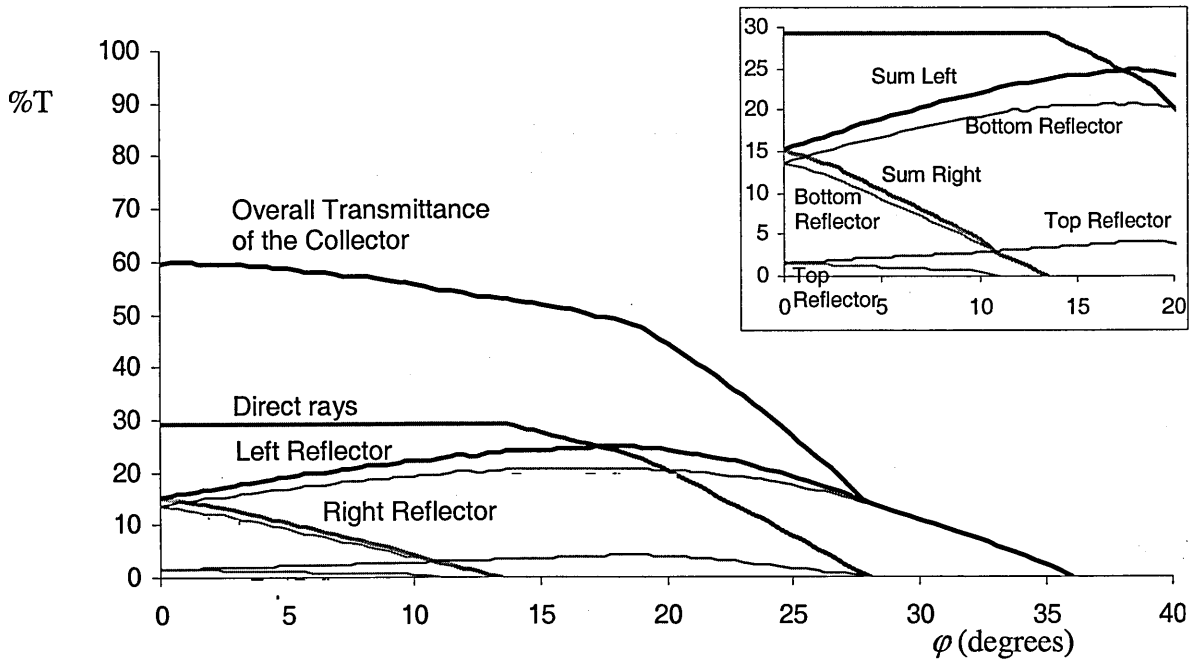


Figure 8.15 **Transmittance plot for a 2 – d concentrator built by coupling two elliptical concentrators. The top cavity has an entry of 410 microns in extent and an exit of 240 microns. The bottom concentrator has an entry aperture of 278 microns in extent and exit aperture of 120 microns.**

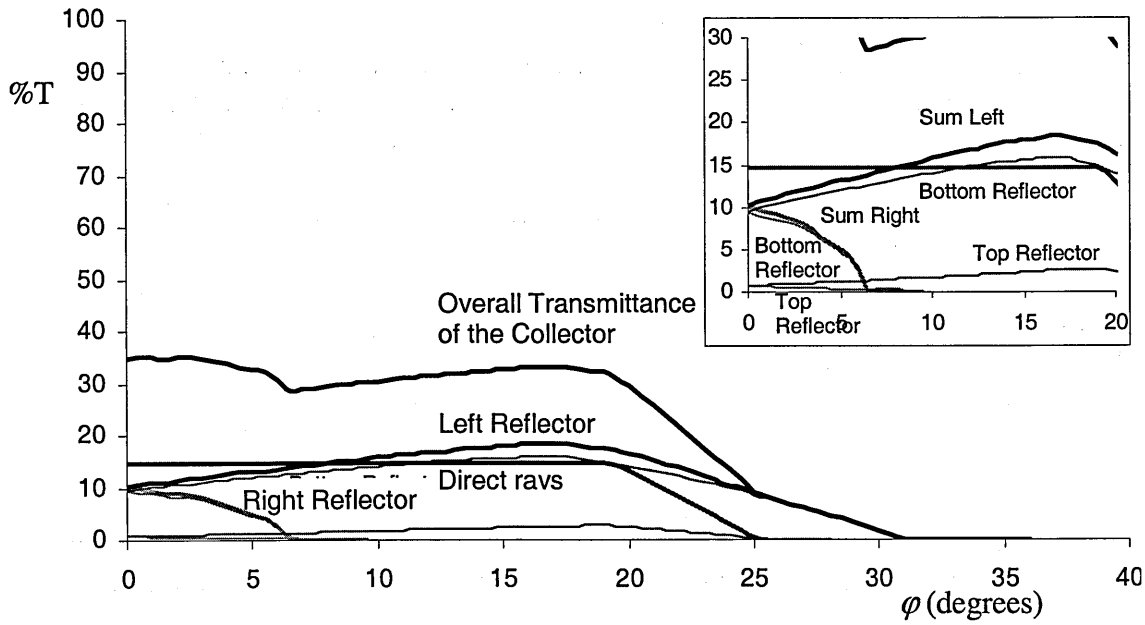


Figure 8.16 **Transmittance plot for the elliptical 2 – d concentrator of figure 8.15 after elimination of the outer structure in order to create an inner active area of 60 microns in extent**

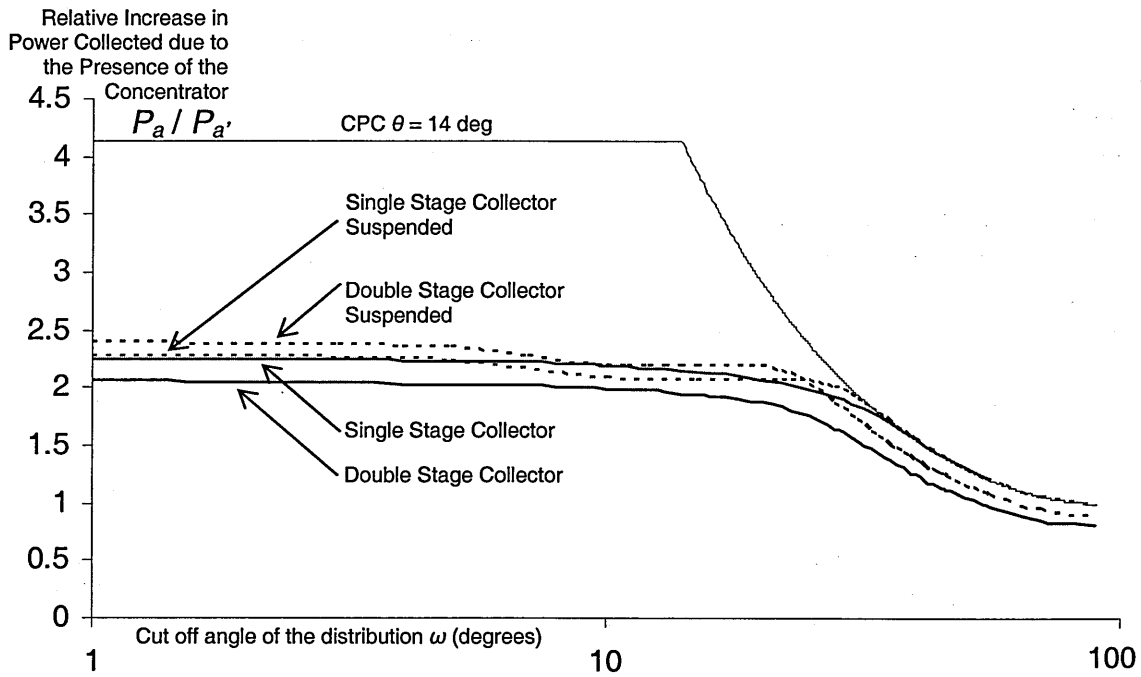


Figure 8.17 Effective concentration power for elliptical concentrators profiles as a function of the cut-off angle of the radiant power distribution. The incoming flux is assumed to be constant for incidence angle below the cut off angle and zero above (square wave).

It is finally interesting to compare the performance obtained from the elliptical concentrators with the performance obtained by a V collector that represents a cross section of a pyramidal collector of the kind obtained by anisotropic wet etching [*Madou, 2003, Chapter 4*]. Concentrators of this kind were produced and incorporated into the first version of the device. (The original design of the device was described in the background part and presented in figure 2.12 [*Shaw et al., 2004*].) The acceptance of a "V" collector was assessed by using ray-tracing. (Williamson's method was employed, as reported in appendix E-6 [*Williamson, 1952*].) The geometry of the wet-etched pit was the following: entry aperture = 475 μm, exit aperture = 107 μm and wafer thickness = 260 μm. The ray-tracing method demonstrated that rays enter either directly or after being reflected once from a sidewall. Direct rays are accepted up to 48.22 degrees. On the contrary, reflected rays are accepted only up to 35.28 degrees from the right reflector and 19.48 degrees from the left reflector. The resulting transmittance is reported as a function of the incidence angle in the diagram of figure 8.18.

The plot shows that more than half the radiation entering the concentrator is lost at any incidence angle, i.e. the collector never reaches 40% transmittance. In fact, the total transmittance is equal to a mere 0.30 and the concentration ratio is 1.34. Notice that this V concentrator has a very wide exit aperture and a large acceptance angle: most of the rays pass through without being reflected: hence its low collection efficiency. Finally, the effective power is constant at 1.66 up to ~ 25 degrees and then starts to decrease accordingly to the usual decrease already seen in the CPC. The elliptical collectors

presented above outperform the wet etching pit in the ideal 2 – d case. However, in the real case, it is relatively easy to obtain cavities with very smooth (even atomically smooth) sidewalls by wet etching, whereas the elliptical cavities showed different patterns of roughness difficult to eliminate. The 3 – d pyramidal collector has a well-defined four-fold symmetry, thus only a small area on each sidewall produces reflections that cross the exit aperture. (On the contrary, 3 – d cavities with cylindrical symmetry would develop an entire annular area producing effective reflections.) The properties and merit of the pyramidal collector are discussed in [*Whatmore et al., 2004*], where similar theoretical results are achieved using a completely different approach.

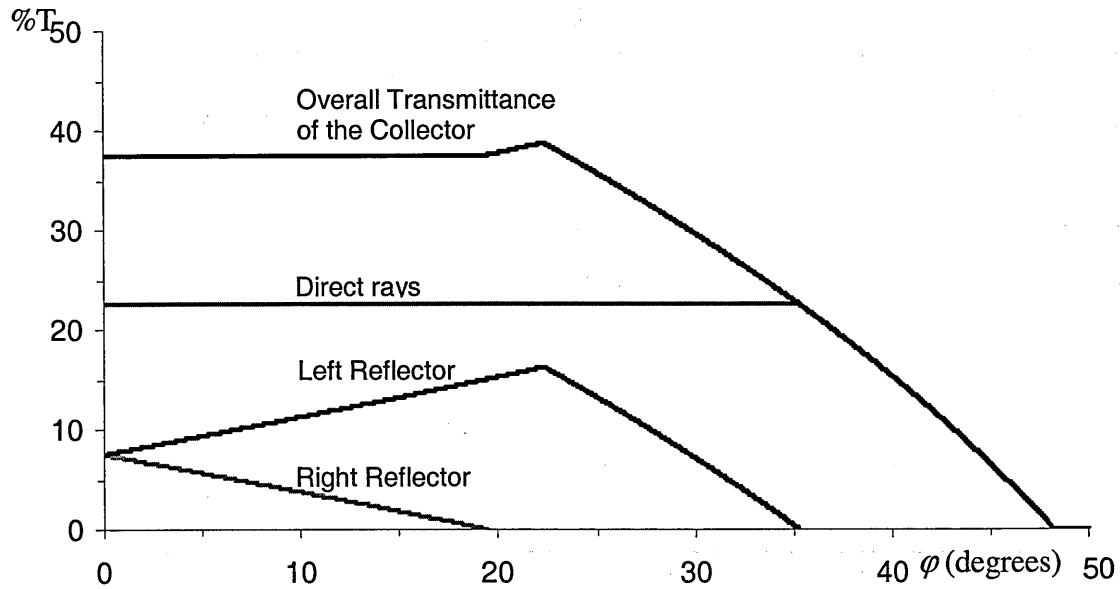


Figure 8.18 Transmittance plot for a 2 – d "V" concentrator which represents the cross section of a wet-etched pit. The cavity has an entry of 237.5 microns in extent and an exit of 53.5 microns. The length of the concentrator is 260 microns.

8.2.2 Simulation of single element performance: Responsivity and Detectivity

In this section the simulation of device performance is presented, based on the background theory reported in section 2.3 and the calculations carried out in chapter 5 and sections 7.1 and 8.2.1. The calculation is concerned with a single element only because the device was only tested one element at a time (following the technique detailed in the experimental part in section 4.1.3).
First, the responsivity of the single element is calculated according to the background theory reported in section 2.3. The intensity responsivity is given by equation 2.11, i.e.

$$\mathcal{R}_i = \frac{i_p}{P_0} = \frac{\eta p A \omega}{G\left(1+\tau_T^2\omega^2\right)^{1/2}} \qquad \text{(2.11rep).}$$

η, the emissivity of the element surface, is considered to be unitary, i.e. corresponding to 100 % IR absorption. This may be far from the true value, especially if no absorbing layer is deposited onto the element surface. However, equation 2.11 is used here to compare the relative performances of different types of device design and the true value

of η can be disregarded. p, the pyroelectric coefficient is assumed to be equal to $3.5 \cdot 10^{-4}$ C $m^{-2}K^{-1}$ [*Kang et al., 1998*]. This pyroelectric coefficient corresponds to a good pyroelectric layer. In practice, the quality of the PZT layer may not be that good in the prototypes produced during this research. (A PZT film with poor performance was shown in figure 8.2.) A represents the area of the individual element. For a full membrane $A = 1.13$ X 10^{-8} m^2 whereas $A = 2.83 \cdot 10^{-9}$ m^2 for the suspended system (disregarding the microbridges and considering only the inner active area). τ_T is the thermal time constant. (It is given by H_m / G.) H_m identifies the thermal mass of the system. H_m is given by the sum of the thermal masses of all the layers:

$$H_m = \sum H_{m_i} = \sum V_i C_{V_i} = \sum A d_i C_{V_i} = \sum A d_i c \rho \qquad (8.1).$$

Here I represents the i^{th} layer, d the thickness, C_V the volume constant thermal capacity, c the specific heat and ρ the density of the layer. The values used for the determination of H_m are reported in table 8.4. Only the main layers composing the heterostructure were considered. The total thermal mass of the element is equal to $4.99 \cdot 10^{-8}$ J K^{-1} for the full membrane and $H_m = 1.25 \cdot 10^{-8}$ JK^{-1} for the suspended system (disregarding the microbridges and considering only the inner active area).

Material	Au	PZT	Pt	SiOx	Unit
d	$1.00 \cdot 10^{-7}$	$1.00 \cdot 10^{-6}$	$1.00 \cdot 10^{-7}$	$4.00 \cdot 10^{-7}$	m
c	$1.29 \cdot 10^{2}$ (a)		$1.33 \cdot 10^{2}$ (a)	$7.8 \cdot 10^{2}$ (b)	J Kg^{-1} K^{-1}
ρ	$1.93 \cdot 10^{4}$ (a)		$2.14 \cdot 10^{4}$ (a)	$2.18 \cdot 10^{3}$ (b)	Kg m^{-3}
C_v	$2.49 \cdot 10^{6}$ (d)	$3.20 \cdot 10^{6}$ (c)	$2.85 \cdot 10^{6}$ (d)	$1.70 \cdot 10^{6}$	J m^{-3} K^{-1}
$H_{m\,i}$	$7.04 \cdot 10^{-9}$	$9.05 \cdot 10^{-9}$	$8.05 \cdot 10^{-9}$	$1.92 \cdot 10^{-9}$	J K^{-1}

(a) [*Shackelford and Alexander, 2001*] (b) [*Wu et al., 1980*], (c) [*Kang et al., 1998*],
(d) Calculated from $C_v = c\,\rho$.

Table 8.4 Values for the calculation of the thermal mass of a single element of the pyroelectric IR sensing array

The term G represents the full losses from the element. This includes the following contributions:

1) The losses by radiation. (In section 7.1 it was demonstrated how these could be disregarded in comparison with other contributions.)
2) The conductive losses to the thermal background (G_T). (The G_T were calculated in table 7.4. Six types of arrays were designed: three with a single bridge and three with two bridges connecting the inner active area to the thermal background as in figure 7.4.)
3) The losses by conduction to the atmosphere from the two faces of the element (G_{air}). The conductivity of air at atmospheric pressure is very low (2.60×10^{-2} $Wm^{-1}K^{-1}$) leading to thermal conductivities of the order of 10^{-7} WK^{-1} (for kinetic conditions below the Knudsen regime). These losses are very small in comparison with the values of G_T and can be disregarded.

Only the losses due to conduction across the microbridges are used for the simulation. The values are reported in table 8.5 (see figure 7.4 for the graphical representation of the elements, relative to the indications reported in table 8.5). The G relative to the full membrane system is equal to 3.91×10^{-4} WK^{-1}.

ρ_A (increment) microns	Width of the bridge μm	*G* fully etched system (WK^{-1})	*G* partially etched system (WK^{-1})
25	12.5	$1.75 \cdot 10^{-6}$	$8.43 \cdot 10^{-6}$
30	15	$2.45 \cdot 10^{-6}$	$9.12 \cdot 10^{-6}$
35	17.5	$3.27 \cdot 10^{-6}$	$9.92 \cdot 10^{-6}$
45	22.5	$1.04 \cdot 10^{-5}$	$1.69 \cdot 10^{-5}$
60	30	$1.82 \cdot 10^{-5}$	$2.46 \cdot 10^{-5}$
75	37.5	$2.79 \cdot 10^{-5}$	$3.42 \cdot 10^{-5}$

Table 8.5 **Values for the calculation of the thermal losses of a single element of the pyroelectric IR sensing array** (refer to figure 3.4 for the system geometry)

The values of $\mathcal{R}_i$ are plotted in figure 8.19. In general, for frequencies below 100 Hz the structures suspended using a single bridge outperforms the structures with two bridges and the structures fully etched through show higher responsivity than their counterpart with full SiO_x/TiO_x membrane. However, the gain obtained from etching through the entire heterostructure is higher for the single-bridge systems (3 to 4.8 times) than for the double-bridge systems (1.2 to 1.6 times). The full-membrane element shows the lowest responsivity. Finally, the responsivity decreases as the width of the bridges increases. The trends highlighted in figure 8.19 are a direct consequence of the trends in the thermal losses. (The trends can be compared with the trends reported in figure 7.3.) Notice that, for frequencies above 100 Hz, the differences tend to disappear. This reflects the fact that, as the IR frequency increases, a smaller time elapses between a peak and a minimum and the role of the losses become less important. Conversely, other factors, such as the thermal mass, tend to prevail. This phenomenon was discussed in section 2.3. The classical theory of IR pyroelectric detection predicts that $\mathcal{R}_i$ increases with the frequency for $\omega << G_T/H_m$ and tends to a constant value equal to $\eta pA/H_m$ afterwards. It is possible to calculate the various G_T/H_m from tables 8.4 and 8.5 and verify that the findings of figure 8.19 effectively follow the classical theory. The value of $3.91 \cdot 10^{-4}$ A W^{-1} represents the upper responsivity limit for the suspended systems.

It is important to state the performance in terms of voltage responsivity (rather than current), since the apparatus for testing the detectors is built to detect a voltage signal, amplified by a FET. In order to evaluate the voltage responsivity, the admittance $|Z|$ of the equivalent circuit has to be introduced. The equivalent circuit of a single element detector was roughly depicted in figure 2.4. The array of 16 by 16 elements contains an additional row of compensation elements, which are shielded from IR radiation. N_C indicates the number of compensation elements connected to the circuit. The compensation elements are employed to filter the actual pyroelectric signal from the changes in current intensity due to the dependence of impedance on the temperature of the array.

The equivalent circuit relative to the device testing set up is drafted in figure 8.20. The sensing element generates an alternate current of intensity i_p. R_e and C_E represent the resistance and the capacitance of the single element respectively. The circuit of figure

8.20 is very similar to the circuit of figure 2.4 after the addition of the compensation circuit, in parallel and with a resistance equal to:

$$R_C = \frac{R_e}{N_C} \tag{8.2}$$

and a capacitance described by:

$$C_C = N_C C_E \tag{8.3}.$$

The circuit of figure 8.20 can be reduced to the circuit of figure 8.21. For such a circuit:

$$i'_p = i_p \frac{N_C}{N_C + 1} \tag{8.4},$$

and

$$C_p = \frac{N_C}{N_C + 1} C_E \tag{8.5}.$$

According to equation 2.12,

$$\mathcal{R}_V = |Z|\mathcal{R}_i = \mathcal{R}_i / |Y| \tag{8.6},$$

where

$$Y = \frac{1}{R_G} + i\omega(C_P + C_A) \tag{8.7},$$

C_A is the capacitance of the FET. C_A is assumed equal to $5.8 \cdot 10^{-12}$ farad. C_p is equal to:

$$C_p = \frac{N_C}{N_C + 1} \varepsilon\varepsilon_0 \frac{A}{d} \tag{8.8},$$

where d is the thickness of the PZT layer, A the area of the element and ε is the relative permittivity of the PZT layer. (ε was set to 260, a typical value; see e.g. table 2.1 or [*Zhang et al., 2001*]). The total resistance (element + compensation) R_G is given by the combination of the DC resistance and AC impedance of the element. Hence:

$$\frac{1}{R_G} = \frac{N_C}{N_C + 1} \frac{A}{d\rho_E} + \frac{N_C}{N_C + 1} \omega C_E \tan\delta \tag{8.9}.$$

Where ρ_E is the electrical resistivity of the pyroelectric element (set to 3 X 10^{10}, which is a typical value [*Whatmore and Watton, 2001*]) and tan δ represents the dielectric loss (tan δ = 0.006 as in table 2.1). $\mathcal{R}_V$ can be calculated by substituting in 8.7 the value of $\mathcal{R}_i$ and expression 8.9.

The values of $\mathcal{R}_V$ are plotted in figure 8.22. The trends mirror very much the findings relative to $\mathcal{R}_i$. For example, the responsivity increases when the system is completely etched through. The gain is lower for double-bridge systems. The bottom line is represented by the full-membrane (non etched) system. For frequencies above 100 Hz, the difference begin to disappear. Notice also that for $\omega << G_T / H_m$ the voltage responsivity is nearly constant. $\mathcal{R}_V$ decreases with ω afterwards. This behaviour finds confirmation in the classical theory [*Muralt, 2001*].

How do these values of $\mathcal{R}_i$ and $\mathcal{R}_V$ relate to the theoretical and practical values most often reported in literature? A direct comparison is difficult. Whatmore [*Whatmore, 1991; Whatmore and Watton, 2001*] and Putley [*Putley, 1970*] discuss responsivity only in terms of arbitrary units and relative variation. (It was commented above on how the

general behaviour predicted for $\mathcal{R}_i$ matches my findings.) In [*Iborra et al., 2002; Muralt, 2001*; *Putley, 1980*], the authors present values of $\mathcal{R}_V$ of a similar order of magnitude to those presented in figure 8.22 (or slightly lower). Other authors tend to reason in terms of NETD (or detectivity) [*Rogalsky, 2003*; *Kruse, 1999*]. In fact, just in terms of responsivity, it is difficult to compare our pyroelectric detector with other thermal detectors based on different principles or different design. Indeed, one should consider the detectivity. However, it is impossible to find an absolute value of detectivity for two reasons. First, little information is available about the final circuit in which the device will be incorporated. In particular, it cannot be foreseen which kind of noise will affect the response (see section 2.4). Furthermore, since this device is indeed a staring array of 16 by 16 elements, one should rather reason in terms of NETD, rather than point detectivity. Nevertheless, the similar order of magnitude of the data reported in literature and the similar trends seem to suggest that the theoretical analysis developed so far retains a certain degree of validity.

When a non-imaging concentrator is applied to a point element detector, the theoretical increase in detectivity can be simply calculated from equation 2.7 (section 2.3).

$$D^* = \frac{A^{1/2}\Delta f^{1/2}}{NEP} \qquad (2.7rep)$$

When a concentrator is applied, the actual area of the element would not change and so the NEP would remain the same (if the noise is dominated by internal mechanism such as thermal or Johnson). However, the area of actual detection would be equal to the cross section of the flow that is accepted, therefore one can write:

$D^*_{w/collector} / D^* = (A^{1/2} / \text{NEP}) / (A'^{1/2} / \text{NEP}) = (A / A')^{1/2}$. (8.10).

Applying the expression for the physical concentration ratio of a generic concentrator (eq. 3.1, i.e. $C = A / A'$) to equation 8.10 one obtains:

$D^*_{w/collector} / D^* = C^{1/2}$ (8.11)

i.e.: the increase in detectivity is exactly equal to the square root of the concentration ratio. The advantage of this configuration can be demonstrated for the ideal CPC considering that each element will receive (if the collection is ideal) the power incoming onto a larger area (i.e. the entry aperture of the collector: $A = 4\pi a^2$) but the noise will be associated with a smaller area (the effective are of the element: $A = 4\pi a'^2$).

To evaluate the theoretical increase in detectivity for the systems analysed in this research, one has simply to calculate the square roots of the concentration values that were previously calculated for the collector profiles of interest. These are reported in table 8.6. It is true that those values were calculated in 2 – d. However, these are used only for comparing the different concentrators rather than with finding absolute values. Furthermore, Winston demonstrated that the 3 – d collection efficiency of a concentrator obtained by rotation around an axis of a 2 – d concentrator is equal to the collection efficiency for the 2 – d concentrator when the sole meridian rays are considered (and slightly lower if one considers also the skewed rays) [*Welford and Winston, 1989, Chapter 4*].

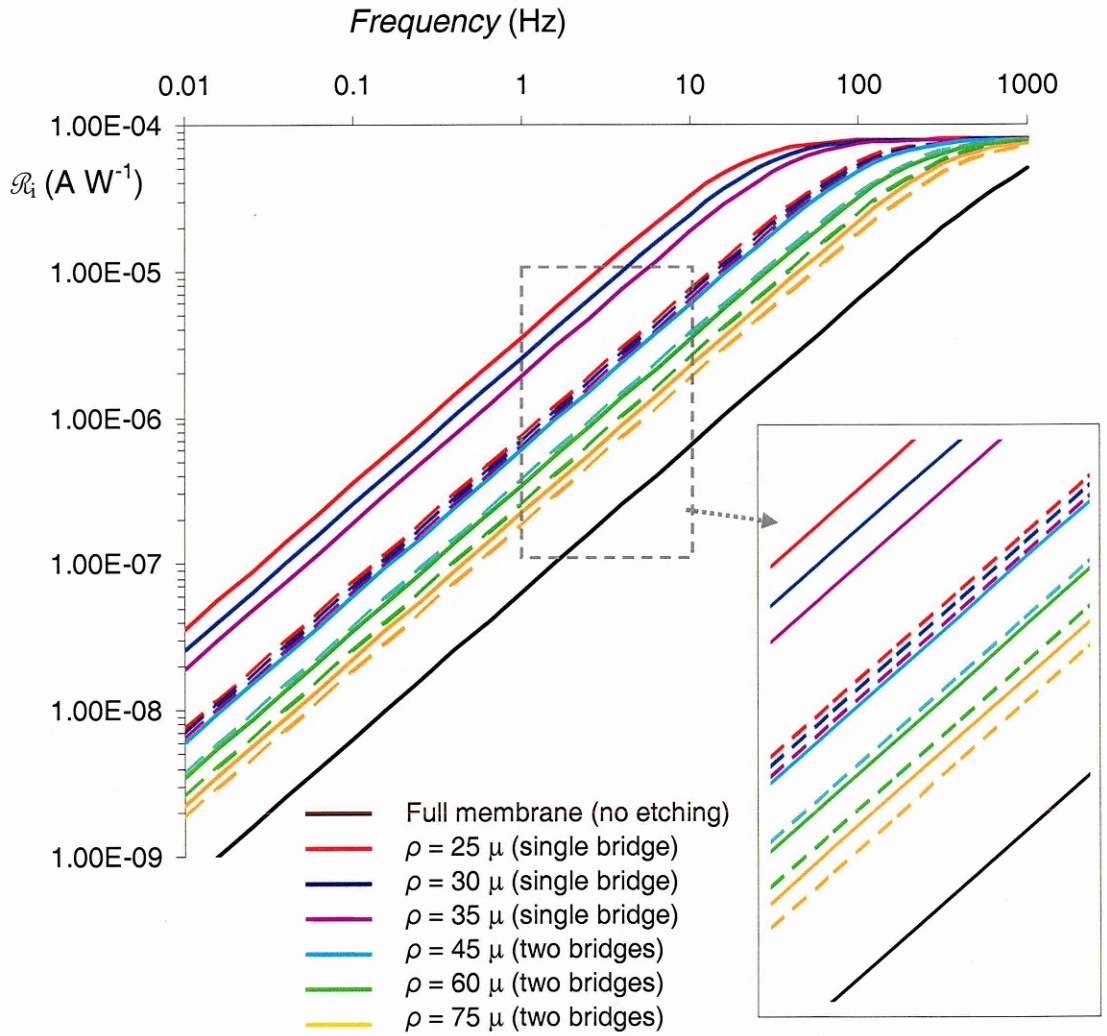


Figure 8.19 **Plots of $\mathcal{R}_i$ Vs. frequency for a single element central circular structure connected to the thermal sink by one or two spiral microbridges of various design** (The dashed lines represent a fully etched system, the full lines correspond to a system that was etched only up to the bottom electrode, leaving the TiO_x/SiO_x membrane unetched)

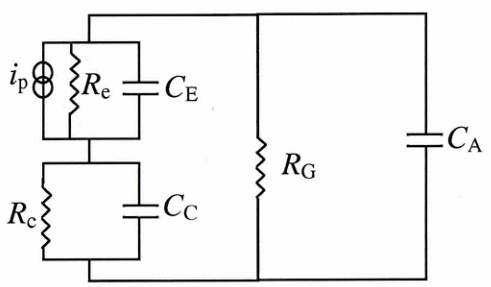


Figure 8.20 **Equivalent circuit for the set up of the testing equipment (testing set up with a single working element connected plus compensation elements)**

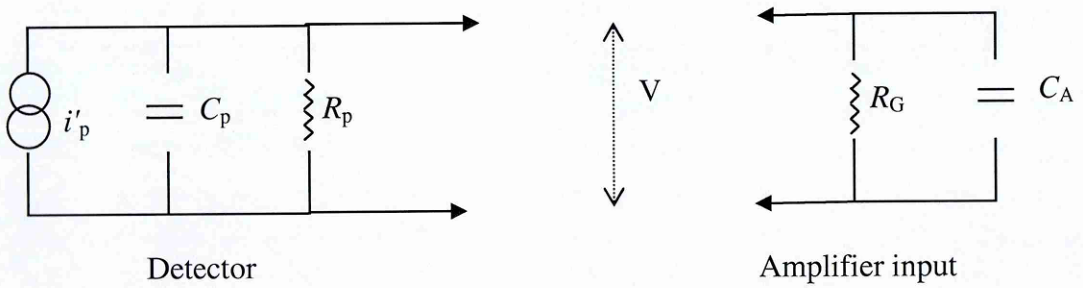


Figure 8.21 **A reduced version of the equivalent circuit of figure 8.20** [*Putley, 1970*]

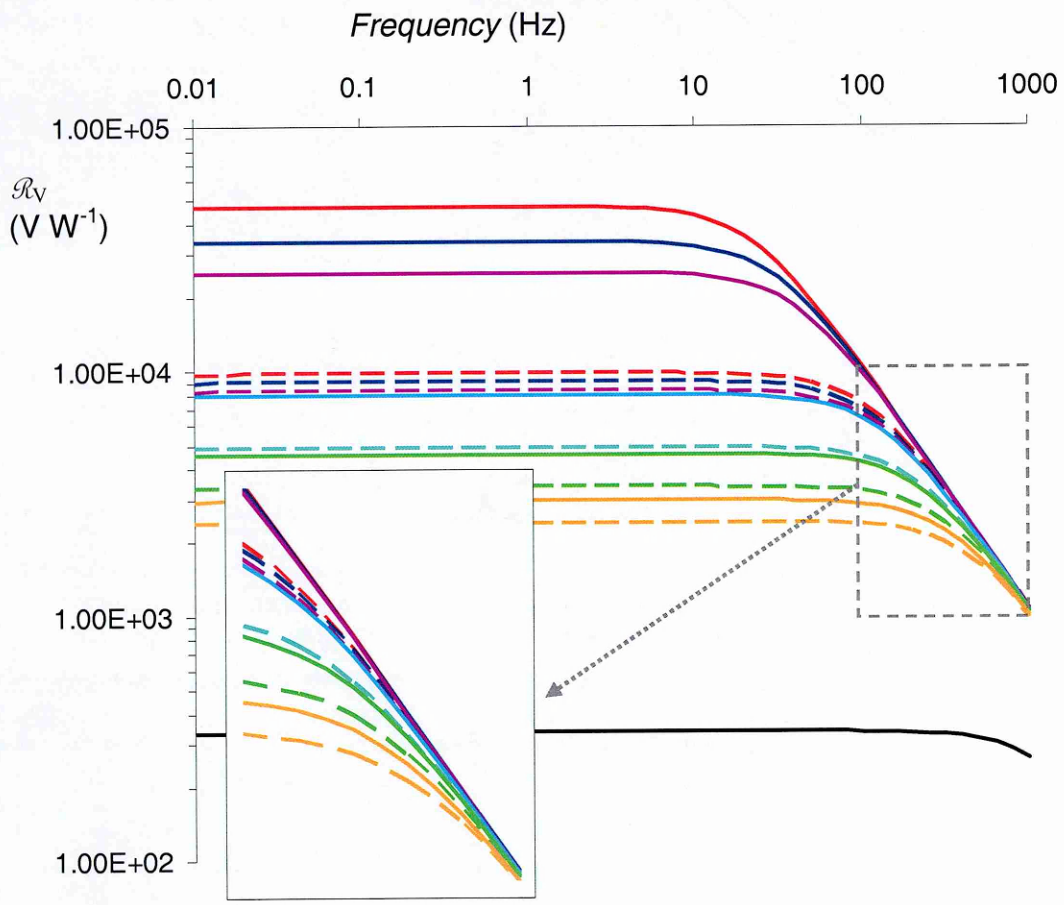


Figure 8.22 **Plots of $\mathcal{R}_V$ Vs. frequency for a single element central circular structure connected to the thermal sink by one or two spiral microbridges of various design** (Same legend of figure 8.19; the dashed lines represent a fully etched system, the full lines correspond to a system that was etched only up to the bottom electrode, leaving the TiO_x/SiO_x membrane unetched)

Type of design	2 – d CPC	2 – d CPC truncated	Long V collector	Short V collector	Single stage ellipse (6.3.5)	Two stages ellipse (6.3.5)	Single stage ellipse (8.2.1)	Two stages ellipse (8.2.1)
Full system	2.00	1.42	1.58	1.33	1.21	1.19	1.27	1.17
Enlarged System	1.89	1.35	1.48	1.36	1.26	1.24	1.33	1.31

Table 8.6 **Theoretical increase in detectivity associated with the introduction of a collecting concentrator for a single element of a pyroelectric sensing array (2 – d case).**

8.2.3 Theoretical analysis of the detection of IR collimated beams

The practical problem of testing the IR sensors was discussed in the experimental part, in section 4.1.3. An apparatus was built to test the response of single elements (figure 4.3). Once the testing apparatus was set up, and a signal from the device obtained, the subsequent problem was to demonstrate the effective signal increase obtained with the implementation of the design. In principle it was relatively easy to assess the effect of isolating the inner structure. It was sufficient to compare the signal from an element with full membrane and an element with an inner area isolated by means of microbridges. The results of figure 8.22 seem to demonstrate that an effective increase in signal is to be expected from most micromachined elements, in spite of the smaller detection area.

The effect of power concentration is more difficult to demonstrate. In effect, the best practice should have been to prove the effective collection efficiency of the single collector (or arrays of collectors) by testing them as through-the-wafer cavities, without the active layer. An early test was attempted using the UV lamp of a mask aligner and assessing the dose passing through with a radiometer. This attempt did not show meaningful results. It is true that the roughness of the sidewalls will scatter UV radiation to a larger extent than IR. (See sections 6.2.6 and 6.3.2 for a discussion on the scattering problem.) Therefore, those results could hardly be representative of the collection obtained. Direct testing of the arrays would have entailed the use of IR laser for a highly collimated beam and a radiometer to assess the dose received. Unfortunately, such equipment was unavailable. See the future work section for a deeper discussion on the direct testing of the collectors.

In the absence of a direct way of measuring, a way of demonstrating the effect of the collimators by simple comparison (i.e. relative increase in signal) had to be devised. Unfortunately, it is not possible to produce an array of elements with areas equal to the entry aperture of the collectors and no concentrators to collect the radiation. In other words it is not possible to build a sensor with all the elements suspended on the same thin membrane. (A silicon wafer is needed as a backing substrate for the active layer.) Furthermore, production of such a device would have entailed a completely different microfabrication process and design. Finally, the idea was proposed of analysing the effect of differently collimated beams. This section deals with the theoretic effect of

collimated beams on the signal detected. Section 8.3.2 reports the experimental results and discusses the correlation of these with the theoretical results.

A highly collimated beam is a beam with small cut off angle (ω). With reference to the apparatus of figure 4.3, there are three ways in which the beam proceeding from the hot plate can be reduced, during the testing of the device. These are schematised in figure 8.23. Firstly, the distance between the hot plate and the detector can be increased (figure 8.23*a*). Secondly, the small shutter that stands between the hot plate and the detector has a variable diameter, which can be decreased (figure 8.23*b*). Eventually, an array of microscopic collimators can be coupled to the device array as showed in figure 8.23*c*.

The effect of the collimation will be analysed first by using the microscopic collimators. These may be simple arrays of through-the-wafer cylindrical cavities, obtained by anisotropic DRIE. In the following, it will be assumed they are perfectly cylindrical and only direct rays pass through them, i.e. the reflected rays are completely adsorbed or scattered. If the sidewalls are 100% reflective (ideal case), then the cylindrical cavities do not have any collimation power. As usual, the 2 – d case will be considered and a perfect square-wave distribution will be assumed (B constant for $\varphi \leq \omega$ and equal to 0 for $\varphi > \omega$). The total power passing through such collimators can be calculated by using simple geometrical considerations. The calculations are reported in appendix I. Once the total power is calculated for each collimator of interest, the ratio gives the total increase in power collected by passing from a small collimator (i.e. diameter equal to 125 μm) to a large collimator (i.e. 205 μm on diameter). The theoretical results are reported in figure 8.24 (solid blue curve). The calculations show that for a cut off angle higher than the maximum acceptance angle of the largest collimator (i.e. $\omega \geq \theta$), the system "sees" the distribution as if it were fully isotropic.

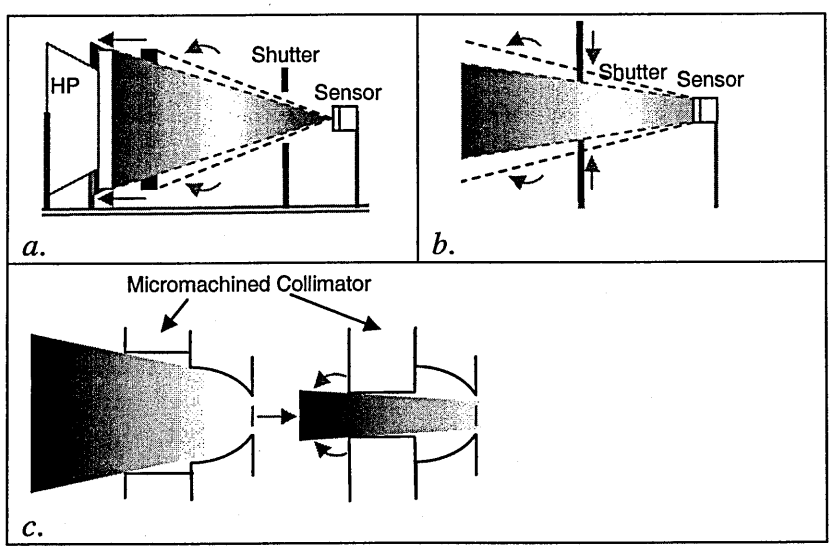


Figure 8.23 Ways of producing a collimated beam for IR detection using the Home made testing set-up (schematic in figure 4.3).

If the sidewalls were partially reflecting (so that a small part of the radiation passes through the collimator after being reflected), the trends reported above would not change in principle: as long as the amount received upon reflection is a small part of the

entire flux, the collimation would be effective, although the shape of the flux distribution would not be represented by a square wave, but maybe a cosine or Gaussian distribution such as those reported in appendix E-1.

In case the collectors were ideal (i.e. 2 – d CPCs), then the increase in signal observed after enlarging the collector would correspond to the maximum increase in power attainable (i.e. the blue curve of diagram 8.24). However, the elliptical collectors are far from ideal. It would be quite complex to calculate the actual increase when using an elliptical collector. One should calculate the transmittance relative to the full system: collector plus collimator. This would require an entire new set of ray-tracing calculations. Fortunately, there is a simpler way to demonstrate the effect of the collectors. It is easier to calculate the expected increase in absence of any signal from the sidewalls (i.e. collectors with collection efficiency equal to zero). In the assumption that all the radiation hitting the sidewalls of the collector is lost, the only contribution would come from the rays that enter the exit aperture directly. In this case, the gain deriving from a larger collimator will be certainly lower. The calculation of the direct rays entering the system (collector plus collimator) is analogous to the treatment of the direct rays for a generic collector (such as that reported in section 5.4). The details are reported in appendix I. The theoretical results are reported in figure 8.24 (dashed green curve).

The diagram of figure 8.24 demonstrates that there is a consistent difference between the increase in presence of totally collecting sidewalls and in presence of totally non-collecting sidewalls (for the concentrator). In principle, it should be possible to discriminate between the two contributions. This would save the ray tracing computation required to obtain the exact power increase required. Very simply all the increase detected beyond what would be expected if the radiation were completely scattered by the sidewalls would demonstrate that the sidewalls are effectively reflecting.

As shown in the plot of figure 8.24, the quantitative effect of the micro-collimators depends on the degree of the collimation of the IR beam at the macroscopic level (i.e. the cut-off angle of the distribution, ω). On the other side, ω depends on the geometry of the set up and the hot plate (see figure 8.25). It is important to assess its effect so one can discriminate between the two sorts of contributions (full collection Vs. no collection). Discrete values for a series of system set up are reported in table 8.7. In the apparatus of figure 4.3 the distance between the hot plate and the shutter was set equal to 10 cm. The distance between the shutter and the sensing array is fixed to 5 cm. Collimation is increased by restricting the aperture of the shutter. This set up corresponds to the series of experimental measurements reported in section 8.3.2. Notice also how the data of table 8.7 are related to the diagram of figure 8.24.

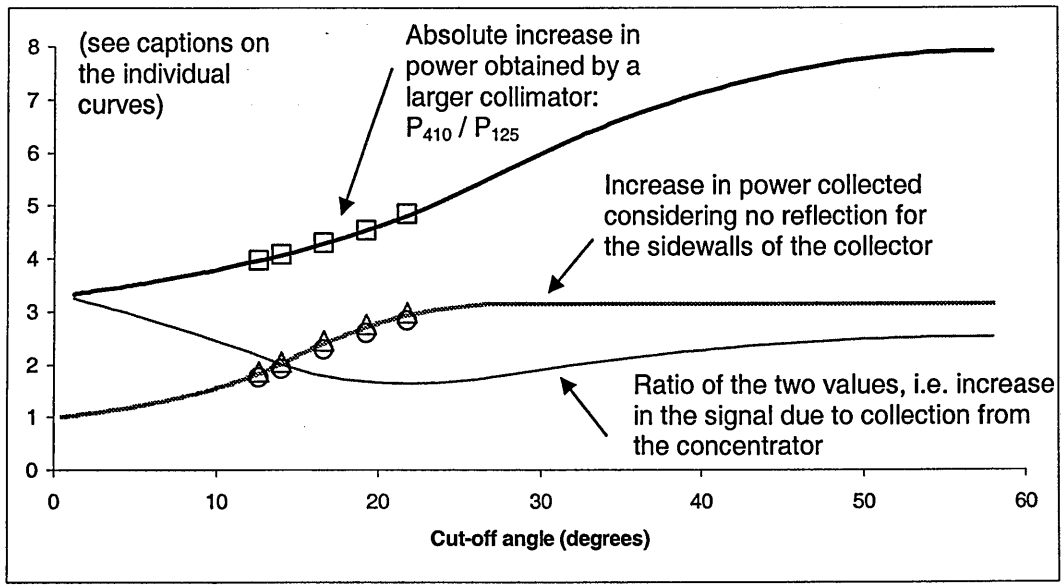


Figure 8.24 The transmission of power through micro-collimators and their effect on the performance of micromachined collectors. Comparison between the case of total transmittance and the case of zero transmittance from the sidewalls.

8.3 Experimental testing of the prototype

This section is dedicated to the testing of the devices. The general performance is described in section 8.3.1. The results with using collimated beams are reported in section 8.3.2. Little time remained, at the end of the research, for the actual testing of the prototypes. The main reasons were: the relatively late set up of testing equipment (the set up was completed in summer 2003); the delays in achieving a working prototype due to the unsuitability of the grey-scale method (section 6.1) and the many problems emerged when other methods were attempted (section 6.2).

Four wafers containing working devices were produced. All samples contained collectors micromachined by DRIE in pure SF_6. The samples denominated PZTDEVICE3 and PZTDEVICE4 were produced using the same PZT solution. They contained the pattern of the early device (i.e. no spiral microbridges or elements isolation). The elements are squared and range in dimensions from 20 to 100 μm (depending on the array). These wafers were also poled by using corona poling. Samples PZTDEVICE5 and PZTDEVICE6 were produced using a Mn-doped PZT solution. They contained the new design pattern. Therefore the elements are circular, with a radius equal to 60 μm. Some of these arrays were later patterned with the spiral microbridges, as detailed in section 8.1.2. Due to the little time remaining, a complete and exhaustive characterisation of the device was not achieved. Experimental testing would play a wider and more complete role in any future extensions of this project. Possible new directions for the project are discussed in details in the future work section.

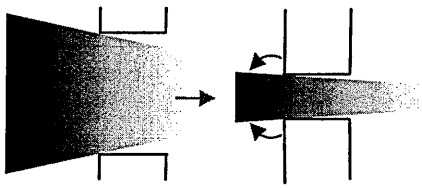
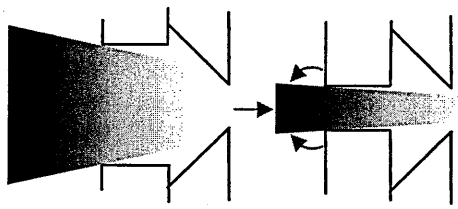
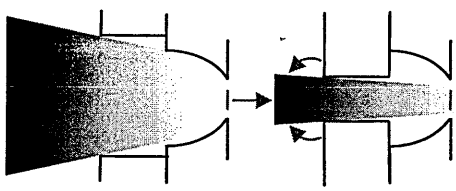
Half width of shutter aperture (mm)	11.25	12.5	15	17.5	20	Marker (plot 8.24)
Cut off angle of the IR beam (degrees)	12.68	14.04	16.70	19.29	21.80	
Configuration						
 Full power crossing the collector: total collection	3.96	4.067	4.28	4.53	4.84	□
 Wet etched pit (figure 1.10)	1.86	2.05	2.44	2.76	2.98	○
 DRIE etched collector (figure 1.11)	1.76	1.92	2.28	2.59	2.83	△

Table 8.7 Theoretical increase in power collected (P_{410} / P_{125}) with a larger micro-collimator

8.3.1 Experimental result: general performance

The electrical properties of the elements were initially tested to evaluate the integrity of the membranes and the quality of the PZT. The testing apparatus was presented in the experimental part (see section 4.1.3).

The capacitance could be measured for three arrays only from sample PZTDEVICE3 after sawing (see section 8.1.3). Although they had been patterned, the presence of a capacitance demonstrated that the elements were not short-circuited. The PZT layer was also supposed to be poled, since the wafer had been previously poled by using corona poling. Although the prototypes were perfectly intact, it was not possible to obtain any IR signal from these arrays when attempting to test them.

The PZT layer in PZTDEVICE4 showed an average dielectric constant of 261 (minimum 170 and maximum 410). This value is compatible with the results often reported in literature and used for the performance simulation of section 8.2.2. One array of the sample (with elements of 100 μm in side) produced a signal once exposed to IR radiation. The array was tested in the testing apparatus with the hot plate at 20 cm from the array case, corresponding to a cut off angle equal to ~ 14 degrees. The hot

plate was set to 250 degrees. The results are reported in figure 8.25. First, the elements of the array were tested with no post-treatment (series: ▲). There is a large variation is signal among different elements, so that the largest signal is 1.6 times the average, which is 3.6 times the minimum signal. This variation may be due to the variation in the dimensions (and shape) of the collectors. Conversely, there is no evidence that the position of the single element within the array affects the intensity of the signal.

Subsequently, a gold coating was deposited onto the sidewalls by evaporation by using a shadowing mask (series: ■). The presence of a reflector on the sidewalls did not seem to improve the response sensibly. Finally, a second array of collectors was added, following the procedure outlined in figure 8.1 (series: ◉). In section 8.2.1 a decrease of about 10% was predicted, due to partial shadowing, i.e. partial scattering of the radiation. Effectively there was a steady decrease for all the elements (ranging from 10% to 50%). The alignment between the bottom and top arrays was checked under the microscope (figure 8.26-*left*) in order to exclude a partial shadowing due to misalignment of the two wafers. If there were no collection from the sidewalls (figure 8.26-*right*), then no decrease in signal should be detected up to a cut off angle of 16 degrees. This seems the first demonstration that a certain degree of collection from the sidewalls is achieved.

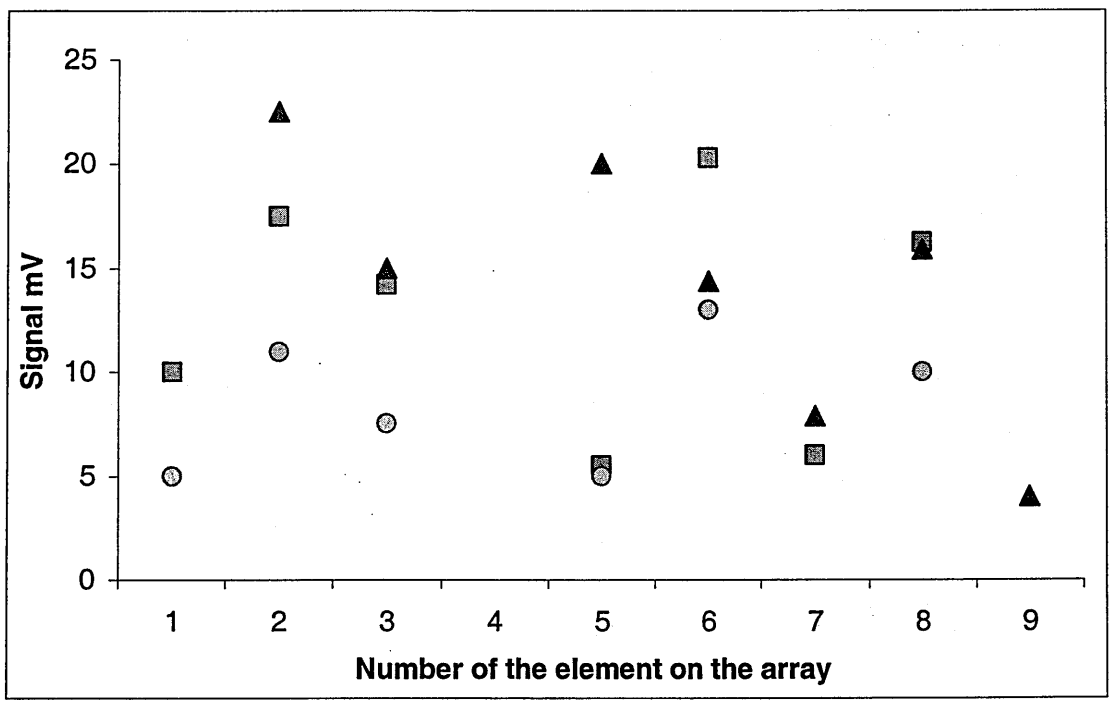


Figure 8.25 Response obtained from an array of sample PZTDEVICE4.
Series: ▲, original response; series: ■, sidewalls of the collector coated in gold; series: ◉, after a second stage is added.

Samples PZTDEVICE5 and PZTDEVICE6 show an average dielectric constant 40% lower than the ideal value of 260. This low dielectric constant seems to suggest a low quality of the PZT layer. Indeed, both the XRD spectra and the overall aspect of the film suggested an unsatisfactory crystallisation, with presence of pyrochlore. (A XRD

spectrum of a PZT film containing pyrochlore phase was presented in figure 8.2). In effects, it was not possible to attain any sensible response from the sample PZTDEVICE5. Sample PZTDEVICE6 yielded many working arrays. The responses were in the range 5 to 7 mV, therefore circa half of the response achievable from the sample PZTDEVICE4. This time, the coupling of a top cavity did not show appreciable decrease in the response. Finally, it was possible to assess the response from two elements of a patterned array. The array was patterned with spirals microbridges (two microbridges). The signal was, in both cases, 5.5 mV (comparable with the response attainable from the full device). However, in all these cases, the signal is so low that is dramatically affected by the noise, so that it is not possible to draft apparent conclusions from the analysis of arrays coming from the sample PZTDEVICE6.

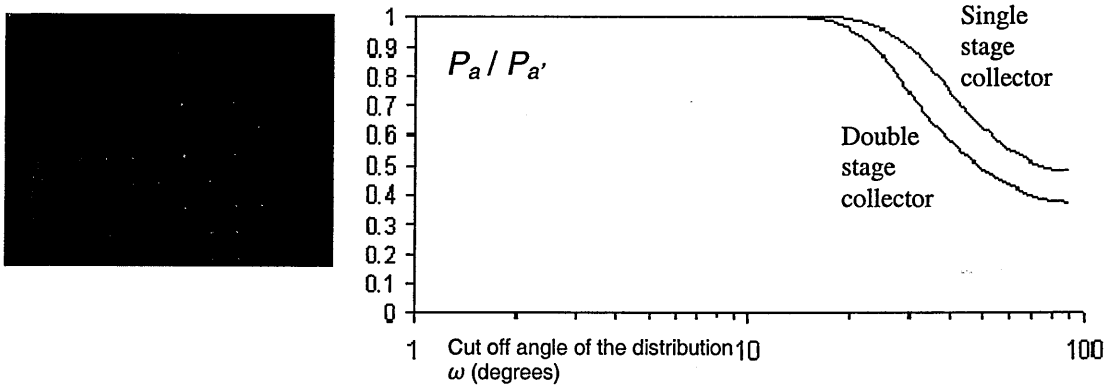


Figure 8.26 Left: View of the two-stage set up taken at the optical microscope. It demonstrates the alignment of the two arrays (top collector plus bottom collector). Right: Power plot (see figure 8.17) considering no collection at all from the sidewalls.

8.3.2 Experimental results: use of collimated beams

An array of "narrow" micro-collimators was aligned and coupled to each array. The array was tested in the usual testing set up (figure 4.3). The array was then coupled to a second array of microcollimators (with the larger diameter), incorporated again into the device and tested again. The results, for the set up of table 8.7, are reported in table 8.8.

It was not possible to test the two-stage configuration with the collimator arrays coupled, because the array holder does not allow the thickness of three wafers. (The arrays would keep on breaking when attempting to fit three sandwiched arrays into the holder.)

In both cases, the increase is far above the maximum theoretical increase reported in figure 8.24. In particular this could be due to the limits of a 2 – d model, which does not keep the skewed rays into account.

Experimental measurement followed for a few months after the end of this PhD research. A paper recently submitted for publication [*Whatmore et al., 2004*] compares the results obtained using microcollimators with the theoretical results obtained by a

different computation model (that works in 3 – d). The results reported in the paper show that there is a certain agreement between the two sets of values (i.e. the theoretical and the experimental performance).

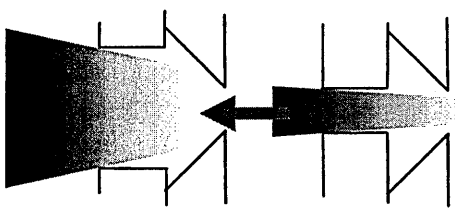
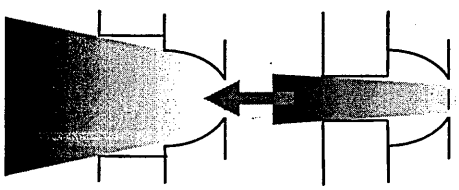
Half width of shutter aperture (mm)	11.25	12.5	15	17.5	20
Cut off angle of the IR beam (degrees)	12.68	14.04	16.70	19.29	21.80
Configuration					
 Wet etched pit (figure 1.10)	5.20	4.63	4.72	4.81	4.64
 DRIE etched collector (figure 1.11)	12.08	11.09	12.64	15.07	9.29

Table 8.8 Experimental increase in signal (V_{410} / V_{125}) with a larger micro-collimator

8.4 Conclusion

A microfabrication route was set up and optimised for producing working prototypes of the novel IR sensing device.

The capacitance could be measured for all the devices produced. The first batch of wafers showed a good quality PZT. Unfortunately, the second batch demonstrated a far lower quality of the active layer. The best response was obtained from unpatterned devices (coming from the first batch), which did not allow thermal isolation of the elements. In other words, it was not possible to obtain any sensible signal from the suspended structures in devices coming from the second batch, although the analysis of the electrical properties showed that these structures were not cracked or short-circuited.

A computation of device performance was accomplished by combining the calculations carried out in previous chapters.

The best response was obtained from a wafer of the first batch, out of which only a few working devices were obtained. The IR response showed a variation of almost 6 times (probably due to the variation in the dimensions of the collectors). Coating the sidewalls in gold did not improve the response. Adding a second array of collectors (i.e. a second stage) decreased the response steadily, as predicted by the theoretic calculations.

Micro collimators were introduced to help clarifying the role of concentrating collectors. The results were compared with the results of the theoretical computation. Unfortunately, having used a 2 – d model that revealed too simplistic, the experimental results are far beyond the maximum increase allowed by the theoretical model. A more recent paper produced by this group demonstrates a better agreement between the experimental results and the results predicted by a different 3 – d model [*Whatmore et al., 2004*].

CHAPTER 9: A DEEPER LOOK TO THE PROCESS OF SILICON ETCHING BY RADICAL FLUORINE IN INDUCTIVELY COUPLED PLASMA REACTORS

A large part of this research entailed micromachining of silicon using fluorine-based gas mixtures. A final process was eventually chosen for producing prototypes, which involved a long silicon etching cycle in pure SF_6 plasmas. An isotropic cycle was also a fundamental part of the class of processes that, although more promising, could not be optimised within the time frame of this research (but would be largely exploited in potential future work). Due to this central role, the process of silicon etching with fluorine was deeply analysed in its kinetics. Two reasons justified this deep study of the process: the first more inherent to this research, the second, of more general purpose. Firstly, a vast effort was devoted in gaining knowledge of the process with the view of building a model to predict the results of the etching, i.e. to simulate the evolution of the contour of the cavities. Current etching simulation tools commercially available (e.g. SPEEDIE [*www-tcad.stanford.edu/*] or SAMPLE [*cuervo2.eecs.berkeley.edu/volcano/*]) are expensive and highly sophisticated. These find their main application in microelectronics, where critical dimensions below 1 μm represent the rule. On the contrary, MEMS often contain cavities or features tens (hundreds) of microns deep or wide. In fact, many of DRIE problems dominant at the scale of a few microns (such as for example bottling, ARDE etc) are less important for larger structures. A simulation tool would not require the level of sophistication of the commercial software. Conversely, simulation tools for large structures should address phenomena emerging at long etching time such as features deformation due to crystalline plane related preferential etching. In particular it would be useful to produce models for predicting the results for large 3 – d structures produced by coupling long isotropic and anisotropic cycles. This would be chiefly important for other fields of application beyond this research, such as microfluidics, microoptics or BioMEMS, where the control over morphology is crucial.

During the etching of silicon using fluorine, a constant effect was observed leading to two important consequences:
- surprising deviation of initially circular cavities from the cylindrical symmetry (original circular mask apertures tend to become squares);
- progressive increasing of surface roughness with the formation of regular patterns, with facets, mainly formed by regular series of parallel ripples, cusps and flat planes.

The extent of these two phenomena can become dramatic. Depending on process conditions and etching time, it can lead to large deformations, unexpected results or failure to achieve the sought contour. Surprisingly, there is hardly any mention of this "large scale" problem in literature. (The literature was reviewed in section 3.5). These effects must be clarified, understood and kept under control when designing and producing MEMS.

On the other side, the detailed analysis of the process is presented here because it was necessary to report succinctly the main findings and hypotheses since these are often referred to in the rest of the thesis. The interpretation of the mechanism of the etching reaction, such as developed during the research and presented here, underlined most of the choices and process optimisation that were reported in the previous chapters. In

particular, this chapter is mainly bound to chapter 6 since the model builds on experimental evidence that was mostly presented in that chapter. In order to make this thesis clearer to read, it was chosen to postpone the scientific discussion at the end of the thesis, rather than intermingling with the results of chapter 6. In fact, albeit this model was developed during the experimental trials and the consequent view of the etching reactions drove most of the operative choices, it is possible to follow the rational path to the microfabrication of the device prototype without referring specifically to the material presented in this chapter.

This chapter is organised as follows. In section 9.1 results are reported that were not directly inherent to the microfabrication of the device (and thus did not find place in sections 6.2 and 6.3) but are required to clarify the nature of the process. The section discusses the major trends of the process (i.e. the dependence of lateral and vertical etch rate on process conditions). Then, the evidence of the preferential nature of the etching mechanism will be presented. After that, the phenomenon of deformation of originally round apertures will be analysed, in more details than those reported in section 6.2.6. Similarly, the analysis of surface roughness of section 8.2.6 will be recalled and expanded. Once the results are reported, a brief discussion follows. In section 9.2 the major findings are compared with the trends reported in literature. Subsequently, a series of hypothesis are assumed, leading to the presentation of a qualitative model to explain the phenomena (section 9.3). After the model, the case for preferential etching effects (relative to different crystalline directions) is made.

9.1 Etching of Si with fluorine-based plasma: additional experimental results

This section reports additional experimental results of the etching of Silicon with SF_6-based plasmas, i.e. etching in absence of passivation-inducing reactants. The literature concerning this process was surveyed in section 3.3 and 3.5. The experimental details were described in section 4.3.3. The results relevant to the microfabrication of the IR sensing device were reported and discussed in sections 6.2.3 and 6.2.6. Section 9.1.1 will present the major experimental trends (shape and contour of the cavities as a function of process parameters). The evidence of crystalline orientation dependent etching (both direct and indirect) will be demonstrated in sections 9.1.2 to 9.1.4.

9.1.1 Shape of the cavities and trends of vertical and lateral etch rates with time and aperture dimension

The main findings, relatively to the shape and scale of cavities etched in pure SF_6 were reported in section 6.2.3. The general behaviour of the process was outlined in order to provide a general background for results presentation. The results showed the following trends: etch rates increased with original mask aperture size (following a logarithmic trend) and etch rates decreased with process time (following a logarithmic or negative exponential trend). For etching times below 2 hours, it was claimed, the contours produced were all roughly similar in shape (almost hemi-ellipses): the etch factor ranged between 1.7 and 2.4, regardless of process parameters and original aperture size. (Subsequently, in section 6.3.1 it was showed how, for etch times above 180 minutes; notable changes in the overall shape can occur when the platen bias is set to zero.) Series of typical cross sections were reported as an example.

This section presents a more detailed analysis of those trends. The vertical and lateral etch rates of the features were assessed by optical microscopy. In this way it was possible to analyse tens of features and build a statistically valid sample. (On the contrary, the laborious SEM analysis of the replicas could provide just one or two measurements for each type of cavity.) The dependence of vertical etch rate and lateral etch rate on original mask aperture diameter (circular holes) are reported respectively in figure 9.1 and 9.2. For clarity of comparison, all the samples reported have been etched for the same time (1 hour).

The increase in etch rates with original mask aperture size can be observed in both diagrams. In both cases, the etch rates can increase up to ~ 3.5 times. It was observed that correlation factors of logarithmic regression improve with process time. (The results for shorter processes are not reported here.) Lateral Etch Rates for etching times below one hour show correlation factors far below one, so that logarithmic regression is meaningless. This is probably not due to truly physical effects, but to errors or limitations in the accuracy of the measurements, which affect the more shallow cavities to a larger extent. The above trends can be generally observed also in the plot reporting the evolution of cavities from squared mask apertures. (The results are not reported here for lack of space.)

Process parameters may affect this logarithmic dependence. As repeated many times through this thesis, the bias power had little or no effect on the vertical etch rate. When bias is raised from 0 to 25 watts no clear increasing trend is observed in the intercept of the logarithmic trend lines. Conversely there is a slight steady increase in the slope from 0 to 15 watts. The slope is affected by a standard deviation of 3.5% whereas the intercepts are scattered with a larger standard deviation (17%). However the highest values correspond to the sample etched at 15 watts and the smallest values belong to the sample etched at 25 watts. A slightly lower scattering affects the lateral etch rate ($\sigma_{slope} = 1.3\%$ and $\sigma_{intercept} = 7.2\%$) and no clear trend can be observed. In figure 6.27, it was showed how the bias power has little influence on the etch factor too.

The addition of oxygen causes a net increase in etch rates both vertical (a 11% increase in the slope against a mere 5.0% in intercept) and lateral (a massive 25% in slope and 26% in intercept). The larger increase of lateral etch rate seems to suggest that the presence of oxygen leads to a decrease in etch factor. The statistical analysis seems to support the evidence that, after long etching cycles, the cavities etched with 10% O_2 in the etching mixture develop effectively a lower aspect ratio than those etched in pure SF_6 (see table 6.2). Although a single sample was etched at reduced chamber pressure (10 mT), the analysis of the trends demonstrated that a decrease in pressure lead to a concrete decrease in vertical etch rates while yielding larger lateral etch rates. Such a decrease in etch factor could be clearly observed in figure 6.27, where the values relative to cavities etched at a pressure of 10 mT lay at the bottom of the diagram. Although the results concerning longer etching processes are not reported here, it was found that both the slope and the intercept of the trend decrease monotonically with process time. The etch factor increases up to 30% for long etching times. Furthermore, the etch factor increases when a backing wafer is coupled to the etching wafer.

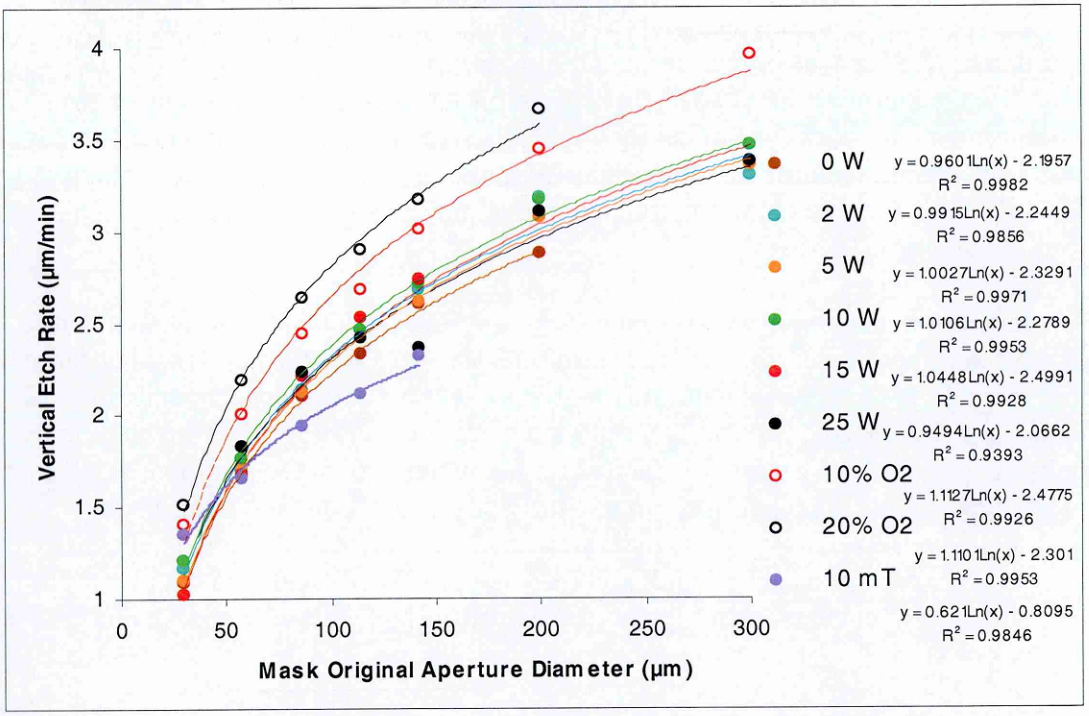


Figure 9.1 **Plot of Vertical Etch Rate (feature depth divided by process time) Vs original diameter of mask aperture (for circular mask apertures). The process time is one hour for all the samples. Regression equations and correlation factors are reported at the right side of the diagram.**

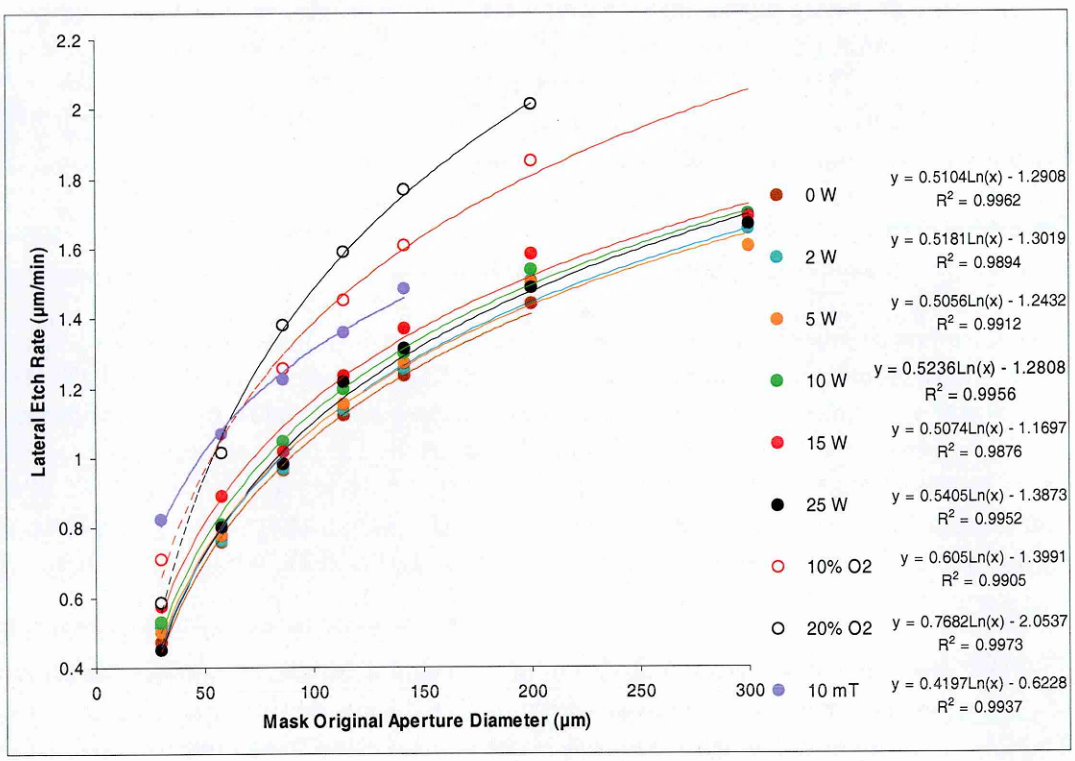


Figure 9.2 **Plot of Lateral Etch Rate (feature undercut divided by process time) Vs original diameter of mask aperture (for circular mask apertures). (For other comments see figure 9.1)**

In order to predict features evolution, it is necessary to build a model that keeps both size and time effects into account. The dependence of vertical and lateral etch rates on time is reported respectively in figure 9.3 and 9.4 for families of cavities having the same original aperture. The data were elaborated from the results reported respectively in figures 9.1 and 9.2. Notice that the data relative to different values of platen power have been incorporated in the same batch to produce averaged trend lines. Etch rates are given in μm/minute. The original mask aperture diameter is indicated beside each series.

The decrease in vertical etch rate with process time can be observed for all the features. The trend demonstrates a good agreement both with logarithmic and exponential regression curves. The behaviour of the lateral etch rate is far less clear. The correlation factors for the regression analysis are too low to be meaningful (therefore, they have not been reported). However, logarithmic trend lines were reported in the diagram just to show the actual tendency of the point to aggregate along series of monotonically decreasing curves. The increase in etch factor with time demonstrates that lateral etch rates decrease faster than vertical etch rates.

The regression analysis reported above was used to build a completely experimental model. This model was used to predict the evolution of features for long etching times. This model, however, failed to approach the results obtained experimentally for long etching times and the relative results are not reported here.

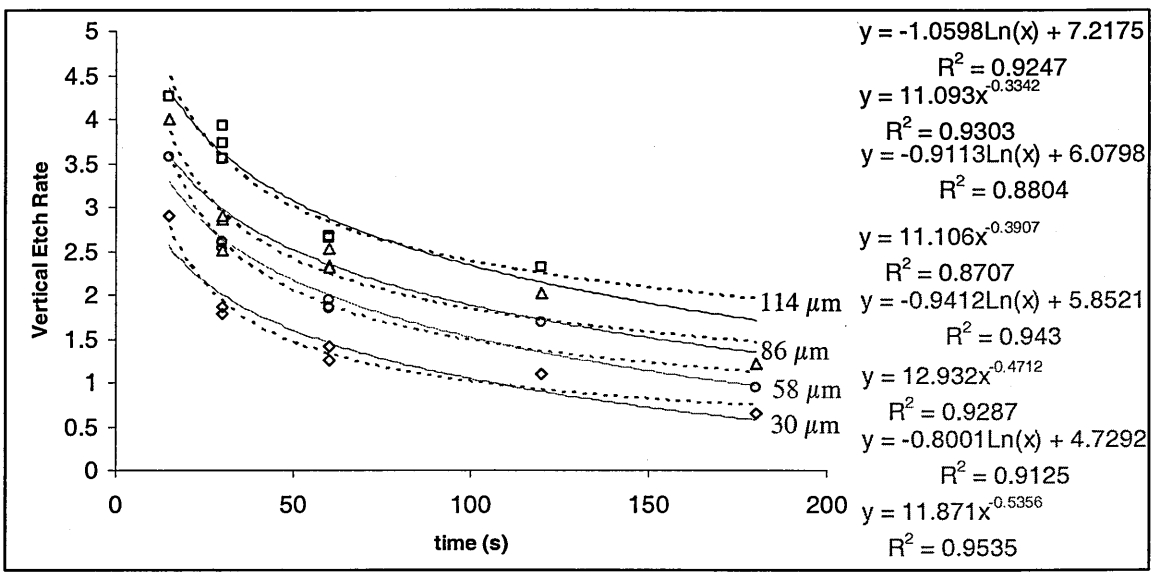


Figure 9.3 **Plot of Vertical Etch Rate (in nm/min) Vs process time for various mask aperture sizes. The colour of the trend line and the markers are indicative of the original feature size, while line pattern changes according the form of the regression relationship. The dotted line represents a logarithmic trend line while the dashed line refer to an exponential relationship. Regression equations and correlation factors are reported at the right side of the diagram.**

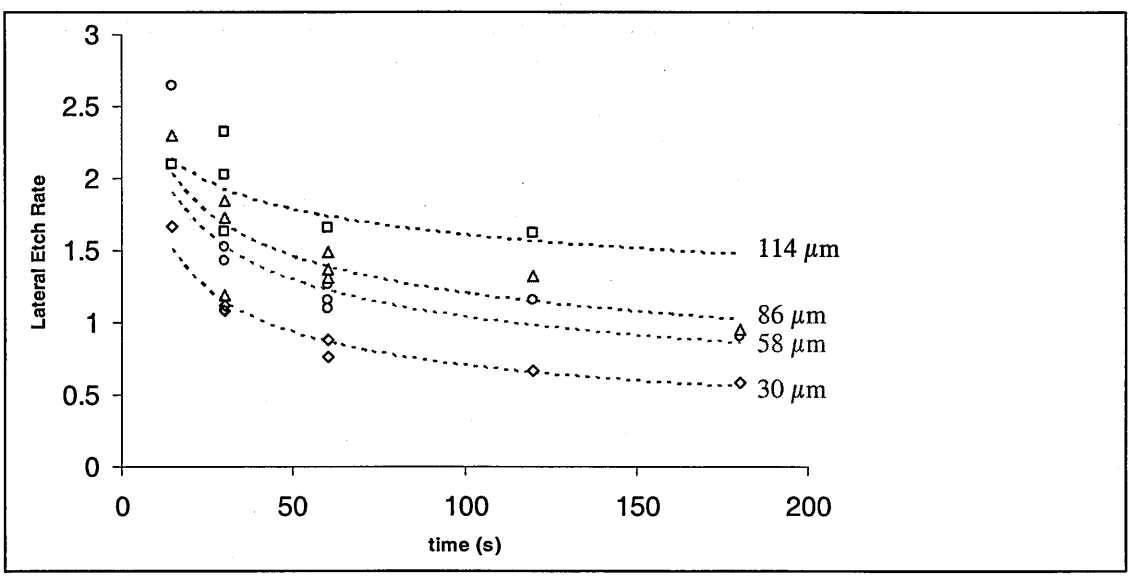


Figure 9.4 **Plot of Lateral Etch Rate (feature undercut divided by process time) Vs process time for various mask aperture sizes (circular holes). Trend lines are presented for every sample. The colour of the line and the marks is indicative of the original feature size.**

9.1.2. *Direct evidence of etching related to the orientation of preferential crystalline planes* (CODE)

The result of anisotropic effects in action during etching is chiefly evident if one observes the outcome of the etching of square-based pillars within a larger aperture, as in figure 9.5. The side view of these pillars shows how the slope of the sidewalls is very near to the typical angle between <111> and <100> planes (54.74°). The pillars were etched with no bias, in pure SF_6-based plasma (same cycle as for the sample of figure 6.44).

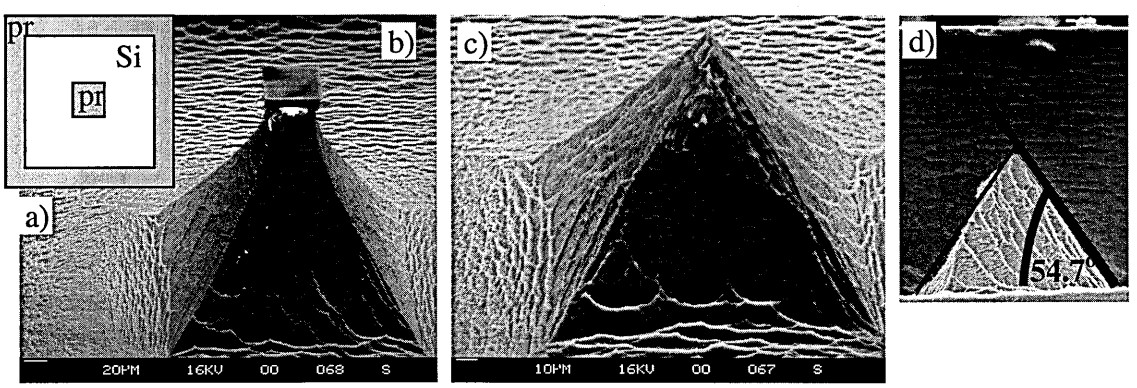


Figure 9.5 **Slowly etching <111> planes arising during etching of a pillar in SF_6 ICP Reactive Ion Etching. a) Mask Pattern, b) Pillar, originally 150 microns large, c) Pillar, originally 100 microns large, d) Front view of the pillar of figure c with indication of the 54.7° angle.**

9.1.3 *Indirect evidence of etching related to the orientation of preferential crystalline planes I: analysis of surface roughness*

The rubber replica of a circular cavity etched in a <100> Si wafer for 1 hour with platen power equal to zero was pictured in figure 6.44. This feature represents a typical cavity etched with the minimum ion flux energy possible (i.e. no platen bias). Zooms relative to different crystalline directions were added to the picture. The surfaces bear the clear signs of CODE. Shikida et al. etched anisotropically a single-crystal Si hemisphere in KOH-based etchant and then characterised the morphology of surfaces developed along different directions [*Shikida et al., 2000*]: their analysis represent a framework to which the results of figure 6.44 can be compared. Moving along the meridian between the (110) and (111) orientation, a transition is observed from a columnar pattern to a stepped surface. These ripples are always bounded by the <111> and <11$\bar{1}$> planes. The steps become wider as the (111) direction is approached until the surface becomes eventually smooth. Notice that seen from the (111) direction perspective, the microstructure may appear as made of a pile of <111> oriented layers of rough triangular shape. This is particularly evident in the surrounding of the <1$\bar{1}$1> plane. In the meridian between the (110) and (100) orientations the usual columnar structure is observed at first. Subsequently, the columns break into a series of pyramidal step as the bottom of the cavity is approached. This typology of surface is expected to show the highest roughness. Then steps become wider and finally smooth surfaces appear again in the (100) direction (bottom of the cavity). Not all morphologies highlighted by Shikida et al. could be observed in the cavity of figure 7.72, probably because the shape is not exactly spherical but it develops as a result of the balance between local preferential etching and the overall tendency towards an isotropic contour, as will be detailed in section 9.3.

The sample of figure 6.44 underwent extensive wet anisotropic etching in KOH solution to highlight more clearly the crystalline-related character of the dry etching (figure 9.6). The wet anisotropic etching process does not seem to change the patterns already present on the surfaces of the cavity. On the contrary, these became more delineated if compared with figure 6.44 or 6.73*a*, the SEM pictures of figure 9.6 demonstrate how the surface patterns developed after wet anisotropic etching results in an amplification of the patterns already present on the contours of the cavities.

A <110> oriented wafer was subjected to the same etching cycle of the sample of figure 6.44. The process yields cavities that possess the same typologies of superficial patterns shown in the replica of figure 6.44, but in different positions (figure 9.7). Notice also that circular apertures tend to develop into hexagonal shape when etching a <110> cut wafer, whereas they tend to become square for a conventional <100> wafer (front views of figure 6.39).

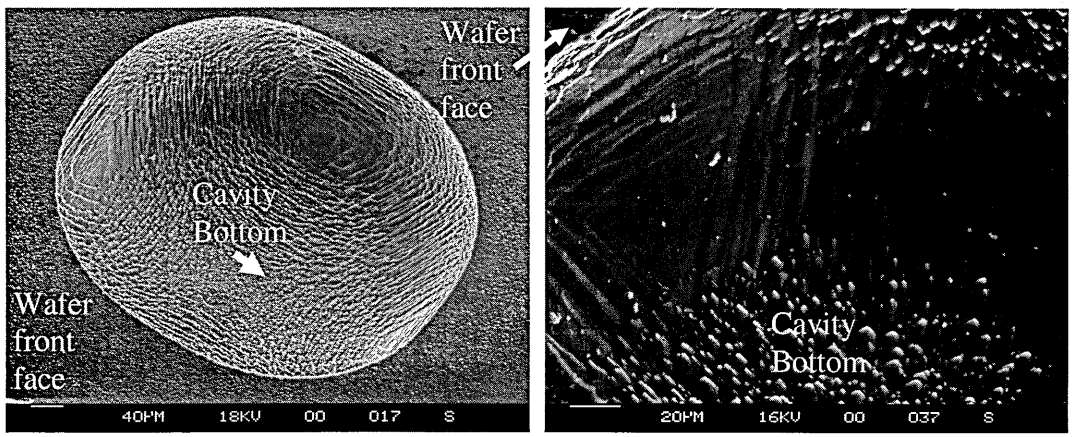


Figure 9.6 **Cavities from samples etched with no platen bias (same sample as for the replica of figure 6.44). The sample was wet etched for 20 minutes (left picture) and then 40 minutes (right picture) in a KOH-based solution (anisotropic etching).**

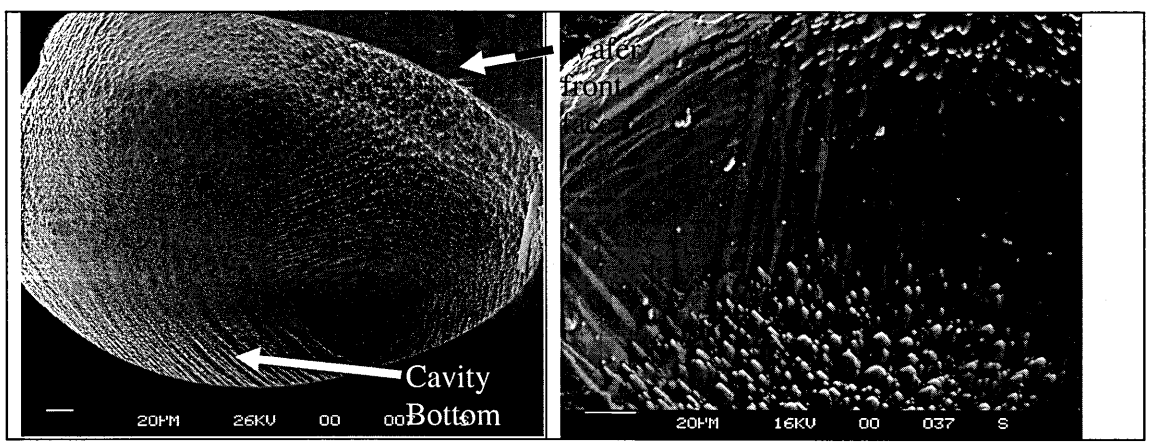


Figure 9.7 **Cavity from a sample etched with no platen bias. The silicon wafer was cut along the <110> plane.**

Through section 6.2.3 it was repeated that an increase in bias power does not induce a notable change in the overall feature aspect ratio (or in the etch factor, e.g. figure 6.27). However, an increase in the energy of the flux may cause dramatic changes in surface quality. A direct inspection of the cross sections of cavities obtained under different process conditions was reported in figure 6.45. It was showed how a transition rough-smooth occurs at the bottom of the cavities as bias power is introduced. Conversely, the sidewalls are not subjected to such a consistent smoothening: they remain visibly rough. However, both the bottom and the sidewalls of the cavities become slightly smoother when O_2 is added to SF_6 in small amounts (~ 10%). From the analysis of the photographs of figure 6.45 and from the analysis of many other samples (not reported here), it was concluded that the parts of the cavity subjected to direct ion flux develop etching fronts far smoother than those parts that are concealed from the ion flux. The quantitative analysis of roughness seem to confirm the above trend. In fact, the plot of figures 6.51 to 6.53 would suggest that the surface "roughness" is highest in the

proximity of the upper aperture of the cavity, i.e. the area that is completely concealed from both ion and radical direct fluxes (compare with the scheme of figure 9.16*b*). The same figures demonstrate also that the roughness of the sidewalls decreases slightly when O_2 is added to the mixture. Roughness is also slightly reduced when pressure is reduced or a backing wafer is bonded to the device wafer. (In both cases the temperature at the immediate etching front surface is expected to increase.)

9.1.4 Indirect evidence of etching related to the orientation of preferential crystalline planes II: evolution of the 3 – d shape of the cavities

Interestingly, although the difference in etch rate between the crystalline planes is visually evident in picture 6.44, no evidence emerges from the analysis of profiles: contours seem to be dictated only (or mainly) by the kinetics of the process. Figure 9.8, elaborated from the contour plots (i.e. the cross sections of the cavities), reports the etch rate as a function of direction angle for cavities of different size and for two different samples (black curves). When the boundaries were compared to the profiles that would be obtained from a pure anisotropic etching (grey curves), no evidence of a minimum in the <111> direction was found. However if the etching is prolonged up to 270 minutes, at zero bias, the preferential etching dramatically affects the overall cavity shape, as shown in figure 6.46.

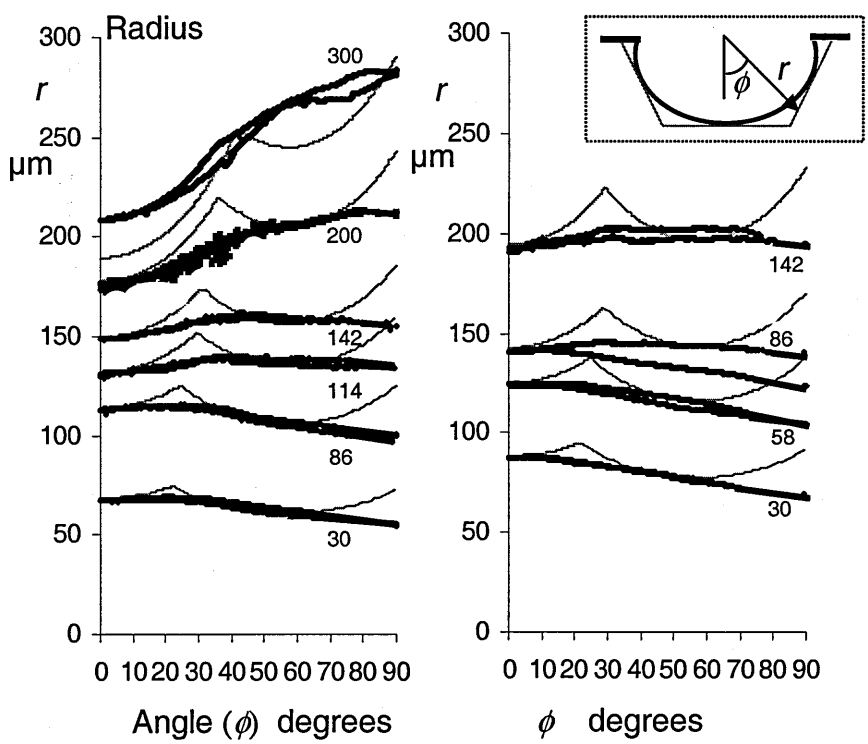


Figure 9.8 Plots of etch depth (*r*) Vs direction angle for the samples etched for 60 minutes at zero bias (left) and 10 bias with 10% O2 in mixture (right) The ideal boundary, developed in wet anisotropic etching is reported in grey. The numbers near the curves represent the original diameter of the mask apertures

On the contrary, considering the evolution of the front section of the cavity, the cavity does not remain circular but encounters a deformation. Circular apertures in <100> oriented wafers tend to become squares as the etching proceeds. (When <110> wafers undergo etching, circular apertures deform towards a fairly hexagonal shape and not a square.) In general, the extent of this deformation depends on process parameters (see an example in figure 9.9). A simple procedure was devised to assess the deviation from the circular shape independently on the scale of the aperture. The optical picture of the apertures (top view) was transformed in b/w images and boxed in a square. The ratio between the area of the outer square and the area of the aperture (in pixels) was computed. The lower limit of this ratio is equal to 1 (when the aperture fills the square completely) and the upper limit is generally 1.273 (when the cavity remains a perfect circle).

The ratio is plotted as a function of original mask aperture diameter (circular holes) for the front face of the wafer in figure 9.10. Conversely, figure 9.11 reports the deformation for the bottom of the features. This deformation was calculated on bottom membranes for though-wafer etching (e.g. the pictures of bottom membranes of figure 6.49) and on the front-view of the rubber silicone replicas from the samples where the etching did not proceed through the wafer (e.g. bottom series of pictures of figure 9.9).

The deformation was always more marked for the front face of the cavities than the bottom (or bottom section). This is qualitatively evident in figure 9.9 comparing the front and bottom view for the same cavities. However, this result can be also demonstrated quantitatively by subtracting each point of figure 9.11 from its respective point of figure 9.10. In this case, the result is always a positive number. In other words, the bottom of a cavity is always subjected to an extent of deformation lower than the top part of the same cavity. Notice that the parts that show a lower degree of deformation correspond to those subjected to the action of direct ion flux and radical flux.

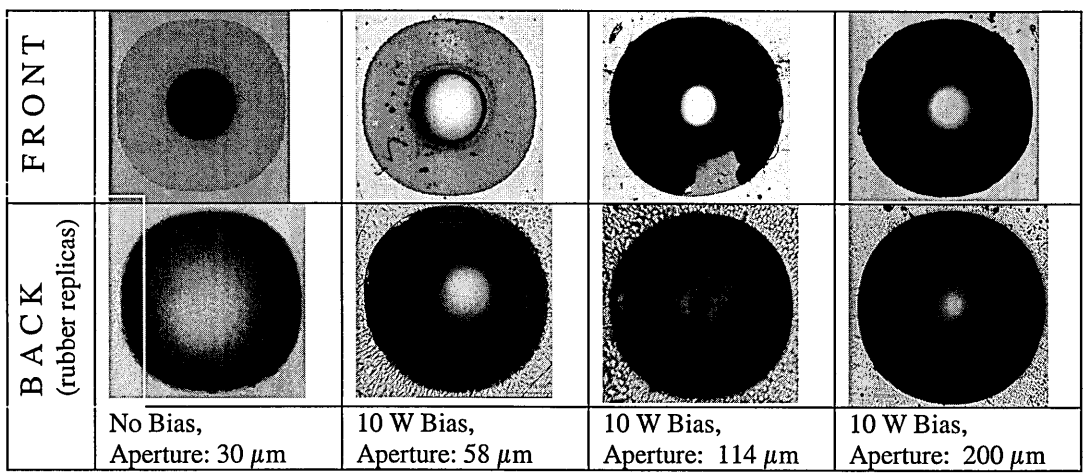


Figure 9.9 **Series of front views (optical microscope) taken from various samples (all etched for 1 hours) showing a different extent of deformation of the originally circular cavities. The scale is different for each picture. The diameter of the cavity is indicated below each picture.**

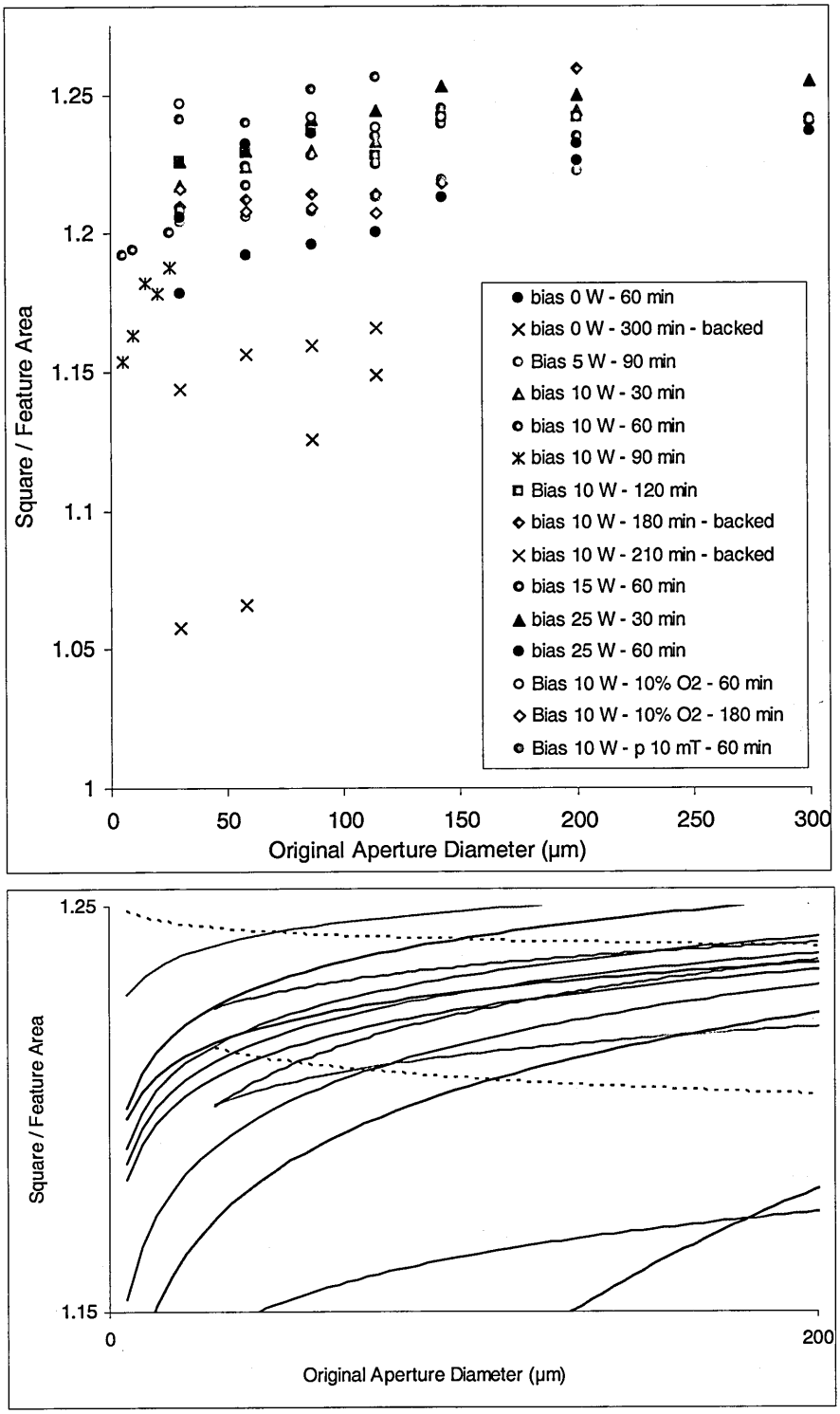


Figure 9.10 The deformation of originally circular apertures after SF_6 etching of monocrystalline Si wafers. Top: experimental data; Bottom: trend lines for the above data. For other comments, see text.

The deformation was more evident at low bias power or in absence of backing wafer. (When a backing wafer is added, the cooling becomes less effective and the temperature of the wafer increases during etching: this is demonstrated by a general decrease in

mask selectivity – see section 4.3.4.) Deformation increased with process time. Furthermore the loss of the original circular shape became more marked for smaller original aperture size. The presence of oxygen in the original etching mixture seems to cause a decrease in the extent and an inversion in trend: larger features showed higher deformation. The trends are far less clear for the opposite side of the cavities.

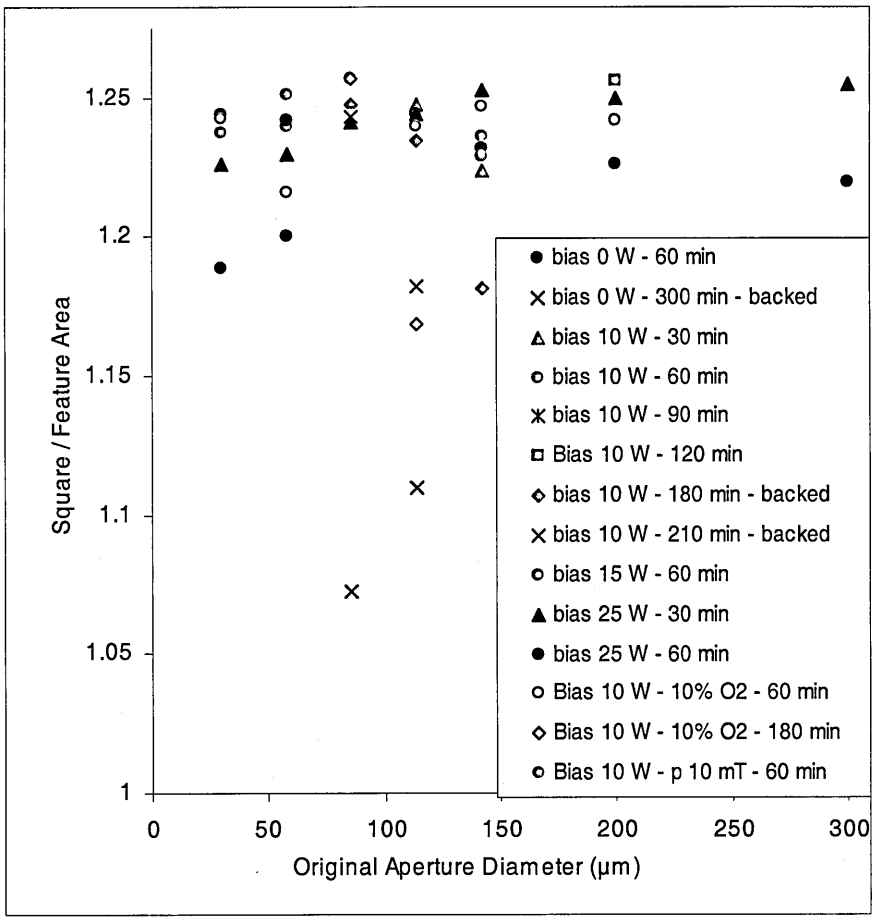


Figure 9.11 The deformation of the bottom part of isotropically etched cavities. For other comments see text.

Due to the isotropic nature of the etching, originally squared apertures tend to develop round corners. When cavities are etched through the wafer, the bottom membranes originated from squared apertures are generally round. For etching times longer than one hour, the memory of the original aperture shape is lost: in other words, squared and circular apertures tend to generate cavities almost identical in shape. In figure 9.12 bottom membranes of (through-the-wafer) cavities originated from squared apertures are reported. As the original dimensions of the cavities become smaller (and the vertical etch rate lower) the membranes resemble more a circle. This demonstrates the isotropic nature of the etching, in particular for the very bottom of the feature, which is directly hit by the ion flux.

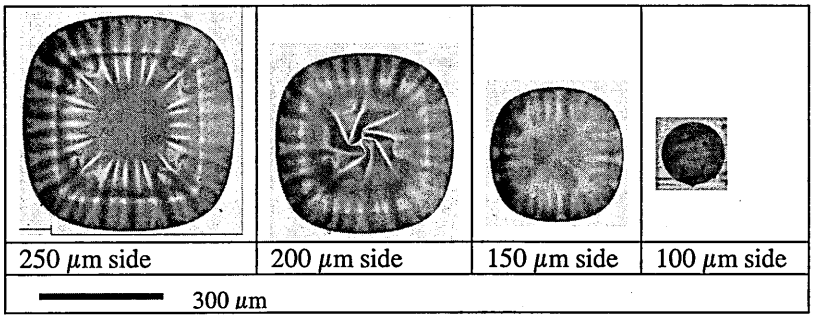


Figure 9.12 Series of front views (optical microscope) taken from the back side of a Silicon Oxide coated Si wafer etched for 3 hours in isotropic etching. The membranes represent the bottoms of cavities etched through the wafer from originally squared cavities. As the original dimensions of the cavities become smaller (and the vertical etch rate lower) the membranes resemble more and more a circle.

9.2 Comparison between the results presented and the major findings and trends reported in literature

In this section the results reported in section 4.2 will be compared with findings for similar processes reported in literature.

9.2.1 Shape of the cavities and the trends of vertical and lateral etch rates with time and aperture dimension

The typical contours of the cavities etched in pure SF_6 are direct expression of the chemistry of the etching process at the feature scale level (see section 3.3). Features of various shapes are observed (or predicted) by different authors according to the mechanism prevailing in the kinetics of the cavity micro-rector. These phenomena will be treated in details in section 9.2. Boundaries similar to those reported in figures 6.26 and 6.48 can be easily found in literature (e.g. in [*Gerodolle and Pelletier, 1991*; *Singh et al., 1992*; *Richter et al., 2001*]. Etch factors of the order of 1.4 were found also after pulse-etching of Si in gaseous XeF_2, although no plasma or ion flux are involved in this etching technique [*Sugano and Tabata, 2002*; *Chu et al., 1997*]. Finally, even wet isotropic etching does not always produce perfectly isotropic boundaries: etch factors higher than one may occur, depending on the kinetic balance between the diffusion of reactant to the etching front and the surface reaction [*Madou, 2003, Chapter 4*; *Schwesinger and Albrecht, 1997*].

The dependence of etch rates on aperture size and time reported in figures 9.1 to 9.4 are not uncommon. The general decrease of etch rate with time is observed by all authors (both experimentally and in most simulation results), when the etching reaction has a chemical nature. In this case, the decrease in etch rate is theoretically predicted by the mass balance. At the steady state, this entails a decrease in the density of the radical flux at the etching front because the etching front grows larger while the mask aperture stays fixed (and so remains the radical flux entering the cavity) [*Mayer and Barker, 1982*; *Gallatin and Zarowin, 1989*]. This decrease is maximum when the surface reaction represents the etch rate limiting step and minimum when the radical diffusion to the

etching front is dominant [*Singh et al., 1992, Harafuji and Misaka, 1995*]. This decrease is not expected when the reaction is mainly ion induced (i.e. of physical nature – sputtering – as opposed to chemically induced) [*Singh et al., 1992, Harafuji and Misaka, 1995*].

The increase in etch rates with aperture size is reported by many authors. Some examples, relative to processes where the ion flux had little or no effect on the etch rates, are plotted in figure 9.13 and 9.14. Notice that these trends do not coincide with the classical ARDE effect (as described in sections 3.3 and 3.5). ARDE has complex and unclear origins and somewhat unpredictable outcomes [*Elwenspoek and Jansen, 1998, Chapter 12 – 14; Bailey and Gottscho, 1995*]. On the contrary, the decrease in etch rates with mask aperture dimensions can be easily explained and predicted advocating the shadowing of the radical flux (see section 9.3). The difference between ARDE and this scaling effect was highlighted (for etching in defect of passivation) in figure 6.25. Harafuji et al. found that, as the coverage of the etching surface increases (that is as the ion contribution becomes more important), the gain in vertical etch rates with aperture sizes decreases [*Harafuji and Misaka, 1995*]. In other words, as the ionic contribution to etching grows, the depth of the features tends to become independent on the size of mask aperture.

The increase in etch rates with feature size in absence of ion bombardment demonstrates the crucial difference from the ARDE effect. For example, Sugano et al. [*Sugano and Tabata, 2002 (bis)*], while etching Si cavities in gaseous XeF_2 (no ionic flux involved), found such an effect. Furthermore, the gain of etch rate with mask aperture size was directly proportional to pressure and inversely proportional to temperature (etch rates tend to decrease in both cases). The pressure has the same effect in the findings of this research. Furthermore, by introducing a backing wafer, similar effects were found: the presence of a backing wafer might be though to lead to an increase in the temperature (since cooling becomes less effective).

It was stressed many times that, for etching times shorter than one hour, other processing parameters (such as the addition of Oxygen or the RF bias applied to the wafer) seem to have a slight effect on the etch rates. This finding was partly corroborated by the technical literature produced by STS, which attributes little or no role to the ion flux [*Ashraf et al., 1999*]. If this may be true for the ICP Multiplex reactor, in other processes, other authors found that the slope of the dependence depends heavily on process parameter such as bias power.

9.2.2 *Direct evidence of etching related to the orientation of preferential crystalline planes* (CODE)

Ulacia et al. published probably the first record of anisotropic effects related to crystalline planes orientation affecting a dry etching process [*Ulacia et al., 1988*]. The authors etched trenches in <111> and <100> cut silicon wafers using a $SF_6/C_2ClF_3/CH_4$ mixture and a RIE plasma process. They noticed the emergence of <111> planes at the bottom of the trenches. This led to trenches with cusp bottoms ("V" grooves) in <100> oriented wafers whereas the bottom of trenches remained flat in <111> Si wafers. It is important to stress that their trenches measured a few microns. Preferential etching

phenomena of a far larger extent were found in this research (for example in figure 9.5). Ulacia et al. measured an ER ratio ($ER_{<100>}$/ $ER_{<111>}$) of about 0.68 in open areas. (They compared this value to the ratio between the bond density in the two planes, i.e. $B_{<100>}$/ $B_{<111>} = 6.8 \text{ X } 10^{14} / 11.8 \text{ X } 10^{14} = 0.58$) Later, similar effects where demonstrated by [*Blauw et al., 2000*] and [*Rangelow, 2001*] after Cryogenic Etching of Si.

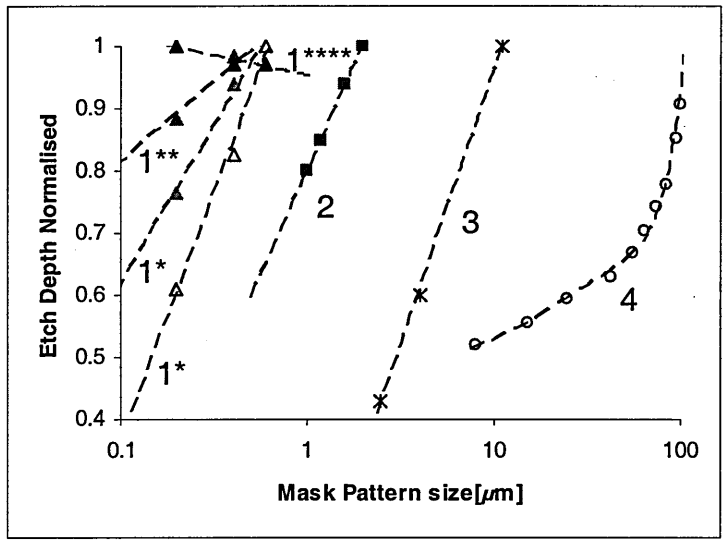


Figure 9.13 Plots of Normalised Vertical Etch Rate Vs Size of Mask Aperture. Data taken from the literature. 1: from [*Harafuji, 1995*] model of RIE, theoretical results; 1*: fluorine coverage / ion coverage = 1, 1**: fluorine coverage / ion coverage = 5, 1***: fluorine coverage / ion coverage = 50, 1****: true isotropic etching (the surface reaction is the rate limiting step). 2: from [*Yamamoto, 1987*] model of RIE, theoretical results. 3: from [*Gerodolle, 1991*] model of RIE, theoretic results. 4: from [*Sugano, 2002*] XeF_2 gas etching, experimental results.

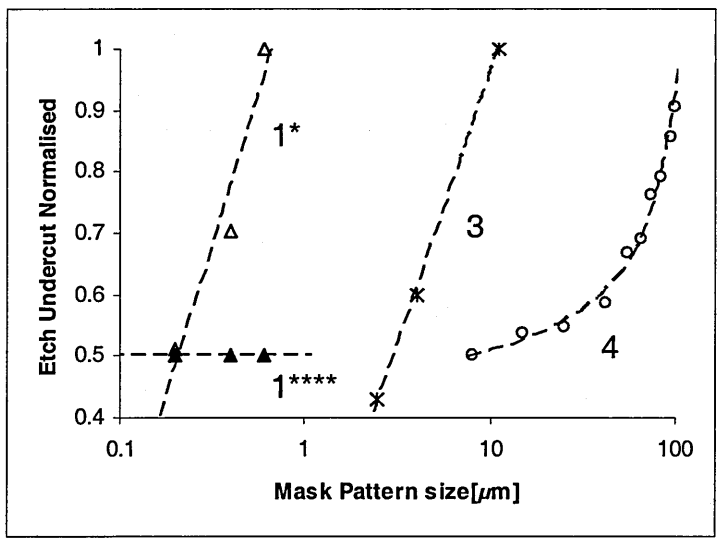


Figure 9.14 Plots of Normalised Lateral Etch Rate Vs size of Mask Aperture. Data taken from the literature. 1: from [Harafuji, 1995] model of RIE, theoretical results; 1*: diffusion limited etching process, 1****: true isotropic etching (the surface reaction is the rate limiting step). 3: from [Gerodolle, 1991] model of RIE, theoretic results. 4: from [Sugano, 2002] XeF2 gas etching, experimental results.

Subsequently, deBoer et al. in their large study on Cryogenic RIE of Silicon in SF_6/O_2 plasma showed many examples of CODE or "crystallographically determined etching" (as they call it) [*deBoer et al., 2002*]. Notably, they showed deep trenches with "V" grooves at the bottom and cavities of more than 100 μm in diameter, where the etching is preferential to such an extent that the bottom of the cavity resembles an anisotropically wet-etched pit. The emergence of large steps, bounded by flat planes, is analogous to the phenomenon found when etching in SF_6/C_4F_8 mixtures (see, e.g. figure 6.34). Finally, they showed a pillar with a well defined geometrical structure, such as the pillars of figure 9.5 (although its faces are not <111> oriented).

It was also showed how even wet isotropic etching of silicon may induce preferential effects, which may lead to the formation of large peaks or steps [*Schwesinger and Albrecht, 1997*].

9.2.3 Indirect evidence of etching related to the orientation of preferential crystalline planes I: analysis of surface roughness

Not many papers detail the roughness of the sidewalls on cavities with complex contours. None was found that analysed roughness quantitatively. This is probably due to the intrinsic difficulties of assessing superficial features in narrow concavities with continuously varying slopes. (Similar measurement problems were reported in the experimental part of this thesis, in section 4.3.5.)

Some authors characterised the roughness of etched silicon after open surfaces or very large apertures were subjected to a short etching cycle (i.e. to a few microns of depth). For example Chandrasekaran et al. analysed the roughness after wet or dry etching of silicon, but no evidence of preferential etching is reported (i.e. not steps nor peaks nor cusps bounded by <111> nor other slowly etching planes) [*Chandrasekaran and Sundararajan, 2004*]. Similarly, Sugano et al. do not refer to any CODE and the nature of the surface roughness (if it is random or periodic) is not clear [*Sugano and Tabata, 2002, (bis)*]. They do claim, indeed that surface roughness increases with etching time and etching depth and etch rate and decreases with surface temperature. These trends could be easily explaining advocating CODE effects (see section 9.3). Sugano et al. found that a maximum roughness of 10 nm is achieved, but the surfaces they characterize are etched only for a very short time and for a few microns [*Sugano and Tabata, 2002, (bis)*].

In [*Richter et al., 2001*], the authors reported on different kinds of surface roughness affecting the sidewalls of cavities obtained by different DRIE processes (in many cases similar to the results of section 6.2.6). They also showed cavities etched in pure SF_6 with smooth sidewalls. However, these trenches were very large and most of the etching front seemed to be directly exposed to radical flux (such as is the bottom of the features of figure 6.45*b*). Cavities with smooth sidewalls were produced by this research too under such conditions. Subsequently they etched buried micro-channels by applying pure SF_6 etching to the bottoms of trenches with heavily passivated sidewalls. In this case, it was possible to observe a roughening on the parts of the cavity that were protected from direct radical flux. The patterns demonstrated in the SEM pictures they

presented are very similar to the sidewalls patterns of figure 6.45. However, they made no reference to CODE effects albeit, in one instance, they presented a picture of small buried micro-channels that appeared to be bounded by flat crystalline planes.

CODE appears clearly in some of the pictures reported in [*Chu et al., 1997*], after pulsed etching of Si in gaseous XeF_2. In this paper, the authors etched cavities from circular and squared mask apertures. The quality of the surfaces and the pattern of roughness that can be observed were strikingly similar to the results reported in section 6.2.6 (figures 6.44 and 6.45).

9.2.4 Indirect evidence of etching related to the orientation of preferential crystalline planes II: evolution of the 3 – d shape of the cavities

The overall deformation of the boundaries to produce flat planes corresponding to crystalline planes was reported by many authors (see section 9.2.2). On the contrary, no evidence could be found in literature that could be compared to the deformation of circular mask apertures. The deformation of a circular aperture to produce a squared cavity can be compared to the classic anisotropic etching of wagon wheel patterns to calculate the degree of anisotropy of a wet etchant solution [*Madou 2003, Chapter 4*]. Sugano et al. [*Sugano and Tabata, 2002*] looked for crystalline anisotropy in the etching of silicon using XeF_2 gases (no ion flux). However, after etching a wagon wheel pattern, they could not find any evidence of preferential etching.

deBoer et al. showed the only example of deformation that could be compared with those reported in section 9.1.4. In [*deBoer et al., 2002*], they showed a high-aspect ratio cavity originating from a circular mask aperture that developed a squared bottom. Perhaps more revealing would be the comparison of the deformation with the effect that a perfectly wet anisotropic etching would have on circular mask apertures. In a perfectly anisotropic etching process, every component that promoted isotropy would be set to zero. The shape of the cavities would be totally determined by the slow etching crystalline planes (in this case the <111> planes). In fact, a quick simulation with a demo version of the software SIMODE ® [*www.gemac-chemnitz.de/*] demonstrates that circular mask apertures tend to become squares if subjected to anisotropic etching. 3 - d images of such cavities are reported in figure 9.15. It can be clearly observed how the deformation increases with time and decreases with aperture diameter. These are exactly the same trends that were found for the cavities etched in pure SF_6 (figure 9.10).

9.3 Analysis and model for the etching of silicon using fluorine radicals

In this section, a qualitative model is proposed for SF_6 plasma etching of Silicon, based on the results reported in sections 9.1, 6.2 and 6.3. An overview of plasma models for DRIE was reported in section 3.3. The focus is on explaining the evolution of features shape and surface roughness. These issues emerge at the feature-scale level and their analysis would require a far more complex feature-scale-level plasma model. The model presented in this section is elaborated from the class of phenomenological models developed by the groups of McVittie [*Singh et al., 1992*], Elwenspoek [*Elwenspoek and Jansen, 1998*] and Oldham [*Oldham et al., 1980*]. Following their lead, other groups

developed software simulations based upon similar principles but more suitable for deeper and larger cavities [*Strasser and Selberherr, 1995; Harafuji and Misaka, 1995*].

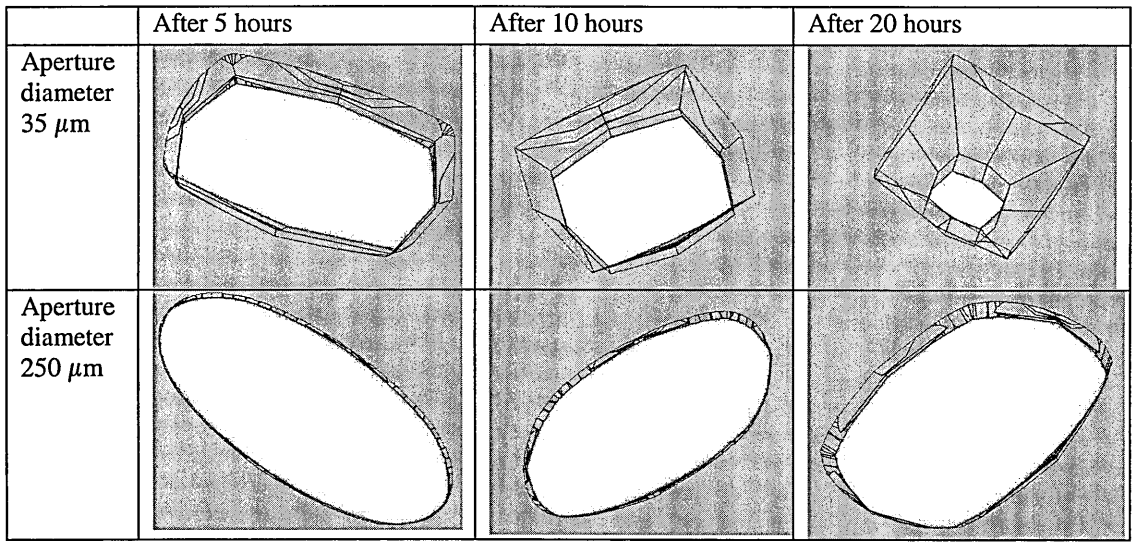


Figure 9.15 3-D images of wet etched features produced by simulating the process with a demo-evaluation version of SIMODE ®. The front of the wafer and cavities sidewalls are pictured in gray. The bottom of the cavities is pictured in white.

9.3.1 Kinetic balance, etch rates and the evolution of the etching front

The two relevant streams of primary particles that reach the etching front within a microscopic cavity are reported in the schematic of figure 9.16*a,b*. These are the radical (fluorine) and ionic (SF_x^+) fluxes. The main inputs of the feature-scale model are the radical angular distribution (RADF), the ion angular distribution (IADF) functions and, finally, the ion energy distribution function (IEDF). Given the sensitivity of these fluxes to the geometry of the cavity and the local conditions, it is extremely difficult to measure these distributions directly. (Furthermore, the STS-ICP Multiples apparatus used for this research does not have any instrument for measuring these fluxes.) Alternatively, they could be derived from higher hierarchies of plasma modeling (such as those that address the dark sheath electrodynamics). Such simulation tools were not available within the framework of this research. To simplify matters, a series of assumptions had to be made. A common assumption is that the ion flux has a Gaussian distribution at the entrance of mask aperture whereas the radical flux is isotropic [*Elwenspoek and Jansen, 1998, Chapter 14*]. IADF and RADF are represented in the plot of figure 9.17. Once inside the cavity, the radical distribution is no longer isotropic, due to the shadowing effects. Besides the primary flux, fluorine radicals can reach the etching front in other two ways, schematized in figure 9.16*c, d*. First, once absorbed, they can diffuse along the surface towards the zones of etching front that are depleted of fluorine (figure 9.16*c*). These zones are found just below the mask, where the radical flux is almost totally shadowed. Secondly, if the sticking coefficient (S_R) is lower than one, then the absorbed fluorine radicals can be back-scattered and retro-diffuse into the cavity (figure 9.16*d*). In both cases, the secondary radicals are most likely to attack the etching front (i.e. the boundary of the cavity) in a truly isotropic fashion.

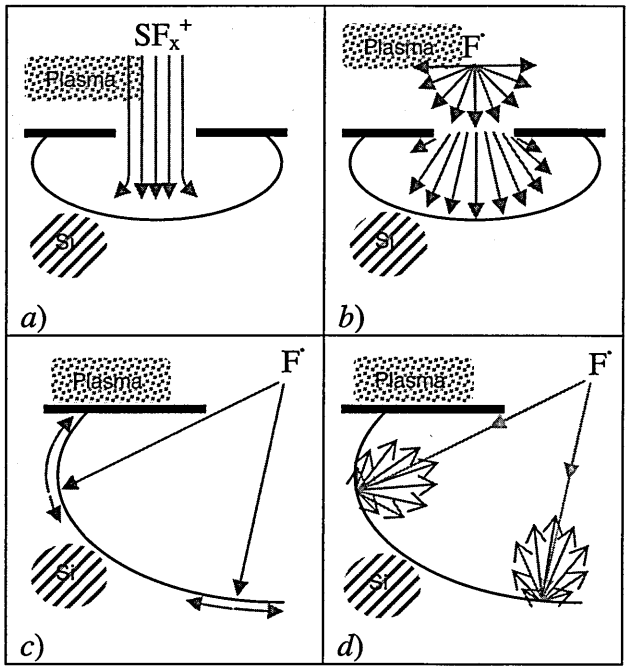


Figure 9.16 Schematic of the main fluxes active in a micro-cavity during SF_6 plasma etching of Silicon. *a)* Ion flux, *b)* Radical flux, *c)* Diffusion of fluorine radicals along the surface, *d)* Back-scattering of fluorine radicals with retro-diffusion.

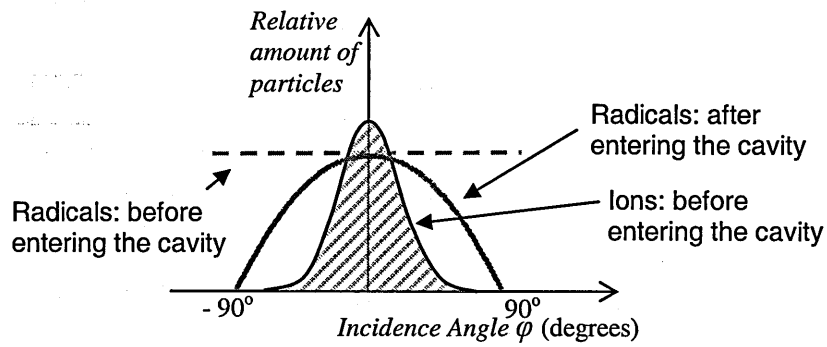


Figure 9.17 Conventional distributions assumed for IADF and RADF.

Once the gas kinetic within the cavity has been clarified, it is crucial to understand how these fluxes interact with the silicon surface. It is important to identify which particles are primarily responsible for the etching reaction and what is the nature of the reactions occurring at the surface. These may be highly complex and non-linear issues, involving considerations of statistical dynamics about adsorption equilibrium. However, for the purposes of this discussion, the following simplifications can be assumed:

1) In pure SF_6 etching of Silicon no passivation occurs: the reactants absorbed on silicon either react or are backscattered, but do not build up;

2) The ions play no direct physical role in etching: the process is chemically induced and the etch rate R has a first order dependence on the radical flux [*Flamm et al., 1981*], i.e.
$R = k_R \phi_R S_R (1 - \chi_R)$ $[Lt^{-1}]$ (9.1)
where ϕ_R is the local radical flux, S_R is the sticking coefficient, and χ_R the relative amount of surface sites occupied by fluorine (k_R is the kinetic constant). In other words, the diffusion of radicals to the surface represents the rate limiting step. (This is clearly expressed also in [*Singh et al., 1992*; *Elwenspoek and Jansen, 1998, Chapter 14; Ashraf et al.,1999*; *Otto et al., 1999*].)

3) For the relatively large features treated in this research, the etch rate may be thought of as the linear combination of three factors: the etch rate related to the synergetic effect of the ions (R_I), the etch rate related to the primary radicals (R_R) and a third factor (R_{Riso}) that includes the etching by secondary radicals (both retro-diffused or surface diffused) [*Strasser and Selberherr, 1995; Harafuji and Misaka, 1995*].

The relative relevance of the three etching factors in determining the etch rate can be assessed by observing the evolution of the etching boundary, which is direct consequence of the balance between them. In effects: R_I is expected to be highly anisotropic, R_R should depend on the "visibility" of etching front from the mask aperture and R_{Riso} is theoretically truly isotropic.

The main reactions involved in the process were reported in section 3.3 and are here repeated:

$$n\mathrm{CF_x^{\cdot}} \rightarrow n(\mathrm{CF_2})_{ads} \rightarrow n(\mathrm{\text{-}CF_2\text{-}})_{ads} \qquad (3.10,rep);$$

$$n(\mathrm{\text{-}CF_2\text{-}})_{ads} + \mathrm{F^{\cdot}} \xrightarrow{(\mathrm{SF_x^+})} n(\mathrm{CF_2})_{ads} \xrightarrow{(\mathrm{SF_x^+})} n\mathrm{CF_x^+} \qquad (3.11,rep)$$

and

$$\mathrm{Si} + \mathrm{F^{\cdot}} \rightarrow \mathrm{Si}\text{-}n\mathrm{F} \rightarrow (\mathrm{SiF_x})_{ads} \rightarrow \mathrm{SiF_x} \qquad (3.12,rep).$$

Although the surface reaction kinetics is far more complex, such a simple model was assumed to describe the interaction of silicon with fluorine radicals. However, the simple model proposed is enough to explain most of the results. A vast survey of the surface science of this reaction, up to the early 90s is in [*Winters and Coburn, 1992*].

The role of the ion-induced etching rate can be clarified analyzing the results. Section 6.2.4 introduced the hypothesis that the ion flux has negligible effect on the shape of the etching contour. The deviation from isotropy was rather induced by shadowing effects. It is now time to demonstrate such a claim, which is partially corroborated by the technical literature disseminated by STS [*Ashraf et al., 1999*]. Their papers attribute little or no role at all to the ion flux in the etching of silicon. The phenomenological models build on the framework reported above were surveyed. In most papers, and in particular in [*Singh et al., 1992*], it is demonstrated how contours very similar to those achieved in this research can be produced without advocating the effect of ion flux.

The similarity is more striking as the cavities are analysed in details:

- the bottom of the features is rounded as it is to be expected when a shadowing effect is in action as in figure 9.18*a* (if ion-induced effects where prominent, the bottom would be flat);
- the etch factor averages around 2: if ion-action had to be kept into account then the expected vertical etch rates would be up to 8 or 10 the lateral etch rates (figure 9.18*a*);
- the typical contour presents a double undercut (figure 9.18*c*): first, just under the mask with no Si left and then a secondary concavity of the profile, which adds to the overall undercut. The undercut directly under the mask (figure 9.18*a*, *b* and *c*) must be explained by a mechanism that brings fluorine to shadowed areas (such as surface diffusion or backscattering of reactants). On the contrary, the secondary undercut can only be explained by shadowing effect (see figures 9.18*b*,*c*).

The literature on plasma-less etching of cavities in XeF_2 gases demonstrated that etch factors higher than one can occur even without the effect of an ion flux (see section 9.2).

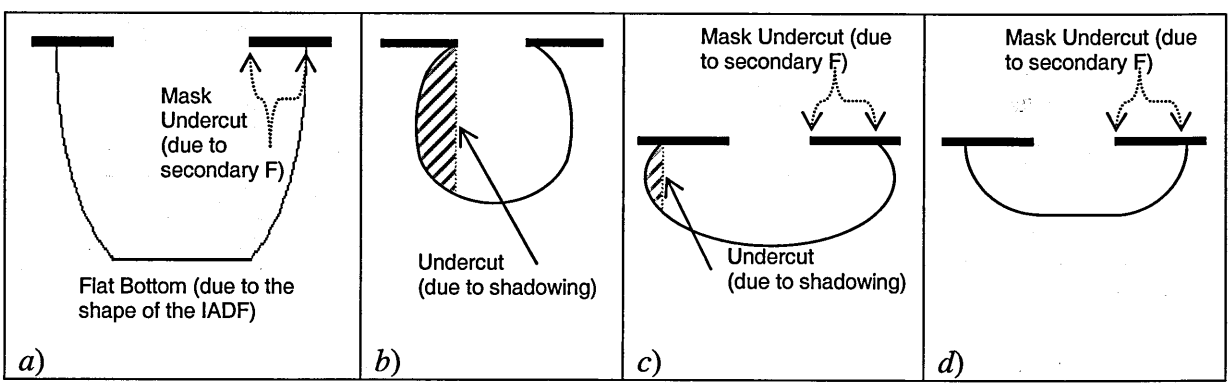


Figure 9.18 Typical boundaries of cavities caused by different kinetic balance within the cavity micro-reactor (schematic). *a*) ion-induced etching and lateral undercut due to secondary radicals, but no etching due to primary radicals, *b*) etching only due to primary radicals (sticking coefficient equal to 1), *c*) etching resulting from the combination of primary component (R_I) and secondary isotropic component (R_I). *d*) Purely isotropic etching.

Other proofs of the scarce effect of ion flux on the shape of the feature come from the dependence of etch rates on process parameter. First, there is no evidence of an increase in aspect ratio when the power flux is increased from 0 to 25 Watts. Secondly, if the vertical etch rate were the sum by the ionic-induced etching and the radical induced etching, then, once the lateral etch rate is subtracted, the remaining term should depend only slightly on the size of mask apertures. (The anisotropic component does not depend on mask aperture but on aspect ratio [*Bailey and Gottscho, 1995*].) On the contrary, it was found that, after subtracting the values of figure 9.2 (Lateral Etch Rates) from the respective values of figure 9.1 (Vertical Etch Rates), the resulting data still have a logarithmic dependence on aperture size. Finally, most models predict a logarithmic dependence of etch rates on aperture size even in absence of ion-related enhancement (but in presence of radical shadowing). Some of the data reported in literature were

gathered in the diagrams of figures 9.13 and 9.14. In analogy with the trends reported in section 9.1 (figures 9.1 and 9.2), some of the trends analysed in literature fit well with a logarithmic least square regression.

A test etching cycle was designed specifically to clarify the role of ion flux. The idea draws from the standard cycles employed for the fabrication of buried micro-channels [*deBoer et al., 2000*]. Cylindrical cavities were etched from circular mask apertures using the standard "deep" unidirectional ASE process (section 4.3.1). Subsequently, a thick C_4F_8 coating was deposited after a long passivation cycle. Finally, these cylindrical cavities were subjected to SF_6 etching for one hour. Typical cavities produced are reported in the cross sections of figure 9.19.

The cylindrical apertures act as a collimator both for the ion and radical flux. However, the collimation affects the radical flux to a far larger since the ion flux already shows a narrow distribution at the entrance of the cavity. A narrow collimated radical flux induces a flat bottom (left picture of figure 9.19), which contrast with the round bottom developed when the radical flux is not well collimated (right picture of figure 9.19). Such behaviour can be predicted by the above assumptions concerning the etching kinetics. R_R was calculated keeping only the shadowing into account ($S \rightarrow 1$), according to the formulae reported in [*Yamamoto et al., 1987*]. Plots of R_R as a function of the incidence angle and x-coordinate along the cavity are reported in figure 9.20. The vector $\boldsymbol{R_R}$ is applied to the etching front and always normal to it. The module of the vector $\boldsymbol{R_R}$ in a point P, along the etching front is equal to an arbitrary constant, multiplied by the local angle of sight. (In other word: the local etch rate is proportional to the incidence angle range within which the incoming radicals are able to hit the point P directly.) The grey line refers to a cavity of the kinds reported in section 6.2.3 (isotropic etching from simple mask apertures). The black line corresponds to a cavity of the kind reported in figure 9.19. In both cases the cavity is elliptical, it has a maximum aperture of 320 μm, a maximum depth of 159 μm and an aperture of 144 μm. In the second case (black line) the cavity is etched at the bottom of a cylindrical collimating cavity of 150 m in depth. Notice how the presence of the collimator yields a flat bottom.

It has to be concluded that even if the ion flux might play some synergetic role in activating the surface reaction, its effect must be negligible if compared with the radical contribution. The effects of the ion beam can be observed mainly locally (i.e. on surface roughness) and affect the evolution of the boundary only for very long etching times (e.g. right picture of figure 6.46). It is therefore assumed, for the purposes of this discussion, that the evolution of surface boundary is determined only by the two factors: R_R and R_{Riso}. The effects of the ion flux on surface roughness and CODE will be analysed separately in section 9.3.2.

A secondary physical mechanism has to be considered in order to introduce a certain amount of fluorine into shadowed area since the etching proceeds directly under the mask (as in figure 9.18*d*). The results point to identify surface diffusion as the main secondary mechanism, prevailing over back scattering of un-reacted fluorine. This is demonstrated by the etching behaviour of square pillars, as shown in figure 9.21. After 1 hour etching in pure SF_6, the sharp corners still maintain an angle of almost 90 degrees (figure 9.21*a*). Back-scattering is a 3 – d mechanism, as showed in figure 9.16*d*.

If back-scattering were the main route to delivery Si to shadowed areas, then the sharp corners of the pillar would be exposed for a 270° angles: this would result in rounding by etching (figure 9.21*b*). (Rounding of corners usually happens after isotropic wet etching [*Madou, 2003, Chapter 4*].) If, however, the fluorine radicals reach these areas along the surface (2 - d diffusion process), then these angles do not represent a particularly weak point. (In other words, from the point of view of the surface, they do not represent any point of high-flow density.) The sharp corners are maintained during etching (figure 9.21*c*). This argument was first advanced by Verdonck et al. [*Verdonck et al., 2002*]. Other authors, on the contrary, assume that retro-diffusion is the prevalent mechanism [*Singh et al., 1994*]. However, it might be that retro-diffusion becomes important in smaller or narrower cavities (i.e. at high Knudsen number) while surface diffusion prevails for large cavities with low aspect ratio and large mask apertures (i.e. large fluxes of reactants).

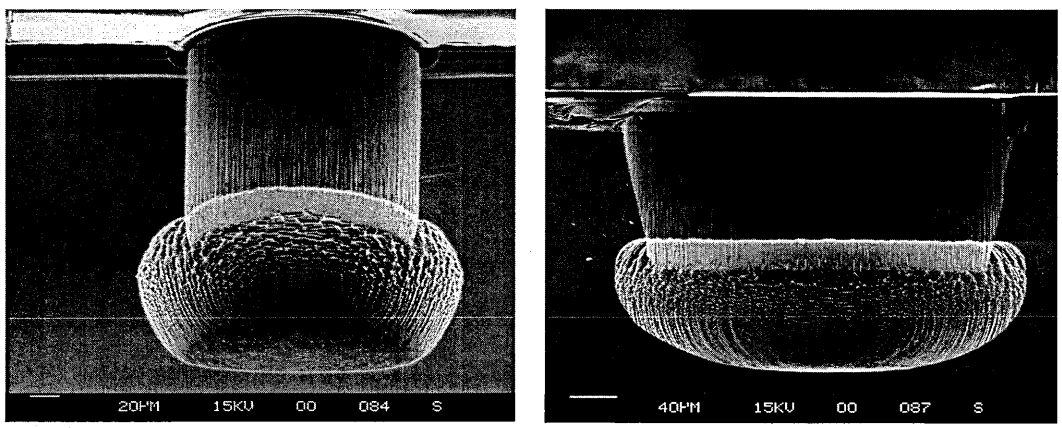


Figure 9.19 Cavities obtained by a three-stages process, modelled on the process traditionally used for producing micro-channels.

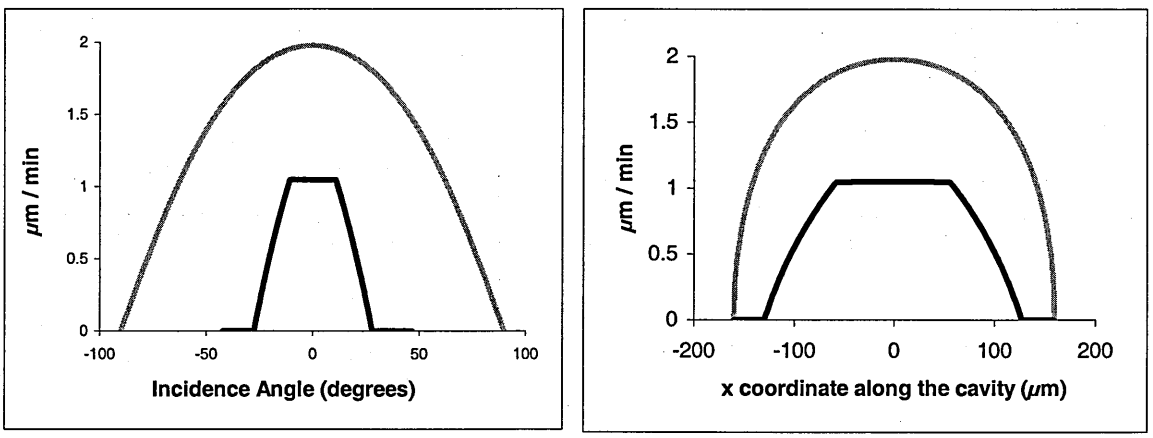


Figure 9.20 Plots of R_R along the etching front as a function of the incidence angle (*left*) and *x*-coordinate along the cavity (*right*). The grey line refers to an elliptical cavity; the black line refers to an elliptical cavity that receives a collimated radical flux (the type of figure 9.19).

This section concludes with the demonstration of how such a model, based on the interaction between primary and secondary fluxes of fluorine radicals, can explain the trends of figures 9.1 to 9.4. The decrease of etch rates with etching time is expression of the simple mass balance and is theoretically expected. It is assumed that the etching is at the steady state. A simple demonstration for the 2 – d case follows. (A demonstration for the 3 – d case, involving the use of differential geometry, is reported in [*Gallatin and Zarowin, 1989*].) Given a constant radical flux Φ_R in [atom $\mu m^{-1} sec^{-1}$] (in 2 – d), the number of particles entering into a cavity of extent $2r$ is equal to $2r\Phi_R$ and is constant on etching time t. If at time t_0 the cavity depth is equal to d_0, then at time $t > t_0$, the etch depth will be $d > d_0$. It is supposed that the surface reaction represents the rate-limiting process step, so that the etching is purely isotropic. It means that the fluorine radicals have time to spread across the entire etching front before reacting. (In other words, $S \rightarrow 0$.) In this case it is $R = k_R \phi_R$. The flux ϕ_R is equal to the ratio between the total number of particles entering the cavity in the unity of time and the length of the etching front (in 2 – d):

$$R = k_R \frac{2r\Phi_R}{2r + \pi d} \tag{9.2}$$

and

$$\frac{R(t)}{R(t_0)} = \frac{2r\Phi_R}{2r+\pi d} \frac{2r+\pi d_0}{2r\Phi_R} = \frac{2r+\pi d_0}{2r+\pi d} \tag{9.3}.$$

Since $d > d_0$, then $R(t) < R(t_0)$. The principle does not change if part of the fluorine reacts before being diffused as long as the process is in a steady state. Conversely, such a strong decrease of etch rate with etching time (or etching depth) is not normally observed in ion-flux-driven processes.

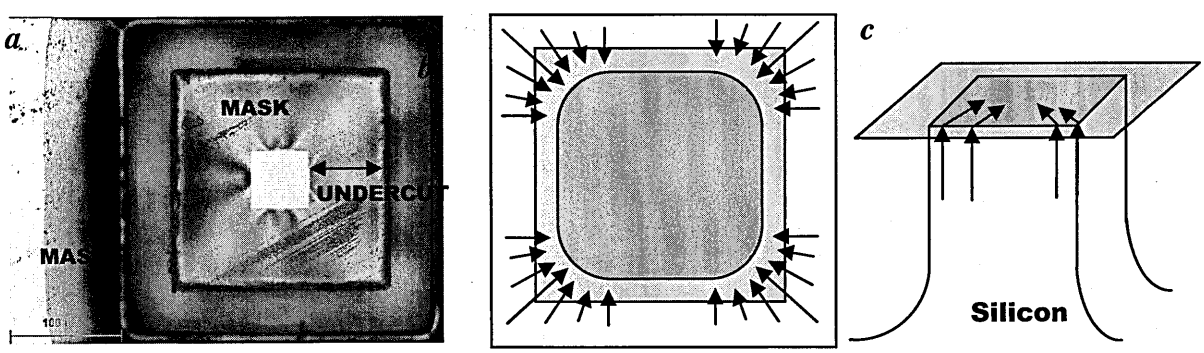


Figure 9.21 Demonstration of convex corners etching under different phenomena: a) results obtained: a pillar maintains sharp corners, b) 3-D diffusion from backscattered fluorine and c) 2-D surface diffusion of fluorine

The decrease in etch rates with size was predicted by most models (as detailed above). It can be theoretically predicted as follows. A 3 – d cavity with a circular mask aperture receives in the time t a number F of atoms equal to $\pi r^2 \Phi_R t$. Φ_R is given (in 3 – d) in [atoms $\mu m^{-2} sec^{-1}$]. Supposing that each F particle removes k cubic microns, then the mass balance at the steady state entails that the total volume of the cavity eroded (V_r) be equal to the sum of the total bits of silicon removed by the sum of each fluorine particle (supposing a reaction rate of 100%):

$V_r = k\pi r^2 \Phi_R t$ (9.4).

In case the etching is truly isotropic, i.e. the chemical reaction represents the rate-limiting factor, and the fluorine radicals are completely diffused before reacting, the profile evolved is of the type reported in figures 9.18*a* and 9.22. The 3 – d shapes can be though of as originated by a π revolution around the y axis of the cross-sections of figure 9.22. The volume can be calculated analytically as:

$$V_r = \pi\int_0^d x^2(y)dy = \pi\int_0^d \left(\sqrt{d^2 - y^2} + r\right)^2 dy = \tfrac{2}{3}\pi d^3 + \tfrac{1}{2}\pi^2 r d^2 + \pi r^2 d \quad (9.5)$$

The geometric notation is reported in figure 9.22. For the cavity of aperture $2R$ it is:

$V_R = \tfrac{2}{3}\pi D^3 + \tfrac{1}{2}\pi^2 R D^2 + \pi R^2 D$ (9.6).

Where D is the etch depth (or lateral undercut) of the cavity. The two equations can be gathered in a system that expresses the mass balance:

$$\begin{cases} \tfrac{2}{3}\pi d^3 + \tfrac{1}{2}\pi^2 r d^2 + \pi r^2 d = k\pi r^2 \Phi_R t & (9.7a) \\ \tfrac{2}{3}\pi D^3 + \tfrac{1}{2}\pi^2 R D^2 + \pi R^2 D = k\pi R^2 \Phi_R t & (9.7b) \end{cases}$$

The solving equation is achieved by dividing equation 9.7*a* by equation 9.7*b* and rearranging:

$4r^2D^3 + 3\pi r^2 R D^2 + 6R^2 r^2 D - (4d^3 + 3\pi r d^2 + 6r^2 d)R^2 = 0$ (9.8).

The radius r was set to 15 μm. Experimentally, for such a feature, the undercut is $d \sim 30$ μm. Once these two parameters are fitted to the experimental results, equation 9.8 can be solved to yield theoretical values of D as a function of R. The values of D (r,R,d) were determined graphically. They are compared with the trends of figure 9.1 and 9.2 in figure 9.23. The above theoretical analysis demonstrates that the etch rates decrease with the size of the aperture. It does not matter what is the balance between R_R and R_{Riso}, as long as the reaction is in a steady state so that the mass balance can be applied. Notice that the experimental trends for the lateral etch rates are similar to what expected from an isotropic (i.e. reaction-rate limited) etching. (Of course, in a true isotropic etching, the lateral etch rate would be higher generally speaking, because the fluorine is equally diffused across the etching front.) This similarity in trend demonstrates that the radicals are delivered to shadowed areas by a secondary (slow) process. Conversely, the experimental trends for the vertical etch rates demonstrate a gain with aperture size larger than expected for a purely isotropic etching. This is due to the additional contribution of shadowing (which is barely involved in determining the lateral etch rate).

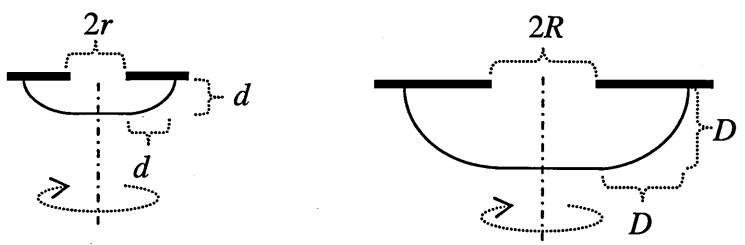


Figure 9.22 Notation used for the theoretical treatment. Purely isotropic etching

The mass balance explains also why, when the rim of the mask breaks down (partially enlarging the original aperture), the etch rate increases as a consequence. This leads to the variation of the scale of the cavities that was observed statistically in sections 6.3.3, 8.1.3 and Appendix G. For this reason, a double mask SiO_2+PR that is less prone to breakdown helps in reducing the variation across the arrays. This mechanism justifies also the degree of scattering of membranes dimensions far higher than what would be expected if the etching were mainly unidirectional.

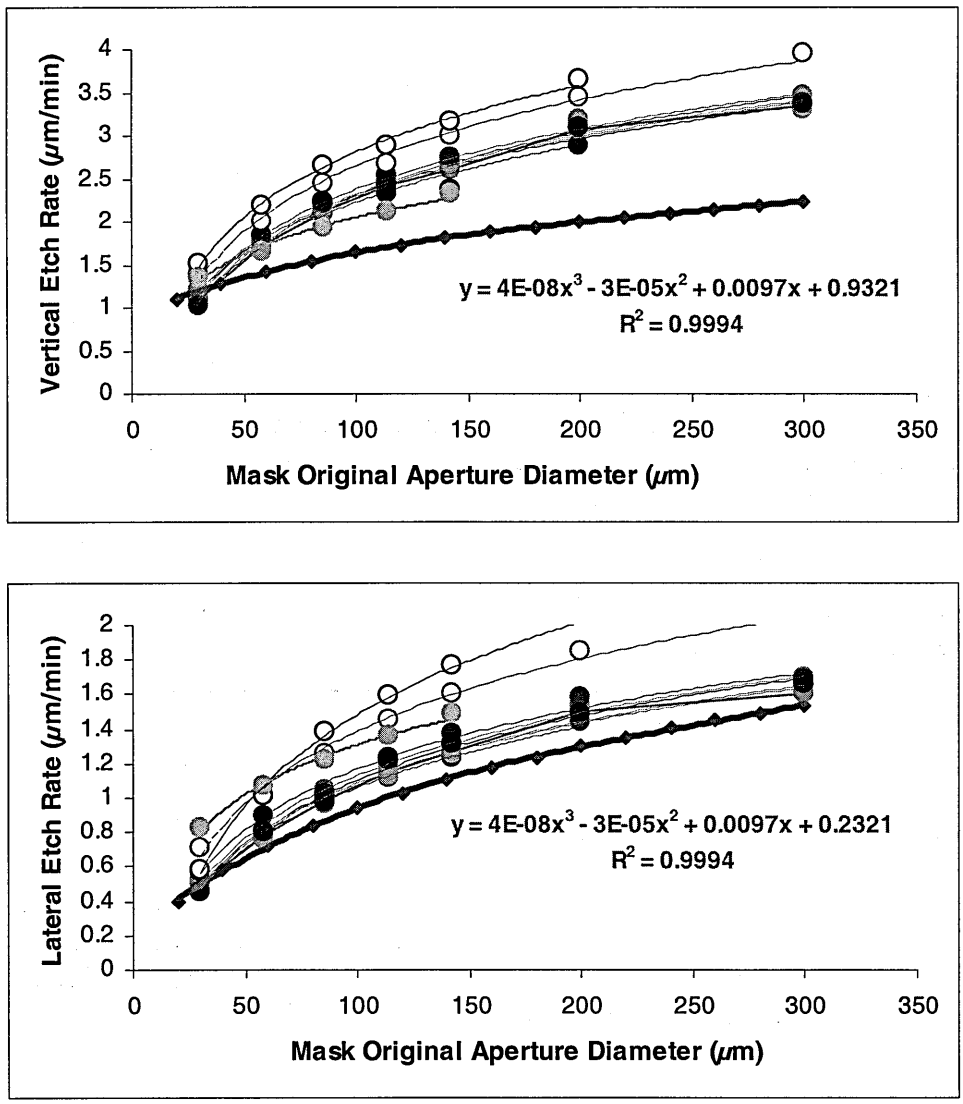


Figure 9.23 Comparison between the trends of figures 9.1 and 9.2 and the theoretical variation of R_{iso} with aperture size

Finally, the variation of the trends and etch factors with other process parameters will be addressed briefly. The results (summed up in table 9.1) can be explained easily in terms of different balance between the primary and secondary radicals fluxes, if one assumes that both fluxes have different properties and induce different geometry. The direct flux (causing the factor R_R) would lead to the geometry of figure 9.18*b*: higher etch factors and higher gains in etch rates with aperture size. The secondary flux (causing the factor

R_{Riso}) would induce the typical contour of figure 9.18*d*, thereby inducing lower etch factors and a lower gain in vertical etch rates with aperture size. The balance between R_R and R_{Riso} is related to the value of the sticking coefficient. If $S \rightarrow 1$, then $R_{Riso} \rightarrow 0$ (i.e. all fluorine atoms react exactly where they hit the etching front). If, on the contrary $S \rightarrow 0$, then the fluorine is totally diffused and the reaction becomes the rate limiting step: the etching is truly isotropic (figure 9.18*d*). Parameters such as pressure, oxygen and presence of a backing wafer can affect the balance between the two fluxes by means of influencing the sticking coefficient. (Here the sticking coefficient is considered as an overall index that determines how much fluorine reacts immediately, but strictly speaking, the diffusion coefficient should be considered as well.) The decrease in aspect ratio and in the gain of etch rates with feature size with a decrease in pressure (and consequent increase in surface temperature) may be justified assuming that the sticking coefficient is reduced and the balance is shifted towards R_{Riso}. Furthermore, it is well known that the diffusion coefficient in a solid increases with temperature. The presence of oxygen plays a more complex role. In principle, oxygen causes the deposition of Si-S-O-based coatings, which lowers the rate of the surface reaction [*Elwenspoek and Jansen, 1998, Chapter 12*]. This would justify the decrease in etch factor: the reaction is slower and the fluorine have more time to diffuse, thereby increasing the secondary fluorine flux (and increasing R_{Riso}). Unfortunately, it was found that oxygen actually causes an increase in both vertical and lateral etch rates. This leads to a contradiction with the above passivation theory, which would conversely predict a decrease in etch rates.

The increase in etch factor with time is due to the fact that the lateral undercut underneath the mask is only due to surface diffusion. The diffusion flux decreases as the cavities become bigger and the etching front gets farther from the mask aperture. Therefore, the lateral etch rate decreases faster with time than the vertical etch rate.

9.3.2 Phenomena ascribed to CODE: a model that includes CODE?

In this section, the outline of the process presented in the previous section will be widened in order to allow a justification of the CODE effects revealed in sections 9.1.2 to 9.1.4. First, It is necessary to introduce a mechanism by which CODE can occur. Then, once this mechanism is clarified, it can be employed to explain the two major CODE phenomena, i.e. the roughening of the contours and the deformation of circular mask apertures. Finally, such a model will be used to explain how process parameters (such as bias power or chamber pressure) affect CODE.

The main steps in the etching of silicon with fluorine are the following [*Winters and Coburn, 1992*]:

1) Arrival of the fluorine radicals to the etching front;
2) Adsorption of the F atoms onto the Si/F reaction layer;
3) Reactions within the Si/F reaction layer, with formation of SiF_4 (or other saturated species such as Si_2F_6 and Si_3F_8);
4) Desorption of saturated species;
5) Out-diffusion of the by-products.

And the total etch rate in the point P is given by [*Bray and Rhinehart, 2001*]:

$$\frac{1}{R}=\frac{1}{R_1}+\frac{1}{R_2}+\frac{1}{R_3}+\frac{1}{R_4}+\frac{1}{R_5} \qquad (9.9).$$

(Each index indicates the rate relative to the respective step numbered above.)

It is clear that, within the framework described in section 9.3.1, the first step (supply of fluorine to the etching front) has been identified as the rate limiting step of the reaction. However, in order to address the etching boundary experimentally developed (figure 9.18*c*), one of the following steps has to be slow enough to allow for part of the fluorine to migrate in areas of the etching front that are shadowed from the radicals flux. The fluorine migration and/or back scattering might be triggered by the inherent repulsion between adsorbed fluorine groups [*Petit and Pelletier, 1986, Carter and Carter,1996*]. The true contour of the cavities may be simulated by assuming R as a linear combination of a direct radical etching rate and a secondary isotropic etching. However, the above model fails to address the true kinetic nature of the process. It also fails to explain the numerous CODE effects revealed by the results (section 9.3).

A conundrum arises from the following line of reasoning: if the etching is diffusion limited (and not reaction limited) how is it possible to observe CODE effects? There are three experimental facts that could offer hints for solving this dilemma:

1) Besides step 1 (fluorine supply), there is at least a second step slow enough to consent a partial redistribution of fluorine. This step may have an inherently crystal orientation related velocity, thus representing the mechanism by which CODE effects arise. That an equilibrium between two different effects might exist was suggested also by Blauw et al. (for what concerns the cryogenic etching of silicon) [*Blauw et al,2000*].
2) Unlike the major deformation obtained in wet anisotropic etching of silicon, the CODE effect presented here are local (i.e. they affect surface roughness, but generally do not impinge on the overall contour shape). CODE builds up in specific areas (i.e. the zones shadowed from direct fluxes). Effects of this extent can be plausibly ascribed to a secondary kinetic contribution.
3) From the literature, it is known that CODE effects may arise locally during wet isotropic etching of silicon. This happens usually in some regions of the HNA ternary diagram (i.e. high HF concentration and low HNO_3 concentration, when the oxidation of Si is the rate limiting step), although the overall shape of the cavity produced may remain almost perfectly isotropic [*Schwartz and Robbins, 1976*]. In other words, there is no evidence of macroscopic steps bounded by <111> flat planes, but there is evidence of roughness, peaks and corners, delineation of defects (which trigger the reaction) and, more generally, CODE [*Schwesinger and Albrecht, 1997*].

How can CODE be related to any actual mechanism involved in the etching reaction? Various authors speculated on this issue. The debate is still at an early stage: although contributions have been made both by the experimental and theoretical point of view, a clear picture has yet to be drawn. As an early consideration, in their vast review, Winters et al. speculate on the evidence that fluorine atoms form a stable chemiadsorbed

layer on the surface of single crystal silicon [*Winters and Coburn, 1992*]. Considering a <100> silicon surface with two dangling bonds for each surface site, it can be expected that fluorine atoms will form a periodic array of -SiF_2 groups on the surface. On the contrary, on a <111> silicon plane, with only one dangling bond, the surface species -SiF is expected to abound. In effects, *ab initio* simulations showed that the energy released by the formation of the Si-F bond is hardly adequate to disrupt the dimer bonds on the (100)-(2X1) reconstructed surface, so that even on <100> planes a -SiF monolayer is first formed [*Carter and Carter, 1996*].

If the adsorbate -SiF_2 is the essential intermediate to the formation of SiF_4 (e.g. through the reaction -SiF_2 + -SiF_2 → SiF_4↑ between two nearest SiF_2 neighbours [*Petit and Pelletier, 1986*]), then on a <111> plane, one Si-Si bond has to be broken to form the -SiF_2 intermediate, thus adding to the activation energy of the overall surface reaction. Petit et al. built a model based on the Ising theory, keeping into account the repulsion among fluorine groups [*Petit and Pelletier, 1986*]. They predicted that the formation of -SiF_2 groups was faster on the <100> planes than on the <111> planes, such as schematized in the plot of figure 9.24. The etch rate in the {111} direction is lower than in the {100} directions. However, as pointed out by Elwenspoek [*Elwenspoek and Jansen, 1998, Chapter 3; deBoer et al., 2002*], such an argument would not be able to explain why the <110> planes etch as fast as the <100> planes: <110> planes have, in fact a single dangling bond per surface site (exactly as the <111> planes).

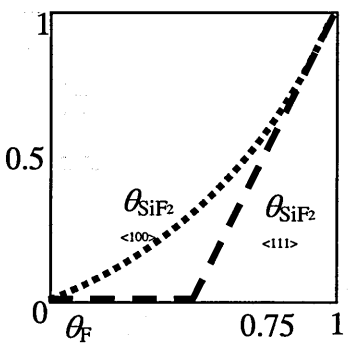


Figure 9.24 A schematic plot showing the coverage of –SiF_2 on a Si surface as a function of the coverage of fluorine. (Both *x* and *y* are measured in monolayers.) Redrawn from [*Petit and Pelletier, 1986*].

A second hypothesis refers to the atomic roughness of a surface. Jackson applied statistical mechanics (Ising theory) to describe the current of nucleation during the growth of a crystal surface from the melt, keeping into account the probability for an atom to remain attached to a solid surface [*Jackson*, 1999]. In fact, the classical equation assumes that all growth sites at the surface crystal are equivalent. This assumption is reasonable for surfaces such as the <100>, where there is no energy barrier to the formation of new layers. Such surfaces are "rough" at the atomic level, i.e. kinks and steps form normally on the surfaces: the activation energy is slight and there is a net gain in free energy. Conversely, the <111> crystal plane is atomically smooth: due to the large step free energy, there is a nucleation barrier to the formation of new layers. (It is the energetic difference in forming new layers on different faces of a crystal

that induces anisotropic growth and, eventually, gives the crystal its characteristic shape.)
However, as Jackson also points out, the difference depends also on the external process parameters. In other words, the small energy gap that differentiates the smooth atomic planes from the rough ones can be filled by many factors. Among them, Jackson lists the increase in temperature (above the "roughening transition temperature" all surfaces are atomically rough and, therefore, equivalent) or a state far from the equilibrium (leading to a very low mobility of the absorbed atoms). In crystal growth, therefore, there is a transition in the growth morphology from faceted or spiky crystals at smaller undercooling to isotropic growth at large undercoolings. At large undercooling the mobility of the incoming particles is so low that very few particles that attach are rejected (independently on the smoothness of the crystal plane onto which they attached). The reaction is very far from the equilibrium, and therefore very fast, and the arrival to the particles onto the growing surface represents the limiting step. In the same way, in isotropic wet etching of Si there is a transition between true smooth surfaces obtained in the high HNO_3 – low HF concentration region, where the process is not surface reaction limited, and the spiky-rough-preferential etching region in the low HNO_3 – high HF concentration region, where the oxidation of Si, with hole injections, represents the rate limiting factor [*Swartz and Robbins, 1976*].

Elwenspoek used a derivation of this theory to explain the transition between isotropic and anisotropic etching of silicon in aqueous solutions [*Elwenspoek and Jansen, 1998, Chapter 3*]. He expresses the kinetic current of etching (the opposite of the nucleation current) as a function of the under-saturation factor, i.e. the chemical potential of the system. At low temperature and for etching solution that give low undersaturation (that is low difference in chemical potential $\Delta\mu$) the etch rate is very slow and depends mainly on the step free energy. The etching is extremely slower for {111} faces than for {100} and {110}. Conversely, at great under-saturation conditions the nucleation barrier breaks down and all single atom cavities act as nuclei. All crystal planes become equivalent and are etched at the same rate.

It may be that CODE is induced by a similar mechanism. Given the practical scope of this research, no theoretical or experimental evidence is given here to demonstrate that. An experimental study by Aliev et al. demonstrated that the activation energy for the formation of an adsorption complex (SiF_2 or SiF_3) is lower for atoms situated on kinks or steps than for atoms situated on terraces [*Aliev and Kruchinin, 1999*]. This seems to suggest that the etch rate is lower on <111> planes because they are smooth: it is far easier to find steps and kinks on "rough" planes such as the <100> and the <110>. The importance of surface disorder for the etching processes was also theoretically demonstrated in [*Carter and Carter, 1996*].

If these hints are correct, when the overall contour of the cavities is kept into account, then the variation of etch rate (R) across the etching front has such an extent to determine the shape of the contour completely. Conversely, at local level (in the 10 μm range) the differences in etch rate are very small and secondary CODE effects may emerge, leading to the formation of the typical patterns of roughness highlighted in figures 6.44 and 6.45. Equation 9.9 can be reformulated as:

$$\frac{1}{R}=\frac{1}{R_1}+\frac{1}{R_2} \tag{9.10}$$

If two points (P_A and P_B) are taken along the etching front, the respective rates are R_A and R_B. The difference in etch rates is given by:

$$R_A-R_B=\frac{R_1^A R_2^A}{R_1^A+R_2^A}-\frac{R_1^B R_2^B}{R_1^B+R_2^B} \tag{9.11}$$

When the points are far and set so that $R_1^A >> R_1^B$, the difference in the reaction rates is negligible and $R_2^A \sim R_2^B \sim R_2$, equation 9.11 reduces to:

$$R_A-R_B=\frac{R_2^2\left(R_1^A-R_1^B\right)}{\left(R_1^A+R_2\right)\left(R_1^B+R_2\right)} \tag{9.12}$$

The difference in the local radical flux is dominant and determines completely the etch rate. There is no space for CODE at this scale level. On the contrary, when the two points are so near that $R_1^A \sim R_1^B \sim R_1$, then equation 9.11 becomes:

$$R_A-R_B=\frac{R_1^2\left(R_2^A-R_2^B\right)}{\left(R_1+R_2^A\right)\left(R_1+R_2^B\right)} \tag{9.13}$$

The difference at the local scale is dominated by the CODE. In a way, it is as these CODE-induced patterns were "superimposed" onto the overall contour. The results reported in section 9.1 did not demonstrate the effects of CODE as dramatically as some examples reported in literature (see section 9.2.2). However, there is a crucial difference: the kind of CODE reported in section 9.2.2 was found in very narrow (< 10 μm) or high aspect ratio structure and under different process conditions (cryogenic etching in presence of a passivating gas). Surface roughness increases with time because the CODE small differences build up with time becoming more evident. For very long etching time and zero platen bias, the CODE builds up to the extent that the overall shape is dramatically changed: the CODE effects are no longer local (see, for example figure 6.46 *right*).

The deformation of the front sections can be explained in a similar way. Since the mask apertures possess cylindrical symmetry, the etch rate is supposed to be equal along all the rings parallel to the wafer surface. Along each ring it is $R_1^A \sim R_1^B \sim R_1$. The small CODE effects build up so that the overall annular section is dictated by CODE and the original circular feature gets deformed along the "diagonal", i.e. the two crossing {110} directions. The amount of deformation decreases with aperture size (figure 9.10) as it is expected from a perfect wet anisotropic etching (figure 9.15). Similarly, the CODE-induced-roughness on the sidewalls increases with deformation; therefore it decreases with the size of the cavity.

How does such a model explain the smoothness of features bottom (figure 6.44)? The areas subjected to direct ion flux show mirror-like smoothness with no evidence of steps. Conversely, the cavities etched with no bias develop a rough bottom altogether (figure 6.45). One could advance the hypothesis that, although having just a slight effect on the development of the etching boundary, the ionic flux nonetheless affects the surface reaction to such an extent to cancel the (small) difference in activation energy between the <111> and the <100> (or <110>) crystalline planes and effectively obliterating CODE. The test structures of figure 9.19 can help clarifying the role of ion

flux in smoothing the etching front. Notice how, due to the higher collimation of the ion flux, only the bottom of the cavity is smooth. The transition is neat: the sidewalls become immediately rough. On the contrary, the conventional cavities, where the ion flux has a Gaussian distribution and is therefore less collimated, show a continuous transition from a smooth bottom to rough sidewalls. In cryogenic deep etching, Blauw et al. found that a strong ion beam can suppress CODE [*Blauw et al., 2000*].

A possible way to the ion synergetic effect (in classical RIE of silicon with fluorine) is that incoming ions destroy locally the atomic Si bond and crystalline framework thereby increasing the fluorine intake [*Singh et al., 1992*]. Furthermore, fluorine adsorption is enhanced at surface damaged sites [*Mayer and Barker, 1982*]. Mayer et al. showed that the energy of ion bombardment could cause considerable lattice disorder in the surface region [*Mayer and Barker, 1982*]. It might be that the ions provide the energy required to break the Si-Si bonds, inducing the formation of a thick -SiF_2 layer on <111> planes too. Alternatively, the may induce a general roughening of the surfaces, erasing the original difference in smoothness between the <111> and the <100> planes. deBoer et al. come to a similar conclusion studying CODE in cryogenic etching equipment [*deBoer et al., 2002*].

The gap in activation energy may become negligible if the local temperature rises above the temperature of roughening transition. Therefore, the etching loses its preferential character. It seems reasonable to expect a decrease in the deformation and an improvement of smoothness when bias power is increased or pressure decreased or when a backing wafer is attached to the etching wafer. In all cases, the overall temperature of the wafer increases, as testified by the net decrease in mask selectivity. In the first case the increase is due to the higher energy of the ions, in the second case to the less effective cooling. Similar effects were found by Blauw et al. [*Blauw et al., 2000*] and by deBoer et al. [*deBoer et al., 2002*] during cryogenic deep etching.

The role of oxygen is less clear. Section 9.3.1 stressed the role of oxygen in depositing a coating that decelerates the surface reaction, thereby increasing the secondary contribution to etching. The role of oxygen in decreasing surface roughness and deformation throws some light upon which stage if the reaction is effectively decelerated. If the reaction rate were reduced while maintaining the CODE, then CODE effects would be observed at a larger extent. For these reasons neither the absorption nor the reaction of fluorine can possibly be decelerated so much by the presence of the oxygen. It could be possible that desorption of reacted fluorine represented the step affected to a larger extent. This phenomenon is know to limit the etch rate in many RIE processes (e.g. in the RIE of PZT). If the de-sorption of SiF_4 is decelerated by the presence of a Si-O-F coating, then, although the atoms on the <100> planes are attacked first, the atoms on the <111> planes have more time to react before the <100> surface becomes again clear from the –SiF_2 groups. This would partially reduce the CODE, and therefore both roughness and deformation. However, once again, the general increase in etch rates with oxygen addition does not fit into this picture.

9.3.3 *Production of complex cavities obtained coupling long anisotropic and isotropic cycles*

The availability of a model able to explain the evolution of complex profiles would be crucial for the production of 3 – d structured micro-cavities. Ideally, for such features, hundreds of microns large, a phenomenological model should provide adequate approximation. For a deeper discussion on the importance of a reliable model for further developments of this project, see the future work section.

This section will outline how the model presented in sections 9.3.1 and 9.3.2 could be applied to the modelling of the complex etching cycles presented in section 6.2.3, 6.2.4 and 6.2.5. Firstly, the evolution of the etching boundary will be briefly discussed, based on the balance of passivation and etching fluxes. Secondly, the above model will be used to provide an explanation for the roughness patterns observed in these cavities.

The evolution of the boundary of the cavities etched by a sequence of long anisotropic and "isotropic" steps (section 6.3.4) can be qualitatively explained in terms of RADF. Starting with three circular mask apertures of different size (figure 9.25*a*), anisotropic cylindrical cavities are etched (figure 9.25*b*). The ARDE affect predicts that the cavities have similar depth if the aspect ratios are comparable, in other words: $d \sim D \sim D$, unless $r << d$. After the anisotropic step, fluorine flows into the cavities in absence of any passivation step ("isotropic" etching) and it is consumed by the sidewalls. The total flux entering the aperture at the instant Δt is equal to $\pi r^2 \Phi_R \Delta t$. The flux increases with the square of the radius. On the contrary, the consumption rate depends on the lateral area of the cavity the flow has moved along in the time Δt, that is: $2 \pi r v_{flux} \Delta t$. If r, R and R are not too different, then the flow is in a similar Knudsen regime and the speed of the flux should be similar. The flux increases with the square of the radius, whereas the consumption rate increases linearly with the radius. As a consequence, the flux will penetrate the larger cavity deeper, hence the different evolution of the sidewalls showed in figure 9.25*c*. If the feature is large enough, then the flux can reach the bottom, etching it in isotropic fashion (figure 9.25*d*). The signs of this mechanism can be easily observed in the SEM pictures of the cavities (figure 9.25*e*). Finally it needs to be stressed that the actual mechanism is more complex than the above picture would suggest, because the shape of the sidewalls changes constantly during etching.

A similar behaviour of the radical flow can be held responsible the shape of the cavities etched in defect of passivation (section 6.2.2) or with SF_6/C_4F_8 mixtures (section 6.2.5). The difference from the previous case is that the fluorine radicals etch through a thin coating continuously deposited during the same etching process. The coating is thin enough to allow etching of the sidewalls so that the sidewalls are enlarged in isotropic fashion. This, also, leads to different patterns of roughness (see section 6.2.6).

Surface roughness, it was said in section 6.2.6, comes in three kinds. The first is represented by a random network of cavities affecting the sidewalls. These can be observed in figure 6.43. Those rough chaotic patterns might be caused by the non-homogeneous consumption of the carbonaceous coating during the etching steps (see

also [*Richter et al., 2001*]). This kind of roughness can be observed both in all the processes attempted (continuous, cycled and with long steps). If the passivation coating is not thick enough, the radicals will etch through it. The small holes that are created will affect surface roughness. Slow-etching planes generally bound these small holes. (It can be clearly observed in figure 6.43.) A part from this kind of roughness, it is also possible to observe overall periodic patterns, clearly due to CODE. The continuous etching in SF_6/C_4F_8 mixtures represents a particular case. The C_4F_8, deposited mainly as a $-CF_2-$ coating, inhibits the reaction, slowing it enough to make large CODE induced effects emerge. Notice that the steps that bound the feature of figure 6.34 are large enough to be compared to the largest CODE effects observed in literature, However, the overall boundary, dictated by the kinetic of diffusion within the cavity, can still be appreciated: it has not disappeared completely and the largely stepped patterns can still be though as superimposed onto the boundary.

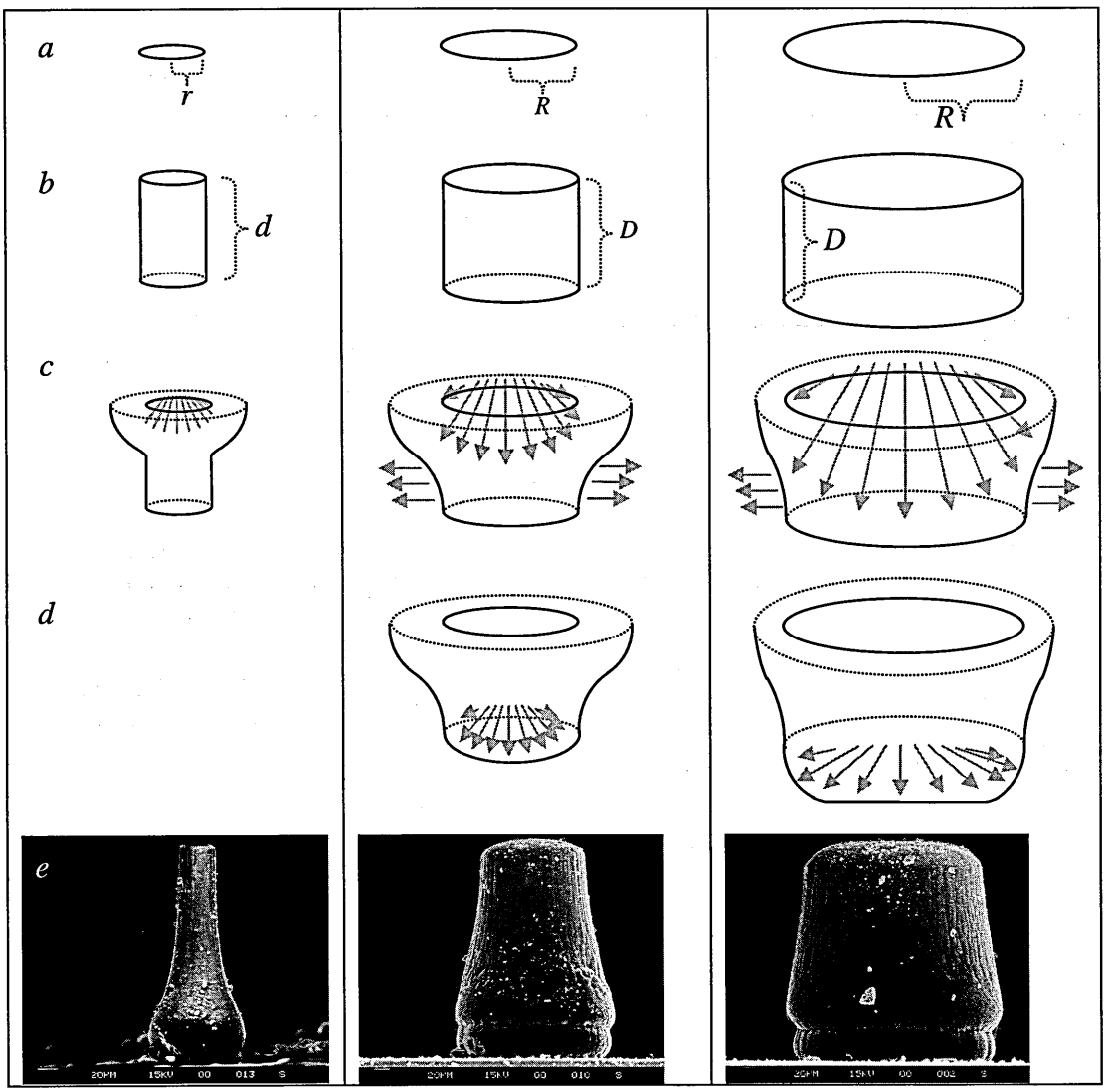


Figure 9.25 Schematic of the evolution of boundaries in pure SF_6 of anisotropic (cylindrical) cavities (figure 9.25*a* to *d*) and examples of experimental results (figure 9.25*e*)

9.4 Conclusion

This chapter was aimed to provide a brief but exhaustive report on the main phenomenology occurring during the etching of silicon with fluorine radicals in a plasma environment.

Firstly, the main experimental evidence presented in previous sections of this thesis was recalled and additional evidence was added, that had been previously left out because not immediately inherent to the matter presented above. A summary of the experimental results is reported in table 9.1.

Results **Processing Parameters**	**Etch Factor**	**Variation of etch rate with aperture size**	**Roughness of the sidewalls**	**Deformation of the circular apertures**
Aperture Size	Slight but steady decrease (~ 10% maximum) with aperture size.	Logarithmic trend in general. The fit improves with etching time.	Decreases with aperture size.	Is more marked for smaller original aperture size.
Time	Increases monotonically with time up to 30%.	Both the slope and the intercept of the trend decrease monotonically with process time	Increases steadily with time.	Increases logarithmically with process time.
Bias Power	No observable effect	Very slight increase in the slope of the trends. No other evidence.	The bottom of the features becomes smooth. Little effect on the sidewalls.	Decreases monotonically with process power.
Reduced Pressure (or presence of a Backing Wafer)	Markedly lower.	Large decrease in vertical etch rates, while increasing the lateral etch rates	Evidence of preferential effects, but reduced in comparison.	General decrease in deformation.
Oxygen in mixture	Slightly lower. Markedly lower for longer cycles.	Net increase in both vertical and lateral etch rates.	The sidewalls become smoother.	Seems to cause a decrease. Larger features are subjected to larger deformation.

Table 9.1: Summary of the experimental evidence. (Etching of silicon in SF_6 plasmas.)

Subsequently, the major experimental evidence reported in literature was surveyed. The major trends are summarised in table 9.2.

Finally, a qualitative model was build up. The model explains the trends on the basis of the balance between a primary etching mechanism and secondary etching mechanism. In table 9.3 the trends of table 9.1 are explained employing the model presented in section 9.3.

Results **Process Parameters**	**Etch Factor**	**Variation of etch rate with aperture size**	**Roughness of the sidewalls**
Aperture Size	Slight increase with aperture size in one case. Inconclusive in others.	Logarithmic trend in general. More complex dependence in XeF_2 gas etching.	
Time	Vertical and lateral etch rates decrease with time.		Increases steadily with time (& etch depth).
Fluorine/Ion Coverage		As the fluorine coverage increases (so that the ionic synergy becomes more important) the slope of the trend decreases and the intercept increases.	
Pressure		The gain of etch rate with mask aperture size is directly proportional to pressure.	

Table 9.2: Experimental or theoretical trends reported in literature. (Etching of silicon in SF_6 plasmas.)

Results Process Parameters	Etch Factor (*)	Variation of etch rate with aperture size (*)	Roughness of the sidewalls	Deformation of the circular apertures
Aperture Size	*It might be due to an increased importance of the secondary mechanism* (**).	The etch rates increase with aperture size because of the mass balance and effect of shadowing.	Anisotropic wet etching (and therefore CODE) predicts that larger apertures deform less than smaller apertures. Due to lower deformation, they present lower surface roughness.	
Time	R_{Riso} decreases faster than R_R with time. In other words, secondary etching decreases with the increase in etching front faster than primary etching.		The differences induced by CODE, although small, build up with time if the etching parameters are kept constant.	
Bias Power	No ionic contribution to the evolution of etching front.		Ions cancel the difference between <111> and <100> planes relatively to the etching reaction.	Ions heat the areas where they hit. Temperature rise locally.
Reduced Pressure (or presence of a Backing Wafer)	As the pressure decreases, the sticking coefficient decreases: more prominence to the secondary flux.		Ions heat the local areas where they hit. Temperature rises locally.	
Oxygen in mixture	Oxygen reduces reaction rate: more prominence to the secondary flux. *Why then reaction rates increase?* (**)	*In the same way, if the etching is more reaction-rate-limited, why does the slope of the trend increase?* (**)	If a coating is deposited, then a third step is competing unbalancing the CODE.	Reduced CODE means reduced deformation. *The inversion in deformation trend demonstrates that O_2 changes the kinetic of the surface reaction.* (**)

(*) These trends are explained on the basis of the balance between the primary and secondary radical fluxes, influenced by the values of *S*.
(**) In italic the trends that the model cannot explain.

Table 9.3: Explanation of the experimental trends on the basis of the model detailed in section 9.3 (Etching of silicon in SF_6 plasmas).

CONCLUSION

This research has demonstrated a novel concept in the collection and sensing of IR radiation. The novelty of the device lies in the design as well as in the microfabrication process. Firstly, the design involves an array of microscopic IR collectors (each coupled to an individual sensing element) and consequent patterning of the active layers to provide thermal isolation of the elements. Secondly, the route to build the prototype includes methods typical of MST, which are here for the first time applied to the fabrication of IR sensors.

In order to optimise the design of the pyroelectric sensor, the background theory and technology of IR radiation sensing was surveyed. This study demonstrated that the radiating power reaching the detector should be maximized and the thermal conductance of the sensor elements to their surroundings minimised to obtain a pyroelectric detector with superior responsivity and detectivity. Various solutions were proposed in the past. Application of MST allows a wider freedom of design: an earlier device produced at Cranfield, upon which this research builds, used pyramidal concentrator cavities obtained by wet anisotropic etching.

Once the physical issues of IR collection were clarified, the thesis surveyed the bulk of the literature in order to establish the optimal design of the concentrators and microbridges and set up a viable microfabrication route. Different types of concentrator profiles were considered. Ways of assessing the collection efficiency of a given collector had also to be reviewed. Non-imaging concentrators revealed to be ideal for the application (in particular CPCs, that offers the maximum theoretical collection efficiency). When the microfabrication route was considered, the choices were almost endless. However, the constraint imposed by the design, reduced the number of viable routes to just a few. Non-contact techniques based on high-density plasma etching were promising and could be conveniently explored. Two techniques were surveyed and discussed. The first entailed employing intermediate sacrificial 3 – d photoresist masks, which would be subsequently transferred into silicon by conventional unidirectional etching. Conversely, the second route would start with conventional binary masks and obtain 3 – d cavities exploiting partially anisotropic plasma etching or slightly modified DRIE cycles. Both routes presented an element of novelty never before attempted in literature and therefore it was impossible to anticipate what results had to be expected. Based on this review, an experimental road map was established.

The theoretical analysis of thermal losses demonstrated the effectiveness of suspending the active elements onto microbridges. A way had to be found of building microbridges as thin and long as possible. After consideration of a few case studies, traditional RIE was chosen for patterning the active layer. After the literature on PZT and metal RIE was reviewed, suitable recipes were set up.

The results concerning the design and microfabrication of the concentrator were then presented. First, conventional and original shapes suitable for incorporation in the device were considered, including a design compatible with the patterning of the elements (the enlarged collectors series). The performance was assessed through a mixture of analytical and computational ways. The theory demonstrated that the

introduction of a concentrator in an anisotropic flux such as that produced by a germanium lens in an IR sensor, might be advantageous. Collectors were compared in terms of concentration ratio (for a cut off angle of 14.48 degrees) and relative power collected. The 2 – d CPC outperforms all the other systems (as expected). Truncation and suspensions (i.e. enlargement) always lead to a decrease in power collection.

A large part of the research was applied to finding a viable route to fabricate arrays of concentrating collectors in silicon wafers. First, a way of producing 3 – d structures by unidirectional transfer of 3 – d structured sacrificial masks (produced by grey scale photolithography) into silicon substrates was attempted. Although contoured masks were easily produced, when unidirectional transferring was carried out it was found that the quality of the contours produced generally worsened with slope and masking materials so that deep through-the-wafers cavities could not be obtained with reasonably smooth sidewalls. This methodology was abandoned. In another set of trials, variously unbalanced processes were attempted in order to obtain contoured cavities using conventional masks. The suitability of partially anisotropic reactive ion etching (with $A < 1$) was assessed. Most methods were unsuitable because produced cavities affected by convex contours, very high roughness, broken profiles and coarse steps (all of which would scatter the radiation rather than converging it). Isotropic etching, although able to approximate only a small part of the ideal CPC contour presented nevertheless the maximum reliability, lowest surface roughness and minimum deformation among all the methods attempted. Being robust and easy to implement, isotropic etching was chosen as a way of producing devices that could provide a measurable response. A more advanced series of trials demonstrated that other problems arose when through-the-wafer etching was attempted.

The approximation to the ideal CPC profile was carried out graphically, by qualitative comparison since more sophisticated computational tools were not available. An array of effective collectors was devised by stacking two wafers 250 μm thick, thereby creating an array of two stage cavities. The computational analysis of an elliptical collector modelled after the statistical analysis of the actual cavities produced by isotropic etching, showed that the maximum increase in power collected would be up to 2.36 times.

Once a viable route to fabricate the collectors had been chosen, the practical problem of patterning the active layer had to be tackled. In fact, the suspension of the active elements was to be obtained by etching spiral microbridges onto the membranes originated as a consequence of through-the-wafer etching. This represented an optimal design, theoretical calculations having showed an expected decrease in thermal losses between 100 and 2000 times. The suspended structures were produced by etching the whole Au/PZT/Pt heterostructure in conventional RIE, after the process had been optimized and suitable recipes set up.

On the basis of the above results, a series of devices were produced. Although the approximation of the overall profile was achieved some serious drawbacks still existed. In particular the overlapping of two wafers created a step on the profile that could scatter away part of the radiation entering the concentrator cavity. In some areas roughness of the surfaces could be compared to the wavelength of the IR radiation to be

collected (This is expected to lead to partial scattering of the radiation.) A large variation of dimensions occurred across the wafer area (particularly affecting the backside membrane). It was not possible to evaluate a priori the reduction on concentration due to these deviations from the ideal profile. Furthermore, dicing the individual devices from the array represented a very crucial step, the repercussions of which had not been considered previously. As a consequence of these problems and of the lack of time, not enough working devices could be obtained to provide a statistically valid series of responses. It was nevertheless possible to obtain a response from a few devices and to compare the experimental results with the device response expected from a theoretical analysis. This comparison was unable to highlight the advantage of the thermal isolation of the active elements. However, it was possible to show some effect that might be due to the action of the collectors' sidewalls. A more recently published paper presents further experimental evidence. The use of an array of micromachined collectors coupled to the device could not demonstrate the effect of the collectors directly because of the inadequacy of the simulation methods used.

The last part of the thesis provided a qualitative model based upon the mass balance upon which the main findings and trends of the silicon etching process could be interpreted. The model was built in parallel with the development of the experimental trials and it drove many operative choices taken during the research. The effects of process parameters on the etch factor and the variation of etch rate with aperture size were explained on the basis the balance between a primary etching mechanism (anisotropic) and secondary etching mechanism (isotropic) and shadowing from the mask aperture. The formation of patterns of roughness on the sidewalls and the deformation of the circular apertures were explained advocating Crystalline Orientation Dependent Etching phenomena. CODE could be reduced or annulated by the action of the ion flux, by increasing the temperature at the etching front or by adding oxygen to the etching mixture.

In conclusion, this research achieved the following accomplishments:

- the optimised design of a novel concept IR sensor was carried out and its performance calculated theoretically;
- working prototypes were fabricated;
- experimental effects probably due to the action of the collectors were measured;
- an original study of the transfer of 3 – d masks into silicon at high selectivity was accomplished (never previously attempted in literature);
- an interesting range of contoured cavities obtainable using a conventional binary mask was mapped out;
- a qualitative model of the etching of silicon using fluorine was built, based on previous models. This allowed a deeper interpretation of the results.

A series of promising methods were devised to demonstrate directly and experimentally the increase in performance with thermal isolation and power collection. These are discussed in the future work section.

FUTURE WORK

This section describes the outline of the future work and sets up a viable way of reaching reliable results. First the main obstacles emerged during the research are recalled: in particular the difficulties related to the microfabrication process and the lack of a way of assessing the concentration power of the collectors produced. To overcome this series of problems, a different sequence of microfabrication operations is suggested. Finally program of research is outlined, including the time potentially involved.

As said above, a first series of problems emerged when attempting to characterise the concentrators in terms of concentration power and the devices in terms of responsivity: in both cases no equipment was available. Of course, it was not conceivable to incorporate each array produced into an actual IR sensor camera to test its performance. A valid alternative could have been to simulate the performance of concentrators obtained experimentally by using ray – tracing software. A method was devised for obtaining the matrix of experimental data that represent the 2 – d cross section profile of a concentrator. These data could be easily processed: a commercial package called OptiCAD has the capability of applying ray - tracing techniques to mirror profiles and surfaces, described either analytically or numerically. Unfortunately, there were not enough resources to acquire this software. Due to this lack of characterisation techniques, key decisions had to be made in due course without a satisfactory amount of elements or data. In particular, at the early stage of direct deep etching there was no chance of assessing the actual performance of the profiles produced and the decision of suitable techniques and a roadmap were decided on the basis of qualitative criteria (i.e. the quality of the surface or the reproducibility of the profiles obtained).

This lack of measurement techniques has been partly filled since an apparatus was made available for testing the response from the individual elements of an array. Now it is possible to test the response and, by comparing relative response, the concentration power of different shapes of concentrators. Unfortunately, this apparatus was assembled only a few months before the end of the research, when most experimental research had already been carried out.

A further series of problems emerged, related to the microfabrication process. Crucial steps and bottlenecks that should have been tackled from the beginning were not given the proper attention. Two steps in particular, namely the dicing of the arrays and the smoothing of the cavities after etching were revealed as fundamental for achieving a high performance prototype. On the contrary, a large part of the research was focussed on the production of concentrators using pure SF_6. This technique produced cavities that were far from the concentrator ideal shape without reaching a satisfactory surface smoothness. (In the end, a smoothing step would be required). In the following, two alternative sequences of microfabrication steps will be suggested: the first is instrumental to the development of new and more effective concentrators; the second is designed for the final production of the device, once the ideal concentrators shape has been achieved.

The schedule presents a crucial difference in comparison with the previous processes. The DRIE stage is postponed at the end of the production, i.e. after sawing. The sequence of operations would be as follows:

1. Ti deposition and oxidation (front side);
2. Ti/Pt electrode patterning (front side);
3. PZT deposition and patterning (front side);
4. A corona poling could be inserted here, if required;
5. Cr/Au electrode patterning (front side);
6. Patterning of the spiral membranes might be carried out at this point: but only partially into the PZT (~ 500 nm etch depth);
7. Patterning of the etch mask on the other side (back). Alignment with the alignment marks partially etched in the PZT layer during step 6;
8. Wafer dicing (before DRIE).

Sawing the entire wafer before etching is largely advantageous in that it would allow the survival of almost all elements and arrays. In this way it is possible to create up to 45 already prepared arrays for each device wafer. These dies can be etched singularly (or in small batches according the dicing) in the DRIE using different parameters settings. Also, after etching, these arrays can be directly introduced in the testing apparatus to assess their response.

The research might proceed in parallel as small sets of 4 or 6 arrays undergo the same etching process. One part of these arrays might be tested directly after DRIE (and subsequently coated in gold or smoothened using a smoothing technique). Other arrays might be used for assessing the profiles of the cavities (using rubber replicas) and eventually simulate the concentration power of the concentrators. In this case one would have an immediate validation of the results both from the experimental and theoretical points of view.

This new sequence would open the road to many possibilities. In fact, many more concentrator shapes could be incorporated into a working device and assessed for IR detection. Only the most promising in terms of response would undergo the subsequent processing phase (coating in gold or smoothening) in order to increase the response further.

This approach could be used to assess different combinations of anisotropic and isotropic cycles. One can start with maximally straight sidewalls (this should correspond to the minimum power collected). Subsequently, progressively longer isotropic cycles can be applied to the cavities to look for the response variation as a function of length of the isotropic etch step. A mask with circles of different diameter could also be produced. In this case cavities could be obtained using the same process but initial mask holes of different diameter. Finally, it would be possible to test the cavities produced by special masks that compensate for the preferential etching.

A drawback of this method is the following: if the wafer has to be supported by the side of the holes onto the frame during sawing i.e. it has to face the saw from the top face), the photoresist of the etch pattern would not survive. This problem can be overcome in two ways:

1) the pattern may be transferred into the SiO_2 layer before sawing and then the photoresist mask can be aligned again over this SiO_2 pattern for each array. This could be done with a minimum alignment error that would not change dramatically the profile of the cavities after etching;
2) if the sawing marks are reported in the DRIE pattern as well, then the wafer can be sawed with the DRIE pattern facing the mask and the photoresist would survive.
The saw marks and the edges of the individual arrays can all be protected during etching by depositing a thick layer of photoresist (by brushing or dipping).

To conclude, the method outlined would allow development of effective concentrators by trial and error given the large variety of working arrays that can be produced. Once the best concentrator shape is found, then the prototyping phase is accomplished. At this point, one can decide to use the same procedure for producing the device arrays. A full wafer should be produced to increase the yield of working arrays.

Alternatively, one can choose microfabrication routes that offer better performance. For example, aiming to minimise surface roughness, one could switch to producing the concentrators by injection moulding or hot embossing in a polycarbonate layer, which is subsequently aligned and mounted onto the sensing array. The previous method would have been used to find the concentrator shape that yields the best performance and therefore there would be no need of producing more than a single metallic mould.

Of course, a theoretical analysis more sophisticated than that presented in this thesis would represent a crucial help for the above procedure. In particular, it would be ideal to compare the actual results with a reliable and sensible modelling of the expected performance at any stage during the microfabrication. For this reason, it is advisable to acquire a commercial simulation package. In particular, OptiCAD® would allow immediate analysis of the optical properties of cavities of any given contours (both numerically or analytically expressed).

REFERENCES

V S Aliev V N Kruchinin *Development of Si (100) Surface Roughness at the Initial Stage of Etching in F_2 and XeF_2 Gases: Ellipsometric Study, Surf.Sci*, 442, 1999, pp. 206 – 214

D M Allen *Anisotropic Etching Microtechnology, Prec.Eng.*, 3, 1981, pp. 161 – 166

H. Andersson, M Ekberg, S Hard, S Jacobsson, M Larsson and T Nilsson *Single Photomask, Multilevel Kinoforms in Quartz and Photoresist: Manufacture and Evaluation, Appl.Opt.*, 29, 1990, pp. 4259 – 4266

G Arthur, C Wallace and B Martin, *A Comparison of Recent Development Models in Optical Lithography Simulation, SPIE*, 3332, 1998, pp. 538 – 549;

G Arthur and B Martin *Enhancing the Development Rate Model in optical Lithography Simulation of Ultra-Thick Resist Films for Applications such as MEMS and LIGA, SPIE* 4404, 2001, pp.209 – 220

H Ashraf, J K Bhardwaj, S Hall, E Guibarra, J Hopkins, A M Hynes, I Johnston, L Lea, S McCauley, G Nicholls and P O'Brien *Defining Conditions for the Etching of Silicon in an Inductive Coupled Plasma Reactor, Mat.Res.Soc.Proc., Boston, USA, November* 29 *– December* 3, 1999. *Available from the www.stsystems.com website*

H Ashraf, J K Bhardwaj, S Hall, J Hopkins, A M Hynes, I Johnston, S McAuley, G Nicholls, L Atabo, M E Ryan and S C Watcham *Advances in Deep Anisotropic Silicon Etch for MEMS, 5th National Conference On Sensors And Microsystems, The Italian Association of Sensors and Microsystems, Lecce, Italy. 2000. Available from the www.stsystems.com website*

S V Babu and E Barouch *Exact Solution of Dill's Model Equations for Positive Photoresist Kinetics, IEEE Trans.El.Dev.Lett.*, EDL-7, 1986, pp. 252 – 253

A Bagolini, L Pakula, T L M Scholtes, H T M Pham, P J French and P M Sarro *Polyimide Sacrificial Layer and Novel Materials for Post-Processing Surface Micromachining, J.Micromech.Microeng.*, 12, 2002, pp. 385 – 389

D Bailey and R A Gottscho *Aspect Ratio Independent Etching: Fact or Fantasy? Jpn.J.Appl.Phys.B*, 34 1995, pp. 2083 – 2088

J Bauer, G Drescher and M Illig Surface Tension, Adhesion and Wetting of Materials for Photolithographic Process *J.Vac.Sci.Technol.B*, 14, 1996, pp. 2485 – 2492

A Bell, Y Huang, O Paul, Y Nemirovsky and N Setter *A Thin Film Pyroelectric Detector, Int.Ferr.* 6, 1995, pp. 231 – 240

A Bertsch, P Bernhard and P Renaud *Microstereolithography: Concepts and Applications, Proc. 8th IEEE Conf. Emerging Technologies & Factory Automation*, 2, 2001, pp. 289 – 298

K Bhardwaj and H Ashraf *Advanced Silicon Etching using high density plasma, SPIE*, 2639, 1995, pp. 226 – 233

K Bhardwaj, H Ashraf and A McQuarrie *Dry Silicon Etching for MEMS, The Symposium on Microstructures and Microfabricated Systems at the Annual Meeting of the Electrochemical Society*, Montreal, Canada. May 4 – 9, 1997. Available from the www.stsystems.com website

M A Blauw, T Zijlstra, R A Bakker and E van der Drift *Kinetics and Crystal Orientation Dependence in High Aspect Ratio Silicon Dry Etching, J.Vac.Sci.Technol.B*, 18, 2000, pp. 3453 – 3461

V T Bly and J T Cox *Infrared Absorbers for Ferroelectric Detectors, Applied Optics*, 33, 1994, pp. 26 – 30

A L Bogdanov and S S Peredkov *Use of SU-8 Photoresist for Very High Aspect Ratio x-Ray Lithography, Micr.Eng.* 53, 2000, pp. 493 – 496

R P Bray and R R Rhinehart *A Simplified Model for the Etch Rate of Novolac-Based Photoresist, Plasma Chem. Plasma Proc.*, 21, 2001, pp. 149 – 161

Canyon Materials *CMI Product Information No.* 01-88. *Available from the www.canyonmaterials.com website*, 2004.

E A Carter and L E Carter *Simulated Reaction Dynamics of Fluorine on Partially Fluorinated Silicon (100) Surfaces, Surf.Sci*, 360, 1996, pp. 200 – 212

M J Carvalho, M Collares-Pereira, J M Gordon and A Rabl *Truncation of CPC Solar Collectors and its Effect on Energy Collection, Solar Energy*, 35, 1985, pp. 393 – 399

S Chandrasekaran and S Sundararajan *Effect of Microfabrication Processes on Surface Roughness Parameters of Silicon Surfaces, Surface & Coatings Technology*, 2004, *In press*

T-K A Chou and K Najafi *Fabrication of Out-of-Plane Curved Surfaces in Si by Utilizing RIE Lag, IEEE-MEMS* '02, 2002, pp. 145 – 148

P B Chu, J T Chenm, R Yeh , G Lin, J C P Huang, B A Warneke and S J Pister *Controlled Pulse-Etching with Xenon Difluoride, IEEE Solid State Sens.Actuat., TRANSDUCERS '97, Chicago*, 1997, pp. 665 – 668

Clariant *AZ4500 Resists Series, Datasheet, Available from the www.azresist.com website*, 2004

J W Coburn and E Kay *Some Chemical Aspects of the Fluorocarbon Plasma Etching Of Silicon, IBM-J.Res.Develop.* 21, 1979

J W Coburn *Plasma-Assisted Etching, Plasma Chem. Plasma Processing*, 2, 1982, pp. 1 – 41

V Comello *ICP Etchers Start to Challenge ECR, R&D Magazine, April* 1993, pp. 79 – 80

D Daly, R F Stevens, M C Hutley and N Davies *The Manufacture of Microlenses by Melting Photoresist, Meas.Sci.Techl.*, 1, 1990, pp. 759 – 766

W Däschner, P Long, R Stein, C-K Wu and S H Lee *General Aspheric Refractive Micro-Optics Fabricated by Optical Lithography Using a High Energy Beam Sensitive Glass Grey-Level Mask J.Vac.Sci.Technol.B*, 14, 1996, pp. 3730 – 3733

M J deBoer, R W Tjerkstra, J W Berenschot, H V Jansen, G J Burger, J G E Han Gardeniers, M Elwenspoek and A van den Berg *Micromachining of Buried Micro Channels in Silicon, J.MEMS*, 9, 2000, pp. 10 – 15

M J deBoer, J G E Gardeniers, H V Jansen, E Smulders, M-J Gilde, G Roelofs, J N Sasserath and M Elwenspoek *Guidelines for Etching Silicon MEMS Structures Using Fluorine High-Density Plasmas at Cryogenic Temperatures, J.MEMS*, 11, 2002 p. 385 – 401

F H Dill, W P Hornberger, P S Hauge and J M Shaw *Characterisation of Positive Photoresist, IEEE Trans.El.Dev.*, ED-22, 1975, pp. 445 – 452;

J Elders, H V Jansen, M Elwenspoek and W Ehrfeld *DEEMO: a New Technology for the Fabrication of Microstructures, IEEE – MEMS '95 Proc.*, 1995, pp. 238 – 243

M Elwenspoek and H Jansen *Silicon Micromachining, Cambridge Studies in Semiconductor Physics and Microelectronic Engineering, Cambridge University Press*, 1998

K P Fahey *Methods for Measurement of Development Parameters in the Manufacturing Line for use in Photolithography Modelling, IEEE Trans.Sem.Manufact.*, 9, 1996, pp. 182 – 190

D L Flamm, V M Donnelly and J A Mucha *The Reaction of Fluorine Atoms with Si*, J.Appl.Phys., 52, 1981, pp. 3633 – 3639

G R Fox and S Trolier-McKinstry, S B Krupanidhi, L M Casas *Pt/Ti/SiO_2/Si Substrates, J.Mater.Res.*, 10, 1995, pp. 1508 – 1515

M T Gale *Replication Techniques for Diffractive Optical Elements, Micr.Eng.* 34, 1997, pp. 321 – 339

G M Gallatin and C B Zarowin *Unified Approach to the Temporal Evolution of Surface Profiles in Solid Etch and Deposition Processes, J Appl. Physics 65, 1989, pp. 5078 – 5088*

A F Gerodolle and J Pelletier *Two-Dimensional Implications of a Purely Reactive Model for Plasma Etching, IEEE Trans.El.Dev.*, ED-9, 1991, pp. 2025 – 2032

C Gimkiewicz, D Hagedorn, J Jahns, E B Kley and F Thoma *Fabrication of Microprisms for Planar Optical Interconnections by use of Analog Gray-Scale Lithography with High-Energy-Beam-Sensitive Glass, Appl.Opt.*, 38, 1999, pp. 2986 – 2990

J M Gordon *Complementary Construction of Ideal Nonimaging Concentrators and its Applications, Appl.Opt.* 35, 1996, pp. 5677 – 5682

J M Gordon *Nonimaging Optical Designs for Laser Fiber Optic Surgery, Opt.Eng.*, 37, 1998, pp. 539 – 542

N T Gordon, C L Jones, D J Purdy *Application of microlenses to infrared detector arrays, Infrared Physics*, 31, 1991, pp. 599 – 604

A J Goss *The Pyroelectric Vidicon – a review, SPIE* 807, 1987, pp.25 – 31

P Griss, P Enoksson, H K Tolvaten-Laaks, P Merilainen, S Ollmar and G Stemme *Micromachined Electrodes for Biopotential Measurements, J. MEMS* 10, 2001, pp. 10 – 15

P S Hauge and J M Shaw *Optical Lithography, Ibid*, pp. 440 – 444

S Hannoe, I Sugimoto, K Yanagisawa and H Kuwano *Enhanced Chromatographic Performance of Silicon-Micromachined Capillary Column with Clean Structure and Interactive Plasma Organic Films, Transducers '97, Chicago*, 1997, pp. 515 – 518

S Hanson *Analysis of PZT Thin Films, Thesis (M.Sc.) - Cranfield University, School of Industrial and Manufacturing Science, Advanced Materials*, 1996.

K Harafuji and A Misaka *Dry Etching Topography Simulator with a New Surface Reaction Model: MODERN, IEEE-Trans.El.Dev.*, ED-42, 1995, pp. 1903 – 1911

J P Holman *Heat Transfer*, McGraw-Hill, New York 1997, 8th Edition

T Horiuchi and H Yaguchi *Curved Resist Surface Fabrication by Scanning a Blue Laser Beam with Positional Dose Distribution, Jpn.J.Appl.Phys.*, 40, 2001, pp. 5474 – 5479

Z Huang, Q Zhang and R W Whatmore *Low Temperature Crystallization of Lead Zirconate Titanate Thin Films by a Sol-Gel Method, J.Appl.Phys.*, 85, 1999, pp. 7355 – 7361

R H Hudson jr, *Infrared System Engineering*, Wiley, USA, 1969

E Iborra, M Clement, L V Herrero and J Sangrador *IR Uncooled Bolometers based on Amorphous $Ge_xSi_{1-x}O_y$ on Silicon Micromachined Structures, J.MEMS* 11, 2002, pp. 322 – 329

F P Incropera, D P deWitt *Introduction to Heat Transfer,* Wiley, New York, 2002

IRISYS – InfraRed Integrated Systems Ltd. *IRI 1011 – The Universal Thermal Imager, Technical Notes from* www.irisys.co.uk, 2004

K A Jackson *Computer Modeling of Atomic Scale Crystal Growth Processes, Journ.Crystal Growth,* 198/199, 1999, pp. 1 – 9

JSR *JSR IX Resists Series*; www.jsr.co.jp, 2004

J K Jung and W J Lee *Dry Etching Characteristics of $Pb(Zr,Ti)O_3$ Films in CF_4 and Cl_2/CF_4 Inductively Coupled Plasma, Jpn.J.Appl.Phys.* 40, 2001, pp. 1408 – 1419

S J Kang, V B Samoilov, Y S Yoon *Low Frequency Response of Pyroelectric Sensors IEEE Trans.Ultr.Ferr.*, 45, 1998, 1255 – 1260

H Keller and C Foster *Novel radio-frequency induction plasma processing techniques, J.Vac.Sci.Tech.A*, 11, 1993, pp. 2487 – 2491

M Kerker *The Scattering of Light, and Other Electromagnetic Radiation, Academic Press, New York*, 1969

D J Kim, W G Oldham and A R Neureuther *Development of Positive Photoresist, IEEE Trans.El.Dev*, ED-31, 1984, pp.1730 – 1736

P B Kirby, E Komuro, M Imura, Q Zhang, Q X Su and R Whatmore *High Frequency Thin Film Ferroelectric Acoustic Resonators and Filters, Int.Ferr.* 41, 2001, pp. 1743 – 1752

L E Kline and M J Kushner *Computer Simulation of Materials Processing Plasma Discharges, Cri.Rev.Solid State Mat.Sci.*, 16, 1989, pp.1 – 35

M Kohli, C Wuethrich, K. Brooks, B Willing, M Forster, P. Muralt, N Setter and P Ryser *Pyroelectric Thin-Film Sensor Array, Sensor.Actuat.A-Phys.* 60, 1997, pp. 147 – 153

P W Kruse *Uncooled Thermal Imaging, Arrays, Systems and Applications* SPIE Press, Bellingham, 2001

V Kudryashov, X C Yuan, WC Cheong and K Radhakrishnan *Grey scale structures formation in SU-8 with e-beam and UV, Microelectr.Eng.*, 67, 2003, pp. 306 – 311

K H Kwon, C I Kim, S J Yun and G Y Yeom *Etching Properties of Pt Thin Films by Inductively Coupled Plasma, J.Vac.Sci.Technol.A*, 16, 1998, pp. 2772 - 2776

W Lang, K Kühl and H Sandmaier *Absorbing Layers for Thermal Infrared Detectors Sensor.Actuat.A-Phys.* 34, 1992, pp.243 – 248

F Larmer and A Schilp, *German Patent DE 4241045*, 1993

Y J Lee, H R Han, J Lee and G Y Yeom *A Study of Lead Zirconate Titanate Etching using Magnetized Inductively Coupled Plasma", Surf.Coat.Tech.*, 131, 2000, pp. 275 – 260

Y Lin, Q Liu, T Tang and X Yao *XPS Analysis of PZT Thin Films after Dry Etching by CHF_3 Plasma, Appl Surf.Sci.* 165, 2000, pp. 34 – 37

H Macé, H Achard and L Pecchoud *Reactive Ion Etching of Pt/PZT/Pt Ferroelectric Thin Film Capacitors in High Density DECR Plasma, Microel.Eng.* 29, 1995, pp. 45 – 48

C A Mack *PROLITH: A Comprehensive Optical Lithography Model, SPIE,* 538, 1985, pp. 207 – 220

C A Mack *Development of Positive Photoresist*, J.Electrochem.Soc., 134, 1987, pp. 149 – 152

M Madou *Fundamentals of Microfabrication* CRC, Boca Raton, 2003 2nd Edition

L D Madsen, L Weaver, H Ljungcrantz and A J Clark *Analysis of the Stress and Interfacial Reactions in Pt/Ti/SiO_2/Si for Use with Ferroelectric Thin Films, J.Electron.Mat.,* 27, 1998, pp. 418 – 425

S Mancha *Chemical Etching of Thin-Film PLZT, Ferroelectrics*, 135, 1992, pp. 131 – 137

T M Mayer and R A Barker *Simulation of Plasma-Assisted Processes etch by Ion-Beam Techniques, J.Vac.Sci.Technol.*, 21, 1982, pp. 10 – 15

S A McAuley, H Ashraf, L Atabo, A Chambers, S Hall, J Hopkins and G Nicholls *Silicon Micromachining Using a High Density Plasma Source, J.Phys.D*, 34, 2001, pp. 2769 – 2774

L Méchin, J C Villégier, P Langlois, D Robbes and D Bloyet *Sensitive IR Bolometers Using Superconducting YBCO Air Bridges on Micromachined Silicon Substrates Sensor.Actuat. A-Phys.* 55, 1996, pp. 19 – 23

E Meeks and P Ho *Plasma Modelling* in *Handbook of Advanced Plasma Processing Techniques*, ed. by R J Shul and S J Pearton, *Springer Berlin*, 2000, pp. 69 – 122

MicroChem LOR™ Lift-Off Resists, Datasheet, Available from the www.microchem.com website, 2004

K R Milkove and C X Wang *Insight into the dry etching of fence-free patterned platinum structures, J.Vac.Sci.Technol.A*, 15, 1997, pp. 596 – 603

R A Miller and J J Bernstein *A Novel Wet Etch for Patterning Lead Zirconate-Titanate (PZT) Thin-Films, Int.Ferr.*, 29, 2000, pp. 225 – 231

A J Moulson and J M Herbert *Electroceramics - Materials, Properties, Applications* Chapman & Hall, London, 1990

P Muralt *Micromachined Infrared Detectors based on Pyrolectric Thin Films, Rep.Prog.Phys.* 64, 2001, pp. 1339 – 1388

G R Nash, T Ashley, N T Gordon, C L Jones, C D Maxey and R A Catchpole *Micromachined Optical Concentrators for IR Negative Luminescent Devices, J. Mod.Opt.*, 49, 2002, pp. 811 – 820

N Neumann, R Köhler and G Hofmann *Pyroelectric Thin Film Sensors and Arrays Based on P(VDF/TrFE), Int.Ferr.*, 6, 1995, pp.213 – 230

A R Neureuther and F H Dill *Photoresist Modeling and Device Fabrication Applications, Symposium on Optical and Acoustic Micro-Electronics, New York*, 1974, pp.233 – 249

S Nicolas, E Dufour-Gergam, A Bosseboeuf, T Bourouina, J-P Gilles and J-P Grandchamp *Fabrication of Gray-Tone Mask and Pattern Transfer in Thick Photoresist, J.Micromech.Microeng.*, 8, 1998, pp. 95 – 98

X Ning *Application of Non-imaging Optical Concentrators to Infrared Energy Detection, SPIE* 1528, 1991, pp. 88 – 91

B Norton, P C Eames and Y P Yadav *Symmetric and Asymmetric Linear Compound Parabolic Concentrating Solar Energy Collectors: The State of the Art in Optical and Thermo-Physical Analysis, J.Amb. Energy,* 12, 1991, pp. 171 – 190

D C O'Shea, Beletic and Poutouns *Binary Mask Generation for Diffractive Optical Elements Using Microcomputers, Appl.Opt.,* 32, 1993, pp. 2566 – 2572

J S Ogle, *U.S. Patent No.* 4,948,458, 14 *August* 1990

W G Oldham *SAMPLE : A General Simulator for VLSI Lithography and Etching Processes: Part I: Application to Projection Lithography, IEEE Trans.El.Dev*, ED-2, 1979, pp. 717 – 722

W G Oldham, A R Neureuther, C Sung, J L Reynolds and S N Nandgaonkar *A General Simulator for VLSI Lithography and Etching Processes: Part II-Applications to Deposition and Etching, IEEE-J.Solid State Circ.*, SC-15, 1980, pp. 520 – 524

Y Opplinger, P Sixt, J M Stauffer, J M Mayor, P Regnault and G Voirin *One Step 3D Shaping Using a Gray-Tone Mask for Optical and Microelectronic Applications, Microel.Eng.*, 23, 1994, pp. 449 – 454

T Otto, H Wolf, R Streiter, A Dehoff, K Wandel and T Gessner *Process and Equipment Simulation of Dry Silicon Etching in the Absence of Ion Bombardment, Microel.Eng.*, 45, 1999, pp. 377 – 391

C Paz de Araujo, J F Scott and G W Taylor *Ferroelectric Thin Films Synthesis and Basic Properties*, Gordon, 1996

B Petit and J Pelletier *Mécanisme d'Anisotropie dans la Gravure du Silicium en Plasma SF_6. Modèle de Gravure, Revue Phys.Appl.*, 21, 1986, 377 – 399

B Ploss, D Lienhard and F Sieber *Thermal Simulation of Micromachined Bridges for Integrated Pyroelectric Sensor Arrays, Microel.Eng.*, 29, 1995, pp. 75 – 78

M R Poor, A M Hurd, C B Fleddermann *PLZT Thin-Film Etching Using Plasma Techniques, IEEE-Int.Symp. Appl.Ferr.(ISAF)VII*, 1991, pp. 702 – 705

Z D Popovic, R A Sprague and G A Neville Connell *Technique for Monolithic Fabrication of Microlens Arrays, Appl Opt* 27, 1988, pp. 1281 – 1284

D R Purdy *Fabrication of Complex Micro-Optic Components Using Photo-Sculpting through Halftone Transmission Masks, Pure Appl. Optics* 3, 1994, pp.167 – 175

E H Putley *The Pyroelectric Detector, Semicon. Semimet.* 5, 1970, pp. 259 – 285

E H Putley *A Method for Evaluating the Performance of Pyroelectric Detectors, Infr.Phys.*, 20, 1980, pp. 139 – 147

A Rabl, N B Goodman and R Winston *Practical Design Considerations for CPC Solar Collectors, Solar Energy*, 22, 1979, pp. 373 – 381

P Rai-Choudhury *MEMS and MOEMS Technology and Applications, SPIE, Bellingham USA*, 2000

I W Rangelow *Dry Etching-Based Silicon Micro-Machining for MEMS, Vacuum*, 62, 2001, pp. 279 – 291

K Richter, M Orfert and H Schuhrer *Variation of Etch Profile and Surface Properties During Patterning of Silicon Substrates, Surf.Coat.Tech.*, 142-144, 2001, pp. 797 – 802

N H Rizvi, P T Rumsby and M C Gower *New Developments and Applications in the Production of 3d Micro-Structures by Laser Micro-Machining, SPIE* 3898, 1999, pp. 240 – 249

A Rogalski *Infrared Detectors: Status and Trends, Prog.Quantum Electronics* 27, 2003, pp. 59 – 210

S K Rotich, J G Smith, A G R Evans and A Brunnschweller *Photoresist Parabolas for Curved Micromirrors, J.Micromech.Microeng.*, 8, 1998, pp. 108 – 110

K Saito, J H Choi, T Fukuda, M Ohue *Reactive Ion Etching of Sputtered PZT Thin Films, Jpn.J.Appl.Phys. Part 2* 31, 1992, pp. 1260 – 1262

B Schwartz and H Robbins, *Chemical Etching of Silicon IV. Etching Technology, J.Electrochem.Soc.* 123, 1976, p.1903 – 1909

N Schwesinger, A Albrecht *Wet Chemical Isotropic Etching Procedures of Silicon - A Possibility for the Production of Deep Structured Microcomponents, SPIE*, 3223, 1997, pp. 72 – 79

J F Shackelford and W Alexander (ed.) *CRC Materials Science and Engineering Handbook, CRC Press, Boca Raton, FL*, 2001

C P Shaw, S Landi, P B Kirby and R W Whatmore, *Development Aspects of an Integrated Pyroelectric Array Incorporating a Thin PZT Film and Radiation Collectors, Ferroelectrics* 63, 2004, pp. 93 – 97

T Shibano, K Nakamura, T Takenaga and K Ono *Platinum Etching in Ar/Cl_2 Plasmas with a Photoresist Mask, J.Vac.Sci.Technol.A*, 17, 1999, pp. 799 – 804

M Shikida, K Tokor, D Uchikawa and K Sato *Surface Morphology of Anisotropically Etched Single-Crystal Silicon J.Micromech.Microeng.* 10, 2000, 522 – 527

Shipley *S1800 Resists Series, Datasheet, Available from the http://electronicmaterials.rohmhaas.com website*, 2004

V K Singh, E S G Shaqfeh and J P McVittie *Simulation of Profile Evolution in Silicon Reactive Ion Etching with Re-Emission and Surface Diffusion, J.Vac.Sci.Technol.B*, 10, 1992, pp. 1091 – 1104

V K Singh, E Q Shaqfeh and J P McVittie *Study of Silicon Etching in CF_4/O_2 Plasmas to Establish Surface Re-Emission as the Dominant Transport Mechanism, J.Vac.Sci.Technol.B*, 12, 1994, pp. 2952 – 2962

R A Smith, F E Jones and R P Chasmar *The Detection and Measurement of Infrared Radiation*, Clarendon Press, Oxford, 1968

R Steingrüber and M Ferstl *Three Dimensional Microstructure Elements Fabricated by Electron Beam Lithography and Dry Etching Technique, Micr.Eng.* 53, 2000, pp. 539 – 542

M B Stern *Pattern Transfer for Diffractive and Refractive Microoptics* Microelectronic *Engineering,* 34, 1997, pp. 299 – 319

E Strasser and S Selberherr *Algorithms and Models for Cellular Based Topography Simulation, IEEE-Trans.CAD*, CAD-14, 1995, pp. 417 – 422

G Suchaneck, R Tews, G Gerlach and G Y Yeom A *Model for Reactive Ion Etching of PZT Thin Films, Surf.Coat.Tech.*, 116-119, 1999, pp. 456 – 460

K Sugano and O Tabata *Effects of Aperture Size and Pressure on XeF_2 Etching of Silicon, Microsyst.Technol.*, 9, 2002, pp. 11 – 16

K Sugano and O Tabata *Reduction of Surface Roughness and Aperture Size Effects for Etching of Si with XeF_2, J.Micromech.Microeng.*, 12, 2002, pp. 911 – 916 (*bis*)

V Sukharev *Multiscale Modeling of Plasma Etch Processing, Vacuum*, 65, 2002, pp. 281 – 289

T J Sulesky and D C O'Shea *Gray-Scale Masks for Diffractive-Optics Fabrication I- Commercial Slide Imagers Appl.Opt.*, 32, 1995, pp. 7507 – 7517; D C O'Shea and W S Rockward *Gray-Scale Masks for Diffractive-Optics Fabrication: II- Spatially Filtered Half-Tone Screens, Ibid.*, pp. 7518 – 7526

R Takayama, Y Tomita, J Asayama, K Nomura and H Ogawa *Pyroelectric Infrared Sensors made of c-Axis-Oriented La-Modified-$PbTiO_3$ Sensor.Actuat.A-Phys.* 21 – 23, 1990, pp. 508 – 512

S H Thornton and C A Mack *Lithography Model Tuning: Matching Simulation to Experiment, SPIE*, 2726, 1996, pp. 223 – 226

M A Title, L M Walpita, W X Chen, S H Lee and W S C Chang *Reactive Ion Beam Etching of PLZT Electrooptic Substrates with Repeated Self-Aligned Mask, Appl.Opt.*, 25, 1986, pp. 1508 – 1510

J I Ulacia, C J Petty and J P McVittie, *Crystal Orientation Dependent Etch Rates and a Trench Model for Dry-Etching, J.Elecrochem.Soc.*, 135, 1988, pp. 1521 – 1525

J J van Glabbeeck, G A C M Spierings, M J E Ulenaers G J M Dormans and P K Larsen *Reactive Ion Etching of Pt/PZT/Pt Integrated Ferroelectrics Capacitors, Mat.Res.Soc.Symp.Proc.*, 310, 1995, pp.127 – 132

A J van Roosmalen, J A G Baggermann and S J H Brader *Dry Etching for VLSI*, Plenum Publ. Corp., New York, 1991

W B Veldkamp and T J McHugh *Binary Optics, Sci.Am.*, 266, 1992, pp. 92 – 97

P Verdonck, A Goodyear, R D Mansano, P R J Barroy, and N S J Braithwaite *Importance of Fluorine Surface Diffusion for Plasma Etching of Silicon, J.Vac.Sci.Technol.B*, 20, 2002, pp. 791 – 796

D P Vijay, S B Desu and W Pan *Reactive Ion Etching of PZT Thin Films Capacitors J.Electrochem.Soc.* 140, 1993, p.2635 – 2639

B Wagner, H J Quenzer, W Henke, W Hoppe and W Pilz *Microfabrication of Complex Surface Topographies Using Gray Tone Lithography, Sens.Act.A,* 46, 1995, pp. 89 – 94

C M Waits, A Modafe and R Ghodssi *Investigation of Gray-Scale Technology for Large Area 3D Silicon MEMS Structures, J.Micromech.*Microeng., 13, 2003, pp. 170 – 177

D Waller and A Safari *Corona Poling of PZT Ceramics and Flexible Piezoelectric Composites, Ferroelectrics,* 87, 1988 pp. 189 – 195

R Watton *Ferroelectric Materials and Devices in Infrared Detection and Imaging, Ferroelectrics*, 91, 1989, pp. 87 – 108

M Weck, S Fischer and M Vos *Fabrication of Microcomponents Using Ultraprecision Machine Tools, Nanotechnology,* 8, 1997, pp. 145 – 148

W T Welford and R Winston *High Collection Non-Imaging Optics, Academic Press Inc.*, USA, 1989

H Wensink, J W Berenschot, H V Jansen and M C Elwenspoek *High Resolution Powder Blast Micromachining, Proc. MEMS Conf. XIII*, 2000, pp. 769 – 774

R W Whatmore *Pyroelectric Ceramics and Devices for Thermal Infra-Red Detection and Imaging, Ferroelectrics,* 118, 1991, pp. 241 – 259

R.W. Whatmore and R. Watton, *Pyroelectric Materials and Devices* in *Infrared Detectors and Emitters: Materials and Devices*, ed. by P. Capper and C.T. Elliot, Kluwer Academic Publisher, USA, 2001

R W Whatmore, C P Shaw, S Landi, Q Zhang and P B Kirby *Micromachined Pyroelectric Infra-red Detectors with Integral Radiation Collectors: Design Fabrication and Testing, In press to be presented at ECAPD 7,* 2004

D E Williamson *Cone Channel Condenser Optics, J.Opt.Soc.Am.*, 42, 1952, pp. 712 – 715

R Winston *Light Collection Within the Framework of Geometrical Optics, J.Opt.Soc.Am.*, 60, 1970, pp. 245 – 249

R Winston *Principles of solar concentrators of a novel design, Solar Energy* 16, 1974, pp. 89 – 95

R Winston and W T Welford *Ideal Flux Concentrators as Shapes that do not Disturb the Geometrical Vector Flux Field: A New Derivation of the Compound Parabolic Concentrator, J.Opt.Soc.Am.,* 69, 1979, pp. 536 – 539 ; R Winston and W T Welford, *Geometrical Vector Flux and some new Non-Imaging Concentrators, Ibid., pp.* 532 – 536

H F Winters and J W Coburn *Surface Science Aspects of Etching Reactions, Surf.Sci.Reports.*, 14, 1992, pp. 161-269

W Witte *Cone Channel Optics, Inf.Phys.*, 5, 1965, pp. 179 – 185

C-K Wu *Method of Making High Energy Beam Sensitive Glasses, United States Patent* 5,078,771, 1992

S Y Wu *Response of Pyroelectric Detectors, IEEE Trans.El.Dev., ED-27*, 1980, pp. 88 – 90

D S Wuu, N H Kuo, F C Liao, R H Horng and M K Lee *Etching of Platinum Thin Films in an Inductively Coupled Plasma, Appl.Surf.Sci.*, 169 – 170, 2001, pp. 638 – 643

D Z Xie, B K A Ngoi, Y Q Fu, A S Ong and B H Lim *Etching Characteristics of TiNi Thin Film by Focused Ion Beam, Appl.Surf.Sci.* 225, 2004, pp. 54 – 58

S Yamamoto, T Kure, M Ohgo, T Matsuzawa, S Tachi and H Sunami *A Two Dimensional Etching Profile Simulator: ESPRIT, IEEE-Trans.CAD*, CAD-6, 1987, pp. 417- 422

J. Yao, J. Su, J. Du, Y. Zhang, F. Gao, F. Gao, Y. Guo and Z. Cui *Coding Gray Tone Mask for Refractive Microlens Fabrication, Microelectr.Eng.*, 53, 2000, pp. 531 – 534

Q Zhang and R W Whatmore *Sol-gel PZT and Mn-doped PZT Thin Films for Pyroelectric Applications, J.Phys.D Appl.Phys.*, 34, 2001, pp. 2296 – 2301

Q Zhang and R W Whatmore Improved Ferroelectric and Pyroelectric Properties in Mn-Doped Lead Zirconate Titanate Thin Films. *J.Appl.Phys.*, 94, 2003, pp. 5228 – 5233

J Zhao, A Wang, P Campbell and M A Green *A 19.8% Efficient Honeycomb Multicrystalline Silicon Solar Cells with Improved Light Trapping, IEEE Trans.El.Dev.* 46, 1999, pp. 1978 – 1983

R Zhou, H Zhang, Y Hao, D Zhang and Y Wang *Simulation of Profile Evolution in Etching-Polymerization Alternation in DRIE of Silicon with SF_6/C_4F_8, IEEE MEMS* '03, Kyoto, 2003. pp. 161 – 164

APPENDIX A
Features and patterns on a High Energy Beam Sensitive Glass Calibration Plate

An HEBS calibration glass plate is used to set up the process of grey scale photolitography. In particular, the HEBS mask allows experimental determination of the correlation between the dose received (i.e. the local optical density of the mask) and the photoresist remaining thickness for a given photolitography setting. The calibration plate contains various patterns and arrays of different shapes (figure A.1). The parts that were used for the feasibility study (described in sections 4.3.2 and 6.1.1 of the main text) are essentially three, as follows.

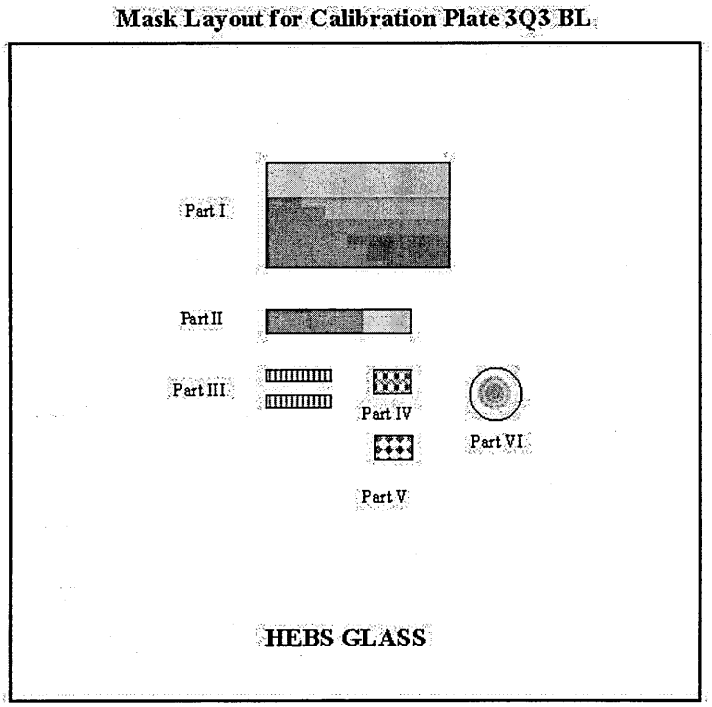


Figure A.1 Layout of an HEBS calibration glass plate (true grey mask)

1) A first pattern contains 100 sets, each of which contains three rectangular test strips (204.8μm x 819.2μm). The sets correspond to 100 grey levels (from totally opaque to totally clear). The optical density of the strips varies according to the series

$$OD = 0.12 + 0.0101i, \qquad \text{where } i = 0, 1, 2 \ldots 99 \qquad \text{(A.1)}$$

2) A second pattern consists of four sets of 37 gratings that encode a series of ramps (blazed gratings) of different length and slope in the photoresist layer. I have generally analysed the results relative to four sets of 6 blazed gratings having periods of 50, 100, 200, 300, 400 and 500 μm. Each grating has 4 periods. 100 grey levels are contained within each period. The variation in local transmittance (or optical density) is peculiar to each of the four set, as reported in table A.1. Since $OD = \log(1/T)$ the results relative to different sets can be compared as in figure A.2.

3) A third area contains arrays of features with curved contour. The shape, size and contour (i.e. number of grey levels) vary from array to array. These are intended for the production of microlenses. The features have been analysed only qualitatively, not considering the optical density curve. Examples of the kind of masks produced in photoresist and silicon oxide are reported in figure A.3.

Set number	Series describing the grey level	
1	$T = 0.759 - 0.0069\ i$	
2	$OD = 0.12 + 0.0101\ i$	$i = 0, 1, 2 \ldots\ldots 99$
3	$T = 0.759 - 0.0061\ i$	
4	$OD = 0.12 + 0.0071\ i$	

Table A.1 **Variation in optical density or transmittance in sets of blazed gratings containing 100 grey levels**

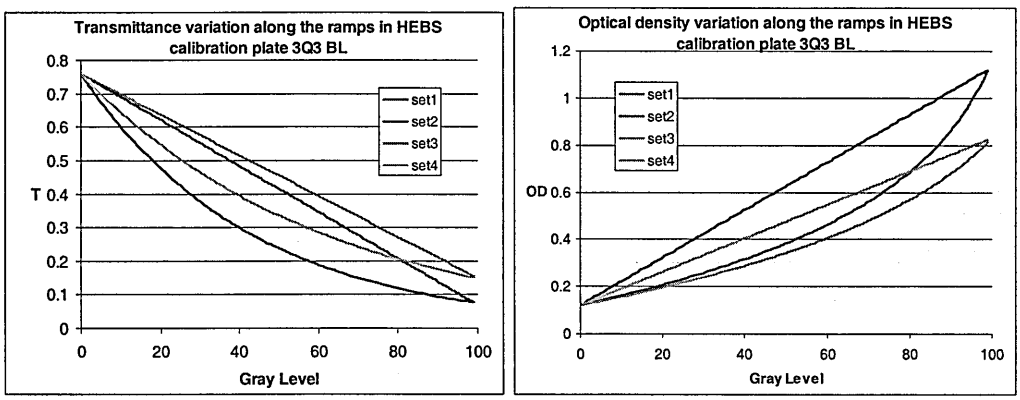


Figure A.2 **Variation in transmittance (a) and optical density (b) in sets of blazed gratings containing 100 grey levels**

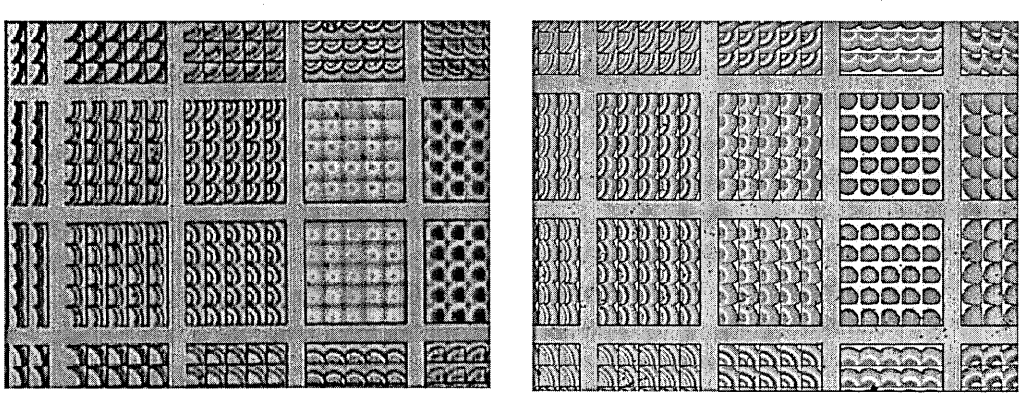


Figure A.3 **Examples of pattern produced by photolithography using the part of the calibration plate containing arrays of microlenses. a) pattern in photoresist, b) pattern transferred into silicon oxide by RIE. The side of each squared array measures 250 microns.**

APPENDIX B

Validation of the results obtained by profilometry to assess the contours of ramps produced in photoresist using the HEBS calibration glass plate.

In this appendix the profiles of contoured protruding ramps are measured by profilometry and AFM. The results are then compared. The comparison is accomplished for ramps smaller and steeper than the ramps that will be considered in this research. If the error that affects profile detection for these smaller ramps is acceptable, it seems reasonable to expect that the measurements will be even more accurate for the larger ramps (100 to 500 μm wide) with more gentle slope. The measurements were performed on the sample denominated "JSR 7.5 X 45" (photolithography process conditions in table 4.2a of section 4.3.2). Each series of ramps was analysed first with the AFM and then by profilometry. The resulting profiles were therefore separately evaluated. The profiles were then graphically overlapped to visually check potential differences. The results are in figure B.1 *a* to *c*. Visually, the profiles seem to overlap pretty well: although differences exist in detecting the total height and length of the ramps, both methods reveal similar slope and evidence of coarse steps in the contours. Only the right-hand side of the ramps was considered for the quantitative analysis (the left side is nominally vertical). After choosing a single ramp from each set, the uppermost tops of the resulting diagrams were overlapped. The two curves were integrated (for each profile) from the maximum height to zero height. The difference between the two integrals yields an indication of the error of the less accurate method (profilometry). The procedure can be written as (with reference to figure B.2):

$$\%\,\varepsilon = \frac{I_{AFM} - I_{Dektak}}{I_{AFM} + I_{Dektak}} = \frac{\left| \int_{x_{top}}^{x_{bottom}} f_{AFM}(x)dx - \int_{x_{top}}^{x_{bottom}} f_{Dektak}(x)dx \right|}{\int_{x_{top}}^{x_{bottom}} f_{AFM}(x)dx + \int_{x_{top}}^{x_{bottom}} f_{Dektak}(x)dx} \qquad \text{(B.1).}$$

The error $\%\,\varepsilon$ is given in table B.1. It can be seen how only in one case the error is higher than 3%. As the scan length of the profilometry measure is reduced (that is the number of data points for each profile is increased) the accuracy increases. Finally, the ramps that will be analysed are more than five times wider than those used for the comparison: accuracy is expected to increase further. Therefore, the profilometry measurement was judged to be reliable for assessing the contour of 3 – d masks within the limits of the purposes of this research.

Ramp type	**Length of the overall scan (μm) for profilometry**	$\%\,\varepsilon$
5 μm x 10 levels	100	0.34
10 μm x 10 levels	100	1.93
20 μm x 10 levels	200	3.19
20 μm x 10 levels	50	0.13

Table B.1 **Percentage error in the profiles revealed by profilometry** (DEKTAK) **as compared to the results from and Atomic Force Microscope** (Digital Instruments Nanoscope 3000)

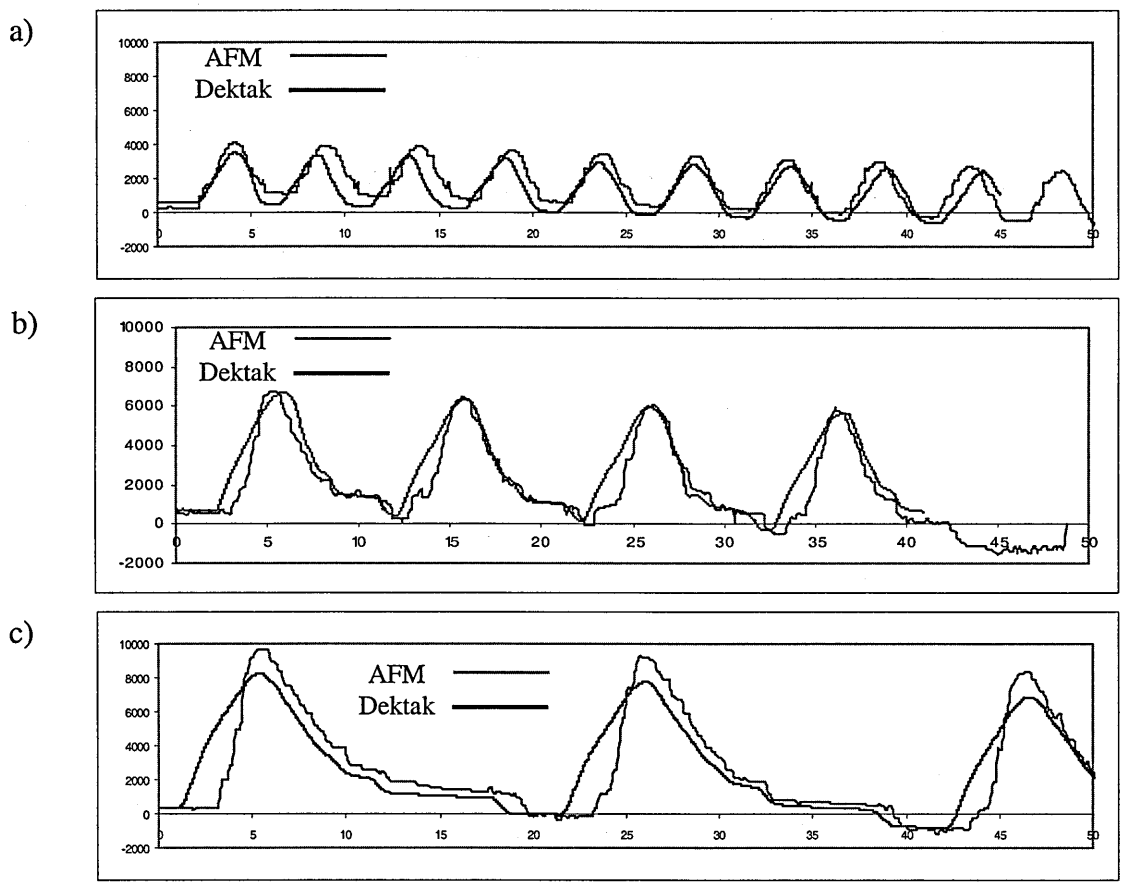


Figure B.1 **Comparison between the profile results obtained by profilometry and Atomic Force microscopy over ramps made by 3 – d photoresist contours:** a) A series of 10 ramps, each ramp is 5 μm wide and consists of 10 grey tone levels; b) Series of 4 ramps. Each ramp is 10 μm wide and consists of 20 gray tone levels. c) Series of 4 ramps. Each ramp is 20 μm wide and consists of 20 gray tone levels. The vertical coordinate is in Angstroms, the abscissa is in μm.

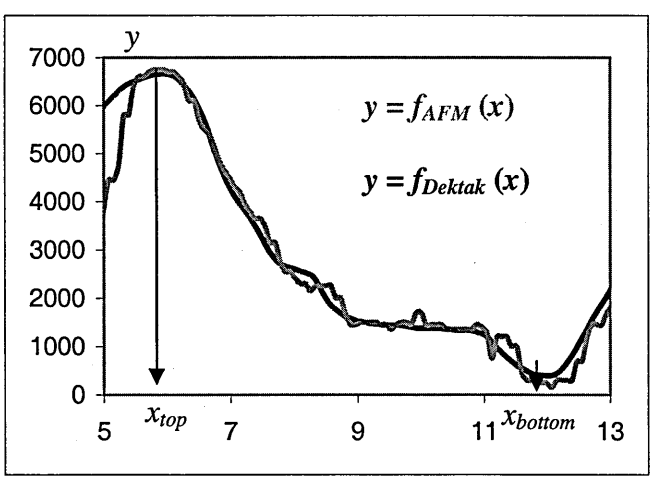


Figure B.2 **Enlargement of one ramp from figure B.1 *b*. The *y* coordinate is in Angstroms, the *x* coordinate is in μm**

APPENDIX C
Procedure for interpolating boundaries from images

The original pictures, taken with the Scanning Electron Microscope are in *.jpg* format. Each pixel of the matrix is indexed with a grey tone (a number between 0 and 255). A generic cross section, such as that reported in picture Figure C.1 cannot be expected to reproduce reliably the major cross section of the cavity because the contour depends on the position and the direction of the cut.

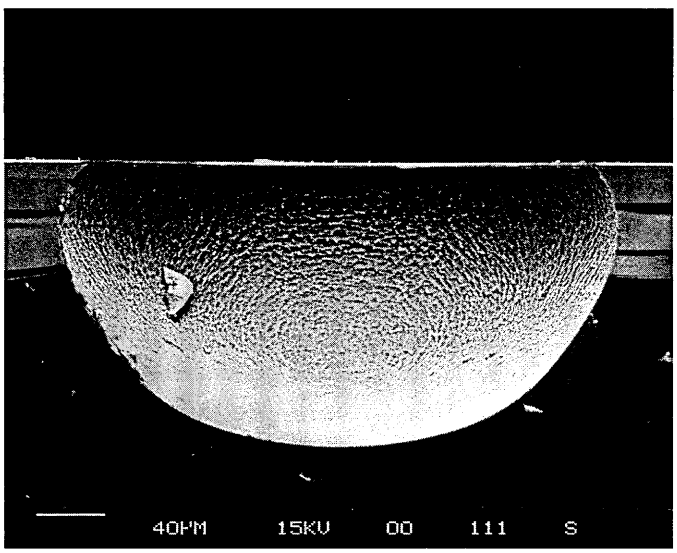


Figure C.1 Example of a cross section obtained from a cavity etched isotropically (i.e. in absence of passivation)

A silicone rubber replica, made by polymer casting yields a more accurate view of the actual feature contour. The front view coincides necessary with the maximum cross section, taken in the direction parallel to the front of the image as in figure C.2. The image is still in *.jpg* format.

To enhance the contrast and highlight the boundary, the picture is transformed into a binary *.bmp* image (Figure C.3). Now the pixels are either white (value equal to 255) or black (value equal to zero).

Finally the picture must be cleaned from any random noise or artefact not related to the actual boundary. It needs to be tilted at 90 degrees to be elaborated by the program (figure C.4).

A Mathcad code can collect the grey value of every single point. A matrix is created, each element corresponding to a pixel with value equal either to 0 (absolute black) or 255 (absolute white). The Mathcad code scans every rows of the matrix, row after row, and records the x coordinate of the boundary point (first pixel of a different colour encountered). The coordinates are collected in a vector, each value representing the local depth (in pixels) of the etching contour. Each coordinate is converted into microns and the curves can be collected as an Excel spreadsheet.

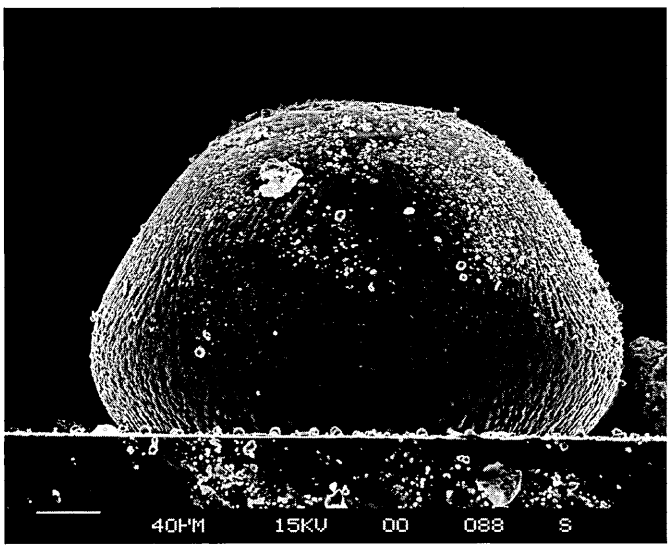


Figure C.2 **Cast replicas obtained from a cavity etched isotropically (i.e. in absence of passivation). The cavity is taken from the same array of the cavity depicted in figure C.1.**

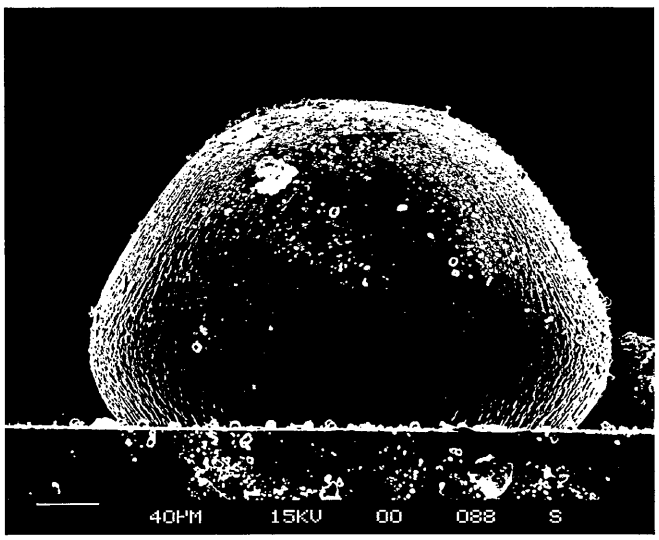


Figure C.3 **Digitalised bit map obtained from the *.jpg* image of figure C2.**

The technique is affected by experimental errors that can induce a discrete scattering in the results:

- The cast may sometimes be slightly deformed by the presence of air bubbles during casting or because it is still too tender when separated from the mould. These kinds of errors are relatively easy to detect during SEM observation,

- If the sample is not perfectly vertical when the picture is taken, then an etch depth is derived slightly more shallow than the actual one,

- Blurring of the image, dust and other picture artefacts can produce an etching figure slightly magnified.

- Since the code can only detect one point for each row, the correlation between the etch depth and point position must be unique. Zones of straight sidewalls or undercut are not detected by the system. Therefore the top part (the slightly undercut zone near to the aperture) is "missing". However the original depth is derived with acceptable accuracy.

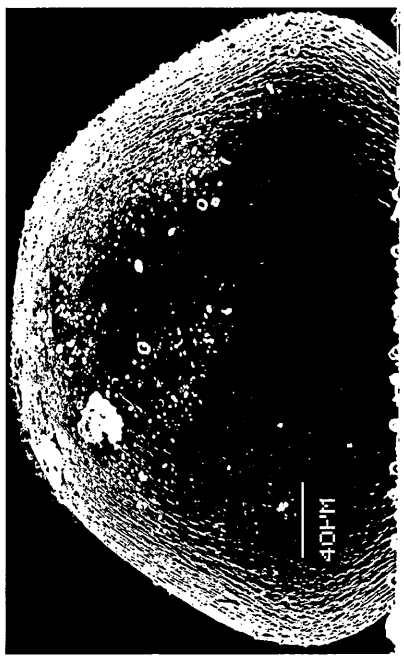


Figure C.4 **Digitalised bit map obtained from the *.jpg* image of figure C.2.**

APPENDIX D

Optical method for the qualitative determination of surface roughness on the sidewalls of contoured cavities

An indirect method to assess the roughness of the sidewalls had to be devised due to the difficulty of obtaining direct measurements (section 4.3.5). This method assesses the roughness from the analysis of the boundary of the SiO_2 membranes that results as a consequence of etching or undercut. First, an optical image of the boundary is taken (as in figure D.1 left). The picture is then digitalised in a black and white bitmap to be elaborated (figure D.1 right). A software code (written in MathCAD) is used to produce a matrix, which contains the x, and y coordinates of the points of the boundary. These data can be plotted (as in figure D.2) and subsequently interpolated.

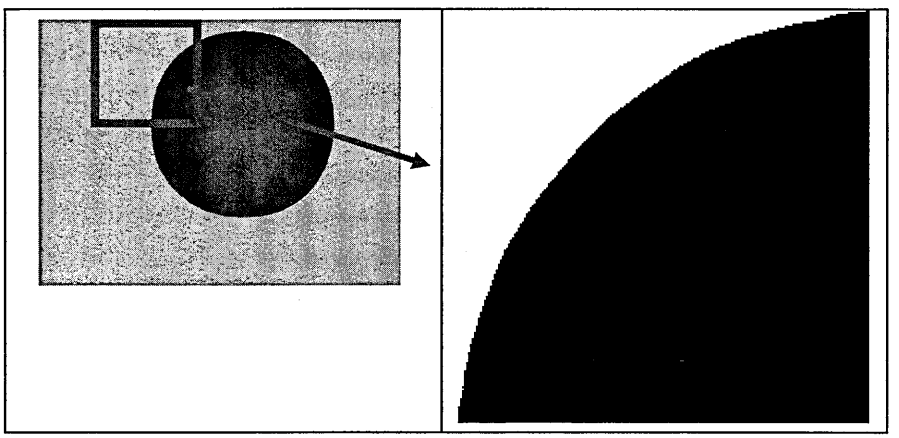


Figure D.1 **Transformation of the optical image of the membrane in a black and white bitmap**

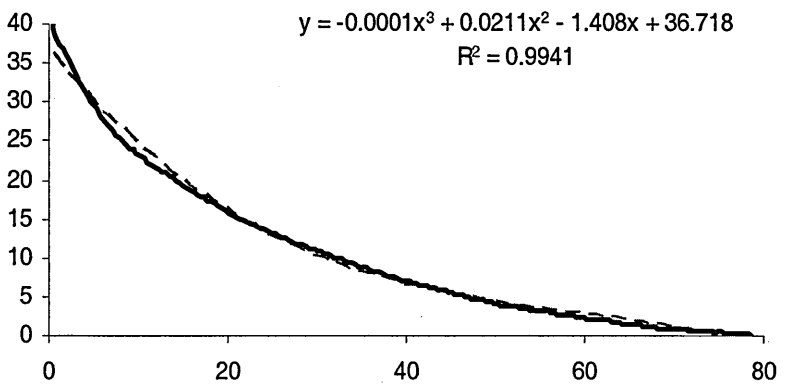


Figure D.2 **Transformation of the optical profile in a numerical matrix of data (thick black line) with least square trend line (dashed grey line). The scale is in microns. The trend line equation and the correlation factor are reported at the top-right corner.**

The values y_i are then filtered by subtracting the respective value obtained from the least square trend line, i.e. $f(x_i)$. A set of data produced after a first filtration from the data of figure D.2 is reported in figure D.3. It is important to notice that, with this simple method it is no longer possible to identify accurately the scale with microns because the

deformations due to the filtration are not kept into account. After a satisfactory number of filtrations have been made the profile may appear as in figure D.4. It is clear that as the number of filtrations increases so does the deformation: hence the accuracy of the method decreases.

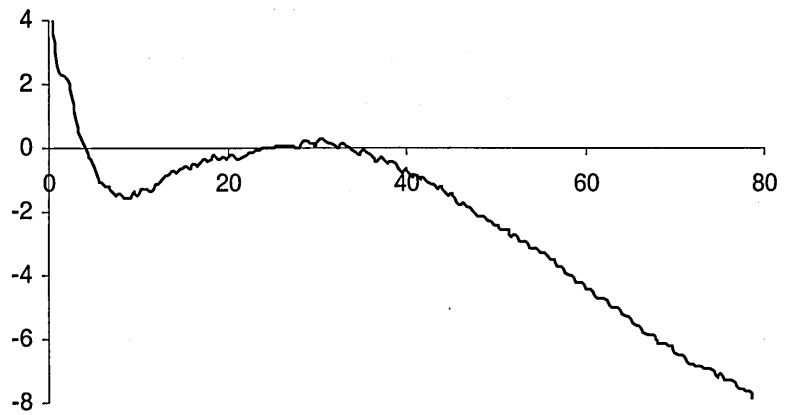


Figure D.3 **The curve of figure D.2 after the waviness has been filtered once. At this point, the scale cannot be considered to represent microns accurately.**

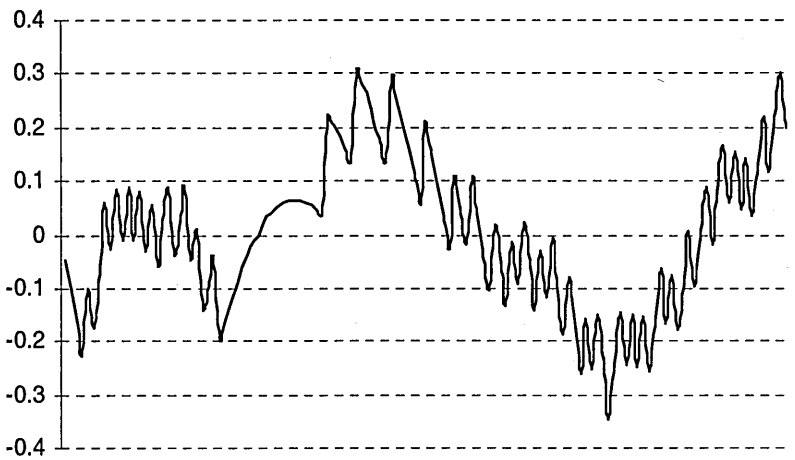


Figure D.4 **The same curve after a subsequent series of filtrations. The vertical scale may be considered to nominally represent microns with the cautions reported in the main text.**

APPENDIX E
Assessment of the performance of various types of design for non-imaging concentrators

This appendix reports mainly the detailed calculations through which the results reported in chapter 5 were obtained. It also contains supplementary diagrams and drawings to complement the issues introduced in chapter 5.The details were removed here as a whole in order to avoid burdening an already long chapter.

Appendix E-1: Types of design analysed

This appendix contains a sketch of all the concentrator design types that are analysed in chapter 5.

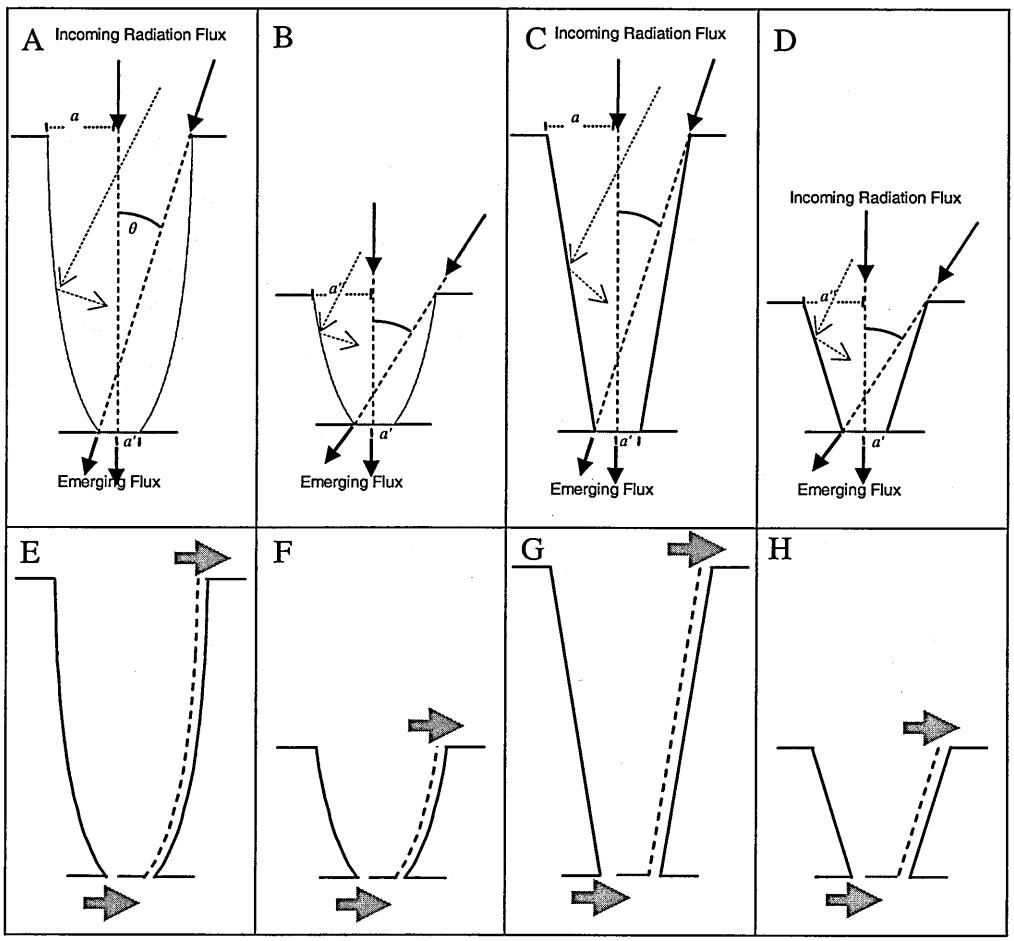


Figure E.1: Typical profiles of concentrators (in 2 – d) analysed theoretically. The proportions between horizontal and vertical dimensions have been maintained. For all drawings a = 300 μm and a' = 75 μm. Figure A represents the 2 – d CPC built with the geometry of table 5.1, which becomes B after truncation (length = 580 μm). Figures C and D represent respectively the V and truncated V collectors. Figures D to H introduce the suspended version of each individual design type.

Appendix E-2: Effect of a cosine and a Gaussian distribution on the performance of a series of 2 – d CPC

This appendix demonstrates the effect on power collected of distributions of a shape slightly more complex than a simple square wave (such as that expressed in equation 5.9). The diagram of figure E.2 plots the ratio between the power collected by the 2 – d CPCs and the power that would be collected by the exit aperture in absence of the CPC ($P / P_{a'}$) as a function of the cut-off angle of the incoming power flux distribution. The analysis is reported for:

1) the squared wave distribution described by equation 5.9 (solid curves);

2) a Gaussian distribution of the kind $B = \exp(-\varphi^2 / 2\sigma^2)$ (dotted curves);

3) a cosine distribution expressed simply by $B = \cos(a\varphi)$ (dashed curves).

The parameters σ and a determine the cut-off angle of the respective distribution. In the above cases σ and a have been tailored so that the cut off angle of the respective distribution matches the cut off angle of the distribution of equation 5.9.

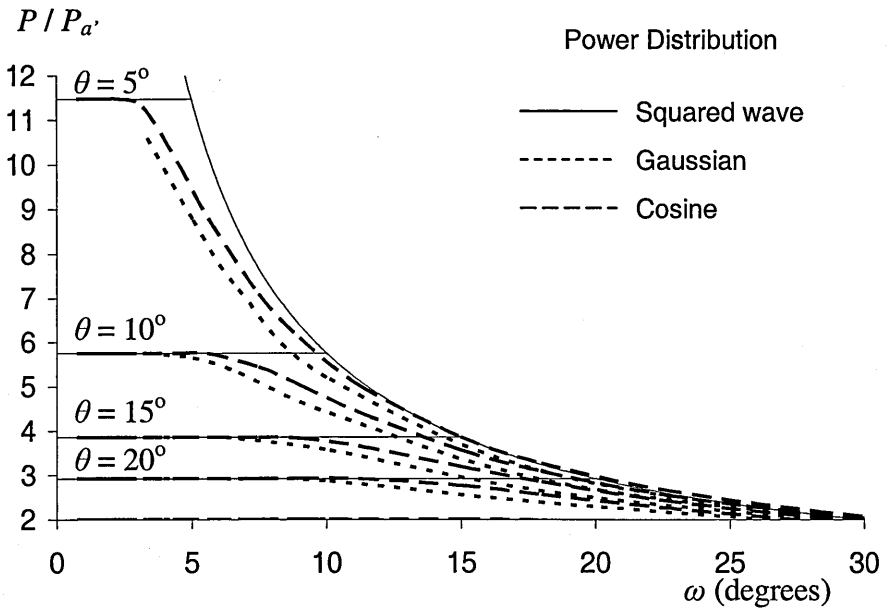


Figure E.2 **Ratio between the power collected by the 2 – d CPCs and the power that would be collected by the exit aperture in absence of the CPC as a function of the cut-off angle of the incoming power flux distribution. The acceptance angle of the CPCs is indicated beside each curve.**

Appendix E-3: Other derivations for the expression of the transmittance of a concentrator as a function of the incidence angle of the beam

This appendix derives an alternative expression of the transmittance, which will confirm the validity of equation 5.15. A generic concentrator receiving a beam of width equal to $2\,a\cos\varphi$ is shown if figure E.3. The grey shaded parts of the beam represent bundles of rays that will pass through the collector (reaching the exit aperture, although this is not shown). The other parts are rejected. The three intervals of collection are called respectively a_1, a_2 and a_3. For such a beam, the transmittance in the point x along the entry aperture ($-a \le x \le a$), $t(x, \phi)$ is either 1 or 0, as shown in the inset of the figure. $T(\varphi)$ can be though as the sum of infinite contributions from $t(x, \varphi)$:

$$T(\phi) = \frac{P(\phi)}{P_0(\phi)} = \frac{\int_{-a}^{a} Bt(x,\phi)\cos(\phi)dx}{2\int_{0}^{a} B\cos(\phi)dx} = \frac{\int_{-a}^{a} t(x,\phi)dx}{2a} \qquad \text{(E.1).}$$

The integral of equation E.1 can be expressed as a sum of intervals (inset of figure E.3):

$$T(\phi) = \frac{\sum_i \left[(x_{AA'})_{i+1} - (x_{AA'})_i\right] t_i}{2a} \qquad \text{(E.2)}$$

The transmittance t_i is only equal to 1 when the intervals $\left[(x_{AA'})_{i+1} - (x_{AA'})_i\right]$ coincide with the intervals a_i (grey zones of figure E.3) and $t_i = 0$ otherwise. The above sum can be written as:

$$T(\phi) = \frac{\sum_i a_i}{2a} = \frac{w}{2a} \qquad \text{(E.3),}$$

which confirms the result of equation 5.15.

The same results can be achieved by tracing any given bundle of rays. The beam can be conceived as made of N rays, equally spaced, each carrying an amount of energy P_N equal to $2\,aB\cos\varphi / N$. The rays between the grey and white area in figure E.3 represent extreme rays of equation $y = \tan[(\pi/2) - \varphi\,]\,x + k_{\lim}(\varphi)$ (as expressed in section 5.3). The extreme rays identify segments of acceptance (a_i) along the entry aperture, as showed in figure E.3. The number of rays contained into a beam of width a_i is given by $a_i N / 2a$. The overall accepted beam width along the AA' (entry aperture) direction is given by $w = \Sigma\, a_i$ and total number of rays accepted is equal to $\Sigma\,(a_i N / 2a)$, that is $N w / 2a$. For a given incidence angle φ the transmittance $T(\varphi)$ is simply given by the number of emerging rays divided by the number of incoming rays, i.e.

$$T(\varphi) = (w N / 2a) / N = w / 2a \qquad \text{(E.4),}$$

and the expression 5.15 has been demonstrated.

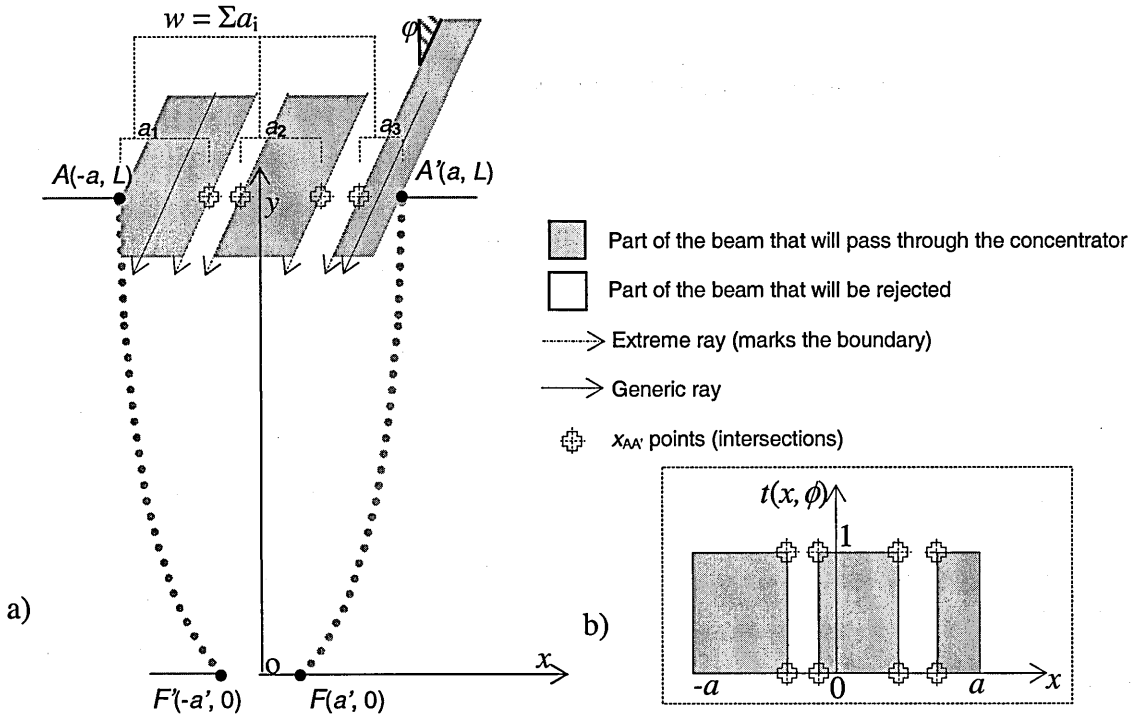


Figure E.3 **a) Geometry of a generic concentrator, showing the axes system (*xoy*) and the coordinates of the rim points. The splitting of the incoming beam in parts of the beam that will be rejected and accepted is symbolically reported at the entry aperture. These beams are bounded by the extreme rays. b) plot of transmittance of a ray as a function of the position (*x*) of the intersection of the ray with the *AA'* line (entry aperture)**

Appendix E-4: The ray-tracing algorithm in two dimensions

Ray tracing is a statistical method based on the iteration of simple rules of geometrical optics. A number of rays are virtually shot through the system. Their trajectory is assessed. The number of rays crossing a surface represents the total power flux (as if each ray represented a bundle of radiations, associated with a unitary amount of power). The number of rays per surface unity corresponds to the energy density. The concentrators treated here work only on reflection. The fundamental laws of reflection of geometrical optics are:

$$\mathbf{i} \cdot \mathbf{n} = \mathbf{r} \cdot \mathbf{n} \qquad \text{(E.5)},$$

$$(\mathbf{i} \times \mathbf{r}) \cdot \mathbf{n} = 0 \qquad \text{(E.6)}.$$

The vectors **i**, **r** and **n** represent the unitary directions of, respectively, the incident and reflected rays and the normal to the surface in the reflection point. Equation E.5 states that the angle of incidence is equal to the angle of reflection. Equation E.6 shows that the three vectors lay on the same plane. According to equation E.6 each of the three vectors can be expressed as a linear combination of the other two. In particular it is

$$\mathbf{i} = \mathbf{r} - 2(\mathbf{r} \cdot \mathbf{n})\,\mathbf{n} \qquad \text{(E.7)}.$$

The algorithm is illustrated in 2 – d in figure E.4. First step is to find the intersection between the incident ray and the curve (contour). The curve can be described by an explicit analytical form or by a finite number of points. The second step requires finding the local slope of the normal to the curve in the intersection. The final step consists in finding the direction of the emerging ray. This can be repeated until the ray has reached the absorber (i.e. has crossed the exit aperture) or has been rejected.

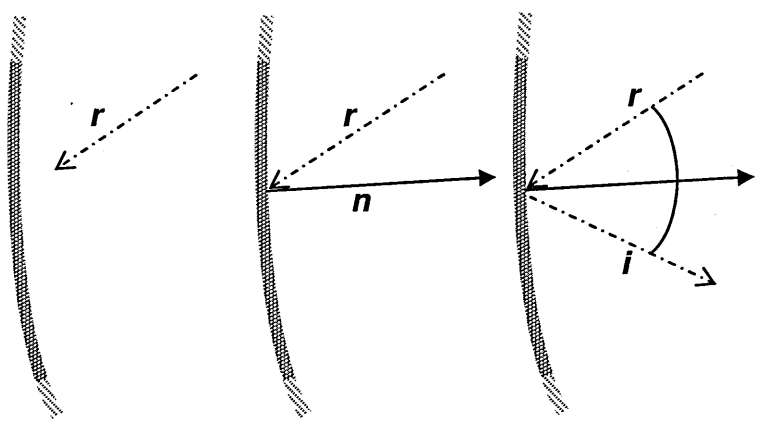


Figure E.4 **Stages of the algorithm for ray tracing procedure in 2 - d**
(redrawn from [*Welford and Winstons, 1989, Chapter 2*])

Appendix E-5 Analytical treatment & ray tracing for the enlarged CPC

In the main body text (section 5.3) it was explained how it is possible to divide the overall beam into parts and compute the respective rejection or acceptance of these parts. The overall width of the accepted beam is then given by the sum of the accepted parts. In section 5.4 the acceptance of direct rays (i.e. the radiation that passes through the concentrator without hit the reflectors) was computed. This appendix shows how the problem of acceptance form the reflected rays is tackled for the enlarged CPC.

Ray tracing is accomplished on the left reflector. Thanks to the mirror symmetry of the system, the behaviour of the right reflector, can be estimated from the results obtained from the left reflector as follows. In a 2 – d enlarged CPC the left reflector (figure E.5) is hit by rays in the range -arctan [$(a - a')/L$] $\leq \varphi \leq$ arctan [$(a + a')/L$]. However, the symmetry of the systems dictates that the acceptance obtained from the left reflector at any incidence angle between - arctan [$(a - a')/L$] and 0 be exactly the same as the acceptance obtained from the right reflector at any incidence angle between 0 and arctan [$(a - a')/L$]. In fact, no rays hit the right reflector for $\varphi >$ arctan [$(a - a')/L$]. Since the results are only computed for $\varphi \geq 0$, the acceptance obtained for the negative values of φ, i.e. $a_{left\ reflector}(-\varphi)$ is summed as a contribution obtained from the right reflector at a positive φ, i.e.:

$$w = a_{direct} + a_{right\ reflector}(\varphi) + a_{left\ reflector}(\varphi)$$
$$= a_{direct} + a_{left\ reflector}(-\varphi) + a_{left\ reflector}(\varphi) \quad \text{(E.8)}$$

Similar results would be obtained computing the contribution on the right reflector using the negative values of φ.

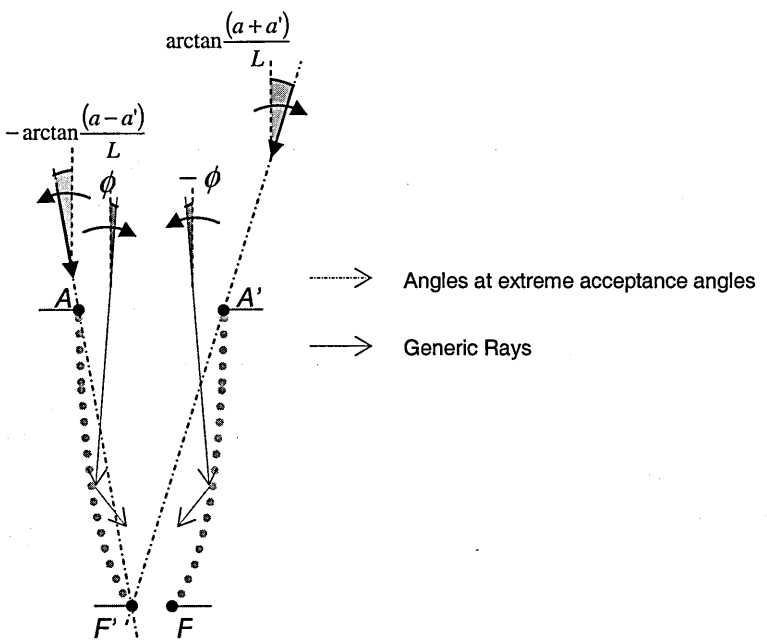


Figure E.5 The extreme angles of acceptance over the left reflector and the demonstration of mirror symmetry between the behaviour of the two left and right reflectors.

Using the mirror symmetry of the 2 – d concentrator design it was demonstrated how the computation can be accomplished on a single reflector and the results can be arranged to yield the overall transmission of the entire collector as in equation E.8. Therefore, the left reflector only will be considered. The incidence angle φ can be comprised in a range -arctan [$(a - a') / L$] $\leq \varphi \leq$ arctan [$(a + a') / L$]. Geometrically, three intervals of acceptance can be identified:

1) If - arctan [$(a - a') / L$] $< \varphi < \theta$ the situation is of the kind depicted in figure 5.4 of the main text for generic rays of incoming angle φ on a 2 – d CPC with acceptance angle θ. It can be seen how, within the overall beam that hits the left reflector (yellow plus pink beam) only a certain part effectively hits the absorber within the active areas (pink part of the beam in figure 5.4).
2) If $\varphi = \theta$ all the rays are collected in the rim (F' from the right reflector, F from the left reflector). Therefore the entire beam width ($2a \cos \varphi$) is collected and the concentration ratio is $C = a / a'$.
3) If $\varphi > \theta$ the rays that hit the reflectors are diverted above F and F' for the properties of the CPC contour. Few of them can pass through the entry aperture, but the geometrical construction assures they will fall between the sidewall and the rim (F or F'). Thus, all rays are loss or rejected.

The computation is greatly simplified if accomplished in the original system where the parabola containing the left reflector lies, with vertex in the origin and axis coinciding with ordinate axis (*i*.e. the reference system of figure 5.4). In this system the parabola containing the left reflector has equation:

$$Y = \frac{X^2}{4A} \qquad \text{(E.9).}$$

where $A = a'(1 - \sin\theta)$.

In this system of reference the incidence angle is $\Phi = \varphi + \theta$ and its limits are (- θ - arctan[$(a + a') / L$] ; 0). The equation of the generic incoming rays is

$$Y = \frac{X}{\tan\Phi} + K \qquad \text{(E.10).}$$

The problem is resolved by determining the values of K (for a given Φ) so that the reflected ray originating from the intersection of the primitive ray (described by equation E.10) with the left reflector (described by equation E.9) meets the entry aperture in the point F' (that is the extreme point of the active area). The coordinates of the generic intersection point ($X_{\Phi,K}$, $Y_{\Phi,K}$) are given by:

$$X_{\Phi,K} = 2\frac{A + \sqrt{A^2 + A(\tan\Phi)^2 K}}{\tan\Phi} \qquad \text{(E.11)}$$

and

$$Y_{\Phi,K} = 2\frac{A + \sqrt{A^2 + A(\tan\Phi)^2 K}}{(\tan\Phi)^2} + K \qquad \text{(E.12)}$$

Following the algorithm presented in E-4 (figure E.4), to find the equation of the reflected ray one has to find the slope of the normal to the curve in the point ($X_{\Phi,K}$, $Y_{\Phi,K}$), i.e.

$$-\frac{1}{Y'_{\Phi,K}} = -\frac{2A}{X_{\Phi,K}} \qquad \text{(E.13).}$$

Finally, the slope of the reflected ray is given by simple considerations of geometric optics and the equation of the generic reflected ray is given by:

$$Y = X\cot\left(2\arctan\left(\frac{2A}{X_{\Phi,K}}\right)-\Phi\right)+Q \qquad \text{(E.14).}$$

The intercept Q is obtained by imposing to the reflected ray the intersection with the left reflector in $(X_{\Phi,K}, Y_{\Phi,K})$ so that:

$$Q = Y_{\Phi,K} - X_{\Phi,K}\cot\left(2\arctan\left(\frac{2A}{X_{\Phi,K}}\right)-\Phi\right) \qquad \text{(E.15).}$$

Finally, the intercept of the extreme rays is found by imposing to the reflected rays (equation E.14) to pass through the starting point of the active area, i.e.

$$Y_{F'} = X_{F'}\cot\left(2\arctan\left(\frac{2A}{X_{\Phi,K}}\right)-\Phi\right)+Q \qquad \text{(E.16).}$$

The point $(X_{F'}, Y_{F'})$ is determined by the construction of the CPC. For a given incidence angle Φ the only incognita of the above equation is K. However, when the correct substitution through equation E.7 to E.15 were made in equation E.16, the result was too complex to be solved not only algebraically but also for numerical values of A, $X_{F'}$, $Y_{F'}$ and Φ. An alternative approach to reverse ray tracing, proceeding from the reflections passing through F' to find the respective primitive rays was equally unsuccessful leading to an equally complex equation.

An iterative ray tracing process allows the determination of the K_{lim}. Graphical examples of ray tracing outcomes are reported in the pictures E.6, E.7 and E.8. For clarity of display, only the reflected rays are reported. The bundles of rays have been marked using different colours just to facilitate the understanding of the diagram. To produce the results of figures E.6, E.7 and E.8 a beam of parallel rays was shot against the left reflector (all with the same incidence angle Φ and all expressed by equation E.10). In the iteration (produced using an Excel[tm] worksheet) the angle is upgraded from $\{-\theta - \arctan[(a+a')/L]\}$ to 0 in Φ (corresponding to the range $-\arctan[(a-a')/L]$ to $\arctan[(a+a')/L]$ in φ). For each value of Φ, 1000 parallel rays are shot with values of K (intercept) in the following range:

$$Y_A - X_A / \tan\Phi \le K \le Y_{F''} - X_{F''} / \tan\Phi \qquad \text{(E.17).}$$

That is between the ray passing through A' and the ray passing through F'' (these are the geometrical limits of the left reflector). The coordinates of A and F' in the system of reference of the original parabola are given by:

$$X_A = -2A\left(\frac{1}{\tan\theta}+\sqrt{\frac{1}{\tan^2\theta}+1}\right) \qquad Y_A = \frac{X_A}{4A} \qquad \text{(E.18)}$$

and

$$X_{F''} = 2A\left(\tan\theta-\sqrt{\tan^2\theta+1}\right) \qquad Y_{F''} = \frac{X_{F''}}{4A} \qquad \text{(E.19).}$$

The reflected ray is calculated, for each ray shot following the algorithm of Appendix E-4, which leads to equations E.11 to E.16. Once these rays are shot, the extreme rays

can be identified graphically by plotting the difference between the vertical coordinate along each ray in the point $X_{F'}$, i.e.

$$Y(X_{F'}) = X_{F'} \cot\left(2\arctan\left(\frac{2A}{X_{\Phi,K}}\right) - \Phi\right) + Q \qquad \text{(E.20)}$$

and the vertical coordinate of the point F' (i.e. $Y_{F'}$). All the rays (or bundles of rays) that yield $Y(X_{F'}) - Y_{F'} > 0$ are accepted (because they fall at the right of F' and therefore within the active area). On the contrary all the rays for which $Y(X_{F'}) - Y_{F'} < 0$ fall into a dead area and are lost. The extreme rays are represented by the zeros of the curves for the reflections of these rays effectively cross the point $(X_{F'}, Y_{F'})$. A diagram of this kind is reported in figure E.9. The cases depicted correspond to the same cases exemplified graphically in figures E.6, E.7 and E.8. Three different cases can be identified:

CASE A:
Only one solution of equation E.20 can exist because only one K_{lim} is found by ray tracing. This corresponds to the case depicted in figure E.6 and the left curve of figure E.9. The rays are limited only by the upper limit K_{lim}. All rays, hitting the left reflector, with $K(\Phi) \leq K_{\text{lim}}$ are collected. The minimum angle at which it is possible to obtain this kind of solution is found by imposing the reflection of the extreme ray to pass through both points A and F'. This simple analytical problem yields the solution arctan [$(a - a' + s) / L$]. For $\varphi \leq$ arctan [$(a - a' + s) / L$].

CASE B:
Two solutions are found using ray tracing (it means that probably equation E.20 should have two solutions). Only the rays are collected for which $K_{\text{lim1}} \leq K(\Phi) \leq K_{\text{lim2}}$. This is the particular case, depicted in figure 5.4. It corresponds also to the graphic display of figure E.7 and the central curve of figure E.9. Rays for which $K(\Phi) < K_{\text{lim1}}$ or $K_{\text{lim2}} < K(\Phi)$, although entering the collector, are reflected in the dead area and are lost.

CASE C:
Below a certain incidence angle, no rays enter the active area: all the reflections occur into the dead zone. This is shown in figure E.8. In fact, the right curve of figure E.9 does not cross the horizontal axis and equation E.20 should not admit solution.

The K_{lim} found at a given incidence angle can be used directly for calculating the respective a_i in the way suggested in the main text (section 5.3) and finally to plot $T(\varphi)$.

This appendix demonstrated how, although it is not viable to calculate analytically the transmittance obtained from an enlarged 2 – d CPC, it is nevertheless possible to assess it numerically using a ray tracing technique. An important note that has to be added concerns the multiple reflections. In figures E.7 and E.8 it can be seen how part of the reflected rays hit the same reflector again. Winston [*Welford and Winston, 1989, Chapter 4*] demonstrated that these rays pass, after multiple reflections, through the exit aperture. In the above calculations it was assumed that they fall into a dead zone. This assumption is justified by a series of practical observation for different incidence angle. The consequent error of this assumption may underestimate slightly the actual transmission of the system, without disqualifying the entire method for comparing different concentrators.

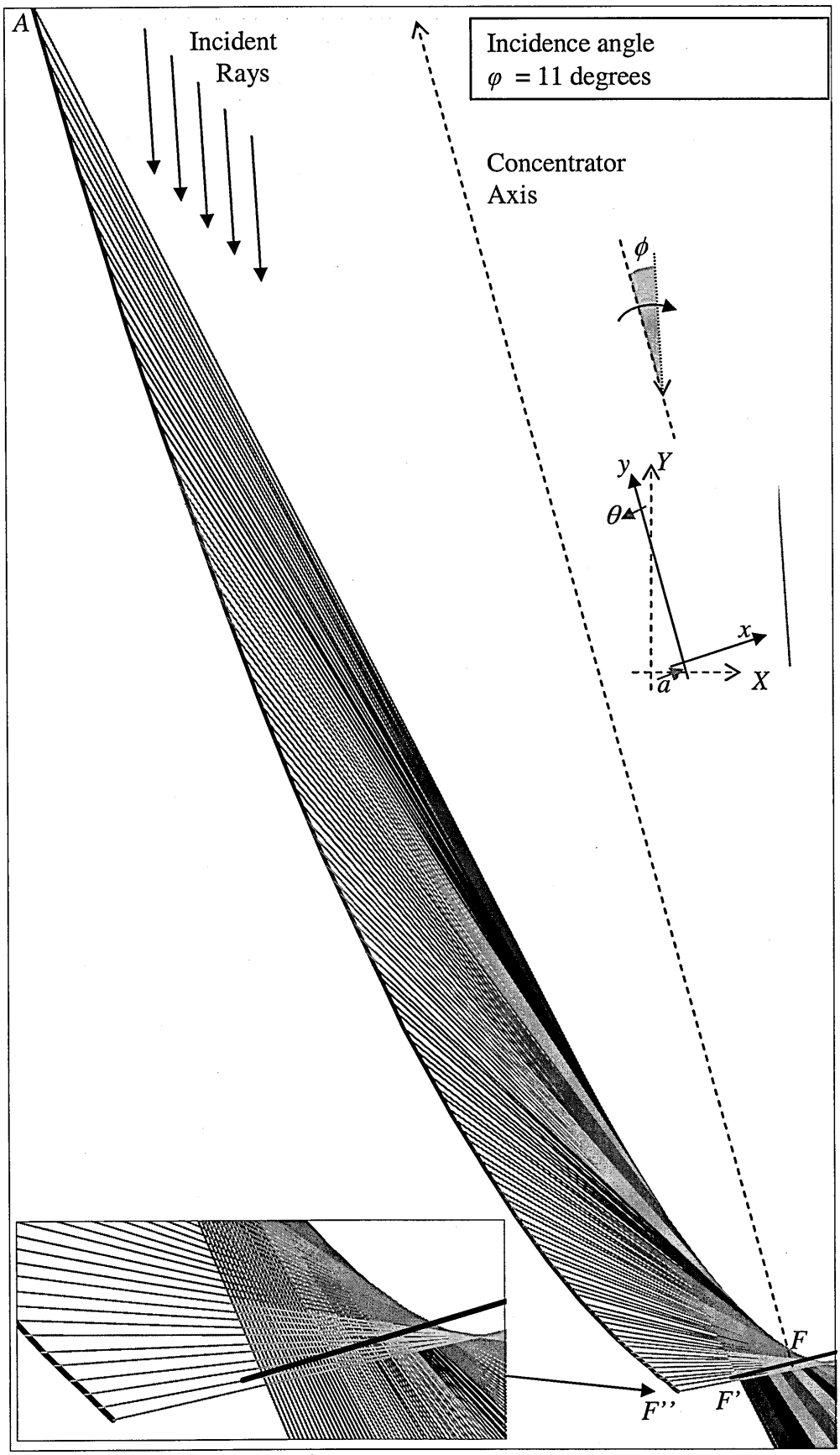


Figure E.6 Graphical example of ray tracing of the left reflector of an enlarged 2 – d CPC. Most reflected rays are accepted.

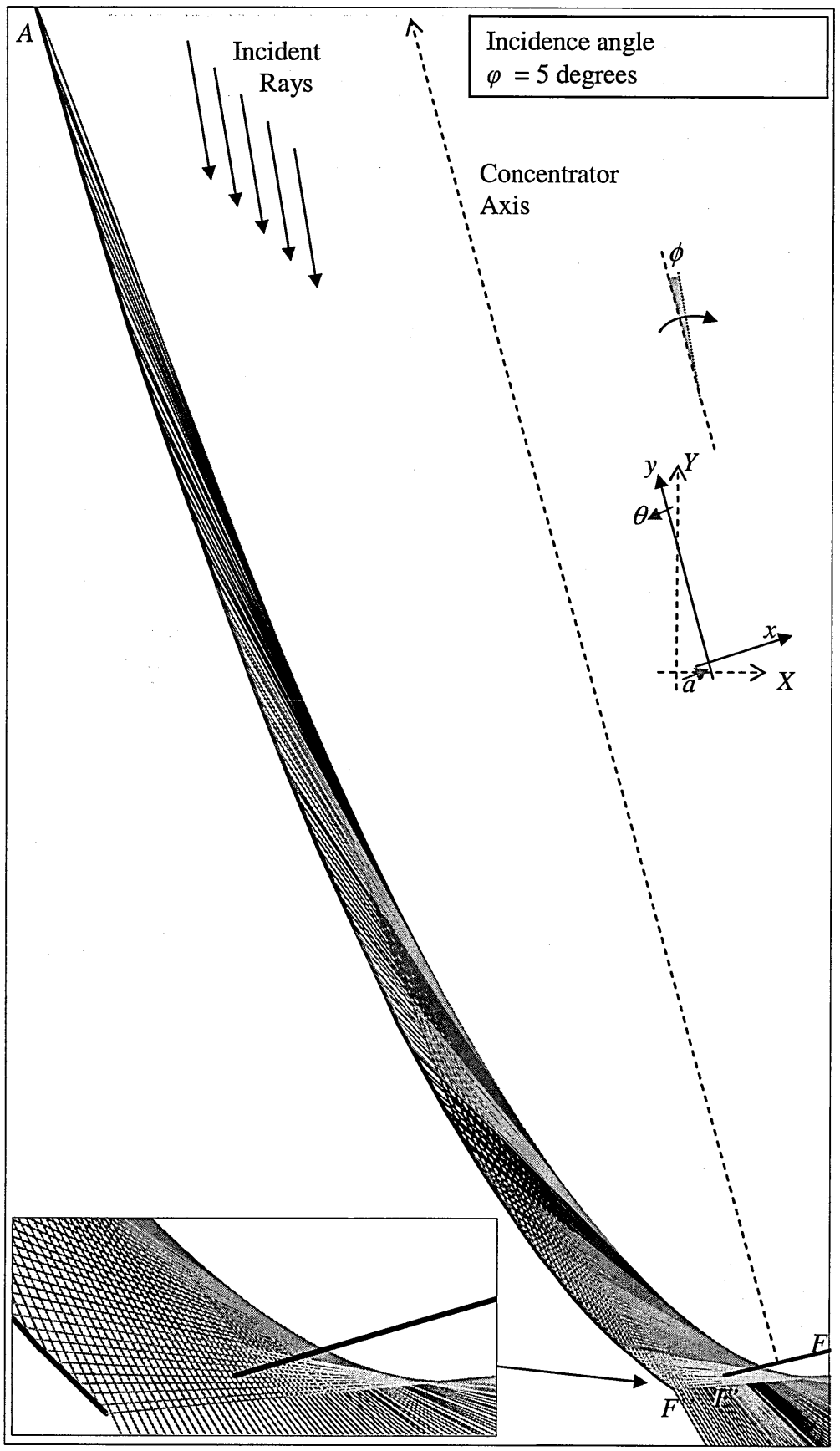


Figure E.7 Graphical example of ray tracing of the left reflector of an enlarged 2 – d CPC. Nearly half of the reflected rays is accepted.

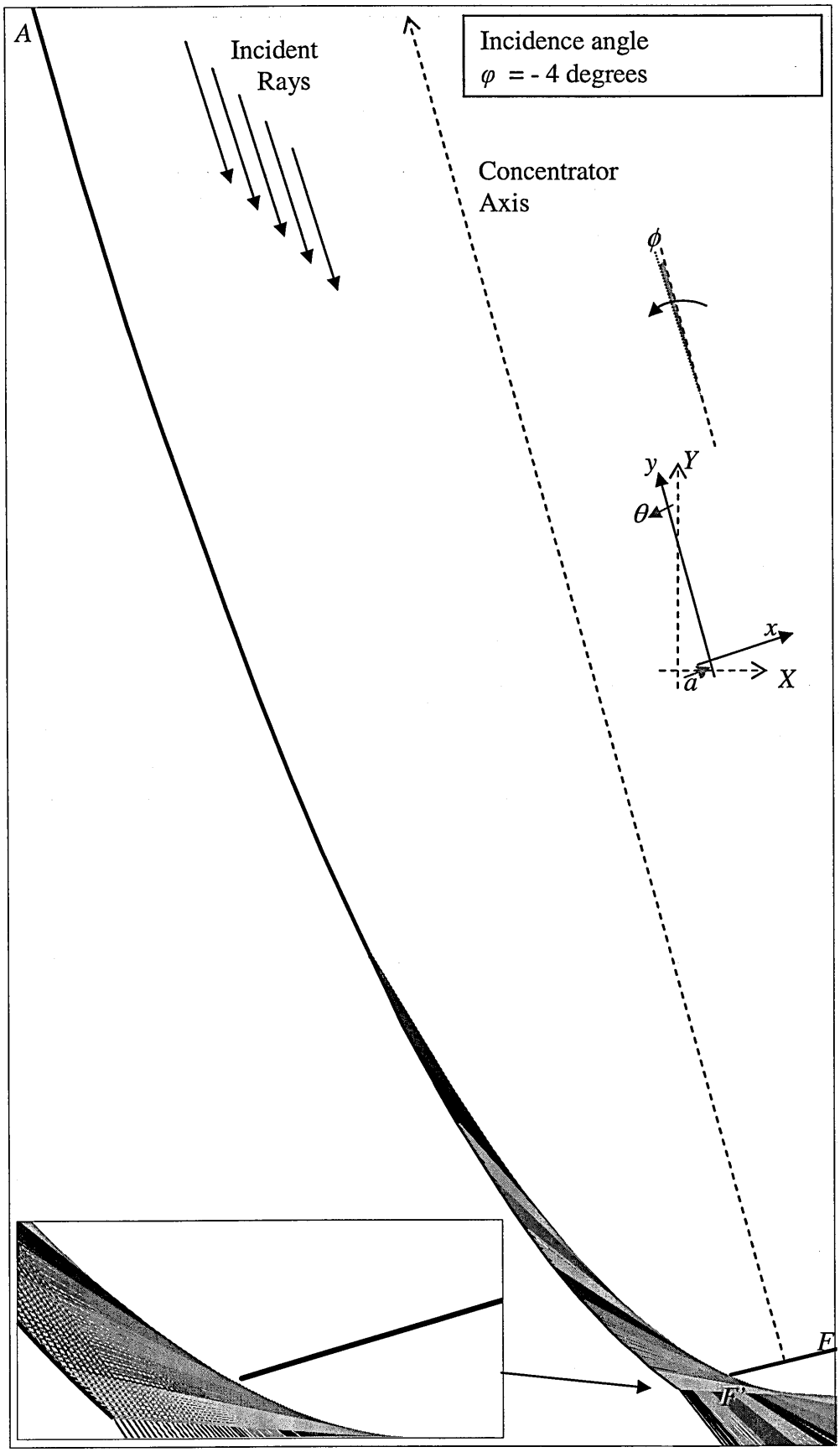


Figure E.8 Graphical example of ray tracing of the left reflector of an enlarged 2 – d CPC. No reflected rays are accepted.

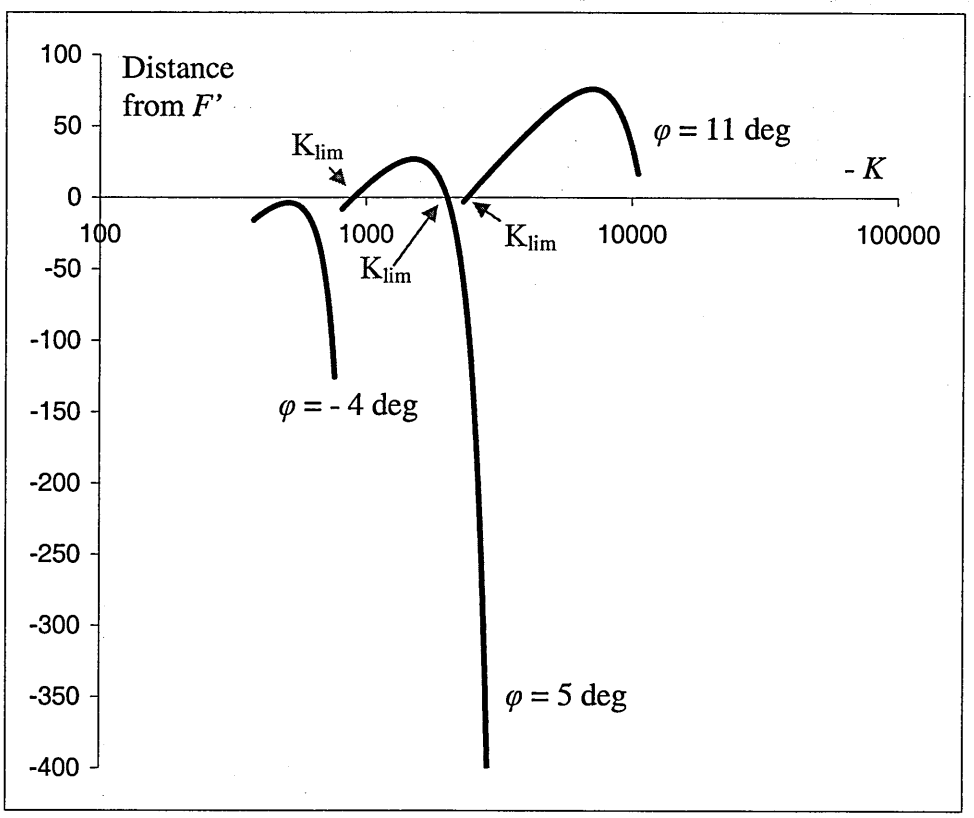


Figure E.9: **The distance from *F'* (along the *Y* axis, i.e. $Y(X_{F'}) - Y_{F'}$) of the reflected rays as a function of the opposite of their intercept (-*K*). The curves are reported for incidence angle (φ) respectively equal to the cases showed graphically in figures E6, E7 and E8. The intercepts of the extreme rays are the zero of the curves (indicated by the arrows)**

Appendix E-6 Analytical treatment of the "V" collectors

The problem of the reflections from the cone or the V collector is particularly complex because a large number of rays may enter after multiple reflections. Williamson introduced a geometric construction that simplifies the computation greatly [*Williamson, 1954*]. This appendix is structured in the following way. First, the geometric construction is illustrated. Subsequently, this construction is applied to evaluate the collection from a given V concentrator. Finally, a similar construction is applied to the enlarged V concentrators.

Figure E.10*a* illustrates the concept of Williamson's construction of virtual concentrators: a series of virtual V concentrators are coupled to the original concentrator by mirror symmetry, forming a star shape. A ray ***r*** that meets the sidewall of the original V can be prolonged along the virtual V, which lies symmetrically across that sidewall. This virtual ray ($\boldsymbol{r_v}$) will be the mirror image of the actual reflected ray (***r'***). If a second reflection (***r''***) occurs, the argument may be repeated. The virtual ray, prolonged into a third V concentrator, will still represent a faithful image of the physical ray twice reflected (***r''***). This process can continue until either the ray (or the virtual ray) intersects the absorber (or its virtual image) or the ray is diverged (and so is the virtual ray). The arrangement of these V creates the regular polygon showed in figure E.10*b*, described by the apertures of the original and mirror collectors. The polygon can be inscribed into a circle ("reference circle") of ray:

$$r = \frac{a'}{\sin\left(\arctan\left(\frac{a-a'}{L}\right)\right)} = a'\sqrt{\frac{L^2}{(a-a')^2}+1} \qquad \text{(E.21)},$$

where a is the half-width of the entry aperture, a' the half-width of the exit aperture and L the length of the concentrator. The reference circle (Figure E.10*b*) can be used, with a certain approximation, to discriminate the rays that will enter the concentrator or that will be rejected, after a certain number of reflections. The upper part of the circle is described by the curve of equation:

$$y = -l + \sqrt{r^2 - x^2} \qquad \left(\text{where } l = \frac{a'L}{a-a'}\right) \qquad \text{(E.22)}.$$

The geometrical limits of computation for the incidence angles of the rays that hit the left reflector are – arctan [$(a - a') / L$] and $+(\pi/2)$. See Appendix E-5 for a discussion on how the data obtained from the sole left reflector can be transformed to allow for the acceptance from both reflectors. The V collector has two extreme angles: α, below which all rays are accepted and β, above which no rays are accepted. The situation is graphically illustrated in figure E.11, using ray tracing after the first reflection (only the reflected rays are shown). If $\varphi = \alpha$, the ray passing through A is tangent to the virtual circumference. Since no ray with $k > k_A$ hits the reflector, all rays intersect the reference circle and are eventually accepted. In analytical terms this extreme ray is found by intersecting equation E.21 with the beams of lines centered in A ($-a$, L):

$$y = m\,x + (L + am) \qquad \text{(E.23)}.$$

Solving the system and putting the determinant of the equation equal to zero yields:

$$(a^2 - r^2)m^2 + 2a(L+l)m + [(L+l)^2 - r^2] = 0 \qquad \text{(E.24)}.$$

The minor root of equation E.24 (minus sign) produces the slope of the ray passing through A tangent to the circumference (m_α). The major root (plus sign) represents the slope of its reflected ray, which starts from A, and is tangent to the circumference on the other side. α is given by:

$$\alpha = \frac{\pi}{2} - \arctan m_\alpha \qquad \text{(E.25).}$$

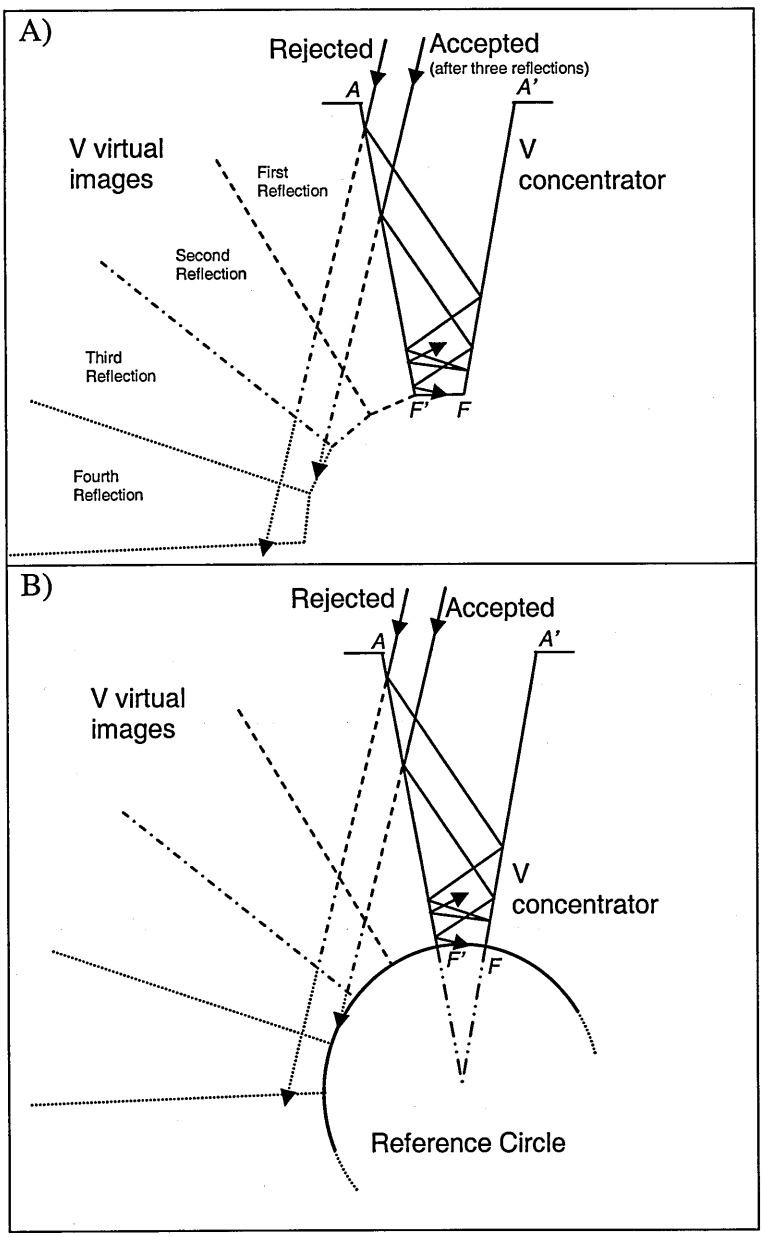


Figure E.10 Williamson contruction for assessing the optical performance of the cone concentrator

For the same argument, at incidence β, the ray passing through A' (a, L) is tangent to the circumference. Since no rays with $k < k_{A'}$ hit the reflector, all rays fall outside the circle and are rejected. Putting into a system equation E.21 with the beam of equation

$$y = m\,x + (L - am) \qquad \text{(E.26),}$$

and setting the determinant equal to zero the resolving equation is found:

$$(a^2 - r^2)m^2 - 2a(L+l)m + [(L+l)^2 - r^2] = 0 \qquad \text{(E.27).}$$

The minor root (minus sign) corresponds to the slope of the sought ray m_β. The other root (plus sign) corresponds to the slope of its reflection. β is equal to:

$$\beta = \frac{\pi}{2} - \arctan m_\beta \qquad \text{(E.28).}$$

The behaviour of the rays after the first reflection for $\varphi = \beta$ is illustrated in figure E.11*c*.

When the acceptance angle is comprised between α and β (figure E.11*b*) the problem of determining the extreme ray for a given incidence angle is reduced to finding the ray of the beam tangent to the circumference of equation E.21. k_{lim}, the intercept of the extreme ray (tangent to the reference circle) at a given incidence angle φ, can be calculated by intersecting the upper circumference with the generic ray of equation:

$$y = \tan\left(\frac{\pi}{2} - \varphi\right)x + k \qquad \text{(E.29),}$$

which one can write as $y = m(\varphi)\, x + k$. The system produces a second degree equation in x whose roots are the abscissas of the intersections. The ray is tangent when the determinant of the intersection equation:

$$(m^2 + 1)r^2 - (k+l)^2 \qquad \text{(E.30)}$$

is equal to zero. Solving in k yields:

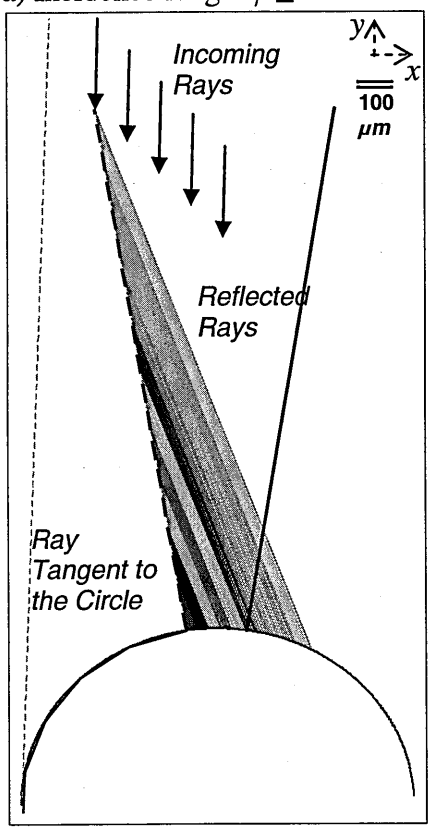
$$k_{\text{lim}} = -l + r\sqrt{m^2 + 1} \qquad \text{(E.31).}$$

Equation E.31 expresses the k_{lim} as a function of the incidence angle. The rays with intercept $k \leq k_{\text{lim}}$ are collected whereas all the others are rejected. The situation is illustrated in figure E.11*b* after the first reflection. The intersection between the line $y = m\,x + k_{\text{lim}}$ (extreme ray) and the line $y = L$ gives the point ($x_{AA'}$, L), which lays on the AA' segment (that is the entry aperture).

$$x_{AA'} = \frac{L - k_{\text{lim}}}{m} \qquad \text{(E.32).}$$

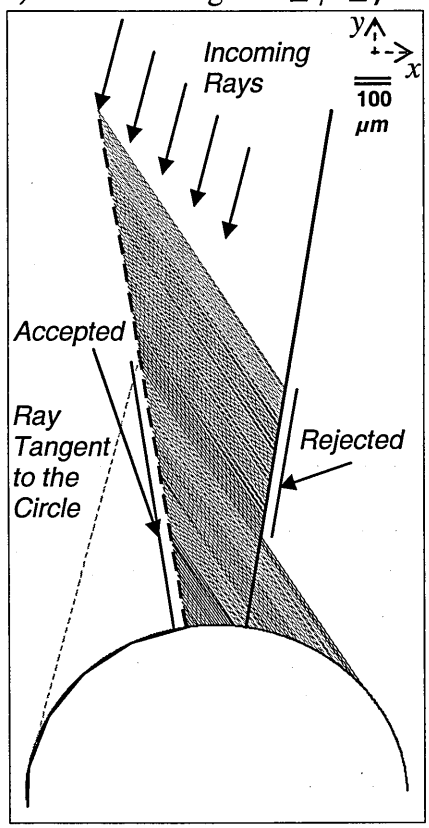
The overall width of accepted beam (along AA') can now be computed as a sum as usual: $w = \Sigma\, a_i$.

a) Incidence Angle $\varphi \leq \alpha$



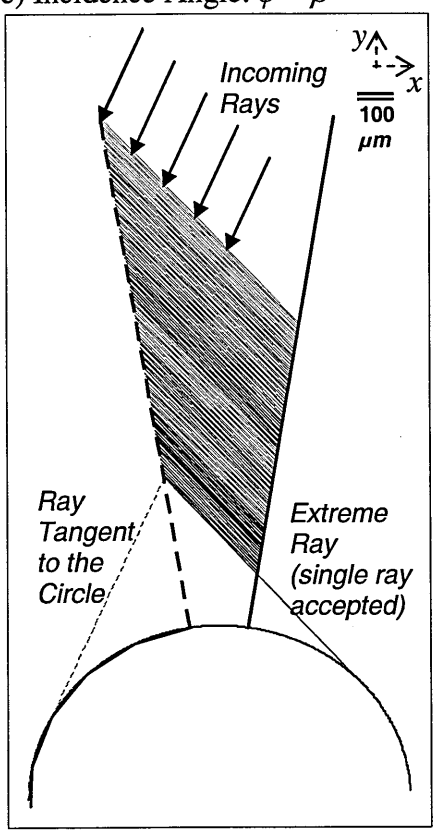
All rays are collected

b) Incidence Angle: $\alpha \leq \varphi \leq \beta$



Part of the rays are collected

c) Incidence Angle: $\varphi = \beta$



All rays are rejected (except the limit ray)

Figure E.11 **Examples of behaviour of the rays after the first reflection in the V concentrator for different incidence angle of incoming rays (φ).**
a) $\varphi < \alpha$,
b) $\alpha < \varphi < \beta$,
c) $\varphi = \beta$.
The primitive rays are not shown.

The construction and method is slightly different for the suspended structure. The way of proceeding is schematised in figure E.12. Instead of building a reference circle, the computation considered the polygon constituted by the exit apertures of the virtual V collectors and, in particular, the active areas. Only the virtual bundles that enter into a virtual active area (grey zones of figure E.12) will eventually cross the entry aperture within the active area.

Given $t = (2a - s)$ and $\gamma = \arctan [(a' - a) / L]$. The generic equation of a ray is:

$$y = \frac{x}{\tan\varphi} + k \qquad \text{(E.33).}$$

And the equations that represent the analytic solutions are expressed in the next table.

Original V conc	**1st reflection**	**nth reflection**	k
$x_V = -a' - s/2$ $y_V = 0$ $x_F = (2a - s)/2$ $y_F = 0$	$x_{V1} = x_V - t\cos 2\gamma$ $y_{V1} = y_V - t\sin 2\gamma$ $x_{F1} = x_V - s\cos 2\gamma$ $y_{F1} = y_V - s\cos 2\gamma$	$x_{Vn} = x_{Vn-1} - t\cos 2n\gamma$ $y_{Vn} = y_{Vn-1} - t\sin 2n\gamma$ $x_{Fn} = x_{Vn-1} - s\cos 2n\gamma$ $y_{Fn} = y_{Vn-1} - s\sin 2n\gamma$	$k_{Fn} = y_{Fn} - \frac{x_{Fn}}{\tan\varphi}$
$x_{F'} = -(2a - s)/2$ $y_{F'} = 0$	$x_{F'1} = x_V - 2a'\cos 2\gamma$ $y_{F'1} = y_V - 2a'\sin 2\gamma$	$x_{F'n} = x_{Vn-1} - 2a'\cos 2n\gamma$ $y_{F'n} = y_{Vn-1} - 2a'\sin 2n\gamma$	$k_{F'n} = y_{F'n} - \frac{x_{F'n}}{\tan\varphi}$

Finally from the intersections between the extreme rays and the entry aperture AA' one can find the various a_i relative to various number of reflections. Finally, the contributions from the right reflector and the direct rays are added, according to the usual sum $w = \Sigma\, a_i$.

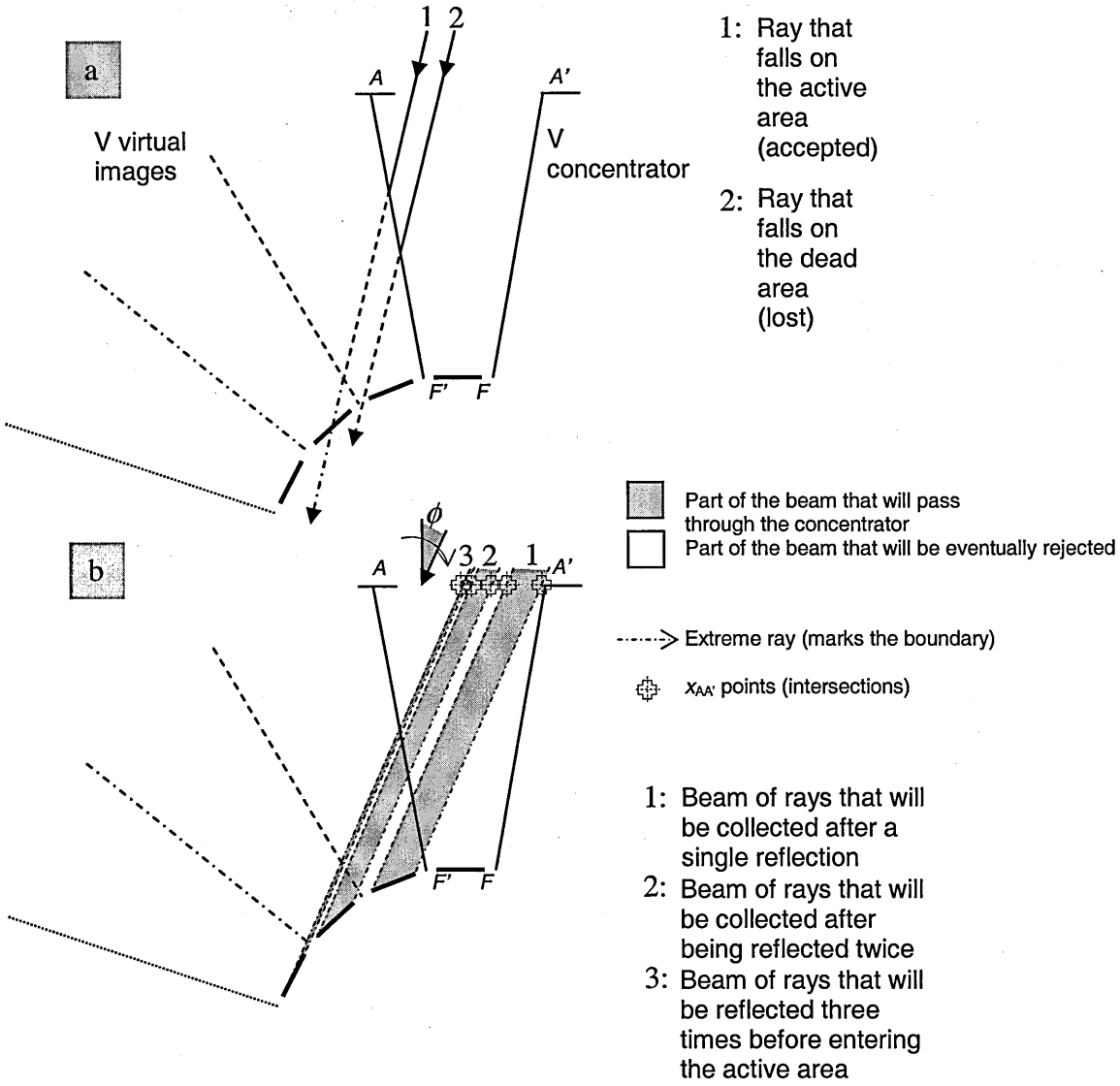


Figure E.12 Williamson construction applied to the enlarged V concentrator with a suspended active area. The accepted parts of the beam for a given incidence angle φ are indicated.

APPENDIX F

Physical modelling of the contrast curves for predicting the 3 – d contours developed in grey scale photolithography

In the main text (section 6.1.1) it was stressed how the ramps profiles may represent, upon manipulation, effective contrast curves of the kind used for DRM [*Fahey, 1996; Arthur et al., 1998; Thornton and Mack, 1996*]. In this appendix the measured profile data are manipulated in order to produce data reporting photoresist remaining thickness Vs dose. These can be considered as experimental contrast curves [*Fahey, 1996; Arthur et al., 1998; Thornton and Mack, 1996*]. The measurement of contrast curves under different process conditions (e.g. development time) is the first step for modelling the photolithographic behaviour of a photoresist material [*Fahey, 1996; Arthur et al., 1998*] Furthermore, this manipulation allows the representation of all the profiles in a single plot, since these become unbound from the width of the single ramp.

It must be said that the mask aligner used has an internal radiometer for assessing the lamp radiance intensity. It is known that these instruments often induce a large error on the absolute values of dose [*Thornton and Mack, 1996*]. However, once the process is set up, many procedures exist for optimising the settings on an actual photolithography system [*Fahey, 1996; Arthur et al., 1998; Thornton and Mack, 1996*]. In the following, a nominal intensity I_{lamp} of 10 $mJs^{-1}cm^{-2}$ is attributed to the lamp. Plots of H Vs Dose (contrast curves) obtained transforming the ramps profiles are reported in figures F.1, F.2 and F.3 (note the change in the x scale). Each ramp contains a hundred grey levels (see appendix A) and there are four ramps per sets. When all four sets are measured, each sample produces 1600 couples of values H Vs dose. However, in this case not all sets were characterised for all the samples. Finally, when the profile is assessed by profilometry, the number of points for each curve can go up to 8000, depending on the resolution of the scan. The results for thick photoresist (AZ4562) seem to show complex behaviour not predicted by the simple assumptions of Dill's model. In particular, curves from samples that have been developed for the same time should overlap, since the inhibitor distribution within the layer is expected to depend only on the overall dose [Dill et al., 1975; *Fahey, 1996*]. In fact, they do not overlap for AZ4562: in figure F.1 and F.2 the curves relative to samples developed for the same time do not overlap. Even the slope of the curves is different (see inset of figure F.2). One is led to conclude that the process for AZ4562 (thick resist) lacks reproducibility. The process needs to be optimised for an individual set of conditions and the knowledge acquired can hardly be applied to any different process conditions.

On the other side, contrast curves for thin photoresist JSR IX575 (figure F.3) present a certain agreement with the classical model, at least in the linear part of the curves. JSR IX575 could yield a more robust process if it were not leading to a very small usable part of the ramp and large deviations from linearity. Furthermore, it is showed in section 6.1.3 how JSR IX575 masks are too thin to be used for through-the-wafer etching. The most striking feature of the diagram of figure F.3 is the presence of similar steps on almost all the ramps, at approximately the same height. This phenomenon seems to confirm the hypothesis, raised in section 6.1.1, that the nonlinearities in the profiles are due to standing waves or other optical effects intrinsic to the interaction of the radiation with the substrate.

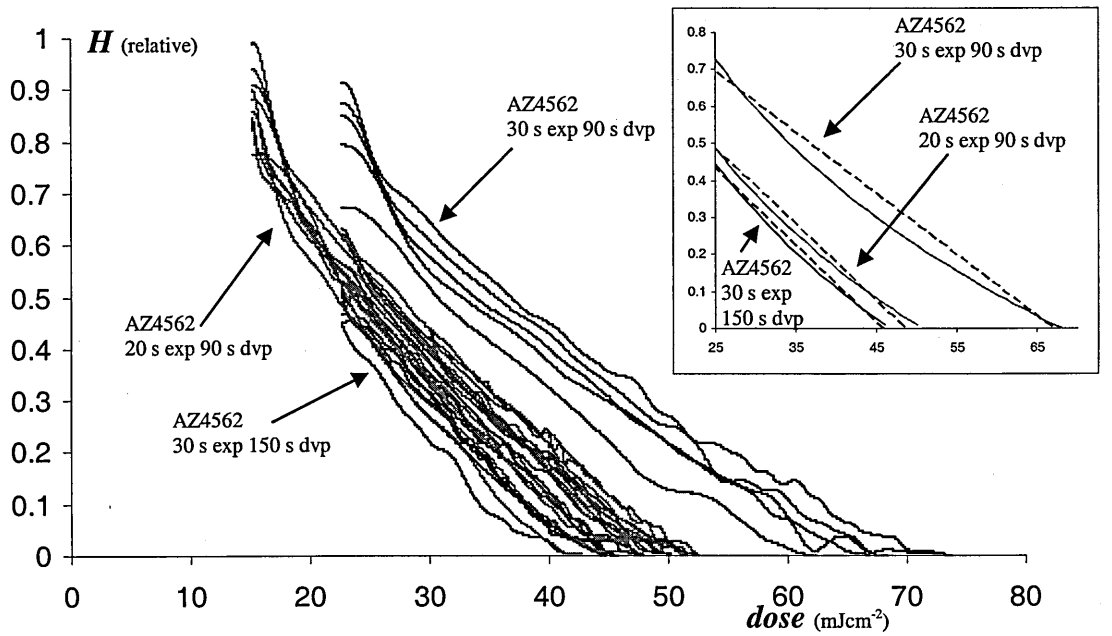


Figure F.1 **Contrast curves for AZ4562 spun at 3000 RPM on bare silicon. Other conditions, relative to the single samples are on the diagram. Inset: overall slope of the contrast curves produced (trend lines).**

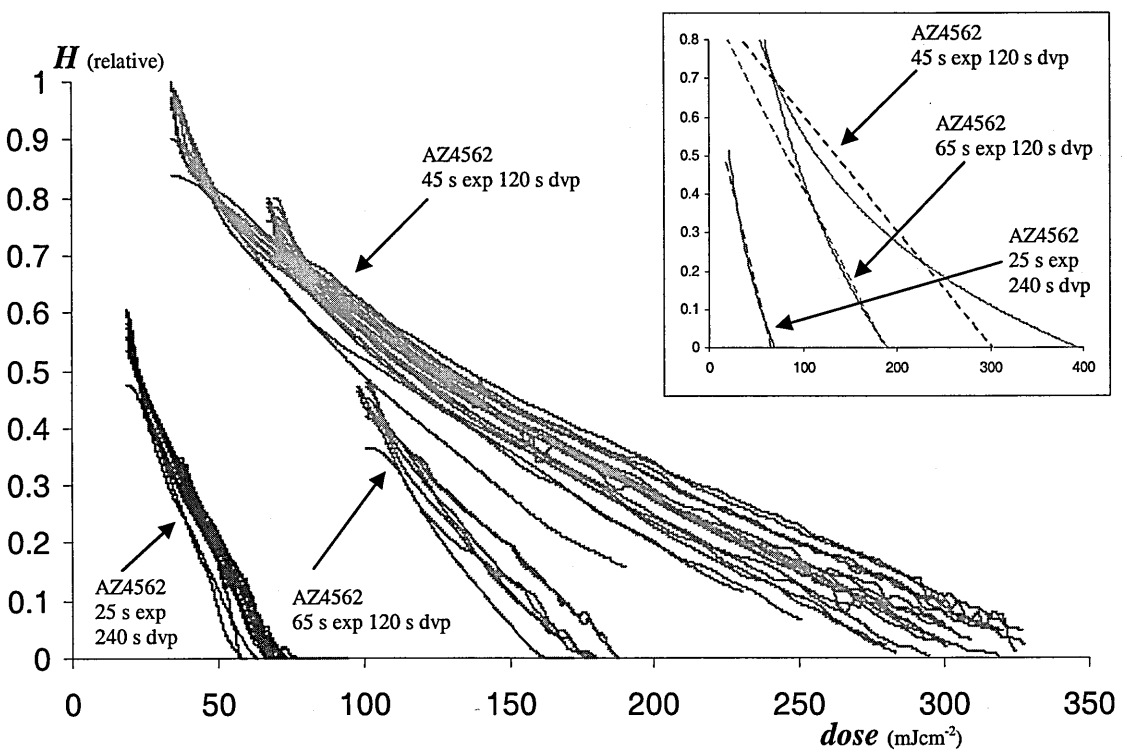


Figure F.2 **Contrast curves for AZ 4562 spun at 2000 RPM on bare silicon. Other conditions, relative to the single samples are on the diagram. Inset: overall slope of the contrast curves produced (trend lines).**

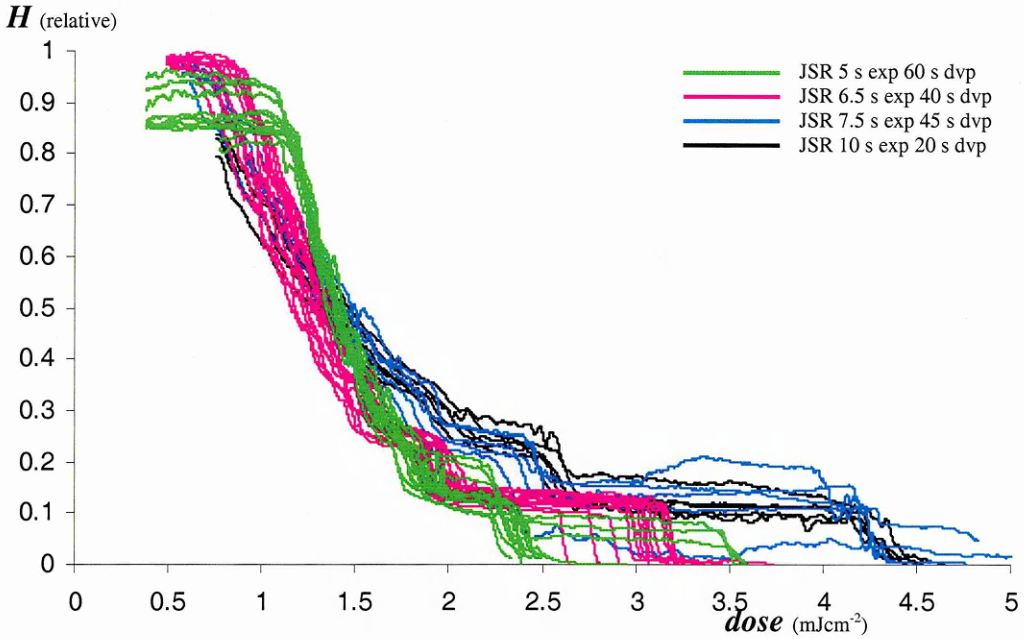
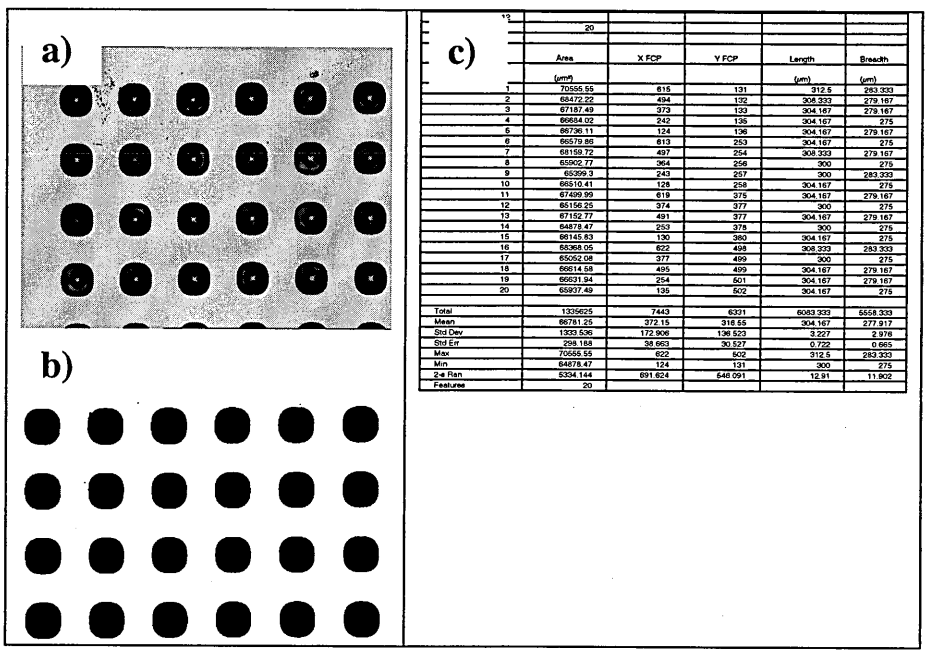


Figure F.3 Contrast curves for JSR IX 575 spun at 2000 RPM on bare silicon. Other conditions, relative to the single samples are in legend.

Next step in a mechanistic approach to process modelling would be to manipulate the *H Vs dose* plots to yield the variation of *R* (etch rate during development) as a function of depth into photoresist *z* (i.e. thickness residual). This further step was beyond the scope of this exploratory research. Furthermore, far more samples would have to be produced to obtain a full set of data for different development rates. Although it was not fully accomplished within the framework of this research, the coupling of the DRM method with the use of an HEBS calibration glass plate presents some very interesting aspect. In particular, it would consent to obtain thousands of data of development rate within a single exposure, thereby eliminating the need of producing tens of samples in the so-called "poor man" DRM method [*Arthur et al., 1998*].

APPENDIX G
Statistical analysis of features dimensions

In order to obtain a sensible estimate of the typical profile of the collectors produced, it was crucial to analyse the variation of the dimensions of the cavities across the wafer area. The statistical analysis was considerably simplified by the use of a software package for image analysis. A picture is taken (figure G.1a) and then digitalized (figure G.1b). At this point, the software can elaborate the picture, counting each black dot as an individual feature. The software is able to provide different pieces of information concerning each feature. The dimensions of the features (which may represent the entry aperture or the exit aperture of the cavities) are collected and computed for each picture. The area of a feature is assessed simply by counting the pixels each feature occupies after calibration. The largest and shortest linear dimensions are computed using the method of the Feret diameters. Finally, the software produces a list with all the information required, which can be directly imported in a worksheet (figure G.1c). The operation is repeated until a full array has been scanned and measured, obtaining a complete statistical sample. Oversized or barely etched cavities (outliers) are handpicked and discarded.



	Area (µm²)	X FCP	Y FCP	Length (µm)	Breadth (µm)
1	70588.55	615	131	312.5	283.333
2	68472.22	494	132	308.333	279.167
3	67187.49	373	133	304.167	279.167
4	66684.02	242	135	304.167	275
5	66736.11	124	136	304.167	279.167
6	66579.86	613	253	304.167	275
7	68159.72	497	254	308.333	279.167
8	65902.77	364	256	300	275
9	65299.3	243	257	300	283.333
10	66510.41	126	258	304.167	275
11	67499.99	619	375	304.167	279.167
12	65156.25	374	377	300	275
13	67152.77	491	377	304.167	279.167
14	64878.47	253	378	300	275
15	66145.83	130	380	304.167	275
16	66368.05	622	498	308.333	283.333
17	65052.08	377	499	300	275
18	66614.58	495	499	304.167	279.167
19	66631.94	254	501	304.167	279.167
20	65937.49	135	502	304.167	275
Total	1336625	7443	6331	6083.333	5558.333
Mean	66781.25	372.15	316.55	304.167	277.917
Std Dev	1333.536	172.906	136.523	3.227	2.978
Std Err	298.188	38.663	30.527	0.722	0.665
Max	70588.55	622	502	312.5	283.333
Min	64878.47	124	131	300	275
2-σ Ran	5334.144	691.624	546.091	12.91	11.902
Features	20				

Figure G.1 Statistical analysis: a) Optical picture, b) Digitalisation and c) Computation of the grey level: features dimensions

It is clear from the example of figure G.1 that, given the four fold symmetry developed by most membranes, the shortest cord represents the "side" of the squared figure, whereas the longest one represents the "diagonal". For the reasons adduced in the text, the shortest measure, i.e. the "side" is considered. Histograms of this measure, relative to the membranes of samples "Device 6" and "Device O2" are reported in figures G.3 and G.4 (the key to the diagrams is in figure G.2). For clarity of display it was necessary to report all the arrays within the same wafer along the same x scale. For these reasons the extremes of the histograms have been cut out for some arrays.

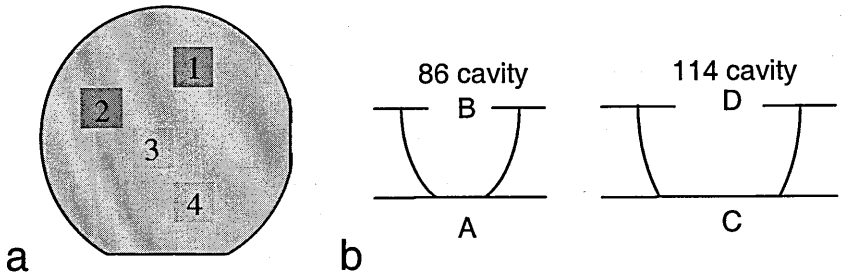


Figure G.2: **Key to the histograms of figures G.3 and G.4. a: position of the array relative to each series (the squares indicate the generic position and not the single array), b: indication of the side of the wafer & type of cavity that was measured**

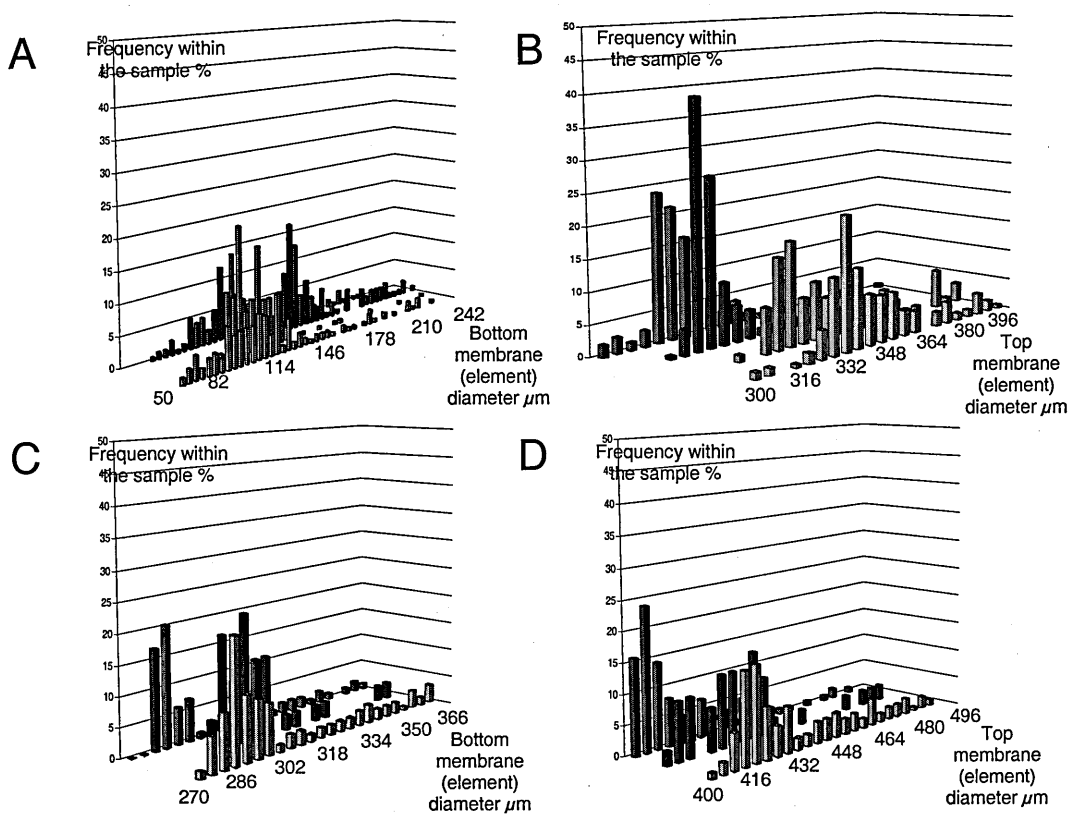


Figure G.3: **Histograms representing the variation in the "breadth" of the membranes across the sample "Device 6" (etched for 210 minutes in pure SF6). Diagrams A and B are relative to cavities with original diameter equal to 86 microns. Diagrams C and D are relative to cavities with mask apertures 114 microns in diameter. Other information in figure G.2.**

A close observation of the histograms reveals that the standard deviations concerning the back membranes are generally of the same order of magnitude of the standard deviations of the front membranes. Therefore, since the back membranes are generally smaller: they are prone to far larger standard error (relative error). The standard deviation for the bottom membranes of the smaller cavity (original mask aperture: 86 microns) is so high that the presentation of an average value is sometimes meaningless.

The large variation leads sometimes to a factor of three between the smaller and the larger value for the sample Device O2 and of five for the sample Device 6.

Some distributions can be assimilated to a normal Gaussian with two tails. Conversely, a few look strongly skewed, in particular distributions G.3c and G.3d, with the bulk of values at the lowest dimensions and a long tail towards increasing dimensions. Both kinds of distribution could be explained advocating the breakdown of the rims of mask apertures. It is known that both vertical and lateral etch rates increase with the diameter of mask apertures, therefore a partial break down in the rim of the masks during etching means an acceleration in etch rate. If almost all the rims break, it may be that most of them break at a certain extent while fewer break at a lower or higher extent. This would explain a two-tailed Gaussian distribution. Otherwise, if only a few of the rims break, then the frequency will decrease with increasing dimensions, inducing a strongly skewed distribution. Since both findings occurred, it is difficult to say which phenomenon tends to dominate.

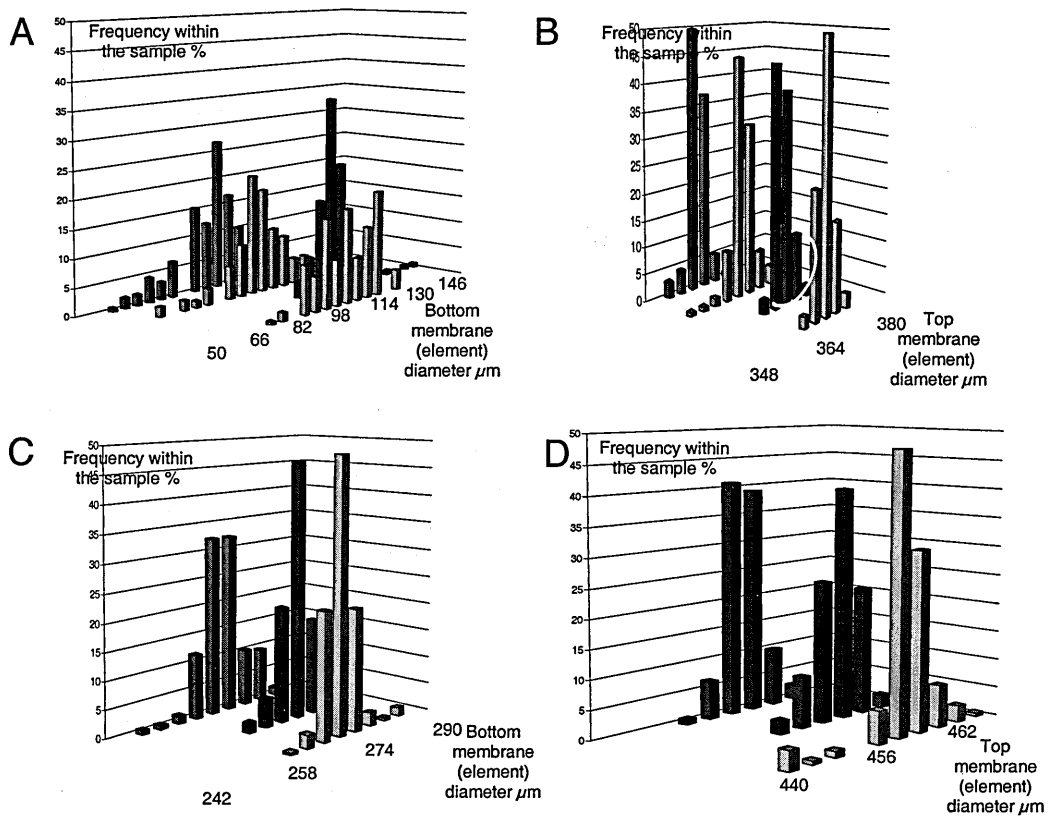


Figure G.4: Histograms representing the variation in the "breadth" of the membranes across the sample "Device O2" (etched for 180 minutes in SF6/O2mixture). Diagrams A and B are relative to cavities with original diameter equal to 86 microns. Diagrams C and D are relative to cavities with mask apertures 114 microns in diameter. Other information in figure G.2.

Finally, the sample Device O2 shows a far lower variance for all the types of membranes. This phenomenon could be simply caused by chance.

The analysis of variance (not reported here) showed that there is evidence of a difference in etch rate average between most of the arrays within each individual sample (effects due to the position of the array on wafer surface). Nevertheless the data relative to each kind of feature have been averaged for each sample in order to produce the values reported in the main text.

Histograms relative to the membranes of samples "PZT DEVICE 4", "PZT DEVICE 5" and "PZT DEVICE 6"are reported in figures G.6 to G.8 (the key to the diagrams is in figure G.5). The histograms for a sample etched to produce the top wafer (ample "TOP WAFER") are reported in figure G.9.

Most distributions can be assimilated to a normal Gaussian with two tails, in particular the ones reporting the dimensions of the top apertures (see discussion above). Notice, however, that most histograms of figures G.7A and G.8A show a long tail at lower dimensions.

Again in most cases the standard deviation (relatively to the average) is larger for the bottom aperture than the top aperture.

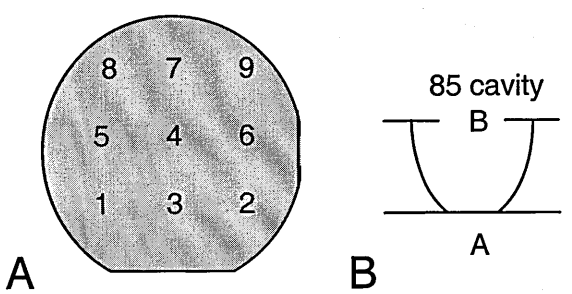


Figure G.5: Key to the histograms of figures G.6 to G.9. A: position of the array relative to each series, B: indication of the side of the wafer and type of cavity that was measured

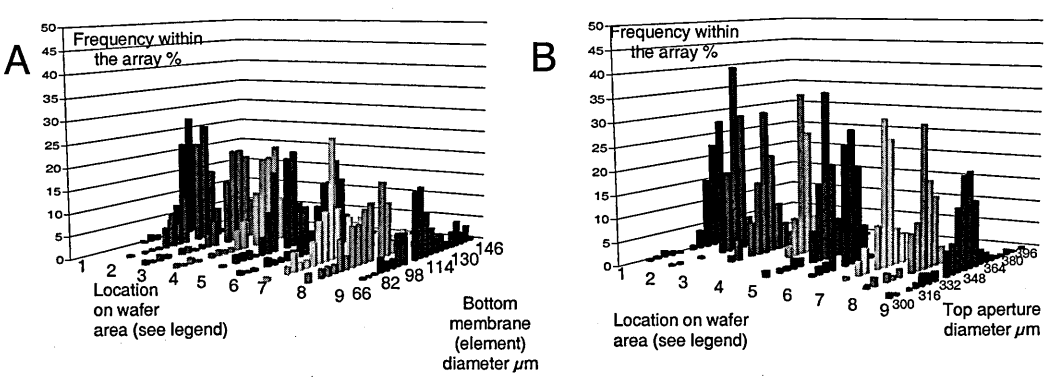


Figure G.6: Histograms representing the variation in the "breadth" of the membranes across the sample "PZT DEVICE 4" (etched for 280 minutes in pure SF6).

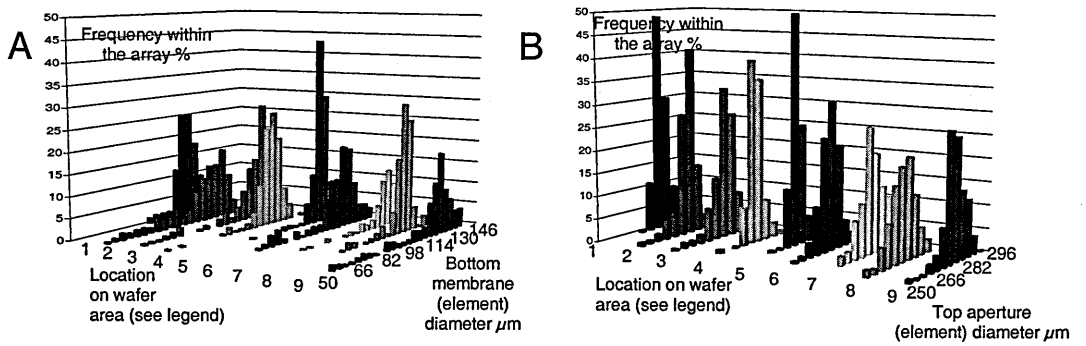


Figure G.7: Histograms representing the variation in the "breadth" of the membranes across the sample "PZT device 5" (etched for 210 minutes in pure SF6).

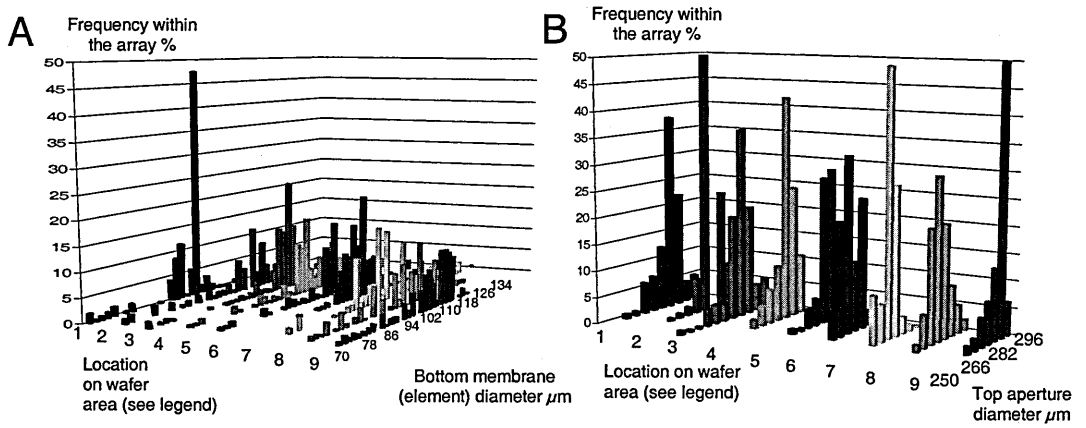


Figure G.8: Histograms representing the variation in the "breadth" of the membranes across the sample "PZT device 6" (etched for 240 minutes in pure SF6).

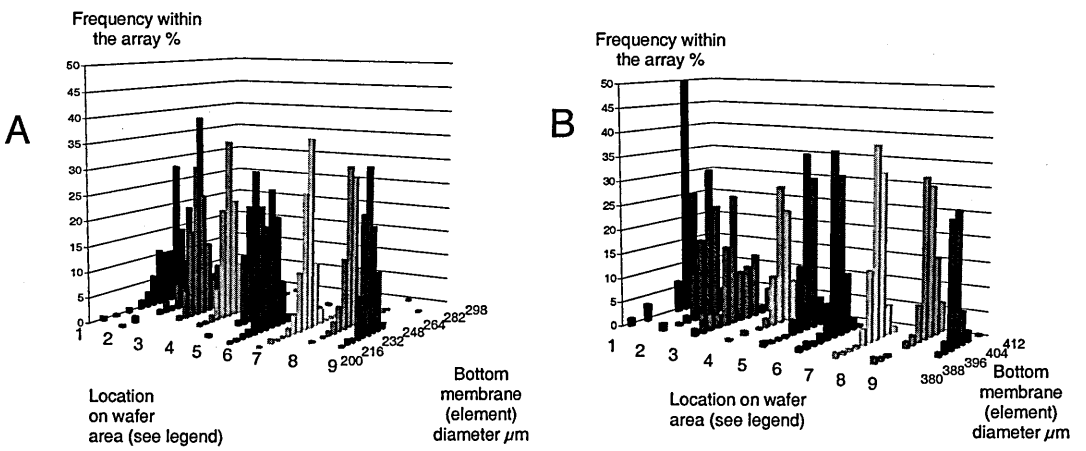


Figure G.9: Histograms representing the variation in the "breadth" of the membranes across the sample produced to top the device-containing wafer (etched for 240 minutes in pure SF6).

APPENDIX H

Analytical treatment & ray tracing for the two-stage elliptical collector

In section 5.3 of the main text it was demonstrated how the overall beam of accepted rays can be divided into bundles of rays and the respective rejection or acceptance of these bundles can be computed separately. It was also demonstrated that in a 2 – d ideal concentrator the bundles are either completely accepted or completely rejected. Under these assumptions, a finite number of rays mark the boundaries between these regions. Finally, it was demonstrated how, thanks to the mirror symmetry of the 2 – d concentrator design, the computation can be accomplished on a single reflector and the results can be arranged to yield the overall transmission of the entire collector. The overall width of the accepted beam is given by the sum of the accepted parts. In this appendix the overall ray-tracing treatment is applied to the 2 – d concentrator obtained by coupling two elliptical cavities. The dimensions of the two-stage collector analysed here reflect the actual average dimensions obtained from the statistical analysis. Although the actual profile of the cavities produced is not perfectly elliptical, the profiles analysed here can be considered akin to experimental results.

Initially, it is convenient to assess the acceptance of the direct rays (i.e. the radiation that passes through the concentrator without hitting the reflectors) separately, since this can be calculated analytically. Expressions for the acceptance as a function of incidence angle were reported in section 5.4. Those expressions were deemed valid for any concentrator contour in absence of convexities, i.e. of centres of scattering. In this particular case, the expressions have to be slightly changed in order to be used. In fact, the profile does contain a convexity, in that the bottom rim of the upper cavity (point A''') lies above the line between the bottom rim of the bottom cavity (point A') and the top rim of the upper cavity (point A''). The direct rays are therefore partially shadowed, as showed in figure H.1. Figure H.1 reports the main angles involved in the computation. Following the indications and the notation reported in the figure, the acceptance of the direct rays can be obtained from considerations of elementary plane geometry:

$$a_{direct} = \begin{cases} 2\,a' & \text{if } 0 < \varphi \leq \arctan\left[(a''' - a') / L1 \right], \\ [a' + a''' - L1 \tan\varphi] & \text{if } \arctan\left[(a''' - a') / L1 \right] < \varphi \leq \arctan\left[(a'' - a''') / L2 \right], \\ [a'' + a' - L \tan\varphi] & \text{if } \arctan\left[(a'' - a''') / L2 \right] < \varphi \leq \arctan\left[(a + a'') / (L1 + L2) \right], \\ 0 & \text{if } \varphi > \arctan\left[(a + a'') / L1 + L2) \right] \end{cases} \quad \text{(H.1).}$$

Notice, that expression H.1 does not represent a simple change in notation, but an actual difference in the transmission of the direct rays, due to the partial shadowing of the beam by the lower rim of the upper cavity.

The suspended version of the elliptical collector is schematically showed in figure G.2. The angles used for the computation are indicated. It can be observed how, this time, the bottom rim of the top cavity (point *A'''*) lies *below* the line connecting the top rim of the top cavity (point *A''*) with the rim of the suspended area (or segment in two dimensions, with extremes *S* and *S'*). Although in the suspended version of the collector the shadowing effect does not impinge on the direct beam, its acceptance cannot be given by the standard equation for direct rays. In fact, since the way of achieving an inner active area is different, a different notation has to be used. In the design, schematised in figure H.2, there is no enlargement of the structure (such as that depicted in figure 5.1) but rather a simple elimination of the outer part of the exit aperture in order to make the design compatible with the actual microfabrication route. The eliminated part is indicated by *s*, in analogy with figure 5.1. The expression for the acceptance segment relative to the direct rays is reported in equation H.2. Notice that the principle does not change (the phenomenology is the same): only the notation is changed in order to make the treatment homogeneous with the notation of chapter 5.

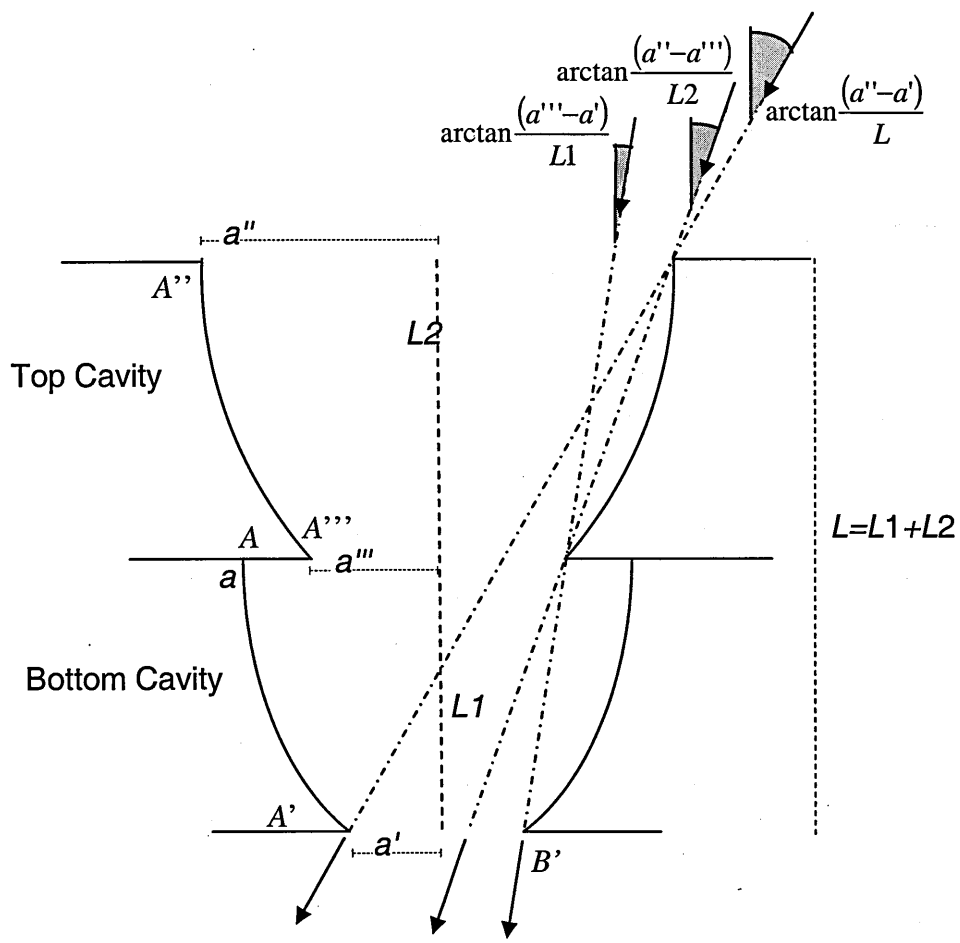


Figure H.1: **Schematic of the profile of a concentrator obtained by coupling two elliptical cavities, reporting the angles used for the computation of the direct rays.**

$$a_{direct} = \begin{cases} 2\,a' - 2\,s & \text{if } 0 < \varphi \leq \arctan\left[\,(a'' - a' + s)\,/\,(L1 + L2)\,\right], \\ [a'' + a' - s - L\tan\varphi] & \text{if } \arctan\left[(a'' - a' + s)\,/\,(L1 + L2)\right] < \varphi \\ & \qquad \varphi \leq \arctan\left[(a'' + a' - s)\,/\,(L1 + L2)\right], \\ 0 & \text{if } \varphi > \arctan\left[(a'' + a' - s)\,/\,(L1 + L2)\right] \end{cases} \quad \text{(H.2).}$$

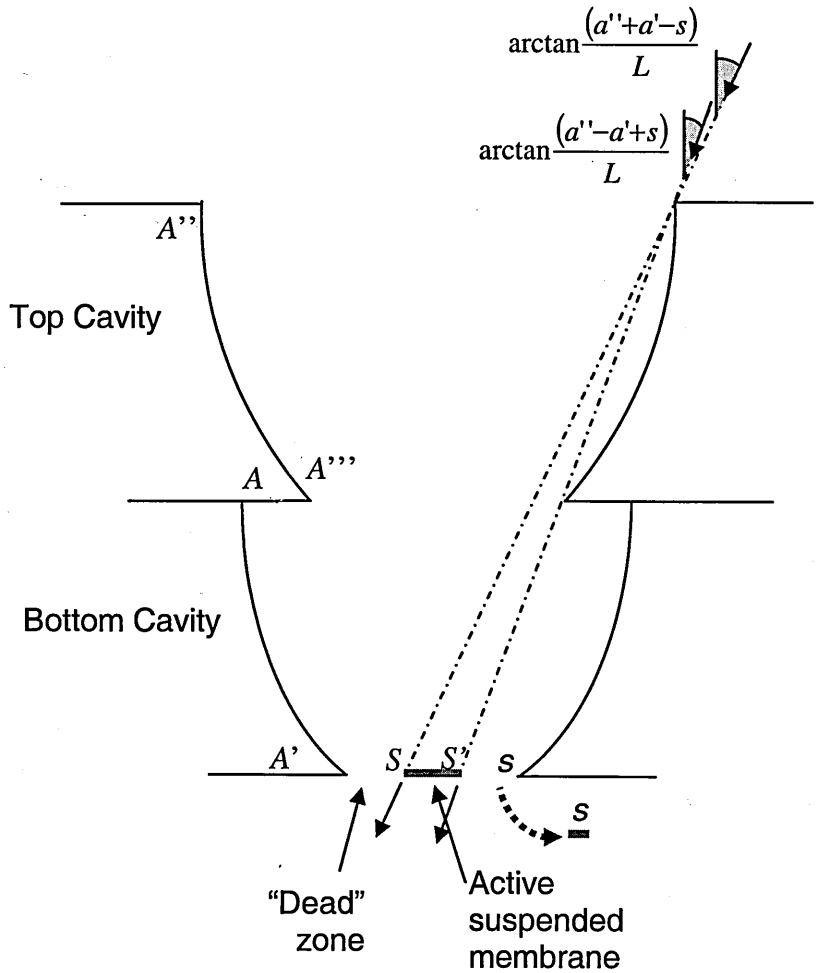


Figure H.2: **Schematic of the profile of a concentrator obtained by coupling two elliptical cavities, reporting the procedure of suspension of the inner active area and the relative angles used for the computation of the direct rays.**

Concerning the reflected rays, an analytical solution was not attempted. On the contrary, the $k_{lim}(\varphi)$ were evaluated using straightforward iterative ray tracing. The intercepts relative to the rays which mark the boundaries between the accepted bundles and the rejected bundles were found in the following way. A beam of parallel rays of equation:

$$y = \frac{y}{\tan\varphi} + k \qquad \text{(H.3)}$$

was shot against the left reflector, which is analytically described by:

$$y = L1 - l1\sqrt{1-\frac{x^2}{a^2}} \qquad \text{for } x < -a' \text{ and } y \le L1 \qquad \text{(H.4}a\text{)}$$

and

$$y = L - l2\sqrt{1-\frac{x^2}{a''^2}} \qquad \text{for } x < -a''' \text{ and } L1 \le y \le L. \qquad \text{(H.4}b\text{).}$$

$l1$ and $l2$ represent the vertical semi-axes of the respective ellipses which generate the bottom and top elliptical collectors. In the iteration (produced using an Excel worksheet) the angle is upgraded from $\{-\arctan[\,(a'' - a') / L\,]\}$ to $\pi / 2$ (or until there are reflections falling inside the exit aperture). For each value of φ, 1000 parallel rays are shot with values of k (intercept) in the range

$$[(L + a'') / \tan\varphi] \le k \le [(a') / \tan\varphi] \qquad \text{(H.5)},$$

i.e. between the ray passing through A'' and the ray passing through A' (the extremes of the left reflector). The reflected ray is calculated, for each ray shot following the algorithm of Appendix E-4. The normal to the reflector is calculated at each of the 1000 points of intersection and the 1000 reflected rays thus computed. Once the reflected rays are shot, the extreme rays can be identified by calculating for each angle the following primitive rays.

1) The primitive ray whose reflection passes through the point A''' ($-a'''$;$L1$) or at nearest. This ray is indicated in figures H.3 and H.4 by a triangle. Called $k_{A'''}$ the intercept of his ray, all rays with $k > k_{A'''}$ for $\varphi > 0$ (or $k < k_{A'''}$ for $\varphi < 0$) produce reflections that hit the top left reflector a second time. It was assumed that these rays do not reach the bottom reflector or the exit aperture. This addresses the shadowing of the reflected rays (in analogy with the shadowing of direct rays, as it was addressed by expression H.1).
2) The primitive rays whose reflections cross the entry aperture at the point $B'(a';0)$. There may be two rays of this kind, one hitting the top left reflector ($k_{B'}{}^{top}$ indicated by a black square in figures H.3 and H.4) and one hitting the bottom left reflector ($k_{B'}{}^{bottom}$ indicated by a grey square in figures H.3 and H.4).
3) the primitive ray which crosses the top reflector in A'''. This ray represents the last ray to hit the top left reflector and it is indicated by a circle in figures H.3 and H.4. Called $k_{A'''}{}^{P}$ its intercept, all rays with $k < k_{A'''}{}^{P}$ for $\varphi > 0$ (or $k > k_{A'''}{}^{P}$ for $\varphi < 0$) hit the bottom left reflector.

Since the reflections that hit the bottom left reflector a second time are assumed to finally enter the entry aperture, all rays for which $k_{B'}{}^{bottom} \le k < k_{A'''}{}^{P}$ for $\varphi > 0$ ($k_{B'}{}^{bottom} \ge k > k_{A'''}{}^{P}$ for $\varphi < 0$) produce reflection that pass (eventually) through the exit aperture. Conversely, all rays with $k_{A'''}{}^{P} < k < k_{B'}{}^{top}$ for $\varphi > 0$ ($k_{A'''}{}^{P} > k > k_{B'}{}^{top}$ for $\varphi < 0$) or $k < k_{B'}{}^{bottom}$ for $\varphi > 0$ ($k > k_{B'}{}^{bottom}$ for $\varphi < 0$) produce reflections that do not cross the entry aperture but hit the right reflector instead. It was then calculated (and therefore assumed) that all these reflections diverge and all these rays are eventually rejected by the concentrator.

A similar treatment may be applied to assess the acceptance of the suspended elliptical concentrator. Also in this case $k_{A'''}$ has to be used in order to address the shadowing (albeit there is no shadowing of direct rays). The other extreme rays, in this case, produce reflections which cross the exit aperture at S and S' (i.e. the extreme of the active inner segment). Since each part of the left reflector (top and bottom) has its own k_S and $k_{S'}$, for a given φ there are up to four extreme rays.

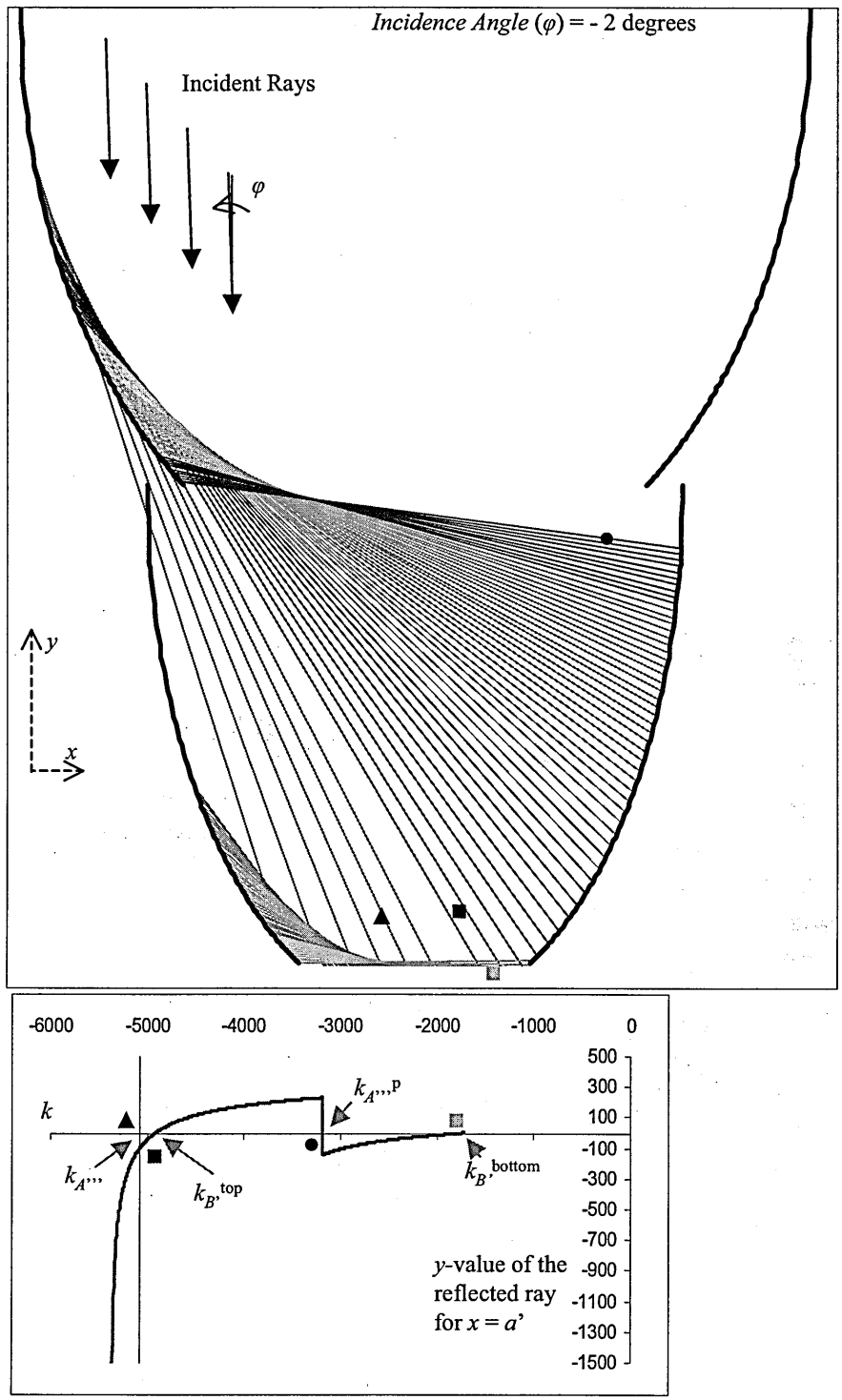


Figure H.3 ***TOP*** **- Graphical example of ray tracing from the left reflector of an enlarged 2 – d CPC for φ = - 2 degrees. The extreme rays (or its nearest rays) are indicated by triangles.** ***BOTTOM*** **- The distance from *B'* (along the y axis, i.e. $y(x_{B'})$) for the reflected rays as a function of the intercept of the respective primitive rays. The incidence angle is the same as for figure *A*. The intercepts of the extreme rays are indicated by arrows. All the parameters of the simulation are indicated in the diagram, for other comments see text.**

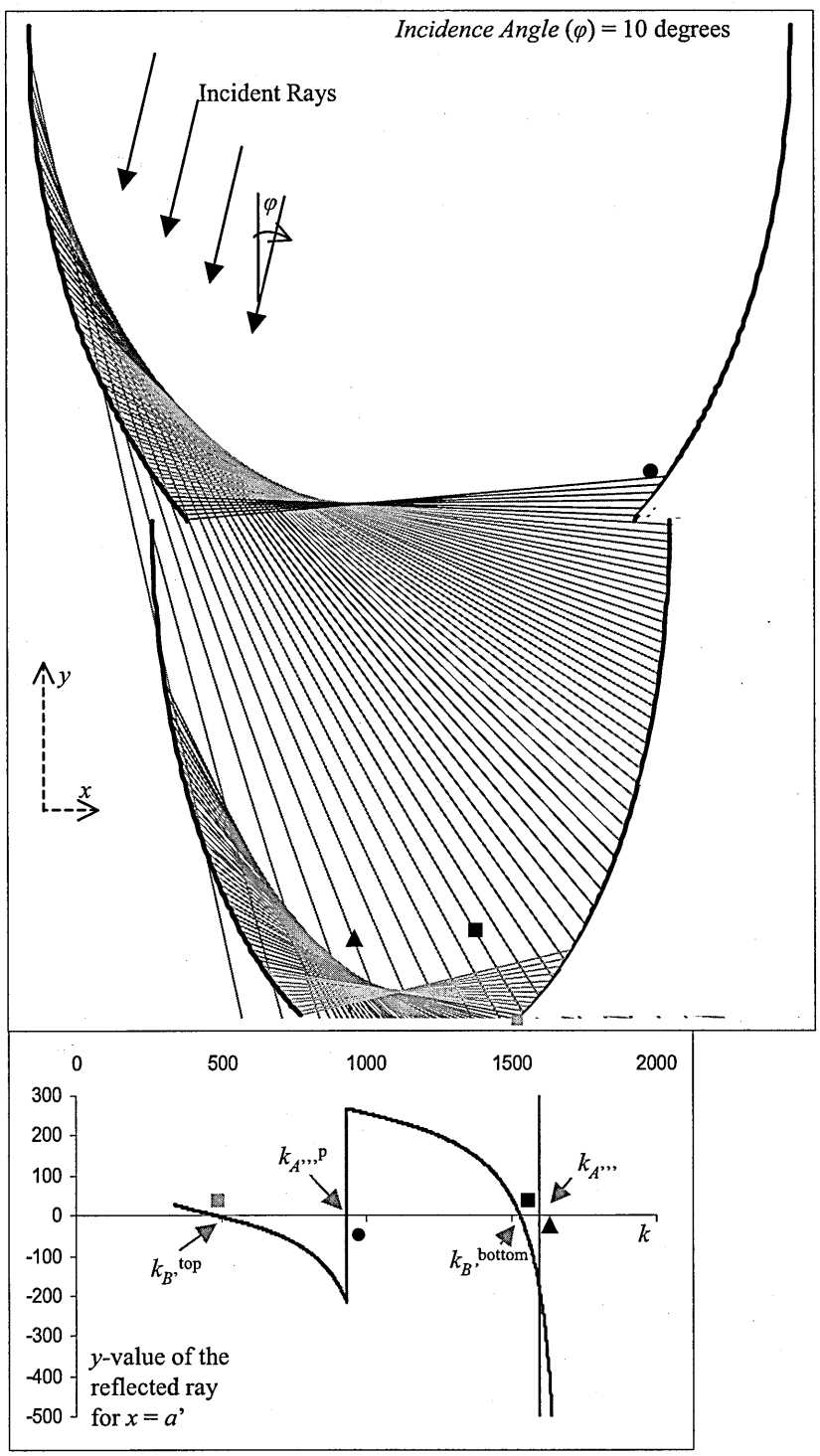


Figure H.4 ***TOP*** **- Graphical example of ray tracing from the left reflector of an enlarged 2 – d CPC for φ = 11 degrees. The extreme rays (or its nearest rays) are indicated by triangles.** ***BOTTOM*** **- The distance from *B'* (along the y axis, i.e. $y(x_{B'})$) for the reflected rays as a function of the intercept of the respective primitive rays. The incidence angle is the same as for figure *A*. The intercepts of the extreme rays are indicated by red arrows. All the parameters of the simulation are indicated in the diagram, for other comments see text.**

APPENDIX I

Analytical treatment of the effect of the introduction of micro-collimators on the collection efficiency of elliptical 2 – d collectors

The analytical calculation of the effect of collimation is reported in this appendix. The calculation is accomplished in 2 – d to be homogeneous with the theoretical treatment of the collectors. The generic expression for the overall power that passes through a 2 – d collimator is given by:

$$P = 4c \int_0^{\min(\theta,\omega)} B\, T_C \cos\varphi \, d\varphi \qquad \text{I.1}$$

The notation "min(θ, ω) indicates that one has always to use the smaller angle between the acceptance angle of the collimator or the cut-off angle of the distribution. The acceptance angle is given by:

$$\theta = \arctan\left(\frac{2c}{L_C}\right) \qquad \text{I.2.}$$

If the collimator is assumed to be a perfect cylinder with straight sidewalls that do not reflect any radiation, the expression for T_C is given by:

$$T_C = \begin{cases} \dfrac{2c - L_C \tan\varphi}{2c} & \text{if } 0 < \varphi \le \theta \\ 0 & \text{if } \varphi > \theta \end{cases} \qquad \text{I.3}$$

In the following, the ratio is calculated between the power that crosses a collimator of width equal to 410 μm (c_{410} = 205 μm) and the power transmitted by a collimator of width equal to 125 μm (c_{125} = 62.5 μm). The power for the generic collimator can be calculated substituting equation I.3 in equation I.1:

$$P = 4c \int_0^{\min(\theta,\omega)} B \, \frac{2c - L_C \tan\varphi}{2c} \cos\varphi \, d\varphi \qquad \text{I.4.}$$

B can be taken outside the integration sign (since it is considered to be uniform with φ) and tan φ is equal to the ratio between the sine and cosine, therefore:

$$P = 4cB \left[\int_0^{\min(\theta,\omega)} \cos\varphi \, d\varphi - \int_0^{\min(\theta,\omega)} \frac{L_C \tan\varphi}{2c} \cos\varphi \, d\varphi \right] \qquad \text{I.5.}$$

L_C and c can be taken out so that equation I.5 becomes:

$$P = 4cB \left[\int_0^{\min(\theta,\omega)} \cos\varphi \, d\varphi - \frac{L_C}{2c} \int_0^{\min(\theta,\omega)} \sin\varphi \, d\varphi \right] \qquad \text{I.6.}$$

And, after integration:

$$P = 4cB \sin(\min(\theta,\omega)) + 2BL_C \left[\cos(\min(\theta,\omega)) - 1\right] \qquad \text{I.7.}$$

Notice that the first term of this expression represents the maximum power flux that crosses an aperture of extent 2c. One can now calculate the ratio P_{410}/P_{125}, considering that the two collimators have the same depth.

$$\frac{P_{410}}{P_{125}} = \frac{2c_{410} \sin\omega + L_C(\cos\omega - 1)}{2c_{125} \sin\omega + L_C(\cos\omega - 1)} \qquad \text{if } \omega < \theta_{125} \qquad \text{I.8}a$$

or

$$\frac{P_{410}}{P_{125}} = \frac{2c_{410}\sin\omega + L_C(\cos\omega - 1)}{2c_{125}\sin\theta_{125} + L_C(\cos\theta_{125} - 1)} \qquad \text{if } \theta_{125} \le \omega \le \theta_{410} \qquad \text{I.8}b$$

or, finally,

$$\frac{P_{410}}{P_{125}} = \frac{2c_{410}\sin\theta_{410} + L_C(\cos\theta_{410} - 1)}{2c_{125}\sin\theta_{125} + L_C(\cos\theta_{125} - 1)} \qquad \text{if } \omega > \theta_{410} \qquad \text{I.8}c.$$

Introducing expression I.2, the trigonometric terms disappear, substituted by square roots. However, the substitution of $\sin\theta$ and $\cos\theta$ with their values as a function of c and L_C makes the above expressions more complex, rather than simplifying them.

Equations I.8(*a, b* and *c*) represent the total power crossing the collectors. In case the collectors were ideal (i.e. 2 – d CPCs), then the increase in signal observed after enlarging the collector would correspond to that expressed by equations I.8. In other words, expressions I.8 represent the maximum increase that can be observed after passing to the larger collector. However, the elliptical collectors are far from ideal. It would be quite complex to calculate the actual increase using an elliptical collector. It would also be meaningless, given the large difference expected between the ideal collection and the actual case. Fortunately, there is a simpler way to demonstrate the effect of the collectors. It is easier to calculate the expected increase in absence of any signal from the sidewalls (i.e. collectors with collection efficiency equal to zero).

The contribution from the direct rays can be easily calculated following the outline of section 5.4. The following expressions for the acceptance of direct rays are valid in a case such as that depicted in figure I.1, i.e. when:

$\arctan\frac{(c-a')}{L1+L_C} \le \arctan\frac{(a-a')}{L1}$ and $\arctan\frac{(c+a')}{L1+L_C} \le \arctan\frac{(a+a')}{L1}$ or, in other words

$\delta_{coll} \le \delta_{ell}$ and $\theta_{coll} \le \theta_{ell}$. The transmittance of the direct rays is given by:

$$T_{direct} = \begin{cases} a' / c & \text{if } 0 < \varphi \le \arctan\left[(c - a') / (L1 + L_C) \right], \\ [c + a' - (L1 + L_C)\tan\varphi] / 2c & \text{if } \arctan\left[(c - a') / (L1 + L_C) \right] < \varphi \text{ AND } \varphi \le \arctan\left[(c + a') / (L1 + L_C) \right], \\ 0 & \text{if } \varphi > \arctan\left[(c + a') / (L1 + L_C) \right], \end{cases} \qquad \text{(I.9).}$$

By introducing equation I-9 into I.1 one can now calculate the ratio: P_{410} / P_{125} for full-membrane concentrators when no reflection from the sidewalls is expected. The expression represents the bottom line of increase in power, i.e. there is no contribution at all from the concentrators.

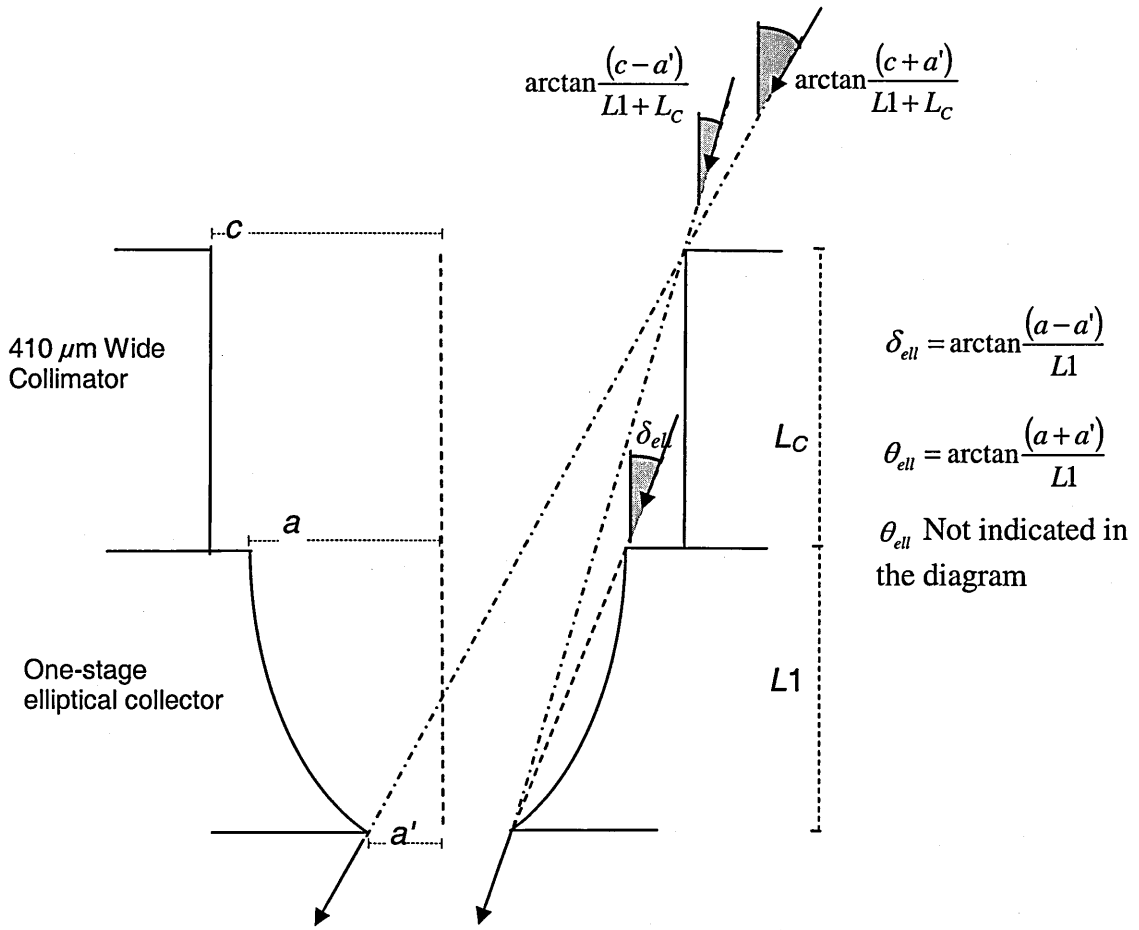


Figure I.1 Schematic of the addition of a micromachined collimator to a single-stage elliptical collector.

The expressions for suspended concentrators, with an inner active area, of the kind reported in Appendix H are slightly different (see figure I.2). Again, if $\delta_{coll} \leq \delta_{ell}^{susp}$ and $\theta_{coll} \leq \theta_{ell}^{susp}$, then:

$$T_{direct} = \begin{cases} (a' - s) / c & \text{if } 0 < \varphi \leq \arctan [\, (c - a' + s) / (L1 + L_C) \,], \\ [c + a' - s - (L1 + L_C) \tan \varphi] / 2c & \text{if } \arctan [\, (c - a' + s) / (L1 + L_C) \,] < \varphi \\ & \qquad \varphi \leq \arctan [\, (c + a' - s) / (L1 + L_C) \,], \\ 0 & \text{if } \varphi > \arctan [\, (c + a' - s) / (L1 + L_C) \,], \end{cases} \quad \text{(I.10).}$$

However, this calculation was not brought to completion, since it was not possible to attain a signal from any suspended systems.

$$\delta_{ell}^{susp} = \arctan\frac{(a - a' + s)}{L1}$$

$$\theta_{ell}^{susp} = \arctan\frac{(a + a' - s)}{L1}$$

δ_{ell}^{susp} Not indicated in the diagram

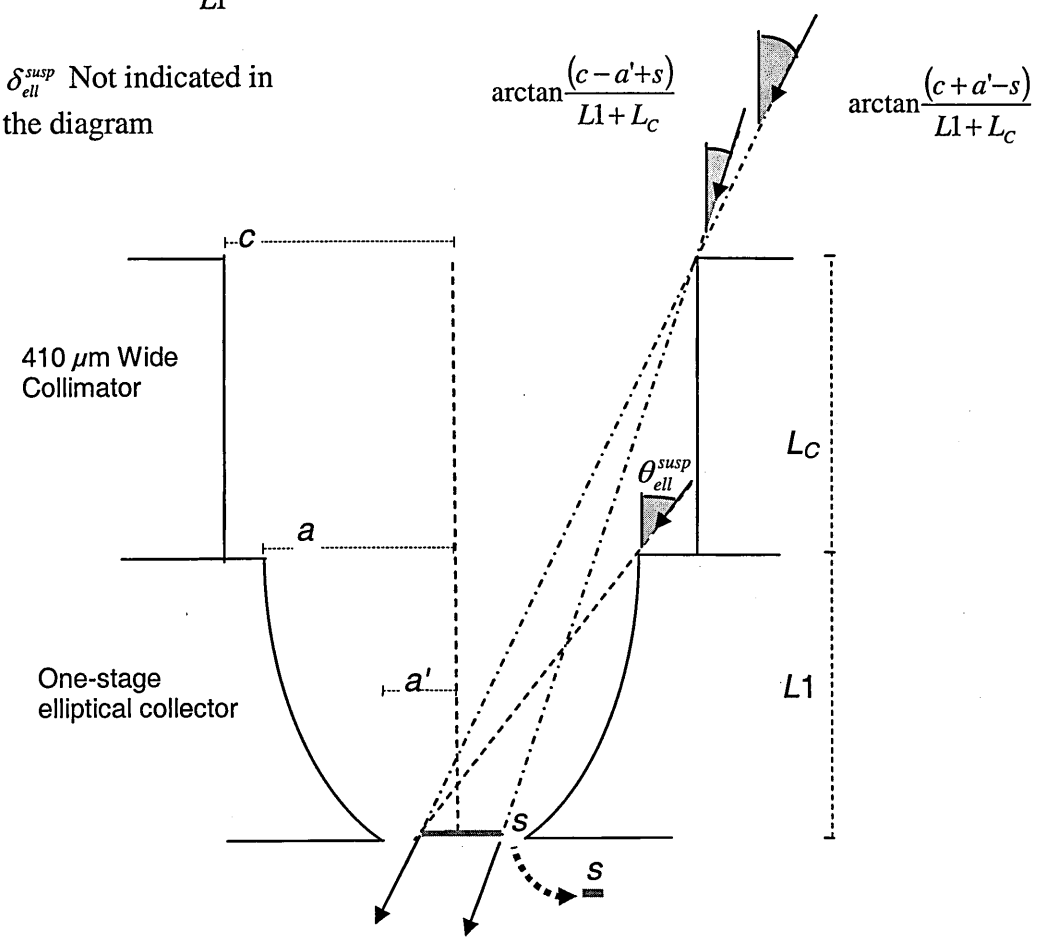


Figure I.2 **Schematic of the addition of a micromachined collimator to a single-stage, suspended, elliptical collector (inner active area).**